ORNL/FEDC-83/1

FED-A
AN ADVANCED PERFORMANCE FED BASED ON LOW SAFETY FACTOR AND CURRENT DRIVE

Y-K. M. PENG
P. H. RUTHERFORD
ET AL.

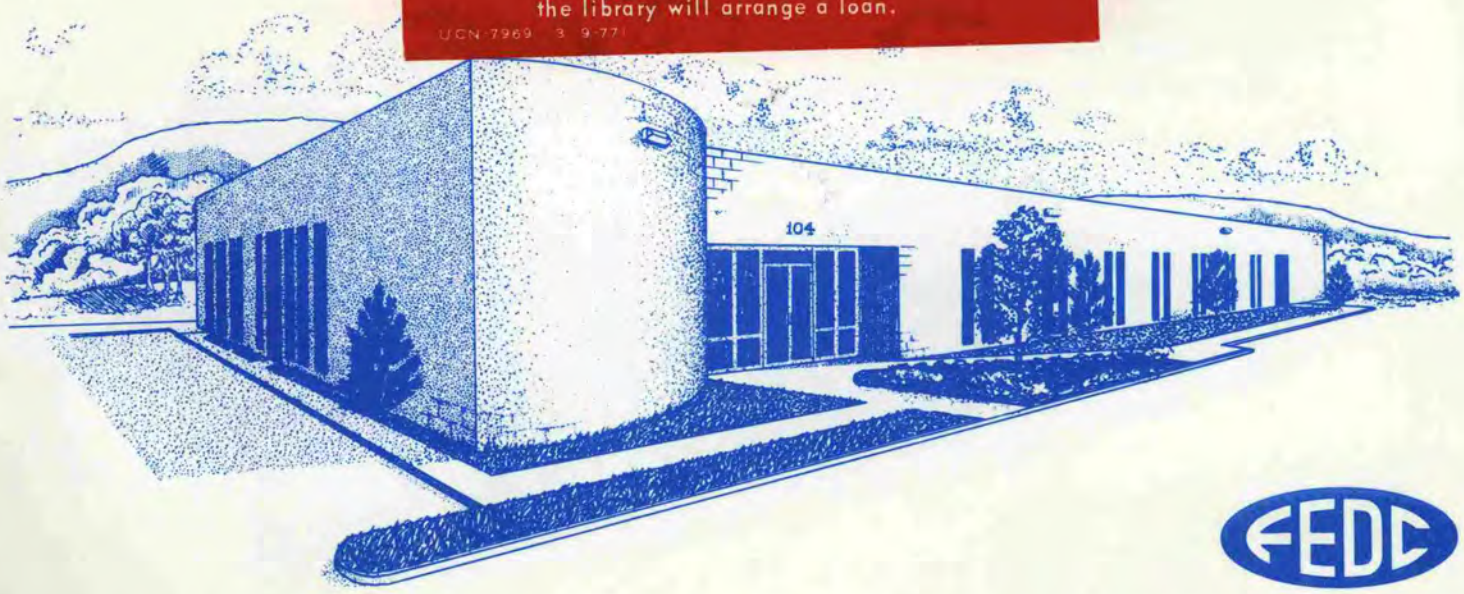

FEDC

FUSION ENGINEERING DESIGN CENTER

Oak Ridge National Laboratory * Oak Ridge, Tennessee

Printed in the United States of America. Available from
National Technical Information Service
U.S. Department of Commerce
5285 Port Royal Road, Springfield, Virginia 22161
NTIS price codes—Printed Copy: A21 Microfiche A01

ORNL/FEDC-83/1
Dist. Category UC-20 c,d

Fusion Engineering Design Center

FED-A, AN ADVANCED PERFORMANCE FED BASED ON LOW SAFETY FACTOR AND CURRENT DRIVE

Y-K. M. Peng
P. H. Rutherford

O. A. Anderson
S. E. Attenberger
R. J. Barrett
S. K. Borowski
T. G. Brown
B. A. Carreras
V. S. Chan
W. S. Cooper
B. A. Cramer
D. Ehst
M. Y. Gohar
D. A. Goldberg
J. R. Haines
L. M. Hively
J. T. Hogan
J. A. Holmes
R. J. Hooper
W. A. Houlberg
B. L. Hunter
H. Iida
S. S. Kalsi
V. D. Lee
C. S. Liu
J. F. Lyon
D. H. Metzler
D. R. Mikkelsen
J. G. Murray
W. D. Nelson
F. W. Perkins
M. Porkolab
R. L. Reid
K. E. Rothe
L. Ruby
C. E. Singer
G. E. Smith
L. Soroka
V. C. Srivastava
L. D. Stewart
D. J. Strickler
E. H. Valeo
F. W. Wiffen
K. F. Wu

Date Published - August 1983

Prepared by the
OAK RIDGE NATIONAL LABORATORY
Oak Ridge, Tennessee 37830
operated by
UNION CARBIDE CORPORATION
for the
U.S. DEPARTMENT OF ENERGY
under Contract No. W-4705-eng-26

CONTENTS

PREFACE

This document is one of four describing studies performed in FY 1982 within the context of the Fusion Engineering Device (FED) Program for the Office of Fusion Energy, U.S. Department of Energy. The documents are:

1. FED Baseline Engineering Studies (ORNL/FEDC-82/2),
2. FED-A, An Advanced Performance FED Based on Low Safety Factor and Current Drive (this document),
3. FED-R, A Fusion Device Utilizing Resistive Magnets (ORNL/FEDC-82/1), and
4. Technology Demonstration Facility — TDF.

These studies extend the FED Baseline concept of FY 1981 and develop innovative and alternative concepts for the FED.

The FED-A study project was carried out as part of the Innovative and Alternative Tokamak FED studies, under the direction of P. H. Rutherford, which were part of the national FED program during FY 1982. The studies were performed jointly by senior scientists in the magnetic fusion community and the staff of the Fusion Engineering Design Center (FEDC). Y-K. M. Peng of the FEDC, on assignment from Oak Ridge National Laboratory, served as the design manager.

LIST OF FIGURES

LIST OF TABLES

LIST OF CONTRIBUTORS

Chapter 1	Y-K. M. Peng (FEDC/ORNL)
Chapter 2	Y-K. M. Peng (FEDC/ORNL) P. H. Rutherford (PPPL)
Chapter 3	P. H. Rutherford (PPPL), Coordinator S. E. Attenberger (ORNL) B. A. Carreras (ORNL) L. M. Hively (FEDC/GE) J. T. Hogan (ORNL) J. A. Holmes (ORNL) W. A. Houlberg (ORNL) J. F. Lyon (ORNL) Y-K. M. Peng (FEDC/ORNL) D. J. Strickler (FEDC/ORNL)
Chapter 4	P. H. Rutherford (PPPL), Coordinator O. A. Anderson (LBL) V. S. Chan (GA) W. S. Cooper (LBL) D. Ehst (ANL) D. A. Goldberg (LBL) C. S. Liu (GA) D. R. Mikkelsen (PPPL) F. W. Perkins (PPPL) M. Porkolab (MIT) L. Ruby (LBL) C. E. Singer (PPPL) L. Soroka (LBL) L. D. Stewart (Exxon/PPPL) E. J. Valeo (PPPL)
Chapter 5	R. L. Reid (FEDC/ORNL), Coordinator K. F. Wu (FEDC/ORNL) K. E. Rothe (FEDC/ORNL) R. J. Barrett (FEDC/B&R)
Chapter 6	G. M. Fuller (FEDC/MDAC), Coordinator S. K. Borowski (FEDC/UM) B. A. Cramer (FEDC/MDAC) M. Y. Gohar (FEDC/ANL) J. R. Haines (FEDC/MDAC) V. D. Lee (FEDC/MDAC) J. G. Murray (FEDC/PPPL) Y-K. M. Peng (FEDC/ORNL) F. W. Wiffen (FEDC/ORNL)

Chapter 7	D. H. Metzler (FEDC/GE), Coordinator J. R. Haines (FEDC/MDAC) H. Iida (JAERI) J. G. Murray (FEDC/PPPL) W. D. Nelson (FEDC/GE) Y-K. M. Peng (FEDC/ORNL) K. E. Rothe (FEDC/ORNL)
Chapter 8	D. J. Strickler (FEDC/ORNL), Coordinator S. S. Kalsi (FEDC/GE) T. G. Brown (FEDC/GAC) R. J. Hooper (FEDC/GE) B. L. Hunter (FEDC/GE) Y-K. M. Peng (FEDC/ORNL) K. E. Rothe (FEDC/ORNL) V. C. Srivastava (FEDC/GE)
Chapter 9	R. L. Reid (FEDC/ORNL), Coordinator G. E. Smith (FEDC/GAC)

ACKNOWLEDGMENTS

We would like to acknowledge the valuable comments by the other members of the Innovative and Alternative Tokamak FED Steering Committee — Dan Cohn, Dan Jassby, Jim Lyon, John Rawls, and John Schmidt — on the initial basic concept of FED-A. The authors also appreciate the encouragement of Tom Shannon, FEDC Manager, and Chuck Flanagan, FEDC Projects Manager.

We wish to acknowledge the dedication, skill, and unflagging cooperation of Kathie Zell, June Jernigan, and Melinda Cofer, who provided the secretarial services essential to preparation of this report. We also wish to thank Paul Fogarty, Bill Kunselman, and Melvin Willey for preparation of many of the drawings and figures.

We express our thanks to the ORNL Fusion Energy Division Reports Office for editing, preparation of the artwork, proofreading, word processing, and final layout of the document. Without their efforts, this report would not have been possible.

This work was supported by the U.S. Department of Energy, Office of Fusion Energy.

ABSTRACT

The FED-A study aims to quantify the potential improvement in cost-effectiveness of the Fusion Engineering Device (FED) by assuming low safety factor q (less then 2 as opposed to about 3) at the plasma edge and noninductive current drive (as opposed to only inductive current drive). The FED-A performance objectives are set to be:

1. ignition assuming International Tokamak Reactor (INTOR) plasma confinement scaling, but still achieving a fusion power amplification $Q \gtrsim 5$ when the confinement is degraded by a factor of 2;

2. neutron wall loading of about 1 MW/m^2, with 0.5 MW/m^2 as a conservative lower bound; and

3. more nearly power-reactor-like operations, such as steady state.

These are equal to or better than the FED Baseline performance objectives. The FED-A study encompasses reviews of our understanding of relevant physics subjects and their projected applications to the FED-A engineering concept, including cost estimates. Major conclusions include the following:

1. With q_ψ(edge) = 1.8 and a cyclic, quasi-steady-state current drive scenario, the near-optimum design is shown to have R = 4.2 m, a = 0.92 m, κ = 1.2, B_{max} = 10 T, and I_p = 4.1 MA, with a full, low voltage OH flux capability and a burn time of about 1000 s. A reduction in the direct total cost of about 30% from the FED Baseline design is estimated.

2. A closely fitted conducting shell with a time constant in the range of 0.5 s should be adequate in avoiding unfavorable growth of the m = 2 kink/tearing mode when q_ψ passes near 2 and in mitigating the impact on the device of a major plasma disruption. An AMAX-MZC copper alloy, continuous, water-cooled first wall with a total thickness of 1.5 cm is shown to provide adequate electrical conductivity, neutron transparency, reactor-relevant heat removal, and mechanical integrity.

3. The lower hybrid wave current drive in a cyclic density operation has the highest physics and engineering merit

in FED-A over other candidate approaches such as fast wave ion cyclotron, electron cyclotron resonance wave, and relativistic electron beams. A relatively simple poloidal field coil configuration is adequate for the quasi-steady-state operation and also significantly reduces the toroidal field intercoil structure.

1. INTRODUCTION

The FED-A study aims to quantify the potential improvement in cost-effectiveness of FED when the aggressive physics assumptions of low safety factor q (less than 2 as opposed to about 3) and noninductive current drive (as opposed to only inductive current drive) are incorporated in the design concept. To quantify these effects, we set ourselves a goal that, without a significant increase in risk of failure, the FED-A performance objectives must be equal to or better than the FED Baseline objectives with a significantly lower cost and, when possible, a closer approximation to the operating conditions of a fusion power reactor.

This study is motivated by the projected cost of the FED Baseline and similar devices such as INTOR. For FED Baseline, the total capital cost is currently estimated to be about $2 billion with a direct cost of about $1 billion in constant 1981 dollars. This cost is largely a reflection of the device size as dictated by the performance objectives of (1) a fusion power amplification $Q \gtrsim 5$, (2) an average neutron wall loading $W_L^N \gtrsim 0.5$ MW/m^2, and (3) a burn pulse of about 100 s with high duty factor ($\sim$65%), together with such physics assumptions as $q_\psi \cong 3.0$ and inductive current drive.

The FED-A study encompasses reviews of the status of our understanding of low q discharges and noninductive current drive processes in tokamaks, their projected applications to FED-A and assessments of the design criteria and requirements (Chaps. 3 and 4), systems trade calculations in the FED-A parameter space to identify a near-optimal design (Chap. 5), assessments of those engineering design features unique to FED-A (Chaps. 6, 7, and 8), and estimates of device cost and schedule (Chap. 9).

2. RATIONALE AND SUMMARY OF CONCLUSIONS

The FED-A performance, which should be better than or equal to the baseline performance, can be characterized as:

1. ignition assuming INTOR plasma confinement scaling, but still achieving a fusion power amplification $Q \gtrsim 5$ when the confinement is degraded by a factor of 2;
2. neutron wall loading comparable to or better than the baseline, suggesting a value of about 1 MW/m^2, with 0.5 MW/m^2 as a conservative lower bound; and
3. more nearly power-reactor-like operations, such as steady state.

Here we present a brief discussion on how low safety factor (Sect. 2.1) and noninductive current drive (Sect. 2.2) are expected to help achieve these performance objectives. We also summarize the major results of the FED-A study (Sects. 2.3 and 2.4).

2.1 LOW SAFETY FACTOR OPERATION

The primary advantages of low safety factor q operation include enhanced plasma beta β and reduced plasma disruptivity in certain circumstances. High beta serves to improve fusion performance and reduce device size, and reduced disruptivity improves the relevance to power reactors of the tokamak concept.

2.1.1 High Beta

The average fusion power density for an FED-like device can be approximated by

$$\langle P_{DT}\ (MW/m^3)\rangle \cong \langle \beta\ (5\%)\rangle^2 [B\ (4\ T)]^4 \ ,$$

where the profile enhancement of fusion power has been included and β is the reacting portion of the total beta. The average neutron wall load at the plasma edge then becomes

$$W_L^N \ (MW/m^2) \cong 0.4(2\kappa^2/1 + \kappa^2)^{1/2}[a \ (m)]<\beta \ (5\%)>^2[B \ (4 \ T)]^4 \ .$$

The latest experimental indications suggest that the volume-averaged beta takes the form (Sect. 3.4)

$$<\beta \ (5\%)> \cong \frac{5}{Aq_\psi} \frac{1 + \kappa^2}{2} \ ,$$

where A is the aspect ratio and q_ψ is the flux-surface-averaged safety factor at the plasma edge. From these we have

$$<P_{DT} \ (MW/m^3)> \cong \frac{25}{A^2 q_\psi^2} \left(\frac{1 + \kappa^2}{2}\right)^2 [B \ (4 \ T)]^4 \ ,$$

$$W_L^N \ (MW/m^2) \cong 10\kappa\left(\frac{1 + \kappa^2}{2}\right)^{3/2} \frac{a \ (m)}{A^2 q_\psi^2} [B \ (4 \ T)]^4 \ .$$

Thus, to achieve high W_L^N, a low q_ψ is desired.

In the event that the beta limit is more a result of limitations in $\varepsilon\beta_p$ (inverse aspect ratio and poloidal beta), we have $<\beta> \propto \varepsilon\beta_p\varepsilon/q_\psi^2$, which will lead to an even stronger q_ψ dependence of $W_L^N \propto q_\psi^{-4}$ in favor of low q_ψ operation. A major emphasis of the FED-A study (Chaps. 5 and 9) is therefore to clarify the effect of lowering q_ψ on performance and cost.

2.1.2 Low Disruptivity

The majority of tokamak experiments have encountered difficulties in achieving $q_\psi < 2$ operations; discharges usually terminate in a disruption as $q_\psi = 2$ at the plasma edge is approached. In the tokamaks that have consistently reached the $q_\psi < 2$ regime (e.g., DIVA, T-10, D-III), the plasma is seen not to disrupt as long as q_ψ at the plasma edge stays significantly below 2. Among these experiments, DIVA appears

to be unique; it has a thick (3-cm) conducting shell closely fitted to the plasma and shows the most resistance to disruptions. Other major emphases of the FED-A study are therefore to assess the effect of a closely fitted conducting shell on plasma disruptivity as q_ψ is lowered through 2 and maintained below 2 (Chap. 3) and to examine the feasibility of a continuous, conducting first wall in FED-A (Chap. 6).

2.2 NONINDUCTIVE CURRENT DRIVE

In the FED Baseline design, based on inductive current startup and maintenance, the plasma burn phase is limited by its projected poloidal flux capability. Only about 5% of the total flux capability is available to maintain the plasma current for the 100-s burn; the greater part is expended in establishing the plasma current. The pulsed nature of an inductively driven tokamak tends to impose serious limitations on the lifetime, availability, and economy of a tokamak reactor. While such potential difficulties are perceived to be less severe in a tokamak FED than in a tokamak power reactor, they nevertheless result in increased cost and complexity of its baseline design concept. It is therefore highly desirable to achieve a significant level of noninductive current drive in FED.

Recent successful demonstrations of lower hybrid current drive (LHCD) in PLT, Alcator-C, Versator II, JIPPT-II, etc., albeit at modest plasma densities, have suggested such a possibility. A successful radio frequency (rf) current drive at such low densities does not necessarily imply an indefinite burn phase at the required density (about 10^{14} cm^{-3}). However, it will permit cyclic current drive operations, such as recharging the solenoid current only at low density, and will hence eliminate shutdown of the plasma current and drastically reduce the cyclic electromagnetic loads. It will also permit the application of nearly full ohmic heating (OH) induction flux capability to the burn phase at high density, which will increase the burn pulse by an order of magnitude (to about 1000 s) and drastically reduce the cyclic thermal loads.

A major emphasis of the FED-A study is therefore to assess the physics viability and limitations of several candidate current drive approaches (lower hybrid wave, fast Alfvén wave, electron cyclotron wave, relativistic electron beam, and neutral beam) in their applications to FED-A (Chap. 4). The study also addresses engineering design concepts for these current drive components (Chap. 7), the impact on the design parameters when the inductive current drive requirements can be reduced or eliminated (Sect. 5.3), and the changes in the poloidal and toroidal magnetic field coil configurations due to the quasi-steady-state operations permitted by cyclic current drive operation (Chap. 8).

2.3 FED-A CONFIGURATION AND MAJOR FEATURES

The FED-A reference configuration, as suggested by the study, is shown in Figs. 2-1 (elevation view) and 2-2 (plan view). The major reference parameters are summarized in Table 2-1. The corresponding reference parameters for the FED Baseline (10-T operation) are also shown for comparison.

It will be noted that the assumption of achieving $q_\psi < 2.0$ during operation for a constant maximum toroidal field strength and a similar $\langle\beta\rangle$ value leads to a smaller machine (R = 4.22 m, which is 0.8 m smaller than FED Baseline) and lower fusion power (P = 255 MW, which is 200 MW less than FED Baseline). The smaller size for FED-A results in a significant reduction in cost.

The first wall design of FED-A is significantly different from that of FED Baseline. The FED-A employs a continuous copper shell with a toroidal time constant of 0.5 s. The FED Baseline employs discrete first wall panels with copper jumpers between shield sections; its toroidal time constant is on the order of 50 ms.

Other major features assumed for FED-A include a common vacuum boundary between the toroidal field (TF) coils and the torus shield, 12 TF coils, and a quasi-steady-state current device capability employing lower hybrid resonance heating (LHRH).

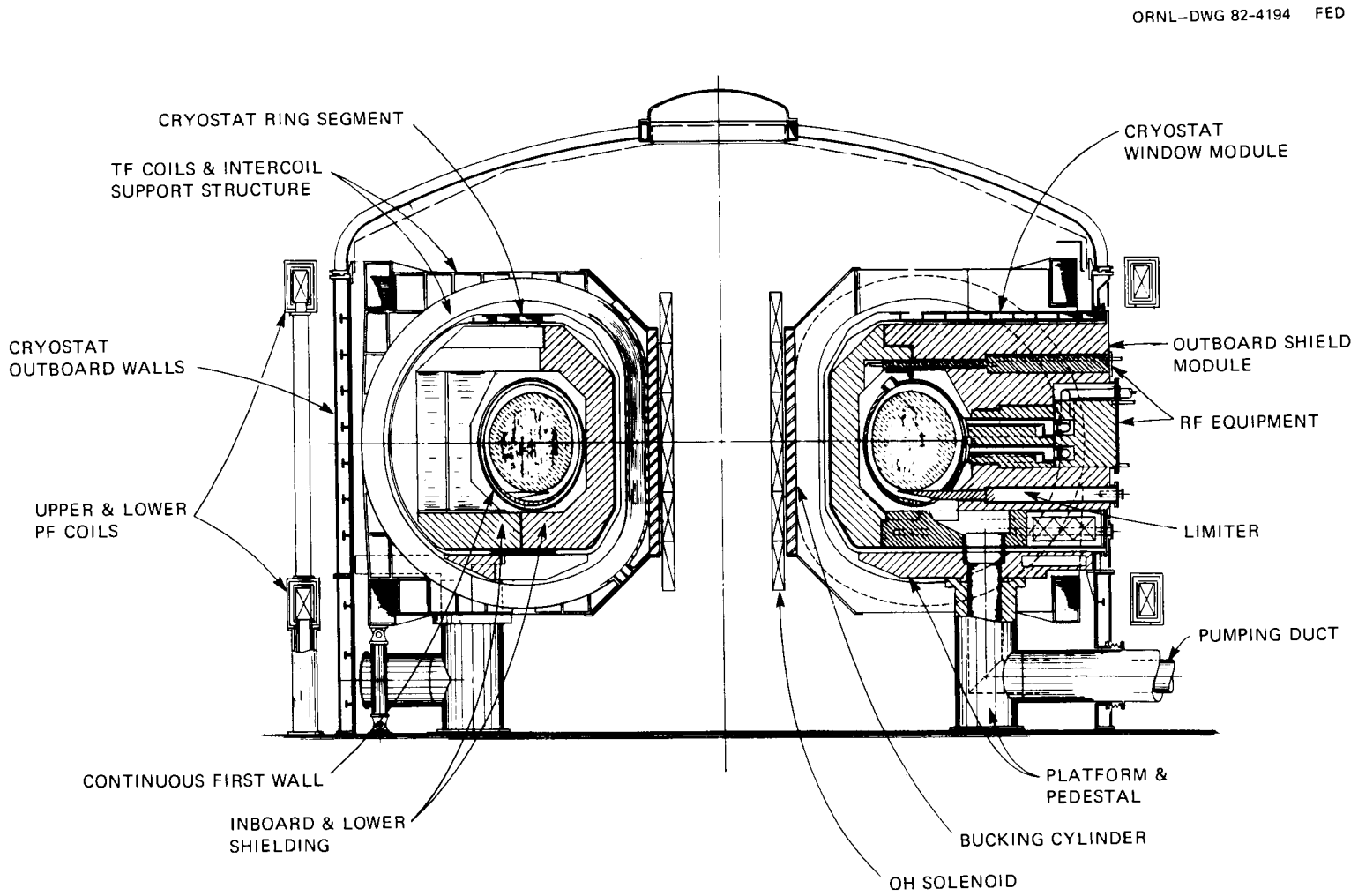

Fig. 2-1. FED-A elevation view.

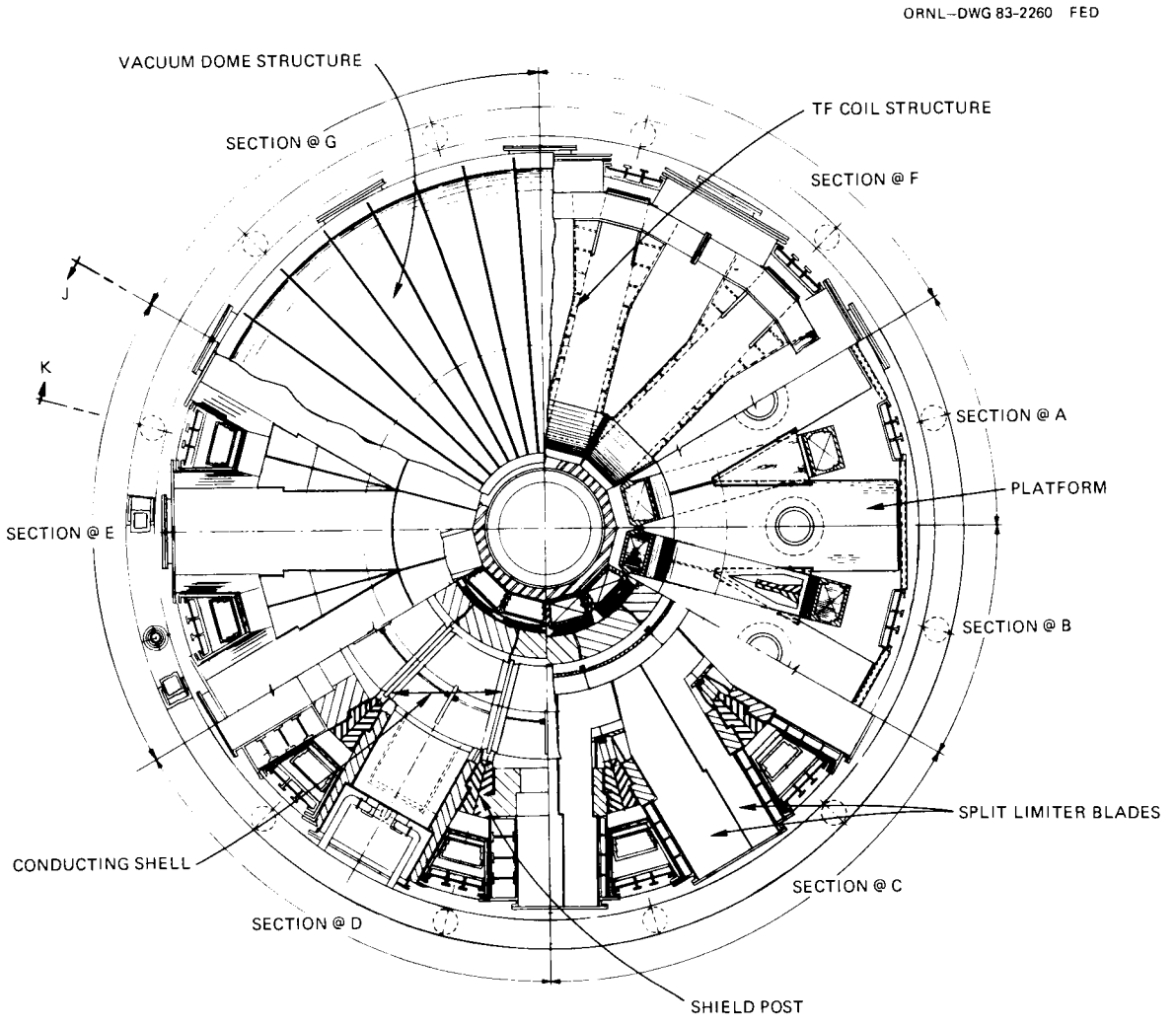

Fig. 2-2. FED-A plan view.

Table 2-1. FED-A reference parameters[a]

Description	Value	
	FED-A	FED Baseline
Major radius, R	4.22 m	5.0 m
Plasma radius, a	0.92 m	1.3 m
Plasma elongation, κ	1.2	1.6
Aspect ratio, A	4.59	3.80
Safety factor (edge), q_ψ, flux surface averaged	1.8	3.2
Plasma current, I_p	4.1 MA	6.5 MA
Total beta, $<\beta>$	6.0%	5.2%
Toroidal field at plasma, B_p	4.98 T	4.60 T
Fusion power amplification, Q	Ignited	Ignited
Toroidal eddy current time, τ_w	~0.5 s	~0.05 s
Other conducting path eddy current decay time, τ_x	~0.1 s	
Average fusion power, P_{DT}	255 MW	450 MW
Average neutron wall load, P_N	1.0	1.0
Burn time, τ_{burn}	~1000 s	~100 s
Number of TF coils	12	10
Maximum toroidal field strength, B_{max}	10 T	10 T

[a]For more extensive listing see Table 5-15.

2.4 SUMMARY OF CONCLUSIONS

The following are the important conclusions of the FED-A study.

2.4.1 Low Safety Factor and High Beta (Chap. 3)

Preliminary analytic and numerical calculations suggest that a closely fitted conducting shell of modest thickness (e.g., b/a = 1.1-1.4, 0.5- to 1.0-cm-thick copper) should be adequate in avoiding plasma disruptions resulting from growth of the m = 2 kink/tearing mode. Such a conducting shell will lengthen the instability time scale to the shell time constant τ_s, making it a significant fraction of the m = 1 sawtooth oscillation time ($\tau_s \sim 0.3\tau_{sawtooth}$). When q_ψ is less than 2 but above 1.5, the conducting shell is also shown to strongly limit the nonlinear growth of the m = 3, n = 2 tearing mode, making it unlikely to interact unfavorably with the m = 1, n = 1 mode and become a cause of disruption. These results are consistent with the latest experimental observations and suggest the use of a continuous conducting first wall in FED-A. The suggested value of τ_s for this purpose is about 0.2 s.

Given that q_ψ values below 2 can be achieved, the latest indication of beta limits suggest that $\langle\beta\rangle$ = 5-6% is possible if κ = 1.6 is assumed. If a value of $\varepsilon\beta_p$ as high as 0.5 could be achieved, the FED-A plasma with a modest elongation of κ = 1.2 would reach $\langle\beta\rangle$ = 6%. Given $\langle\beta\rangle$ = 6%, transport calculations with standard confinement assumptions (INTOR models) indicate that ignition can be reached in FED-A. Operation with $Q \geq 5$ remains achievable when confinement degradation due to toroidal field ripple, diffusion and loss of fusion alpha particles, or finite-beta-induced transport is included. The enhanced transport due to sawtooth activities within the q = 1 surface is found to represent a severe threat to the plasma performance of FED-A at low q and high beta.

2.4.2 Current Drive (Chap. 4)

A quasi-steady-state current drive scenario with cyclic plasma density or conductance is suggested as the desirable design approach for

FED-A. Among the many possible approaches to current drive in tokamaks, lower hybrid wave current drive has had the most experimental success and has a sound theoretical basis. The experimental results indicate efficiencies that follow the empirical relationship I (kA)/P (kW) $\sim$ $8T_e$ (keV)/Rn (10^{14} cm^{-2}). This relationship is in accord with theoretical predictions if the energies of the suprathermal current-carrying electrons bear a fixed relationship to the electron temperature; however, since in many present-day experiments the current-carrying electrons already have energies of 100 keV or more, the current drive efficiency may not continue to improve in future large devices as strongly (i.e., linearly) with further increases in electron temperature. Because of the inverse dependence of efficiency on plasma density, cyclic current drive approaches are seen to enhance the effective current drive efficiency by an order of magnitude over steady-state operations at a fixed high density. Despite these attractive features, the lower hybrid wave is nevertheless perceived to have a serious limitation in wave penetration at high density.

Other current drive approaches are assessed with regard to their potential to avoid this limitation, but with less physics basis. Fast Alfvén and electron cyclotron waves do not suffer from limited access at high density and hence can be used to sustain steady-state burn. The efficiency of these approaches is estimated to be about 0.1 A/W at densities of about 1×10^{14} cm^{-3}, leading to a fusion power amplification $Q \sim 5$ for FED-A.

Relativistic electron beam (REB) current drive represents an approach with the potential to maintain a steady-state burn at high Q. While this approach can also facilitate plasma initiation, nonclassical beam penetration into the tokamak plasma configuration and large anomalous enhancement of plasma resistivity during beam slowing down need to be assumed to make this approach viable.

Finally, negative-ion-based neutral beams with energies in the range of 400 to 800 keV are found to be appropriate for current drive in FED-A but have limited efficiency. A novel concept of tranverse field focusing is discussed as a possible scheme to implement the required beam system.

2.4.3 Cost-Effective FED-A Designs (Chap. 5)

Assumming a constant achievable $\varepsilon\beta_p$ (e.g., 0.5), INTOR-like confinement scaling, and several conventional design constraints, it is found that the capital cost of FED-A decreases with decreasing q_ψ. As q_ψ is decreased from 2 to 1.5, roughly a 13% reduction in cost is indicated, whether Q or wall loading is held constant. The cost is found to be insensitive to variations in elongation κ when Q is held constant, but the neutron wall load scales favorably as κ.

A maximum field of 10 T at the TF coils appears optimum for FED-A for minimum total capital cost and unit capital cost, both for a constant ignition margin and for constant neutron wall load. In The 10-T case is about 17% lower in cost than the 12-T case. This difference is lowered to about 8% when the Nb_3Sn unit cost in the 12-T case is reduced to equal that of the NbTi cost. When the plasma major radius is reduced by assuming noninductive current drive startup to compensate for a shortfall in OH flux, the cost is found to be essentially unchanged for constant neutron wall load and to decrease by a maximum of about 9% for constant Q when R is decreased from 4.2 m to 3.5 m.

With these findings, the near-optimum, cost-effective FED-A design is suggested to have R = 4.2 m, a = 0.92 m, B_{max} = 10 T, I_p = 4.1 MA, q_ψ = 1.8, and κ = 1.2, with a full OH flux capability permitting quasi-steady-state operation with burn times around 1000 s (Tables 2-1 and 5-15).

2.4.4 Continuous Conducting First Wall (Chap. 6)

Following a comparison of the electromagnetic, material, neutronic, mechanical, and thermodynamic properties of 316 stainless steel, 5083 aluminum alloy, and AMAX-MZC copper alloy with the design criteria, it is suggested that a continuous first wall of water-cooled copper represents the best choice for FED-A (see Fig. 2-3). With a total thickness of 1.5 cm (including a 0.5-cm coolant passage) it provides the best combination of electrical conductivity ($\tau_s \gtrsim 0.5$ s to mitigate disruption impact), neutron transparency (tritium breeding ratio of 1.2), and reactor-relevant heat removal (coolant temperature up to 320°C).

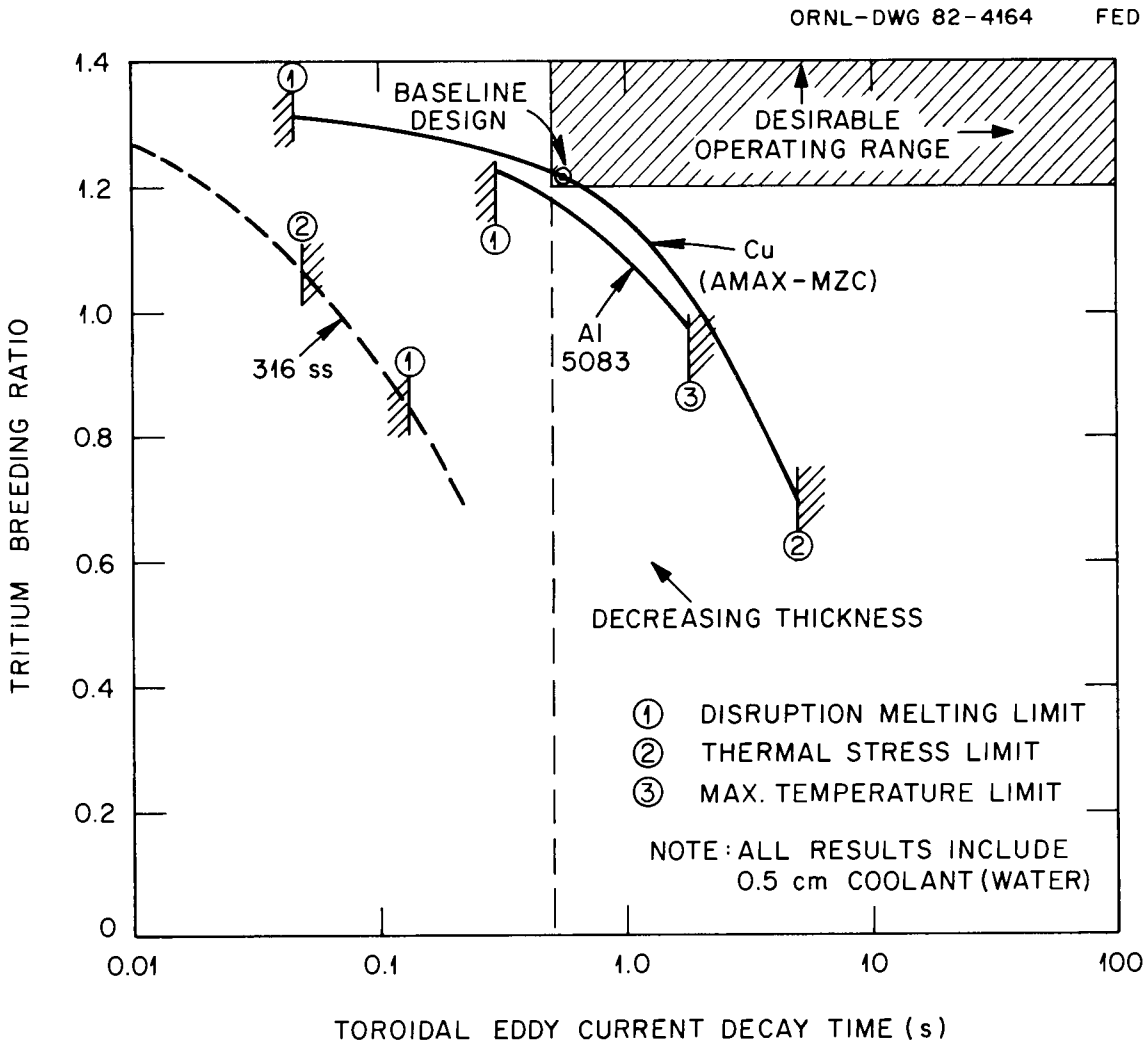

Fig. 2-3. Comparison of continuous conducting first wall performance among candidate materials. While Cu AMAX-MZC and Al 5083 appear nearly satisfactory in tritium breeding ratio and toroidal eddy current decay time, the aluminum alloy has limited reactor relevance because of its low melting temperature.

A simple bolted design to join the shell sectors offers high potential for good electrical conductivity across the sector joints. No structural difficulties are indicated for this first wall concept by the preliminary assessments.

2.4.5 Current Drive Component Design Concepts (Chap. 7)

In the FED Baseline design, the plasma current is driven solely by a large OH transformer. It is bulk heated by ion cyclotron resonance heating (ICRH) with electron cyclotron resonance heating (ECRH) for startup assist. This system requires about 4 m^2 of valuable access at the midplane and costs about $70 million for the 50 MW of power injected. The addition of the current drive system will cause a further impact on the device access, unless some approach or combination of approaches could be devised to perform all the required heating and current drive functions. Four current drive concepts are proposed to do this, namely, REB, LHRH (with modulated density), ECRH, and fast wave ion cyclotron (FWIC). These concepts, along with those of the baseline, are evaluated in a trade study. Each combination evaluated (a total of 40) is weighted for its physics and engineering credibility. Because of the lack of an experimental database for the REB and FWIC, these concepts are assigned low credibility, even though they score high marks in potential engineering cost-effectiveness. The favored concept utilizes the baseline heating and startup systems, a low voltage OH transformer with about 40 V•s and LHRH for current drive. The most credible operating scenario appears to be one in which the plasma density is modulated to allow good efficiency of the LHRH current drive at low density to recharge the OH transformer. The full transformer volt-seconds are then used during the burn, which lasts about 1000 s. Recharging takes tens of seconds; hence, the device duty factor is about 90% in this quasi-steady-state mode.

In the equipment configuration part of the study, emphasis is placed on the LHRH systems. Arrangements leading to high availability through modular construction are developed. Array (grill) modeling gives insight into the effects of module failure on the launched spectrum.

Guidelines for choosing array parameters, such as width, spacing, etc., are developed for current drive waveguides and launcher systems where hundreds of waveguide elements are required to launch tens of megawatts.

2.4.6 Magnetics and Configuration (Chap. 8)

The relatively simple poloidal field (PF) coil configuration proposed for the FED Baseline remains appropriate for FED-A during quasi-steady-state operation, although coil currents need to be modified. With steady-state plasma current and 1000-s burn pulses, a significant reduction in the TF intercoil structure is indicated. The segmentation approach to the continuous first wall is shown not to introduce difficulties to the basic FED device configuration.

2.4.7 Device Cost (Chap. 9)

Based on costing algorithms nearly identical to those for the FED Baseline, the FED-A design as currently perceived is estimated to have a direct total cost about 30% less than that of the FED Baseline.

3. LOW SAFETY FACTOR AND HIGH BETA

In this chapter we review the status of tokamak plasmas at low safety factor values ($1.5 \leqslant q_\psi < 2$) as a means of achieving low plasma disruptivity and high beta in FED-A. Approaches and design requirements aimed at reducing or even eliminating the probability of major disruptions of the plasma during $q_\psi < 2$ operation are a main subject of discussion. Given reliable low q operation, FED-A plasma beta values and plasma performance are also assessed.

Plasma disruption is a major concern both in operating present-day tokamaks at low q values and in design studies of future large tokamaks. The status of our present understanding is summarized in Sect. 3.1, where it is argued that a large m = 2, n = 1 tearing mode island appears to be necessary for major plasma disruptions, whether it overlaps with an m = 3, n = 2 island or the limiter in the process. Although a significant fraction of low q tokamak discharges are found to terminate with disruptions, the use of either a closely fitted conducting shell or external helical windings appears to permit low q ($1.2 \leqslant q_\psi < 2$) discharges, at least in the case of modest elongations.

Plasma stability in the presence of a conducting shell is the subject for Sects. 3.2 and 3.3. In an analytic assessment in Sect. 3.2, it is shown that a nearby, finitely conducting shell constrains the m = 2 kink/tearing instability to a nonrotating mode, which is unstable when q_o (safety factor on axis) is close to 1 ($q_o \gtrsim 0.9$ in the case calculated). The instability growth rate of the m = 2 mode is dictated by the shell time constant; catastrophic development of this instability can be avoided if the shell time constant is a significant fraction of the sawtooth period, during which q_o decreases from 1 to values as low as 0.6. This suggests that a shell time constant above 0.2 s should be adequate for avoiding disruptions in FED-A.

In Sect. 3.3, a set of numerical calculations for the m = 3, n = 2 modes, when $q_\psi < 2$, in the presence of a nearby shell is summarized. It is pointed out that the presence of a conducting shell near the plasma suppresses the m = 3, n = 2 mode and decreases the chances of major disruptions for $q_\psi < 2$ tokamak plasmas, as long as $q_\psi > 1.5$. The

presence of a nearby conducting shell is therefore suggested to be effective in avoiding disruptions in low q discharges. (Chapter 6 is devoted to a more detailed assessment of the conducting first wall design criteria and concepts.)

Sections 3.4 and 3.5 are concerned with estimates of the FED-A plasma beta and plasma performance, respectively. In Sect. 3.4 it is shown that based on ideal MHD stability, $\langle\beta\rangle$ in FED-A is limited to about 3.2% for $q_\psi = 1.8$, $A = 4.6$, and $\kappa = 1.2$. To achieve beta values up to about 6%, it may be necessary to increase elongation, decrease q_ψ, or invoke the stabilizing effects of energetic particles in reactor-grade plasmas. As shown in Chap. 5, the FED-A systems trade studies suggest that it may not be cost-effective to require full elongation at low q_ψ values. An elongation of 1.2 is therefore assumed for the present FED-A concept.

Transport calculations of FED-A performance are discussed in Sect. 3.5. The sensitivity of the performance to variations in q_ψ, toroidal field ripple, diffusion and loss of fusion alpha particles, and finite-beta-induced transport enhancements is the main topic. It is pointed out that, while the performance is likely to degrade because of all of these processes, the finite-beta-induced transport, in conjunction with the enhanced transport due to sawtooth activities within the $q = 1$ surface, represents the most severe threat to plasma performance of FED-A at low q and high beta.

3.1 PLASMA DISRUPTIVITY AT LOW q

J. T. Hogan (ORNL)

Operation at low q is sought in order to obtain high values of β_T with the smallest $\varepsilon\beta_p$. Early experience with ohmically heated tokamaks[1] suggested that the maximum stored energy was obtained with $q_\psi \cong 2$. Hence, the scaling of confinement properties with additional heating, at $q_\psi \lesssim 2$, is an important topic.

There is a complication, however, in that typical experience in tokamak experiments shows that the fraction of discharges ending in disruptions increases with $q_\psi \lesssim 4$ and reaches $\approx$50% at $q_\psi \cong 2$. These

values are only approximate because many large devices are not designed to withstand repeated disruption; hence, systematic exploration of disruptions is discouraged. Experiments carried out in smaller devices have been encouraging, however, especially the results of the DIVA experiment,[2] in which disruption-free operation at low q was attained. This has led to a study of conducting shell options for FED-A.

3.1.1 Models for Disruptivity

Several models have been proposed for the disruption process. Wesson[3] suggests that a large m = 2, n = 1 (2/1) island contacting the limiter will produce a catastrophic loss of confinement. Carreras et al.[4] propose that the dynamic evolution of overlapping 3/2 and 2/1 islands leads to abrupt field line ergodization and confinement loss. The boundaries for machine operation limited by the overlap criterion have been surveyed by Monticello and White.[5] Various plasma-wall studies[6-8] have suggested that MHD activity is not the only cause but that increased limiter heating, possibly resulting from enhanced MHD convection losses, leads to the injection of substantial amounts of limiter material into the plasma, and the plasma is thereby extinguished with an intolerably high radiative loss.

3.1.2 Experimental Studies: Ohmically Heated Plasmas

Direct experimental study has mainly been conducted on smaller machines because of the high disruption frequency in the low q regime. The JIPPT-II group has reported observations of both the 2/1-limiter contact and the 3/2-2/1 overlap situations.[9] However, only in the case of limiter contact with the 2/1 case do they see the "hard," or major, disruption. The 3/2-2/1 overlap case leads to recurrent "soft" (internal) disruptions in this experiment.

Progress has recently been reported on low q, disruption-free regimes. The CLEO device has been operated at low q ($1 \lesssim q_\psi \lesssim 2$) in two modes: as a helically assisted, low q tokamak (HALQT), obtained with $\ell = 3$ stellarator windings, and in a pure tokamak mode with gettering,

accurate position control, and controlled gas puffing.[10] Tokamak confinement at low q was found to be consistent with empirical scaling. However, the use of $\ell = 3$ windings reduced the HALQT minor radius by 30%, hence reducing the confinement time. Values of $q_L \sim 2.5$ for pure tokamaks and $q_L \sim 1$ for HALQT are reported.

The TORIUT-4 tokamak has produced low q discharges with the addition of a nonresonant 3/1 winding.[11] The 3/1 island is thought to produce ergodization of the major 2/1 island and hence to suppress its growth. The ergodization does, however, reduce the effective plasma radius, and thus a penalty in confinement would result if such a scheme were attempted in FED. Furthermore, the effect of the conducting shell was found to be significant. With b/a = 1.13, where b is the radius of the conducting shell, stable discharges with $q_L = 1.2$ could be attained. With b/a = 1.5, however, the $q_L \leq 2$ regime could not be reached at all without the 3/1 windings, and even so, the group reports that $q_L^{MIN} = 1.8$ because of 1/1 coupling to the 3/2 mode. The 3/1 winding also allowed a wide margin of flexibility in vertical field programming. With b/a = 1.5 and $q_L \cong 2$, a ±1.3% change in B_l destroyed the discharge with the 3/1 coil off; however, a ±4.5% variation in B_l could be allowed with the 3/1 coils energized. This would be significant for FED operation, because optimization with respect to tearing modes in the (relatively) cold edge must compete with optimization of the q profile for high beta transport and with shape considerations for pumped limiter or divertor efficiency. Hence, a wide margin for variation would be helpful.

3.1.3 Experimental Studies: Neutral-Beam-Heated Plasmas

Many experimental groups are currently engaged in beta optimization studies, and the low q regime is favored. New information on the disruptivity issue from two of these studies (PDX, D-III) is discussed here.

Current programming

The PDX group[12] has obtained some high beta results using rapid current programming. This technique was previously used to produce high β_p values in ohmically heated tokamaks[13] and could be further explored in the future as a means to higher $\bar{\beta}$. In discussing the disruptivity issue, however, we idealize the PDX technique.

Also, it has been found in analysis of ISX-B results[14] that the ideal MHD instability growth rates may be reduced (and hence confinement may be enhanced) if the q profile is chosen to be flat in the center. The j profile has, correspondingly, a relatively large gradient near the edge. The question is, thus, whether these profiles can be maintained on FED-like time scales.

These observations suggest that if plasma current is rapidly decreased and then restored, we can expect to produce just the kind of flattening of the q profile needed for ideal MHD. A simulation of this scenario for PDX-like parameters is shown in Fig. 3-1. The current density profile has the ideal MHD favorable "wing" at 150 ms. The q profile is flattened in the center, as desired (Fig. 3-2). However, the evolution of edge tearing modes during the current programming phase adds a complicating factor. As seen in Fig. 3-3, the 2/1 and 3/2 modes are excited with sizable island width when q_L is increased to >2. In fact, the 3/2 and 2/1 overlap and the ergodic region thus produced can touch the limiter. A disruption could occur, according to the JIPPT-II criterion; both the necessary conditions (islands and limiter contact) are present.

Recent high beta results

The D-III group has recently achieved record values of $\bar{\beta}_T$ (Ref. 15). As regards the disruptivity issue, the pattern observed seems to conform to other tokamaks in the low q regime. It is reported that the disruptivity rate is about 50% during the beam pulse in the high beta regime ($B_T \sim 6$ kG, $q_\psi \sim 1.7$, $\bar{\beta} \sim 4.6\%$, $\beta_p \sim 0.08$) and that all discharges disruptively terminate when the beam heat source is removed. Evidently

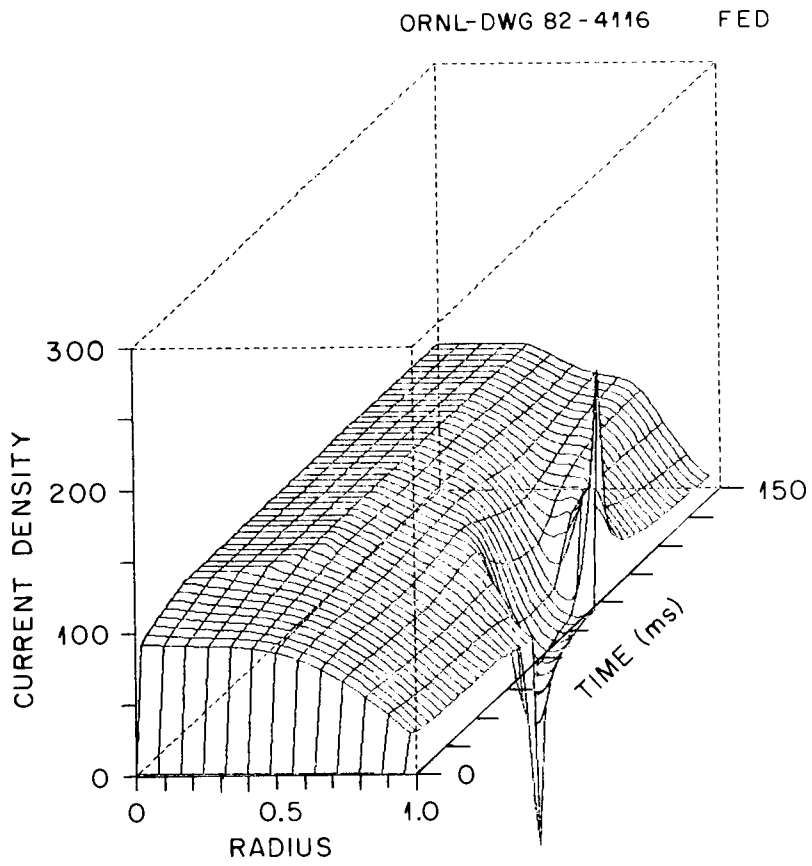

Fig. 3-1. Evolution of the current density radial profile as the current is programmed from 300 kA to 200 kA and then back up to 300 kA. A suitable j(r) profile for ideal MHD stability is obtained at 150 ms. (Parameters are chosen to resemble the PDX tokamak, although a detailed comparison is not attempted.)

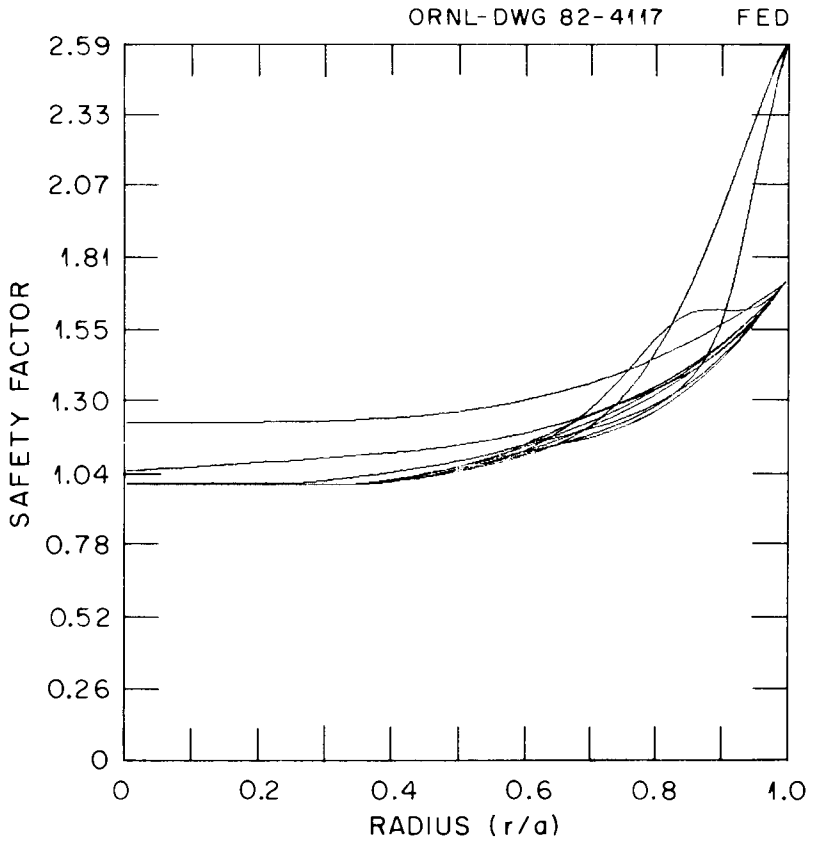

Fig. 3-2. Evolution of the q(r) profile during current programming. q(a) drops from 2.6 to 1.7, then goes back up to 2.6 as I_p is varied.

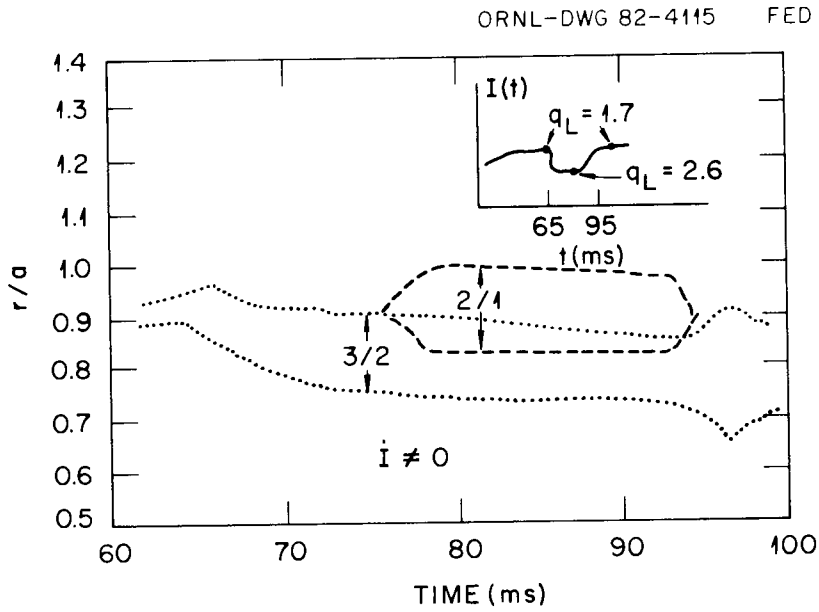

Fig. 3-3. Evolution of saturated magnetic island widths as I_p varies. Both the 2/1 and 3/2 have significant radial (r/a) width. They overlap each other, and the ergodic zone touches the limiter in this case, at least when $q_{lim} \geq 2$.

the beam input power is needed to sustain the ultra-Murakami ($M \sim 9$) densities $\bar{n}_e \sim 6\text{-}7 \times 10^{13}$ cm^{-3} achieved with 250 torr·L·s^{-1} gas puffing. The lack of a rise in disruptivity frequency associated with high $\bar{\beta}$ is encouraging.

3.1.4 Summary

The disruptivity picture has received a more detailed description in the past year, and the prospects for eventual solution remain good, if sufficient attention is given to this area. With several indirect measurements of the q profile, close control of the plasma position and plasma-wall interaction appears needed to achieve sustained disruption-free operation in the low q regime. When $q_\psi \gtrsim 2$, external helical windings are seen to improve the control of the plasma. A closely fitted conducting shell is seen to permit very low q ($q_\psi \geqslant 1.2$) operations for modestly elongated plasmas. No fundamental obstacle to reducing disruptivity in large tokamaks has presented itself, but it is a challenging problem of optimization and control during plasma operation.

3.2 EFFECT OF A FINITELY CONDUCTING SHELL ON TOKAMAK STABILITY AT LOW q

P. H. Rutherford (PPPL)

Operation of a tokamak with very low values of the limiter safety factor q_a is generally prevented by the onset of kink/tearing instabilities, leading to plasma disruptions. This section provides an estimate of the effect of a conducting shell on these instabilities and the condition of the shell in avoiding disruptions.

Theoretically, in the absence of a conducting shell, a tokamak with central safety factor q_o equal to unity is unstable to the $m = 2$, $n = 1$ mode for virtually all typical current profiles $j_z(r)$ (Ref. 16) although stability can be achieved at $q_a \geqslant 2.6$ for specially tailored profiles.[17] For $q_a < 2$, this mode takes the form of a strongly growing kink instability with a resonant surface [where $q(r) = 2$] that lies in the vacuum region outside the plasma. If $q_o < 1$, the $m = 1$ tearing mode becomes

unstable (resulting in "sawtooth" oscillations), but the stability of higher m modes is improved. In particular, the m = 2 mode is stable if $q_o \lesssim 0.9$ for typical current profiles.[16] In the sawtooth mode of tokamak operation, which generally exhibits superior confinement, the q_o value is believed to decrease slowly from unity to values as low as 0.6-0.7, after which it is rapidly restored to unity through a fast relaxation (expansion) phase of the sawtooth.[18-20] Thus, a "sawtoothing" tokamak may be expected to be alternatingly stable and unstable to m = 2 modes.

For $q_a > 2$, the m = 2 instability will take the form of a tearing mode, whose growth in amplitude in the nonlinear regime may be so slow[21] that it does not reach measurable amplitudes on the time scale of a sawtooth period; indeed, strongly sawtoothing tokamaks are generally free of large m = 2 oscillations. For $q_a < 2$, however, the m = 2 kink instability would be expected to grow on a hydromagnetic time scale, much shorter than the sawtooth period.

Experimental results from PDX tend to confirm at least some aspects of this picture.[22] In particular, a major disruption most often occurs very soon after the fast relaxation phase of the sawtooth. Sometimes a strong m = 2 oscillation is seen just after the sawtooth and immediately before the disruption. At other times, this strong m = 2 mode is not seen, but it should be noted that a strongly growing, nonrotating kink may not be readily observable with conventional diagnostics.

3.2.1 Kink/Tearing Mode in the Presence of a Conducting Shell

The stability of the m = 2 mode can be greatly improved by the addition of a perfectly conducting shell at a radius r = b, close to the plasma surface. With $q_o = 1$, current profiles can be found that are theoretically stable to all kink/tearing modes, including the m = 2 mode, for q_a values as low as 1.8, provided a conducting shell is placed at $r/a \leqslant 1.2$ (Ref. 17). The DIVA tokamak has reported disruption-free operation at $q_a < 2$ with a 3-cm copper shell placed at r/a = 1.2 (Ref. 23). If the shell is imperfectly conducting, a rotating kink mode might still

be effectively stabilized,[24] but a nonrotating kink will remain unstable, with a reduced growth rate that will be related to the resistive time constant of the shell.

A reactor-prototypical vacuum vessel with low toroidal resistance ($\lesssim$0.1 mΩ) has been proposed for FED-A and certain future large tokamaks. A pertinent question is: Can such a vacuum vessel, perhaps equipped with m = 2 helical conducting straps, sufficiently impede the growth of the m = 2 kink so that significant amplitudes are not attained during the part of the sawtooth period that is m = 2 unstable? If so, relatively disruption-free operation with $q_a < 2$ might be achieved.

The boundary condition to be applied at a thin resistive shell, with its thickness d much less than its radius b, is

$$\left[\frac{(rB_r)'}{B_r}\right]_b = \frac{b}{\lambda} \tanh \frac{d}{\lambda} , \tag{3-1}$$

where $[]_b$ denotes the discontinuity across the shell, $\lambda = (\eta_w c^2/4\pi\gamma)^{1/2}$ is the resistive skin depth of the shell, γ is the growth rate of the mode, and the prime denotes differentiation with respect to r. The condition to be applied on the inner side of the shell is

$$\left.\frac{(rB_r)'}{B_r}\right|_b = -m - \gamma\tau_S , \tag{3-2}$$

where $\tau_S = 4\pi bd/\eta_w c^2$ is the resistive time constant of the shell. In deriving Eq. (3-2), we have taken $d \ll \lambda$, noting that the shell exerts a strong stabilizing effect on long wavelength kink modes even if its resistive skin depth significantly exceeds its thickness (a stabilizing effect requires only that $\lambda^2 \lesssim bd$).

For the simplest case of uniform current density, and therefore uniform q value within the plasma, the dispersion relation for kink modes with complex frequency ω can easily be shown to be

$$\frac{(\omega - \omega_E)^2 \tau_H^2}{2(m - nq)^2} = 1 - \frac{1}{m - nq} + \frac{(a/b)^{2m}}{1 - (a/b)^{2m} + 2im/\omega\tau_S}, \qquad (3\text{-}3)$$

where $\tau_H = [4\pi\rho a^2 B_\theta (a)^2]^{1/2}$ is a hydromagnetic time and $\omega_E = mv_\theta/r$ describes the effect of plasma rotation, arising either from a radial electric field or from diamagnetic effects. Without the conducting shell ($\tau_S \to 0$), the m = 2, n = 1 kink is unstable whenever $1 < q < 2$, and the unstable mode has a growth rate on the order of τ_H^{-1} and rotates with the plasma. However, in the more usual case, where $\tau_S \gg \tau_H$, and provided the shell is sufficiently close to the plasma [$b/a < (q - 1)^{-1/4}$], the rapidly growing m = 2 kink is stabilized by the high effective conductivity of the shell and becomes a rapidly oscillating kink with frequency $\omega = \omega_E \pm \omega_K$, where $\omega_K \sim \tau_H^{-1}$ is the frequency of the stable kink obtained from Eq. (3-3) by setting $\tau_S = \infty$ and $\omega_E = 0$. This oscillatory mode is weakly damped by shell resistivity, except in the very atypical case where $\omega_E > \omega_K$, in which event the "backward" wave with $\omega = \omega_E - \omega_K$ is established by shell resistivity. Of more significance is a slowly growing, nonoscillatory mode that presents the greatest threat in the case of a resistive shell and is the main topic of this discussion.

3.2.2 Nonrotating Mode in the Presence of a Resistive Shell

In order to evaluate the stability of this nonrotating kink/tearing mode as the tokamak evolves through a sawtooth period, we consider the "two-step" current profile shown in Fig. 3-4, which is analytically tractable.[17] Specifically, we assume a uniform current density j_o in a central core of radius c with safety factor q_c, surrounded by a "pedestal" of uniform current density pj_o extending to r = a, with an edge safety factor q_a. The adjustable parameters are related by $c^2/a^2 = (q_c/q_a - p)/(1 - p)$. Just after the fast relaxation phase of the sawtooth, we take $q_c = 1.0$, p = 0.2, and c/a = 0.76, with g_a just above 1.5. In this case, Fig. 3-4 shows that the current profile roughly approximates the "flattened model" of Ref. 16. Here the limiter should not necessarily

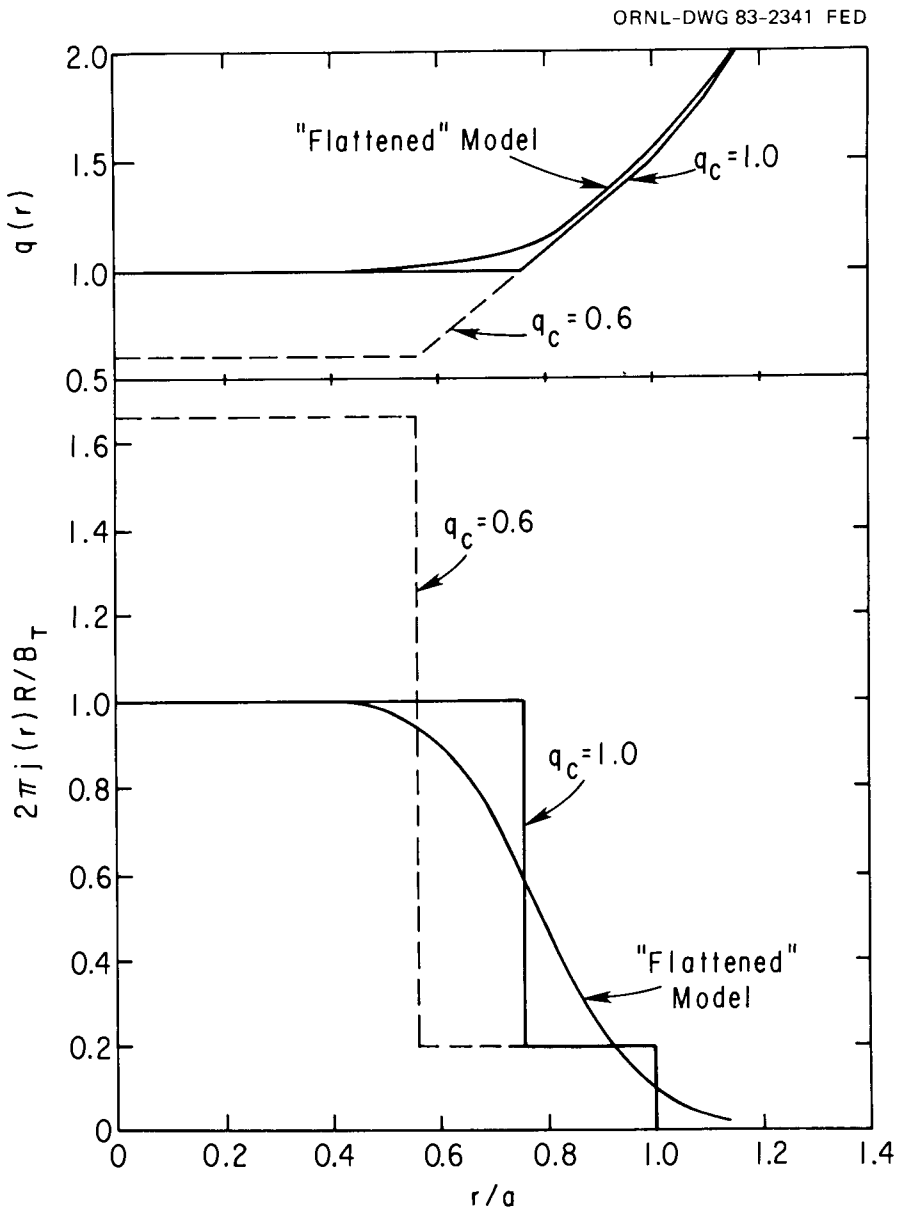

Fig. 3-4. The "step model" current profile used in the calculations and its comparison with the "flattened" model of Ref. 16. During the sawtooth, the profile evolves from q_c = 1 (solid line) to q_c = 0.6 (broken line). The radius r = a corresponds to the outer edge of the current channel; the limiter radius will be somewhat larger, perhaps r = 1.1a.

be identified with r = a, but with a somewhat larger radius, say r = 1.1a, where the smoothed current density vanishes. During the slow rise phase of the sawtooth cycle, q_c decreases, while q_a and the current density in the outer part of the plasma remain fixed. The step model parameters evolve according to $p = 0.2q_c$, $c/a = 0.68q_c^{1/2}/(1 - 0.2q_c)^{1/2}$. The broken curve in Fig. 3-4 shows the profile when $q_c = 0.6$.

The growth rate of the slow nonrotating kink can easily be shown to be

$$\frac{\gamma\tau_S}{2m} = \frac{N}{D} ,$$

where

$$N = \frac{1 - p}{m - nq_c} - 1 + \frac{pq_a}{q_c(m - nq_a)} \left\{ 1 - \frac{1 - p}{m - nq_c} \left[1 - \left(\frac{c}{a}\right)^{2m} \right] \right\} \qquad (3\text{-}4)$$

and

$$D = -N + \left(\frac{c}{b}\right)^{2m} \frac{1 - p}{m - nq_c} + \left(\frac{a}{b}\right)^{2m} \frac{pq_a}{q_c(m - nq_a)} \left\{ 1 - \frac{1 - p}{m - nq_c} \left[1 - \left(\frac{c}{a}\right)^{2m} \right] \right\} . \qquad (3\text{-}5)$$

Figure 3-5(a) shows the growth rate at the most vulnerable moment, just after the fast relaxation phase of the sawtooth ($q_c = 1.0$, $p = 0.2$), as a function of shell position; for $b/a > 1.61$, the mode is not stabilized even by a perfectly conducting shell, and the growth rate becomes infinite on the time scale of τ_S. These rough estimates appear consistent with some recent experimental observations (see Sect. 3.1.2).

In Fig. 3-5(b), we have plotted the growth rate of the m = 2 mode as a function of q_c for a sawtooth cycle extending to $q_c = 0.5$, for $b/a = 1.4$. The mode is stable for $q_c < 0.87$, and the accumulated growth

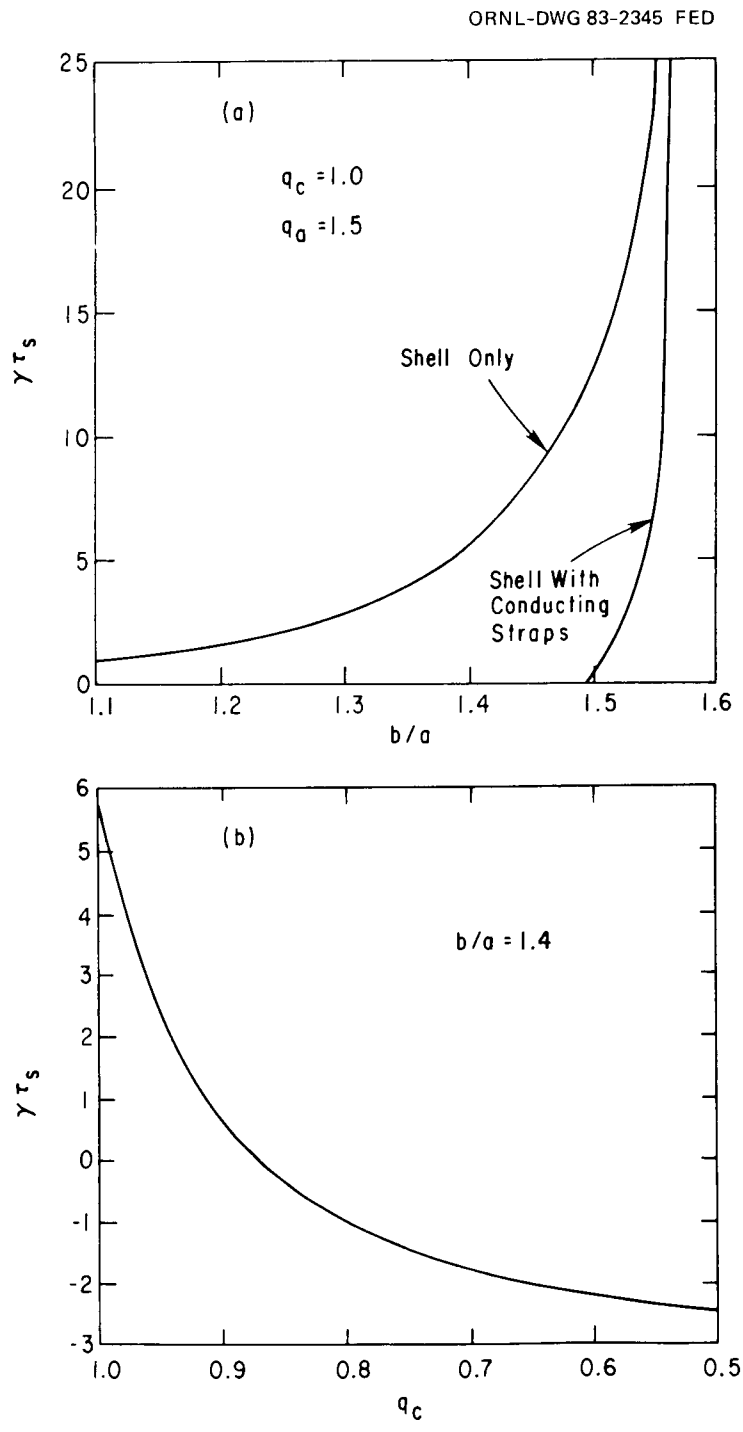

Fig. 3-5(a). The growth rate of the m = 2 mode just after fast relaxation of the sawtooth (q_c = 1.0) for various positions of the resistive shell and for the case of a shell equipped with helical conducting "straps." (b). The growth rate of the m = 2 at different stages of a sawtooth period for the case of a resistive shell at b/a = 1.4; the mode is damped if q_c < 0.87.

vanishes for any sawtooth cycle extending to q_c values lower than about 0.65. The average growth rate γ during the unstable phase of the sawtooth, lasting about a third of the total sawtooth period, is about $2\tau_S^{-1}$. Since a few exponentiations ($\sim$2) can presumably be tolerated during this phase before disruption is induced, the condition for effective stability can be expressed roughly as $\tau_S \gtrsim 0.3\tau_{sawtooth}$.

For a continuous shell of minor radius b and thickness d, the resistive time constant is τ_S (s) = [1.3b (m)]d (cm)/[η_W ($\mu\Omega\cdot$cm)]. Thus, a 0.5-cm-thick copper shell (η_W = 1.7 $\mu\Omega\cdot$cm) of minor radius 1.1 m gives τ_S = 0.4 s, more than adequate to provide effective stability even for very long sawtooth periods. On the other hand, a stainless steel shell (η_W = 80 $\mu\Omega\cdot$cm) must be about 2.2 cm thick if the sawtooth period is 200 ms.

The stabilizing effect of a poorly conducting shell can be greatly enhanced if it is equipped with m = 2, n = 1 passive helical conducting windings, perhaps in the form of copper "straps" wrapped on the outside of the shell. Since all possible phases of the m = 2 mode must be stabilized, there must be two independent windings in which separate currents $\pm I_1$ and $\pm I_2$ can be induced, as shown in Fig. 3-6. Assuming the copper to be perfectly conducting, these windings act like a perfectly conducting shell except for a "leakage" flux, which (for an m = 2 mode excited in the windings shown in Fig. 3-6) takes the form of a perturbation term like $B_r \sim \exp(6i\theta - 3i\phi)$, localized in radius to the neighborhood of the shell. Retaining such a term in the analysis, we find that the boundary condition to be applied to the m = 2 mode on the inner side of the shell becomes

$$\left.\frac{(rB_r)'}{B_r}\right|_b = -14 - 2\gamma\tau_S \ , \qquad (3\text{-}6)$$

where τ_S still refers to the finitely conducting continuous shell. In Fig. 3-5(a), we include the growth rate of the m = 2 mode for our model current profile just after the fast relaxation phase of the sawtooth (q_c = 1.0, p = 0.2) as a function of the position of this composite

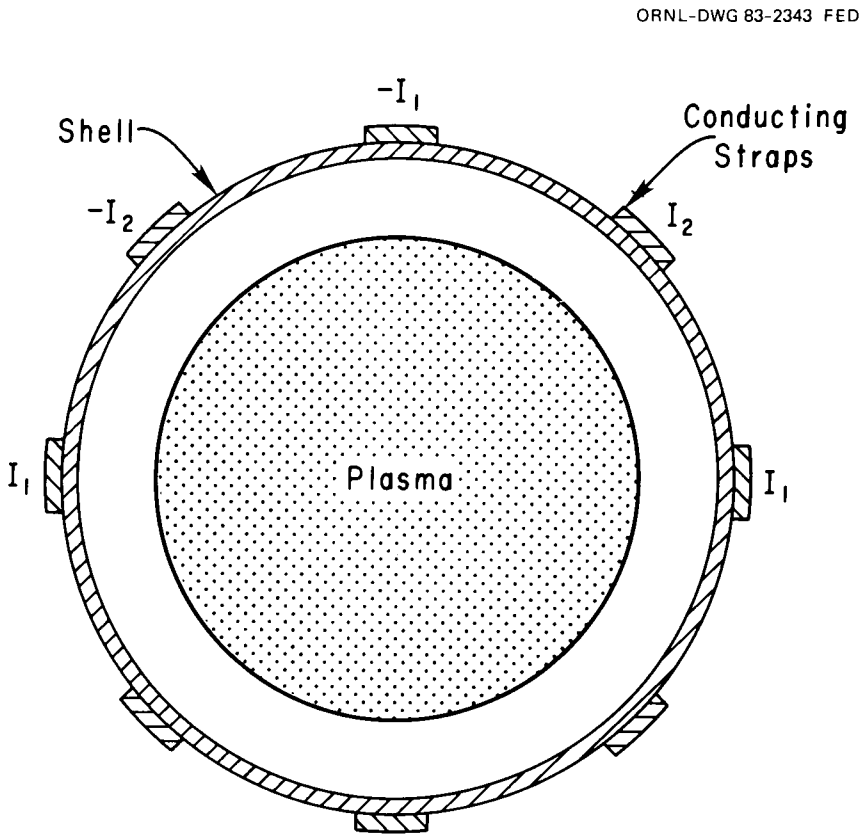

Fig. 3-6. Schematic diagram of the placement of m = 2, n = 1 helical conducting "straps" on a resistive shell.

shell. The mode is completely stabilized if $b/a < 1.49$. At $b/a = 1.55$, the growth rate is about the same as that for a shell at $b/a = 1.42$ without the copper straps [see Fig. 3-5(a)].

3.2.3 Sawtooth Time Scale

For ohmically heated discharges, sawtooth periods range from about 1 ms in small tokamaks ($a \sim 12$ cm) to as much as 10 ms in large present-day devices ($a \sim 40$ cm). The observations seem to be consistent with theoretical models that express the sawtooth period as some combination of the resistive "skin" time and the plasma "heating" time,[25-27] although there are disagreements as to the exact nature of the reconnection process that characterizes the fast relaxation phase.[28] Such models predict that the sawtooth period should increase both with plasma size (as a^2) and with central electron temperature, although the latter dependence is not well verified because the ohmic data are limited to cases with $T_e(0) \sim 1$ keV. In ohmic plasmas, sawtoothing is undoubtedly aided by "thermal instability," in which peaking of $T_e(r)$ leads to peaking of $j(r)$, which, in turn, further exacerbates the peaking of $T_e(r)$.

For neutral-beam-heated discharges, sawtooth periods tend to be somewhat longer, ranging up to 50 ms in moderate q plasmas in PLT[29] and PDX.[30] With $q_a \lesssim 2$ in PDX, the sawtooth period is about 25 ms (Ref. 30). The increase in sawtooth period relative to ohmically heated discharges is partly due to the higher central electron temperatures [$T_e(0) \sim 1.5$-3.0 keV] by injection heating. Reduced thermal instability is probably the other important contributor to the lengthening of the sawtooth period. The dominant term in the electron power balance, coupling to hotter ions, has a "stable" inverse dependence on electron temperature. Extrapolation of these results to next-generation tokamaks [$a \sim 80$ cm, $T_e(0) \sim 10$ keV] operated at low q_a values indicates sawtooth periods ranging up to about 400 ms. However, detailed measurements of the location of $m = 1$, $n = 1$ magnetic fluctuations during sawteeth in low q_a PDX discharges[30] suggest that much of the current profile

peaking (from $q_c \cong 1.0$ to $q_c \cong 0.9$) occurs relatively quickly, perhaps during the first 4 ms of a 25-ms sawtooth. If this holds generally, then the "effective" sawtooth period in a next-generation tokamak may be only about 200 ms. Scaling from this value, the upper range of the "effective" sawtooth period in FED-A [$a \sim 90$ cm, $T_e(0) \sim 20$ keV] is estimated to be $\tau_{sawtooth} \sim 0.5$ s.

Our analysis is predicated on the assumption that major disruptions arise from m = 2 instabilities, and we have ignored other modes, in particular the m = 3, n = 2 tearing mode. In fact, Ref. 17 shows that the m = 3, n = 2 mode is stable for "step model" current profiles with q_a just above 1.5, as shown in Fig. 3-4. More general profiles with $q_a < 2$ and a conducting shell stabilizing the m = 2 mode tend to be unstable to the m = 3, n = 2 mode. However, nonlinear calculations of saturated tearing modes show that the m = 3, n = 2 magnetic island does not grow large enough to overlap neighboring islands (m = 4, n = 3 and m = 5, n = 3).[31] Thus, the preconditions for major disruptions may not arise if m = 3, n = 2 is the dominant unstable mode. A more detailed numerical assessment of this mode is given in Sect. 3.3.

3.2.4 Summary

In conclusion, we have found that a finitely conducting shell with $\tau_S > 0.3\tau_{sawtooth}$ placed at $b/a \leqslant 1.4$ should effectively stabilize the m = 2 kink mode in a tokamak when q_a is varied to below 2. Here, a is the radius of the edge of the current channel; the limiter radius will be about 1.1a and the limiter q value will be about 1.8. In FED-A, a shell time constant of about 0.5 s which is suggested by the need to limit the induced electromagnetic effects during disruption (Sect. 6.1), should then be adequate for an estimated $\tau_{sawtooth} \sim 0.5$ s during burn. If the shell can be equipped with m = 2, n = 1 passive helical copper "straps," the same degree of stability can be achieved with a shell placed at $b/a \leqslant 1.55$.

3.3 NONLINEAR STABILITY ASSESSMENTS AT $q < 2$

B. A. Carreras and J. A. Holmes (ORNL)

Experimental results from several tokamaks[23,32-34] indicate that a disruption-free operational regime is obtained when the safety factor at the plasma boundary $q(a_p)$ is less than 2. The presence of a conducting shell in some of these devices could play a role in attaining this regime. To interpret such results and to investigate the role of the conducting shell, we have studied the stability of tearing modes for $q(a_p) < 2$. For our studies a reduced set of resistive MHD equations was used.[35] This set of equations has been useful for understanding disruptions caused by the $m = 2$, $n = 1$ (2;1) tearing mode in $q(a_p) > 2$ tokamak discharges.[36] The main features of these disruptions have been well described using the cylindrical limit of these equations. Therefore, we begin the present studies with the same basic model.

When $q(a_p) > 2$, the (2;1) tearing mode is generally believed to be the cause of major disruptions, because it is the tearing mode with the largest potential energy. This is reflected in the large magnetic island width associated with this mode. Disruptions may be triggered by the overlap of the $m = 2/n = 1$ (2/1) magnetic island with some other island present in the plasma, with the 3/2 magnetic island being the most likely candidate.[36] If the value $q(0)$ of the safety factor at the magnetic axis is held fixed while $q(a_p)$ is decreased, the 2/1 magnetic island increases (Fig. 3-7). Its island width achieves maximum value for $2.5 \leqslant q(a_p) \leqslant 3$. In this $q(a_p)$ range, the chances of island overlap are therefore greatest, and so is the likelihood of disruptions. The stabilization of the (2;1) tearing mode below $q(a_p) = 2.5$ is due to the effect of the conducting wall boundary condition at the plasma edge. Therefore, this boundary condition does not give a good description of tearing modes in a conventional tokamak when $q(a_p)$ is near 2. For $q(a_p) < 2$ the most unstable mode, besides the (1;1) mode, is the (3;2) mode. A potential cause of disruptions for $q(a_p) < 2$ discharges is then the overlap of the 3/2 magnetic island with the 1/1 island. We investigate

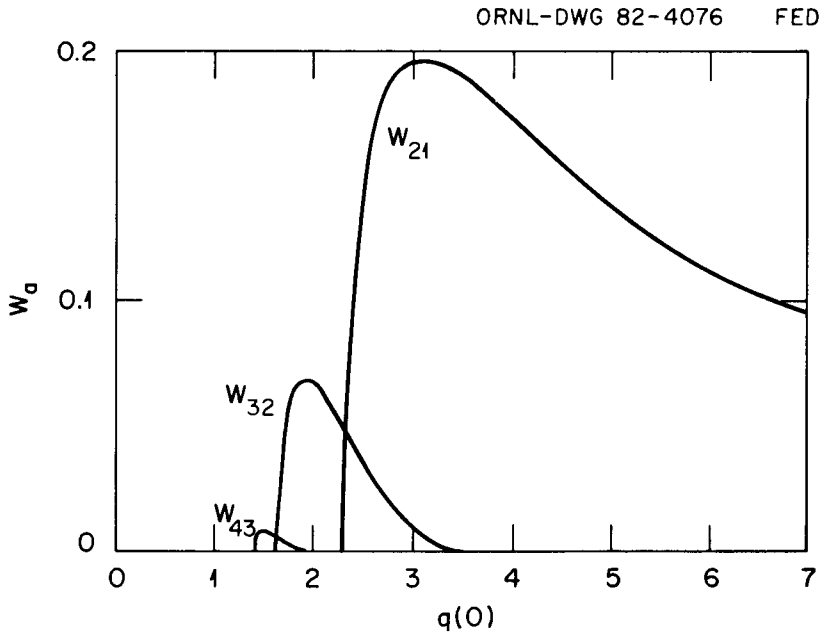

Fig. 3-7. Magnetic island width as a function of $q(a_p)$ for the (2;1), (3;2), and (4;3) tearing modes. Here $q(0) = 1.08$.

the stability properties of this mode and its possible role in low q disruptions. The present investigation is limited to low beta plasmas.

3.3.1 Stability Properties of the (3;2) Tearing Mode

To study the stability properties of the (3;2) tearing mode it is useful to parameterize the safety factor profile,

$$q(r) = q(0)[1 + (r/r_0)^{2\lambda}]^{1/\lambda} \quad . \tag{3-7}$$

The RST code[37] has been used for the numerical calculations.

Using the conducting wall boundary condition, the (3;2) mode is always stable for $q(0) < 1$. Increasing $q(0)$ causes the mode to become unstable, with a linear growth rate increasing with $q(0)$ (Fig. 3-8). The growth rate has its maximum value for $q(0) \approx 1.3$ and then decreases, becoming stable when $q(0) = 1.5$ and the 3/2 singular surface is no longer in the plasma. With increasing λ, the toroidal current gradient increases, causing the (3;2) mode to become more unstable (Fig. 3-8).

The fact that the (3;2) tearing mode is stable for $q(0) < 1$ seems to indicate that its role in low q tokamak disruptions cannot be important. That would leave only the (1;1) mode as a possible cause of disruptions, and these would be limited to internal disruptions only. However, the present results have been obtained using a conducting wall boundary condition at the plasma edge. We can relax this condition by introducing a highly resistive region between the plasma edge at $r = a_p$ [broken line in Fig. 3-9(b) and (c)] and the conducting wall at $r = a_w$. This precludes the rigorous study of the effect of a vacuum region when the resonant surface moves close to the plasma edge. However, it is judged to be a reasonable model to study wall effects on the stability of internal modes.

In Fig. 3-9(a), the toroidal current density profile is shown for an equilibrium with $q(0) = 0.95$, $q(a_p) = 1.9$, $\lambda = 4$, and $a_p = a_w$, which is stable to the (3;2) tearing mode. When the conducting wall is moved away from the plasma, keeping the other equilibrium parameters fixed,

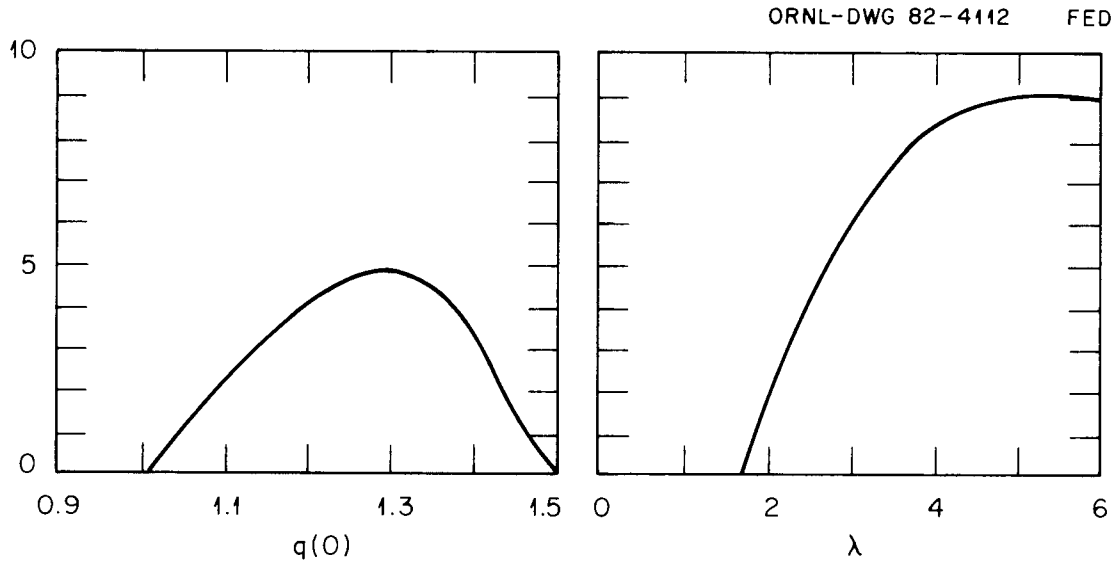

Fig. 3-8. Linear growth rate of the (3;2) tearing mode (a) as a function of q(0) with $\lambda = 2$, $S = 10^5$, and $q(a_p) = 4.1$ and (b) as a function of λ with $q(0) = 1.08$, $S = 10^5$, and $q(a_p) = 4.1$.

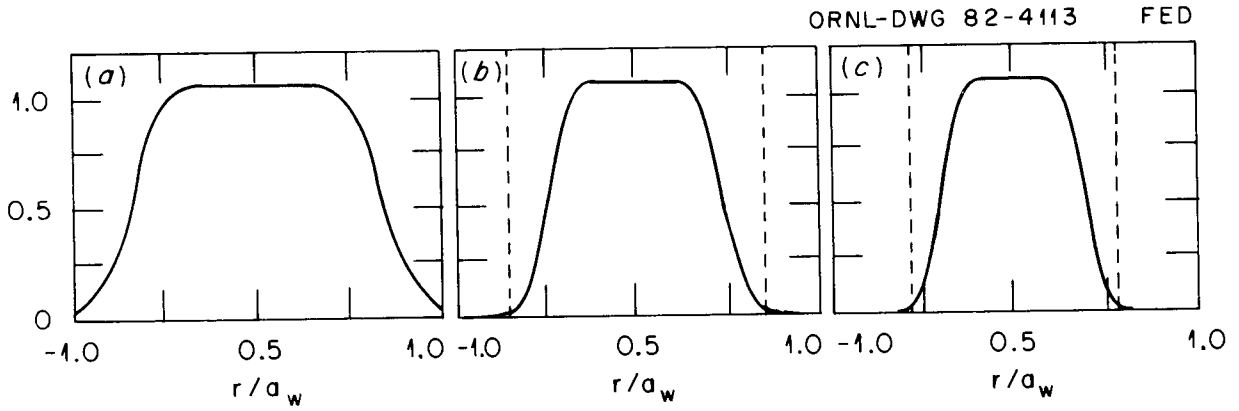

Fig. 3-9. Toroidal current density profile for an equilibrium with $q(0) = 0.95$, $q(a_p) = 1.9$, and $\lambda = 4$ for (a) $a_p = a_w$, (b) $a_p = 0.7a_w$, and (c) $a_p = 0.57a_w$.

the (3;2) mode becomes unstable. When $a_p = 0.7a_w$ [Fig. 3-9(b)], the mode's linear growth rate is $\gamma_{32} = 2.2 \times 10^{-3}\tau_{hp}^{-1}$ for $S = 10^5$, and when $a_p = 0.57a_w$ [Fig. 3-9(c)], $\gamma_{32} = 3.2 \times 10^{-3}\tau_{hp}^{-1}$ for the same value of S. This shows the importance of the wall stabilization effect for the low q discharges and the role of the conducting shell in suppressing these modes.

Toroidal effects can also be important in destabilizing the (3;2) tearing mode. The (2;2) mode, which is generally unstable, could drive the (3;2) mode through toroidal coupling. This has been experimentally observed in Wendelstein VIIA.[38] We are at present investigating the effect of this toroidal coupling.

3.3.2 Effect of Sawtooth Oscillations

The linear stability properties provide some guidance on potential scenarios for disruptions at low q. Through nonlinear, single-helicity calculations we obtain an estimate of the 3/2 island size and therefore an estimate of the possibility of overlapping with other islands. For all equilibria considered, the 3/2 magnetic island width is at most a few percent of the plasma radius, even when the conducting wall is away from the plasma. It never reaches a size comparable to the 2/1 island before a $q(a_p) > 2$ disruption. Therefore, to reach a disruptive situation a further enhancement of the island width is necessary. This could come about through multiple-helicity nonlinear interaction.

The (1;1) tearing mode in its nonlinear evolution causes a sawtooth oscillation[39] that brings q(0) above 1. This suggests that the (1;1) mode could nonlinearly destabilize the (3;2) mode, through quasilinear deformation of the toroidal current profile when q(0) relaxes to 1, and induce a stronger nonlinear interaction between the magnetic islands associated with these modes. We have investigated numerically the plausibility of such a destabilizing mechanism. We have considered an equilibrium stable to the (3;2) tearing mode, with $q(0) = 0.95$, $\lambda = 4$, $q(a_p) = 1.9$, and $a_p = a_w$ [Fig. 3-10(a)]. The nonlinear evolution of the (1;1) tearing mode involves a fast growth of the 1/1 magnetic island to a topology flip and finally to full magnetic field line reconnection

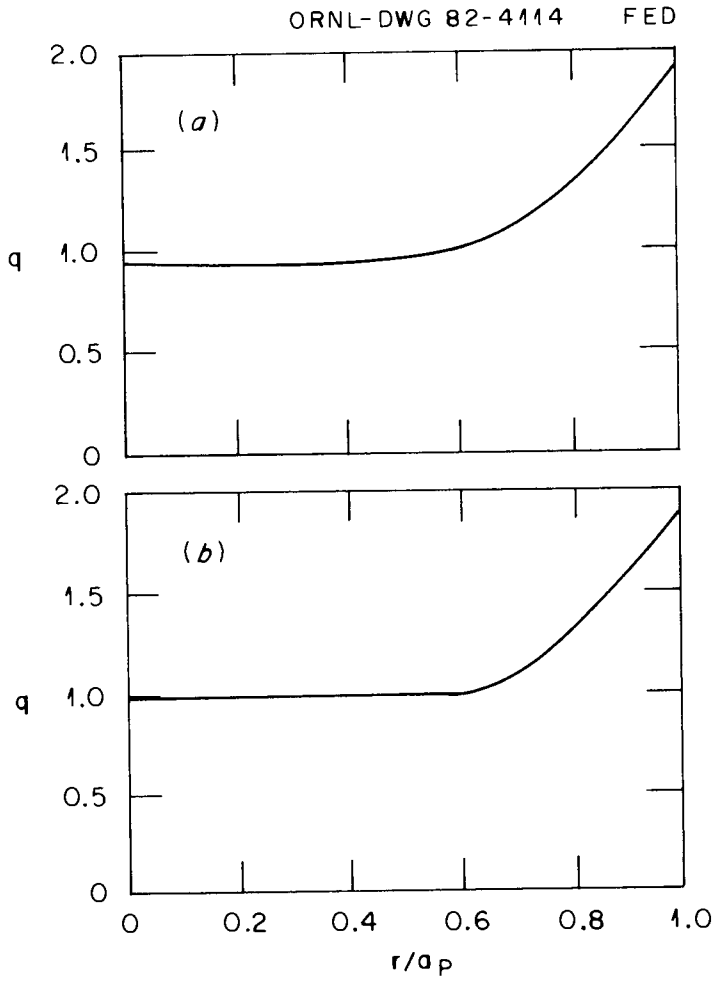

Fig. 3-10. q profile before and after the (1;1) mode nonlinear sawtooth evolution described in the text.

across the plasma center. After reconnection, the q profile is ≥ 1 in the whole plasma [Fig. 3-10(b)]. However, neither the q profile modification nor the nonlinear coupling through modes such as the (4;3) is found to be sufficient to destabilize the (3;2) mode in the calculation.

3.3.3 Conclusions and Future Work

From the present results we can conclude that the presence of a conducting shell near the plasma can play an important role in suppressing the (3;2) mode and hence in decreasing the chances of major disruptions for $q(a_p) < 2$ tokamak plasmas as long as $q(a_p) > 1.5$. Even without a conducting shell, the probability of disruption via the (3;2) tearing mode with $q(a_p) < 2$ appears to be smaller than with $q(a_p) > 2$. However, further work must be done to complete our understanding of stability for such plasmas: (1) multiple-helicity calculations with the conducting wall away from the plasma and (2) the extension of such calculations to toroidal geometry.

To complete our understanding of low q disruptions, we must also modify the present codes to include a nearby vacuum region surrounding the plasma. This will make it possible to study the case in which the $q = 2$ surface is between the plasma edge and the conducting wall and to address the possible problems of transition into the low q regime.

3.4 IDEAL MHD STABILITY LIMITS AT LOW q_ψ

D. J. Strickler, Y-K. M. Peng (FEDC/ORNL)

The projected performance of FED-A (Sect. 3.5) is based largely on the assumption that a nearby highly conducting first wall will allow a value of q_ψ as low as 1.8 through avoidance of plasma disruptions when q_ψ is decreased through 2. Such a wall has also been shown to cause ideal MHD limits on plasma beta to be set by pressure-driven (high n) modes through a stabilizing influence on low n and axisymmetric modes.

There exist theoretical and experimental studies suggesting that the ideal MHD approach to beta limits may be pessimistic. Data from the Impurity Study Experiment (ISX-B) indicate that the achieved limits are

more closely correlated with the quantity $\varepsilon\beta_p$ [$\varepsilon = a/R_o$, $\beta_p = 8\pi\langle p\rangle / B_p(a)^2$] than with $\langle\beta\rangle$ ($\langle\beta\rangle = 8\pi\langle p\rangle/B_t^2$), and beta limits quoted from the literature[40] have been surpassed in this tokamak. Recent theoretical work, however, shows that beta limits with respect to ballooning modes in tokamaks improve when energetic ions are present and finite Larmor radius effects are included, and this has been offered as a possible explanation of ISX-B observations.[41] Although it is difficult to quantify this work as it applies to FED-A, it may enhance ideal beta limits by as much as 20-30% (Ref. 42). Also recently, it was shown[43] that pressure profile modifications could substantially alter high n, stable beta limits (by >40% in D-shaped FED equilibria) for otherwise fixed parameters. More recently, an approximate formula for the beta limit in low q cases with optimized profiles has been proposed:

$$\langle\beta\rangle \cong \frac{0.25}{Aq_\psi}\,\frac{1+\kappa^2}{2}\,, \tag{3-8}$$

which appears consistent with recent experimental indications (e.g., PDX, D-III, and ISX-B) and ideal MHD stability calculations (e.g., PEST code). In this section, we apply pressure profiles similar to those optimized for FED equilibria in estimating an ideal MHD beta threshold for the FED-A plasma with a mild elongation of 1.2 and a relatively large aspect ratio of 4.6.

3.4.1 Previous Low q_ψ Calculations

The stabilizing influence of low values of q_ψ and a flat q profile on high n, ideal ballooning modes has been demonstrated in several studies. In the work of Charlton et al.[44] a conducting wall at a radius 20% greater than the plasma minor radius sufficiently stabilized external kink modes so that threshold values of $\langle\beta\rangle$ with respect to all ideal MHD mode numbers were defined largely by $n = \infty$, which is also shown to improve with decreasing q. Similar results had been obtained by Todd et al.,[40] whose q dependence calculations were carried out using a geometry roughly the same as FED-A (i.e., a circular plasma with aspect

ratio A = 4.6) with limiting values of $\langle\beta\rangle$ for $q_\psi < 2$ of about 2% without profile optimization. By further optimizing equilibria through flattening and raising the q profile (i.e., $q_o > 1$, where q_o is the value of q at the magnetic axis) while holding the pressure profile fixed, Cooper[45] has obtained circular equilibria in ISX-B geometry (A = 3.4) that are stable to ideal ballooning modes at $\langle\beta\rangle > 4\%$. However, these equilibria tend to have a hollow current profile.

In general, if high n modes are a limiting factor in the performance of FED-A plasmas, as may be implied by the presence of a close and highly conducting first wall, the low value of q_ψ serves to compensate for what is lost (in theory) through a near-circular plasma cross section and moderately high aspect ratio.

3.4.2 Ideal Stability Limit in FED-A

Equilibria with representative FED-A parameters (i.e., R_o = 4.22 m, a = 0.92 m, B_t = 5.0 T, κ = 1.2) and monotonically increasing q profiles with boundary values of q_o = 1.0 and q_ψ = 1.8 (Fig. 3-11) were tested for high n, ideal MHD stability using the General Atomic MBC code.[46] Equilibrium A (Fig. 3-12) was generated using a pressure profile P(x) with a one-parameter exponential dependence on the normalized poloidal flux $x = (\psi - \psi_o)/(\psi_L - \psi_o)$ as an integral of

$$\frac{dP}{dx} = A \frac{e^{-\alpha x} - e^{-\alpha}}{1 - e^{-\alpha}}, \quad P(1) = 0 . \tag{3-9}$$

For $\langle\beta\rangle$ = 2.9%, β_p = 1.2, this equilibrium exhibits an annular region of high n instability, consistent with results from the literature mentioned above.

Following the analysis of Ref. 43, equilibria with pressure profiles of the form

$$\frac{dP}{dx} = A[e^{-\alpha(1-x)} - 1] + B(e^{-\gamma} - e^{-\gamma x}) \tag{3-10}$$

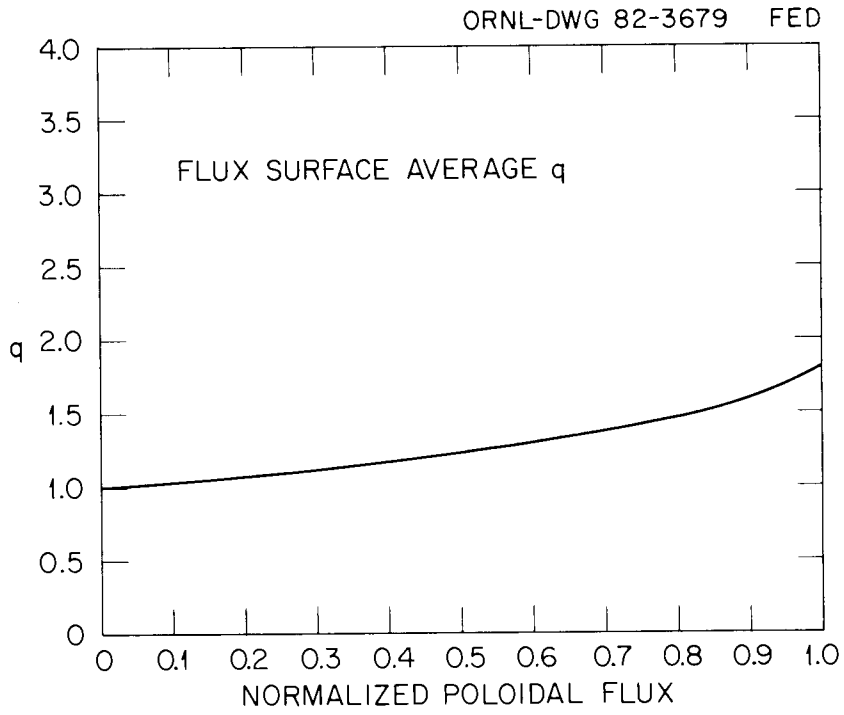

Fig. 3-11. $q(\psi)$ profile for FED-A equilibria tested for high n, ideal MHD stability.

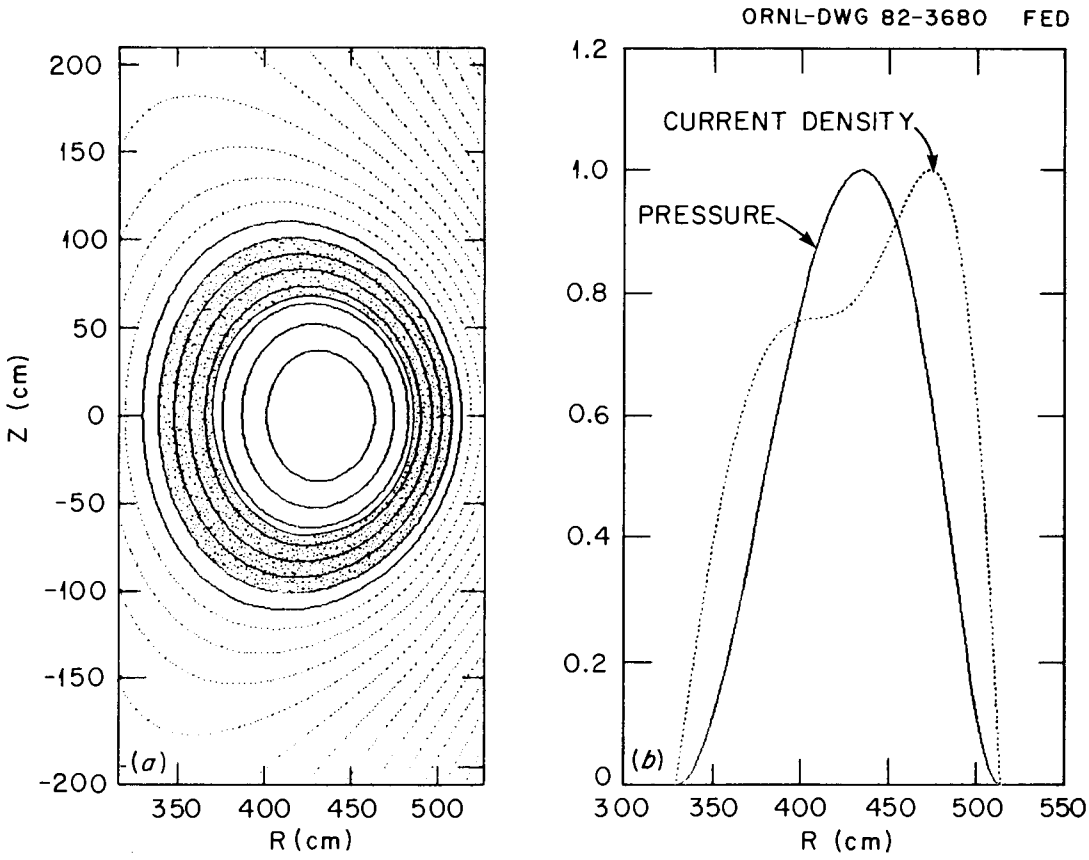

Fig. 3-12. Equilibrium A exhibits (a) an annular region of instability for $\langle\beta\rangle$ = 2.9%, β_p = 1.2, using (b) the pressure profiles based on Eq. (3-9).

and carefully chosen parameters tend to follow closely the boundary of the region of instability (i.e., the contour of marginal stability) in the shear ($s = d\ \ell n\ q / d\ \ell n\ \rho$) and pressure ($dP/d\psi$) derivatives and in general give higher stable beta values for a given q profile. Equilibrium B (Fig. 3-13), with a pressure profile of the form in Eq. (3-10), is found to be stable to ballooning modes at $\langle\beta\rangle = 3.2\%$ and $\beta_p = 1.4$, a substantial improvement ($\sim$50%) over limits using single-parameter profiles. The eigenvalues of the second-order ordinary differential equation for $n = \infty$ stability,[47] negative for unstable flux surfaces, are shown in Fig. 3-14 for equilibria A and B.

Both equilibria have broad current profiles with steep gradients at the outer edge of the plasma, but equilibrium B more clearly displays a "shoulder" on the large major radius side (i.e., less outward shift of the current peak), qualitatively consistent with recent marginally stable equilibria optimized with respect to reproducing diagnostic data from high beta ISX-B experiments.[48] The ISX-B analysis suggests that the improved pressure profile of Eq. (3-10) is the more realistic representation. The conclusion is that for FED-A equilibria with $\kappa = 1.2$, the beta threshold set by ideal pressure-driven MHD modes appears to be $\langle\beta\rangle \cong 3.2\%$.

This value is significantly lower than the reference value of $\langle\beta\rangle = 6\%$ (see Table 5-15). However, several factors can be invoked to increase $\langle\beta\rangle$. First, the theoretical limits are almost certainly pessimistic, in that they neglect finite gyration radius and other nonideal effects that are strongly stabilizing for high n modes. Second, it is probable that the optimum q profile has not been found. For example, operation with $q(0) < 1$ should be favorable for ballooning stability, provided the internal sawteeth can be tolerated. A further decrease in q_ψ would be beneficial, as would a decrease in aspect ratio and, of course, an increase in elongation beyond 1.2. The impact of varying κ, A, or q_ψ on the FED-A concept is presented in Chap. 5.

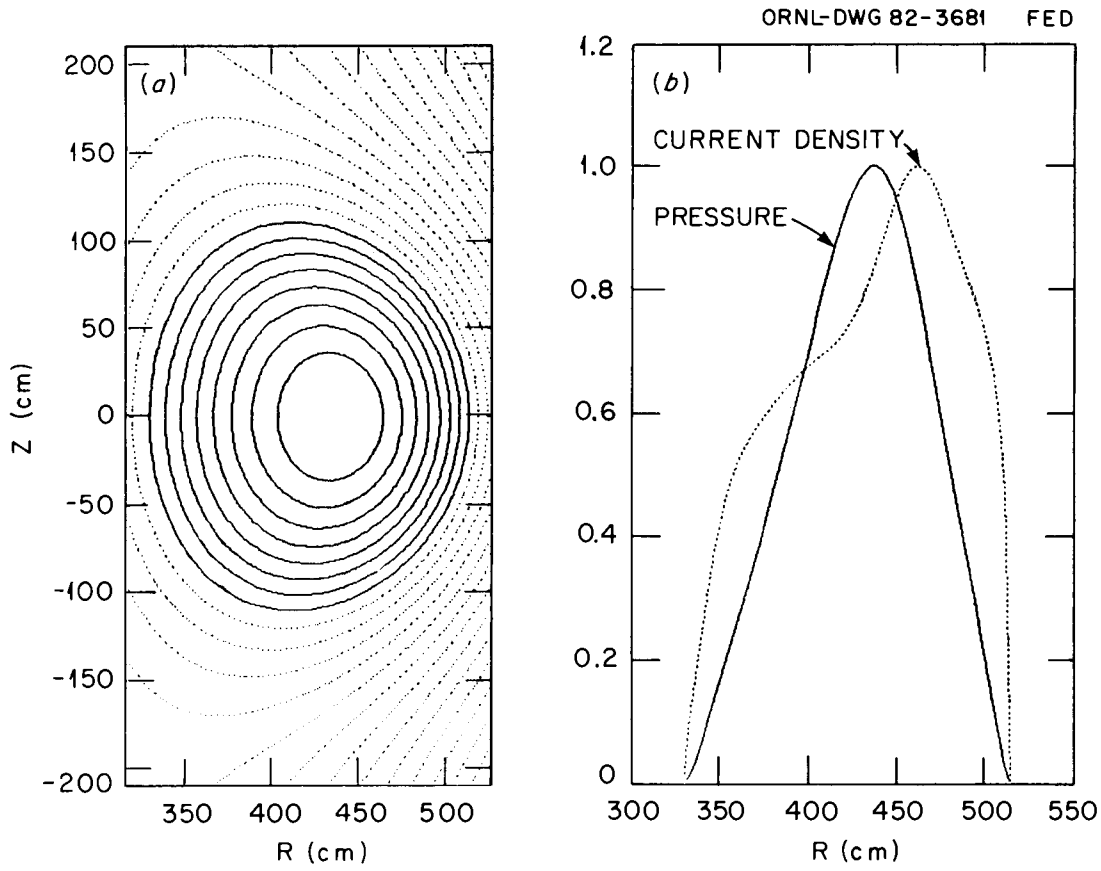

Fig. 3-13. Equilibrium B is found to be stable to ballooning modes for $\langle\beta\rangle$ = 3.2%, β_p = 1.4. Shown are (a) poloidal flux surfaces using (b) the pressure profile of Eq. (3-10).

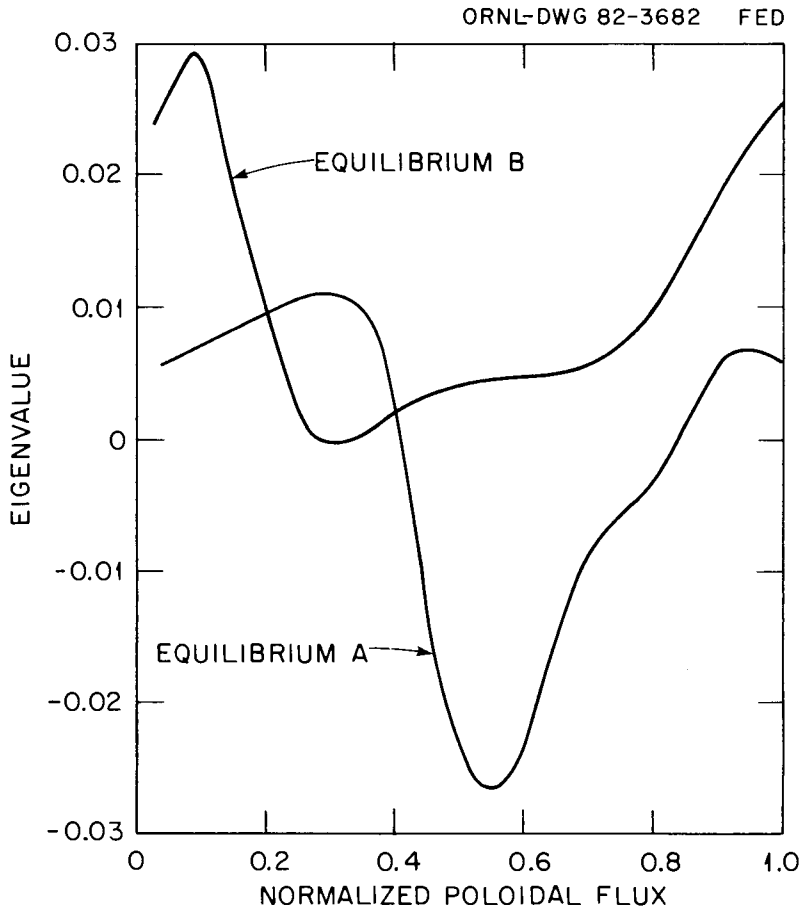

Fig. 3-14. Eigenvalues of the differential equation for n = ∞ stability, negative for unstable flux surfaces, are shown for equilibria A and B.

3.5 PLASMA PERFORMANCE ESTIMATES

W. A. Houlberg (ORNL), S. E. Attenberger (ORNL), L. M. Hively (FEDC/GE)

Transport calculations have been carried out for the FED-A concept to assess its performance and sensitivity to plasma current, losses induced by toroidal field ripple, radial diffusion of the fast alpha particles, prompt loss of alpha particles born on banana-trapped orbits, and finite-beta-induced electron conduction losses. The POPCON option in the 1-1/2-D WHIST transport code[49] is used for these assessments with a model heating profile to simulate heating in the ion cyclotron range of frequencies (ICRF). The toroidal field ripple contours were obtained from the FED-A toroidal field (TF) coil design. Ripple conduction losses include ripple-trapped particles in both the collisional and collisionless detrapping regimes and three regimes of banana-trapped particles. A multienergy group model is used for radial diffusion of the fast alpha particles and coupled with a classical model for collisional energy relaxation on the background electrons and ions. Since toroidal field ripple may lead to the loss of all banana-trapped alpha particles, an approximate assessment of this potential loss was made for the FED-A design by reducing the alpha heating by the fraction of particles born on trapped orbits. Finite-beta-induced transport is evaluated with the Carreras-Diamond resistive pressure-driven model with enhanced transport inside the $q = 1$ region, which has had success in modeling ISX-B high β_p results. It is found that the operating characteristics of FED-A are sensitive to these issues, especially the enhanced transport within the $q = 1$ region.

3.5.1 Baseline Performance and Sensitivity to Plasma Current

In Fig. 3-15 the contours of constant toroidal field ripple (peak-to-average) for FED-A, calculated with the BARC13 code[50] assuming a uniform current density in the 12 TF coils, are shown superimposed on the flux surfaces for a low beta ($<\beta_T> \cong 1.7\%$) MHD equilibrium. In these calculations, the major radius is $R_o = 422$ cm, minor radius in the midplane $a = 92$ cm, elongation $\kappa = 1.2$, triangularity $\delta = 0.1$, vacuum

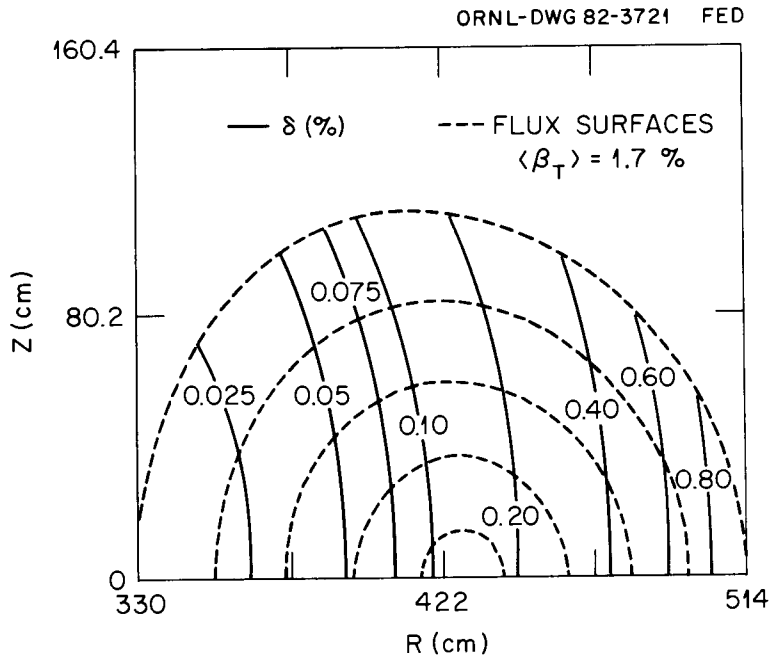

Fig. 3-15. Peak-to-average ripple contours for FED-A with δ_a = 1.0% and q_a = 1.8.

toroidal field at the chamber center $B_T = 4.98$ T, and safety factor at the plasma edge $q_\psi(a) = 1.8$. A 15-cm scrape-off layer in the midplane extending into a toroidal limiter is included in the transport calculations. The ripple at the outside edge is $\delta_a \cong 1\%$; at the magnetic axis, $\delta_m \cong 0.15\%$. At higher beta the magnetic axis shifts outward and the ripple increases; for example, at $\langle\beta_T\rangle \cong 6.2\%$, $R_m \cong 442$ cm, and $\delta_m \cong 0.18\%$. The increase in ripple with increasing beta is automatically accounted for by flux surface averages of the ripple loss terms using a data set for $\delta(R,Z)$ and the time evolution of the axisymmetric MHD equilibrium.

The baseline performance was determined using the reference INTOR model for transport, that is, three times neoclassical[51] plus anomalous contributions to electron conduction and particle diffusion, given by

$$\chi_e^{an} = 5D^{an} = \frac{5 \times 10^{17}}{n_e\ (cm^{-3})}\ (cm^2/s)\ .$$

Thermal conduction due to toroidal field ripple was added to the ion energy transport using the same models Hastie and Hitchon applied to INTOR:[52]

$$Q_i^{ripple} = Q^{RP} + Q^{BD1} + Q^{BD2} + Q^{RT} + Q^{H}$$

$$Q^{RP} = -Q_1 \int_{u_0}^{u_1} A(u) e^{-u} u^3 du \qquad Q^{BD1} = -Q_1 \int_{u_1}^{u_2} A(u) e^{-u} u^5/u_1^2 du$$

$$Q^{BD2} = -Q_1 \int_{u_2}^{\infty} A(u) e^{-u} u_2^5/u_1^2 du \qquad Q^{RT} = -Q_2 \int_{u_t}^{u_3} A(u) e^{-u} u^5 du$$

$$Q^{H} = Q_2 \int_{u_3}^{\infty} A(u) e^{-u} u_3^5 du \qquad Q_1 = \frac{\delta_o^2}{4\sqrt{2}} \frac{N_c}{R_o} v_{ti} \rho_{\theta i}^2 n_i T_i'$$

$$Q_2 = 0.33\delta_o^{3/2} G(\alpha) \frac{v_{ti}^2 \rho_i^2}{R_o^2 \nu_{ti}} n_i T_i' \qquad A(u) = \frac{n_i' T_i}{n_i T_i'} + \frac{e\phi'}{kT_i'} + u - \frac{3}{2}$$

$$u_0^2 = \frac{1.75\sqrt{\pi}\nu_{ti}}{\nu_*} \qquad u_1^2 = \frac{1.5\sqrt{\pi}\nu_{ti} N_c^2 q^2}{\nu_*}$$

$$u_2^5 = \left(\frac{0.4\sqrt{\pi}\nu_{ti} N_c q R_o B_T}{c\phi'}\right)^2 \qquad u_t^2 = u_0^2 \left(\frac{\varepsilon}{\delta_o}\right)^{3/2} \frac{1}{N_c q}$$

$$u_3^5 = \left(\frac{\sqrt{3N_c}\, q \nu_{ti} R_o^2}{v_{ti} \rho_i}\right)^2 \qquad v_{ti} = \left(\frac{kT_i}{m_i}\right)^{1/2}$$

$$\nu_{ti} = \frac{4\sqrt{2\pi}}{3} \frac{n_i e^4 \ell n\, \Lambda}{\sqrt{m_i}(kT_i)^{3/2}} \qquad \nu_* = \frac{\varepsilon^{3/2} \nu_{ti}}{R_o q}$$

In this scheme, Q^{RP} represents the ion heat flux due to ripple-plateau diffusion,[53] Q^{BD1} and Q^{BD2} are the high and low collisionality regimes, respectively, of banana-drift diffusion,[54-56] Q^{RT} is the collisional regime of ripple-trapped diffusion,[57,58] and Q^{H} is the collisionless detrapping regime of ripple-trapped diffusion.[59,60] The radial electric field parameter,

$$\xi = \frac{e\phi'}{kT'} ,$$

was set to $\xi = 0$ in the following calculations except in the evaluation of u_2, where $\xi = 1$ was used to prevent nonphysically large values of Q^{BD1} (Ref. 52).

The auxiliary power contours for the FED-A baseline are shown in Fig. 3-16. The heating profile was taken to be a Gaussian, $H(p) \propto \exp[-2\rho/a_o)^2]$, with 50% of the power delivered to the ions. Ignition occurs for $\langle n \rangle \geq 1.25 \times 10^{14}$ cm^{-3}, with thermally stable ignited operation

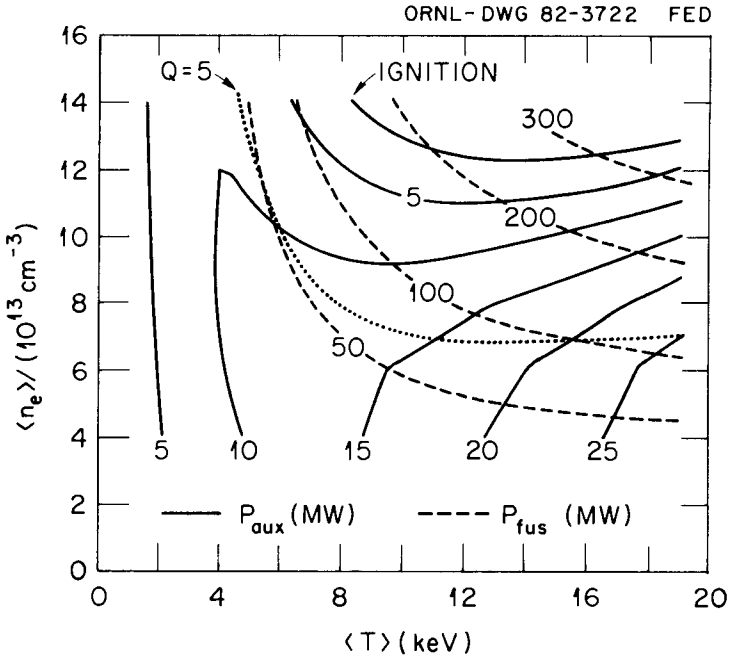

Fig. 3-16. Auxiliary heating and fusion power contours with a Gaussian source for FED-A with the reference transport model and q_a = 1.8. Also shown is the Q = 5 contour.

yielding a power output in excess of 250 MW. Also shown is the Q = 5 contour, which can be reached with densities as low as $\langle n \rangle = 7.0 \times 10^{13}$ cm^{-3}. The corresponding average toroidal and poloidal beta contours are shown in Fig. 3-17.

The ripple conduction losses are dominated by the ripple-trapped (Q^{RT}) and collisionless detrapping (Q^{H}) contributions. The spatial region in which local ripple wells exist, $\alpha^* < 1$, evolves from low beta to high beta as shown in Fig. 3-18, where

$$\alpha^* = \frac{RB(\vec{B}_p \cdot \vec{\nabla}B)}{N_c \delta(R,Z) B_T^3}$$

is calculated from the superposition of the ripple component of the toroidal field onto the axisymmetric field determined from the solution of the Grad-Shafranov equation.[61] B_T and B_P represent the local toroidal and poloidal components, respectively, of the axisymmetric field, and $B = |B|$. The collisionless detrapping term is limited by two approximations that tend to overestimate the conduction losses. First, the height of the ripple-trapped region is assumed to be small compared to the plasma radius; this breaks down at both the axis and the edge. The second approximation is the neglect of the impact of the radial electric field on the drift orbits.[60] Combining these two effects may reduce the thermal losses by a factor of 2.

In Fig. 3-19, the auxiliary power contours and the Q = 5 contour are shown for a case in which the plasma current is reduced so that $q_\psi(a_o) = 2.2$. The major reason for the reduced operating performance is the increased ripple conduction losses. Although the Q = 5 contour is not changed significantly, ignition is no longer in the potential operating range. In both the INTOR and FED designs a greater tolerance to ripple losses is found when current is reduced, principally because of the larger machine sizes.

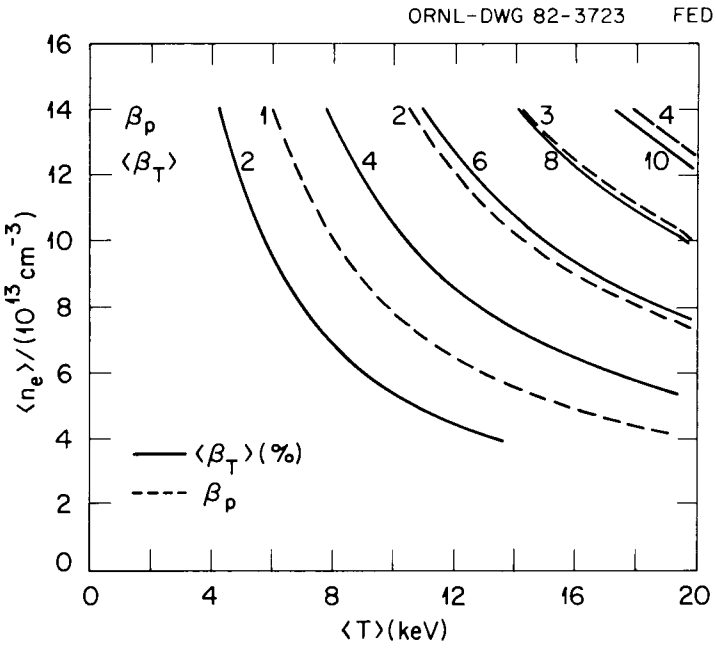

Fig. 3-17. Average toroidal and poloidal beta contours for FED-A with the reference transport model.

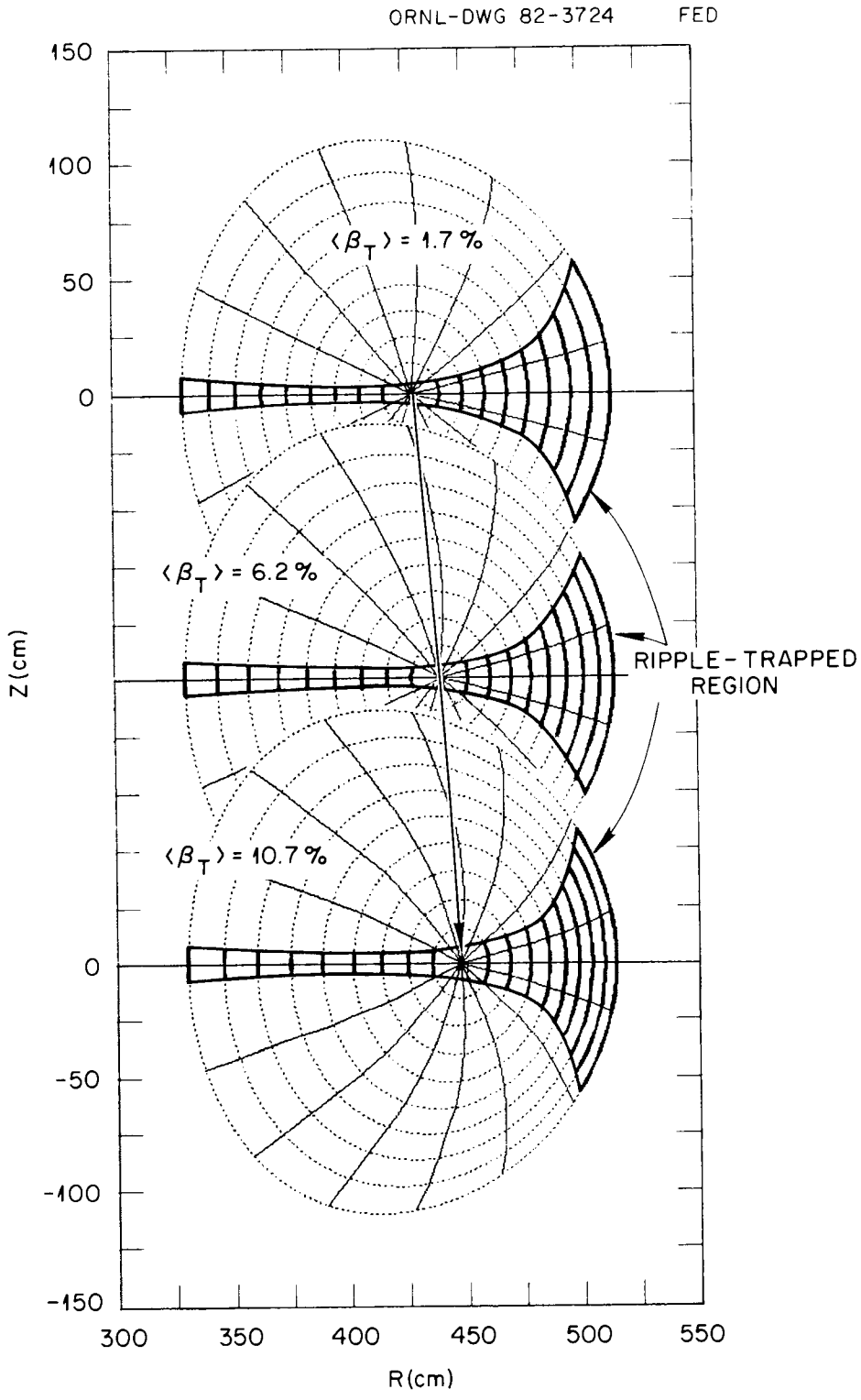

Fig. 3-18. Evolution of the ripple-trapping region ($\alpha^* < 1$) in FED-A with $q_a = 1.8$ as average beta increases.

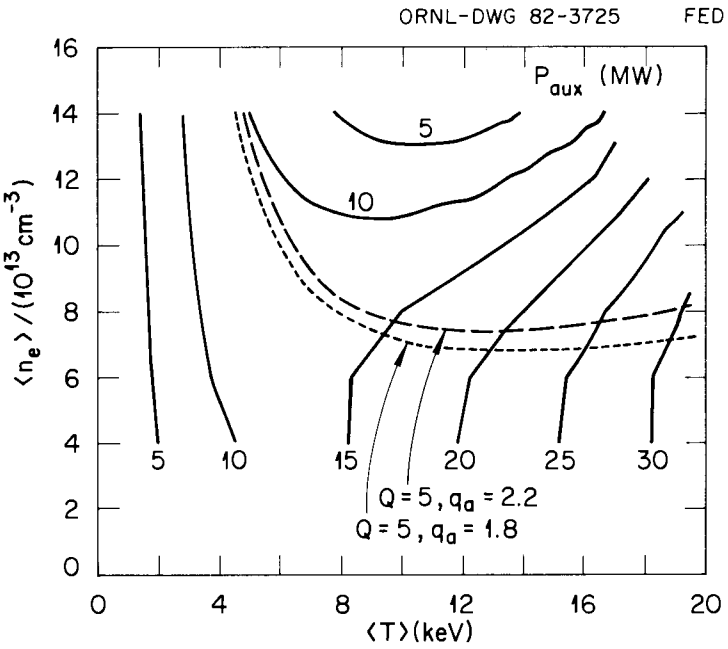

Fig. 3-19. Auxiliary heating power contours with a Gaussian source for FED-A with q_a = 2.2. Also shown are the Q = 5 contours for q_a = 2.2 and 1.8.

3.5.2 Sensitivity to Alpha Heating Dynamics

One area of physics for reactor plasmas that is generally not investigated in depth is the alpha heating process. Standard calculations, as in the baseline calculations of Sect. 3.5.1, include local thermalization with Coulomb collisions determining the division of power between electrons and ions. Radial diffusion of the fast alpha particles during thermalization can be an important consideration in assessing fusion reactor performance. Classical thermalization leads to a fast alpha density profile, $n_{f\alpha}$, which is strongly peaked on axis because the source profile, $S_\alpha \propto n^2\langle\sigma v\rangle$, and the thermalization (slowing-down) time, $\tau_{SD} \propto T^{3/2}/n$, both increase toward the plasma center, and $n_{f\alpha} \propto S_\alpha \tau_{SD}$. Even a small radial diffusion coefficient, when combined with the large gradients of $n_{f\alpha}$ in the plasma core, can produce a significant radial flux and broaden the heating profile.

A multienergy group radial diffusion model for the fast alphas can be coupled to the usual set of fluid transport equations to examine the sensitivity to diffusion. Letting $n_{\alpha j}$ designate the fast alpha density in energy group j and neglecting upscattering events, the continuity equations for the highest (j = 1) and lower (j ⩾ 2) energy groups can be written as[62]

$$\frac{\partial n_{\alpha 1}}{\partial t} = - \frac{1}{V'(\rho)} \frac{\partial}{\partial \rho} [V'(\rho)\tilde{\Gamma}_{\alpha 1}(\rho)] + n_D n_T \langle\sigma v\rangle_{DT} - \frac{n_{\alpha 1}}{\tau_{s1}} ,$$

$$\frac{\partial n_{\alpha j}}{\partial t} = - \frac{1}{V'(\rho)} \frac{\partial}{\partial \rho} [V'(\rho)\tilde{\Gamma}_{\alpha j}(\rho)] + \frac{n_{\alpha j-1}}{\tau_{sj-1}} - \frac{n_{\alpha j}}{\tau_{sj}} .$$

For collisional energy relaxation the downscattering time from group j to group j + 1, τ_{sj}, is only a function of the background plasma parameters and the energy interval around E_j; that is, interactions between fast alpha particles can be neglected:

$$\tau_{sj} = \frac{\tau_{so}}{3} \ln\left[\frac{1 + (E_{j-1/2}/E_c)^{3/2}}{1 + (E_{j+1/2}/E_c)^{3/2}}\right] ,$$

where τ_{so} is the characteristic energy relaxation time on electrons and E_c is the critical energy at which energy relaxation on electrons and ions is equal.[63] The simplest form for the particle flux is to assume that the main driving term for $\tilde{\Gamma}_{\alpha j}$ is the density gradient for that energy group; then,

$$\tilde{\Gamma}_{\alpha j} = -D_{\alpha j}\left\langle |\nabla\rho|^2 \right\rangle \frac{\partial n_{\alpha j}}{\partial \rho} .$$

This form should be valid for physical models in which the magnetic geometry or background plasma is responsible for the diffusion.

In Fig. 3-20 we show the effect of increasing $D_{\alpha j} = D_{\alpha o}$ on the $Q \geq 5$ region for FED-A. For comparison, the particle diffusion coefficient for thermal ions in existing experiments is about 5000 cm^2/s. In recent calculations for INTOR, Yushmanov[64] showed that diffusion of fast banana-trapped alpha particles in a toroidal field with $\sim$1% ripple can lead to diffusion coefficients much larger than those considered in Fig. 3-20.

An estimate of the maximum loss of heating due to loss of banana-trapped alpha particles can be made by reducing the source of fast alphas by the fraction of alpha particles born on trapped orbits (i.e., a "prompt" loss). The source of fast alphas should be uniform on a flux surface and have an isotropic distribution. Then the trapped fraction of all alphas born on a flux surface is just the flux surface average of the local fraction,

$$f_T = \left\langle (1 - |B|/|B|_{max})^{1/2} \right\rangle_f ,$$

where $|B(R,Z)|$ is determined from the MHD equilibrium. As beta increases, two effects can reduce f_T by as much as 50%. First, the increasing

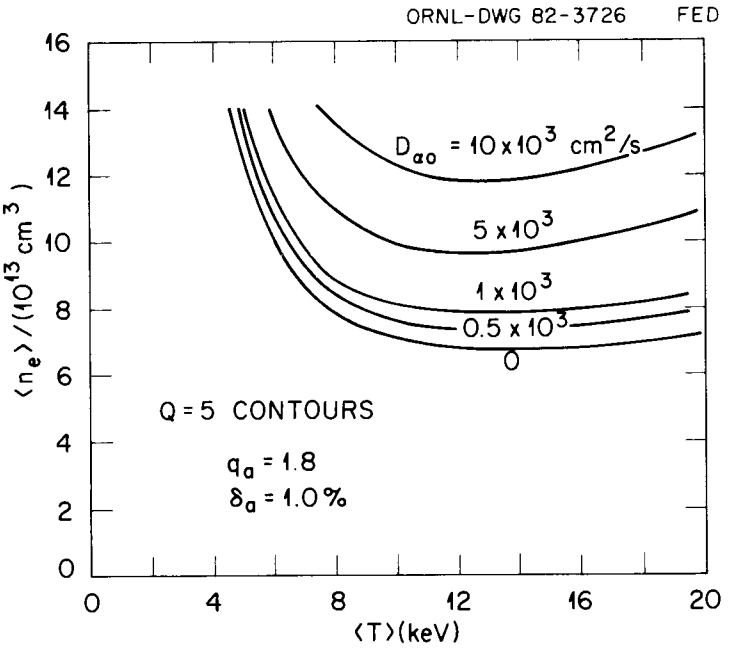

Fig. 3-20. The effect of increased fast alpha diffusion on the Q = 5 contour in FED-A with q_a = 1.8 and the reference transport model.

poloidal contribution to $|B|$ on the outside of the plasma reduces the variation in $|B|$ from the outside to inside; second, the decreasing plasma volume on the outside relative to the inside shifts the flux surface weighting away from where most trapped particles are born. For $\langle n \rangle = 1.2 \times 10^{14}$ cm^{-3} and $\langle T \rangle = 10$ keV, about 20% of the alphas are born on trapped orbits with the effect on the auxiliary power contours shown in Fig. 3-21. Pitch angle scattering into the trapped region could result in an additional energy loss.

3.5.3 Finite-Beta-Induced Transport

ISX-B results have shown a degradation in electron energy confinement with increasing poloidal beta. A model for this enhanced transport has been derived by Carreras et al.,[65] based on resistive pressure-driven modes, although extension to plasma parameters in the reactor regime is subject to several uncertainties. In applications to ISX-B results it was found that the best fit consisted of a component of χ_e valid at low beta (about half the usual INTOR model) added to a finite beta component (twice the Carreras-Diamond theoretical result),[66]

$$\chi_e = 0.5\chi_e^{an} + 2\chi_e^{CD} ,$$

where

$$\chi_e^{CD} = 3.0 \times 10^{13} \left[\frac{A_i n_e(0) \times 10^{-13}}{T_e(\rho)}\right]^{1/2} \frac{Z_{eff}}{I_a} \frac{q(\rho)}{q(a)}$$

$$\times \frac{R_o}{(a/R_o)^{1/2}} \left[\frac{\beta_o q^2(\rho)}{SL_p}\right]^{3/2} \text{cm}^2/\text{s} ,$$

and

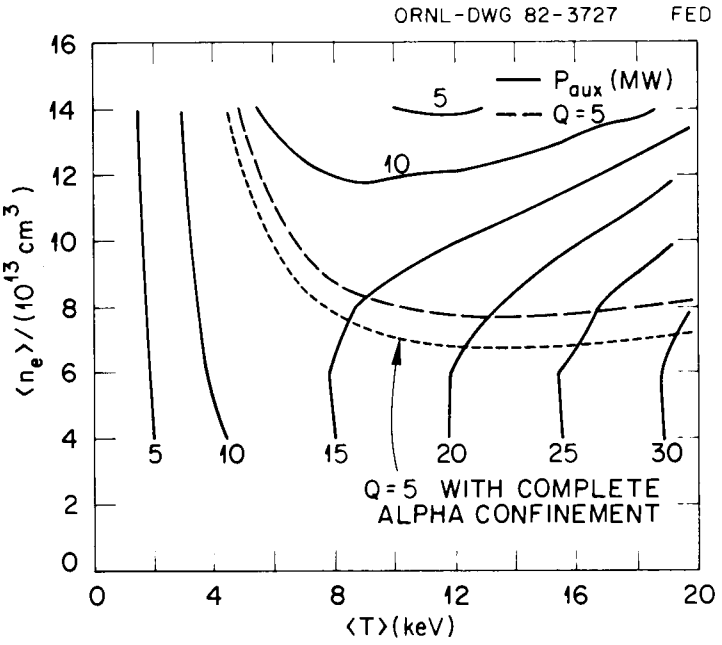

Fig. 3-21. Auxiliary heating power contours with a Gaussian source and q_a = 1.8 for FED-A, where the heating contribution from all alpha particles born on banana-trapped orbits has been removed. The Q = 5 contour with heating from the trapped alphas is also shown.

$$\beta_o = \frac{P(0)}{B^2/2\mu_o} ,$$

$$S = \frac{\rho}{q(\rho)} \frac{\partial q}{\partial \rho} ,$$

$$L_p = -\left[\frac{1}{P(0)} \frac{\partial P(\rho)}{\partial \rho} \right]^{-1} ,$$

A_i is the ion mass in units of the proton mass, and other units are expressed in centimeters, electron volts, values per cubic centimeter, and amperes. In addition, the transport coefficients must be enhanced inside the q = 1 region to simulate the effects of sawtooth activity.

Applying this model to FED-A, we get the results shown in Fig. 3-22, where the Q = 5 contour is illustrated for several cases. The best results are for the base case, where it was assumed that there was no enhanced transport inside the q = 1 region and no beta-enhanced transport. Reducing the baseline electron conduction losses by a factor of 2 and adding both of the MHD contributions while maintaining $q_a = 1.8$ pushes the q = 5 contour to near $\bar{n} = 1.4 \times 10^{14}$ cm^{-3} and $\bar{T} = 16$ keV. The major contributions to this enhanced transport are the assumed model for the enhanced transport inside q = 1 and the calculated size of the $q \leqslant 1$ region, but not the resistive pressure-driven contribution. Dropping the resistive pressure-driven contribution only lowers the Q = 5 contour to $\bar{n} \cong 1.2 \times 10^{14}$ cm^{-3}. This domination can also be seen in the intermediate Q = 5 contour, where q_a is raised to 2.2 and net confinement improves due to the reduction of the size of the q = 1 region even though the resistive pressure-driven contribution increases transport losses. Both of these MHD effects need further analysis before definitive conclusions are drawn about their impact on performance of machines with parameters similar to FED-A because of the low q_a and low resistivity. This analysis only serves as a further illustration that MHD-enhanced transport effects may play a critical role in reactor performance.

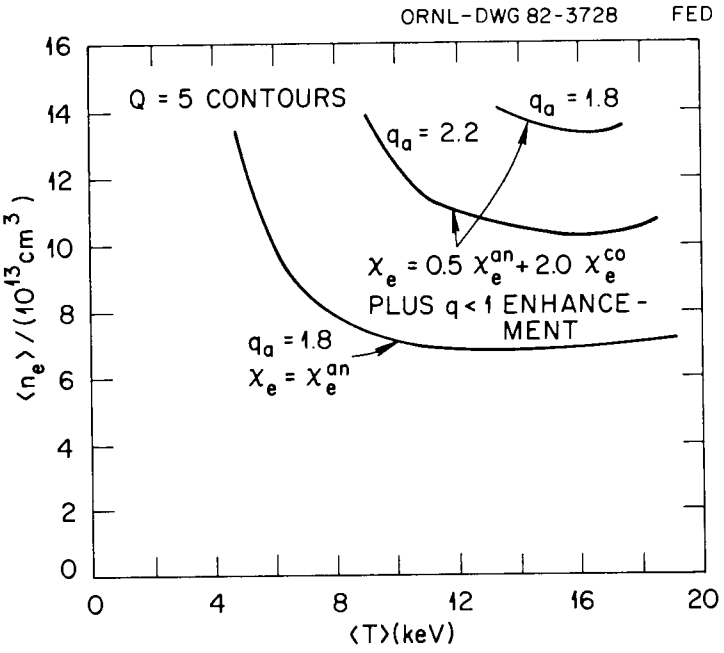

Fig. 3-22. Q = 5 contours for FED-A showing the effects of MHD-induced transport due to m = 1 activity and pressure-driven resistive modes.

3.5.4 Summary

Assuming the capability of low q_ψ ($\geq$1.8) and high $\langle\beta\rangle$ ($\leq$6%) operations in FED-A, its potential performance ranges have been assessed using the POPCON approach. It is found that, assuming an INTOR type of scaling, performance is not strongly degraded by toroidal field ripple-enhanced transport of either the bulk ions or the fusion alpha particles, although ignition may no longer be accessible in FED-A. When the safety factor is increased to 2.2, a relatively modest degradation is again indicated. The most serious potential impact on performance is found to result from the enhanced plasma transport within the q_ψ = 1 surface when it extends to large values of minor plasma radius. Further analysis is needed in this area.

REFERENCES

1. V. S. Strelkov, in *Proceedings of the 5th European Conference on Controlled Fusion and Plasma Physics, Grenoble, 1975.*
2. DIVA Group, Nucl. Fusion 20, 271 (1980).
3. J. Wesson, Nucl. Fusion 18, 87 (1978).
4. B. Carreras et al., Phys. Fluids 23, 1811 (1980).
5. D. Monticello and R. White, PPPL-1674, Princeton Plasma Physics Lab., Princeton, N.J., July 1980.
6. ASDEX Group, in *Proceedings of the 5th International Conference on Plasma-Surface Interactions, Gatlinburg, Tennessee, 1982.*
7. DITE Group, D. Goodall, presenter, in *Proceedings of the 5th International Conference on Plasma-Surface Interactions, Gatlinburg, Tennessee, 1982.*
8. R. Clausing, in *Proceedings of the 5th International Conference on Plasma-Surface Interactions, Gatlinburg, Tennessee, 1982.*
9. K. Toi et al., Nucl. Fusion 22, 465 (1982).
10. T. Edlington et al., paper IAEA-CN-41/S2 presented at the 9th International Conference on Plasma Physics and Controlled Nuclear Fusion Research, Baltimore, September 1982; to be published in the proceedings.
11. Z. Yoshida et al., paper IAEA-CN-41/S5 presented at the 9th International Conference on Plasma Physics and Controlled Nuclear Fusion Research, Baltimore, September 1982; to be published in the proceedings.
12. R. Fonck and the PDX Group, in *Proceedings of the 5th International Conference on Plasma-Surface Interactions, Gatlinburg, Tennessee, 1982.*
13. S. Mirnov, Sov. Phys.-JETP 12, 65 (1970).
14. B. A. Carreras et al., paper IAEA-CN-41/P4 presented at the 9th International Conference on Plasma Physics and Controlled Nuclear Fusion Research, Baltimore, September 1982; to be published in the proceedings.

15. T. Ohkawa and the D-III Groups, paper IAEA-CN-41/A2 presented at the 9th International Conference on Plasma Physics and Controlled Nuclear Fusion Research, Baltimore, September 1982; to be published in the proceedings.

16. H. P. Furth, P. H. Rutherford, and H. Selberg, Phys. Fluids 16, 1054 (1973).

17. A. H. Glasser, H. P. Furth, and P. H. Rutherford, Phys. Rev. Lett. 38, 234 (1977).

18. S. von Goeler, W. Stodiek, and N. Sauthoff, Phys. Rev. Lett. 33, 1201 (1974).

19. B. B. Kadomtsev, Fiz. Plazmy 1, 710 (1975).

20. R. B. White, D. A. Monticello, M. N. Rosenbluth, and B. V. Waddell, in *Plasma Physics and Controlled Nuclear Fusion Research. Proceedings of the 6th International Conference, Berchtesgaden, 1976*, Vol. 1, Int. Atomic Energy Agency, Vienna, 1977, p. 569.

21. P. H. Rutherford, Phys. Fluids 16, 1903 (1973).

22. K. M. McGuire, Princeton Plasma Physics Laboratory, Princeton, N.J., personal communication.

23. M. Maeda et al., in *Plasma Physics and Controlled Nuclear Fusion Research. Proceedings of the 7th International Conference, Innsbruck, 1978*, Vol. 1, Int. Atomic Energy Agency, Vienna, 1979, p. 377.

24. T. H. Jensen and M. S. Chu, GA-A16669, General Atomic Co., San Diego, Calif., 1982.

25. B. V. Waddell et al., Nucl. Fusion 18, 735 (1978).

26. K. M. McGuire and D. C. Robinson, Nucl. Fusion 19, 505 (1979).

27. Equipe TFR, in *Plasma Physics and Controlled Nuclear Fusion Research. Proceedings of the 6th International Conference, Berchtesgaden, 1976*, Vol. 1, Int. Atomic Energy Agency, Vienna, 1977, p. 279.

28. M. A. Dubois, D. A. Marty, and A. Pochelon, Nucl. Fusion 20, 1355 (1980).

29. K. Bol, in *Plasma Physics and Controlled Nuclear Fusion Research. Proceedings of the 7th International Conference, Innsbruck, 1978*, Vol. 1, Int. Atomic Energy Agency, Vienna, 1979, p. 26.

30. K. M. McGuire et al., PPPL-1946, Princeton Plasma Physics Lab., Princeton, N.J., 1982.

31. W. Park, personal communication.

32. V. M. Leonov, "Ohmic Heating and Neutral Beam Injection Studies on the T-11 Tokamak," in *Plasma Physics and Controlled Nuclear Fusion Research. Proceedings of the 8th International Conference, Brussels, 1980*, Vol. I, Int. Atomic Energy Agency, Vienna, 1981, p. 393.

33. A. B. Berlizov, "Low q Discharges in the T-10 Tokamak," in *Plasma Physics and Controlled Nuclear Fusion Research. Proceedings of the 8th International Conference, Brussels, 1980*, Vol. I, Int. Atomic Energy Agency, Vienna, 1981, p. 23.

34. D. Overskei et al., "Low q Operations in Alcator," in *J. Magn. Magn. Mater.* 2, 363 (1979).

35. H. R. Strauss, Phys. Fluids 19, 134 (1976).

36. B. V. Waddell et al., Phys. Rev. Lett. 41, 1386 (1978).

37. H. R. Hicks et al., J. Comput. Phys. 44, 46 (1981).

38. G. Cattanei et al., "Neutral Injection Heating in Wendelstein VII-A Stellarator," presented at the 9th International Conference on Plasma Physics and Controlled Nuclear Fusion Research, Baltimore, September 1982; proceedings to be published.

39. B. V. Waddell et al., Nucl. Fusion 16, 528 (1976).

40. A. M. M. Todd et al., Nucl. Fusion 19, 743 (1979).

41. K. T. Tsang and D. J. Sigmar, "Stabilization of Ballooning Modes by Energetic Particles in Tokamaks," unpublished.

42. W. A. Cooper, Nucl. Fusion 22, 835 (1982).

43. D. J. Strickler, Y-K. M. Peng, and D. K. Lee, *Pressure Profile Effects on the Ballooning Mode Stability of the FED Tokamak*, ORNL/TM-8040, Union Carbide Corp. Nuclear Div., Oak Ridge Natl. Lab., 1982.

44. L. A. Charlton et al., Phys. Rev. Lett. 43, 1395 (1979).

45. W. A. Cooper, Plasma Phys. 24, 437 (1982).

46. R. W. Moore, *MBC — A Ballooning Stability Code for Finite Toroidal Mode Number*, GA-A16243, General Atomic Co., San Diego, Calif., 1981.

47. D. Dobrott et al., Phys. Rev. Lett. 39, 943 (1977).

48. R. W. Wieland et al., "A Pressure Profile Analysis of High Beta ISX-B Plasmas Using MHD Equilibrium Geometry," submitted to Nuclear Fusion.

49. W. A. Houlberg, S. E. Attenberger, and L. M. Hively, Nucl. Fusion 22, 935 (1982).

50. The model is described by J. C. Whitson and W. I. Van Rij, J. Appl. Phys. 47, 3291 (1976). The FED-A computations were performed by L. M. Hively.

51. F. L. Hinton and R. D. Hazeltine, Rev. Mod. Phys. 48, 239 (1976).

52. R. J. Hastie and W. N. G. Hitchon, "Energy Loss Due to Ripple Effects in INTOR," in EURFuBRU/XII-2/81/EDV 70, European Contribution to the Third Workshop Meeting, Phase IIa, December 1981.

53. A. H. Boozer, Phys. Fluids 23, 2283 (1980).

54. J. N. Davidson, Nucl. Fusion 16, 731 (1976).

55. K. T. Tsang, Nucl. Fusion 17, 556 (1977).

56. R. Linsker and A. H. Boozer, Phys. Fluids 25, 143 (1982).

57. T. E. Stringer, Nucl. Fusion 12, 689 (1972).

58. J. W. Connor and R. J. Hastie, Nucl. Fusion 13, 221 (1973).

59. P. N. Yushmanov, Nucl. Fusion 22, 315 (1982).

60. K. C. Shaing and J. D. Callen, *Neoclassical Ripple Transport in Tokamaks*, UWFDM-416, University of Wisconsin, Madison, 1981.

61. R. J. Godston and H. H. Towner, Nucl. Fusion 20, 781 (1980).

62. E. G. Corman et al., Nucl. Fusion 15, 377 (1975).

63. J. D. Callen et al., in *Plasma Physics and Controlled Nuclear Fusion Research. Proceedings of the 5th International Conference, Tokyo, 1974*, Vol. 1, Int. Atomic Energy Agency, Vienna, 1975, p. 645.

64. P. N. Yushmanov, "Confinement of High-Energy Trapped Particles in the Rippled Magnetic Field," U.S.S.R. Contribution to the 4th Workshop Meeting, Phase IIa, March 1982.

65. B. A. Carreras et al., "MHD Activities and Neutral-Beam-Driven Transport Effects in ISX-B Tokamak," presented at the 9th International Conference on Plasma Physics and Controlled Nuclear Fusion Research, Baltimore, September 1982; proceedings to be published.

66. M. Murakami et al., "Beta Scaling Experiments in ISX-B," presented at the 9th International Conference on Plasma Physics and Controlled Nuclear Fusion Research, Baltimore, September 1982; proceedings to be published.

4. CURRENT DRIVE

In this chapter we review the status of noninductive current drive in tokamaks and examine how it may be incorporated into the FED-A concept. A major purpose here is to shed light on the impact of current drive on design requirements and plasma operation scenarios.

Among the many possible approaches to tokamak current drive, lower hybrid waves have been the most successful experimentally and have been the subject of intensive theoretical studies. Two sections are devoted to discussion of this technique: first, a summary of the experimental basis for the lower hybrid current drive (Sect. 4.1), and second, a theoretical assessment of lower hybrid current drive scenarios in FED-A (Sect. 4.2). It is pointed out that essentially all the lower hybrid current drive experiments (PLT, Alcator-C, JIPPT-2, WEGA, Versator II, and WT-II, but excepting JFT-2) have indicated efficiencies that follow the empirical relationship of I (kA)/P (kW) $\sim 8T_e$ (keV)/Rn (10^{14} cm^{-2}), which is generally in accord with theoretical predictions. However, the present relationship between the suprathermal current carriers (typically electrons on the order of 100 keV) and the electron temperature ($\lesssim$1 keV) may not be preserved as the electron temperature is increased to reactorlike values, because of the inverse dependence of efficiency on plasma density. Cyclic current drive approaches, in which plasma density and conductivity are periodically lowered to allow for current drive in short durations with high efficiency, are discussed in Sect. 4.2. The overall current drive efficiency can be improved by an order of magnitude over steady-state current drive operation. Despite these attractive features, the lower hybrid wave is nevertheless perceived to have a potential limitation in wave penetration at high density.

The prospect for high density, steady-state current drive using fast Alfvén waves is discussed in Sect. 4.3. This approach has the advantage of assured wave propagation to the plasma center over a wide density range. Preliminary assessments of the design requirements and of ways to implement this approach in FED-A are discussed. Another rf current drive scheme largely free from limitations on access to the plasma center is the electron cyclotron wave (Sect. 4.4). While the

wave-plasma interaction process here is relatively well understood, this approach is distinct in that it aims to increase the perpendicular energy of a select group of electrons moving in Doppler resonance with the wave. An anisotropic resistivity is created, allowing these electrons to acquire a net momentum (and hence a current) in the direction of the waves. The efficiencies of these two approaches are estimated to be around 0.1 A/W for densities around 10^{14} cm^{-3}, leading to a fusion power amplification Q of about 5 for FED-A.

The prospect of high current drive efficiency and high Q at high densities by pulsed injection of relativistic electron beams is discussed in Sect. 4.5. Assuming that the background plasma resistivity is anomalously enhanced during beam slowing-down, the relativistic electron beam (REB) current drive efficiency is estimated to be an order of magnitude above other current drive schemes. If there were a means of ensuring adequate beam penetration into the tokamak plasma configuration, this scheme apparently could provide both current drive and plasma heating.

Finally, the use of neutral beams as a current drive option is discussed in Sect. 4.6. In the case of steady-state current drive, it is found that beam energies in the range 400 to 800 keV at a power level of about 50 MW will be needed to maintain a current of about 4 MA in FED-A. However, with a cycling density approach, a time-averaged power of only 5 MW is needed for FED-A. A novel concept of a negative-ion-based neutral beam using transverse field focusing is also discussed as a possible scheme to implement the required beam system.

Aside from issues of current drive component development, none of the current drive approaches to be discussed here appears to introduce dramatic alterations to the FED Baseline configuration (Chap. 7). The choice of candidate current drive scenarios is therefore largely predicated on the considerations of physics viability. A quasi-steady-state current drive scenario with cyclic plasma density or conductivity then suggests itself as a desirable design philosophy, not only because it appears to have a broad physics basis and makes the FED-A concept more nearly reactor-prototypical, but also because it does not exclude from

the design high Q, steady-state operation if current drive studies eventually permit it. An assessment of the current drive engineering design issues is presented in Chap. 7.

4.1 EXPERIMENTAL BASIS FOR LOWER HYBRID CURRENT DRIVE

M. Porkolab (MIT)

In this section we summarize the present status of lower hybrid current drive (LHCD) experiments. This summary includes the latest results presented at the Third Joint Varenna-Grenoble International Symposium on Heating in Toroidal Plasmas, Grenoble, France, March 22-26, 1982[1-7] and at the Ninth International Conference on Plasma Physics and Controlled Nuclear Fusion Research, Baltimore, September 1-8, 1982.[8-12] In addition, results from a few earlier publications on LHCD in tokamaks are included.[13-15] We do not review some earlier works[16-20] that were instrumental in clarifying the basic concepts of current drive theory.[21]

4.1.1 Examples of Typical Experimental Results

Lower hybrid rf current drive has been observed in tokamaks with and without ohmic heating (OH) electric fields. While current drive experiments operated at low densities ($\bar{n} < 10^{13}$ cm^{-3}) and low frequencies ($f \cong 0.8$ GHz) have achieved the longest current drive pulses, recent experiments on Alcator-C have extended current drive operation to densities as high as $\bar{n} \cong 5 \times 10^{13}$ cm^{-3}. It is believed that this high density operation is achieved in the Alcator-C experiments by the use of high frequencies ($f = 4.6$ GHz). This was possible since the high magnetic field in Alcator-C (B_T = 6-10 T at the plasma) allowed wave penetration even for relatively low values of $N_{\|}$ ($\cong 2$). In particular, in many of the experiments (e.g., PLT and Alcator-C) the grill used was built originally to provide an optimal power spectrum at 0, π, 0, π phasing, rather than at 0, $\pi/2$, π, $3\pi/2$, which is usually used for current drive experiments.

In Fig. 4-1 we show a typical time sequence of a current drive shot from PLT.[1] Here the waveguides are phased 90°, and 100 kW of rf power

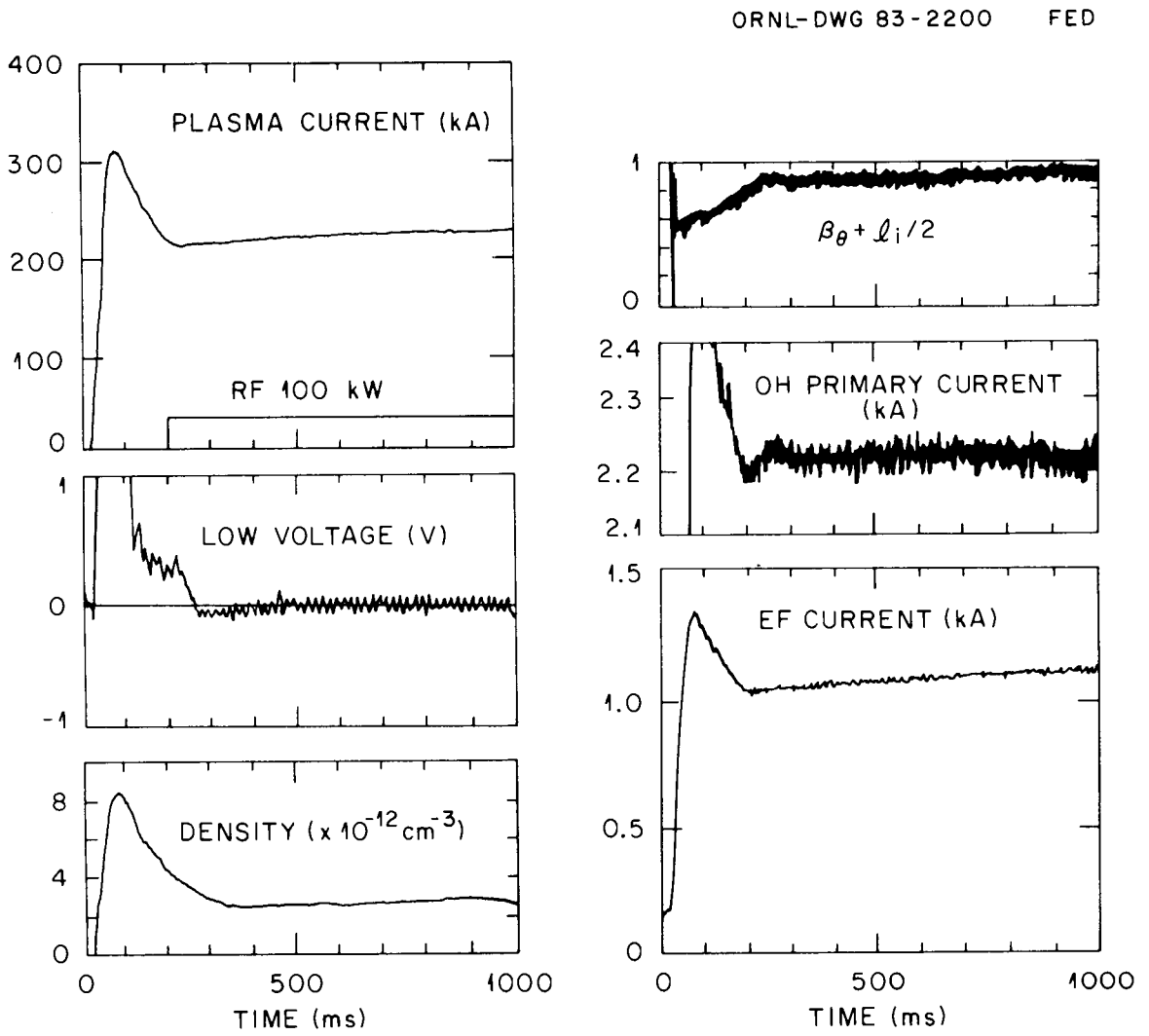

Fig. 4-1. Evolution of plasma current, loop voltage, plasma density, $\Lambda = \beta_\theta + \ell_i/2$, OH primary, and equilibrium field current during a current drive shot in PLT. The rf power is 100 kW, and it is on from 200 to 1000 ms. The Λ signal is derived from I_p and I_{EF}.

is applied for 800 ms after the primary ohmic current is terminated. We see that the loop voltage is initially driven negative and then approaches the zero value. The density is initially $\bar{n} \cong 8 \times 10^{12}$ cm^{-3} (to suppress runaways) and then is maintained flat at $\bar{n} \cong 3 \times 10^{12}$ cm^{-3}. Such flat-top currents were recently maintained for as long as 3 s. Hence, inductive effects can be ignored, and pure rf current maintenance is observed here.

By increasing the rf power, it was possible to ramp the current in PLT. For example, applying 370 kW of rf power for 200 ms produced a current ramp of 80 kA/s at $\bar{n} = 3 \times 10^{12}$ cm^{-3}.

In Fig. 4-2 we show high energy x-ray spectra from PLT. It is usually found in current drive experiments that while the hard x-ray spectrum coming from high energy electrons hitting the limiter decreases, the bulk-plasma-produced hard x-ray spectrum increases during application of the rf. At the same time, the $2\omega_{ce}$ emission increases. These phenomena indicate formation of a high energy tail within the plasma volume near the center of the discharge. Radial scans of the x-ray emission confirm this both in the PLT and the Alcator-C tokamaks. These results indicate that a high energy tail extends from bulk thermal energies to several hundred kiloelectron volts.

In Fig. 4-3 we show LHCD results from the recent Alcator-C experiments.[11] Here 100 kA of current is produced upon application of 210 kW of rf power at a density of $\bar{n} = 2.5 \times 10^{13}$ cm^{-3}. We see that slowly rising or flat-top currents can be produced with a loop voltage that is initially negative and slowly rises to zero. Current ramping was also observed. For example, at a density $\bar{n} = 1.4 \times 10^{13}$ cm^{-3}, a value of $d/dt(\bar{n}I/P) \cong 0.16(A \cdot 10^{14}$ cm^{-3}/W$\cdot$s) was produced upon application of 0.5 MW of power. In Alcator-C flat-top currents were maintained for 100-200 ms with powers up to 600 kW and densitites up to $\bar{n} \cong 5 \times 10^{13}$ cm^{-3}.

Regarding the stability of these discharges, in many current drive experiments rf probes in the shadow of the limiter detect rf emission at $\omega > \omega_{pi}$ (Refs. 4, 6, 9, 11). These oscillations are believed to be electrostatic waves with the dispersion relationship $\omega \cong \omega_{pe} \cos\theta$, which are driven unstable by the anisotropic distribution function due

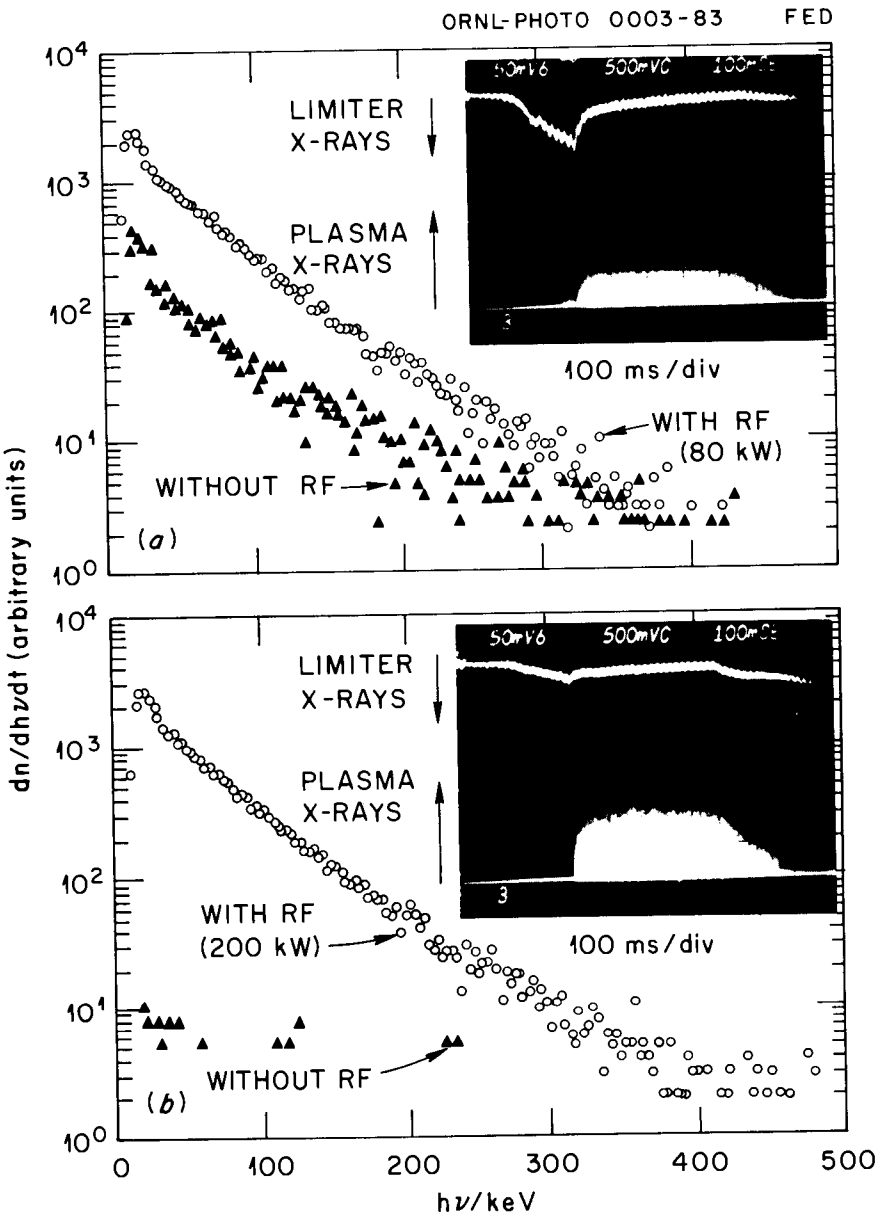

Fig. 4-2. (a) Hard x-ray spectrum with and without rf at a line-averaged density $\bar{n}_e = 3 \times 10^{12}$ cm^{-3} in PLT. The inset shows the time evolution of the plasma x rays and the limiter x rays (inverted scale). The rf power is 80 kW, and it is on from 300 to 700 ms. (b) Hard x-ray spectrum with and without rf at a line-averaged density $\bar{n} = 6 \times 10^{12}$ cm^{-3}. The rf power is 200 kW, and it is on from 300 to 700 ms.

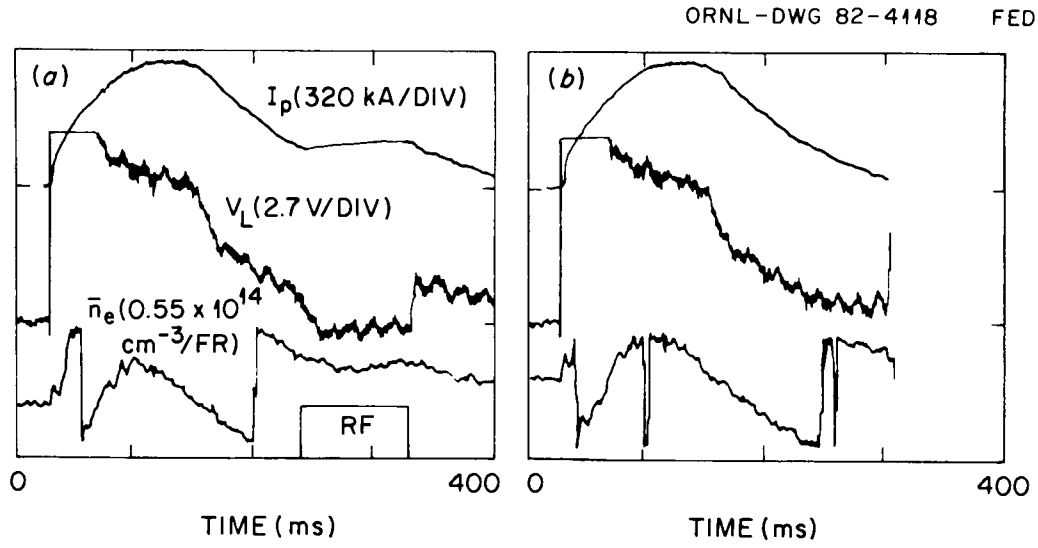

Fig. 4-3. I_p, V_L, and $\bar{n}_e$ (a) with and (b) without rf injection in Alcator-C. ΔP_{rf} = 210 kW, relative waveguide phasing is $\pi/2$, and B = 8 T.

to the anomalous Doppler effect[22] or perhaps by an electron beam formed on the tail. In some experiments at low densitites, such oscillations are observed even before the rf power is injected.[4,11] These oscillations result in spikes on the loop voltage that tend to limit the current drive efficiency, as shown in Fig. 4-4(a) (Versator II[4,11]). However, it was found that upon application of 20-50 kW of electron cyclotron resonance heating (ECRH) at f = 35 GHz, the rf activity on the probe and the loop voltage spikes both disappeared, and increased current drive efficiency resulted [Fig. 4-4(b)]. Similar results were found in other experiments.[6,9] It is believed that the ECRH fields scatter energetic electrons in perpendicular velocity space, thus driving the distribution function more isotropic and hence more stable (the lower hybrid fields flatten and populate the distribution function primarily in the $v_{\|}$ space).

A common feature of many experiments is the preferential relative phasing of 90° (or even less for PLT) of adjacent waveguides during efficient current drive. In Fig. 4-5 we show results from the Versator II experiment that demonstrate this effect.[15] Thus, traveling waves in the direction of initial OH electron drift are preferred for current drive.

4.1.2 Comparison of Experimental Results

In Table 4-1 we summarize the results from a number of recent tokamak LHCD experiments. We see that with the exception of PLT and Alcator-C, in all experiments the OH field is on while the rf power is applied. This makes the interpretation of these experiments somewhat difficult. However, in these experiments the change in the loop voltage is directly proportional to the rf current drive (assuming that supra-thermal electrons carry the current). During current drive, the electron temperature usually drops in these experiments. Thus, loop voltage drops cannot be blamed on electron heating (and hence increased conductivity). The typical rf power input varies in the range $P \cong 40\text{-}600$ kW, with the record having been achieved in Alcator-C. In particular, driving currents at high densities requires significant amounts of power.

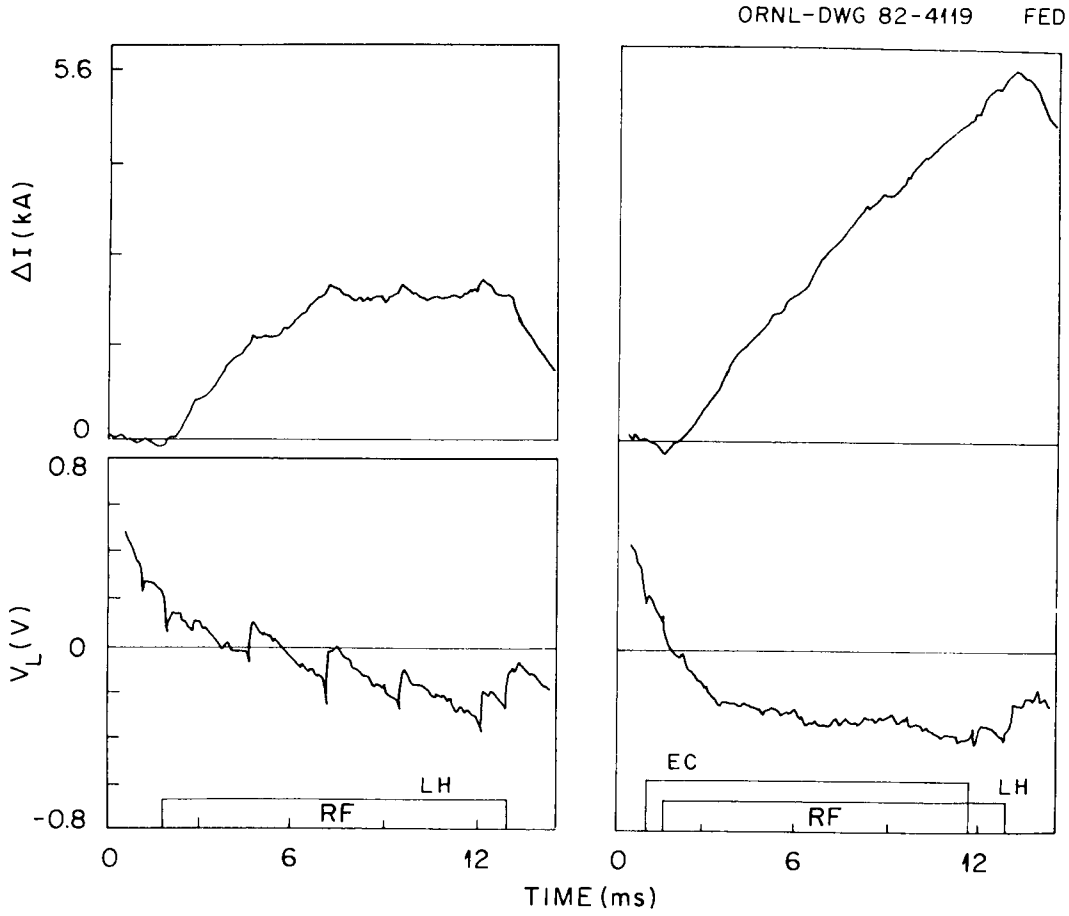

Fig. 4-4. Plasma current increase ΔI and loop voltage V_ℓ during (a) LHCD and (b) LHCD (P = 30 kW) and ECRH (P = 50 kW) added. $\Delta I = \Delta t I_{rf}/\tau_L/R$ (Versator II).

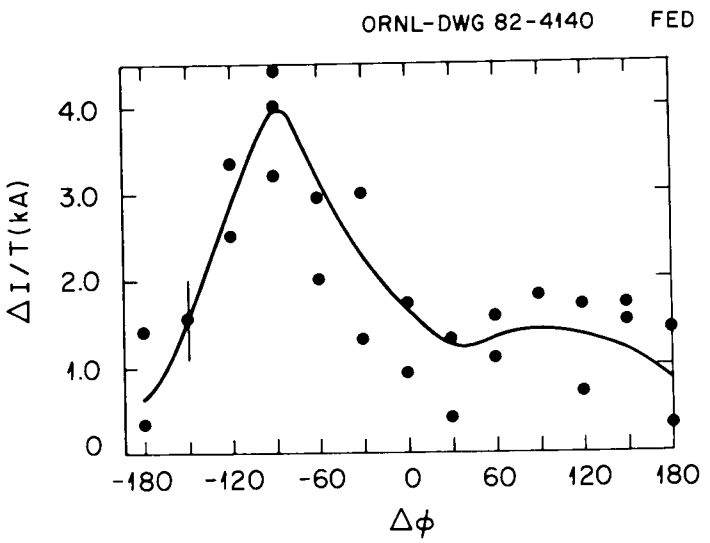

Fig. 4-5. Current increment ΔI_T normalized to rf power transmission coefficient, T, as a function of array phase $\Delta\phi$ with a 4-ms rf pulse in Versator II.

Table 4-1. Experimental parameters during LHCD experiments

Device	R (cm)	f (GHz)	P_{rf} (kW)	P_{rf}/A (kW/cm^2)	Grill [Number × d (cm)]	I_{rf} (max) (kA)	Δt_{rf} (ms)	$\bar{n}_{max}$ (cm^{-3})	$N_{\parallel}$ (estimated at $\phi = \pi/2$)
JFT-II	90	0.75	150	2	4 × 1.4	35	40	6×10^{12}	2-8
JIPPT-II	91	0.80	150		2	40	20	8×10^{12}	1-4
WT-II	40	0.91	100	1	4 × 1.8	10	20	6×10^{12} (1×10^{13})	1-8
WEGA	72	0.80	50 (150)	2	4 × 3.5 4 × 2.0	50	40	7×10^{12} (1.3×10^{13})	1-4
Versator-II	40	0.80	40 (100)	1	4 × 2.4	40	10-30	6×10^{12} (1×10^{13})	1-4
PLT	132	0.80	400	2	6 × 3.7	165 420	3500 300	7×10^{12} (1.2×10^{13})	1-2.5
Alcator-C	64	4.60	600	9	4 × 0.8 (× 4)	200	200	5×10^{13}	1-2.5

The grills (waveguide arrays) used in these experiments are typically 4-waveguide arrays (with the exception of Versator II and PLT, where 6-waveguide arrays are also used). Thus, the $N_{\|}$ spectrum is wide, with $\Delta N_{\|}/N_{\|} \cong 1$. The high current drive efficiency obtained in some of these experiments may be due to the wide $N_{\|}$ spectra and especially to the low values of $N_{\|}$, which allow interactions with relatively high energy electrons. However, as the density is increased, it becomes increasingly difficult for relatively low values of $N_{\|}$ (<1.8) to penetrate the plasma. This introduces a "density limit" in most experiments such that $\omega_{pe}^2/\omega_{ce}^2 \lesssim 1$. This problem can be ameliorated by proper grill design in future machines, but we may anticipate a somewhat lower current drive efficiency than that observed in some of the present experiments.

Regarding the rf currents generated, we see from Table 4-1 that typically $I_{rf} \cong 50$ kA, but in Alcator-C and PLT $I_{rf} \cong 200$ kA. Furthermore, in PLT $I_{rf} \cong 420$ kA has been achieved in some cases. The pulse lengths vary widely from 10 ms in small machines to 3.5 s in PLT. In nearly all the experiments $t_{rf} \gtrsim t_{L/R}$, so that current penetration and diffusion are ensured. Furthermore, the electric field diffusion time is typically shorter than the L/R time, so that changes in the loop voltage show up relatively soon after the rf power is turned on.

In earlier experiments a critical "density limit" was observed, above which the current drive efficiency dropped dramatically. Since in most experiments the driving frequency was $f \cong 800$ MHz, the density limit observed was $\bar{n} \cong 7 \times 10^{12}$ cm^{-3}. It was concluded that rf current drive may operate only in the "slideaway" regime.[22-24] However, recent experiments in both PLT and Alcator-C have shown that current drive may be operative even when initially there is a negligible fraction of the electrons in an energetic tail (see Fig. 4-2). On the other hand, the rf populates the energetic tail by several orders of magnitude, both in number density and in energy.[1,12] Furthermore, in Alcator-C rf current drive has been produced at densities up to $\bar{n} = 5 \times 10^{13}$ cm^{-3}. At these densities all the available rf power ($P \cong 600$ kW) was necessary to maintain the flat-top current. Hence, in Alcator-C the density limit is not yet determined (only a power limit was reached). Furthermore,

current drive in PLT was recently observed at densities up to $\bar{n}$ = 1×10^{13} cm^{-3} when the initial target plasma was produced with higher initial ohmic discharge currents, so that the initial electron temperature was higher than in previous experiments.[12] Finally, in the presence of OH fields, rf current drive effects are observed both in WEGA and PLT (although the loop voltage is not driven to zero) up to $\bar{n} \cong 1.3 \times 10^{13}$ cm^{-3}. These results indicate that the cause of the so-called "density limit" may be inadequate wave penetration and/or insufficient rf power. Further, higher initial electron temperatures may be beneficial for efficient LHCD. It is likely, however, that at low densities where runaway (slideaway) effects are significant (especially in the presence of ohmic fields), the existence of a preformed energetic electron tail would reduce the power necessary to drive a given amount of rf current (and hence result in an apparently "overefficient" current drive as compared with theory).

From Table 4-2 we see that the current drive efficiencies vary in the range $nI/P \cong 0.1\text{-}1.9 \times 10^{13}$ cm^{-3}·A/W. A more meaningful comparison among different machines requires a normalization of the power to the major radius R of the device. According to Fisch,[25] $nI/P = K(N_{\|})T_e/R$, where $K(N_{\|}) = 0.02(J/P_d)$, which depends on wave power spectra and wave type. For lower hybrid waves, $J/P_d \cong 20$. In Table 4-2 we list nIR/P. As a further normalization, we may divide these results by the bulk electron temperature. We see that with the exception of the JFT-II experiment, all devices are within a factor of 2 of each other by using either the initial or the final electron temperature. Considering the large variety of devices and the differences between the various waveguide launchers [which are characterized by $K(N_{\|})$ in the above equation] the efficiencies seem to be remarkably close. Taking Fisch's theory, with $J/P_d \cong 20$ as is appropriate for moderately suprathermal resonant electrons, we get $RnI/PT = 4 \times 10^{14}$ cm^{-3} × cm·A/W·keV. This is within a factor of 2 of the experimental values. If we allowed larger values of J/P_d (to allow for higher phase velocities), then we would get higher theoretical predictions for J/P_d. The agreement with the experiments, especially with the PLT and Alcator-C results, is considered to be good, especially when we consider the crudeness of the theoretical evaluation

Table 4-2. Current drive efficiency

Device	T_e (keV)	nI/P $\left(\frac{10^{13}\ cm^{-3}\cdot A}{W}\right)$	nIR/P $\left(\frac{10^{14}\ cm^{-3}\cdot cm\cdot A}{W}\right)$	nIR/PT_e $\left(\frac{10^{14}\ cm^{-3}\cdot cm\cdot A}{keV\cdot W}\right)$
JFT-II	0.8	0.14	1.3	1.6
	(0.5)			(2.6)
JIPPT-II	?	0.70	6.3	
WT-II	0.17	0.15	0.6	3.5
	(0.03)			(20)
WEGA	1.2	0.70	5.0	4.2
	(0.5)			(10)
Versator II	0.25	0.40	1.6	6.4
	(0.15)			(11)
PLT	1.2	0.6-0.8	7.9-10.6	6.6-8.8
	(1.0)			(7.9-10.6)
Alcator-C	∿1.5	1.3-1.9	8.3-12.1	5.5-8.1
	(1.3?)			(6.3-9.3?)

Note: The temperatures in parentheses are the values after application of the rf pulse.

of the launched wave $N_{||}$ spectra, toroidal effects, radial profiles, etc. It is likely that a more accurate treatment of the waveguide spectra would yield a closer agreement between experiment and theory. This is indeed what is found in the case of both Versator II and PLT, for which a combined toroidal ray tracing transport code calculation by Bonoli and Englade[4,26] finds good agreement with the experiment, at least at densities $\bar{n} \lesssim 8 \times 10^{12}$ cm^{-3}. These code calculations also show that the initial gap between the applied parallel phase velocities (as determined by grill geometry) and thermal velocity in experiments such as PLT[1] and others can be resolved if toroidal upshifts of $N_{||}$ are allowed (which requires ray tracing with multibounce ray trajectories). At higher densities ($\bar{n} \gtrsim 1 \times 10^{13}$ cm^{-3}) there is still a discrepancy between theory and experiment in PLT and Versator II (the theoretical efficiencies do not drop as rapidly as the experiments would indicate). Finally, we note that other theoretical mechanisms have also been proposed by Liu et al.[27] to close the gap between the thermal velocity and the launched phase velocities. In Fig. 4-6 we show a plot of the data from Table 4-2, namely, a plot of nIR/P vs T_e. We see that we can approximate all the results (with the exception of JFT-II) with the relationship $n(10^{14}\ \text{cm}^{-3})I(A)R(cm)/P(W)T_e(keV) \cong 7.4$. This should be compared with the Fisch result mentioned earlier, which gives 4.

4.1.3 Summary

Here we provide a brief summary of the status of LHCD experiments. From the PLT and Alcator-C experiments, we conclude that rf maintenance of toroidal currents without OH assist has been demonstrated in the density range $\bar{n} = 2 \times 10^{12}$-$5 \times 10^{13}$ cm^{-3}. We see that with the possible exception of JFT-II, all the experiments yield current drive efficiencies within a factor of 2 above the Fisch value assuming moderately suprathermal resonant electrons but close to or slightly below the Fisch value assuming the highly suprathermal current carriers that are observed. Considering the crudeness of these estimates (both theory and experiment), the agreement is considered to be remarkably good. The JFT-II results

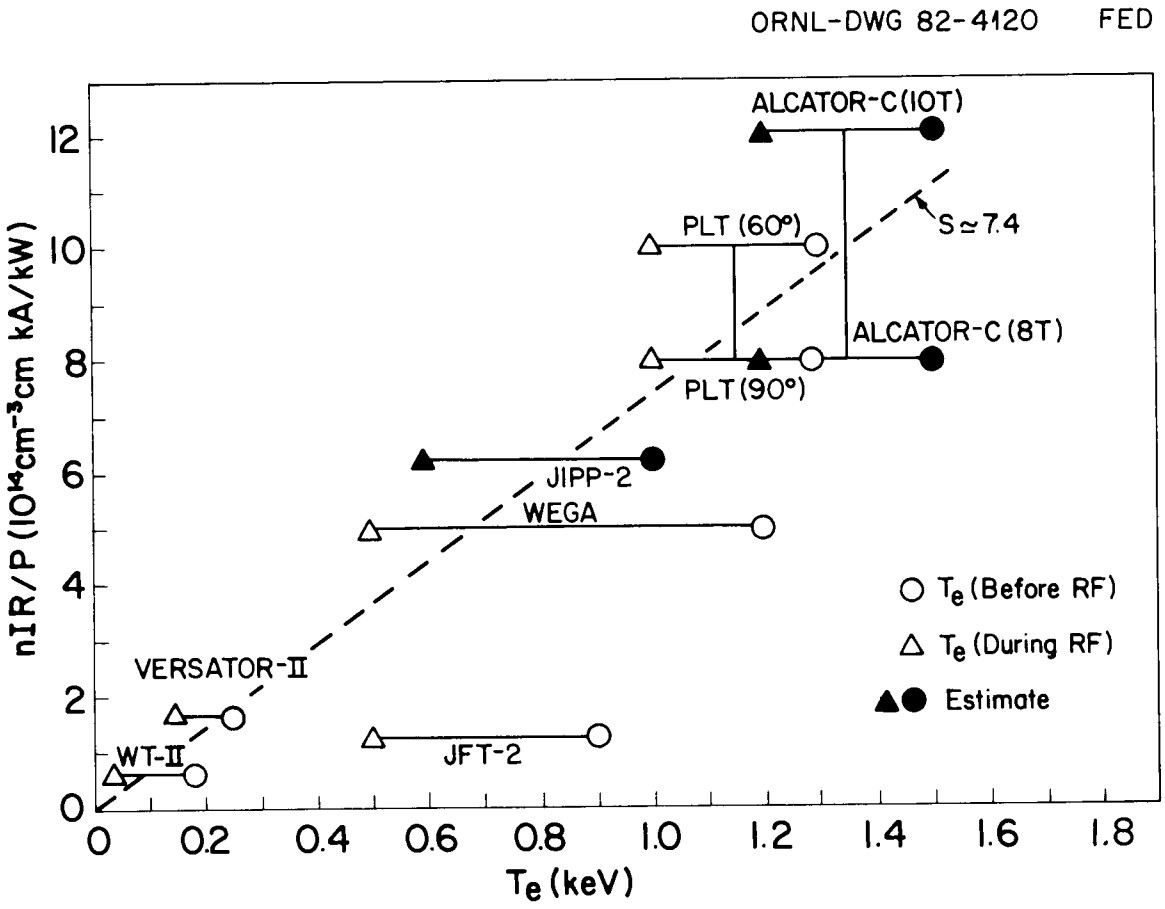

Fig. 4-6. Current drive efficiency vs T_e in various LHCD tokamak experiments.

indicate somewhat lower efficiencies. Physically, this can be explained by noticing the relatively high $N_{\parallel}$ content of the JFT-II coupler (which had 1.4-cm waveguide gaps, whereas in all other experiments, with the exception of the Versator II 6-waveguide grill, the gap size was 2.5-3.7 cm). In fact, for JFT-II it was reported that the observed distribution function had a plateau on the electron distribution function in the medium energy range, 3-15 keV; thus, for efficient current drive it is desirable to have couplers rich with low $N_{\parallel}$ content (which, nevertheless, are still accessible).

Finally, we note that the power level on Alcator-C will soon be raised to the 1-MW level. Based on existing results, this power should allow us to test current drive at the 150- to 200-kA level and at densities up to $\bar{n} \cong 1 \times 10^{14}$ cm^{-3}. The power level and pulse length will also be increased on PLT to allow larger currents to be driven for pulse lengths up to 10 s in lower density plasmas. On PLT and Versator II, new 2.45-GHz S-band rf systems will be installed that will test scaling of the density limit with frequency for a given device.

4.2 LOWER HYBRID CURRENT DRIVE SCENARIOS

E. J. Valeo, F. W. Perkins, and P. H. Rutherford (PPPL)

Theoretical studies[21,28] and recent experimental evidence[11,12,29] have demonstrated the possibility of driving currents in large tokamaks that are comparable to those induced by the ohmic transformer. These positive results motivate a closer look into the possibility of using lower hybrid waves to produce current in FED in some combination of three possible modes:

1. Steady state. The lower hybrid wave would provide essentially all of the current in an operational mode with a pulse length limited by considerations other than induction flux. There would be essentially no ohmic transformer.
2. As a means to recharge the transformer. The tokamak would operate in a cyclic mode in which the rf source overdrives the plasma current during a period τ_1, followed by a period τ_2 during which the transformer provides the current.

3. For pulse length extension. The rf system would provide start-up capability, and the volt-seconds saved thereby would be used to substantially lengthen the discharge pulse length.

An assessment of the LHCD efficiencies and conditions in these modes is provided here.

Heating and current drive in the lower hybrid frequency range have several attractive features. (1) High power sources are commercially available. (2) The relatively short wavelengths involved allow launchers with no need for dielectric loading materials exposed to the plasma. (3) The plasma impedance is comparable to that of free space, so that the circulating power in the antenna structure is not large. (4) The method's feasibility has already been demonstrated experimentally for quasi-steady-state pulses lasting several seconds. Although the plasma density in current experiments has been at best a factor of 4 below that anticipated for FED-A, the rf power flux already achieved is adequate for FED.

4.2.1 Steady-State Current Drive

There are fundamental limitations on the possibility of achieving steady-state current drive with lower hybrid waves as the plasma density and temperature are increased. The critical parameter is the parallel wave index $n_{\|} = k_{\|} c/\omega$. Its value is bounded both above and below if it is necessary only for the wave trajectories to penetrate to the center of the discharge and for the wave energy not to be deposited in the plasma before the center is reached.

The lower bound $n_{\|,min}$ comes from the requirement of wave accessibility.[30] Suppose the wave frequency is substantially above the resonance frequency in order to minimize wave-ion interaction; that is,

$$\omega = 2\pi f >> \frac{\eta}{(1 + \eta^2)^{1/2}} (\Omega_e \Omega_i)^{1/2} , \qquad (4\text{-}1)$$

with $\eta \equiv \omega_{pe}/\Omega_e = 0.63 n_{20}^{1/2}/B_5$. Here, n_{20} is the electron density in units of 10^{20} m^{-3} and B_5 is the magnetic field strength in units of 5 T. In dimensional units, Eq. (4-1) becomes

$$f\ (\text{Ghz}) >> \frac{1.2 n_{20}^{1/2}}{(1 + \eta^2)^{1/2}} \tag{4-2}$$

for a 50:50 deuterium-tritium (DT) plasma. Then, only waves with sufficiently large $n_\parallel$, well approximated by

$$n_\parallel > n_{\parallel,\min} = (1 + \eta^2)^{1/2} + \eta\ , \tag{4-3}$$

propagate at a given n.

The upper bound, $n_{\parallel,\max}$, follows from the desire that only negligible current be generated outside some specified radius r_o; that is,

$$J_{rf}(r) = \frac{n_e e f_e(v_1)(v_2^2 - v_1^2)}{2} < J(r) \tag{4-4}$$

for $r > r_o$. Here v_1 and v_2 are, respectively, the local minimum and maximum parallel phase velocities of the lower hybrid waves. The electron distribution function, $f_e(v)$, has been assumed constant in the interval $v_1 \leqslant v \leqslant v_2$. This approximation, equivalent to assuming that the quasi-linear collision frequency exceeds the Coulomb collision frequency, is well satisfied at rf powers needed for significant current generation. Assuming, conservatively, that for $v < v_1$ the distribution function is Maxwellian at the local electron temperature T_e, and estimating J(r) by

$$J(r) \lesssim J(0) = \frac{cB}{2\pi R} \tag{4-5}$$

[$q(0) \cong 1$], we have the lower bound on E_1, the energy of electrons with velocity v_1:

$$\frac{E_1}{T_e} \geq \frac{E_{min}}{T_e} \equiv \ell n \left[\frac{R}{\rho_e} \frac{\eta^2}{4(2\pi)^{1/2}} \left(\frac{1}{n_{\parallel,2}^2} - \frac{1}{n_{\parallel,1}^2} \right) \right] . \tag{4-6}$$

Here $\rho_e = v_{th,e}/\Omega_e$ is the electron gyroradius. If we assume $n_\parallel \cong 1.7$, with a fairly narrow spectral width

$$\frac{n_{\parallel,1} - n_{\parallel,2}}{n_\parallel} \cong 0.2 , \tag{4-7}$$

then the value of the logarithm is about 6. Relating E_{min} to $n_{\parallel,max}$ via the relativistic formula for the electron kinetic energy, inequality (4-6) translates into the upper bound

$$n_\parallel \leq n_{\parallel,max} = \frac{1 + \alpha}{\alpha^{1/2}(2 + \alpha)^{1/2}} \tag{4-8}$$

on $n_\parallel$ for $r > r_o$. Here $\alpha = 6T_e/mc^2 = 0.12T_{10}$, with T_{10} the temperature in units of 10 keV.

The region of propagation is then bounded by $n_{\parallel,min}$ (a function of $n_{20}^{1/2}/B_5$ determined by the need to avoid mode conversion) and $n_{\parallel,max}$ (a function of T_{10} determined by the need to avoid damping in the outer regions of the plasma).

In order to demonstrate the severity of these constraints, we have plotted in Fig. 4-7 both $n_{\parallel,min}$ and $n_{\parallel,max}$ as a function of radius for an FED-like plasma with density and temperature profiles of the form

$$\begin{aligned} n(r) &= n(0)(1 - r^2/a^2)^{1/4} , \\ T(r) &= T(0)(1 - r^2/a^2)^{3/2} , \end{aligned} \tag{4-9}$$

with $n(0) = 10^{20}$ m^{-3}, $T(0) = 35$ keV, $a = 1.2$ m, $R = 5$ m, and a toroidal magnetic field strength $B = 5.5$ T. The profiles are similar to the flat density and peaked temperature profiles observed in existing machines. The combination of relatively low central density and high central

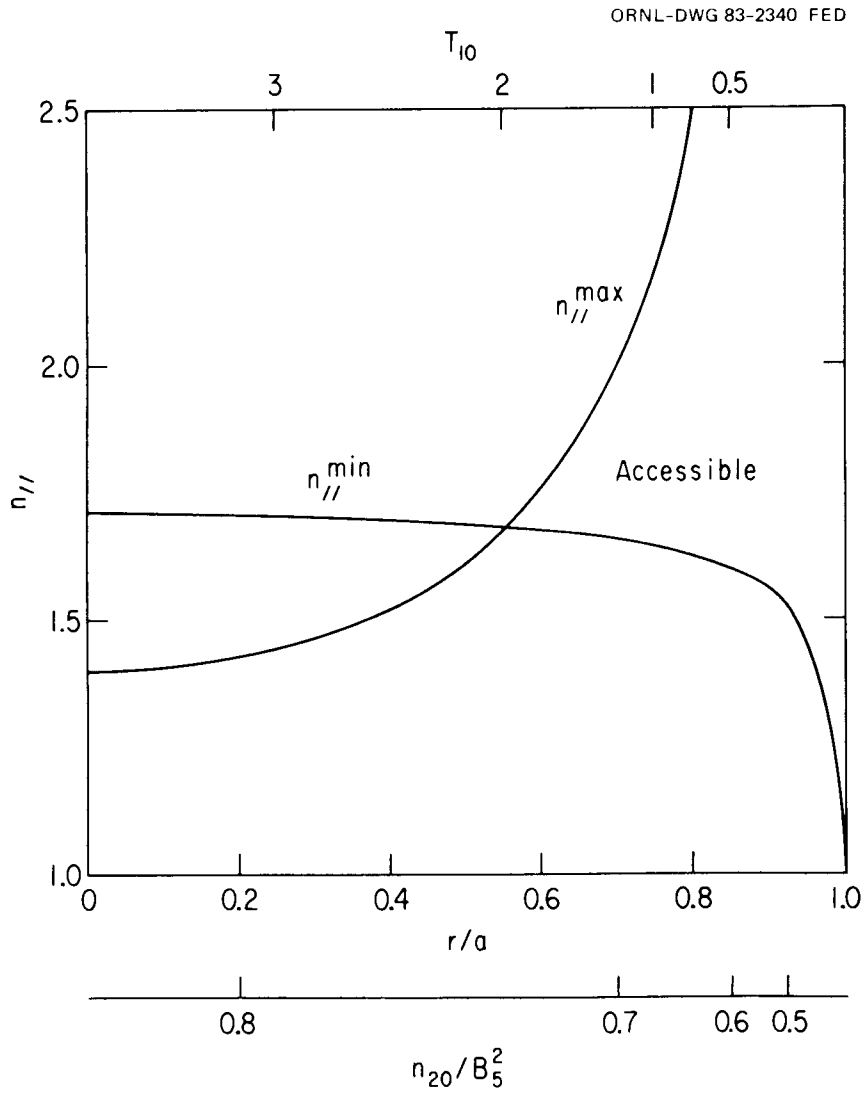

Fig. 4-7. Region accessible by steady-state LHCD when the wave frequency is much above resonance and the plasma density and temperature are given by Eq. (4-9).

temperature is a choice that follows from an optimization of Q (thermonuclear power output/rf power input) with the plasma beta bounded by stability considerations.[31] The maximum Q (about 6 for FED) is obtained for a density-weighted average (ion) temperature of 16 keV, which yields T(0) = 35 keV. The core region of the plasma ($r < 0.6a$) is not accessible. Damping of the waves in the outer regions of the plasma can be reduced by lowering the electron temperature or by narrowing the temperature profile, but the penalty in reduced thermonuclear output is probably too severe. The damping of the waves can also be reduced by further narrowing the wave spectrum, but, because of the relative insensitivity of the logarithm in Eq. (4-6), a spectral width of not more than $\Delta n/n = 3 \times 10^{-2}$ would be needed for penetration to the center of an FED plasma.

We have confirmed these estimates [Eq. (4-9)] for the profiles by computing current generation and power deposition profiles with a code that includes toroidal ray tracing, electron quasi-linear diffusion, and lower hybrid wave damping on the self-consistently calculated electron distribution. We have been unable to find a combination of incident spectral shapes and wave launching positions that leads to current generation for $r < 0.7$ m.

If we succeed in achieving wave penetration by accepting some combination of lowered density, electron temperature, or spectral width or by increasing the magnetic field strength, then we are left with the issue of current drive efficiency; that is, how much power must be expended per ampere generated. The ratio of the local steady current density generated J to the local power absorbed per unit volume P_d has been calculated,[21,28] including electron-electron and electron-ion collisions; the effects of self-consistent, two-dimensional (2-D) variation of $f_e(v_\parallel, v_\perp)$; and relativistic effects.[32] These results, including an additional enhancement (≅15%) due to current carried by bulk electrons as a result of the momentum imparted by collisions between the bulk and plateau electrons, are displayed in Table 4-3 for several relevant energies. Here I(MA) is the current generated in megamperes, P(MW) is the rf power dissipated in megawatts, R_5 is the major radius in units of 5 m, and $\bar{E}_{100}$ is the mean energy of electrons in the plateau region

Table 4-3. LHCD efficiency (based on the theory by Fisch et al.)

	$\bar{E}_{100}$				
	1	2	3	4	5
$8.33 \frac{I(MA) \cdot R_5 \cdot n_{20}}{P(MW) \cdot \bar{E}_{100}^{1/2}}$	1.0	1.08	1.08	1.11	1.10

$$\bar{E} = \frac{E_1 + E_2}{2} , \tag{4-10}$$

measured in units of 100 keV. We have assumed

$$\frac{E_2 - E_1}{\bar{E}} << 1 . \tag{4-11}$$

This efficiency estimate (Table 4-3) is, of course, an upper bound, since there are other potential loss channels for the suprathermals, such as electron cyclotron emission and radial diffusion. The efficiences in Table 4-3 can be combined with the lower bound on $n_{\parallel}$ given in Eq. (4-3) to determine efficiency vs η. These results are shown in Fig. 4-8, where we have taken the average energy of the current carriers to be $E_{max}/2$ with E_{max} determined from $n_{\parallel,min}$. Efficiencies of about 0.08 A/W are then to be expected for the FED parameters quoted above if the current were generated at the plasma center.

4.2.2 Cyclic Current Drive

The limitations on accessibility of the plasma interior and on steady-state efficiency can be obviated by cyclically driving the plasma current with rf power.[33] For lower hybrid waves, both the electron temperature and plasma density would ideally be lowered from reactor values during the drive phase, which alternates with the high temperature and density "burn" phase. These reductions would both eliminate the accessibility problem and increase the drive efficiency. Lowering

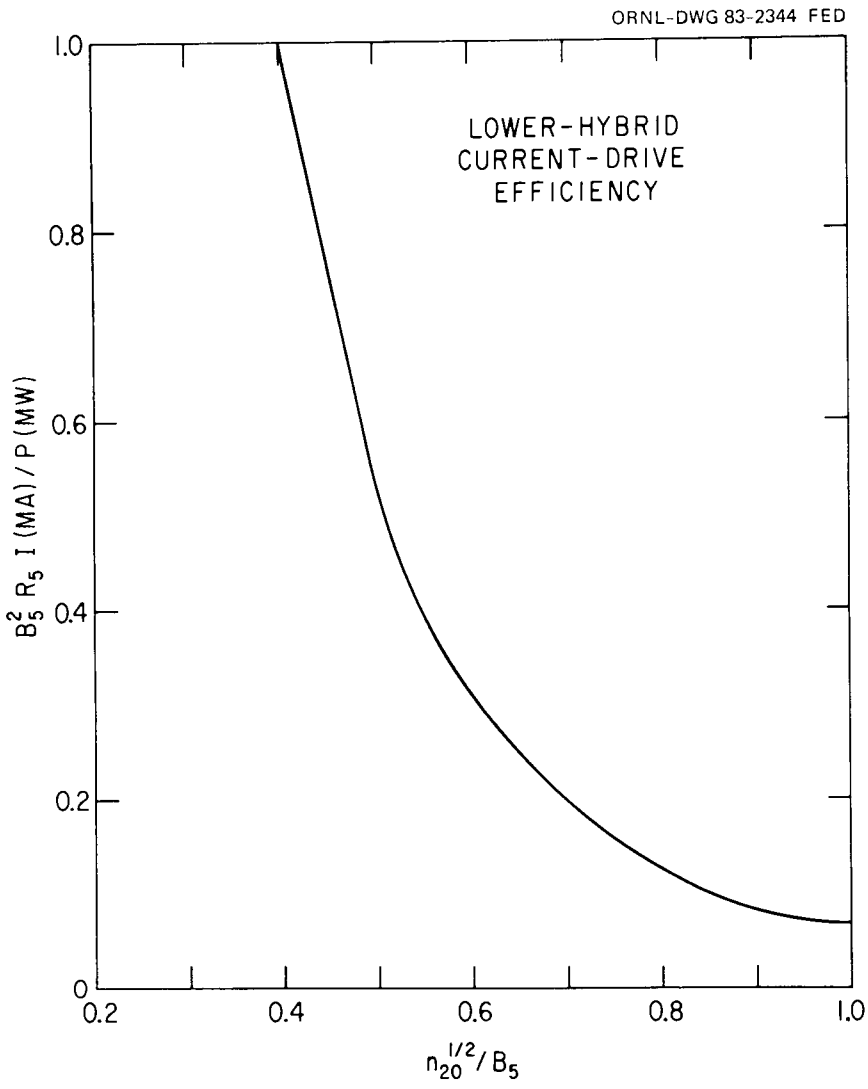

Fig. 4-8. LHCD efficiency vs $n_{20}^{1/2}/B_5$ in FED-A.

the temperature has the additional benefit of reducing the L/R time for relaxation to steady state and therefore the rf energy expended for a given increment in current.

The essential results for the cyclic case can be obtained simply from the equivalent circuit shown in Fig. 4-9. The subscripts p and t refer, respectively, to quantities associated with the plasma and the ohmic transformer. Dissipation in the transformer circuit has been neglected for simplicity, and M designates the mutual inductance between

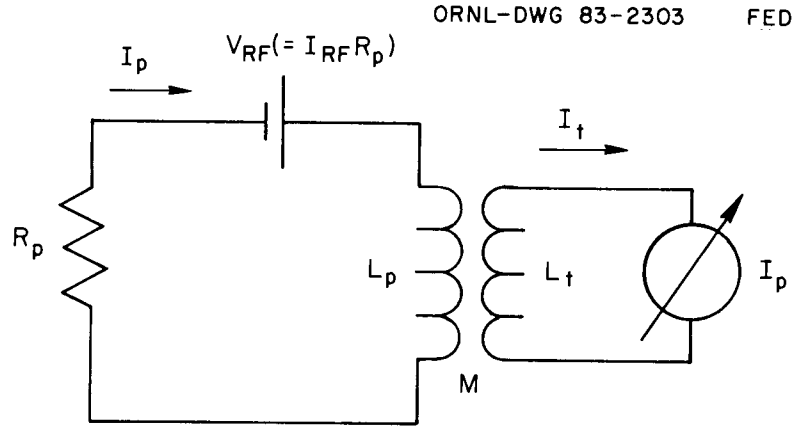

Fig. 4-9. Equivalent circuit for the plasma (p) and transformer (t) during rf current drive.

the plasma and transformer. The rf current source appears in the circuit as an effective voltage $V_{rf} = R_p I_{rf}$, with I_{rf} the current that the source would support in steady state. Coupled equations for the current in the transformer and plasma loops can be combined into the single equation

$$L_{eff} \frac{dI_p}{dt} + R_p I_p = V_{rf} - V_{t,eff} \qquad (4\text{-}12)$$

for plasma current by introducing an effective inductance $L_{eff} = L_p - M^2/L_t$ (approximately L_p, since $L_t \sim M \ll L_p$) and an effective transformer voltage $V_{t,eff} \equiv (M/L_t)V_t \sim V_t$. The requirements that the plasma and transformer currents be cyclic both lead to the constraint

$$\int dt\ (I_{rf} - I_p)R_p = 0\ , \qquad (4\text{-}13)$$

where the time integral is over a complete cycle. Consider, for illustrative purposes, the case in which I_p oscillates weakly about its mean value $\bar{I}_p$. This may actually be desirable in practice, since the variation of the magnetic stresses associated with poloidal flux swings would be minimized. For simplicity, assume that R_p and I_{rf} each take on alternately two values, one during the current generation/transformer recharge phase (subscript 1) and the other during the decay phase (subscript 2). Let $I_{rf} = f\bar{I}_p$ (where the overdrive factor $f > 1$) during the drive phase

and $I_{rf} = 0$ during the decay phase. Then the ratio R_E of energy expended for cyclic drive compared with steady drive is easily obtainable from Eq. (4-13) as

$$R_e = \frac{\tau_1 (P/I)_1}{(\tau_1 + \tau_2)(P/I)_2} \left(1 + \frac{R_2\tau_2}{R_1\tau_1}\right), \tag{4-14}$$

with $(P/I)_j$ the power needed per unit current for steady drive in phase j. Assuming that the principal variation of P/I is with density, we have

$$R_E = \frac{n_1}{n_2} \frac{1}{1 + \tau_2/\tau_1} \left(1 + \frac{R_2\tau_2}{R_1\tau_1}\right). \tag{4-15}$$

The times τ (resistivities R) are directly (inversely) proportional to the current relaxation rates and therefore vary as $T_e^{3/2}$ ($T_e^{-3/2}$). Setting

$$\frac{\tau_1}{\tau_2} = \frac{T_1^{3/2}}{(f - 1)T_2^{3/2}} \tag{4-16}$$

and $R_2\tau_2/R_1\tau_1 \cong 1/(f - 1)$, we finally obtain

$$R_E = \frac{n_1}{n_2} \left[1 + \frac{(f - 1)T_2^{3/2}}{T_1^{3/2}}\right]^{-1} \frac{f}{f - 1}. \tag{4-17}$$

The corresponding ratio of the cyclic rf power required compared with steady drive is

$$R_p = \frac{f(P/I)_1}{(P/I)_2} \cong f \frac{n_1}{n_2} \quad ; \tag{4-18}$$

if, for example, $n_2 = 10^{14}$ cm^{-3}, $n_1 = 10^{13}$ cm^{-3}, $T_2 = 16$ keV, $T_1 = 3$ keV, and $f = 2$, then $R_E = 2 \times 10^{-2}$ and $R_p = 0.2$. Instead of a steady power

of 33 MW required to drive a 4-MA current with 100-keV electrons in steady state, only 7 MW would be required if the density and temperature could be cycled as suggested.

The effective voltage generated by the rf source could also be used during a start-up phase in order to conserve transformer flux for a subsequent long pulse, low resistance burn phase. Estimating the start-up flux requirement for FED as roughly 50 V•s and desiring a start-up phase of $\lesssim$100-s duration yields an rf-induced loop voltage requirement of $\sim$0.5 V (ignoring the flux contribution from vertical field coils). For the 7-MW source discussed above, the steady-state I_{rf} equals 8 MA at a plasma density $n = 10^{13}$ cm^{-3}. The plasma resistivity R_p must therefore be at least 0.06 $\mu\Omega$, which implies a temperature no greater than $\overline{T}$ = 4.5 keV during this start-up.

A possible limitation to the cyclic and start-up schemes is the difficulty in keeping the plasma sufficiently cool at the required high rf power level. If the average plasma temperature rises above 4.5 keV, the resistivity may be too small to effectively employ these schemes. Since the energy content of the low density, low temperature plasma is about 700 kJ, the energy confinement time must be kept to <100 ms.

4.2.3 Conclusions

The following statements can be made concerning LHCD in FED-A.

1. High temperature, high density operation, desirable for the optimization of Q, will probably lead to lower hybrid power deposition and a current source in the plasma periphery, assuming <T> < 15-20 keV and a flat density profile.
2. Steady-state current drive efficiency during burn will probably be no greater than 0.1 A/W.
3. Cyclic schemes are desirable because they minimize demands on the OH transformer, reduce fatigue due to pulsing of poloidal field energy, and greatly increase the time-averaged power and energy efficiency. Current drive efficiencies of 1 A/W are achievable in principle. One potential problem is the difficulty of maintaining the desired low temperatures in the low density current drive phase while dissipating rf power on the order of 10 MW in the plasma.

4.3 FAST WAVE CURRENT DRIVE: PROSPECTS FOR A PURELY STEADY-STATE FED

F. W. Perkins (PPPL)

The success of LHCD experiments (Sect. 4.1) has created the possibility of a true steady-state tokamak reactor. The transit-time magnetic pumping (TTMP) interaction between superthermal electrons and the fast Alfvén wave represents an approach that can also maintain a plasma current carried by energetic electrons. This approach is currently perceived to have several advantages over lower hybrid waves in a steady-state reactor. These include (1) antenna coincident with the first wall, (2) assured wave propagation to the plasma center and no wave propagation accessibility limitation on the energy of resonant tail electrons, and (3) complete compatibility with heating in the ion cyclotron range of frequencies (ICRF). The assessment presented here shows that a 40-MW, 62-MHz, fast wave current drive capability can be included in the FED-A ICRF heating system to drive a 4-MA current, provided $T_{eo} > 15$ keV.

4.3.1 Overview

The true steady-state tokamak is very attractive as a fusion reactor, and the recent success of LHCD experiments[11-13] has shown that traveling waves can maintain a tail of high energy electrons that carry the current. This section investigates the possibility that the high energy electron current could be maintained by the TTMP[34] interaction between the fast Alfvén wave and the electrons. The fast Alfvén wave provides several advantages over the lower hybrid wave in the area of reactor engineering. First, the frequency (62 MHz) and wave launcher are entirely compatible with ICRF heating, so that a separate high power rf heating system is not required. Second, the long parallel wavelength ($\lambda_{\|} \approx 2.4$ m) readily tunnels through the plasma scrapeoff layer, permitting the antenna to be coincident with the first wall. Lower hybrid antennas are quite sensitive to the plasma density at the antenna location and further require that the wave propagate through the turbulent scrapeoff plasma. Third, the fast Alfvén wave does not have a wave propagation accessibility limit on the energy of electrons that interact with

the wave. This allows wave propagation to the plasma center and creates the possibility of improved current drive efficiency.

The distinctive property of fast wave current is the weakness of the electron TTMP absorption process — a feature that is responsible for important advantages and disadvantages of fast wave current drive. On the beneficial side, the weak absorption ensures wave propagation to the plasma center. In fact, many passes through the plasma by the wave will be needed for absorption, a property that fast wave current drive shares with the present LHCD experiments in research tokamaks at low density. However, weak absorption also allows other channels of energy absorption to compete with electron TTMP. In particular, the fast wave can be damped via cyclotron harmonic damping by fusion alpha particles for almost any harmonic number ℓ. This follows from the fact that the energy E_α of fusion alpha particles satisifies $E_\alpha >> 1/2M_\alpha V_A^2$, where V_A is the Alfvén speed. In a reactor, cyclotron harmonic damping can be avoided if the frequency is chosen to satisfy $2\Omega_T < \omega < 2\Omega_D$. These inequalities can be satisfied if the plasma aspect ratio exceeds $R/a = 5$. Experimental demonstrations of fast wave current drive in a pure deuterium plasma would require that $\Omega_D < \omega < 2\Omega_D$, which implies $R/a > 3$. Hence FED-A can demonstrate fast wave current drive in a deuterium plasma and, with increased aspect ratio, can explore current drive in a DT plasma and the possible interaction with fusion alpha particles. In the DT case, fast wave current drive calls for a frequency $\nu = 62$ MHz, while standard second harmonic ICRF heating of deuterium requires $\nu = 75$ MHz. ($B_T = 5$ T is assumed.) Clearly, the same rf generator can be built to supply both frequencies.

The weak wave-particle interaction also forces fast wave current drive to operate in a mode that differs from the present LHCD experiments. Our calculations show that if the plasma current were to be carried entirely by a high energy tail, as is the case in present lower hybrid experiments, then the number density of tail electrons would not be sufficient to absorb the fast wave. Therefore, fast wave current drive must operate in a regime where Maxwellian electrons are responsible for the wave absorption. The wave-induced current takes the form of a

modest deformation of the Maxwellian distribution at high (but not too high) energies, typically $\varepsilon \approx 4\text{-}5 \times T_e$.

High central electron temperatures are particularly beneficial to the efficiency of fast wave current drive. Not only does the central electron density decrease (assuming constant beta), but also the energy of the current-carrying electrons increases as T_e. The efficiency improves as T_e^2. Let us also note that the fast wave will be preferentially absorbed in the central region of the plasma, where the highest energy near-Maxwellian electrons reside. In many ways, fast wave current drive is complementary to LHCD. Fast wave current drive works best in the dense, high beta, high T_e plasmas where LHCD encounters its greatest difficulties.

At 62 MHz, the fast wave antenna must launch a traveling Alfvén wave with $\lambda_{\|} = 2.4$ m. This corresponds to a toroidal mode number $n = 12$. The phased-array antenna fits entirely within the nominal ICRF launcher port, which has a 2.4-m toroidal extent. It is important to emphasize that the individual elements in this array are simply ICRF antennas with a common large-area Faraday shield. Each element is a basic ICRF antenna, which will have to be used for ICRF heating in any event. Additional requirements imposed by fast wave current drive are the size and contiguous location of the individual antennas and an ability to tune the resonant elements of the antenna over a modest range in frequency. The additional cost to install fast wave current drive launchers on FED-A should be small.

Our calculations show that the fast wave current drive installation sketched in Fig. 4-10 should be able to maintain a 4-MA plasma current with 40 MW of power, provided $T_{eo} > 15$ keV. The fast wave absorption is very weak — about 20 passes through the plasma are required for absorption. We show that the high Q toroidal eigenmodes ($Q \sim 700$) observed[35] in many tokamak experiments are consistent with other mechanisms of absorption being substantially less than the electron TTMP predicted for FED-A (in the absence of significant fusion alpha particles).

Our observations are that fast wave current drive is the most attractive method for maintaining a current in a pure steady-state

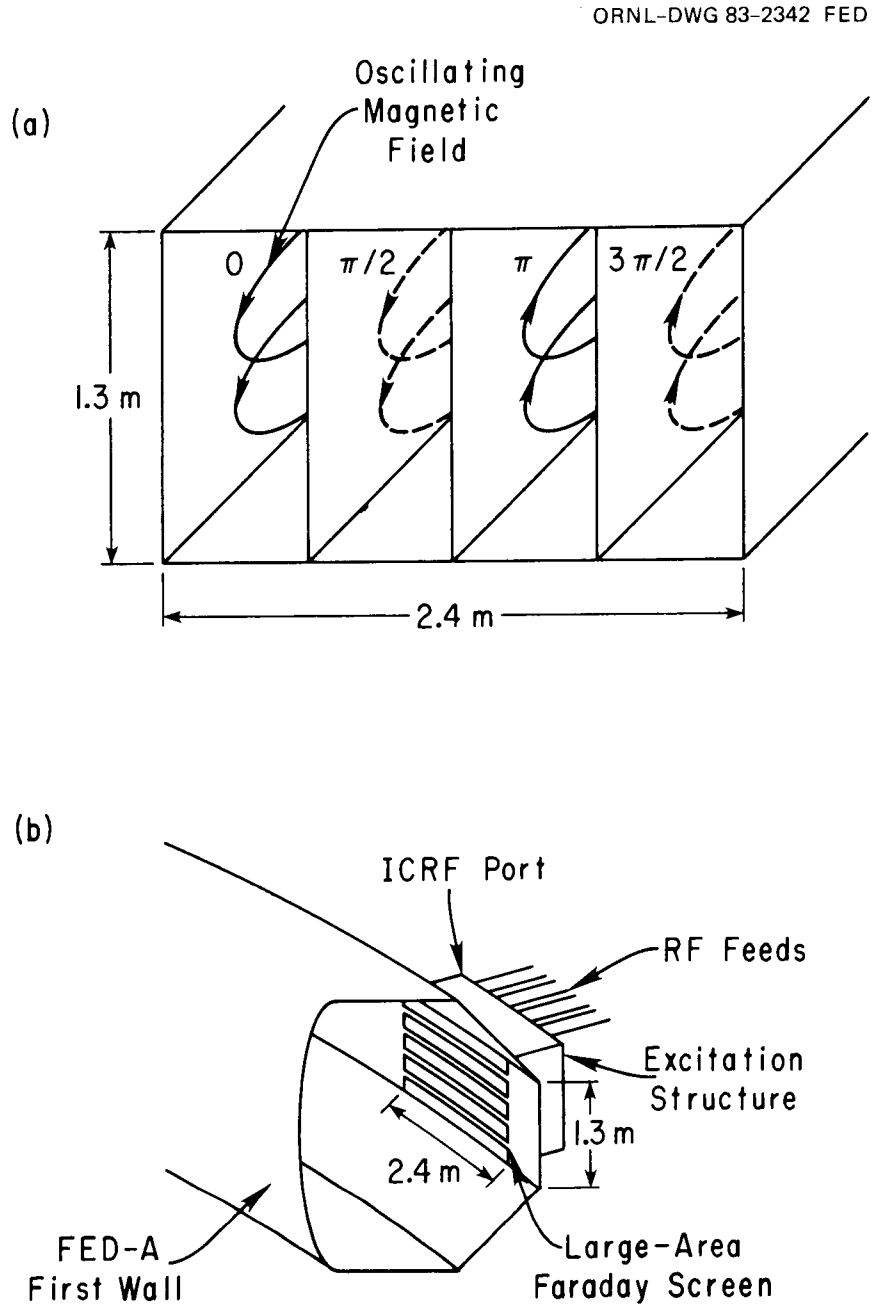

Fig. 4-10. Fast wave current drive antenna configuration. (a) Geometry and phasing of oscillating magnetic field. Because the component of the oscillating magnetic field along the steady magnetic field $\vec{B}_o$ is the dominant electromagnetic field in the fast wave, the antenna-plasma coupling occurs via the magnetic, not the electric, field. The magnetic field in each element has the configuration appropriate to a TE waveguide mode. The excitation can be via waveguide or coils. (b) Installation of the antenna. The large-area Faraday screen is simply a series of slots in the FED-A first wall and therefore does not interrupt toroidal current or first wall coolant flows.

tokamak when $T_{eo} > 15$ keV, that the experimental data available to date support the requirement that electron TTMP dominate other wave absorption processes, and that a fast wave current drive capability can be included in the ICRF heating system for minimal additional cost. The crucial parameter for fast wave current drive is the central electron temperature. The value to be expected for FED-A depends on the still uncertain electron energy confinement in the temperature range 8 keV $< T_e <$ 20 keV. Injection heating experiments in TFTR should make clear what electron temperatures can be expected in FED-A. If T_{eo} exceeds 15 keV, then fast wave current drive can provide an energy-efficient, steady-state tokamak.

Section 4.3.2 presents the basic physics of fast wave propagation and damping. Section 4.3.3 deals with the traveling wave antenna. Section 4.3.4 sketches experiments that could be performed on possible upgrades for TFTR.

4.3.2 Fast Wave Basics

Fast wave propagation. The fast wave is simply the extension of the MHD compressible Alfvén wave into the frequency (ω) regime above the ion cyclotron frequency (Ω). In its simplest version, one can write the equations governing the wave fields as[36]

$$\left(\frac{\omega_{pi}^2}{\Omega^2 - \omega^2} - n_\parallel^2 + 1\right) E_{ox} = i\left[\frac{\omega_{pi}^2 \omega}{\Omega(\Omega^2 - \omega^2)}\right] E_{oy}$$

$$- i\left[\frac{\omega_{pi}^2 \omega}{\Omega(\Omega^2 - \omega^2)}\right] E_{ox} + \left(\frac{\omega_{pi}^2}{\Omega^2 - \omega^2} - n_\parallel^2 + 1 - n_\perp^2\right) E_{oy} = 0 \ , \quad (4\text{-}19)$$

where we have assumed a dependence, in a slab plasma,

$$\vec{E} = \vec{E}_o \exp(i\vec{k}_\perp \cdot \vec{\chi} + ik_\parallel z - i\omega t) \ ,$$

$$n_\perp = k_\perp c/\omega \ , \quad (4\text{-}20)$$

$$n_\parallel = n_\parallel c/\omega \ ,$$

as well as the polarization

$$\vec{E}_o = \begin{pmatrix} E_{ox} \\ E_{oy} \\ 0 \end{pmatrix} \quad \vec{k}_\perp = k_\perp \hat{x} \ , \tag{4-21}$$

corresponding to high plasma conductivity along field lines (in the z-direction). Here ω_{pi} is the ion plasma frequency, $\vec{E}$ the wave electric field, k the wave number, and n the wave refractive index. The resulting dispersion relation is

$$k_\perp^2 = \frac{\omega^2}{V_A^2} \frac{\{1 - [\Omega(\Omega + \omega)/\omega_{pi}^2](n_\parallel^2 - 1)\}\{1 + [\Omega(\omega - \Omega)/\omega_{pi}^2](n_\parallel^2 - 1)\}}{1 + (n_\parallel^2 - 1)(\omega^2 - \Omega^2)/\omega_{pi}^2} \ , \tag{4-22}$$

where V_A is the Alfvén velocity, given by

$$V_A^2 = B^2/4\pi nM \ , \tag{4-23}$$

M being the ion of mass. Since the inequality $\omega_{pi}^2 >> \Omega^2$ is satisfied over the plasma, the terms involving $n_\parallel^2$ can be ignored (since $n_\parallel \approx 2$) and the fast wave dispersion relation becomes

$$k_\perp^2 = \frac{\omega^2}{V_A^2} = \omega^2 \left(\frac{\omega_{pi}^2}{c^2 \Omega^2} \right) . \tag{4-24}$$

The wave polarization then takes the form

$$E_{ox} = -i \left(\frac{\omega}{\Omega} \right) E_{oy} \ , \tag{4-25}$$

$$B_z = \frac{c}{V_A} E_{oy} \ ,$$

$$B_x = -n_\parallel E_{oy} \ ,$$

$$B_y = -in_{\parallel} \left(\frac{\omega}{\Omega}\right) E_{oy} \ .$$

Many properties of the fast wave are evident from these straightforward considerations. In our application, the frequency is chosen to lie midway between the tritium and deuterium second harmonic frequencies, so that we can choose $\omega = 2\Omega$, $M = 2.5M_p$ (proton mass) with good accuracy. Fast wave properties of interest include the following.

1. The perpendicular wavelength,

$$\lambda_{\perp} = \frac{c}{2\omega_{pi}} \approx \frac{12 \text{ cm}}{(n_{14})^{1/2}} \ , \tag{4-26}$$

is small compared to the minor radius of FED-A. It follows that geometrical optics describes the fast Alfvén wave well, and it will be refracted into regions with low phase speed (high density regions), naturally leading to high wave intensities as it accumulates in the plasma center.

2. The cutoff density,

$$n_c = (1.5 \cdot 10^{11} \text{ cm}^{-3})(n_{\parallel}^2 - 1) \approx 5 \times 10^{11} \text{ cm}^{-3} \ , \tag{4-27}$$

is low so that wave propagation begins right at the plasma surface.

3. The compressional (B_z) component of the wave magnetic field is by far the largest electromagnetic field component. This motivates antenna configurations that provide an oscillating toroidal magnetic field. Antennas couple to the fast Alfvén wave by magnetic, not electric, fields.

4. Provided $n_{\parallel}^2 > 1$, there are no resonances to absorb the wave. Wave absorption proceeds via wave-particle interactions.

5. In the main body of the plasma, the dispersion relation [Eq. (4-22)] can be simplified to be

$$\omega^2 = k_\perp^2 V_A^2 + 5k_\parallel^2 V_A^2 \ , \tag{4-28}$$

leading to a parallel group velocity of

$$V_{g\parallel} = \frac{\partial \omega}{\partial k_\parallel} = \frac{5 n_\parallel V_A^2}{c} \ , \tag{4-29}$$

which is very slow (about 2×10^8 cm/s in FED-A). Consequently, even weakly damped fast Alfvén waves (say, $Q \sim 100$) can propagate 3 m the long way around the torus, and toroidal eigenmodes are not likely to exist.

Electron TTMP interaction. Calculation of the damping rate for fast wave-electron interactions involves straightforward, but lengthy, kinetic theory calculatons. The two key results are that the intensity damping decrement is given by

$$2\gamma = \omega \frac{\pi^2 mn}{2B^2} \left\langle \left(v_\perp^2 - \frac{2T_e}{m} \right)^2 \frac{\partial f_o}{\partial v_\parallel} \right\rangle \ ,$$

where

$$\left\langle \left(v_\perp^2 - \frac{2T_e}{m} \right)^2 \frac{\partial f_o}{\partial v_\parallel} \right\rangle = \int_0^\infty 2\pi v_\perp \, dv_\perp \left(v_\perp^2 - \frac{2T_e}{m} \right)^2 \left(\frac{\partial f_o}{\partial v_\parallel} \right)_{\omega/k_\parallel} \ , \tag{4-30}$$

and the parallel wave electric field is given by

$$eE_\parallel + i \frac{k_\parallel B_z T_e}{B} = 0 \ . \tag{4-31}$$

Here f_o denotes the velocity distribution function for electrons. Equation (4-31) simply states that the total parallel force on the electrons vanishes; it is the generalization of the high conductivity

limit to include the magnetic gradient force. Evaluating Eq. (4-30) for a Maxwellian distribution leads to

$$2\gamma = \omega(\sqrt{\pi}/2)\beta_e \varepsilon^{1/2} e^{-\varepsilon} , \tag{4-32}$$

where

$$\varepsilon = \frac{m\omega^2}{2k_\parallel^2 T_e} = \frac{mc^2}{2n_\parallel^2 T_e} \tag{4-33}$$

is the energy of the resonant electrons in units of T_e. The attenuation $e^{-\Delta}$ via TTMP interaction per pass of the fast wave through the central plasma is of interest. It can be estimated (since $v_{g\perp} \cong V_A$) by

$$\Delta = \frac{2\gamma a}{V_A} = \pi^{3/2} \left(\frac{a}{\lambda_\parallel}\right)\left(\frac{M}{m}\right)^{1/2} \beta_{eo}^{3/2} \varepsilon e^{-\varepsilon} , \tag{4-34}$$

where β_{eo} refers to the central electron beta. Let us adopt the values

$$\lambda_\parallel = 2.4 \text{ m} ,$$

$$a = 1 \text{ m} ,$$

$$\beta_{eo} = 0.05 ,$$

$$n_o = 2 \times 10^{14} \text{ cm}^{-3} ,$$

$$T_{eo} = 15 \text{ keV} .$$

Evaluating Eq. (4-34), we find

$$\Delta \approx 1.5\varepsilon e^{-\varepsilon} ,$$

and we find $\Delta \sim 0.1\text{-}0.05$ for $\varepsilon = 4.5$. The current will be carried by 75-keV electrons when $T_{eo} = 15$ keV. This regime produces 20-pass absorption and $(2\gamma/\omega) \approx 10^{-3}$, values that are not unreasonably small.

Clearly, difficulties with wave absorption will be experienced if the energy of the resonant electrons is increased to 150 keV in a Maxwellian distribution. Evidently the energy of the resonant electrons increases directly as T_e, with the consequent increase in the energy efficiency of current drive.

Our estimates rest on the electron distribution function being close to Maxwellian. Will a modest distortion of a Maxwellian distribution produce sufficient current? To answer this, let use require the current carried by unidirectional Maxwellian electrons with an energy exceeding ε to be larger than the current density,

$$\frac{ne}{\sqrt{2\pi}}\left(\frac{T_e}{m}\right)^{1/2} e^{-\varepsilon} > \frac{B_z c}{2\pi R} = j \ . \tag{4-35}$$

Our standard numerical values produce

$$e^{-\varepsilon} > \left(\frac{mc^2}{T_e}\right)^{1/2} \frac{B_z}{\sqrt{2\pi} Ren} \approx 2 \times 10^{-3} \ .$$

The inequality is modestly satisfied as long as electron TTMP interaction is strong ($\varepsilon \leqslant 4$). Altogether, the parameters of FED-A are appropriate to support fast wave current drive.

Efficiency. The efficiency of fast wave current drive is estimated to be, for constant β_{eo},

$$\eta = 0.09 \left(\frac{T_{eo}}{15 \text{ keV}}\right)^2 \frac{A}{W} \ .$$

The low efficiency comes from the rather high value of central electron density used in our estimates. The improvements in efficiency, which scale as T_{eo}^2, result from decreases in central density while maintaining constant β_{eo} and from the increased energy of current-carrying electrons. Clearly, at T_{eo} = 20 keV, fast wave current will be adequately efficient.

At constant T_{eo}, fast wave attenuation scales as $n_{eo}^{3/2}$. It may well be that fast wave current drive could operate with $\Delta \approx 10^{-2}$ (100-pass absorption) and $n_{eo} = 10^{14}$ cm^{-3}, bringing η up to $\eta = 0.1$ A/W at $T_{eo} = 10$ keV.

Interaction with fusion alpha particles. If the fast wave frequency is raised so that a cyclotron harmonic interaction with fusion alpha particles becomes impossible to avoid, then the overall damping can be estimated by using unmagnetized ion theory and computing the perpendicular ion Landau damping. The one-dimensional (1-D) velocity distribution for fusion alphas is

$$\frac{\partial f}{\partial u} = - \frac{K}{u^2} , \tag{4-36}$$

where, for an equal DT mixture,

$$K = (1/4)\langle\sigma v\rangle n_e \tau_s \approx 4 \times 10^{-4} \left(\frac{T}{10 \text{ keV}}\right)^{7/2} .$$

The resulting damping decrement is

$$\frac{2\gamma}{\omega} = \pi V_A^2 \left(- \frac{\partial f}{\partial u}\right) = \pi K \sim 10^{-3} , \tag{4-37}$$

which makes damping on fusion alpha particles comparable to electron TTMP. In a reactor, strong wave interaction with fusion alpha particles must be avoided, as well as interaction with cyclotron harmonic resonances of the majority plasma ions. The frequency must be intermediate between the second harmonic tritium and deuterium frequencies. In this case, the only deleterious wave-particle interactions are second harmonic resonances with imperfectly stripped impurities. It is hoped that in a reactor, these concentrations will be small and only in the surface layers.

Toroidal eigenmodes. High Q toroidal eigenmodes have been noted on several research tokamaks. Measurements[35] yield values of

$$Q \equiv \frac{\omega}{2\gamma} \sim 4 \times 10^2\text{-}10^3 \ ,$$

which demonstrates that fast waves can propagate toroidally with weak damping. The mechanism causing damping in these measurements is not known; electron TTMP would be far too weak in these low beta devices. A wall absorption coefficient of 10^{-2} could account for the results. This points to the need for maintaining $\Delta > 10^{-2}$. Thus, experimental observations to date do not preclude the fast wave current drive scenario presented here, but they have generated no experimental demonstration of plasma heating or wave propagation where electron TTMP is the dominant mechanism.

4.3.3 Antenna

The traveling wave antenna is shown schematically in Fig. 4-10. For our purposes it consists of four elements, each element producing an excitation field at the Faraday shield,

$$B_{zm}(z) = B_z \cos\left[\frac{4\pi}{\ell}\,(z - z_m)\right] e^{-i(m\pi/2+\omega t)} \ ; \qquad (4\text{-}38)$$

the elements have the spacing

$$z_m = \frac{m\ell}{4} \ , \qquad m = 0,\ 1,\ 2,\ 3 \ . \qquad (4\text{-}39)$$

Such an excitation can be provided by re-entrant waveguides[37] or by coils located within the individual elements.

The power spectrum of this antenna is given by

$$P(k_\parallel) = \frac{128\pi^2}{\ell^3}\left[\frac{\sin^2(k_\parallel \ell)}{\sin^2(k_\parallel \ell/8 - \pi/4)}\right]\left[\frac{\cos^2(k_\parallel \ell/8)}{(k_\parallel^2 - (4\pi/\ell)^2)^2}\right] \ , \qquad (4\text{-}40)$$

where the first set of brackets represents the effect of phasing the elements and the second set of brackets gives the power spectrum associated with an individual antenna element. This power spectrum has a peak at $k_{\|} \ell = 2\pi$. In the vicinity of this peak, the variation with $k_{\|}$ can be well approximated by

$$P(k_{\|}) = \text{const} \frac{\sin^2(\delta k_{\|} \ell)}{(\delta k_{\|} \ell)^2} , \tag{4-41}$$

where

$$\delta k_{\|} = k_{\|} - \frac{2\pi}{\ell} .$$

Hence, if $k_{\|} = 2\pi/\ell$ corresponds to $n_{\|} = 2$, most of the power spectrum lies in the region $n_{\|} = 1.5\text{-}2.4$.

There is an important contribution to the spectrum for a wave traveling in the backward direction with $k_{\|} = -6\pi/\ell$. This wave has one-third the wavelength of the desired forward-going wave and will be absorbed by electrons with one-third the speed. The backward current drive by this backward-going wave is small because of the low velocity and thus does not alter the current drive by the forward wave. It does contribute a potential source of energy inefficiency, however. Fortunately, it is possible to reduce the coupling of the backward wave to the plasma by recessing the antenna into the first wall. Since the evanescent spatial decay rate of the backward wave is three times that of the forward wave, it is possible to arrange for the backward wave to experience substantial evanescence while the desired forward wave experiences little. Thus most of the power into the plasma will lie in the range $n_{\|} = 1.5\text{-}2.5$.

4.3.4 Possible Experiments in TFTR Upgrade

A possible upgrade for TFTR proposes long pulse operation at a toroidal field of 2 T. Fast wave current drive in a proton plasma would

be best accomplished at three-halves of the proton cyclotron frequency, $\nu = 3/2\nu_{pc} = 45$ MHz. A phased array of four ICRF launchers in contiguous ports would generate an n = 5 traveling wave with $\lambda_{\|} = 2\pi R/n = 3.2$ m, yielding $n_{\|} = 2.1$. The key question is whether TFTR will obtain $T_{eo} \sim$ 10 keV and an adequate central electron $\beta_{eo} \sim 5 \times 10^{-2}$ at a toroidal field of only 2 T. Clearly, machines of the TFTR scale represent the best opportunity to provide the needed demonstration of fast wave current drive.

4.4 ELECTRON CYCLOTRON CURRENT DRIVE

V. S. Chan and C. S. Liu (GA Technologies, Inc.)

Electron cyclotron heating (ECH) is probably one of the best understood rf heating schemes. A number of experiments, carried out on mirror machines and tokamaks,[38,39] have demonstrated that ECH is effective in increasing the perpendicular electron energy. These experimental results are generally consistent with the linear theory of propagation and damping of the fast electromagnetic waves, that is, the ordinary and the extraordinary modes.

For FED parameters, the theory predicts that both of these modes can be effectively absorbed in a single pass under high temperature conditions. ECH has a number of distinctive features. The heating is localized, with the power deposited near the cyclotron resonance layer, where the electron cyclotron frequency $\Omega_c = eB/mc$ matches the applied microwave frequency ω. The resonance surface is accessible to these waves provided the plasma is underdense, that is, $\omega > \omega_{pe} \equiv (4\pi ne^2/m)^{1/2}$. This is to be differentiated from other rf schemes in which accessibility to the center of the plasma requires launching a wave spectrum with proper parallel wave numbers, thus necessitating careful design of the launching structure, especially in the case of launching a traveling wave. Electron cyclotron resonance heating is paced more by the technological development of high frequency gyrotrons. In view of this distinction, ECH as a candidate for current drive has advantages over other schemes in terms of wave penetration, antenna coupling, and a well-understood absorption mechanism consistent with linear theory.

4.1.1 Physics

In order to drive a current with electron cyclotron waves, it is necessary to selectively heat electrons traveling in one direction. This can be accomplished by launching the electron cyclotron waves from either the high field side or the low field side of the torus and having the waves completely absorbed before they cross the cyclotron resonance surface. This can be achieved in high temperature plasmas where single-pass Doppler resonance absorption takes place. The mechanism can be understood as follows. A traveling cyclotron wave is used to asymmetrically increase the perpendicular energy of electrons moving in the same direction as the waves. On account of the v^{-3} dependence of the Coulomb collision frequency on the electron velocity v, the ions become less resistive to this group of electrons. An anisotropic resistivity is thus created. As a consequence, the electrons acquire a net momentum in the direction of the waves, balanced by an equal and opposite momentum acquired by the ions. This results in the generation of a toroidal current. The current drive efficiency in current generated per unit power absorbed has been obtained by Fisch and Boozer,[40]

$$\frac{I_{ECH}}{P_{ECH}} = \frac{3}{(5 + Z_i)} \frac{v_e^2 u_0^2}{2\pi R \omega_{pe}^2 e \ \ell n \ \lambda} \quad \text{(cgs)} , \tag{4-42}$$

where

$v_e = (T/m)^{1/2}$ is the electron thermal velocity,

R = major radius of device,

Z_i = charge of ions,

and

$u_0 = [\omega - \Omega(x)]/k_{\parallel} v_e$ is the Doppler-shifted resonance velocity.

Clearly, the efficiency is very sensitive to u_0, which is determined not so much by the parallel wave number spectrum launched, but by how strongly a particular mode is damped at a given u_0. The farther

away from the cyclotron resonance layer a mode is completely absorbed, the larger are u_0 and thus the efficiency. Assuming a Maxwellian plasma, the absorption rates for different modes can be self-consistently evaluated based on linear theory. It is found that at high temperature conditions when single-pass absorption is achieved, the following u_0 values can be achieved:

Mode	u_0
Ordinary	1.5
Extraordinary	1.5
Electrostatic (Bernstein)	3.0

Bernstein waves, the most efficient of the the three, can be excited at the fundamental resonance via upper hybrid mode conversion from fast extraordinary waves. At the second harmonic, Bernstein waves are excited near the cyclotron resonance layer, again via coupling to electromagnetic waves. Other ways of confining the waves far away from the cyclotron resonance have also been suggested in order to increase u_0. Detailed studies of these ideas have yet to be carried out.

Assuming $u_0 = 3$ for the optimum situation of $Z_i = 1$ and $\ell n\, \lambda \cong 17$, the efficiency becomes

$$\frac{I_{ECH}\ (MA)}{P_{ECH}\ (MW)} = \frac{0.04 T_{10}}{R_5 n_{20}}\ , \tag{4-43}$$

where T is normalized to 10 keV, n is normalized to 10^{20} m^{-3}, and R is normalized to 5 m. This expression has been verified by a 2-D (in velocity space) Fokker-Planck calculation, where the ECH is modeled by a quasi-linear diffusion operation in velocity space. The agreement between the numerical results and Eq. (4-43) is excellent, as depicted in Fig. 4-11. No correction factor is necessary to account for the two-dimensional effects. When ECH current drive is compared with LHCD, the

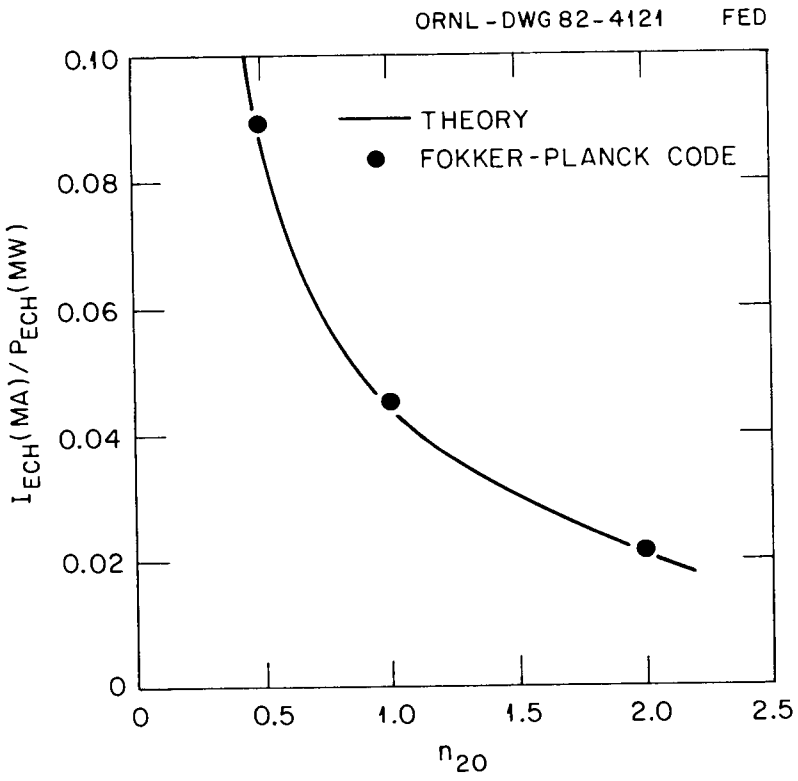

Fig. 4-11. ECH current drive efficiency as a function of density n_{20} for $T_{10} = 1$ and $R_5 = 1$.

latter is more efficient for wave resonance energy above 100 keV for the same density and with temperatures within the FED operating range.

Since ECH is very efficient in increasing the perpendicular energy of electrons, trapped particle effects due to the presence of the toroidal magnetic mirror may be a factor in decreasing the efficiency of ECH current drive, especially when low parallel velocity electrons take part in the current drive process. The trapped particle correction has been calculated in Refs. 41-43. This is depicted in Fig. 4-12, where the current drive efficiency is plotted as a function of the inverse aspect ratio (or minor radius). It can thus be concluded that ECH current drive is most efficient in sustaining a current near the magnetic axis where the trapped particle interference is minimal. Recent experiments performed at the Culham Levitron[44] demonstrated rf current sustainment by ECH; the results were consistent with the Fisch-Boozer theory. Trapped particles were not important in these experiments.

4.4.2 FED Considerations

Taking the current drive efficiency as given by Eq. (4-43), one can obtain some possible limits on Q, the ratio of fusion power output to rf power input in a steady-state tokamak, which ultimately determines the practicality of a particular current drive scheme. If we take the fusion power output to be

$$\bar{P}_{DT}\ (MW/m^3) = 2.6 n_{20}^2 \frac{\ell n(1 + 0.63 T_{10}^{3.5})}{T_{10}} \qquad (4\text{-}44)$$

and the plasma volume to be $V = 2\pi^2 a^2 \kappa R$, where a is the minor radius and κ is the vertical elongation of the plasma, then

$$Q = 2.9 \beta_5 R_5 q_* B_5 \frac{2\kappa}{1 + \kappa^2}\ , \qquad (4\text{-}45)$$

where we have expressed the density in terms of the plasma β_5 ($= 0.64 n_{20} T_{10}/B_5^2$). Here beta is normalized to 5%, q_* is the engineering

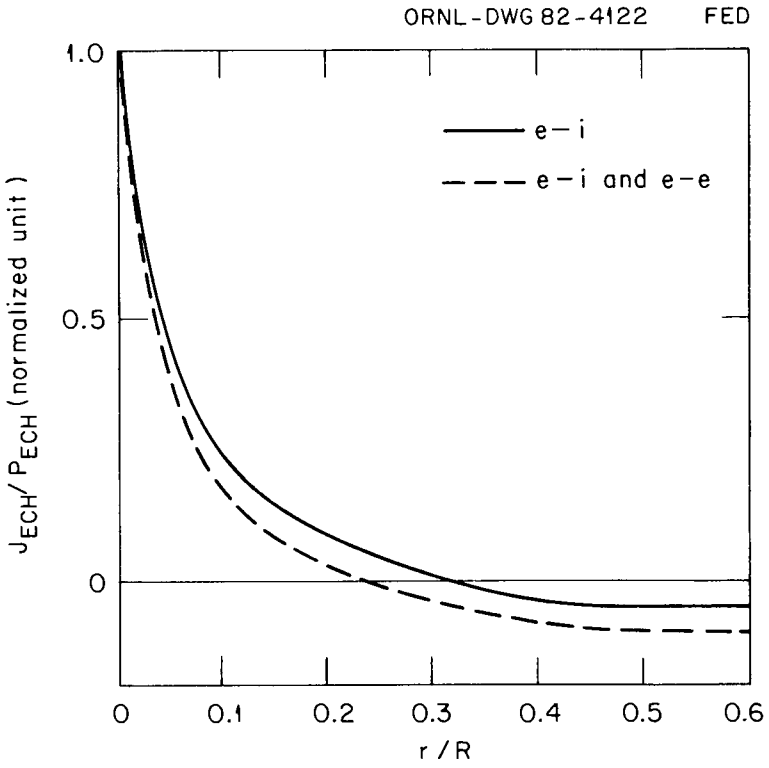

Fig. 4-12. ECH-driven current density per unit power as a function of r/R with electron-ion collisions only (solid line) and with electron-ion and electron-electron collisions (dashed line).

q value, B is normalized to 5 T, and the temperature is taken to be 16 keV. For typical FED-A parameters,

$$a = 0.9 \text{ m} ,$$
$$R = 4.2 \text{ m} ,$$
$$\kappa = 1.2 ,$$
$$B = 5 \text{ T} ,$$
$$q_* = 1.6 ,$$

and assuming a beta value of 6% (a minimum requirement for economical operation), Q is calculated to be $\cong 4.6$. Other correction factors or a beta limit of less than 6% will further lower Q. The corresponding wave frequency for a magnetic field of 5.0 T is 140 GHz, which translates to a cutoff density of 2.2×10^{20} m^{-3}. The density corresponding to $\beta = 6\%$, $T_e = 10$ keV, and B = 5.0 T is 1.7×10^{20} m^{-3}, which is below the cutoff density. Hence, wave penetration should not be a problem.

To implement ECH current drive on FED, microwave antennas capable of launching pure modes (ordinary or extraordinary) must be used. A number of setups can be visualized. Extraordinary waves launched from the high toroidal side of the torus with suitable launch angles can pass through the resonance layer relatively undamped and transfer their energy to the Bernstein waves via upper hybrid mode conversion. Alternatively, ordinary waves can be launched from the low field side at a specific angle that will lead to strong coupling with the extraordinary waves and subsequently to the Bernstein waves, again via the upper hybrid layer. Coupling to Bernstein waves via the second harmonic cyclotron resonance is also possible. However, this would require a much higher frequency for the same magnetic field. Present-day tokamaks with ECH capabilities, such as Doublet III at GA Technologies and PDX at Princeton Plasma Physics Laboratory, can be used to test the practicality and efficiency of these coupling schemes.

Like other rf current drive schemes, the efficiency of ECH current drive goes down inversely with density, which, for an acceptably high value of Q, places a limit on the operating plasma density and thus the

fusion power output. However, unlike other schemes, ECH does not appear to have the problem of a limited operating window in density and temperature due to difficulties with wave penetration. It is also less susceptible to nonlinear processes, and the possibility of directly channeling energy to ions is virtually nonexistent.

4.4.3 Concluding Remarks

A truly steady-state operation with ECH current drive does not appear to be the most promising scheme, based on our physics understanding to date, because of the low efficiency. However, a number of alternative scenarios can be visualized in which ECH can be used advantageously to share the load of the inductive current drives.

The "cyclic density" discharge scenarios proposed for lower hybrid waves can also be realized with electron cyclotron waves. With the alternate application of an inductive driver and an ECH driver (for a relatively shorter period), a close-to-constant toroidal current can be maintained in principle for an indefinite period of time.

Electron cyclotron resonance heating can also be used to generate a "seed" current in the start-up phase of the FED operation in combination with preionization, thus saving valuable transformer volt-seconds. The possibility of enhancing the efficiency by the combination of an ohmic field and ECH has yet to be studied in detail, although preliminary investigation of LHCD in combination with an inductive field shows that such enhancement may be possible.

According to Fisch and Boozer,[40] the anisotropic resistivity is generated by increasing the energy of a selected group of electrons. It appears plausible, then, that a combination of ECH and LHCD may create a "bootstrap" effect, leading to the enhancement of the overall efficiency. Preliminary numerical studies[41-43] using a 2-D Fokker-Planck code have given no indication of such a "bootstrap" effect. The overall efficiency obtained so far is at best additive. However, these results are only preliminary, and this is certainly an area that warrants detailed investigation, both experimentally and theoretically, in the future.

4.5 RELATIVISTIC ELECTRON BEAM CURRENT DRIVE

D. Ehst (ANL)

The use of a relativistic electron beam (REB) for current maintenance, an idea pursued by a number of researchers over the past decade,[45-53] benefits from two phenomena associated with REB injection into a plasma. First, REB technology development has been focused on pulsed power injection, rather than continuous wave (cw) operation. Second, the bulk of theoretical and experimental evidence demonstrates that the plasma's electrical resistivity is increased by orders of magnitude during REB injection. As a result, REB current maintenance could be achieved by repetitive injection ("overdrive") of an REB current with a simultaneously oscillating resistivity. Several authors[54-56] have discussed how the injection of pulsed power can reduce the time-averaged power requirement for current drive when combined with density or resistivity oscillations.

The performance of REB injection is distinguished from alternatives by two features. First, this driver realizes the advantages of pulsed power current drive without significant changes in the macroscopic plasma parameters (density, temperature, current, Z_{eff}), since the resistivity is enhanced by phase space activity (e.g., by the two-stream instability). Second, extremely large resistivity enhancements are possible under these conditions, so that most of the injected energy is transferred to the poloidal magnetic fields associated with the (subthermal) drift of the electron distribution. The principal energy dissipation is then neoclassical Joule heating, the average power consumption being close to $\langle P_d \rangle \approx I_0^2 R$.

The use of REB injection was identified as a possible candidate for FED-A by an earlier survey,[57] which compared a large number of drivers. Figure 4-13 displays the normalized ratio of current density to dissipated power density and shows the potential superiority of the REB current drive when the resistivity enhancement factor α is large. It should be noted that in the present theory of REB current drive, centrally peaked driven current densities are assumed in a zero-dimensional

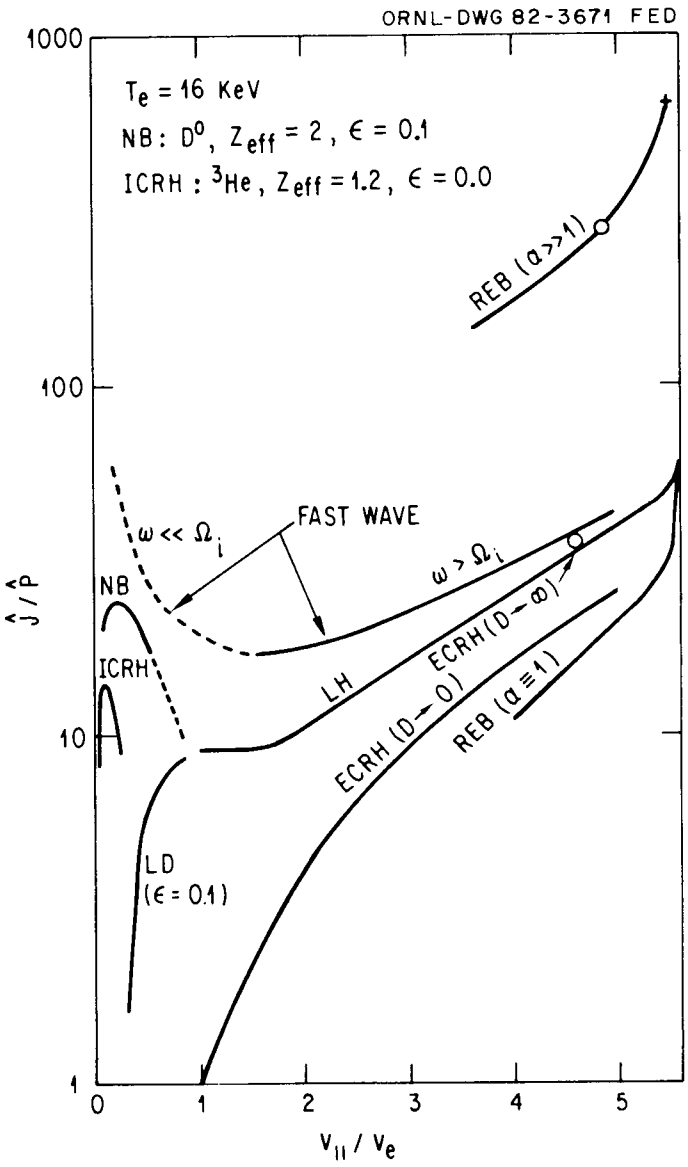

Fig. 4-13. Normalized current density to power density ratio for various drivers in the DEMO reactor at T_e = 16 keV and $n_e = 1.0 \times 10^{20}$ m^{-3}. REB has W_d = 4.0 MJ. The neutral deuterium injection (NB) calculation assumes Z_{eff} = 2 and A^{-1} = 0.1 and includes the benefits of neoclassical effects. ^{3}He minority heating (ICRH) assumes Z_{eff} = 1.2 and A^{-1} = 0.0; the result deteriorates if neoclassical effects are included. ECRH results are shown in the linear (D → 0) and high power, nonlinear (D → ∞) limits. The lower hybrid (LH) wave is shown at high phase speeds, but neoclassical effects may reduce $\hat{j}/\hat{p}$ for Landau damping (LD) at slow speeds. The fast wave benefits from TTMP, but at slow phase speeds (dashed line), neoclassical effects are a concern.

analysis, which does not address the issue of REB penetration and current profile evolution. This issue, other deficiencies in the model, and possible remedies are discussed in Sect. 4.5.4.

For a reactor, the circulating electric power associated with REB current drive is less than a few percent of the gross electric output. This is shown graphically in Fig. 4-14. A corollary is that the REB system is relatively insensitive to the electric conversion efficiency of the driver hardware (18% vs 91% in the illustration). In contrast, the fast wave and neutral beam drivers may require a circulating power for cw current maintenance that is a large fraction of the gross power. In this case, the net power production is quite sensitive to the efficiency of the power delivery system, as shown for two values of neutral beam efficiency.

While our investigation centers on the issue of steady-state current drive, we point out other applications. In particular, the tokamak discharge may be initiated completely by the REB, without the aid of a transformer or rf (ECRH) assistance. This was demonstrated on SPAC VI,[58] in which the neutral gas fill was ionized and heated to several hundred electron volts and the full plasma current was created with a single shot (about 1 kJ) from the REB source. The return current heating mechanism[59] also appears adequate to consider using the REB for heating to ignition.

4.5.1 Comparison of Theory and Experiment

All experimental REB work so far has involved only single-pulse injection, so the increase in toroidal current, ΔI, is the relevant measurement. The increase is predicted to be[56,57]

$$\Delta I = \frac{2\pi R_0 mc}{eL} (\gamma_d \beta_d - \gamma_s \beta_s) , \qquad (4\text{-}46)$$

where R_0 is the major radius, L is the toroidal current's self-inductance, c is the speed of light, and e and m are the electron charge and rest mass, respectively. The relativistic mass ratio is γ and $\beta \equiv \sqrt{1 - \gamma^{-2}}$.

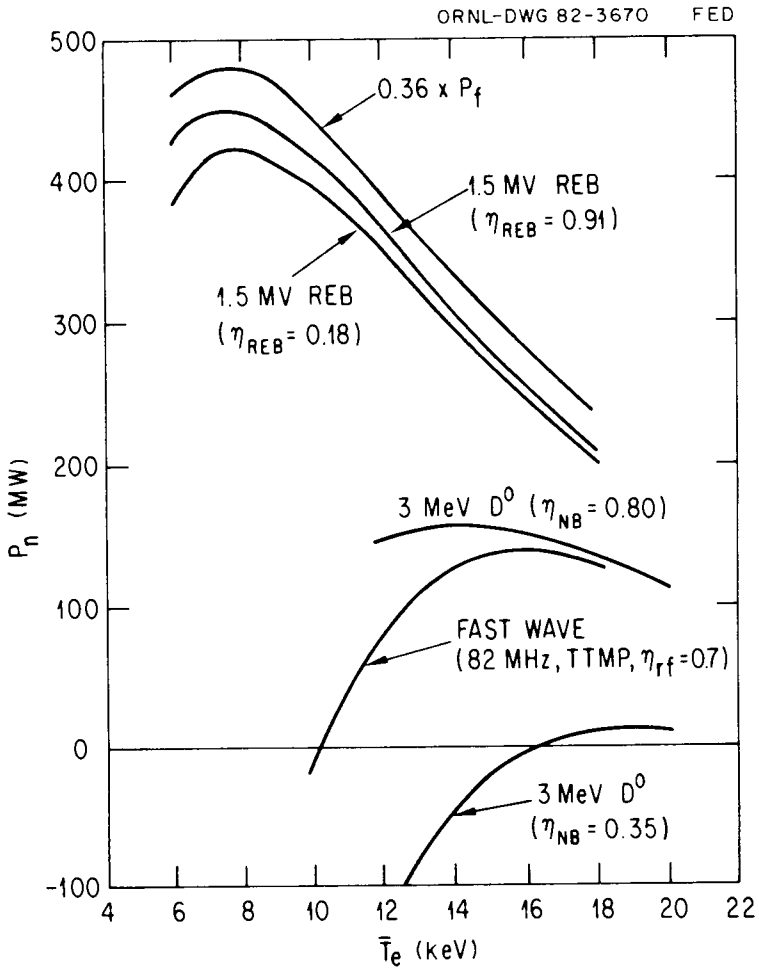

Fig. 4-14. Gross power ($0.36 \times P_f$) for DEMO reactor and net electric power for three driver candidates operating at different average temperatures; R_0 = 5.2 m and I_0 = 9.0 MA. Detailed discussion of these results is available in Ref. 57.

The subscript d refers to the initial value when the relativistic electrons leave the diode, and s refers to the value when the REB has slowed down to the point that the reverse electromotive force (emf) has gone to zero. Specifically, the theory provides

$$\beta_s = \frac{(I_0 + \Delta I)\beta_d}{I_{d_0}}$$

and

$$\gamma_s = (1 - \beta_s^2)^{-1/2} ,$$

where I_0 is the toroidal current before the REB pulse and I_{d_0} is the total stacked REB current immediately after the diode pulse. If the diode operates for a pulse width t_{t-o} and the toroidal transient time for a relativistic electron is $t_{tr} = 2\pi R_0/(\beta_d c)$, then the stacking factor is t_{t-o}/t_{tr}, and the stacked current is related to the instantaneous cathode current I_c by $I_{d_0} = t_{t-o} I_c / t_{tr}$. The kinetic energy delivered in the pulse is

$$W_d = (\gamma_d - 1) \frac{mc^2}{e} I_c t_{t-o} .$$

The theory assumes a resistivity enhancement α during the beam's slowing-down period, and this should be observable as a rapid onset of ΔI after diode operation. The current increase should occur in a period that is short compared to the classical L/R time,

$$\Delta t \approx (L/R)/\alpha . \qquad (4\text{-}47)$$

Additionally, the analytic formulas above assume a diode pulse width even shorter than the beam slowing-down time,

$$t_{t-o} << \Delta t . \qquad (4\text{-}48)$$

We compare these predictions with the results of four experiments.

SPAC V[53] was a toroidal vacuum chamber at Nagoya University with $R_0 = 0.11$ m and a specific inductance estimated in the range $L/2\pi R_0 = 0.17\text{-}0.48$ μH/m. Since it had no transformer, the initial toroidal current was identically zero, $I_0 = 0$. For typical experimental values, $\gamma_d = 2$ (∿500 kV) and $W_d = 2.6$ kJ ($I_{d_0} = 2.2$ MA), the analytic formulas predict $\Delta I = 15$ kA if $L/2\pi R_0 = 0.2$ μH/m. Experimental values are larger, $\Delta I \approx 30\text{-}40$ kA. This discrepancy is not surprising, since the condition in Eq. (4-48) was not satisfied. Fast $\dot{B}_p$ probes showed[60] that $t_{t\text{-}o} \approx \Delta t \approx 100$ ns, and we would thus expect larger ΔI values. However, for this large a value of W_d, $\gamma_d\beta_d >> \gamma_s\beta_s$, so Eq. (4-46) would predict $\Delta I \propto \gamma_d$, and we find that this linear relationship was in fact observed[53] on SPAC V.

A larger device, SPAC VI,[58] was also built at Nagoya with $R_0 = 0.24$ m. In this case $t_{t\text{-}o} \approx 80$ ns $<< \Delta t \approx 700$ ns, so the analytic theory should hold. Since the torus is prefilled with a cold plasma (≈20-30 eV) from a gun, the classical $L/R \gtrsim 1$ ms. Thus, the observed Δt of ≲1 μs is evidence for a large resistivity enhancement, $\alpha \gtrsim 10^3$. For the particular shot reproduced in Fig. 4-15, $\gamma_d = 3.5$ (1.3 MV) and $W_d = 8$ kJ ($I_{d_0} = 1.2$ MA); $I_0 = 0$ since there is no transformer. We would expect ΔI as low as 15 kA for a peaked current density ($L/2\pi R_0 = 0.4$ μH/m) or as high as 30 kA for a hollow current density ($L/2\pi R_0 = 0.2$ μH/m). As shown in the figure, the observed $\Delta I = 28$ kA, which is within the bounds predicted. The experimentalists also cite a monotonic increase in ΔI with γ_d, as we would expect from the theory.

Experimental results on a racetrack torus at Cornell[61] also demonstrate large resistivity enhancements with $\Delta t \approx 1$ μs and $\alpha \gtrsim 10^2$. In a typical shot there is an initial current $I_0 \approx 300$ A and $\gamma_d = 1.3$ (150 kV). However, insufficient REB energy is supplied to reliably test Eq. (4-46). If the full beam energy (≈40 J) were trapped in the torus and if the relativistic electrons had $v_\perp << v_\parallel$, then the stacked current for $I_c = 4.5$ kA, $t_{t\text{-}o} = 60$ ns, and $t_{tr} = 45$ ns would be $I_{d_0} = 6.1$ kA, corresponding to ΔI in the range 1.4-3.9 kA, depending on the specific inductance. The problem is that the beam is launched at a large pitch

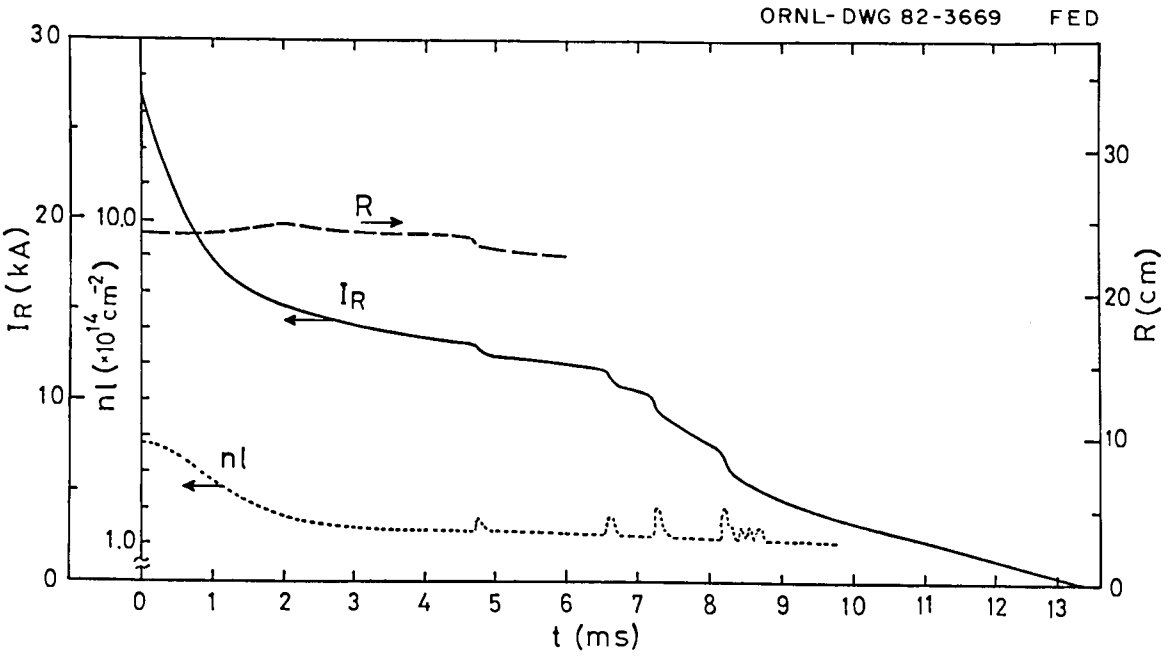

Fig. 4-15. Time variations of the net ring current (I_R), the major radius (R), and the plasma line density ($\overline{n}_\ell$) on SPAC VI.

angle ($v_\perp \approx v_\parallel$), which reduces the toroidally circulating current. This is compounded by an increase in t_{tr} (≈80 ns) due to the slower $v_\parallel$ of the relativistic electrons, further reducing I_{d_0}. Moreover, some injected energy may be lost to the limiter. Thus, I_{d_0} is uncertain within a factor of 2 or 3 (the experimental limits), and β_s may be considerably larger than the ideal case assumed by the theory. Consequently, by reference to Eq. (4-46), it would not be surprising to find ΔI much less than 1 kA. The observed value, $\Delta I \approx 1.4$ kA, falls within the upper bounds predicted, but uncertainty in I_{d_0} prevents a definitive comparison with the theory.

The most ambitious effort so far was the Physics International/UCLA collaboration[62] on Macrotor. Current increments were successfully obtained in this tokamak with $R_0 = 0.95$ m and initial currents as high as 50 kA. A typical example from the data is $\gamma_d = 1.78$ (a 400-kV beam) with $I_{d_0} = 87$ kA, corresponding to $W_d = 840$ J; this assumes about 50% beam loss to the back of the diode after injection. All the constraints are satisfied to validate the analytic theory: the pulse width, $t_{t-o} \approx$ 60 ns, was much less than the current rise time, $\Delta t \approx 1$ μs; the resistivity enhancement was large, $\alpha = (L/R)/\Delta t \approx 10^3$, assuming $T_e \approx 40$ eV initially; and the REB was launched toroidally, with zero pitch angle. In this case Eq. (4-46) predicts $\Delta I = 4.2$-6.8 kA for $I_0 = 45$ kA and $L/2\pi R_0$ in the range 0.41-0.25 μH/m. This agrees well with the experimental values, which were in the range $\Delta I = 5$-8 kA. A sample tokamak waveform is shown in Fig. 4-16. The REB pulse occurs at 4 ms into the discharge in the figure.

Additional data in the report showed that ΔI is nearly independent of I_0 but is proportional to γ_d in the Macrotor experiment. As discussed above, this is a natural consequence of the theory when $\beta_s << \beta_d$, that is, when the injected energy W_d is large enough that $(I_0 + \Delta I) << I_{d_0}$. A detailed, shot-by-shot comparison of theory and experiment has not been performed, partially because of the difficulty in estimating the injected ("trapped") energy and thus the value of I_{d_0}.

We conclude this subsection with a summary of single-shot REB experimental observations compiled from the four devices listed above.

ORNL–PHOTO 4371-82 FED

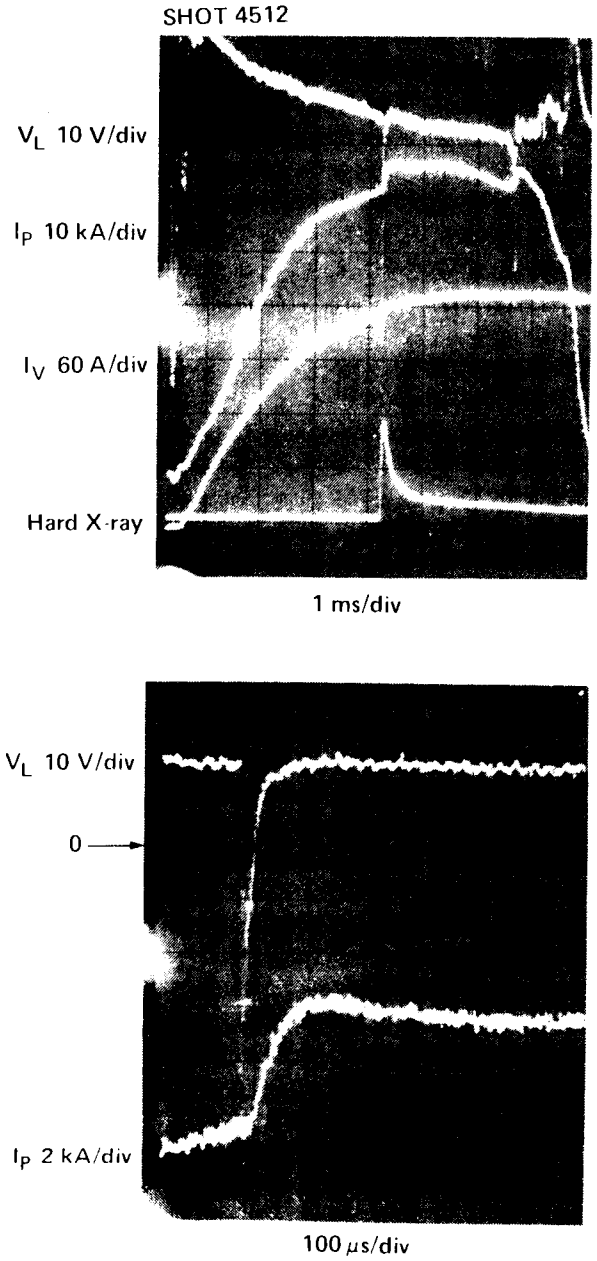

Fig. 4-16. Tokamak waveforms for an H_2 plasma with coinjection of an REB into Macrotor. The second sharp increase in I_p is believed to be due to a disruption. The apparent slow rise of ΔI_ϕ, which is exemplified in the lower photograph, is not real. As is discussed in the text, the actual rise time is ≈1 μs.

- Preionization of fill gas was achieved;[53,58] a partially ionized fill was supplied by a plasma gun and the REB completely ionized the neutrals. For this purpose the REB may achieve plasma breakdown as well as or better than ECRH.
- Current generation was achievable without any transformer-driven ohmic current.[53,58]
- REB-assisted startup allowed ohmic current initiation at a reduced loop voltage.[62] Thus, a hybrid OH/REB system could reduce initial voltages on the conducting FED-A first wall and also extend the burn length by conserving the OH volt-seconds.
- Significant plasma heating was observed, presumably due to the return current. On SPAC VI, spectroscopy indicated that T_i was raised from $\sim$30 eV to 800 eV at $n_e \approx 10^{13}$ cm^{-3} with a single REB pulse.[58] The beta and β_p values were claimed to be 0.05 and 2.0. It is not clear that the ions were truly a thermal distribution, however. Diamagnetic signals on Macrotor[62] also indicated plasma heating. Hence, the REB may serve well for auxiliary heating,[59] although the issue of penetration and heating near the magnetic axis is unsettled.
- At low densities ($n_e < 10^{13}$ cm^{-3}), runaway (or slideaway) discharges can be created with single-pulse injection and maintained for long periods with almost zero loop voltage.[62] The results are strikingly similar to low density current maintenance with lower hybrid waves.
- Current drive at high density was achieved, as demonstrated by the current increments generated in the four experiments. In Macrotor[62] and on the Cornell racetrack,[61] n_e was as large as 2×10^{13} cm^{-3}; SPAC V[53] was successful with $n_e \approx 1 \times 10^{14}$ cm^{-3}. Unlike LHCD, there are no theoretical or experimental density limitations to REB current drive.

4.5.2 REB System for FED-A

According to the theoretical assumption, the plasma resistivity should return to its classical value immediately after ΔI has reached its peak, so the current will ohmically decay to its initial, preinjection

value of I_0 in a time period $\delta t \approx (\Delta I/I_0)(L/R)$, where we assume $\Delta I << I_0$. Using Eq. (4-46) and noting that $\Delta t << \delta t$ in a hot plasma, we find that the time-averaged power required to keep the current oscillating near the I_0 value is

$$\langle P_d \rangle = W_d/\delta t = \frac{\gamma_d - 1}{\beta_s} \frac{I_0^2 R}{\gamma_d \beta_d - \gamma_s \beta_s} . \qquad (4\text{-}49)$$

The normalized quantity $\langle P_d \rangle / I_0^2 R$ is a function of the two beam parameters γ_d and W_d as well as the tokamak parameters R_0 and I_0. We have plotted this ratio for FED-A in Fig. 4-17. The dashed portions of the curves correspond to $\beta_s \geq 0.4$ and the solid portions above the open circles correspond to $\beta_s \leq 0.1$; our analytic REB theory is valid in the range $0.1 \lesssim \beta_s \lesssim 0.4$.

Our first observation is that the beam parameters can be arranged such that $\langle P_d \rangle$ is approximately twice the conventional OH value. If we assume $I_0^2 R$ is about 1 MW, we have $\langle P_d \rangle \approx 2.0$ MW. A variety of beams can achieve this low $\langle P_d \rangle$ — for example, a 250-kV beam with W_d = 250 kJ per pulse and a repetition rate $(\delta t)^{-1}$ = 8 Hz or a higher energy beam (e.g., 1.0 MV) with W_d = 1.0 MJ and $(\delta t)^{-1}$ = 2.0 Hz. Lower energy beams may be cheaper due to the smaller energy storage and lower voltages involved, but the higher repetition rate increases the total number of shots required from the pulsed power system. Since high reliability is demanded from the FED-A we would opt for the higher energy, lower repetition rate beams. For reference purposes we have designed a 1.5-MV system with parameters listed in Table 4-4.

The plasma diode delivers 1.47 MJ at 1.533 MV with a nominal pulse width t_{t-o} = 1 μs and a cathode current I_c = 959 kA. Assuming that a cathode current density $j_c \approx 1$ kA/cm^2 is possible for this pulse width, a cathode area A_c = 959 cm^2 is required. These voltages and currents are somewhat larger than those designed for the 0.2-μs Rayo source under construction at Sandia.[63] (A microsecond configuration for Rayo has also been designed.) The plasma anode has proven effective on the toroidal experiments[53,64] at the megavolt level with hundreds of kiloamperes, but for relatively short (100-ns) pulses. The longer pulse

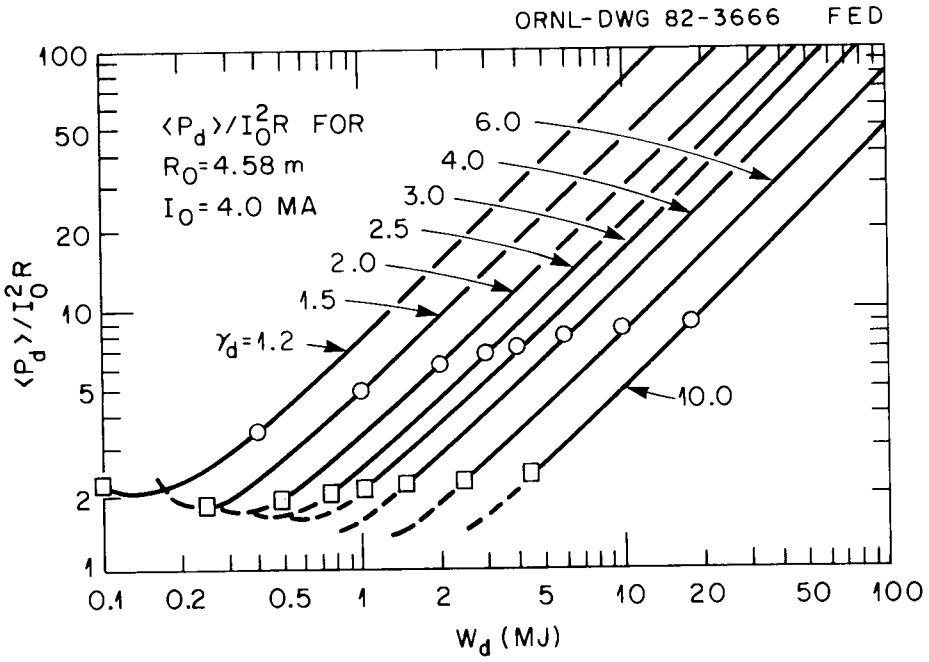

Fig. 4-17. Time-averaged power dissipation for FED-A driven by REB: R_0 = 4.58 m, I_0 = 4.0 MA.

Table 4-4. REB current drive system for FED-A

Symbol	Value	Meaning
R_0	4.58 m	Major radius
I_0	4.0 MA	Toroidal current
R	0.061 μΩ	Toroidal resistance
L	13.3 μH	Toroidal self-inductance
n_e	1.6×10^{20} m^{-3}	Average electron density
P_f	255 MW	Fusion power
V_d	1.533 MV	Diode voltage
γ_d	4.0	Initial mass ratio
W_d	1.47 MJ	Kinetic energy into plasma
β_s	0.4	Electron velocity at maximum ΔI
$<P_d>$	2.13 MW	Time-averaged power dissipation
δt	0.69 s	Interpulse period
α	4×10^3	Resistivity enhancement
t_{t-o}	1 μs	Diode pulse width
I_c	959 kA	Cathode current

width will simplify the transmission line design through the blanket/shield since an impedance match will be unnecessary. Moreover, cathode currents this large should permit the use of magnetic insulation, which minimizes the transmission line cross-sectional area.

Figure 4-18 displays one possible route for the coaxial feed in FED-A, assuming a single-blade pumped limiter is selected. The cathode, shown in detail in Fig. 4-19, is located between the limiter and the first wall, and the return current flows to the anode enclosure behind the cathode, which is at ground potential. The diode is thus well protected from normal and disruptive thermal loading. The relativistic electrons are launched from the open (higher density plasma) side of the diode and follow the toroidal field lines, moving poloidally according to the rotational transform. If the REB is not completely current neutralized, it will move inward in minor radius due to interactions with the plasma and the conducting first wall. Radial motion and partial beam trapping were observed on Macrotor,[62] but it is to be expected that some beam loss will occur due to reincidence on the top of the limiter blade. It will thus be necessary to inject energy in excess of 1.47 MJ, perhaps with an identical, synchronous diode operating at another toroidal location.

The vacuum transmission line is separated from a water line by a double ceramic window several meters beyond the first wall. The insulator is large, in order to reduce the electric field strength and inhibit surface breakdown. The vacuum dimensions appear adequate to minimize neutron degradation of the insulator and allow a reasonable lifetime.

Beyond the reactor, the line extends to the nearby power supply building, where it is connected to a 1.25-μF water capacitor. The power train is shown in Fig. 4-20. The water capacitor, which is discharged through a high voltage spark gap, must hold the full charge for several hundred microseconds; assuming a field strength of ∿30 kV/cm, this requires a water tank ∿7 m in radius, assuming a 4-m ceiling. The capacitor is similar in volume to the water tank of PBFA I, currently operating at Sandia. The capacitor is charged through a 1.5-MV air-core pulse transformer[65] with a 42:1 turns ratio. The 36.5-kV input is

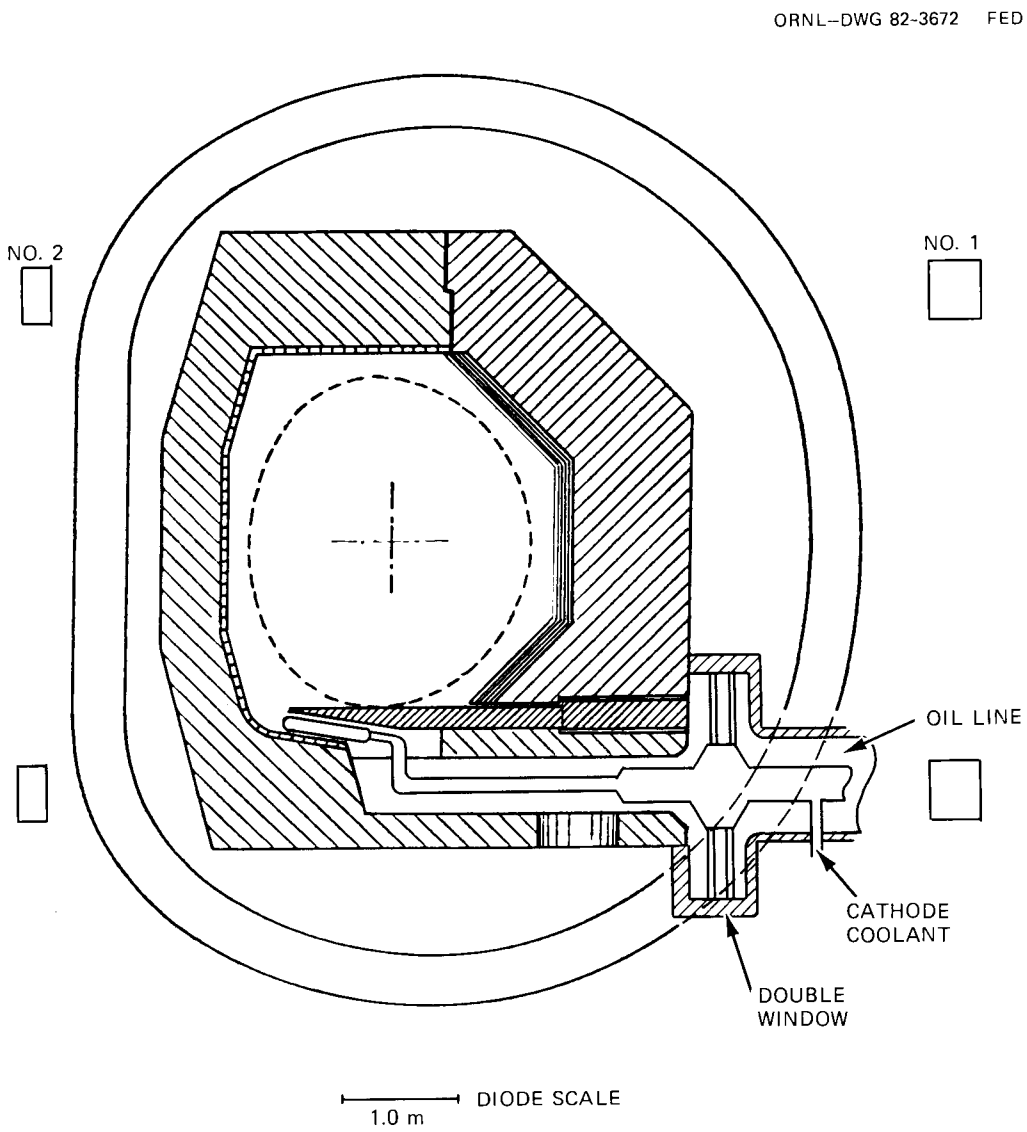

Fig. 4-18(a). Elevation view.

ORNL-DWG 82-3675 FED

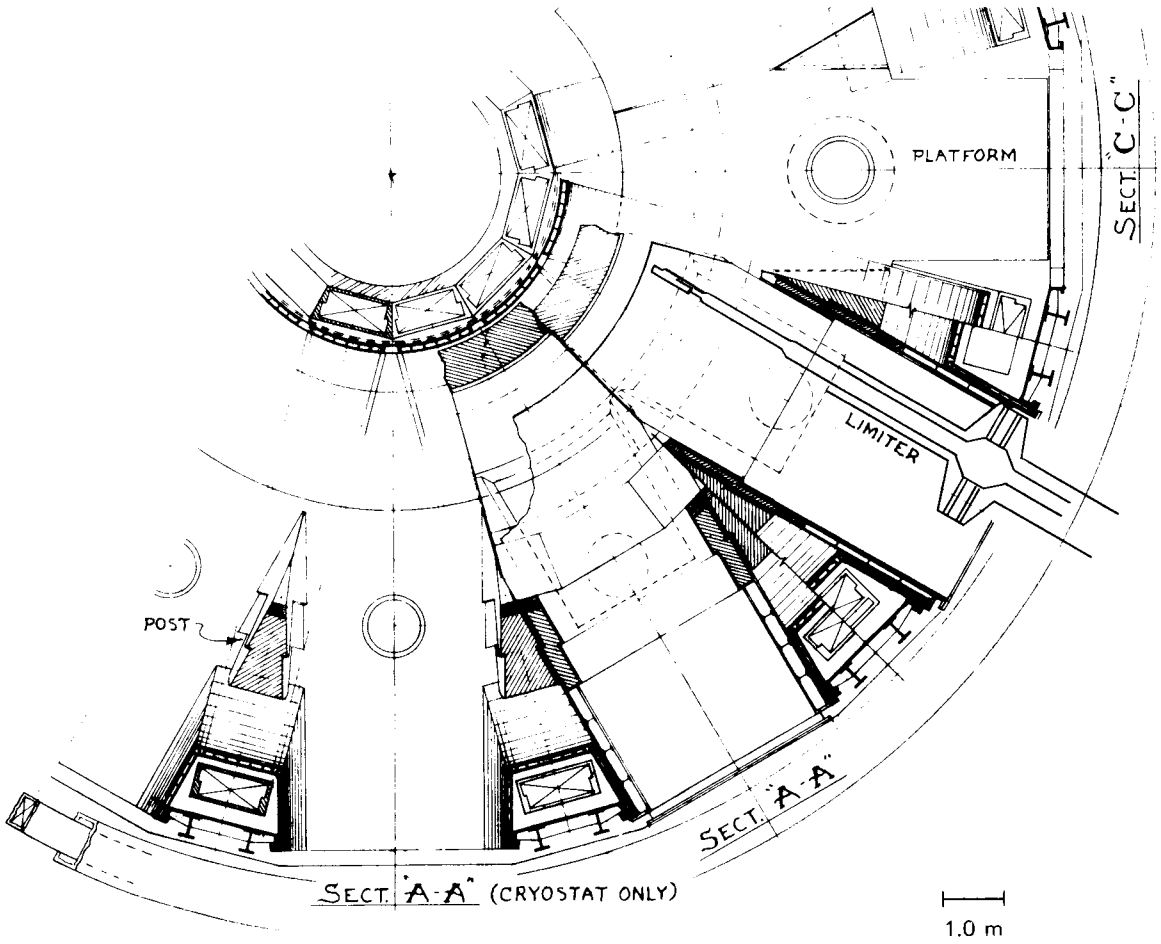

Fig. 4-18(b). Plan view of diode location with bottom limiter option.

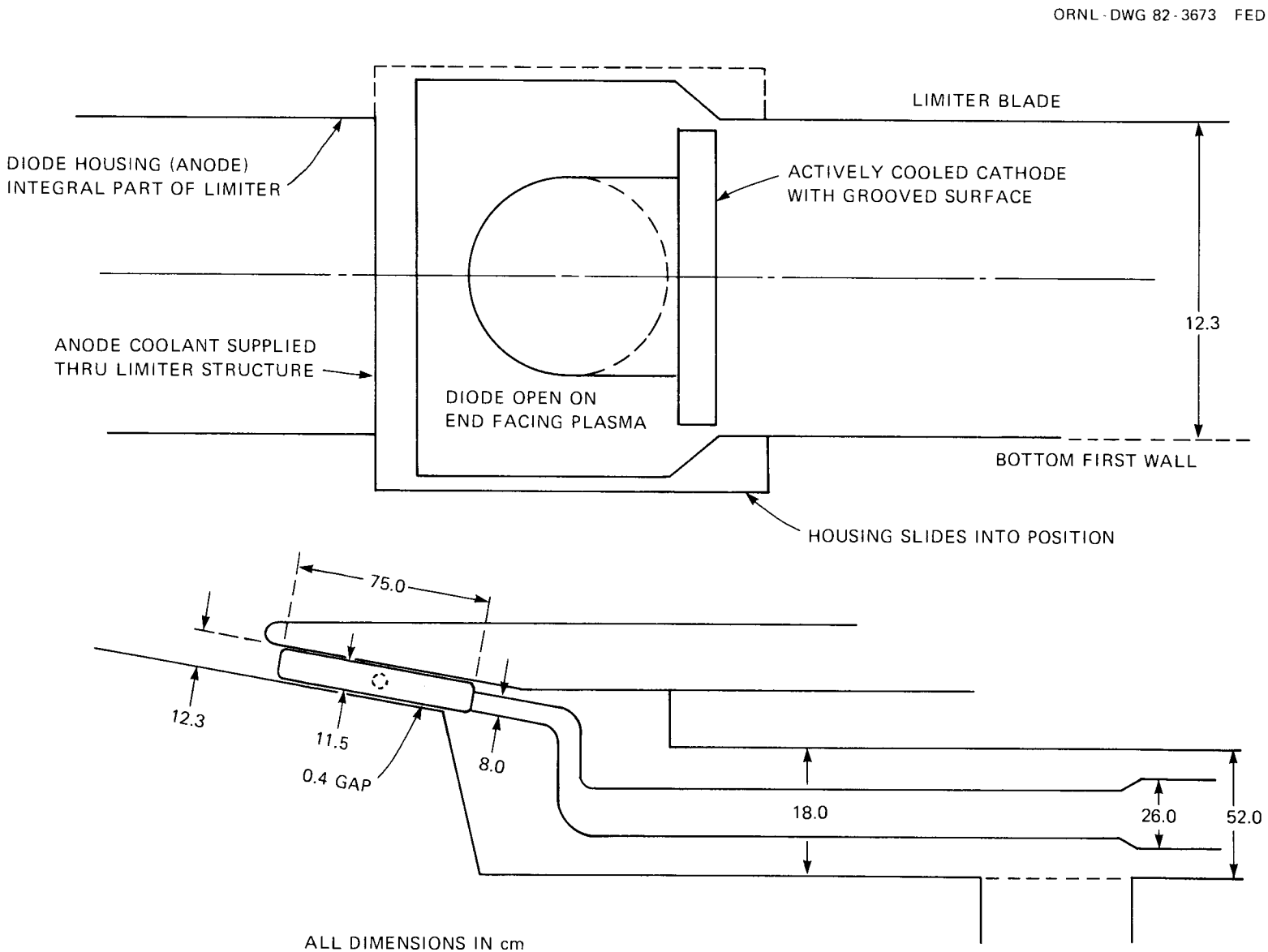

Fig. 4-19(a). Detail of typical diode for FED-A.

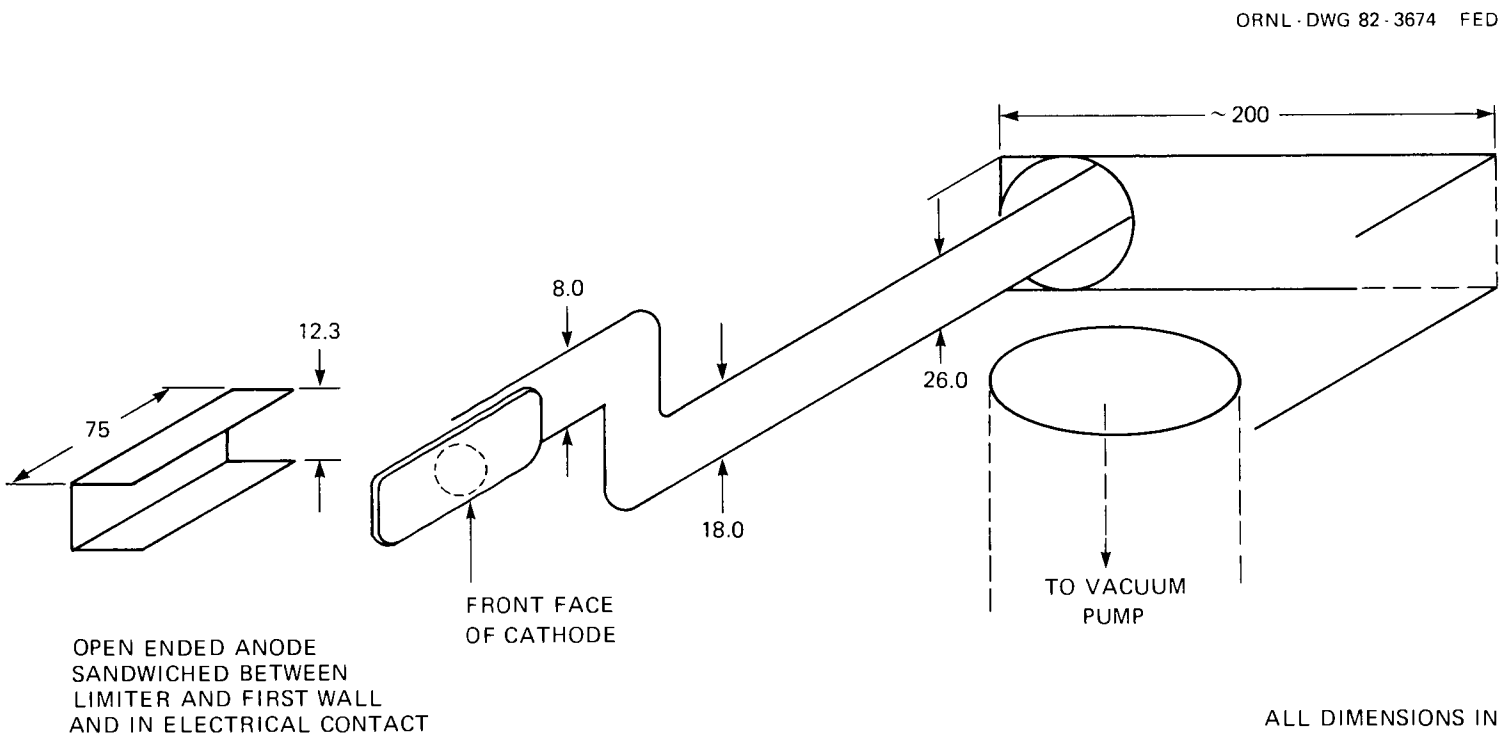

Fig. 4-19(b). Detail of typical diode for FED-A.

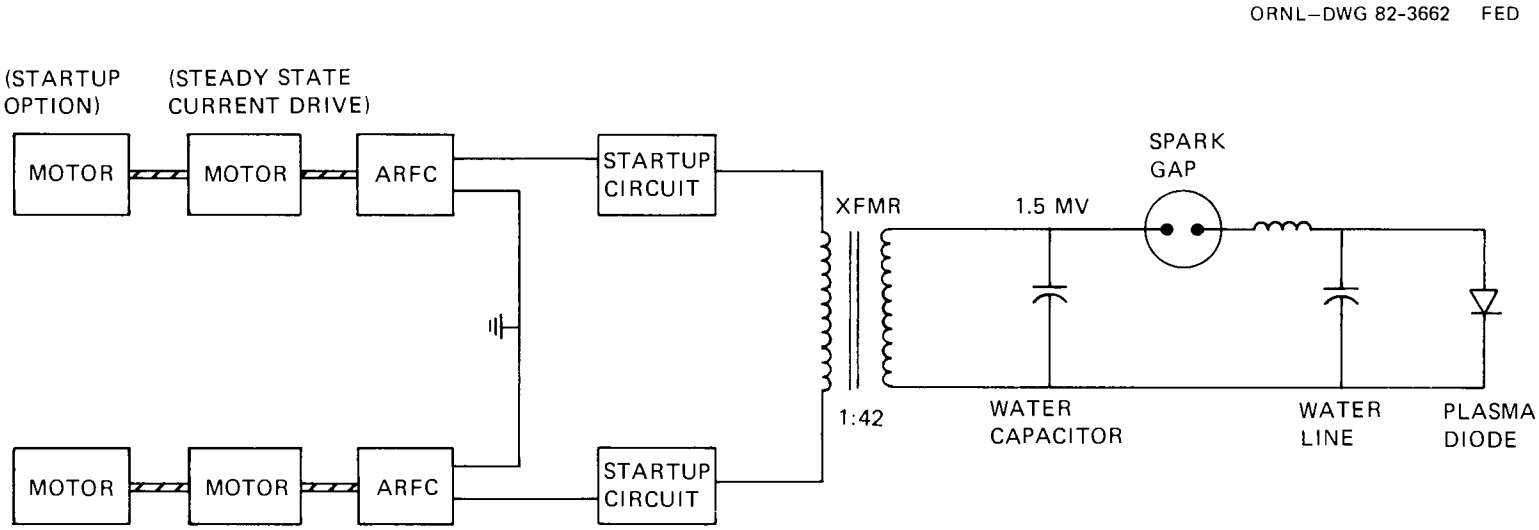

Fig. 4-20. Diode power train for microsecond pulse width.

supplied by two center-tapped active rotary flux compressors (ARFCs)[66] that deliver the energy with a 430-μs pulse halfwidth. Each ARFC is a compact, rotating energy storage device that would be powered by a 1900-hp dc or synchronous motor. The ARFC system has not been optimized. For example, one large ARFC could drive the transformer, but the pulse halfwidth would be nearer 500 μs and the transformer might require a larger turns ratio. The ARFC/transformer/water capacitor power train should be reliable with an acceptably long lifetime. The spark gap is the life-limiting component ($\sim 10^7$ shots), but it can be easily serviced at 6-month intervals during FED-A scheduled maintenance. Each diode delivers $\langle P_d \rangle$ = 2.13 MW and requires an electric input of 2.98 MW for an η_{REB} = 71%. Each diode power train costs ≈$3-4 million for steady-state current drive, assuming no special pulse shaping or compression is required. As suggested earlier, two such systems may be needed if beam trapping in the plasma is poor.

4.5.3 Plasma Operation with REB

It is proposed that with minor modifications the system described in Sect. 4.5.2 can initiate, heat, and ramp up the FED-A discharge. Figure 4-21 shows the projection of a single γ = 4 electron injected into a torus with a vertical field $B_v = 1.2 \times 10^{-3}$ T at R = 5.2 m with a decay index n_0 = 0.175 and no toroidal current. Such an initial equilibrium is established with about -10 kA in EF coil 1 and +20 kA in EF coil 2, as labeled in Fig. 4-18. Judicious choice of the EF currents permits contained orbits with a variety of diode locations. Electron energy loss shrinks the orbit so it will miss the diode on subsequent passes. Based on Eq. (4-43), a ΔI = 14 kA occurs from the initial REB pulse. The vertical field will be increased to maintain a toroidal equilibrium and to draw the current channel toward the center of the vacuum chamber as additional toroidal current is added with each REB pulse. Closed flux surfaces are expected after very few REB pulses.

The plasma can be heated by raising the kinetic energy per REB pulse relative to the steady-state current drive requirement. Reference to Fig. 4-17 shows that an increase of W_d from 1.47 MJ to 20 MJ decreases

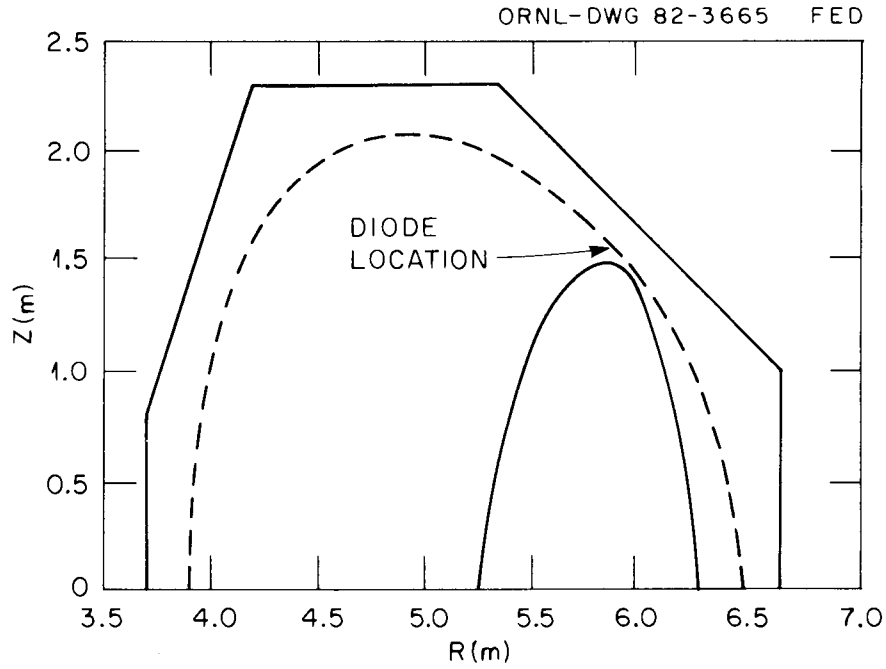

Fig. 4-21. Electron orbits for initiating discharge; the vertical field has a positive field index and is created with two pairs of EF coils.

the current drive efficiency and increases the heat input rate by about an order of magnitude. A start-up scenario was analyzed using the following equations:

$$I_0 = \frac{\langle P_d \rangle}{20.4RW_d} (\beta_d \gamma_d - \beta_s \gamma_s) , \tag{4-50}$$

$$R = 1.94 \times 10^{-6} T_e^{-3/2} , \tag{4-51}$$

$$\langle P_d \rangle = W_d / \delta t , \tag{4-52}$$

$$\beta_s = 0.147 I_0 / W_d , \tag{4-53}$$

$$B_v = (I_0/R_0)[\ell n(8A) - 1.25 + \beta_p] \times 10^{-7} , \tag{4-54}$$

$$U^{EF} = 680 \times 10^6 (B_v/0.42)^2 , \tag{4-55}$$

$$V_\ell = 64 \times \dot{B}_v , \tag{4-56}$$

where T_e, $\langle P_d \rangle$, and β_p were taken from the POPCON neutral beam start-up simulations for FED, given in Ref. 67. Quantities are given in metric units and kiloelectron volts. Since there is no need for a transformer the current ramp can be fairly slow, and a 20-s start-up was selected, which minimizes the EF coil power requirement at $\dot{U}^{EF}$ = 35 MW. The vertical field gives an inductive assist to the REB current drive via the $\dot{B}_v$-induced emf. It appears possible to keep the loop voltage V_ℓ below a few volts.

Figure 4-22 displays the heat input, current, T_e, and fusion power for a low density ($\bar{n}_e = 0.6 \times 10^{20}$ m^{-3}) start-up. It is proposed to operate two diodes out of phase for 6 s. Initially, high power heating ($\langle P_d \rangle$ = 13.6 MW) is achieved with W_d = 1.47 MJ per pulse but with each ARFC operating at a high repetition rate, $(\delta t)^{-1}$ = 4.6 Hz. The ARFC/

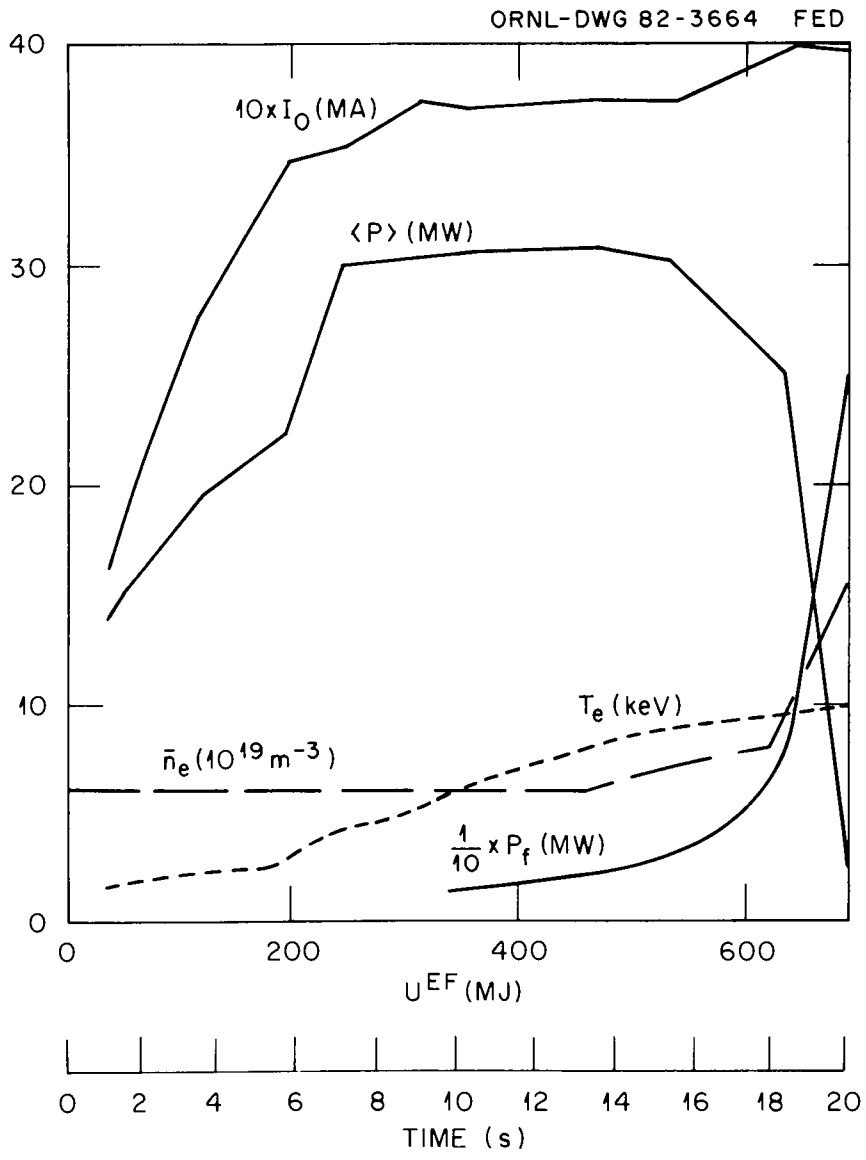

Fig. 4-22(a). REB heating and current ramp for 20-s startup; the vertical field is increased so EF energy increases at constant power.

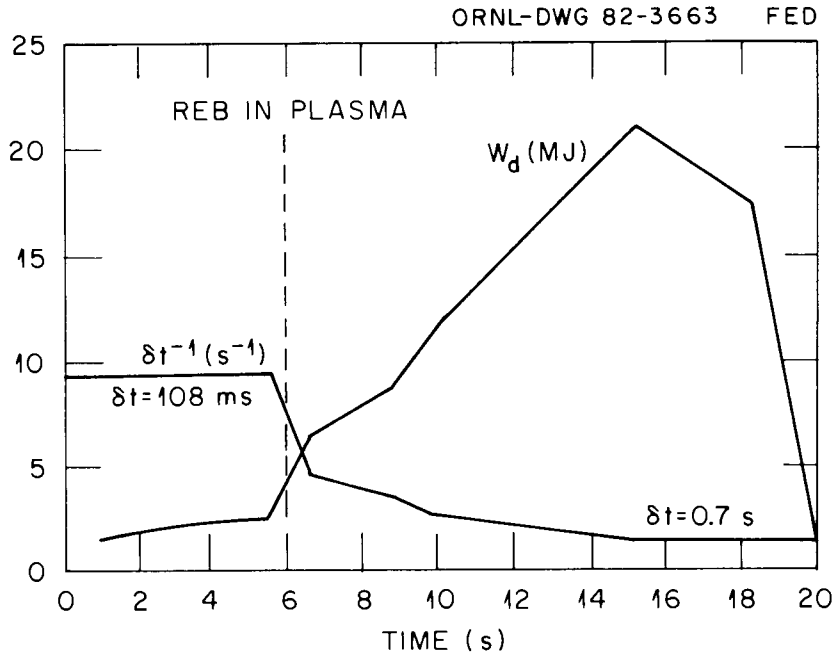

Fig. 4-22(b). Corresponding energy per pulse and repetition rate; two diodes are used.

transformer system can operate at these higher rates for several seconds without significant cost increments. At 6 s the diodes are switched in phase and the rate is reduced to the steady-state value, $(\delta t)^{-1}$ = 1.4 Hz, while W_d is increased to 21 MJ, keeping $\langle P_d \rangle \approx 30$ MW. Thus, if the REB heating option were selected the ARFC rating would be increased from the current drive requirement to 5.6 MJ. An additional start-up motor, rated for 3130 hp cw, would be attached through a clutch to each current drive motor and disconnected during the steady-state operating period. This REB system is attractive because the capital costs do not increase in linear proportion to the power output, since the motors and ARFCs can be overpowered by large factors for the short (20-s) period required for auxiliary heating.

4.5.4 Experimental Needs and Theoretical Topics of Interest

The principal question regarding REB current drive revolves around the issue of relativistic electron orbits in the tokamak. For an ideal axisymmetric tokamak, neoclassical theory predicts radial penetrations of only a few centimeters as $\gamma_d = 4$ electrons lose energy and canonical angular momentum in the presence of the reverse emf. Therefore, there is concern that REB can support only hollow current density [j(r)] equilibria with unacceptably low beta. To make REB a truly viable candidate for current drive in a large tokamak, these concerns must be addressed theoretically as follows:

- The permissible hollowness of j(r) needs to be understood. A number of studies,[68,69] motivated by the accessibility limitations of LHCD, have found attractive stability properties for various hollow profile equilibria.
- Higher γ_d permits somewhat larger radial penetration in neoclassical theory.[49,70] Since high voltage, high energy REB sources are available, the option of high voltage ($\sim$50 MeV) may deserve further consideration.
- Electrons, as is well known, do not behave in tokamaks as predicted by neoclassical theory. Numerous experimental studies[71-73] of relativistic electron transport have been made (LT-3, ORMAK, TFR,

Pulsator, PLT), and the anomalously large transport has been variously attributed to ergodic magnetic field topology, internal disruptions, and magnetic islands. Most remarkable is a set of calculations[72] demonstrating that $\gamma_d \approx 10$ electrons can traverse large fractions of the minor radius in a few hundred toroidal transits in the presence of strong, nonaxisymmetric islands and yet remain completely *contained* within the plasma. If magnetic helicity does not occur naturally in tokamaks, it might be transiently induced during diode operation by extending the diode's center conductor and winding it along a helical path partway around the torus, inside the vacuum pump duct.

- An additional uncertainty in axisymmetry is that the self-fields of the REB may be strong enough to locally perturb the tokamak equilibrium field, considering that the cathode current density can exceed that of the plasma current density. The Cornell device clearly demonstrated the REB's ability to divert the toroidal field during diode operation.[61] In order for the REB to "dig a hole" into the plasma column it would have to propagate a distance without being current neutralized (by the return current).
- Even if the REB cannot provide a strong current source on axis, it is conceivable that the nonlinear activity of nonaxisymmetric MHD modes might serve to fill in the central current density, perhaps in a manner analogous to the relaxation of skin currents during the start-up of ohmic discharges. Intensive study of this possibility has already started for conventional tokamaks.[71,74-77]
- Ions, having a larger mass, appear to behave approximately as predicted by neoclassical theory and to readily contribute to current drive (neutral injection on DITE). Recent studies[78] have demonstrated the desirability of using pulsed neutral injection on INTOR/DEMO to minimize the time-averaged power for current drive, but these proposals require periodic temperature reductions to increase the return current resistivity. Intense pulsed ion beams[79] may achieve the same effects without varying plasma temperatures or density and may achieve better penetration than the REB. The technology is similar to that for the REB, and, if a plasma diode can be used, it would circumvent beam transport problems associated with neutral[78] and charged ion injection.[80]

- Hybrid scenarios with REB and a transformer could prove valuable to FED-A. The obvious choice would be to use REB's demonstrated ability to ionize the fill gas and generate toroidal current without a transformer and subsequently maintain a very long ohmic discharge with a low loop voltage.
- The REB may enhance tokamak reactor prospects if used in combination with another driver. For example, the fast wave might provide current density on axis while the REB could broaden j(r) or provide stabilizing force-free currents[81] near the plasma boundary.

A one-dimensional theory of REB current drive that is being developed (at ANL) can quantitatively address ideas such as those above. Subroutines will be developed for transport code analysis of the temporal and spatial evolution of REB-driven currents.

While intense pulsed ion current drive can be tested on a small machine (a proposal was made at Cornell), it appears necessary to test REB penetration on a larger device for which the neoclassical orbit width is a small fraction of the minor radius. The appropriate tokamak would thus require $I_0 \gtrsim 100$ kA, and multipulse injection would be required in order to sustain I_0 for a period long enough for the current density profile to reach equilibrium. Figure 4-23 shows the REB requirements for an experiment on TEXT ($R_0 = 1.0$ m) for 100 kA and 400 kA. In either case, $\langle P_d \rangle \approx 2I_0^2 R$. Since $I_0 R$ on TEXT is always about 2 V, an average power of 400 to 1600 kW is needed. For example, a 1.5-MV beam ($\gamma_d = 4$) must be injected with $W_d = 8$ kJ every 20 ms. Such high repetition rates appear reasonable for short bursts ($\sim$1 s) from equipment now under development at Sandia.

Should experiments prove successful on a device such as TEXT, they could be followed by more ambitious demonstrations around 1985. Two options are attractive. When Doublet-III is reconfigured as a big D, it would be an appropriate test bed for generating several megamperes over some tens of seconds. A more challenging test for any noninductive drive, however, would be current maintenance for many L/R times (several minutes in a hot tokamak) to ensure that the current density evolves to a true steady state. For this reason a superconducting tokamak would be

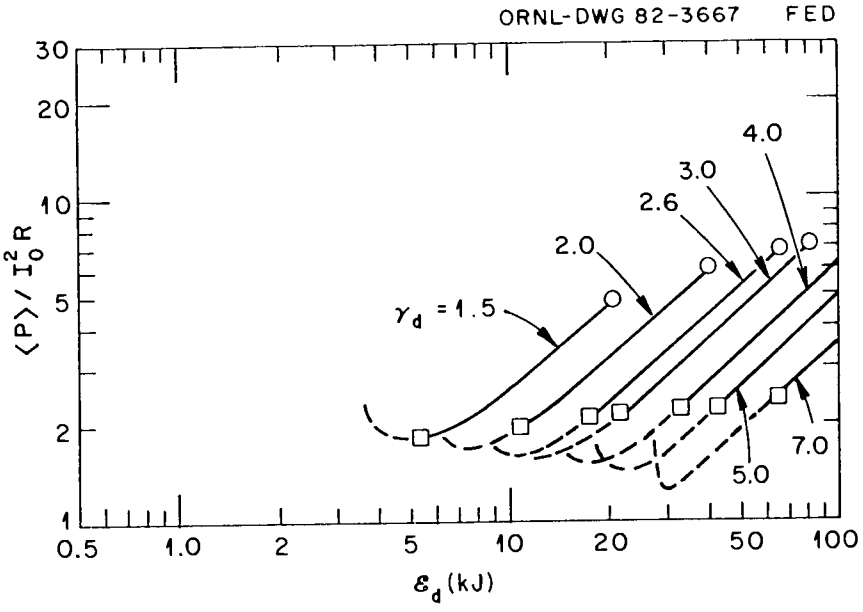

Fig. 4-23(a). Average power required on TEXT (R_0 = 1.0 m) to maintain I_0 = 400 kA.

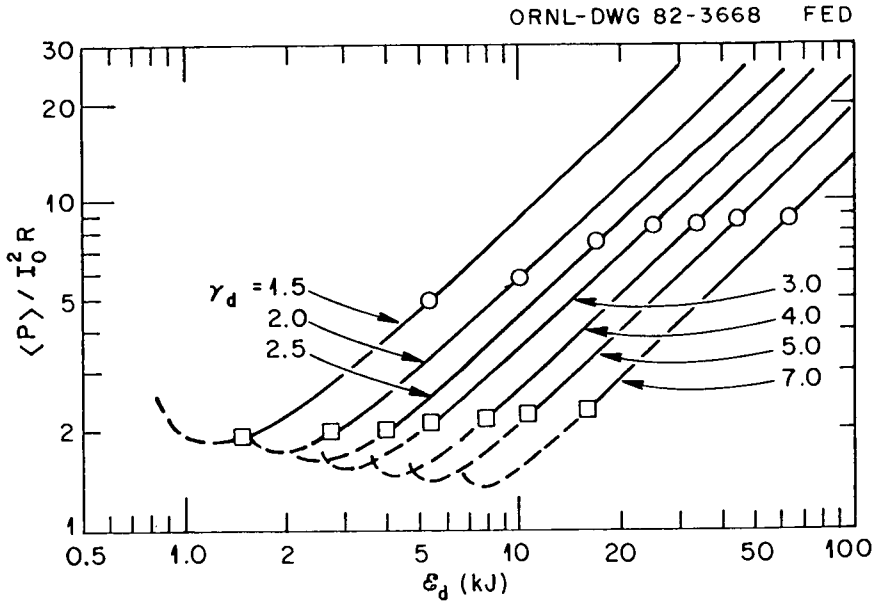

Fig. 4-23(b). Average power required on TEXT (R_0 = 1.0 m) to maintain I_0 = 100 kA.

appealing. Beyond this date, if time is available before incorporation into the FED-A or ETR design, a simultaneous test of both long pulse and high current generation should be done. A very long toroidal field capability ($\sim 10^3$ s) would be essential to adequately test for current drive.

To summarize the prospects for REB current drive, experimental results to date are in good agreement with the simple theory. An extension of this simple theory to FED-A promises a robust, inexpensive driver system that appears to be compatible with a reactor environment and requires very little circulating power, without the need for density or temperature oscillations. The outstanding issues are the question of effective penetration to the center of a large tokamak and the long-term evolution of the otherwise hollow current density profile. Such concerns relating to relativistic electron transport will require further theoretical and experimental study in order to be resolved. Considering its potential for creating a truly steady-state plasma, as well as other applications (e.g., initiating the toroidal current without a transformer), the REB merits continued study as a current drive option.

4.6 NEUTRAL BEAM CURRENT DRIVE

L. D. Stewart (Exxon/PPPL); D. R. Mikkelsen, C. E. Singer (PPPL); O. A. Anderson, W. S. Cooper, D. A. Goldberg, L. Ruby, and L. Soroka (LBL)

Here we discuss two reactor-relevant neutral beam current drive options: the strict steady-state mode and the periodic internal transformer mode. Section 4.6.1 presents the results of modeling strict steady-state drive. The optimum beam energy for FED-A is found to be $\sim$800 keV. Section 4.6.2 presents the results of an internal transformer mode study, in which a 400-keV beam energy is found to be a reasonable choice for FED-A. Beam energies of 400-800 keV dictate negative ion beam technology. In Sect. 4.6.3, recent advances and new ideas in negative ion beam technology are integrated into 800-keV and 400-keV injector concepts for FED-A.

4.6.1 Steady-State Current Drive

A two-fluid zero-dimensional (0-D) model has been used to calculate the maximum beam-driven current for beam powers of 25 and 50 MW and beam energies of 400 and 800 keV. The 0-D model is calibrated with results from BALDUR, a 1-D plasma transport code, and IO, a 3-D neutral beam injection and 2-D tokamak orbit code. The power balance of the original version of the 0-D code[82] was extended to include beam target fusion reactions and an ion energy confinement time of five times the INTOR electron energy confinement time.

The 0-D model parameters for energy confinement, thermonuclear and beam target fusion power, and ion-electron temperature equilibration power were set to match the thermal equilibrium of a BALDUR simulation of FED-A heated by 50 MW of 400-keV D^0. The simulation had $\langle n_e \rangle = 1.3 \times 10^{14}$ cm^{-3}, $\langle T_e \rangle = 13$ keV, and $\langle T_i \rangle = 15$ keV; it produced thermonuclear and beam target fusion powers of 250 and 33 MW, respectively. The 0-D model for the beam-driven current I_{bd} was calibrated with the IO calculations, which include average drag, pitch angle scattering, and the finite-aspect-ratio, trapped electron correction to the beam-driven electron return current. For the BALDUR reference case, the beam-driven current was 2.2 MA.

The original 0-D model was used to find the conditions that would minimize the cost per watt of fusion power in a steady-state, beam-driven FED-A. The result is a high density, high fusion power (P_f = 350-400 MW), low electron temperature ($T_e \sim 10$ keV) plasma that requires $\sim$130 MW of 400-keV D^0 or 80 MW of 800-keV D^0 to drive 4 MA of current.

Cheaper, less ambitious alternatives are possible with more moderate fusion powers ($P_f \sim 250$ MW) and beam powers ($P_b < 50$ MW). The new 0-D model described above was used to vary n_e, T_e, and T_i to find the largest beam-driven current for fixed P_f and P_b. The search was constrained by requiring that $\langle \beta_e \rangle + \langle \beta_i \rangle \leq 6\%$ and that there be sufficient power in both the electron and ion channels to overcome the assumed empirical transport losses.

The maximum beam-driven current for 400- and 800-keV D^0 beams with P_b = 50 and 25 MW is shown as a function of P_f in Fig. 4-24. Note that

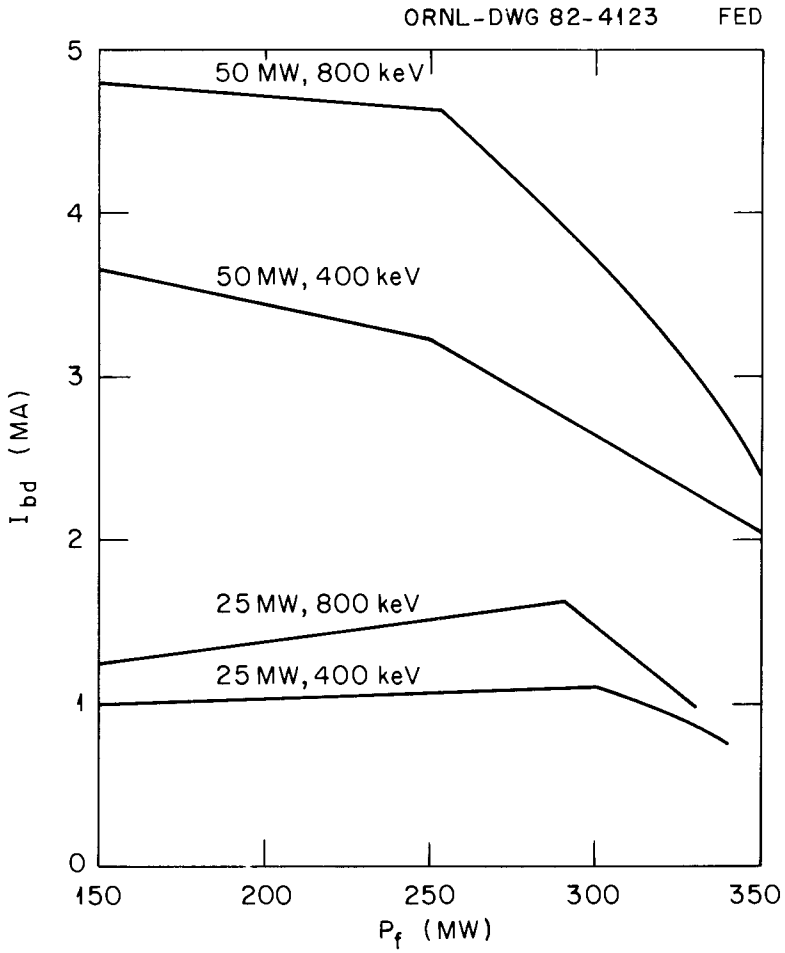

Fig. 4-24. Neutral-beam-driven current as a function of fusion power (P_f) in FED-A for beam energies of 400 keV and 800 keV and beam powers of 25 MW and 50 MW.

50 MW of 800-keV D^0 is sufficient to drive a steady-state FED-A with $I_p \sim 4$ MA and $P_f \sim 250$ MW, and 50 MW of 400-keV D^0 could drive ~3 MA. With only 25 MW of beam power, there is insufficient power to achieve thermal equilibrium with $P_f \sim 350$ MW, and the beam-driven current is only ~1-1.5 MA.

4.6.2 Internal Transformer Driven by Beams

In the internal transformer mode of operation,[83] the plasma current is built up periodically during a relatively short, low density plasma phase (drive phase), then is allowed to decay slowly for a small fraction of the plasma L/R time (coast phase). This mode of operation is discussed in Sect. 4.2 in connection with current drive by lower hybrid waves.

The beam-driven internal transformer mode has been modeled and the average neutron flux that can be obtained using 120-keV and 400-keV beams has been computed. Results for 400-keV beams are summarized in Table 4-5. The optimization was constrained by choosing the FED-A working parameters established in May 1982: major radius R = 4.22 m, plasma radius a = 0.92 m, plasma elongation κ = 1.2, plasma current I_p = 4.1 MA, thermal plasma pressure ratio $\langle\beta\rangle$ = 6.0%, and toroidal field at plasma center B_t = 4.98 T. Energy losses[84] were described by an anomalous electron energy confinement time $\tau_{Ee} \approx \kappa(a/2)^2/\chi_e^{INTOR}$, where χ_e^{INTOR} = $5 \times 10^{17}/n_e \cdot cm^2/s$. The average residence time of a plasma deuteron resulting from beam injection was taken to be τ_p^{eff} = 1.0 s, which may be overly conservative for a plasma density of 10^{13} cm^{-3}. Impurities consist of a helium fraction n_{He}/n_e = 5% and krypton. Z_{eff} = 6 was chosen in Table 4-5 for the drive phase because this represents approximately the value at which benefits of increasing resistivity during the drive phase are canceled by a decrease in efficiency of driving the primary current. Current drive efficiency and fusion power output were calibrated to ion orbit and transport code calculations, as described elsewhere.[84] The coast and drive phase parameters in Table 4-5 were found by optimizing neutron wall loading per unit of cost using previous costing estimates,[82,84] which suggest that every additional 14 MW of

Table 4-5. Plasma parameters for beam-driven internal transformer mode

Parameter	Coast	Drive	Average[a]
n_e = electron density (10^{14} cm^{-3})	2.1	0.11	
T_e = electron temperature (keV)	9.0	6.1	
T_i = ion temperature	9.1	29	
$Z = Z_{eff}$	1.2	6.0	
τ = pulsed length (s)	27	2.0	(total = 33 s)[a]
τ_{skin} = skin time (s)	120	20	
P_b = heating power (MW)	0	44	5.3
P_α = alpha heating (MW)	58	0.01	48
Q = average power multiplication			44
η_{drive} = current drive efficiency (A/W)		0.20	0.77
C_V = relative tokamak cost			370
C_b = relative cost of beams			115
P_w = neutron wall loading (MW/m^2)	1.4	0.0001	1.2

[a]Beams are assumed on for an additional 2.0 s for heating to ignition. Fusion power is neglected for 2.0 s of pumpout and 2.0 s of heating in addition to the 2.0 s of current drive shown here.

400-keV neutral beam power applied to the plasma would require a 10% increment in the total cost of the system. In computing the averages in Table 4-5, a 3-s transition time, during which fusion production is insignificant, was assigned. This is consistent with the observations that fusion power is reduced by one-half when the density decreases by three-fourths and that the sum of the energy confinement time for deignition and thermal inertia time for reignition is 4 s for 44 MW of applied beam power.

Total capital costs could be reduced by using only 20-25 MW of applied beam power, which would still be sufficient to allow continuous operation of FED-A with current driven by the internal transformer effect of turning on and off the beam-driven current. This would, of course, require a longer current drive time and would reduce the time-averaged neutron wall loading by ∿10%. The margin for thermonuclear ignition is a more significant concern, but this could be addressed by planning for staged implementation of up to 50 MW of applied heating power.

Previous work suggests that less than 50 MW of the full energy component of 120-keV beams would also be sufficient for continuous drive with FED-A design parameters in the ignited phase of the internal transformer cycle. The long drive phase and the large port space required make this option unattractive in the long term, but an early starting date for FED-A could be guaranteed by fitting smaller amounts of 120-keV beams to ports that would be refitted eventually with higher energy beams. At the other extreme of much higher energies, 800 keV or higher gives only modest improvement in the performance of internal transformer action. However, higher beam energies may have the technological advantage of fewer beam lines and ports for a given power.

4.6.3 400-keV and 800-keV Negative-Ion-Based Neutral Beam Systems

Recent advances and new concepts in negative-ion-based neutral beam systems have enhanced the attractiveness of these systems for tokamak applications. New developments, including (1) demonstration of dc H^- ion source operation at over 5 A per meter of source length,[85] (2) the

concept of using strongly focusing electrostatic structures for low gradient dc acceleration of high current sheet beams and transport of these beams around corners,[86,87] and (3) the development of oxygen-iodine chemical lasers, configured to allow the D^- beam to pass through the laser cavity,[88] provide a realistic possibility of efficient conversion of negative ions to neutral atoms by photodetachment of one electron from the negative ion.

Two options were considered: (1) a 400-keV, 50-MW system and (2) an 800-keV, $\leq$100-MW dc system. Most of the effort was put on the second option, as it was the more demanding. This system was thought through to the preconceptual stage, meaning that space and vacuum requirements, electrode shapes and sizes, component feasibility, and overall system performance (e.g., currents, voltages, beam admittance) were considered, but no detailed engineering study was performed.

A plan view of the proposed beam line is shown in Fig. 4-25. The beam line design uses electrostatic strong focusing provided by alternating transverse electric fields[86,89] [the transverse field focusing (TFF) concept] in the pumping/transport section, in the main accelerator, and in the neutron shield. The main accelerator raises the D^- beam energy from 200 to 800 keV with low gradients (nowhere exceeding 40 kV/cm). The transverse fields can be expected to inhibit total column breakdown by preventing the acceleration of locally produced electrons and positive ions through more than one stage. TFF sections are also used to transport the beam around two 60° bends in the channel through the neutron shielding. These bends, plus the duct configuration in the transport section (shown schematically in the insert in Fig. 4-25), prevent line-of-sight shinethrough of neutrons. Each sheet beam is 1.1 m high and 1.5 cm wide in the transport section and carries 5.5 A. The beams are generated by surface-conversion negative ion sources of the types being developed at LBL and BNL; there are six of these sources per beam line, each 1.1 m high, with three per channel. Each source has its own isolation valve. The beams from each set of three sources are aimed to intersect at the target.

Pumping is by cryopumps capable of on-line regeneration, under development at LLNL.[90] A 200-keV transport section is provided for beam

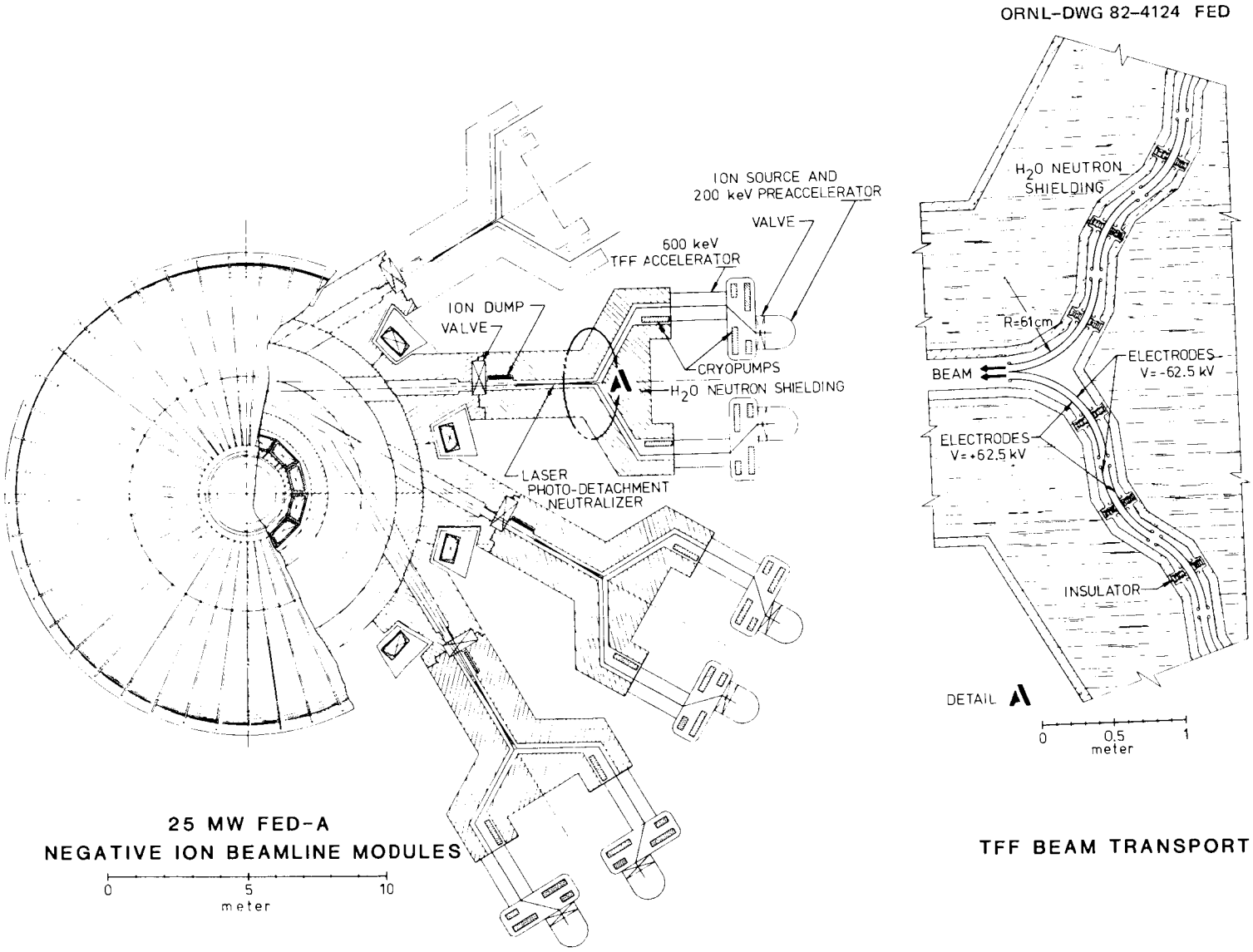

Fig. 4-25. 25-MW FED-A negative ion beam line modules with TFF.

matching and pumping; additional pumping is provided after acceleration to the final beam energy of 800 keV.

After transport around the final 60° bend, the negative ion beam passes through an array of vertically oriented laser cavities, where approximately 97% of the negative ions are converted to neutral atoms by electron photodetachment. The length of this array in the beam direction is 3 m. Suitable lasers in the 10-kW range are now under development in programs funded by the U.S. Air Force. These oxygen-iodine chemical lasers operate at a wavelength of 1.3 μm, which corresponds to a photon energy adequate to remove the electron from a D^- ion but inadequate to strip the electron from common impurity ions such as O^- and OH^- or to create D^+ ions. The beam in the neutralizer is about 3 m high but very thin (a few centimeters) in the narrow direction, which permits efficient use of the lasers. This narrow cross section also permits electrostatic deflection of the remaining 3% of the negative ions and any impurities into an ion dump at one side of the beam.

The beam line vacuum vessel is a double-walled chamber constructed of low activation 5254 aluminum alloy; the volume between the walls is filled with water for neutron moderation and absorption. The shielding thickness shown, 1 m, is probably thicker than necessary. First estimates indicate that the 1.5-m-thick neutron plug at the end of the beam line will attenuate the direct-streaming 14-MeV neutrons by a factor of 10^5 and that the ducts and bends will attenuate the slow neutrons by a factor of 10^3 to 10^4. More work is required in this area to obtain better estimates of these numbers and to verify that hands-on maintenance can be performed on the sources.

A single beam line would inject 25 MW of 800-keV deuterium atoms into FED-A; four ports would therefore be required for injection of 100 MW. For current drive, tangential injection would be used, as is shown in Fig. 4-25. Analysis of a similar system[91] operating at 250 keV indicated an overall system power efficiency on the order of 70%. A higher overall power efficiency can be expected at 800 keV.

The major uncertainties center around the TFF acceleration and transport sections and the laser photodetachment neutralizer. Transport has been demonstrated in an electron device using a similar principle,[92]

but the first experimental demonstration of acceleration and transport of negative ion beams at relevant current densities by a TFF device will not take place for 2-3 years, as presently scheduled. Laser development is proceeding independently of magnetic fusion energy research and is probably a lower risk item than is the TFF accelerator. This beam line design requires an extrapolation by a factor of about 1.4 in deuterium negative ion current density at the ion source beyond what has been achieved experimentally at LBL. This is the expected progress in negative ion source development, which appears consistent with the probable time scale of an FED-A device.

REFERENCES

Heating in Toroidal Plasmas. Proceedings of the 3rd Joint Varenna-Grenoble International Symposium, vol. 2, EUR7979EN, Commission of the European Communities, Brussels, 1982.

1. J. E. Stevens et al., p. 455.
2. M. Porkolab et al., p. 469.
3. K. Uehara and T. Nagashima, p. 485.
4. S. C. Luckhardt et al., p. 529.
5. K. Ohkubo et al., p. 543.
6. S. Tanaka et al., p. 615.
7. G. Tonon et al., p. 623.

Papers presented at the 9th International Conference on Plasma Physics and Controlled Nuclear Fusion Research, Baltimore, September 1-8, 1982; proceedings to be published.

8. G. Tonon et al., IAEA-CN-41/C-1-1.
9. S. Tanaka et al., IAEA-CN-41/C-1-3.
10. T. Amano et al., IAEA-CN-41/C-3.
11. M. Porkolab et al., IAEA-CN-41/C-4.
12. W. Hooke et al., IAEA-CN-41/C-5.
13. T. Yamamoto et al., *Phys. Rev. Lett.* 45, 716 (1980).
14. M. Nakamura et al., *Phys. Rev. Lett.* 47, 1902 (1981).
15. S. C. Luckhardt et al., *Phys. Rev. Lett.* 48, 152 (1982).
16. K. L. Wong, *Phys. Rev. Lett.* 43, 438 (1979).
17. R. McWilliams et al., *Phys. Rev. Lett.* 44, 245 (1980).
18. K. L. Wong et al., *Phys. Rev. Lett.* 45, 117 (1980).
19. R. J. Lahaye et al., *Nucl. Fusion* 20, 218 (1980).
20. R. L. Freeman et al., *Plasma Physics and Controlled Nuclear Fusion Research. Proceedings of the 7th Conference, Innsbruck, 1978*, vol. 1, Int. Atomic Energy Agency, Vienna, 1979, p. 157.
21. N. Fisch, *Phys. Rev. Lett.* 41, 873 (1978).
22. V. V. Parail and O. P. Pogutse, *Nucl. Fusion* 18, 303 (1978).
23. A. A. M. Oomens et al., *Phys. Rev. Lett.* 36, 255 (1976).

24. B. Coppi et al., *Nucl. Fusion* 16, 309 (1976).
25. N. Fisch, *Nucl. Fusion* 21, 15 (1981).
26. P. Bonoli and R. Englade, to be published.
27. C. S. Liu et al., *Phys. Rev. Lett.* 48, 1479 (1982).
28. C. F. F. Karney and N. J. Fisch, *Phys. Fluids* 22, 1817 (1979).
29. S. Bernabei et al., PPPL-1919, Princeton Plasma Physics Lab., Princeton, N.J., July 1982.
30. T. H. Stix, *The Theory of Plasma Waves*, McGraw-Hill, New York, 1962, p. 60.
31. P. Rutherford, personal communication (1982).
32. N. J. Fisch, *Phys. Rev. A* 24, 3245 (1981).
33. N. J. Fisch, in *Heating in Toroidal Plasmas. Proceedings of the Third Joint Grenoble-Varenna International Symposium, Grenoble, 1982.*
34. N. J. Fisch and C. F. F. Karney, "Current Generation with Low-Frequency Waves," *Phys. Fluids* 24, 27 (1981).
35. D. Q. Hwang and R. W. Gould, "Measurements of the Complex Plasma Loading Impedance of the Magnetosonic Cavity Modes," *Phys. Fluids* 23, 614 (1980).
36. F. Perkins, "Heating Tokamaks via Ion-Cyclotron and Ion-Ion Hybrid Resonances," *Nucl. Fusion* 17, 1197 (1977).
37. F. Perkins, "An ICRF Waveguide," in *Proceedings of the 4th Topical Conference on Radio Frequency Plasma Heating*, University of Texas, Austin, 1981, paper B13.
38. M. Gilgenbach et al., *Phys. Rev. Lett.* 44, 647 (1980).
39. C. P. Moeller et al., *Phys. Fluids* 25, 1211 (1982).
40. N. J. Fisch and A. H. Boozer, *Phys. Rev. Lett.* 45, 720 (1980).
41. V. S. Chan et al., *Nucl. Fusion* 22, 787 (1982).
42. J. G. Cordey et al., *Plasma Phys.* 24, 73 (1982).
43. T. M. Antonsen et al., *Phys. Fluids* 25, 1295 (1982).
44. D. F. H. Start et al., *Phys. Rev. Lett.* 48, 624 (1982).
45. S. Yoshikawa, *Phys. Rev. Lett.* 26, 295 (1971).
46. K. Ikuta, *Jpn. J. Appl. Phys.* 11, 1684 (1972).
47. J. Benford, B. Ecker, and V. Bailey, *Phys. Rev. Lett.* 33, 574 (1974).

48. P. Gilad, B. R. Kusse, and T. R. Lockner, *Phys. Rev. Lett.* 33, 1275 (1974).

49. D. W. Swain, P. A. Miller, and M. M. Widner, SAND-75-0214, Sandia Natl. Labs., Albuquerque, 1975.

50. A. Mohri et al., *Phys. Rev. Lett.* 34, 574 (1975).

51. M. Masuzaki et al., *Jpn. J. Appl. Phys.* 14, 1413 (1975).

52. A. Mohri et al., in *Plasma Physics and Controlled Nuclear Fusion Research. Proceedings of the 6th International Conference, Berchtesgaden, 1976*, vol. III, Int. Atomic Energy Agency, Vienna, 1979, p. 395.

53. A. Mohri et al., in *Plasma Physics and Controlled Nuclear Fusion Research. Proceedings of the 6th International Conference, Berchtesgaden, 1976*, vol. III, Int. Atomic Energy Agency, Vienna, 1979, p. 311.

54. N. J. Fisch, PPPL-1772, Princeton Plasma Physics Lab., Princeton, N.J., 1981.

55. N. J. Fisch, in *Proceedings of the 4th Topical Conference on Radio Frequency Plasma Heating*, University of Texas, Austin, 1981, paper B-1.

56. D. A. Ehst and V. Bailey, "Theory of Steady State Toroidal Current Maintenance with a Pulsed Relativistic Electron Beam," submitted for publication.

57. *STARFIRE/DEMO, A Demonstration Tokamak Power Plant Study, Interim Report*, ANL/FPP/TM-154, Argonne Natl. Lab., Argonne, Ill., 1982.

58. A. Mohri et al., in *Plasma Physics and Controlled Nuclear Fusion Research. Proceedings of the 8th International Conference, Brussels, 1980*, vol. I, Int. Atomic Energy Agency, Vienna, 1981, p. 511.

59. D. A. Hammer and K. Papadopoulos, *Nucl. Fusion* 15, 977 (1975).

60. K. Narihara et al., *Proceedings of the 3rd International Topical Conference on High Power Electron and Ion Beam Research and Technology, Novosibirsk, 1979*, vol. I, p. 70.

61. G. A. Proulx and B. R. Kusse, *Phys. Rev. Lett.* 48, 749 (1982).

62. V. Bailey et al., PIFR-1466-1, Physics International Co., 1982.

63. J. J. Ramirez, SAND-81-1459, Sandia Natl. Labs., Albuquerque, pp. 124 ff.

64. V. Bailey et al., *Proceedings of the 4th International Topical Conference on High Power Electron and Ion Beam Research and Technology, Palaiseau, 1981.*

65. G. Rohwein, SAND-81-1459, Sandia Natl. Labs., Albuquerque, 1982, pp. 118 ff.

66. W. L. Bird et al., *Proceedings of the 3rd IEEE International Pulsed Power Conference, Albuquerque, N.M., 1981.*

67. C. A. Flanagan et al., *Fusion Engineering Device Design Description*, ORNL/TM-7948/V1, Union Carbide Corp. Nuclear Div., Oak Ridge Natl. Lab., 1981.

68. D. A. Ehst et al., *J. Fusion Energy* 2, 83 (1982) and several references therein.

69. Ya. I. Kolesnichenko et al., paper IAEA-CN-41/W8 presented at the Ninth International Conference on Plasma Physics and Controlled Nuclear Fusion Research, Baltimore, September 1982; to be published in the proceedings.

70. D. A. Spong, ORNL/TM-5147, Union Carbide Corp. Nuclear Div., Oak Ridge Natl. Lab., 1976.

71. I. H. Hutchinson and A. H. Morton, *Nucl. Fusion* 16, 447 (1976).

72. G. Fussman et al., in *Plasma Physics and Controlled Nuclear Fusion Research. Proceedings of the 7th International Conference, Innsbruck, 1978*, Vol. I, Int. Atomic Energy Agency, Vienna, 1979, p. 401.

73. C. W. Barnes and J. D. Strachan, PPPL-1879, Princeton Plasma Physics Lab., Princeton, N.J., 1982.

74. T. H. Stix, *Phys. Rev. Lett.* 36, 521 (1976).

75. S. V. Mirnov and I. B. Semenov, *Fiz. Plazmy* 4, 50 (1978).

76. Yu. N. Dnestrovskii, D. P. Kostomarov, and A. M. Popov, *Fiz. Plazmy* 5, 519 (1979) [*Sov. J. Plasma Phys.* 5, 289 (1979)].

77. B. Carreras, H. R. Hicks, and B. V. Waddell, *Nucl. Fusion* 19, 583 (1979).

78. C. E. Singer and D. R. Mikkelsen, PPPL-1936, Princeton Plasma Physics Lab., Princeton, N.J., 1982.

79. W. M. Manheimer and N. K. Winsor, *Nucl. Fusion* 21, 1559 (1981).

80. J. M. Dawson and K. R. MacKenzie, PPG-470, Center for Plasma Physics and Fusion Engineering, University of California at Los Angeles, 1980.

81. D. A. D'Ippolito et al., *Phys. Fluids* 21, 1600 (1978).

82. D. R. Mikkelsen and C. E. Singer, *Optimization of Steady-State Beam-Driven Tokamak Reactors*, PPPL-1924, Princeton Plasma Physics Lab., Princeton, N.J., 1982.

83. P. U. Tiger et al., *SLPX — Superconducting Long-Pulse Experiment, Final Report on Scoping Study*, vol. II, Part I, Princeton Plasma Physics Lab., Princeton, N.J., 1978, p. 3-23.

84. C. E. Singer and D. R. Mikkelsen, *Continuous Tokamak Operation with an Internal Transformer*, PPPL-1936, Princeton Plasma Physics Lab., Princeton, N.J., 1982.

85. K. W. Ehlers and K. N. Leung, "Self-Extraction H^- and D^- Ion Source," paper presented at the 24th Annual Meeting of the APS Division of Plasma Physics, New Orleans, November 1-5, 1982.

86. O. A. Anderson, "The TFF Accelerator for Fusion Reactor Injection," paper presented at the 24th Annual Meeting of the APS Division of Plasma Physics, New Orleans, November 1-5, 1982.

87. W. S. Cooper, O. A. Anderson, D. A. Goldberg, and J. Fink, "Improved Negative-Ion Based Neutral Injection System," paper presented at the 24th Annual Meeting of the APS Division of Plasma Physics, New Orleans, November 1-5, 1982.

88. M. W. McGeoch, in *Proceedings of the 2nd International Symposuim on Production and Neutralization of Negative Hydrogen Ions and Beams*, Brookhaven Natl. Lab., Upton, N.Y., 1980, p. 304.

89. P. T. Kirstein, G. S. Kino, and W. E. Waters, *Space-Charge Flow*, McGraw-Hill Book Co., New York, 1967, p. 255.

90. T. H. Batzer, Lawrence Livermore Natl. Lab., personal communication.

91. J. H. Fink, "Effective Photo-Neutralization of Negative Hydrogen Ion Beams," paper presented at the 24th Annual Meeting of the APS Division of Plasma Physics, New Orleans, November 1-5, 1982.

92. H. A. C. Hogg, "Periodic Electrostatic Beam Focusing," *Proc. IEEE*, Part B, Suppl. 10-12, 1016 (1958).

5. COMPARATIVE ASSESSMENT OF COST-EFFECTIVE FED-A DESIGNS

The FED-A is proposed to be a low q_ψ device with provisions for noninductive current drive. System trade studies were conducted using the FEDC systems code to define the impact of variation in physics parameters and technology requirements on FED-A performance and cost. The major topics addressed in these studies are shown in Fig. 5-1 and are summarized as follows:

- impact of the safety factor q_ψ, the plasma elongation κ, and the maximum field at the toroidal field (TF) coil B_{max} on performance and cost;
- impact of Q on cost;
- impact of providing partial noninductive current start-up on performance and cost; and
- impact of tungsten inboard shielding on performance and cost.

The features and characteristics chosen from each trade study were combined into a single design. The parameters, performance, and cost of this selected FED-A configuration were determined and are included.

5.1 GUIDELINES AND GROUND RULES

The following general guidelines were adopted for the FED-A trade studies:

- start-up and 100 s of burn provided by a conventional PF system,
- 1000 s of burn provided by partial noninductive current drive,
- 30,000 cycles (at 1000 s of burn per cycle),
- maximum dose rate to TF coil insulation limited to 1×10^9 rad,
- slow (20-s) plasma current start-up with rf assist or current drive,
- all superconducting PF coils external to the TF coils,
- a maximum field of 8 T in the ohmic heating (OH) solenoid,
- pumped limiter impurity control system,
- plasma heating provided by rf injection,
- magnetic field ripple at the plasma edge maintained at a value of 1.0% (peak-to-average) or less,

ORNL-DWG 82-4125 FED

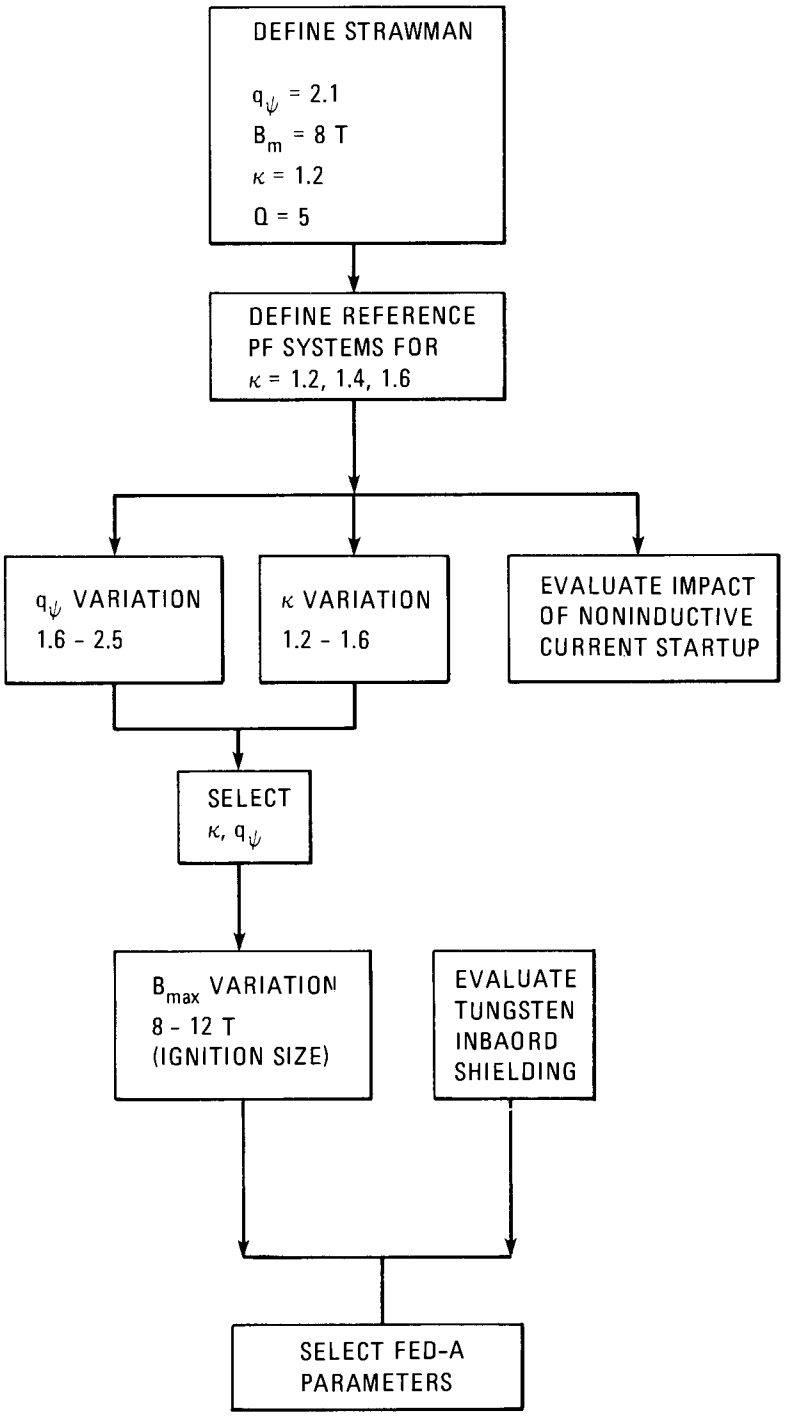

Fig. 5-1. Flow chart for FED-A trade studies.

- plasma average temperature set at 10 keV,
- energy confinement time based on INTOR scaling,
- $\varepsilon\beta_p = 0.50$, where ε is the inverse aspect ratio and β_p is the poloidal beta, so that $\beta \propto (1 + \kappa^2)$, where κ is elongation, and
- a separate vacuum boundary for torus and TF coils.

It should be noted that the last of these guidelines is replaced by a common vacuum boundary in the assessment of design configuration (Sect. 8.4). However, the major conclusions of this chapter are not expected to be altered by this change.

5.2 DEPENDENCE ON q_ψ, κ, Q, AND B_{max}

Trade studies to determine the impact of q_ψ, κ, Q, and B_{max} on tokamak performance and cost were performed using the FEDC systems code. The methodology used in these studies is to set a plasma minor radius leading to a neutron wall load. The thickness of the inboard bulk shielding is then made consistent with the radiation damage criterion of the TF coil insulation. The plasma aspect ratio is finally set to satisfy the 100-s inductively maintained burn time. Equilibrium field (EF) coil currents in the FEDC systems code are scaled as a function of plasma current and coil location from reference values consistent with MHD equilibrium calculations (Sect. 8.1). Reference EF configurations were defined by these calculations for values of plasma elongation κ = 1.2, 1.4, and 1.6 for typical FED-A parameters.

5.2.1 Impact of Safety Factor q_ψ

This study was done for a near-circular, natural plasma shape characterized by a plasma elongation of 1.2 and for a maximum field of 8 T at the TF coils. This natural shape can be provided by a relatively simple PF system consisting of two EF ring coils and an OH solenoid. The reference PF configuration used in this study is shown schematically in Fig. 5-2. Figure 5-3 shows the influence of q_ψ on neutron wall loading, relative cost, fusion power, and Q for a plasma minor radius of

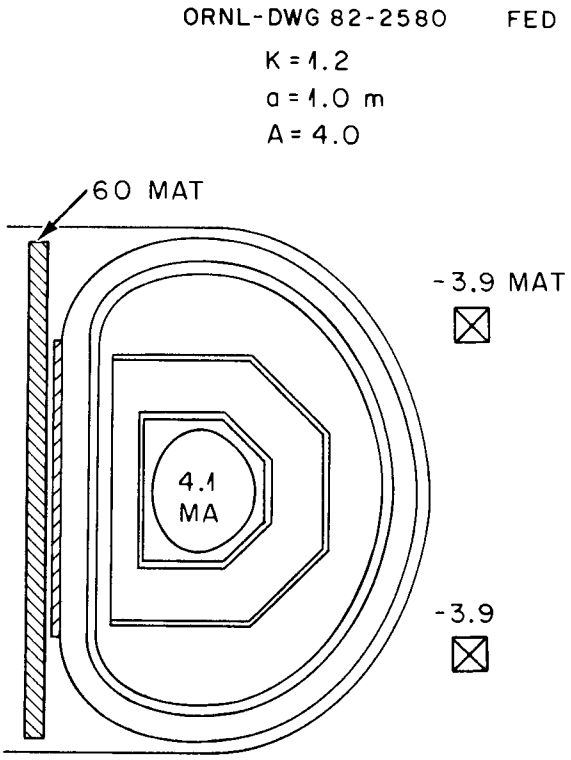

Fig. 5-2. Reference PF system for a near-circular plasma.

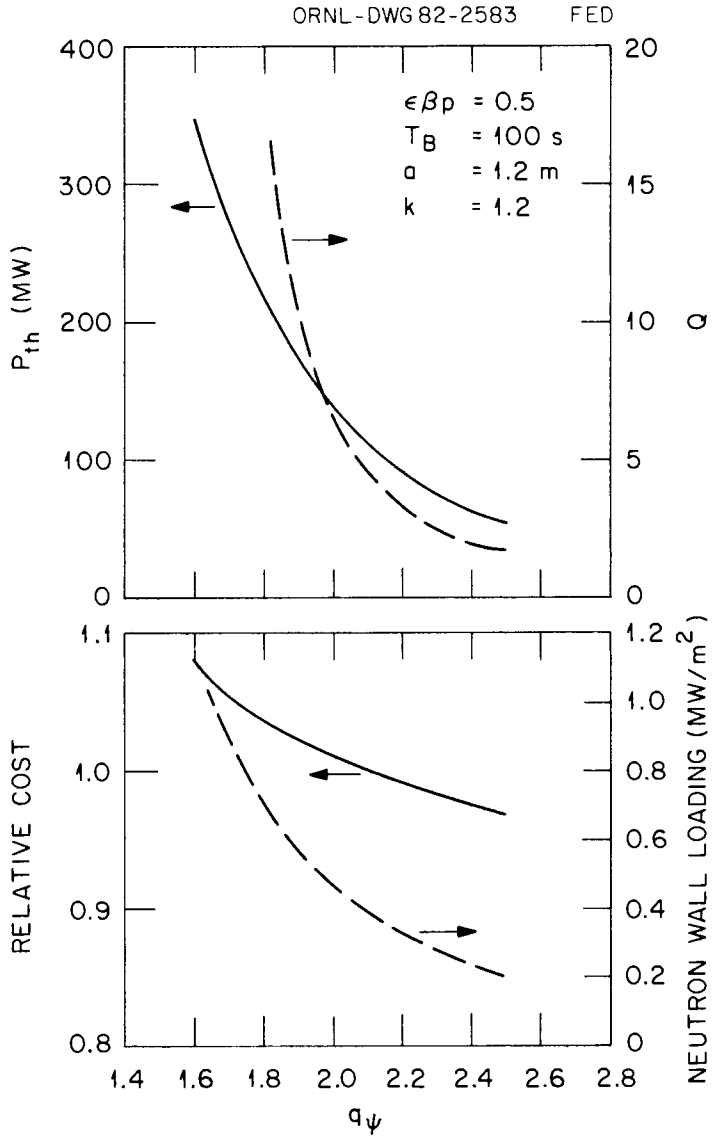

Fig. 5-3. Performance and cost as a function of q_ψ for a plasma minor radius of 1.2 m.

1.2 m. Note that capital cost is normalized to the value achieved at $q_\psi = 2.1$. Decreasing the value of q_ψ for a fixed plasma minor radius achieves substantial increases in Q, fusion power, and neutron wall loading for relatively small increases in capital cost. Decreasing the value of the plasma minor radius at a given value of q_ψ results in decreased Q, power, wall loading, and cost, as indicated by comparing the results of Figs. 5-3, 5-4, and 5-5 for plasma minor radii of 1.2, 1.0, and 0.8 m, respectively.

It is of interest to compare costs at constant performance. Table 5-1 shows self-consistent parameters for a constant value of Q = 5 for plasma minor radii of 1.2, 1.0, and 0.8 m. The relative capital cost is seen to decrease with a decreasing plasma minor radius achieved by decreasing values of q_ψ. Cost is decreased by 13% with a reduction in plasma minor radius from 1.2 to 0.8 m and a corresponding reduction in q_ψ from 2.06 to 1.46. Note that neutron wall loading increases from 0.42 to 0.62 MW/m^2 as plasma minor radius and q_ψ decrease.

Table 5-2 is similar to Table 5-1 except that the neutron wall loading is held constant at 0.5 MW/m^2 as plasma minor radius is reduced from 1.2 to 0.8 m and the value of q_ψ is also reduced from 1.96 to 1.55. The cost reduction with reduced q_ψ is also approximately 13%. Note that in this case, Q decreases as plasma minor radius decreases.

The conclusion from this study is that for constant performance, the lowest value of q_ψ allowed by plasma disruption and stabilizing criteria is desirable for capital cost minimization.

5.2.2 Impact of Plasma Elongation κ

This study examines the influence of plasma elongation on performance and cost at $q_\psi = 2.1$ for a maximum toroidal field of 8 T. The study was done for a theoretical scaling of beta with plasma elongation at constant β_p, for $\beta \propto (1 + \kappa^2)$, and for a more pessimistic scaling that beta is independent of plasma elongation. The last scaling was modeled in the systems code by requiring $\beta_p \propto 1/(1 + \kappa^2)$. In conjunction with the independence of beta from elongation, energy confinement time was enhanced by a linear scaling with elongation, $\tau_E \propto \kappa$, as suggested by recent experiments (e.g., ISX-B).

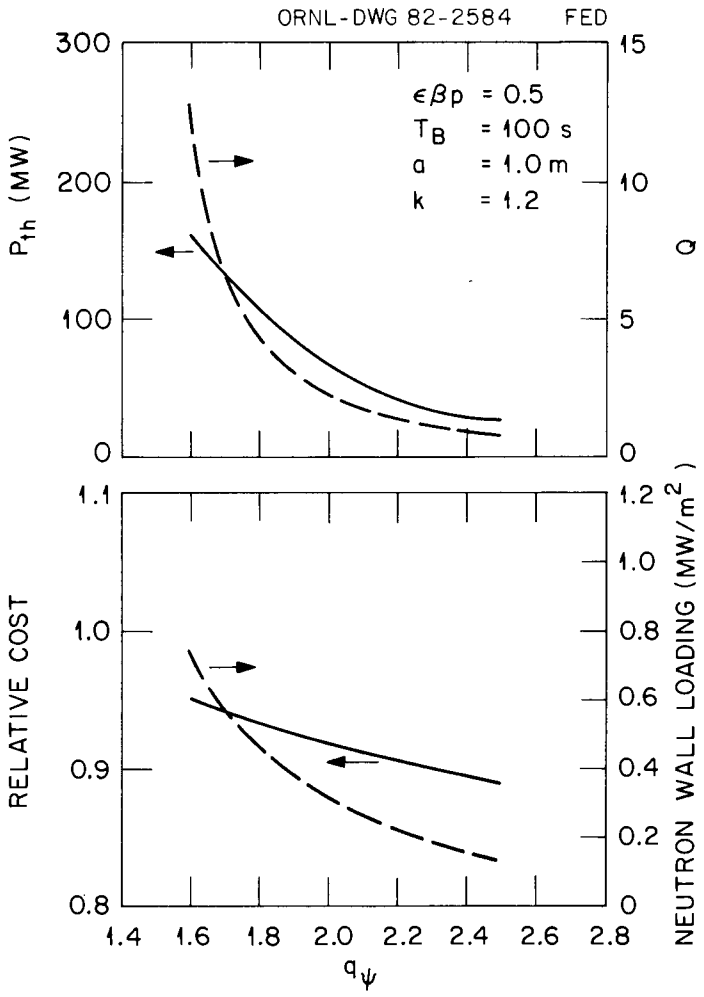

Fig. 5-4. Performance and cost as a function of q_ψ for a plasma minor radius of 1.0 m.

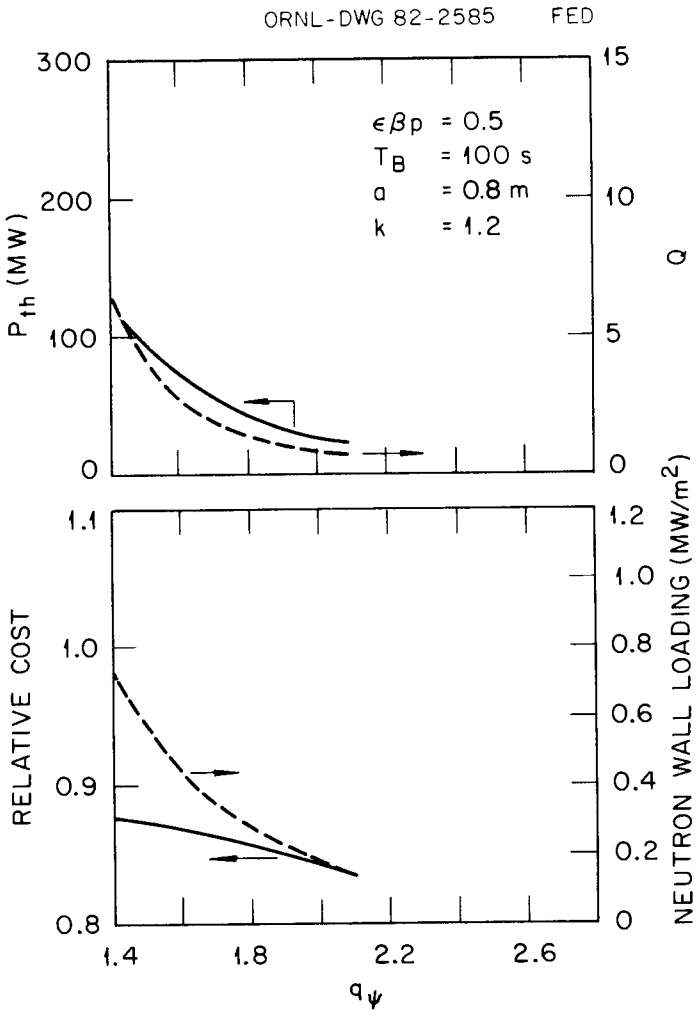

Fig. 5-5. Performance and cost as a function of q_ψ for a plasma minor radius of 0.8 m.

Table 5-1. Parameters and cost for a near-circular plasma at a value of Q = 5.0

	Plasma minor radius, a (m)		
	1.2	1.0	0.8
κ	1.2	1.2	1.2
A	3.62	4.10	4.82
R_o (m)	4.34	4.10	3.86
q_ψ	2.06	1.76	1.46
β (%)	6.6	7.4	8.5
B_T (T)	3.43	3.55	3.68
B_{max} (T)	8.0	8.0	8.0
I_p (MA)	4.4	3.7	3.0
P_{th} (MW)	120	115	105
L_w (MW/m^2)	0.42	0.50	0.62
$\$_R$	1.005	0.940	0.875

Table 5-2. Parameters and cost for a near-circular plasma at a constant value of L_w = 0.5 MW/m^2

	Plasma minor radius, a (m)		
	1.2	1.0	0.8
κ	1.2	1.2	1.2
A	3.67	4.10	4.75
R_o (m)	4.40	4.10	3.80
q	1.96	1.76	1.55
β (%)	7.1	7.4	7.7
B_T (T)	3.46	3.55	3.64
B_{max} (T)	8.0	8.0	8.0
I_p (MA)	4.5	3.7	2.9
P_{th} (MW)	150	115	80
Q	7.5	5	3
$\$_R$	1.015	0.940	0.872

The elongated plasma required additional shaping coils (relative to the near-circular configuration in Fig. 5-2), as shown in Figs. 5-6 and 5-7 for the reference PF configuration with plasma elongations of 1.4 and 1.6, respectively. Note that these additional coils have currents in the same direction as the plasma current and hence reduce the net flux linkage to the plasma during start-up. This must be compensated for by increasing the flux capability of the OH and outer EF coils; this is done by increasing the tokamak major radius, resulting in increased cost.

Figure 5-8 shows that relative cost, neutron wall loading, Q, and fusion power can decrease with decreasing values of plasma minor radius for a fixed κ, assuming the more favorable scaling of beta with κ. As κ is increased from 1.2 to 1.6, performance increases for a given value of plasma minor radius, but so does cost, as is evident by comparing Figs. 5-8 through 5-10.

Table 5-3 shows self-consistent parameters for a value of Q = 5 as κ is increased from 1.2 to 1.6. It is noted that as plasma elongation is increased, the minor radius decreases and the aspect ratio increases. The effect of a favorable scaling of beta with κ is essentially nullified by the increased aspect ratio, which tends to lower beta. The net effect is that cost is essentially unchanged ($\sim$4%) as κ increases from 1.2 to 1.6. However, neutron wall loading does increase from 0.40 MW/m^2 to 0.55 MW/m^2. This could be an important consideration for engineering testing applications. Table 5-4 shows the breakdown of the direct capital cost for this variation of κ at constant Q.

Table 5-5 shows self-consistent parameters for a constant value of neutron wall loading of 0.5 MW/m^2 as κ is varied from 1.2 to 1.6. Again, cost is relatively insensitive to κ ($\sim$5%) over the variation considered. Note that increasing values of κ result in decreased values of Q at a constant neutron wall loading.

The effect of the alternate scaling of κ on β_p and τ_E [$\beta_p \propto 1/(1 + \kappa^2)$, $\tau_E \propto \kappa$] for a constant value of Q = 5 is presented in Table 5-6. This scaling results in a cost increase of 18% as κ is increased from 1.2 to 1.6. Note that beta decreases due to the increased aspect ratio resulting from the κ increases.

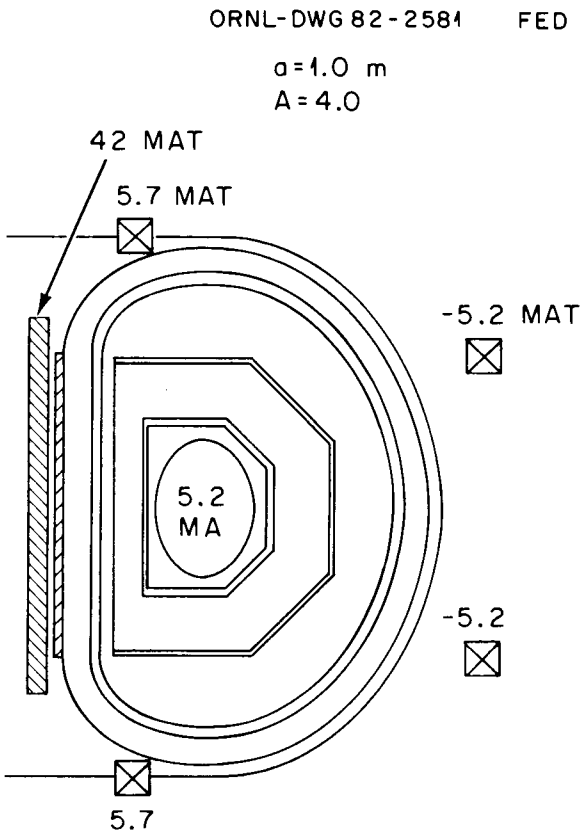

Fig. 5-6. Reference PF system for a plasma elongation of 1.4.

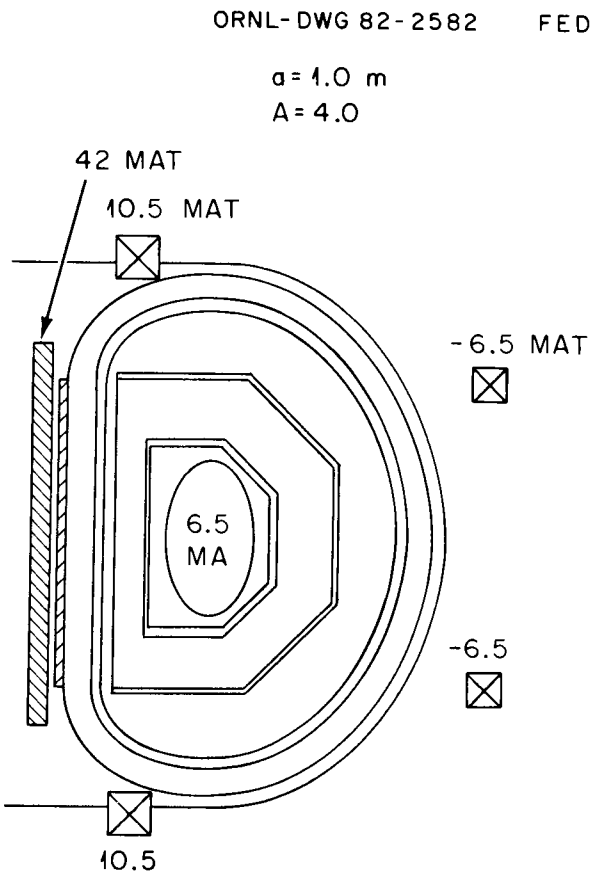

Fig. 5-7. Reference PF system for a plasma elongation of 1.6.

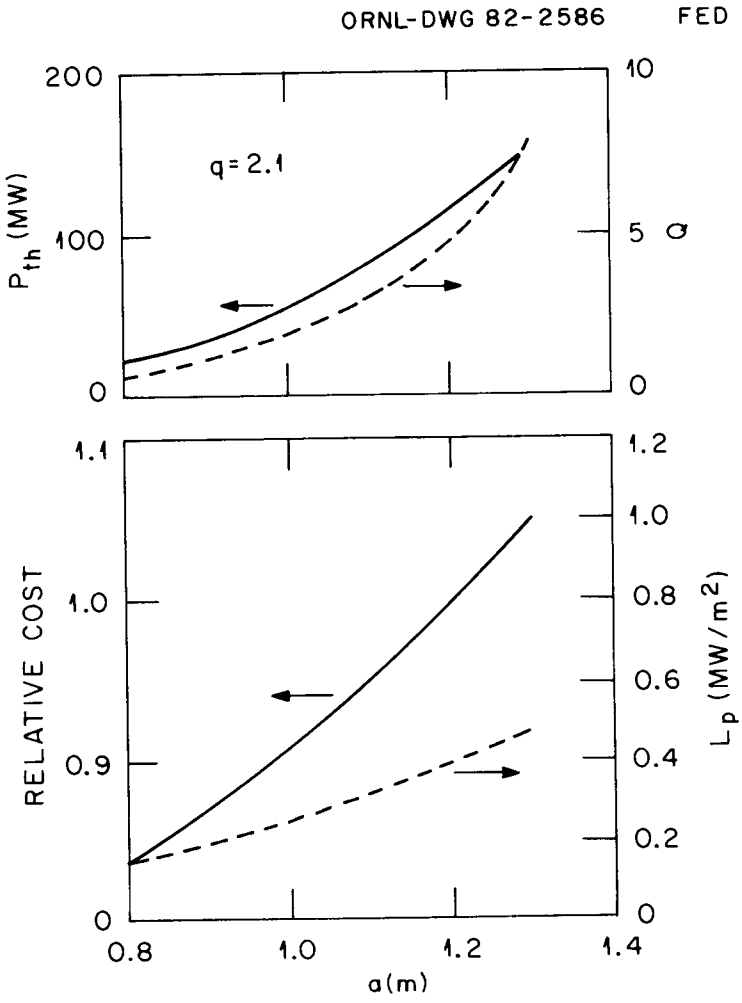

Fig. 5-8. Performance and cost as a function of plasma minor radius at a constant value of κ of 1.2.

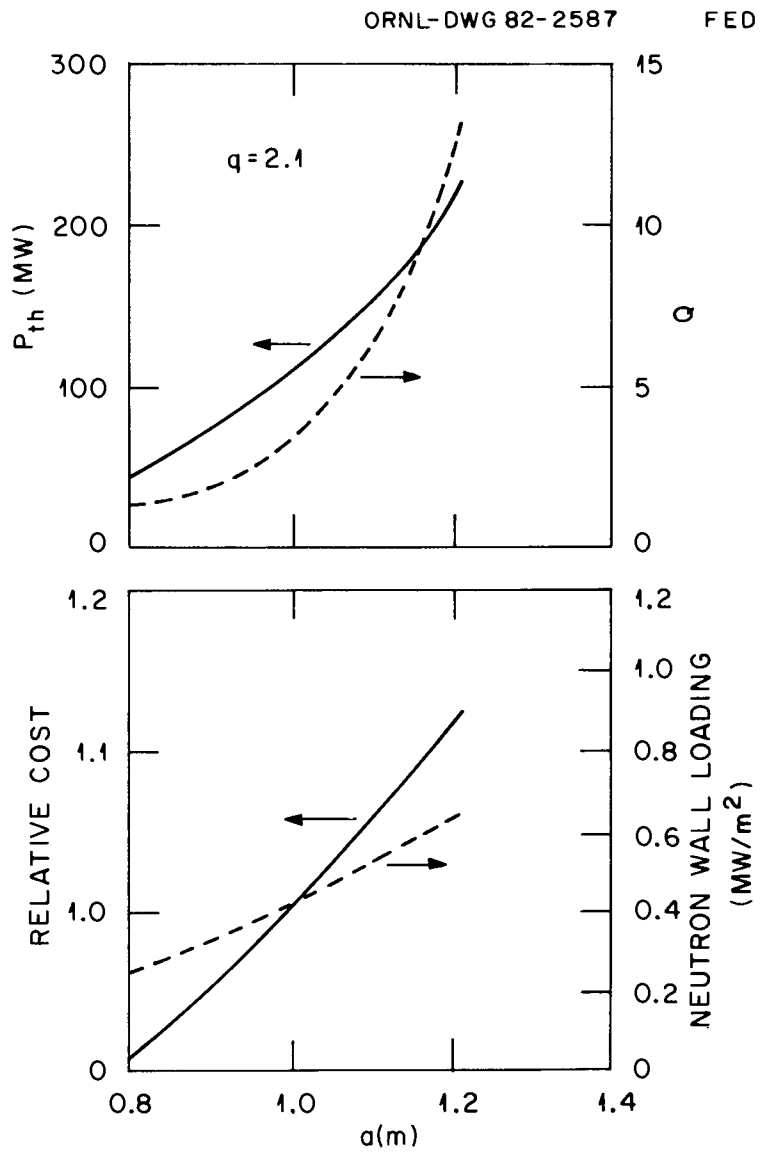

Fig. 5-9. Performance and cost as a function of plasma minor radius at a constant value of κ of 1.4.

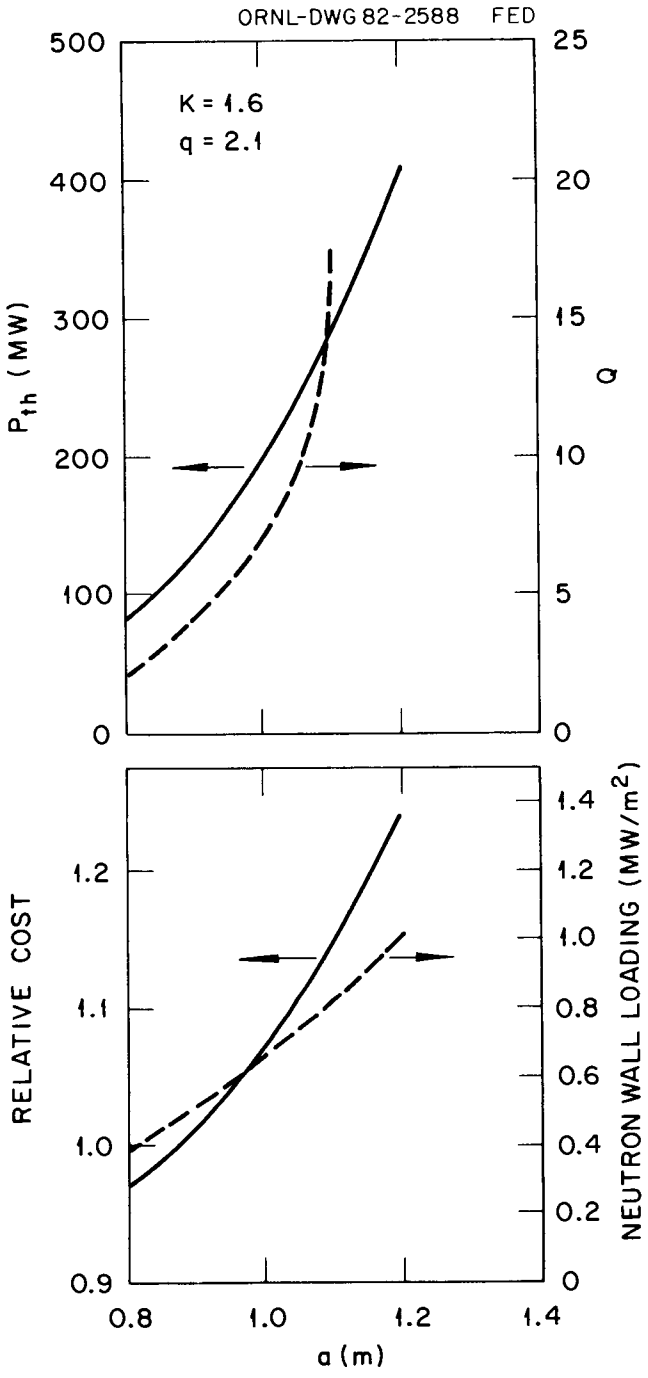

Fig. 5-10. Performance and cost as a function of plasma minor radius at a constant value of κ of 1.6.

Table 5-3. Comparison of elongated and near-circular plasmas for Q = 5 (theoretical beta scaling) with B_{max} = 8.0 T, $\varepsilon\beta_p$ = 0.5, and T_B = 100 s

	Plasma elongation, κ		
	1.2	1.4	1.6
q	1.2	1.2	1.2
a (m)	1.2	1.06	0.93
A	3.6	4.2	4.7
R_o (m)	4.32	4.45	4.37
β (%)	6.4	6.1	6.2
B_T (T)	3.42	3.78	3.92
I_p (MA)	4.3	4.2	3.9
P_{th} (MW)	115	135	150
L_w (MW/m^2)	0.40	0.50	0.55
$\$_R$	1.0	1.03	1.04

Table 5-4. Summary of cost (in millions of dollars) for elongated and near-circular plasmas for Q = 5 with B_m = 8.0 T, q = 2.1, $\varepsilon\beta_p$ = 0.5, and T_B = 100 s

	Plasma elongation, κ		
	1.2	1.4	1.6
Shield	50.0	51.9	52.0
TF coils	66.7	73.0	72.7
PF coils	46.7	48.2	48.2
Plasma heating	66.4	72.7	78.5
Electrical	23.0	23.6	23.7
Heat transport	14.8	16.8	18.0
Facilities	143.8	143.6	142.4
Other	154.9	155.9	156.0
Total	566.3	585.7	591.5
Relative cost	1.0	1.03	1.04

Table 5-5. Comparison of elongated and near-circular plasmas for L_w = 0.5 MW/m^2 with B_{max} = 8.0 T, $\varepsilon\beta_p$ = 0.5, and T_B = 100 s

	Plasma elongation, κ		
	1.2	1.4	1.6
q	2.1	2.1	2.1
a (m)	1.32	1.06	0.90
A	3.45	4.2	4.78
R_o (m)	4.55	4.45	4.30
β (%)	6.9	6.1	6.1
B_T (T)	3.41	3.78	3.92
I_p (MA)	5.0	4.2	317
P_{th} (MW)	160	135	130
Q	9	5	4
$\$_R$	1.06	1.04	1.01

Table 5-6. Comparison of elongated and near-circular plasmas for Q = 5 assuming beta is independent of κ with B_{max} = 8.0 T and T_B = 100 s

	Plasma elongation, κ		
	1.2	1.4	1.6
q	2.1	2.1	2.1
$\varepsilon\beta_p$	0.50	0.37	0.29
a (m)	1.2	1.19	1.17
A	3.6	3.99	4.24
R_o (m)	4.32	4.75	4.96
β (%)	6.4	4.9	4.2
B_T (T)	3.42	3.83	4.03
I_p (MA)	4.3	5.0	5.8
P_{th} (MW)	115	130	135
L_w (MW/m^2)	0.40	0.38	0.35
$\$_R$	1.00	1.11	1.18

The conclusions drawn from this study of the effects of plasma elongation are as follows:

1. Cost is insensitive to plasma elongation for a constant value of Q, assuming constant β_p scaling of beta with κ. However, neutron wall loading scales favorably with elongation.
2. Assuming no beta improvement with elongation, near-circular plasmas are favored.

5.2.3 Impact of Power Amplification Q

The change in relative capital cost as a function of Q for q_ψ = 1.8 and 2.1 is shown in Fig. 5-11. The maximum TF coil field is maintained at 8 T, and Q is varied by varying the plasma minor radius. The aspect ratio is then determined consistent with maintaining flux linkage requirements from the PF system to provide 100 s of burn.

Figure 5-11 indicates that cost sensitivity to Q is a rather weak function. Q can be increased from a value of 5 to a value of 15 for an increase of approximately 9% in the capital cost. This result, plus the advanced physics assumptions of FED-A, suggests that it should be cost-effective to require that ignition be a nominal goal for FED-A.

5.2.4 Impact of Maximum Toroidal Field B_{max}

The impact of maximum toroidal field on performance and cost was investigated with q_ψ = 1.8 and κ = 1.2. Maximum fields of 8-12 T were chosen. The TF windings for the 8- to 10-T maximum field coils were composed of NbTi superconductor and copper. The 11- and 12-T windings feature a graded conductor with the 0- to 10-T portion of NbTi and copper and the high field portions of Nb_3Sn and copper.

The current densities and unit costs of the winding packs were varied as a function of maximum toroidal field. The cost of the winding packs was based on \$90/kg for NbTi and \$255/kg for Nb_3Sn conductor. The 11- and 12-T conductors were graded and costed assuming NbTi up to 10 T and Nb_3Sn for the remainder of the winding. The current density over the winding pack varies from 2500 A/cm^2 at 8 T to 2200 A/cm^2 at 10 T for

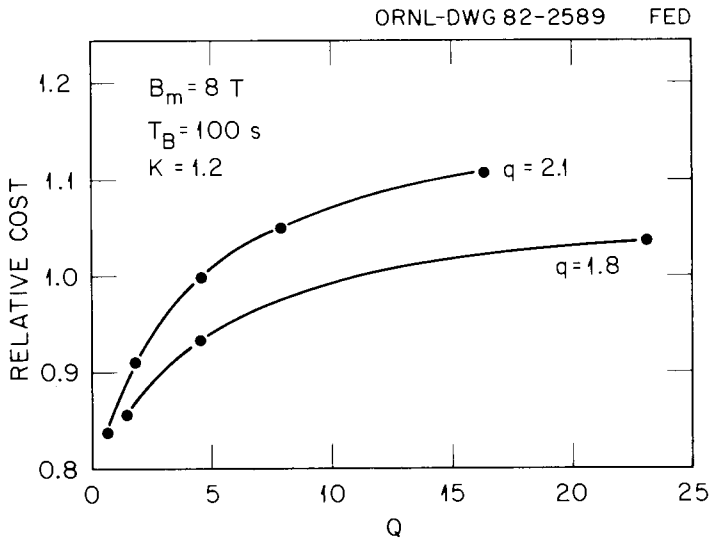

Fig. 5-11. Relative capital cost as a function of Q at a constant B_{max} of 8 T.

the NbTi winding. For the graded conductor the current density for the NbTi portion is taken as 2200 A/cm^2; the higher field Nb_3Sn portions vary from 1970 A/cm^2 at 11 T to 1700 A/cm^2 at 12 T. A more detailed discussion of the TF coil concepts for different field strengths is given in Sect. 8.2. The resulting average winding pack current densities and unit costs are shown in Table 5-7 as a function of maximum toroidal field.

The resulting relative capital cost as a function of maximum toroidal field and plasma minor radius is presented in Fig. 5-12. Note that 100 s of burn is maintained throughout by varying the plasma aspect ratio and that $\varepsilon\beta_p = 0.5$. In general, this figure shows that the cost increases for an increasing minor radius (B_{max} constant) or for an increasing value of B_{max} (plasma minor radius constant). A boundary of marginal ignition is also shown in Fig. 5-12, relating maximum field, plasma size, and capital cost. Little capital cost difference is noted for configurations sized for 8 T to 10 T, but going to 12 T requires a cost increase of $\sim$17% relative to the 10-T configuration. Tables 5-8 and 5-9 present a summary of parameters and a cost breakdown along the ignition boundary, respectively. It is seen that although the 10-T case suffers a 40% increase in TF coil cost over the 8-T case, this increase is compensated for by a decreased cost for the shield, PF coils, and electrical systems due to a reduced minor radius (Table 5-9). This compensation is no longer effective for the 12-T case because of the overwhelming increase of TF coil cost (about 100%) over the 10-T case, coupled with the smaller reduction in other components, which results from the increased major radius due to large increases in the TF coil build.

It is also of interest to determine the cost variation with maximum field at constant neutron wall loading. The boundaries for neutron wall loadings of 1.0 MW/m^2 and 1.5 MW/m^2 are shown in Fig. 5-13. It is seen that the capital cost achieves a minimum value at 10 T. At the 1.0-MW/m^2 level, a cost increase of $\sim$10% is encountered in either decreasing B_{max} to 8 T or increasing B_{max} to 12 T.

Table 5-7. Current density and unit cost as a function of maximum toroidal field assumed in the system analysis

B_{max} (T)	J_{Nb_3Sn} (A/cm^2)	J_{wp}[a] (A/cm^2)	$/$kg_{wp}$	Conductor composition
12	1700	2100	124	Nb_3Sn, NbTi, Cu
11	1970	2177	107	Nb_3Sn, NbTi, Cu
10		2200	90	NbTi, Cu
9		2370	90	NbTi, Cu
8		2500	90	NbTi, Cu

[a]Winding pack overall current density.

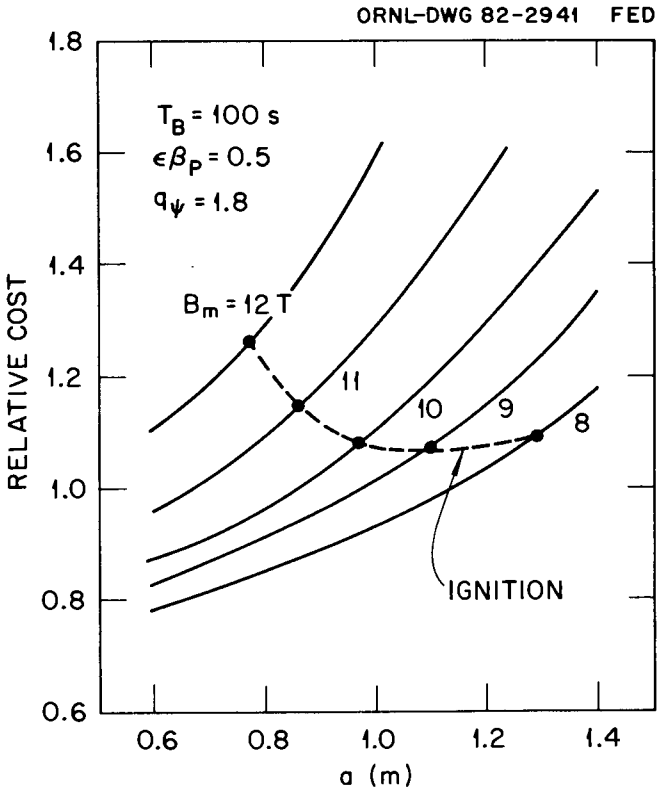

Fig. 5-12. Relative capital cost as a function of plasma minor radius and maximum toroidal field. A boundary of marginal ignition is indicated.

Table 5-8. Ignition FED-A parameters vs B_{max}, where $q_\psi = 1.8$, $\kappa = 1.2$, $\varepsilon\beta_p = 0.50$, and $T_B = 100$ s

	B_{max} (T)		
	8	10	12[a]
J_{wp} (A/cm^2)	2500	2200	2100
J_{OA} (A/cm^2)	1675	1515	1245
TF coil megampere-turns	82	115	163
a (m)	1.29	0.97	0.77
A	3.62	4.77	6.35
R_o (m)	4.67	4.63	4.89
β (%)	8.6	5.7	4.0
B_T (T)	3.51	4.96	6.69
I_p (MA)	5.5	4.1	3.2
PF flux (Wb)	84	73	70
L_p (MW/m^2)	0.86	1.13	1.42
P_{fus} (MW)	280	275	290
$\$_R$	1.09	1.08	1.26

[a] Graded NbTi/Nb_3Sn.

Table 5-9. Cost summary at marginal ignition as a function of B_{max}

	B_{max} (T)		
	8	10	12
Shield	60.4	51.8	49.3
TF coils	81.0	113.1	223.0
PF coils	61.3	44.0	35.7
Plasma heating	60.0	59.2	61.3
Electrical	39.9	31.9	29.4
Heat transport	20.7	21.0	23.4
Facilities	148.3	143.6	143.2
Other	146.4	146.3	147.6
Total	618.0	610.9	712.9
Relative cost	1.09	1.08	1.26

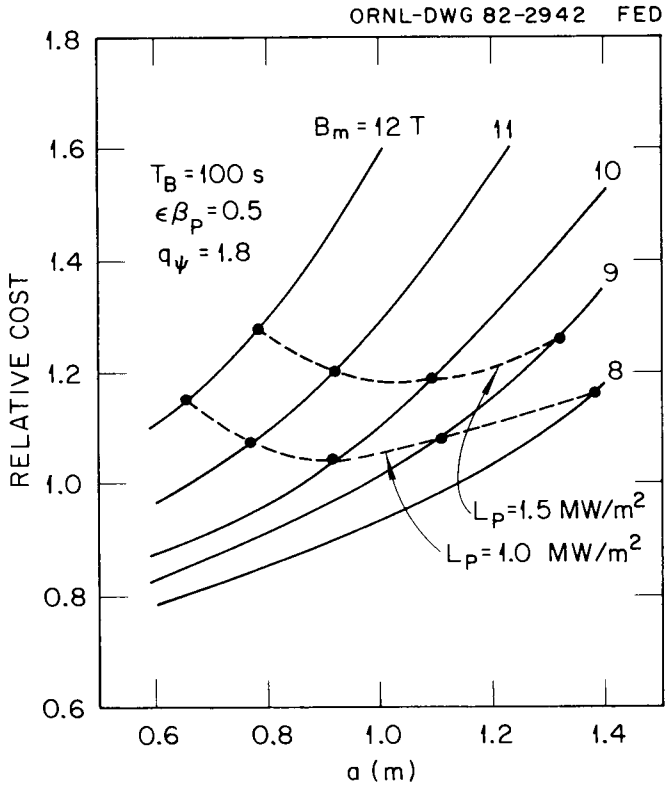

Fig. 5-13. Relative capital cost as a function of plasma minor radius and maximum toroidal field. Lines of constant neutron wall loading are indicated.

For the constraints considered in this study, it appears that B_{max} = 10 T is appropriate for FED-A, and higher toroidal field strengths are neither necessary nor desirable.

Because of the potential significance of this conclusion, it is of interest to assess its sensitivity to some of the assumptions imposed in this study. Figure 5-14 shows the impact of reducing the fixed value of $\varepsilon\beta_p$ from 0.5 to 0.4 for tokamaks sized to achieve ignition and 100 s of burn. Again, the 10-T case achieves a minimum cost, which is about 20% below that of the 12-T case.

The sensitivity of this conclusion to the unit cost of Nb_3Sn was also assessed and is shown in Fig. 5-15. It is seen that if the unit cost of the Nb_3Sn and NbTi conductors is assumed to be the same, the relative total cost of the 12-T device would decrease from 1.26 to 1.17. This is still about 8% higher than the 10-T device, for which the total relative cost is 1.08.

The effect of varying B_{max} on unit capital cost (capital cost divided by the plasma fusion power) is also examined. Figure 5-16 shows that the unit capital cost generally decreases either as plasma minor radius increases with constant B_{max} or as B_{max} increases with constant plasma minor radius. Again, an inductive plasma burn time of 100 s and $\varepsilon\beta_p$ = 0.5 are maintained. The boundary of marginal ignition is also indicated in Fig. 5-16. It is seen that the unit capital cost increases 2% by going from 8 T to 10 T. However, a unit capital cost increase of $\sim$10% is incurred by going from 10 to 12 T. Therefore, the conclusion that B_{max} = 10 T is nearly optimal for FED-A is not sensitive to the assumed values of $\varepsilon\beta_p$ or the superconductor cost (whether capital cost or unit capital cost).

5.3 REDUCING MAJOR RADIUS WITH PARTIAL NONINDUCTIVE START-UP

The purpose of these calculations is to determine the impact of relaxing the induction requirement for start-up and 100 s of burn in FED-A. Removing this requirement would allow the OH solenoid to be reduced, with an accompanying reduction in the major radius. The

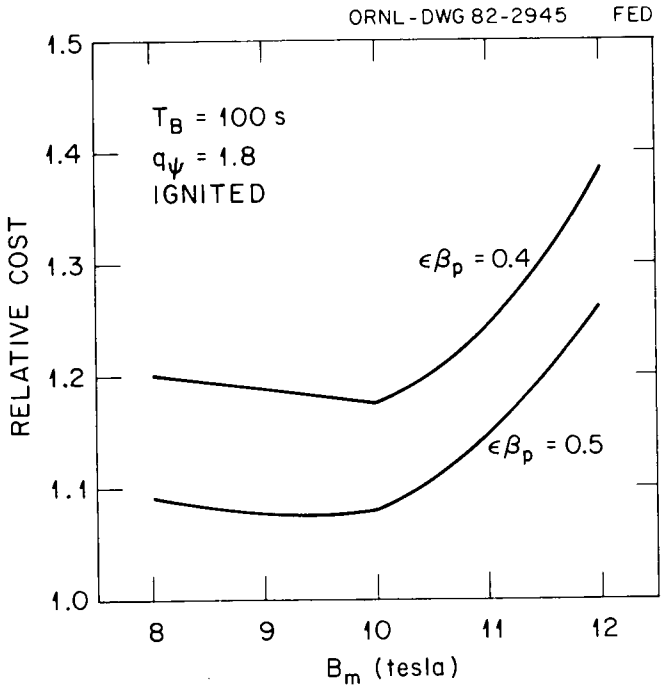

Fig. 5-14. Relative capital cost as a function of $\varepsilon\beta_p$ and maximum toroidal field.

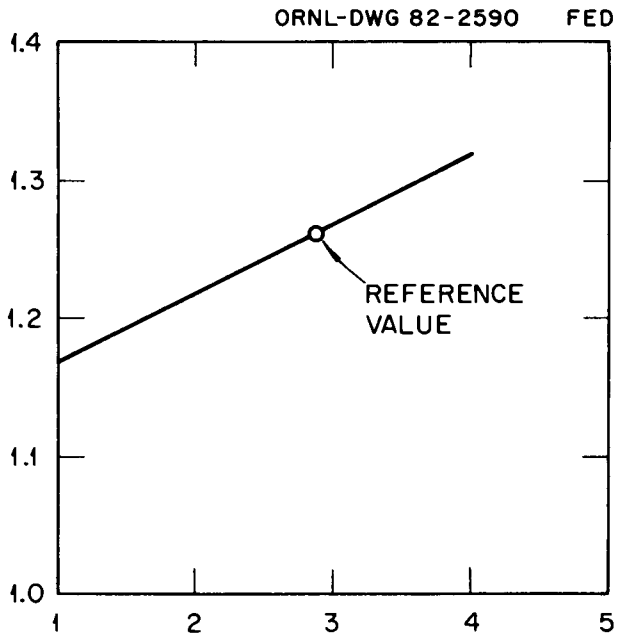

Fig. 5-15. Relative capital cost as a function of the ratio of the unit conductor cost of Nb_3Sn to NbTi.

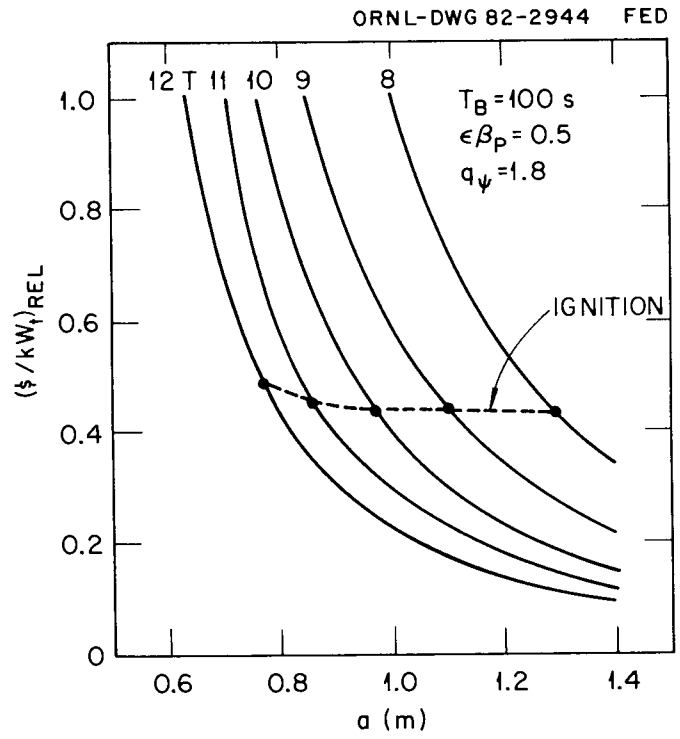

Fig. 5-16. Unit cost [$/kW(t)] as a function of plasma minor radius and maximum toroidal field. A boundary of marginal ignition is indicated.

reduced flux from the smaller solenoid is assumed to be augmented by noninductive current drive in order to achieve start-up and maintain burn at desired values.

This study is done for three cases. In the first case we maintain a constant plasma minor radius as the major radius is reduced, allowing the inductive start-up and burn capability to decrease. This is expected to decrease plasma performance due to decreased toroidal field at the plasma with B_{max} kept constant. In the second case we maintain constant neutron wall loading by increasing the plasma minor radius as the major radius and the OH solenoid are reduced. In the third case we maintain constant Q (e.g., ignition) by increasing the plasma minor radius as the major radius is decreased. Constraints for each case calculated here include B_{max} = 8 T and q_{ψ} = 2.1.

Results for a constant plasma minor radius at 1.2 m are presented in Fig. 5-17, which shows that cost can be reduced approximately 25% by reducing the major radius from 4.3 to 2.8 m. However, at a major radius of 2.8 m, performance is greatly decreased; fusion power is approximately 15 MW, compared with 112 MW at a 4.3-m major radius, and neutron wall loading is approximately 0.1 MW/m^2, compared with 0.4 MW/m^2 at a 4.3-m major radius. The maximum field in the OH solenoid was maintained at 7 T as the major radius was reduced. At a major radius of 3.24 m, the bore of the solenoid consists only of space for the solenoidal winding plus gaps. Beyond this major radius, the solenoidal field is reduced to zero, and the reduction in major radius continues until the center of the device consists only of a solid bucking cylinder. The conclusion drawn is that reduction of the major radius, even to the extreme where the OH solenoid is removed, is not cost-effective due to the deleterious impact on performance.

Results for constant neutron wall loading are shown in Fig. 5-18. The major radius was reduced from 4.3 m to 3.8 m at a constant neutron wall loading of 0.4 MW/m^2. Below a major radius of 3.8 m, this neutron wall loading could not be achieved under the constraints of a fixed B_{max} and a fixed value of poloidal beta times inverse aspect ratio. Cost decreases with decreasing major radius and achieves a shallow minimum by

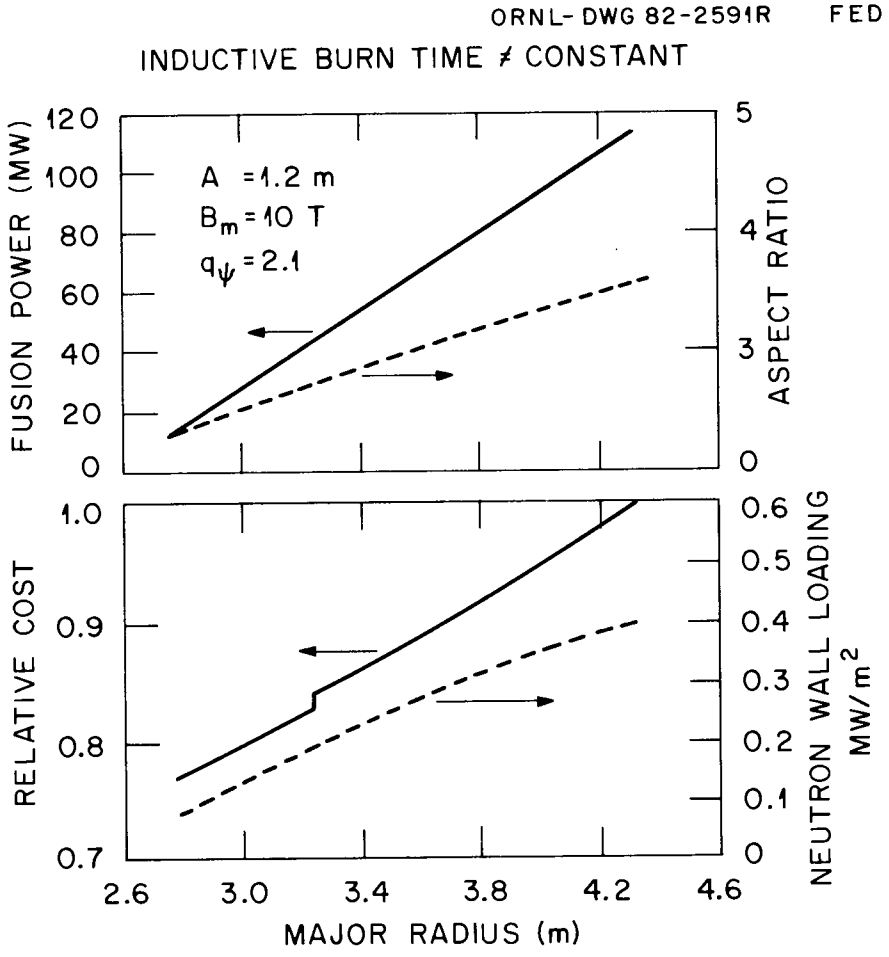

Fig. 5-17. Relative capital cost, fusion power, neutron wall loading, and aspect ratio as a function of major radius for constant values of plasma minor radius and maximum toroidal field. The requirement for an inductive plasma current start-up is relaxed as the major radius is reduced from 4.3 m.

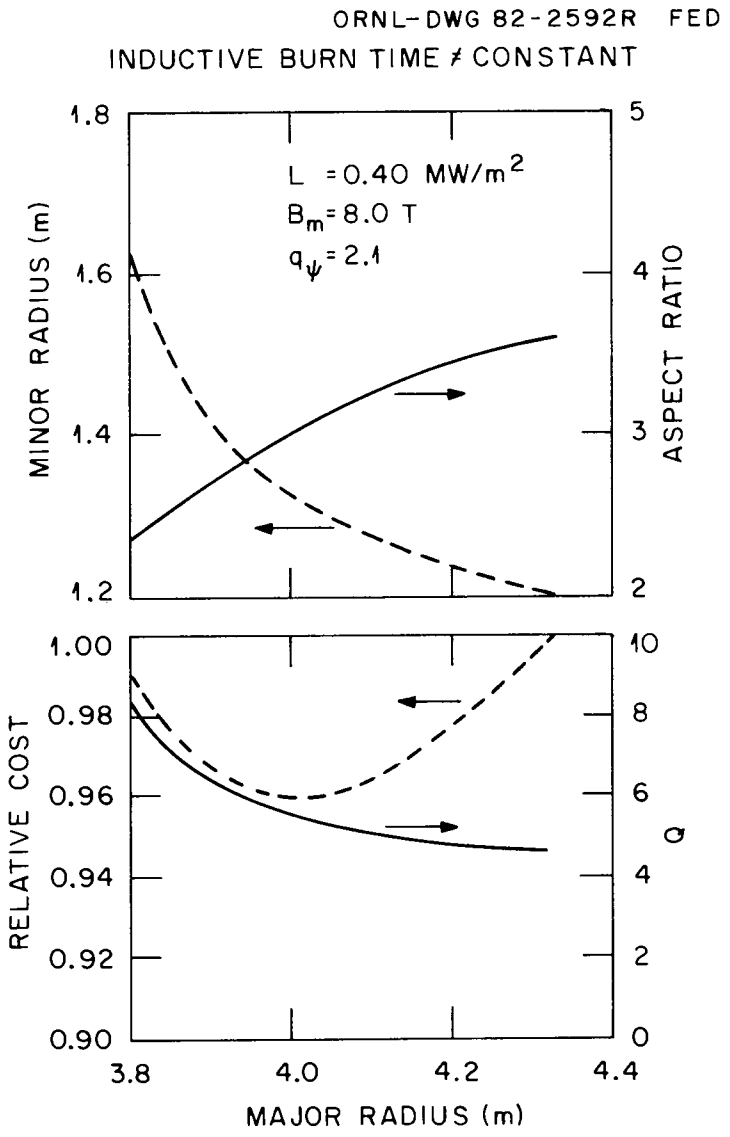

Fig. 5-18. Relative capital cost, Q, minor radius, and aspect ratio as a function of major radius for a constant value of neutron wall loading. The requirement for an inductive plasma current start-up is relaxed as the major radius is reduced from 4.3 m.

only 4%. Further reduction in the major radius requires cost increases in the EF coils, electrical systems, shield, and facilities that more than offset the cost reduction in the TF coils and heating system, as shown in Table 5-10. Assuming the requirement of constant neutron wall loading, reducing the plasma major radius does not provide a significant cost saving even when the cost of noninductive current start-up is ignored.

Results for constant Q are shown in Fig. 5-19. The major radius was reduced from 4.63 to 3.52 m while maintaining ignition conditions. Under these conditions, a 15% reduction in cost was achieved, but at a reduced neutron wall loading (0.89 MW/m^2 as opposed to 1.13 MW/m^2). Further reduction in the major radius results in a cost increase. Again, the flux linkage from the PF system was not required to provide full inductive start-up and burn as the major radius was decreased. A cost breakdown by system and a listing of selected plasma parameters as a function of major radius are shown in Tables 5-11 and 5-12, respectively. The low aspect ratio encountered at reduced major radius provides poor utilization of the maximum TF field but does allow high values of beta, as seen in Table 5-12. Assuming the requirements of constant performance characterized by ignition, reducing the plasma major radius and assuming partial noninductive start-up provides a moderately significant cost saving.

5.4 USING TUNGSTEN INBOARD SHIELDING

If tungsten is used as the inboard shield material, the thickness of the shield can be reduced because the neutron attenuation of tungsten is better than that of stainless steel. For this study, the e-fold thickness (the thickness required to attenuate the neutron flux by a factor of 2.718) of tungsten was taken to be 75% of the e-fold thickness of stainless steel.

Tokamak configurations at ignition for a maximum TF field of 10 T using stainless steel and tungsten inboard shields are presented in Table 5-13. The tungsten shield is thinner by 14 cm than a stainless steel shield, leading to a reduction in the tokamak major radius of

Table 5-10. Summary of costs (in millions of dollars) for variation in major radius at constant neutron wall loading (partial noninductive current start-up)

	R_o = 4.32 m	R_o = 4.0 m	R_o = 3.8 m
Shield	50.0	49.3	53.7
TF system	66.7	51.3	36.5
PF system	46.6	48.4	62.5
Heating system	66.4	61.1	56.9
PF electrical system	19.2	20.8	32.0
Facility	143.8	143.3	146.9
Other	173.6	171.3	170.3
Total cost	566.3	545.5	558.8
Relative cost	1.0	0.963	0.987

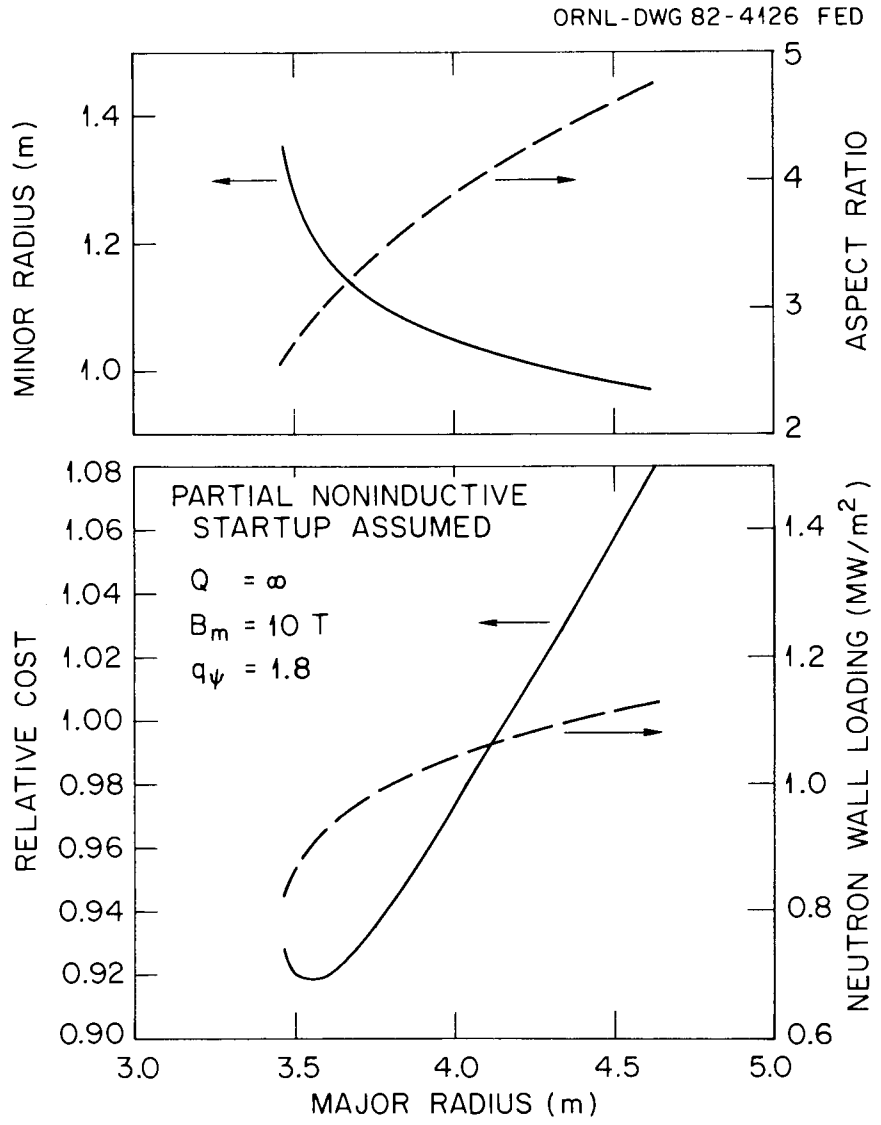

Fig. 5-19. Relative capital cost, neutron wall loading, minor radius, and aspect ratio as a function of major radius at ignition. The requirement for an inductive plasma current start-up is relaxed as the major radius is reduced from 4.3 m.

Table 5-11. Summary of costs (in millions of dollars) for variation in major radius at ignition (partial noninductive current start-up)

	R_o = 4.63 m	R_o = 3.65 m	R_o = 3.52 m
Shield	51.8	44.7	45.2
TF system	113.1	54.9	46.6
PF system	44.0	41.2	44.7
Heating system	59.2	52.0	51.2
PF electrical system	18.7	18.8	22.5
Facility	143.6	139.4	140.2
Other	180.6	170.6	169.8
Total cost	611.0	521.6	520.2
Relative cost	1.08	0.922	0.919

Table 5-12. Selected parameters as a function of major radius for ignited plasmas (partial noninductive current start-up)

	Major radius, R (m)		
	4.63	3.65	3.52
A	4.77	3.17	2.82
a (m)	0.97	1.15	1.25
q_ψ	1.8	1.8	1.8
Beta (%)	5.7	10.9	13.8
B_T (T)	4.96	3.29	2.82
B_{max} (T)	10	10	10
I_p (MA)	4.1	5.5	6.1
P_{th} (MW)	275	215	210
L_w (MW/m^2)	1.13	0.95	0.89

Table 5-13. Comparison of inboard shield configurations at ignition (B_{max} = 10 T, q = 1.8, T_B = 100 s)

Parameter	Reference stainless steel shield	Tungsten shield
Δ_s (m)	0.58	0.44
a (m)	0.95	0.895
A	4.82	4.84
R_o (m)	4.58	4.33
β (%)	5.6	5.6
B_T (T)	4.97	5.13
I_p (MA)	3.98	3.86
P_{fus} (MW)	255.0	241.0
L_p (MW/m^2)	1.08	1.15
$\$_R$	1.064	1.047

25 cm. However, the unit cost of fabricated tungsten is about twice that of stainless steel, and the density of tungsten is also about twice that of stainless steel. For the same volume, the cost of tungsten therefore would be approximately four times that of steel. The net impact of this shield material is found to be 2% in favor of the tungsten shield as shown in Table 5-13. The reduced cost of the smaller tokamak components using the tungsten inboard shield is essentially nullified by the higher cost of the tungsten shield itself, as shown in Table 5-14.

It is concluded that the choice of shield material has little impact on total capital cost, at least for a device the size of FED-A.

5.5 REFERENCE FED-A PARAMETERS

A set of reference parameters for FED-A has been chosen based on these results and is given in Table 5-15. The parameters include a maximum field of 10 T, a plasma safety factor of 1.8, 12 TF coils with size limited by the ripple requirement, and ignition assumed. In addition, a forced-cooled OH solenoid was used, which allows reducing the space between the bucking cylinder and winding pack by 10 cm, providing a greater flux capability. Also, a combined vacuum boundary is assumed, as suggested by the FED Baseline studies, in place of separate vacuum boundaries for the torus and TF coils. This allows a saving of 15 cm in the inboard radial build of the tokamak. The cost of this version of FED-A is about 70% of the cost of the 1981 FED Baseline, based on the systems code estimates. More detailed cost estimates can be found in Chap. 9.

5.6 CONCLUSIONS

The conclusions drawn from the trade studies for FED-A are summarized as follows:

1. The capital cost decreases with decreasing q_ψ for constant Q or constant neutron wall loading. A 13% cost reduction is indicated when q_ψ is reduced from 2.0 to 1.5.

Table 5-14. Summary of costs (in millions of dollars) for stainless steel vs tungsten shield

	Reference stainless steel	Tungsten 90%
Shield	50.5	63.8
TF coils	110.2	99.1
PF coils	42.3	38.4
Plasma heating system	59.1	57.2
Electrical system	31.2	29.5
Heat transport	20.3	19.4
Facilities	143.0	140.3
Other	145.9	145.0
Total	602.5	592.7
$\$_R$	1.064	1.047

Table 5-15. Reference parameters for FED-A

Description	Value
Geometry	
Major radius, R	4.22 m
Plasma radius, a	0.92 m
Plasma elongation, κ	1.2 m
Aspect ratio, A	4.59 m
Scrape-off layer	0.15 m
Plasma	
Average ion temperature, $\langle T_i \rangle$	10 keV
Safety factor (edge), q_ψ (flux-surface-averaged)	1.8
Effective charge (during burn), Z_{eff}	1.5
TF ripple (peak-to-average), edge	1.0%
Plasma current, I_p	4.1 MA
Average electron density, $\langle n_e \rangle$	1.7×10^{14} cm^{-3}
$\varepsilon\beta_p$	0.5
Total beta, $\langle\beta\rangle$	6.0%
Toroidal field at plasma, B_T	4.98 T
Q	Ignited
Operating mode	
Burn time, t_{burn}	100 s, 1000 s[a]
Fusion power, P_{fus}	255 MW
Pumpdown time, t_p	30 s
Start-up/shutdown time, t_{ss}	26 s/26 s
Number of full field current pulses/lifetime	3×10^4
Average number of burn pulses in each current pulse	10
Lifetime	10 years
Torus eddy current times (L/R)	
Conducting vessel	$\sim$1 s
Other conducting path	$\sim$0.2 s

Table 5-15 (cont'd)

Description	Value
First wall/armor	
Coolant	H_2O
Average neutron wall load at plasma edge	1.2 MW/m^2
Average neutron wall load at first wall	1.0 MW/m^2
Average thermal wall load	TBD[b]
Shield	
Inboard shield material	Stainless steel
Inboard thickness (excluding spool armor, gaps, scrapeoff)	62 cm
Dose rate to TF coil insulation	1×10^9 rad
Time after shutdown to permit personnel access (2.5 mrem/h)	36 h
Outboard shield thickness (stainless steel)	120 cm
Maximum structure temperature	200°C
Vacuum	
Initial base pressure	10^{-7} torr
Preshot base pressure	10^{-5} torr
Postshot bast pressure	3×10^{-4} torr
Pressure at duct inlet during burn	10^{-2} torr
Particle flux (molecular) to be pumped	$<10^{23}$ s^{-1}
TF coils	
Number	12
Peak design field at winding, B_m	10 T
Conductor winding current density, J_w	2200 A/cm^2
Overall current density, J_{OA}	1720 A/cm^2
PF coils	
Total flux capability	67 Wb
EF flux	24 Wb
OH flux	43 Wb
Total maximum ampere-turns	51 MAT
Maximum EF ampere-turns	6 MAT
Maximum OH ampere-turns	45 MAT

Table 5-15 (cont'd)

Description	Value
OH maximum field allowable at coil	7 T
OH current ramp time	30 s
Conductor winding pack current density, J_{wp}	1400 A/cm^2
Plasma heating	
Start-up	
Initiating voltage with rf assist only	<10 V
Current rise time	20 s
Start-up ECH power	3.5 MW
Time duration for ECH assist	20 s
Frequency	120 GHz
Bulk heating (including start-up)	Lower hybrid
Power	25 MW
Current drive	
Start-up	
Lower hybrid current	
Rise time	20 s
Power	10-20 MW
Frequency	1-3 GHz
Others (REB, FWIC, ECH)	TBD
Current maintenance	
Lower hybrid	
Power	25 MW
Frequency	1-5 GHz
Others (REB, FWIC, ECH)	TBD

[a] 100 s provided by PF system in the absence of noninductive current drive, 1000 s with partial noninductive current drive.

[b] To be determined.

2. Cost is insensitive to plasma elongation at a constant value of Q, assuming the theoretical scaling of beta; however, the neutron wall loading scales nearly linearly with elongation κ.
3. Assuming no beta improvement with elongation, near-circular plasmas are favored.
4. A maximum toroidal field of 10 T appears to be optimum for FED-A on the basis of capital cost and unit capital cost for marginal ignition or for constant neutron wall loading, subject to the constraints of inductive start-up and 100 s of burn. For ignition, the cost increases 17% in going from 10 T to 12 T. At a constant neutron wall loading of 1.0 MW/m^2, the cost increases 10%.
5. The cost impact of tungsten inboard shielding in place of stainless steel is slight, approximately 2%, when marginal ignition requirements and 10-T maximum toroidal field are maintained.
6. Providing partial noninductive current start-up is cost-effective, giving a $\sim$15% cost reduction by allowing a reduced major radius and a reduced flux OH solonoid while maintaining a constant value of Q and a maximum field of 10 T. For a constant neutron wall loading, partial noninductive start-up is not cost-effective, as only a 4% cost reduction is realized. It is suggested that a full OH solenoid capability be maintained in FED-A for long pulse burn ($\sim$1000 s) in quasi-steady-state operation.
7. High Q ($\sim$15) by increasing the plasma size requires only a modest increase in capital cost ($\sim$10%) relative to the case of Q = 5.
8. A combination of features such as low q, slow plasma start-up, natural plasma shape, and combined vacuum boundary allows a capital cost reduction for FED-A of $\sim$30% relative to the 1981 FED Baseline configuration.

6. CONDUCTING FIRST WALL

A conducting first wall is perceived (Sect. 3.2) to be effective in permitting disruption-free burn and in mitigating disruption impact. In FED-A the first wall must also be compatible with test module operation, simple to maintain, and consistent with the reactor-relevant heat removal.

The achievement of effective disruption mitigation is related in large part to achieving a long eddy current decay time in the first wall to shield the device from the disruption's electromagnetic impact. The requirements for this feature are discussed in Sect. 6.1. Compatibility with test module operation will require a neutronically thin first wall, as discussed in Sect. 6.2. Simple maintainability is closely related to the simplicity of the mechanical design features. These requirements are discussed in Sect. 6.3. In addition, reactor-relevant heat removal represents a desirable characteristic that should be achieved without compromising the preceding requirements. This objective is interpreted as removing first wall coolant at temperatures high enough to result in useful power production. This requirement is also discussed in Sect. 6.3. With these requirements as a guide, a discussion of the conducting first wall design options is then presented in Sect. 6.4.

6.1 ELECTROMAGNETIC CRITERIA

The torus designs of recent fusion devices such as TFTR, PLT, and Doublet III were influenced strongly by inductive plasma start-up requirements. Start-up has been characterized for these devices by high starting loop voltages (up to and above 100 V) over short time duration (up to tens of milliseconds). In order for this voltage to penetrate the structure and initiate the plasma current rapidly, the electrical resistance of the toroidal metallic structure is required to be relatively high, typically above hundreds of microhms. These properties are also required to permit active control fields to penetrate the structure rapidly, a condition generally perceived to be necessary to maintain the desired plasma position. The metallic shell that makes up the first

wall in these devices is also the vacuum vessel and is relatively thin — on the order of a fraction of a centimeter. Shields (in the case of TFTR, for instance) are placed fairly far from the plasma.

As the fusion device designs have become more reactorlike and the burn times are extended to tens or hundreds of seconds, the bulk shields have been moved closer to the plasma and shield materials include large quantities of steel. The short duration, high voltage approach to plasma start-up and control is no longer desirable or straightforward.

Long burn times permit consideration of low voltage, long duration start-up scenarios. This tends to remove the necessity of high resistance shells in the vicinity of the plasma. In addition, for large devices with large plasma energy content, disruption effects become a much more serious threat to viable device operations. Slow dissipation of disruption energy through a longer plasma current decay time during disruption may be accomplished by increasing the toroidal skin time of a conducting first wall.

While detailed electromagnetic calculations are needed to better quantify the first wall parameters, the following subsections present some guidelines for the electromagnetic properties of the torus. The symbols used in the following discussion are defined in Table 6-1.

6.1.1 Disruption Mitigation

Present plasma disruption scenarios include two phases, the thermal quench phase followed by the current quench phase. Possible prevention of the thermal quench phase (island overlap and field line ergodization) through design features of the torus is discussed in Sect. 3.2. One approach requires the design of helical current paths in the wall close to the plasma. This approach is not presented as a requirement in this section because there is evidence that if the current quench can be prevented,[1] the plasma conditions may be restored after a thermal quench. The discussion here is focused on the current quench phase and the first wall conductance requirement.

First, it is assumed that a closely fitted shell with a large toroidal eddy current decay time ($\tau_{t,w}$) is needed for plasma position

Table 6-1. Definition of electromagnetic parameters for continuous first wall

Symbol	Unit	Definition
R	ohm	Resistance = $\frac{\rho L}{A}$
τ	second	Eddy current decay time
ψ	weber	Poloidal flux
ρ	ohm·meter	Electrical resistivity
L	meter	Length of conductor
A	square meter	Cross-section area of conductor
Subscripts		
t		Toroidal eddy current
p		Plasma
w		Conducting wall close to the plasma
x		Conducting structure far from the plasma
VF		Vertical field
SU		Start-up

control (Sect. 6.1.2). It is estimated that $\tau_{t,w}$ should be on the order of 0.5-1.0 s. The current quench time (leading to energy deposition on first wall) is assumed to be approximately equal to the vertical field eddy current decay time ($\tau_{VF,w}$), which is assumed to be roughly half of $\tau_{t,w}$. This time scale should be long enough to keep the energy deposition from resulting in structural damage.

The loop voltage (exterior to the shell) during a current quench can be approximated by $\psi_{ext}/\tau_{t,w}$, where ψ_{ext} is the external poloidal flux linked to the plasma current. The magnitude of ψ_{ext} in FED-A is estimated to be about 20 Wb. The voltage standoff is therefore approximately 20-40 V/turn, eliminating the possibility of arcing across the gaps in the device shield and structure.

6.1.2 Plasma Position Control

Under perturbations (including the disruptive thermal quench), the plasma can move relative to a dominant conducting shell only in the vertical field eddy current time scale (τ_{VF}). The amount of plasma displacement in this time scale is largely dependent on the proximity of this conducting shell. To minimize plasma displacement in short time scales, it is desired to place the dominating shell at the first wall, that is, to have $\tau_{VF,w} \gg \tau_{VF,x}$. The eddy current time scale for the shell near the plasma should be much larger than the same time scales for components further away from the plasma.

6.1.3 Start-Up Considerations

It is assumed that the resistance of the plasma during start-up should be comparable to that of the first wall. With intense rf assist, the resistance of a small radius plasma at $\sim$1 keV is approximately 10 $\mu\Omega$. The permissible resistance of the wall next to the plasma is therefore assumed to be 10-50 $\mu\Omega$.

The time scale of plasma start-up (τ_{SU}) is, on the other hand, bounded below by $\tau_{t,w}$, the toroidal eddy current time constant of the conducting first wall. In the absence of rf current drive, τ_{SU} is also

bounded above by the permissible resistive loss of inductive flux in FED-A. Figure 6-1 shows a typical case of rf-assisted start-up in FED-A. By maintaining the electron temperature above 2 keV through start-up, the total resistive volt-seconds dissipated during a 20-s start-up can be limited to as low as 5 Wb.

Table 6-2 lists the desired electromagnetic properties of the conducting first wall.

6.2 MATERIALS AND NUCLEAR CRITERIA

The selection of the material for any reactor component is invariably a compromise between the desired properties for optimum performance and the actual properties of available materials. Desirable performance properties for a continuous first wall include low electrical resistivity, high thermal conductivity, and high neutron transmission. Since no one material provides ideal values in all of these areas, available materials must be compared in terms of their limitations. This section explores these limitations.

6.2.1 Candidate Materials and Databases

The material specified for the first structural wall in the FED Baseline design is austenitic type 316 stainless steel (316 SS). This steel is specified because it is paramagnetic, has adequate physical and mechanical properties, and can be used with a maximum service temperature of at least 450°C. Furthermore, there is extensive experience with the use of austenitic stainless steels in elevated temperature power conversion systems. In particular, 316 SS has been more extensively studied for its response to neutron irradiation than has any other alloy. However, there are disadvantages associated with this alloy. Its relatively poor thermal conductivity sets limitations on the tolerable heat loading on the first wall and on the section thickness usable in the first wall. The poor electrical conductivity of this steel together with the limits on section thickness also limit the minimum electrical resistance that can be achieved in a continuous first wall.

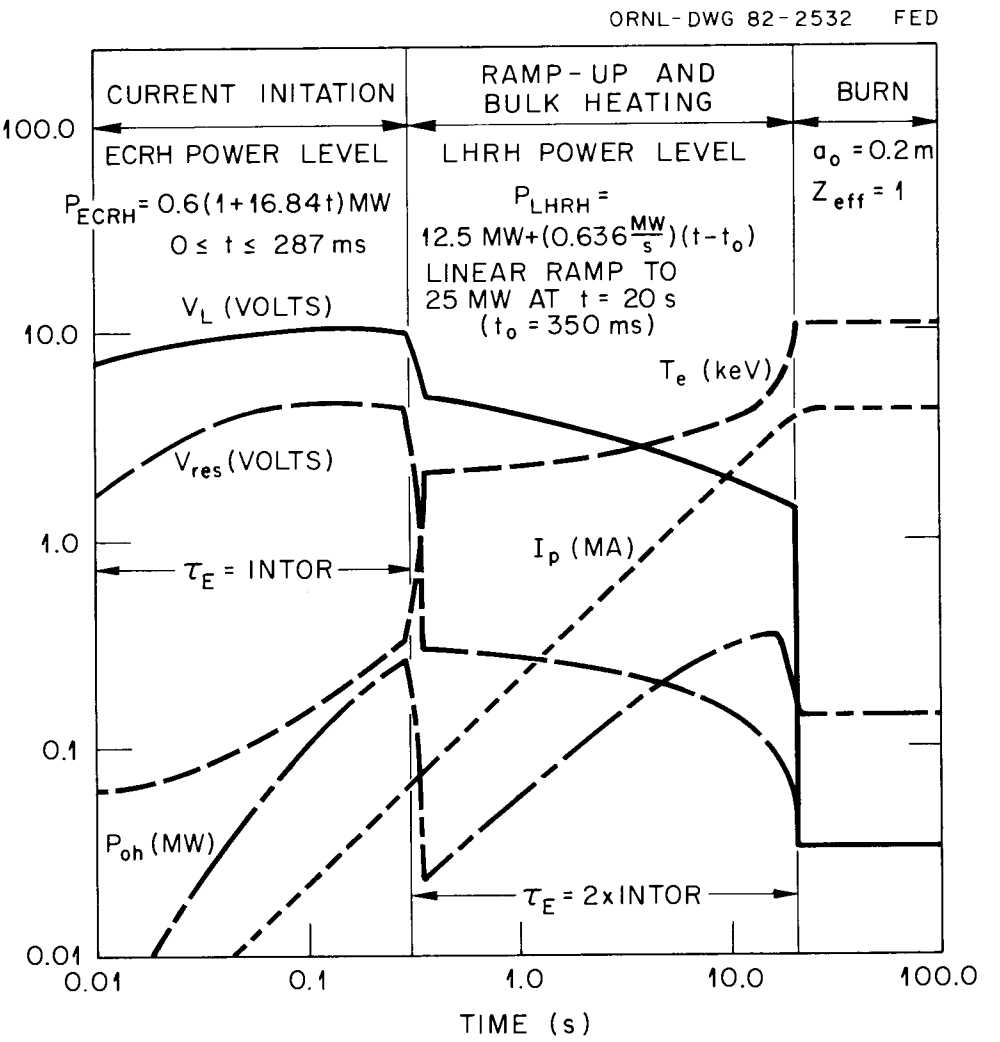

Fig. 6-1. Typical rf-assisted start-up scenario for FED-A.

Table 6-2. Electromagnetic design objectives for continuous conducting first wall

- Disruption mitigation

  ψ_{ext} (plasma)/$\tau_{t,w}$ < voltage standoff $\cong$ 20-40 V

  $\tau_{t,w}$ = 0.5 s > $\tau_{VF,w}$ = 0.2 s

  $\tau_{t,x}$ = 0.05 s > $\tau_{VF,x}$ $\sim$ 0.02 s

- Start-up

  20 s $\gtrsim$ $\tau_{t,w}$ and $\tau_{t,x}$

  R_p < R_w

- Position control

  $\tau_{VF,w} \gg \tau_{VF,x}$ with closely fitted conducting shell

Two alternative alloy systems with much higher electrical conductivity have been examined for the continuous first wall. These are the aluminum and copper alloy systems. These alloy systems also have much better thermal conductivity than does 316 SS, so that section thickness limits are relaxed for these materials. The major generic liability of the aluminum and copper alloys is their loss of strength with increasing temperature. This raises questions about their suitability for use in power-producing fusion reactors, even if they prove suitable for use in FED-A.

Comparisons have been made on the basis of a specific alloy for each of the three alloy systems. These alloys, identified in Table 6-3, are 316 SS, the aluminum alloy 5083 (Al 5083), and the developmental copper alloy AMAX-MZC (Cu AMAX-MZC).

As mentioned above, the database on 316 SS is extensive. The physical and mechanical behavior of the unirradiated material is available in handbooks, and the fabrication technology is well developed. A large database exists for the effects of irradiation on 316 SS, although the largest part of the database is for conditions well outside the temperature range of FED-A operation. (In particular, most irradiations have been at temperatures of 400°C or higher.)

The aluminum alloy 5083 is a standard wrought product of the aluminum industry. It is a weldable, moderately strong, and corrosion-resistant alloy used in sheet, plate, and rod form for pressure vessels and other structural applications. This alloy is not precipitation hardened, so it does not overage during service. It can be used in the annealed condition or can be deformed to achieve somewhat higher strength levels. The properties of this alloy are available for room-temperature service, but data for elevated temperature service are sparse. Specialized data on irradiation effects on this particular alloy are generally not available, but similar alloys have been used in research fission reactors; some projections can be made from these data to predict the irradiation behavior of Al 5083.

The reference copper alloy is Cu AMAX-MZC, a relatively new alloy developed to combine good conductivity, high strength, and elevated

Table 6-3. Composition of candidate alloys evaluated for the FED-A continuous first wall

Alloy	Alloy base	Nominal alloying additions (wt %)
316 SS	Fe	17 Cr, 12 Ni, 2.5 Mo, 2 Mn, 1 Si, 0.08 C
5083	Al	4.4 Mg, 0.7 Mn, 0.15 Cr
AMAX-MZC	Cu	0.6 Cr, 0.1 Zr, 0.03 Mg

temperature service potential. It is alloyed with magnesium, zirconium, and chromium but contains at least 98.9% copper. The alloy is heat treatable, and maximum strength properties are achieved by cold working and then aging. This required strengthening process would make welding of the alloy difficult, so prolonged use at elevated temperatures can lead to overaging and loss of strength. It may, however, be suitable for use in the continuous first wall. Data adequate for conceptual design have been developed by the alloy supplier. The alloy has not been evaluated for its performance in a neutron irradiation environment. Isolated data are available on irradiation effects on quite different copper alloys. Thus, further experimental results would be necessary to adequately predict the service response of Cu AMAX-MZC.

6.2.2 Material Damage

The design of the continuous first wall, presented in Sect. 6.4, is based on allowable limits for critical properties. These limits are different for each of the three candidate alloys and are based on the properties of the alloys before they are put into service. A predictive knowledge of the effect of the service environment on these properties is required to ensure adequate performance and acceptable lifetime of the first wall.

The properties of the candidate alloys may change during service as a result of long-term exposures to elevated temperatures and to the reactor neutron flux. While a full database is not available, the service conditions are relatively modest, and effects on properties can be estimated from the available data.

The continuous first wall of FED-A is water cooled. Allowable maximum structural temperatures, based on strength properties, are taken as 400°C for the 316 SS, 200°C for the Al 5083, and 350°C for the Cu AMAX-MZC. The neutron wall loading of FED-A is approximately 1.2 MW/m^2, equivalent to a total neutron flux of 4.3×10^{14} $n/cm^2 \cdot s$. The goal service life of the reactor is 1.2 $MW \cdot year/m^2$, equivalent to a total neutron fluence at the front surface of the first wall of 1.4×10^{22} n/cm^2. The response of the candidate wall materials to this

fluence can be calculated in terms of the atom displacements and gas production from (n,α) and (n,p) reactions. These parameters, given in Table 6-4, can be used to compare the fusion reactor service to data generated in various radiation effects evaluation programs to predict the effects of service on properties.

Most of the physical properties of metal alloys are relatively immune to service in an irradiation environment at temperatures in the range of interest here. Changes in the electrical resistivity and the thermal conductivity resulting from irradiation at 60°C and above can be anticipated to be in the range of 1 to 10%. Of greater concern is the potential swelling caused by the formation of cavities (voids or bubbles) during neutron irradiation. In 316 SS, irradiations producing responses bracketing the parameters in Table 6-4 caused swelling of less than 0.25% throughout the temperature range 55-650°C. The aluminum alloy 5083 has not been studied, but in somewhat similar alloys at 55°C, swelling was not appreciable until fluences producing approximately 40 dpa were achieved. Swelling in aluminum alloys decreases for temperatures above 55°C. Very scanty data on copper show that swelling in the unalloyed metal occurs for neutron irradiation at temperatures between 225 and 425°C, with peak swelling at about 325°C. As in more thoroughly studied metals, alloying is effective in suppressing swelling in copper. While the performance of Cu AMAX-MZC will require experimental verification, swelling of only a few percent should be assumed until data are available.

The mechanical properties of these alloys can also be affected by the irradiation service. The general effects of irradiation are an increase in strength properties and a loss of ductility. These are also the effects expected in the FED-A continuous first wall.

Available data for 316 SS and for aluminum alloys similar to Al 5083 show that irradiation producing 10 to 20 dpa at FED service temperatures will increase both the yield and the ultimate tensile strength. Similar strengthening should be expected in the Cu AMAX-MZC, although supporting data are not available. Total elongation for stainless steel and aluminum alloys is reduced to the range 5-10% by irradiation conditions similar to those anticipated for FED-A. The uniform elongation can be

Table 6-4. Calculated irradiation response of candidate first wall alloys to integrated service of 1.2 MW•year/m^2

Alloy	Atom displacements (dpa)	Helium generation (appm)	Hydrogen generation (appm)
316 SS	12.8	186	670
Al 5083	17.5	382	359
Cu AMAX-MZC	17.2	120	656

more severely reduced, with values as low as a few tenths of 1% measured for some conditions. However, these lower uniform elongation values accompany high yield strengths and total elongation of 5% or more, indicating the ability to carry design loads based on unirradiated yield strength values. As with other properties, there are no experimental data on the ductility of irradiated Cu AMAX-MZC.

Data are not available on the fatigue, irradiation creep, or stress relaxation of the candidate alloys under FED-A conditions. Experimental determination of these properties will be required to verify the first wall design.

6.2.3 Neutronic Performance

The impact of the first wall material and thickness on the neutron transmission to test zones outside the first wall is examined in this section. Type 316 stainless steel, Al 5083, and Cu AMAX-MZC are considered in the analysis; other materials were considered in Ref. 2. The analysis is based on determination of the performance of a tritium breeding blanket module. Lithium oxide material (Li_2O) is the tritium breeder with 316 SS the structural material. The reflector zone is composed of water and 316 SS, employed to reduce the neutron and energy leakage to the shielding zone and to serve as a coolant header for the blanket. Water is the coolant for the first wall and the tritium breeding module. The compositions and dimensions used in the analysis are listed in Table 6-5. For each first wall material, the thickness is varied while the module (the tritium breeding and reflector zone) is unchanged. The first wall model consists of three layers, as given in Table 6-5 and Sect. 6.4.2.1. The second layer is 1 cm thick, simulating the coolant (water) channels. The thicknesses of the other two layers, t_1 and t_2, are sized from simple thermal hydraulic considerations as follows:

$$t_1 = \alpha t_2 \ ,$$

$$t_1 + t_2 + 1 = t \ ,$$

Table 6-5. Parameters used for first wall neutron transparency analysis

Zone description	Zone thickness (cm)	Zone composition (percentage by volume)
First wall	t_1 (var)	100% first wall material
	1.0	75% H_2O, 25% first wall material
	t_2 (var)	100% first wall material
Tritium breeding zone	48	90% Li_2O (0.7 density factor), 5% 316 SS, 5% H_2O
Reflector	15	75% H_2O, 25% 316 SS

where t is the total first wall thickness in centimeters and α is 0.162, 0.072, and 0.22 for 316 SS, Al 5083, and Cu AMAX-MZC, respectively (see Ref. 3).

The calculations were performed with the ANISN discrete ordinates code 06-3 in cylindrical geometry with an S_8 angular quadrature set. A 67-multigroup cross-section library (46 neutrons, 21 photons) collapsed from the CTR library (DLC-41C)[4] with a P_3 approximation for the scattering cross section was used. The MACKLIB-IV library[5] was employed to calculate the nuclear response functions. The analysis in this section is focused on three areas: (1) neutron transparency from the first wall to the blanket, (2) tritium breeding ratio in a blanket module, and (3) energy deposition per fusion neutron.

The neutron transparency, or neutron current, through the first wall to blanket modules is shown in Fig. 6-2 as a function of first wall thickness for the three reference alloys. The Al 5083 first wall produces the highest neutron leakage to the blanket, reflecting the difference in the absorption cross sections. Type 316 stainless steel shows slightly more neutrons absorbed in the first wall than the copper alloy. This contradicts expectations based on the neutron absorption rate in each material. In fact, the neutron absorption rate in the copper first wall is higher than in 316 SS, but the neutron multiplication from (n,2n) reactions in the copper reverses the impact on the neutron leakage to the blanket. Also, the relative difference in the leakage rate for these two materials decreases as the first wall thickness increases, due to the diminishing effect of the Cu(n,2n) reaction rate. Figure 6-3 shows the neutron flux at the front surface of the breeding zone as a function of the first wall thickness for the three materials normalized to 1.3-MW/m^2 neutron wall loading.

Figure 6-4 shows the tritium breeding ratio as a function of the total first wall thickness for the three candidate materials. Also shown are the two components of the breeding, from ^{6}Li and ^{7}Li isotopes, for each candidate alloy. The Al 5083 first wall has the lowest impact on the tritium generation because aluminum has the smallest inelastic and absorption cross sections compared with 316 SS and Cu AMAX-MZC. The results indicate that about two-thirds of the loss in the tritium

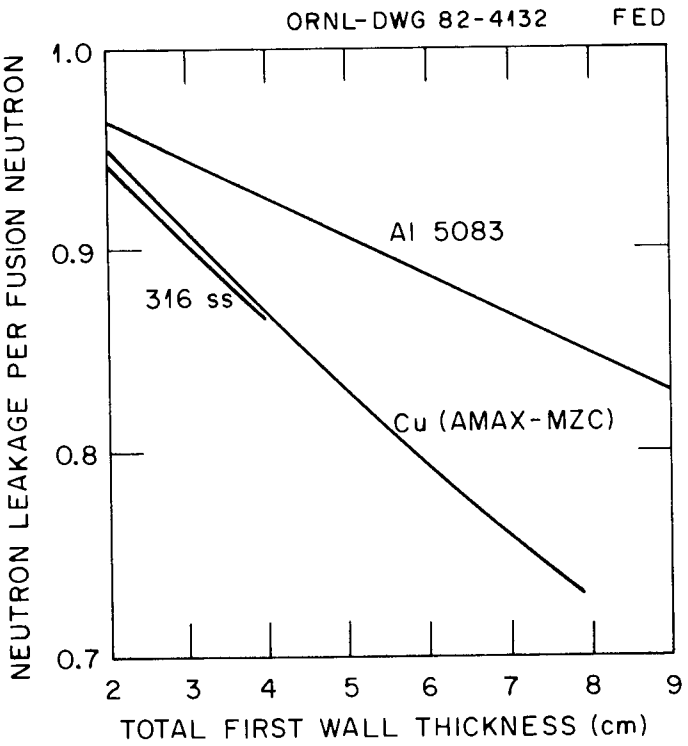

Fig. 6-2. Neutron transparency (neutron current) through the first wall to the blanket test modules as a function of the first wall thickness for different materials. The first wall thickness includes both metal structure and water coolant.

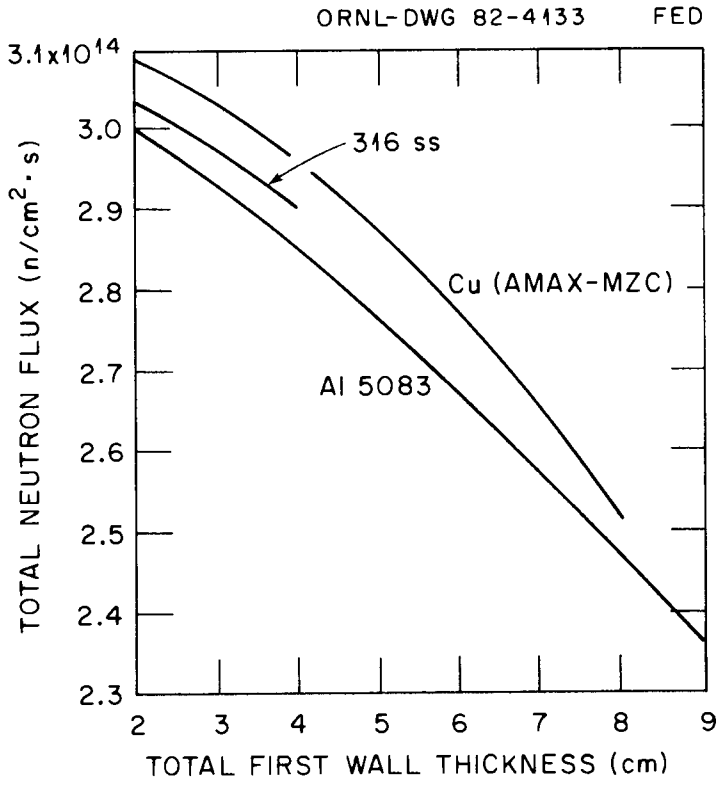

Fig. 6-3. Total neutron flux at the front surface of the blanket as a function of the first wall thickness for different materials normalized to 1.3-MW/m^2 neutron wall loading.

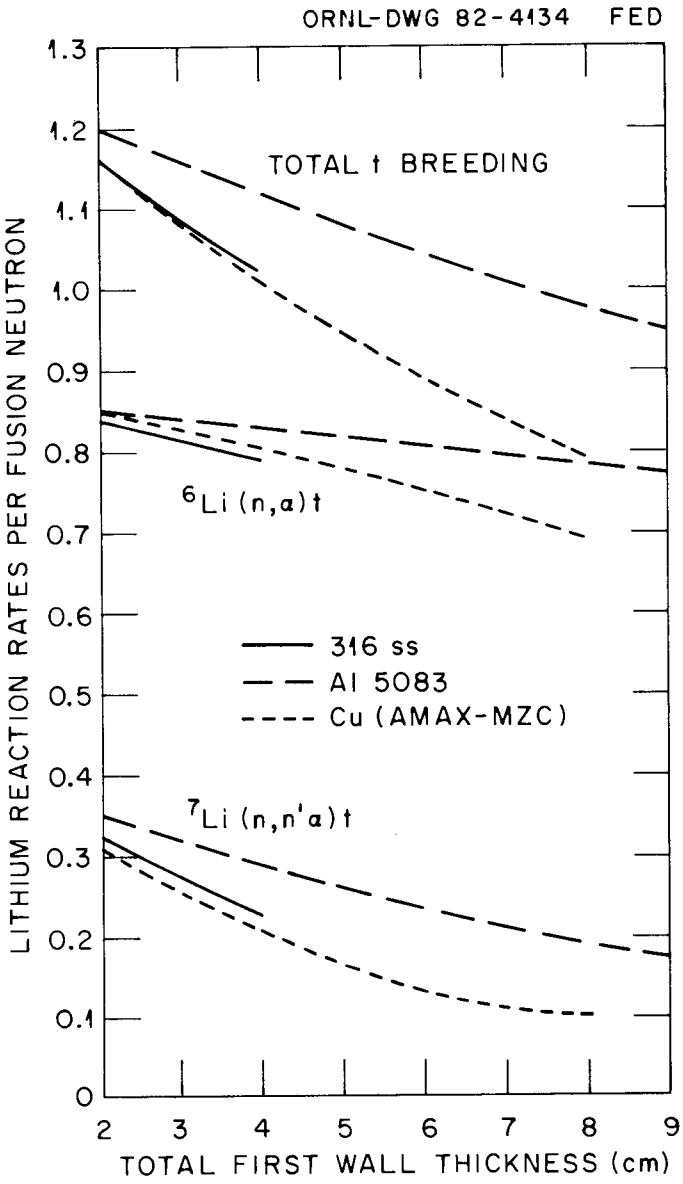

Fig. 6-4. Tritium breeding ratio for a full blanket as a function of the first wall thickness for three first wall materials. The total wall thickness includes both metal and water.

breeding ratio caused by increasing the first wall thickness is due to the reduction in the $^{7}Li(n,n'\alpha)t$ reaction rate.

The energy deposition per fusion neutron is given in Fig. 6-5 as a function of the first wall thickness for the candidate materials. The copper alloy first wall produces the highest energy multiplication of the three candidates. Figure 6-6 shows the percentage of the total power that is deposited in the first wall. The maximum power densities deposited in 2-cm first walls of 316 SS, aluminum alloy, and copper alloy are 11.9, 7.3, and 14.3 W/cm^3 per 1.0 MW/m^2 of neutron wall loading, respectively. The increase in the first wall thickness causes an increase in the maximum power density for 316 SS and the copper alloy. This results from the increase of neutron absorption in the energy range below 1 MeV. For the aluminum alloy the maximum power density is not sensitive to the first wall thickness, because the neutron absorption is quite small. A 10% increase in the maximum power density of the first wall occurs with a change in the first wall thickness from 2 to 4 cm for 316 SS or from 2 to 8 cm for Cu AMAX-MZC.

6.2.4 Materials Activation

The level of radioactivity produced by neutron captures in the first wall material impacts three areas of concern to fusion reactor operation: safety, maintenance, and radioactive waste (radwaste) management. The facility safety is affected through the level of decay heat (and thus the requirement for active cooling at shutdown) and through the inventory of activation products that could be released during an accident. The first wall material contribution to the radiation field of the shutdown reactor determines the level of personnel access for maintenance. The rate of decay of this activity determines the waiting time after shutdown before access and maintenance are possible. The activation level and decay characteristics over longer time periods also determine the radwaste management, including the requirements for long-term storage, possible recycle, and final disposal.

Activation calculations have not been run specifically for the continuous first wall of FED-A. However, general behavior can be

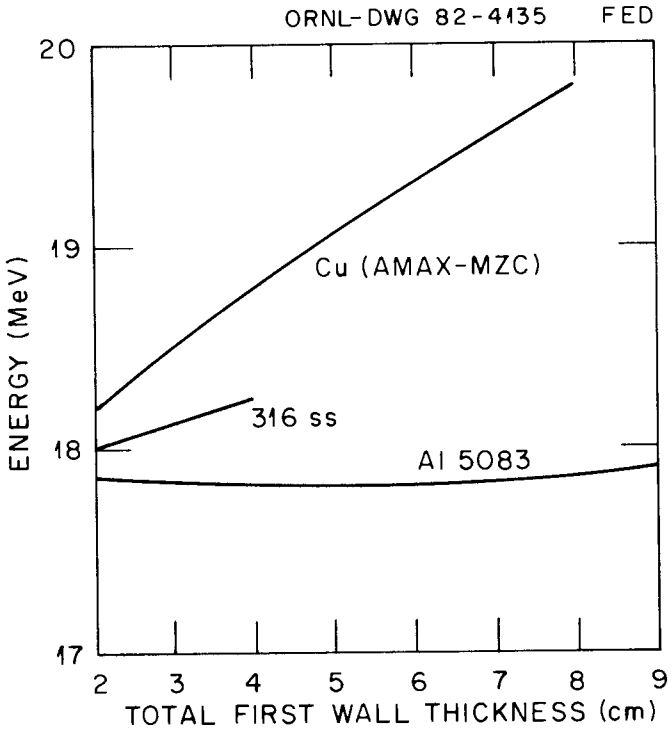

Fig. 6-5. First wall and blanket energy deposition per fusion neutron as a function of the first wall thickness and composition.

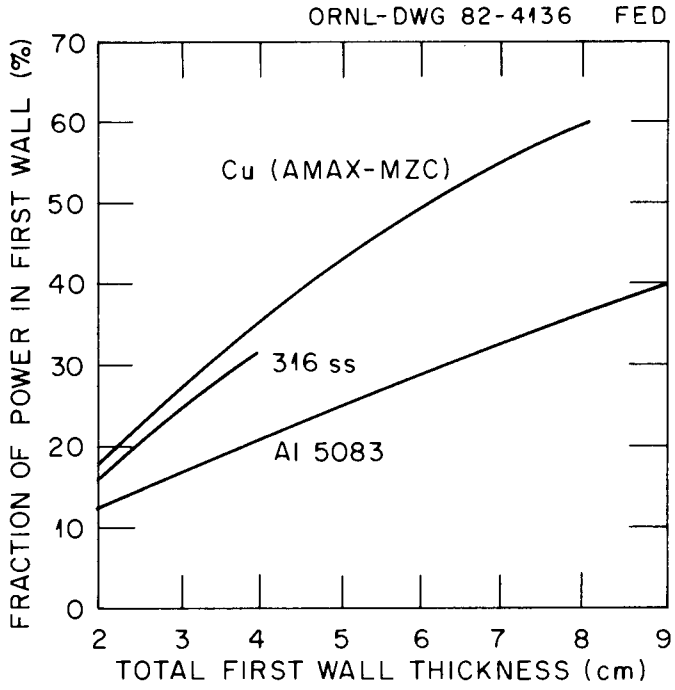

Fig. 6-6. Percentage of the total power deposited in the first wall as a function of wall thickness for the candidate alloys.

inferred from similar calculations for other fusion reactors, which are adequate to show the differences between the three alloys compared in this analysis.

The base elements in the three reference alloys, Fe, Al, and Cu, are activated to approximately equal levels by equal first wall exposures. The difference between the three elements, if measured about 1 h after shutdown, would be only on the order of 10%. Addition of the alloying elements, to form the reference materials, will change the activation level significantly only for the case of the nickel contained in 316 SS. Since the activation level of nickel is about an order of magnitude greater than that of iron, for equivalent reactor service times the 12% Ni in 316 SS will raise the activity level to about twice that of pure iron.

The decay of the shutdown activity level in the three alloys shows greater composition dependence than does the shutdown level. For pure aluminum, significant decay of activity occurs between 1 and 14 days after shutdown, with decay by a factor of 10^6 reached after 14 days. The activity of aluminum is essentially constant for longer times, dominated by the 7.3×10^5-year half-life of ^{26}Al. Iron decays to 10% of shutdown activity within a day of shutdown and remains at that level for 1 month. Significant further decay begins at about 6 months, with decay by 6 orders of magnitude achieved in 15 years and 12 orders of magnitude in just over 30 years. The decay of copper is the slowest of the three alloy base elements considered; decay to 10^{-6} of shutdown activity requires about 100 years.

Major changes in the decay characteristics can result from alloying these three elements. In Al 5083 the magnesium, with decay characteristics like iron, holds the activity level well above that of pure aluminum in the time period from 1 day to 20 years, with domination by the ^{26}Al achieved only for longer times. The magnesium and chromium in Al 5083 have no comparable effects. In 316 SS the nickel dominates decay in the period between 10 and 100 years, with decay characteristics like copper. For times longer than 100 years, the activity level is controlled by the 2.5% Mo in 316 SS; the dominant isotope is ^{93}Mo, with a half-life of 3.5×10^3 years. The decay characteristics of Cu AMAX-MZC

are not affected by the small additions of Cr, Zr, and Mg to the copper base of this alloy.

In summary, the activation levels and decay characteristics of the three reference alloys show no differences of overriding importance. At shutdown, the activity in 316 SS will be higher than in the other two alloys by about a factor of 2. The decay characteristics of Al 5083 will give it the lowest activity of the three in the period 1 week to 10 years, with the advantage (about a factor of 100) set by the manganese level in the alloy. For times beyond 100 years the copper alloy will have the lowest activity, as no longer half-life isotopes are produced in this alloy.

6.2.5 Tritium Inventory and Permeation

The material used for the first wall will control the inventory of tritium retained in the wall and the rate of tritium permeation and release to the coolant stream. The major mechanisms involved in the tritium movement through the metal wall are injection into the wall as energetic ions; diffusion in the wall material, driven by concentration and temperature gradients; recombination to molecules at the surface; and release from the surface. Exact calculations of these processes are complicated by lack of knowledge of the surface cleanliness conditions (e.g., oxide films on water-side surfaces), by internal traps in the metal (impurities, alloying elements, irradiation-produced defects), and by uncertainty in the operating conditions, especially the distribution of wall temperatures around the reactor.

Tritium inventory and permeation rates have been calculated for the stainless steel first wall of INTOR[6] based on a considerable body of experimental data. The same model has been used to calculate these quantities for the FED-A case, for stainless steel, copper, and aluminum first walls.[6] The calculation assumed clean surfaces, constant temperature distributions at all sections of the wall (determined by the coolant outlet temperature), and equivalent tritium trapping properties for all three alloys. Other parameters used in the calculations are given in Table 6-6 and in Ref. 6.

Table 6-6. Tritium inventory and permeation rate for candidate first wall materials[a]

Parameter	Units	Copper wall	Stainless steel wall	Aluminum wall
Tritium flux to wall	ion/cm^2·s	1.25×10^{16}	1.25×10^{16}	1.25×10^{16}
Wall area	m^2	225	225	225
Wall thickness	mm	5	5	5
Wall temperature				
Coolant side	°C	155	155	155
Plasma side[b]	°C	160	232	163
After 1-year continuous operation				
Permeation rate	g/s	0	3.9×10^{-9}[c]	0
Inventory	g	56	190	36
After 30-year continuous operation				
Permeation rate	g/s	1.5×10^{-7}[c]	6.8×10^{-7}	1.1×10^{-7}
Permeation rate	g/year	4.8	21	3.5
Inventory	g	250	360	180

[a] Calculations by M. I. Baskes (Sandia-Livermore) based on INTOR model in FED-INTOR/TRIT/81-01 and FED-INTOR/TRIT/82-4, Ref. 6.

[b] Temperature gradients for the same heat load on each material.

[c] Permeation has not reached steady state for these two cases.

As indicated in Table 6-6, after operation equivalent to 1 year there will be no permeation through the copper or aluminum wall into the coolant water. Permeation through the stainless steel wall will be at a very low rate. The contained tritium inventory after the 1-year operation will be 36 g for an aluminum wall, 56 g for a copper wall, or 190 g for the stainless steel wall. If the reactor operates for 30 years (equivalent full power operating time), permeation rates at the end of that time will be in the range 3 to 20 g/year, and the inventory will range from 180 to 360 g. The differences between materials are small, relative to the uncertainties in the assumptions made in the calculations.

The sensitivity of inventory and permeation rates to the parameters used in calculations has been discussed in the INTOR study[6,7] and is not repeated here. Within the level of uncertainty in the calculation, it must be concluded that the selection among the three candidate materials for the continuous first wall will not have a major impact on the tritium requirements or the tritium release rate of the FED-A.

6.3 MECHANICAL CRITERIA

The first wall for FED-A must satisfy its performance objectives in a severe environment. This environment is characterized by high temperatures, high neutron flux, and local regions of high physical sputtering. In addition to the objectives of a long disruption-induced current time constant via low first wall shell resistance (Sect. 6.1) and test module compatibility — high neutron transparency (Sect. 6.2), several mechanical design objectives should be considered. These include:

1. reactor-relevant heat removal — temperatures in the coolant sufficiently high to generate useful power,
2. high reliability,
3. reasonable fabrication and assembly requirements, and
4. high maintainbility.

The design criteria motivated by these objectives are proposed in this section.

6.3.1 Heat Removal and Utilization

For the first wall to be reactor-relevant, it must operate at temperatures corresponding to coolant temperatures that ensure the generation of useful power. For a steam cycle to be effective, the coolant outlet temperatures should be $\gtrsim$300°C. The capability to operate at temperatures significantly above 300°C is assumed here.

6.3.2 Reliability

The reliability of a system is generally related to the number of functions it performs. The lower the number of functions, the higher the potential reliability. The first wall for FED-A snould perform only those functions that are either unavoidable because of its location or desirable by virtue of the overall FED-A objectives, that is, low disruption probability and effective disruption mitigation. The vacuum boundary is assumed to be removed from the conducting first wall location.

6.3.3 Maintainability

The principal concern for maintainability is the ability to readily repair damage to the first wall. We assume that the first wall will be assembled into a continuous torus from sectors that can be removed between outer legs of the adjacent TF coils. Major damage will then require replacement of a first wall sector. Minor damage will require access to the internal surface of each sector.

In order to ensure replacement within a reasonable period of time, it is required that there be no fluid interface between adjacent first wall sectors. The sector joints will be entirely mechanical, and close attention will be given to the speed of making and breaking a joint with remote techniques.

Access will be provided to the inner surface of each sector without disassembly of either the joints or the principal sector support system. If coolant lines must be disconnected to gain access, close attention

will be given to the design of the disconnects to ensure compatibility with remote handling tools.

6.3.4 Fabrication and Assembly

The shell segmentation shall be such that all sectors of the shell are similar and can be fabricated on one set of tooling fixtures. The surface of the sector joints shall be machined to smoothness and planar requirements adequate to ensure that the electrical resistance of each joint is <1 μΩ. Each sector will contain provisions for tooling pads machined on the outboard surface of the sectors for alignment during assembly employing optical survey equipment.

6.4 CONDUCTING FIRST WALL DESIGN OPTIONS

This section presents an evaluation of factors important in selecting the conducting first wall configuration and design features. As a result of this process, the following features were identified as baseline characteristics:

- a common vacuum boundary between the TF magnet system and the torus, located at the outer surface of the bulk shield and separate from the conducting first wall,
- a continuous conducting first wall made from Cu AMAX-MZC and using water as a coolant, and
- a mechanical joint attachment of the first wall sectors.

6.4.1 Design Selection

After summarizing the selection of a continuous first wall design concept we discuss the comparisons made to suggest the use of Cu AMAX-MZC with water as coolant (Sect. 6.4.2) and the considerations that lead to the choice of a mechanical joint attachment of the first wall sectors (Sect. 6.4.3). Structural design considerations are reviewed in Sect. 6.4.4.

6.4.1.1 Domain in design parameters

Based on the preceding considerations, a thick first wall is desirable to establish a high conductivity surface near the plasma. However, a thick wall has an undesirable impact on the transmission of neutrons through the first wall to the testing and tritium breeding modules. Possible trade-offs for these two performance parameters are illustrated qualitatively in Fig. 6-7, showing tritium breeding ratio performance as a function of toroidal eddy current decay time for different material systems. Three limits, shown in this figure, can be determined for each wall material based on thermal and structural performance requirements. Upper limits on wall thickness (and thus maximum toroidal eddy current decay time) are established based on maximum allowable temperatures and thermal stresses. A lower limit on the toroidal eddy current decay time results from the requirement to inhibit melting of the first wall during plasma disruptions. For toroidal eddy current decay times lower than this limit, the energy deposited during the current quench phase of a plasma disruption causes melting because there is not enough time to conduct the heat away from the heated surface.

Design criteria assumed for FED-A first wall concepts, as suggested by the discussion in the preceding sections, are listed in Table 6-7. The toroidal eddy current time $L/R = 0.5$ s for the conducting first wall and a calculated tritium breeding ratio of >1.2 are considered to be desirable guidelines. The maximum temperature and temperature difference for each of the first wall material candidates (stainless steel, aluminum, and copper) are required to ensure adequate thermal and structural performance.

6.4.1.2 Selection process

The general approach for the selection of the first wall concept is illustrated in Fig. 6-8. For convenience in referencing this chart, the design features in the far right column are numbered from 1 to 9 starting at the top. This figure was constructed as a systematic approach to

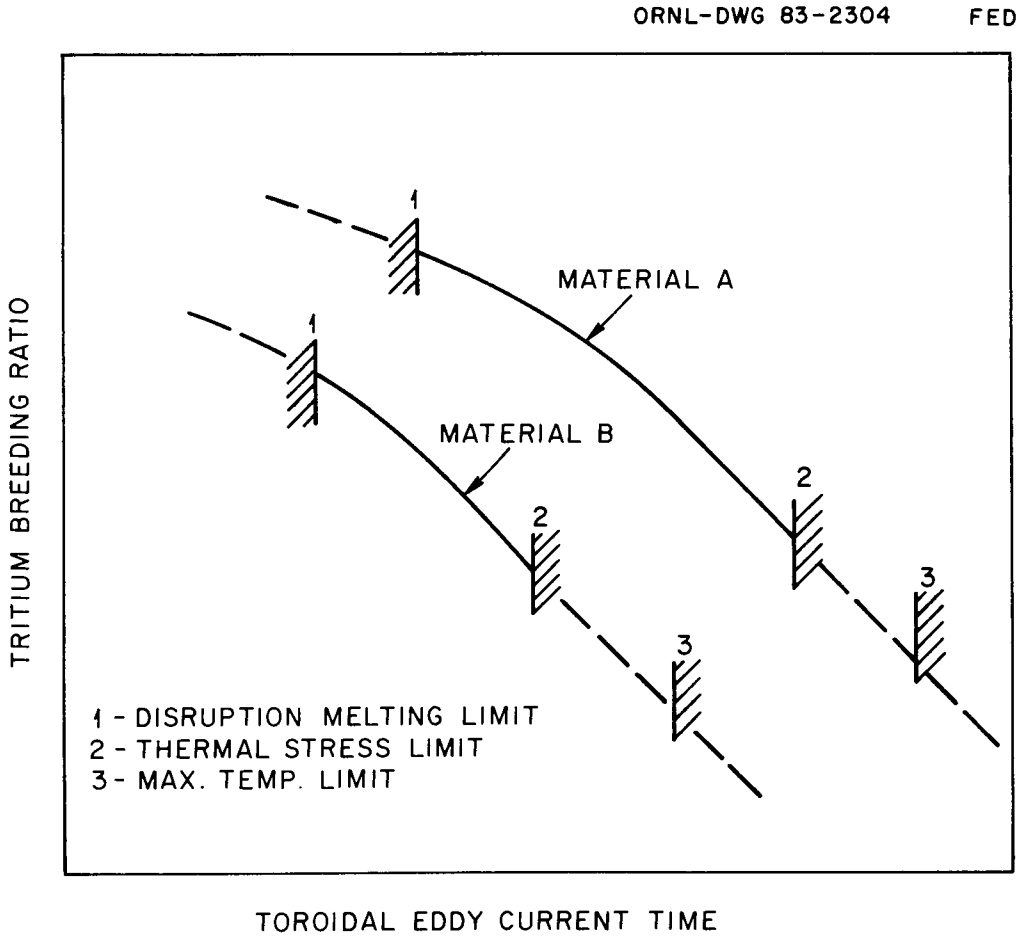

Fig. 6-7. Illustration of first wall performance domain with mechanical limitations.

Table 6-7. Design criteria assumed for FED-A first wall design

Parameter	Material	Condition
Toroidal eddy current time L/R of conducting first wall	NA[a]	∿0.5 s
Tritium breeding ratio	NA	⩾1.2
Maximum first wall temperature	316 SS	400°C
	Al 5083	200°C
	Cu AMAX-MZC	350°C
Maximum temperature difference from heated surface to cooled surface (required because of thermal stress limit), ΔT	316 SS	140°C
	Al 5083	75°C
	Cu AMAX-MZC	100°C

[a]Not applicable.

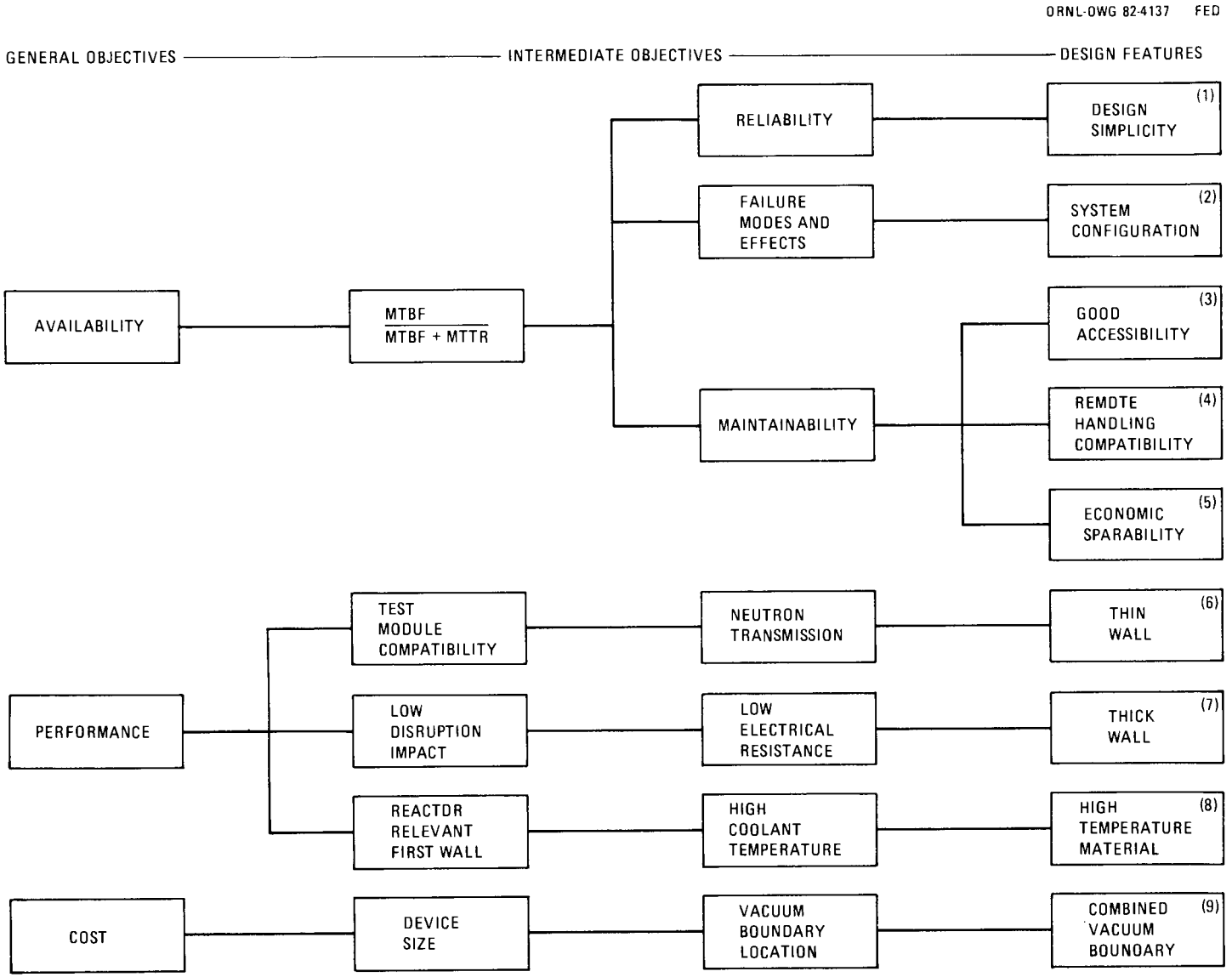

Fig. 6-8. Design selection process for FED-A first wall.

identifying and structuring design trade-offs. For instance, availability is achieved by minimizing the failure frequency of a component and the downtime required to repair a failure. In the design process, however, we seldom achieve high reliability without reducing maintainability. A case in point is modularization to achieve low replacement time, which often introduces more disconnects (which are subject to failure) than if the component were fully integrated in a permanent way. Hence, the question always persists: "Should there be modularization, and if so, at what level — subsystem, assembly, or component?"

The qualitative nature of the trade-offs suggested by this chart is the subject of the following discussion. Most of this discussion addresses features of the first wall. However, because of the impact of first wall design decisions on the rest of the torus, there is also some reference to torus features.

For the first feature of the first wall, design simplicity, the trade-off is identified as a study of the effect on reliability of removing the vacuum boundary from the first wall and moving it outward to the vicinity of the outer shield surface.

The second feature, system configuration, refers to the failure modes of the first wall and their effect. The least damaging failure mode with a loss of coolant applies to the case in which the first wall does not function as a vacuum boundary. In the case of water coolant, a significant leak will lead to loss of plasma confinement. In addition to the need to repair the first wall, decontamination will be required to eliminate the oxygen from the walls. No hazards are expected since the volume of water lost is expected to be small.

In the case of the helium coolant option, the coolant pressures are much higher than for water and coolant loss due to wall failure will be accompanied by a much higher energy dissipation. This will more likely be in the form of a major rupture, possibly accompanied by fragmentation. However, for pressures less than 1000 psi this failure mode is not considered a major device problem.

Good accessibility to the first wall (feature 3) is coupled with remote handling requirements (feature 4). Generally, they work in the

same direction. A first wall that can be removed separately from the shield will result in a much better spare parts cost situation (feature 5). This is because no shield spares are required while the first wall is being replaced.

A thin wall (feature 6) is required to permit high energy (14-MeV) neutron transmission. However, the objective of lower electrical resistance pushes in the direction of a thick wall (feature 7).

A thick wall, on the other hand, is limited by thermal stress conditions and material properties plus design complexity (e.g., multi-layered coolant passage geometry). Therefore, high temperature materials are needed to make the power production capability more efficient (feature 8).

Considerations of the location of vacuum boundary recognize the potential cost savings in reduced device size. These savings may be realized in combining the torus vacuum boundary with the TF coil cryostat (feature 9).

6.4.1.3 Choice of continuous first wall features

The design features examined following the selection process are illustrated in Fig. 6-9. They involve five levels of design options: the location of the vacuum boundary, the configuration of the first wall, the conducting material, the first wall coolant, and the concept of assembly.

The selected features are indicated in the figure by checkmarks and are discussed in the subsequent sections. They are:

- vacuum boundary located at the outer shield surface and common with the magnet system cryostat,
- first wall sectors assembled into a continuous shell,
- first wall using high conductivity copper alloy,
- water coolant, and
- bolted shell sectors.

The rationale for selecting these features can be summarized as follows. The outer surface of the shield was chosen as the vacuum boundary instead of the first wall for one principal reason. It separates

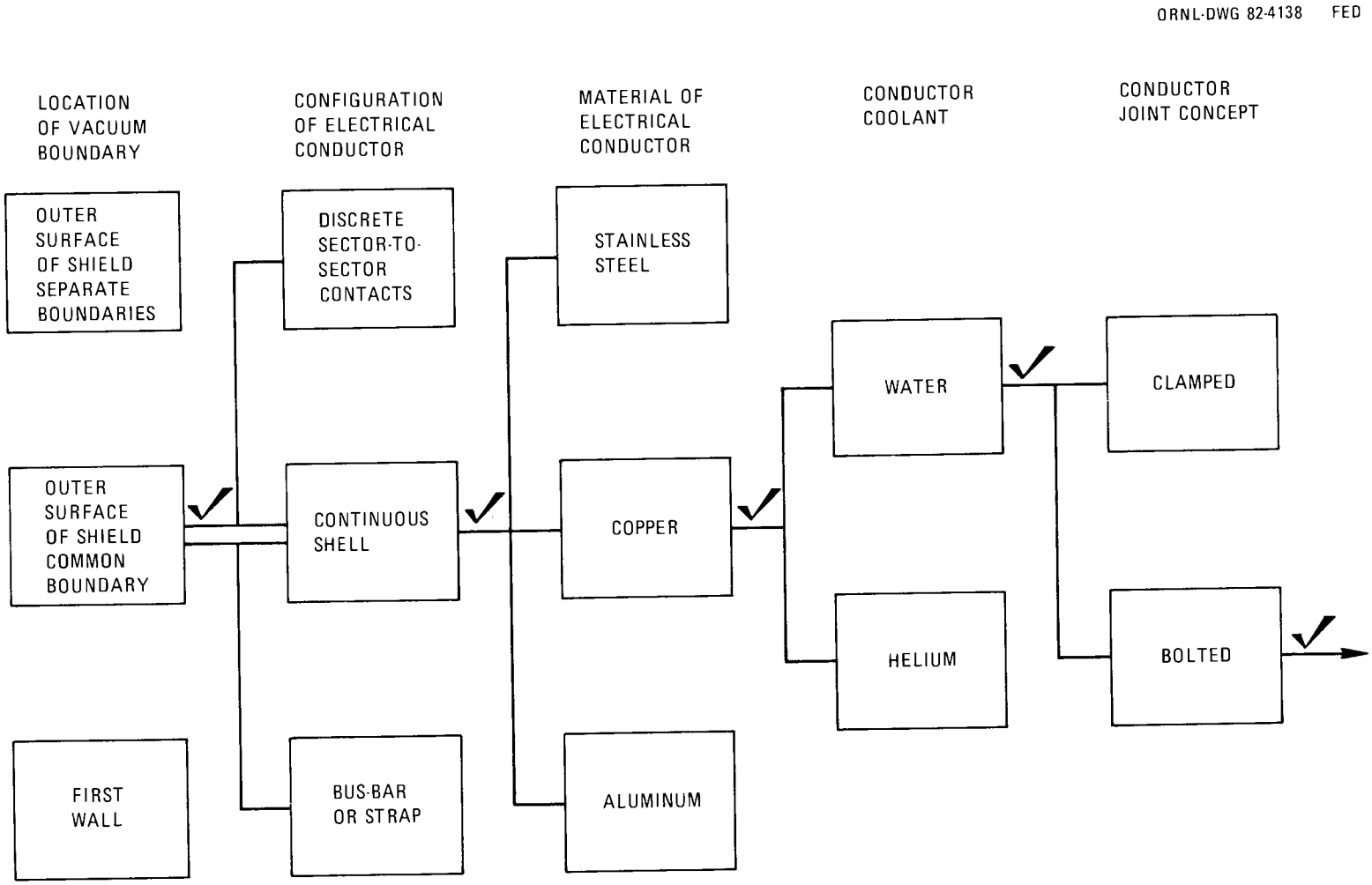

Fig. 6-9. Conducting first wall design options.

the function of providing vacuum integrity from the first wall, thereby making both the first wall and the vacuum boundary more reliable. The common vacuum boundary for the torus and the magnet cryostat was selected over separate vacuum boundaries because of the impact on device size. Other studies[8,9] have shown that employing a common boundary, especially in the region of the vertical inboard wall, may save as much as 15 cm in major radius. This reduction in overall device size may result in cost reductions of $50-80 million.

The continuous shell conductor concept was chosen rather than the discrete sector-to-sector contact because the shell has a much higher potential for achieving a long eddy current time than does the discrete contact type, which has limited contact area. It was chosen over the passive bus-bar concept because the remote installation techniques are perceived to be simpler and more reliable. In addition, achieving passive cooling in the bus-bar significantly limits its conductivity because of maximum material thickness limitations.

The choice of material for the conductor is based on two factors: the ability to satisfy the time constant requirement of about 0.5 s and the ability to accept a coolant temperature of 320°C for water. Stainless steel could not satisfy the time constant requirement of about 0.5 s; the maximum time constant for reasonable shell thickness is 0.05 s. Aluminum cannot be operated at temperatures above 200°C, so it is not an appropriate material for generating useful power with the first wall heat.

Water was chosen for the conducting shell coolant. For a copper shell, the calculated tritium breeding ratio is 1.21, with a toroidal eddy current decay time of about 0.55 s. It can be operated to produce useful power with a water coolant outlet temperature of 320°C. If helium is used its outlet temperature should be $\sim$600°C, which exceeds the copper temperature limit. A detailed comparison among the material and coolant candidates is given in Sect. 6.4.2.

A simple bolted technique rather than clamping was selected for joining the sectors. Though the clamping technique appears to permit easier maintenance procedures, relatively large thermal expansions in the clamping strap lead to uncertainties in joint face pressures at high

temperatures. The strap technique will be retained as a backup design approach. A detailed discussion of these mechanical features is given in Sects. 6.4.3 and 6.4.4.

6.4.2 Material and Coolant Selection

The three structural materials considered for the continuous first wall are Al 5083, Cu AMAX-MZC, and 316 SS. The properties used for thermal and structural analyses are listed in Table 6-8. Given the mechanical features of the continuous first wall, it becomes possible to compare in detail the performances of the candidate materials and coolants. These comparisons include electromagnetic and thermodynamic performances and disruption damage. These, coupled with the neutronic performance discussed in Sect. 6.2.3, will allow for a clear-cut selection of the first wall material and coolant.

6.4.2.1 Electromagnetic performance

The toroidal eddy current decay time L/R of the first wall was identified as a key design parameter for the FED-A first wall. If a high enough toroidal eddy current time (low resistance) can be achieved, it is expected that the damage caused by disruptions (Sect. 6.4.2.3) as well as the likelihood of disruptions (Sect. 4.2) can be reduced. The design guideline of toroidal eddy current time is about 0.5 s and is given in Table 6-2.

The toroidal electrical resistance (R_T) of the continuous first wall for the three candidate materials is shown in Fig. 6-10 as a function of the overall wall thickness. The maximum allowable wall thicknesses leading to the minimum resistances are indicated in this figure. These maximum thicknesses are based on thermal and structural performance requirements for a continuous first wall with a single row of coolant passages (discussed in Sect. 6.4.2.2). The resistances shown in Fig. 6-10 include the contributions from contact resistance at the interface between shell segments. A minimum contact pressure of 0.7 MPa (100 psi) is assumed between adjacent first wall sectors (Sect. 6.4.3.6).

Table 6-8. Material properties for alloys considered for conducting first wall

	316 SS (250°C)[a]	Al 5083 (100°C)[a]	Cu AMAX-MZC (200°C)[a]
Density (mg/m^3)	7.9	2.7	8.9
Thermal conductivity (W/m·K)	17.8	170	310
Specific heat (J/kg·K)	534	900	400
Thermal expansion coefficient (K^{-1})	17×10^{-6}	24×10^{-6}	18×10^{-6}
Electrical resistivity (μΩ·cm)	90	8.3	3.5
Elastic modulus (GPa)	190	69	138
Yield strength (MPa)	140	130	97 (360)[b]
Ultimate strength (MPa)	430	270	200 (400)[b]
Allowable design stress (MPa)	93	87	55

[a]For fully annealed condition.

[b]For worked and aged material.

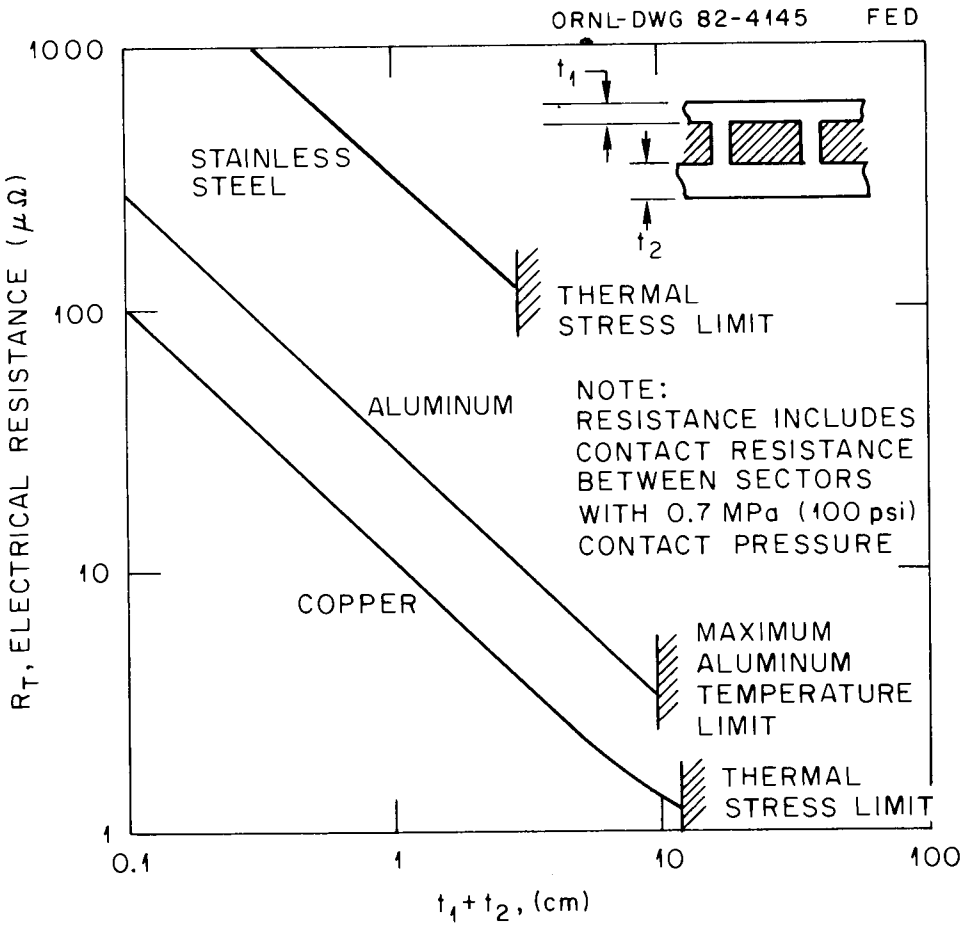

Fig. 6-10. Electrical resistance of FED-A first wall candidate materials.

A continuous first wall constructed of 316 SS has a minimum electrical resistance (R) of 120 μΩ limited by thermal stress considerations. The inductance (L) of the continuous first wall was calculated to be about 6 μH. Therefore, the maximum toroidal eddy current time L/R of a stainless steel wall is 50 ms. Values of L/R = 1.7 s with aluminum and 5.2 s with copper are possible.

6.4.2.2 Thermal-hydraulic performance

The thermodynamic performance of first walls was evaluated for the three structural materials (stainless steel, copper, and aluminum) and two coolants (water and helium gas). The surface heat flux and neutron wall loading used for these analyses were 0.25 MW/m^2 and 1.0 MW/m^2, respectively (Table 5-15).

Structural material temperatures. Maximum temperatures and temperature differences through the first wall surfaces are presented in Figs. 6-11, 6-12, and 6-13 for the three structural materials. (The first wall configurations considered for these studies are also described in Sect. 6.4.4.4 as having a single layer of coolant passages that run toroidally within each sector.) Nominal water coolant flow conditions of a bulk outlet temperature of about 100°C, a coolant passage depth of 0.5 cm, and a convection heat transfer coefficient of 1.0 $W/cm^2 \cdot K$ were assumed for this structural material evaluation. Based on the temperature limits listed in Table 6-7 (Sect. 6.4.1), maximum allowable skin thicknesses are identified in each of the figures and are listed in Table 6-9.

The stainless steel can be adequately cooled if the surface on the plasma side t_1 is less than 0.8 cm thick, while the surface away from the plasma t_2 (backside), which experiences neutronic heating only, can be as thick as 2.1 cm. Therefore, the total thickness of the stainless steel first wall is 3.4 cm (for a 0.5-cm-thick coolant passage). The maximum copper and aluminum first wall thicknesses are not the design thicknesses, but rather the upper limits considered in trade-off studies of first wall electrical resistance and neutron transmission to test modules.

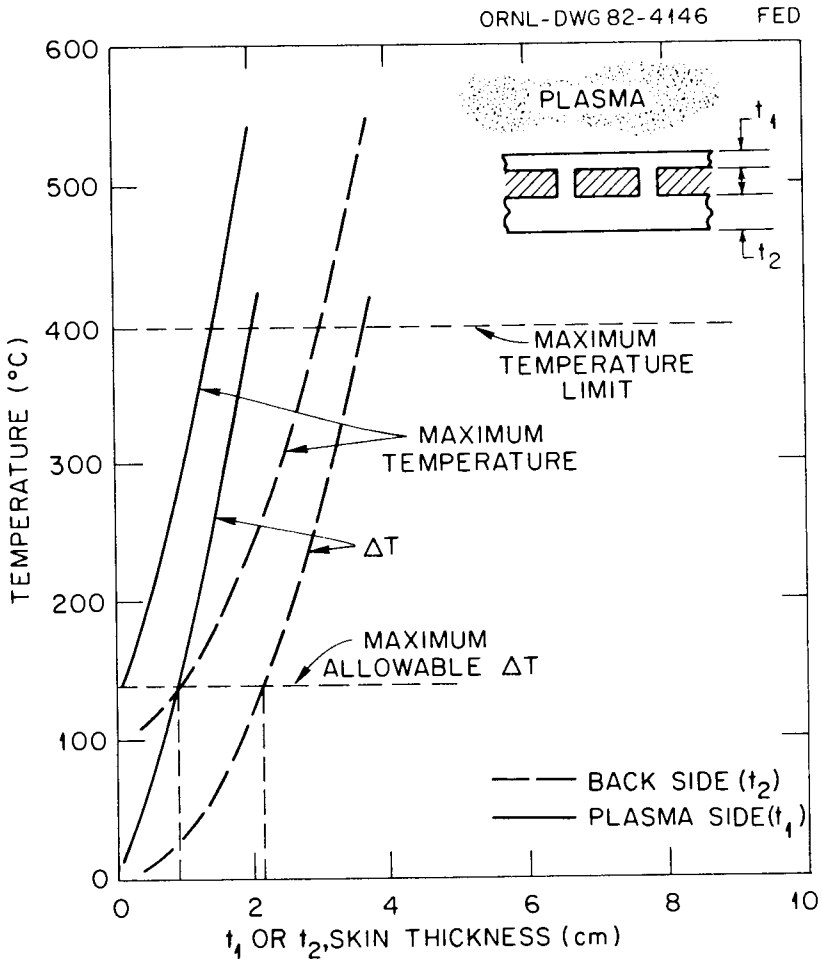

Fig. 6-11. Upper limits on stainless steel skin thickness.

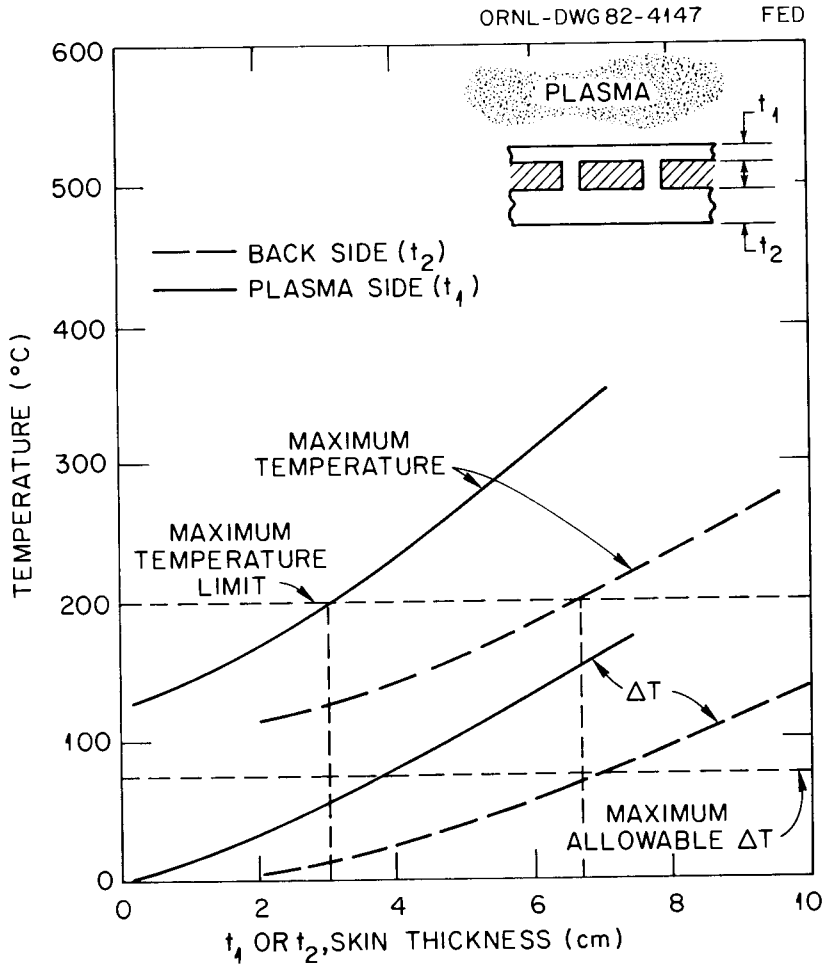

Fig. 6-12. Upper limits on aluminum skin thickness.

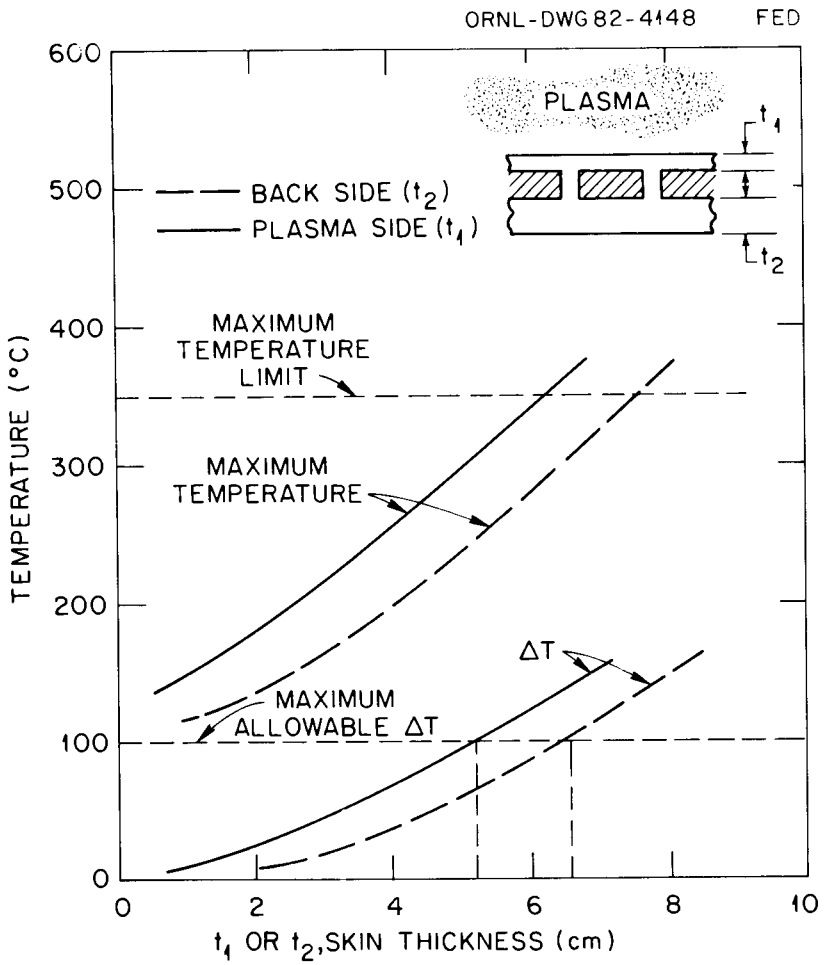

Fig. 6-13. Upper limits on copper skin thickness.

Table 6-9. Upper thickness limits for FED-A first wall based on thermal-hydraulic considerations

Material	Maximum temperature limit (C°)	Maximum ΔT through skin (C°)	Maximum t_1 (cm)	Maximum t_2 (cm)	Maximum wall thickness[a] (cm)
Stainless steel	400	140	0.8	2.1	3.4
Aluminum	200	75	3.0	6.7	10.2
Copper	350	100	5.2	6.6	12.3

[a]Assumes 0.5-cm-thick water coolant passage.

Water coolant. Water coolant flow performance was evaluated for each structural material. The maximum allowable skin thicknesses for stainless steel, t_1 = 0.8 cm and t_2 = 2.1 cm, were used for all three materials. Reference water coolant flow parameters are listed in Table 6-10.

To inhibit subcooled boiling of the water throughout the coolant passages, the maximum temperatures at the interface between the wall and coolant must remain below the saturation temperature at the outlet pressure. For these analyses, a margin of 10°C was provided between the maximum water temperature and the saturation temperature at the calculated outlet pressure. The reference water inlet temperature and pressure are 60°C and 0.7 MPa (100 psi), respectively.

Figure 6-14 shows the sensitivity of the water pumping power requirement to changes in the coolant passage size for each structural material. A large coolant passage size is desirable from a pumping power viewpoint. However, a small size is desirable from a neutron transmission viewpoint. The reference depth of 0.5 cm represents a reasonable compromise between these conflicting performance parameters. The 14-MeV neutron flux attenuation due to 0.5 cm of water is only 7%. For the baseline design of a 1.5-cm-thick copper wall, the reduction in the tritium breeding ratio caused by the presence of the 0.5-cm-thick water coolant passage is only 0.02 out of a total tritium breeding ratio of about 1.2. The relatively low pumping powers for the 0.5-cm-thick passages are 1.3 kW for aluminum, 3.0 kW for stainless steel, and 4.8 kW for copper.

Helium coolant. The thermal-hydraulic performance of helium coolant with stainless steel, aluminum, and copper first walls was investigated. Skin thicknesses of t_1 = 0.8 cm and t_2 = 2.1 cm were assumed, as with the water coolant performance evaluation. The helium inlet temperature was assumed to be 60°C. Maximum structural temperatures were constrained to be 400°C for stainless steel, 200°C for aluminum, and 350°C for copper.

The effect of coolant passage size on helium pumping power is shown in Figs. 6-15, 6-16, and 6-17 for pressures ranging from 1.0 MPa (150 psi) to 5.0 MPa (750 psi). At a helium coolant system outlet pressure of 5.0 MPa and a coolant passage depth of 2.0 cm, the pumping power is

Table 6-10. Water coolant flow performance parameters (0.5-cm-thick water coolant passage)

Flow condition	Stainless steel	Aluminum	Copper
Inlet temperature (°C)	60	60	60
Inlet pressure [kPa (psi)]	690 (100)	690 (100)	690 (100)
Outlet pressure (°C)	121	118	123
Pressure drop [kPa (psi)]	6.4 (0.93)	3.8 (0.55)	8.6 (1.2)
Mass flow (kg/s)	450	340	530
Pumping power (kW)	3.0	1.3	4.8

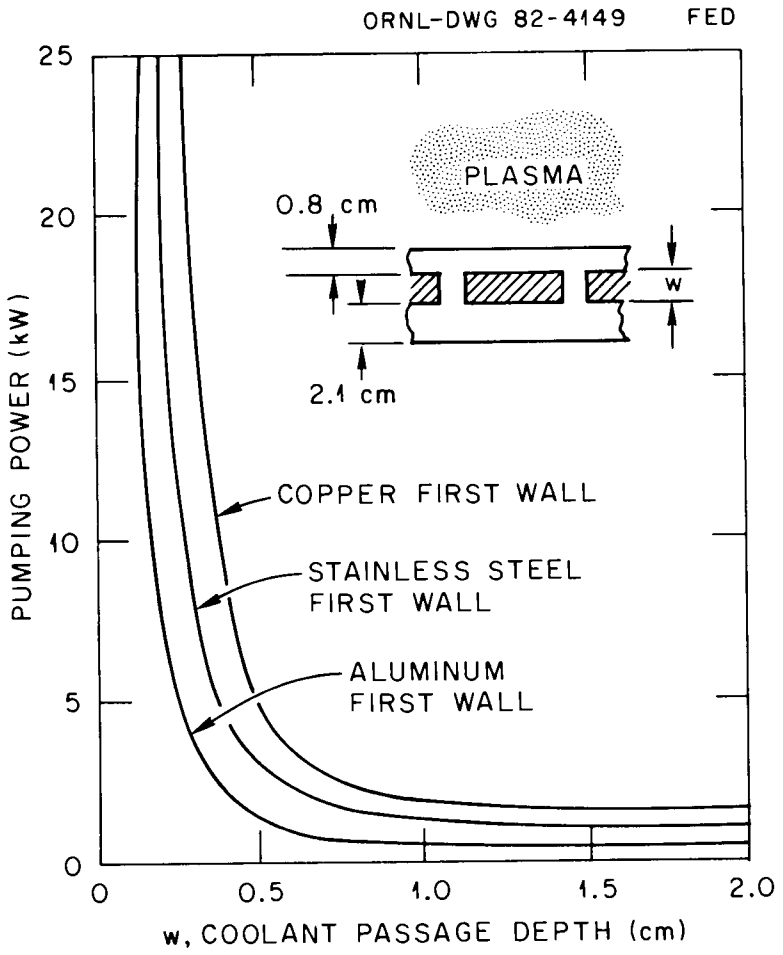

Fig. 6-14. Effect of water coolant passage size on pumping power.

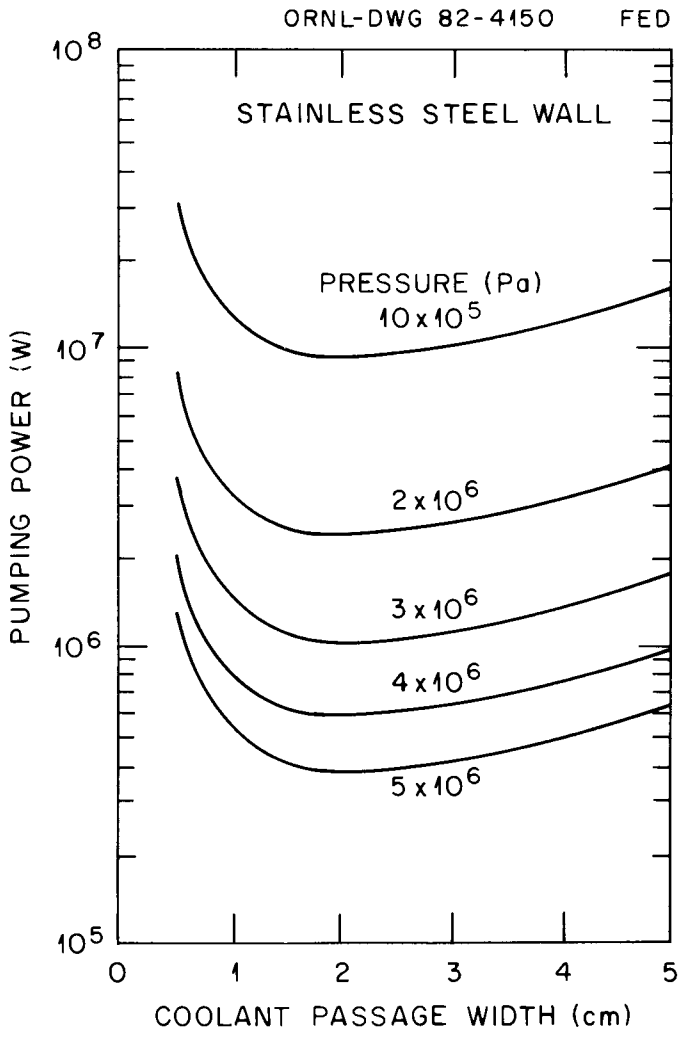

Fig. 6-15. Helium pumping power requirements for cooling a stainless steel first wall.

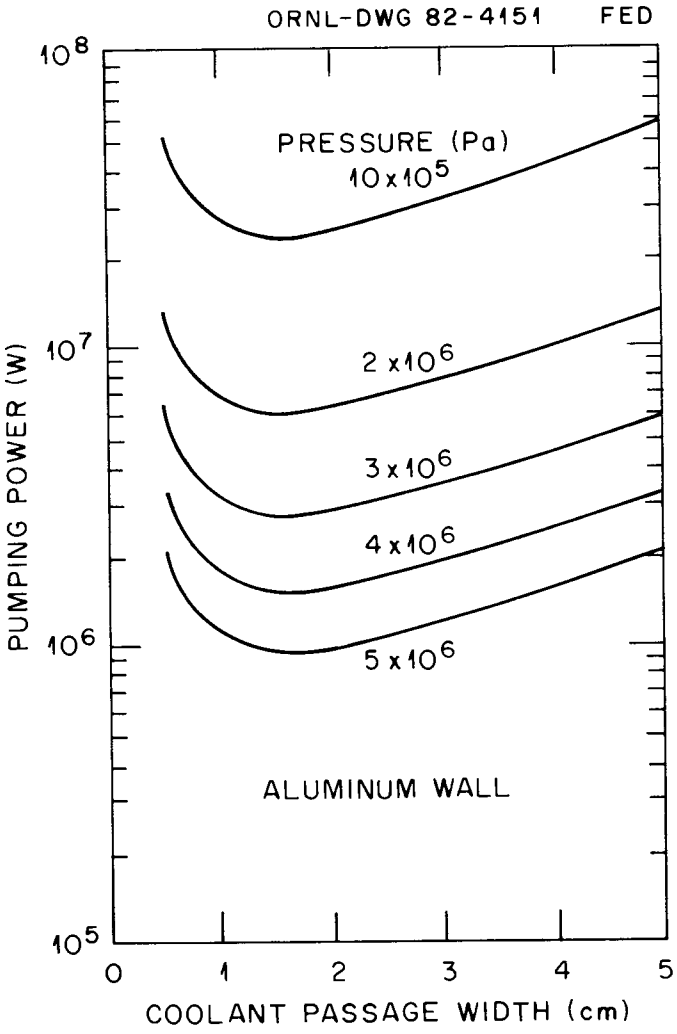

Fig. 6-16. Helium pumping power requirements for cooling an aluminum first wall.

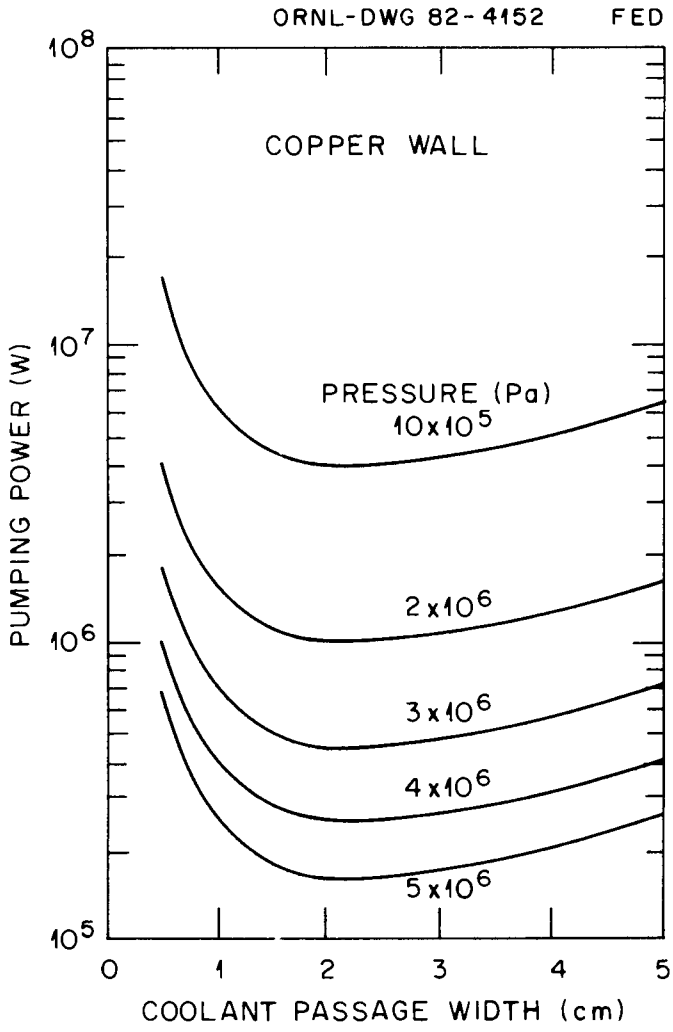

Fig. 6-17. Helium pumping power requirements for cooling a copper first wall.

380 kW for a stainless steel first wall, 1000 kW for an aluminum first wall, and 160 kW for a copper first wall. These pumping powers are much higher than the water coolant system pumping powers of 3.0 kW for stainless steel, 1.3 kW for aluminum, and 4.8 kW for copper. However, all of these pumping powers are insignificant compared to the overall reactor power requirements.

Reference helium coolant flow system parameters are listed in Table 6-11.

Considerations for power production. To investigate the reactor relevance of the FED-A continuous first wall design concept, the impact of operating with reactorlike coolant flow conditions on the first wall thermal-hydraulic performance was examined.

Water coolant flow conditions similar to those used for the STARFIRE commercial reactor design study[10] were assumed. The inlet and outlet water temperatures were 280°C and 320°C, respectively. The inlet pressure was fixed at 15.2 MPa (2200 psi). For these coolant flow conditions and a 400°C limit on the stainless steel temperatures the maximum stainless steel skin thicknesses are t_1 = 0.4 cm and t_2 = 1.5 cm. The resulting minimum electrical resistance and maximum toroidal eddy current times for a stainless steel continuous first wall are 180 μΩ and 0.03 s (120 μΩ and 0.05 s for low temperature coolant), respectively.

For a copper first wall with a maximum temperature of 350°C, the maximum skin thicknesses are t_1 = 0.9 cm and t_2 = 2.3 cm. This corresponds to a minimum electrical resistance of 3.5 μΩ, and a maximum toroidal eddy current time of about 1 s can be obtained with a copper wall, even for reactorlike water coolant flow conditions.

The performance parameters for the high temperature water coolant flow system are listed in Table 6-12. Coolant temperatures of about 600°C are required for feasible power-producing cycles with helium coolant. This coolant temperature is not compatible with a copper wall, which has an upper temperature limit of 350°C. Therefore, water was selected as the first wall coolant because of its relevance to power-producing conditions (outlet temperature of 320°C) in a copper wall.

Table 6-11. Helium coolant flow system performance parameters

Flow conditions	Stainless steel	Aluminum	Copper
Inlet temperature (°C)	60	60	60
Inlet pressure [MPa (psi)]	5.0 (750)	5.0 (750)	5.0 (750)
Outlet temperature (°C)	126	91	150
Pressure drop [kPa (psi)]	7.0 (1.0)	13 (1.8)	5.0 (0.8)
Coolant passage width (cm)	2.0	2.0	2.0
Mass flow rate (kg/s)	340	500	240
Pumping power (kW)	380	1000	160

Table 6-12. Thermal-hydraulic performance of power-producing copper wall

Coolant	Water
Inlet temperature (°C)	280
Outlet temperature (°C)	320
Inlet pressure [MPa (psi)]	15.2 (2200)
Pressure drop [MPa (psi)]	0.024 (3.5)
Mass flow rate (kg/s)	650
Pumping power (kW)	22

Also, the pumping power required with water is lower than that required with helium.

Thermal performance of reference design. Based on the thermal-hydraulic performance studies discussed here, a 1.5-cm-thick copper first wall that includes a 0.5-cm-thick water coolant passage appears as a preferred candidate for the reference design. The temperature profile through the wall is shown in Fig. 6-18. The maximum copper temperature is only 160°C, which is well below its 350°C upper limit. Water coolant flow performance parameters for the baseline design are shown in Table 6-13. The pumping power is only 1.6 kW.

6.4.2.3 Disruption damage

Melting or vaporization of the first wall during plasma disruption remains a major challenge in tokamak reactor concepts. The nominal disruption heating parameters are listed in Table 6-14. The scenario for the FED Baseline disruption heating (documented in Ref. 8) was assumed, with the energies scaled to correspond to FED-A parameters. During the 2-ms thermal quench phase, 80% of the plasma thermal energy (56 MJ) is deposited on first wall and limiter surfaces. The limiter receives 75% of this energy through plasma ion impingement, and the first wall receives 25% of the energy through radiation.

The energy deposited during the current quench consists of 17 MJ of plasma thermal energy, including 3 MJ of magnetic energy transferred to plasma thermal energy (Ref. 11). This energy is assumed to be deposited on 20% of the inboard, top, or bottom surface area in a nonuniform heating distribution with a peak-to-average heating ratio of 2. The current quench duration was treated as a variable since it is a function of the toroidal eddy current time of the continuous first wall.

For long current quench durations (long toroidal eddy current times) the first wall will not experience any melting or vaporization. The minimum current quench duration that results in no first wall melting was determined for each of the three structural materials. It is found that for current quench durations longer than 9 ms for copper, 27 ms for stainless steel, and 60 ms for aluminum, no melting will

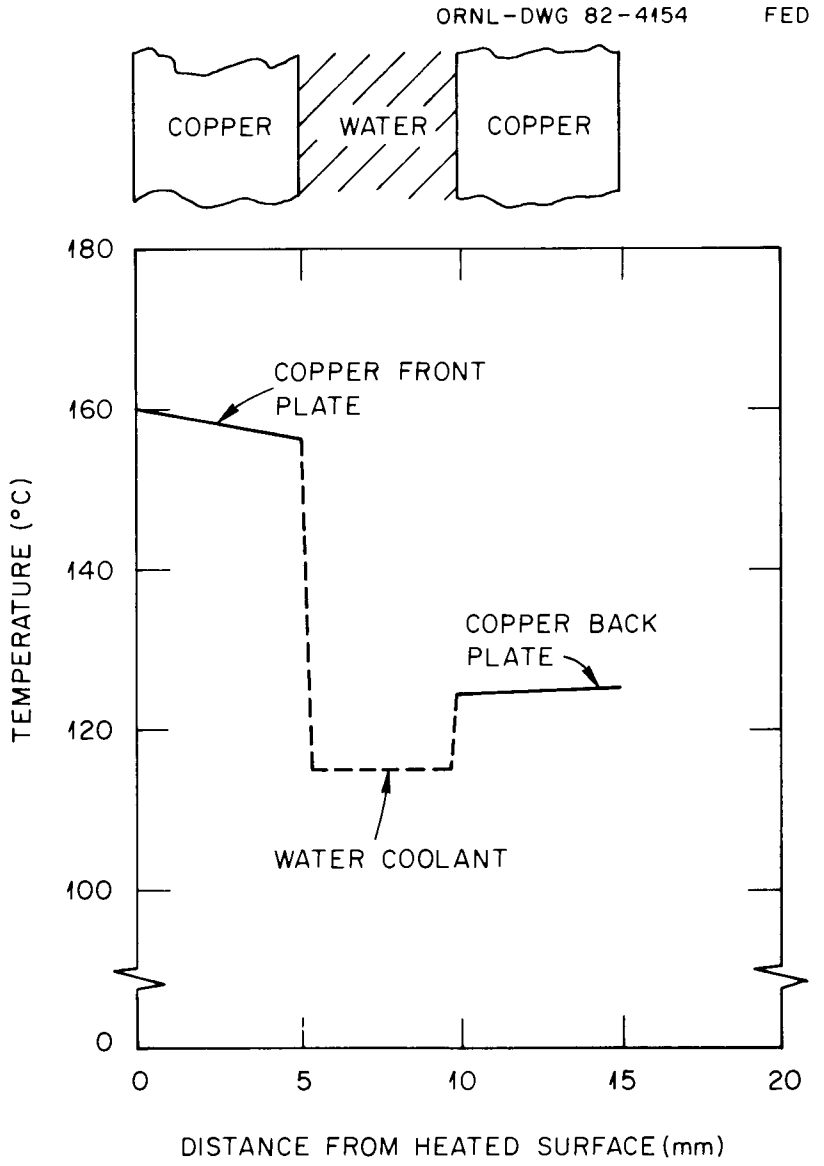

Fig. 6-18. Temperature profile through baseline first wall design.

Table 6-13. Thermal-hydraulic performance of baseline first wall design

Inlet temperature (°C)	60
Outlet temperature (°C)	115
Inlet pressure [MPa (psi)]	0.69 (100)
Pressure drop [kPa (psi)]	4.2 (0.6)
Mass flow rate (kg/s)	360
Pumping power (kW)	1.6

Table 6-14. Disruption parameters assumed for FED-A first wall

	Nominal value
Thermal quench	
Time (ms)	2
Energy (MJ)	56
To limiter (%)	75
To first wall (%)	25
Peaking factor	
Limiter	2
First wall	1 (uniform deposition)
Current quench	
Time (ms)	Dependent on toroidal eddy current time
Thermal energy (MJ)	14
Magnetic energy (MJ)	3
Region of deposition	Inboard, top, and bottom
Extent of region (%)	20
Peaking factor	2

occur. Estimating the current quench duration to be one-fifth of the toroidal eddy current time L/R, the minimum first wall toroidal eddy current times required to inhibit melting of the first wall are 45 ms for copper, 135 ms for stainless steel, and 300 ms for aluminum.

As discussed in Sect. 6.4.2.1, these copper and aluminum toroidal eddy current times can easily be provided, but for stainless steel the maximum permissible L/R = 50 ms, compared with the estimated 135 ms required to inhibit melting. Therefore, erosion of the first wall during plasma disruptions can be avoided by using either copper or aluminum.

6.4.2.4 Choice of Cu AMAX-MZC with water coolant

Based on this discussion and assuming that the thermal and structural performance requirements are satisfied, the key first wall performance parameters are seen to be toroidal current decay time and neutron transmission. Since thick walls are desirable from an electromagnetic performance viewpoint (low electrical resistance and high current decay time) and thin walls are desirable from a neutron transmission and tritium breeding viewpoint (Sect. 6.2.3), these two conflicting performance parameters need to be quantified.

This trade-off is presented in Fig. 6-19. Three possible limits are shown in the figure. First, the maximum temperature limits are 350°C for Cu AMAX-MZC, 200°C for Al 5083, and 400°C for 316 SS. These temperature limits result in an upper limit on wall thickness and therefore an upper limit on toroidal current decay time. Second, the maximum temperature differences allowed through the wall are 100°C for Cu AMAX-MZC, 75°C for Al 5083, and 140°C for 316 SS. These limits also correspond to an upper limit on wall thickness and toroidal current decay time. Third, the lower bound on the toroidal eddy current decay time corresponds to the point at which melting of the first wall occurs during plasma disruptions. For shorter decay times, the energy deposited during the current quench phase of the plasma disruption cannot be conducted away from the heated surface fast enough to prevent surface melting.

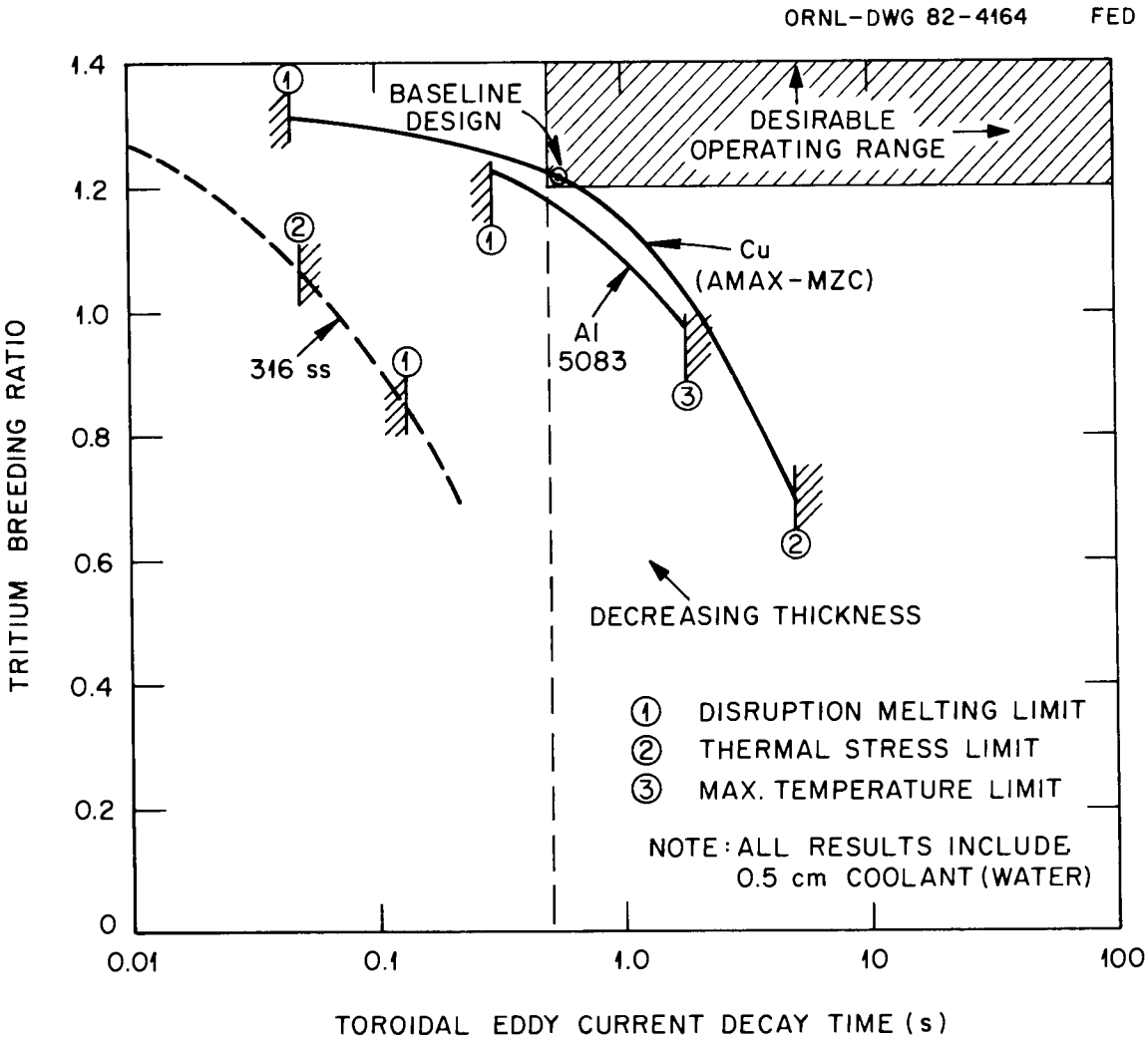

Fig. 6-19. Electromagnetic and neutronic performance trade-off study results.

From the figure, it can be seen that 316 SS cannot be configured to satisfy all of the conditions. It cannot operate below a time constant of 135 ms because of disruption-induced melting. On the other hand, it cannot operate above a time constant of 50 ms because the temperature differences through the wall exceed the 140° limit.

Aluminum comes very close to providing the desired combination of breeding ratio and eddy current decay time. Either a 0.5-s current decay time or a tritium breeding ratio of 1.20 cm can be achieved. However, because of its low maximum temperature ($\leq$200°C), which leads to limited potential in power production, it is considered less than satisfactory.

The best combination of electromagnetic performance and tritium breeding ratio is obtained with the copper baseline wall design. This consists of a 1.5-cm-thick, double-wall-construction shell. The toroidal eddy current time is 0.55 s, and the tritium breeding ratio is 1.22. Even though the FED-A design requires an outlet temperature as low as 123°C, copper's potential to operate at an outlet temperature of 320°C makes it a much more desirable first wall candidate.

6.4.3 Torus Configuration

A description of the torus is necessary here because of its close interaction with the first wall. The torus is composed of twelve 30° sectors with the following major structures: common vacuum boundary cryostat, inboard shield module, outboard shield module, pumped limiter, shielded vacuum duct module, continuous first wall, and torus support platform and pedestal. The general configuration of these structures is shown in Fig. 6-20.

6.4.3.1 Common vacuum boundary cryostat

The common vacuum boundary cryostat is a built-up structure of thin-gage panels with structural ribs. The double-wall panels form the common vacuum boundary between the plasma and the TF magnet vacuums. The plasma vacuum boundary on the outboard wall is closed by the flanged

ORNL–DWG 82-4139 FED

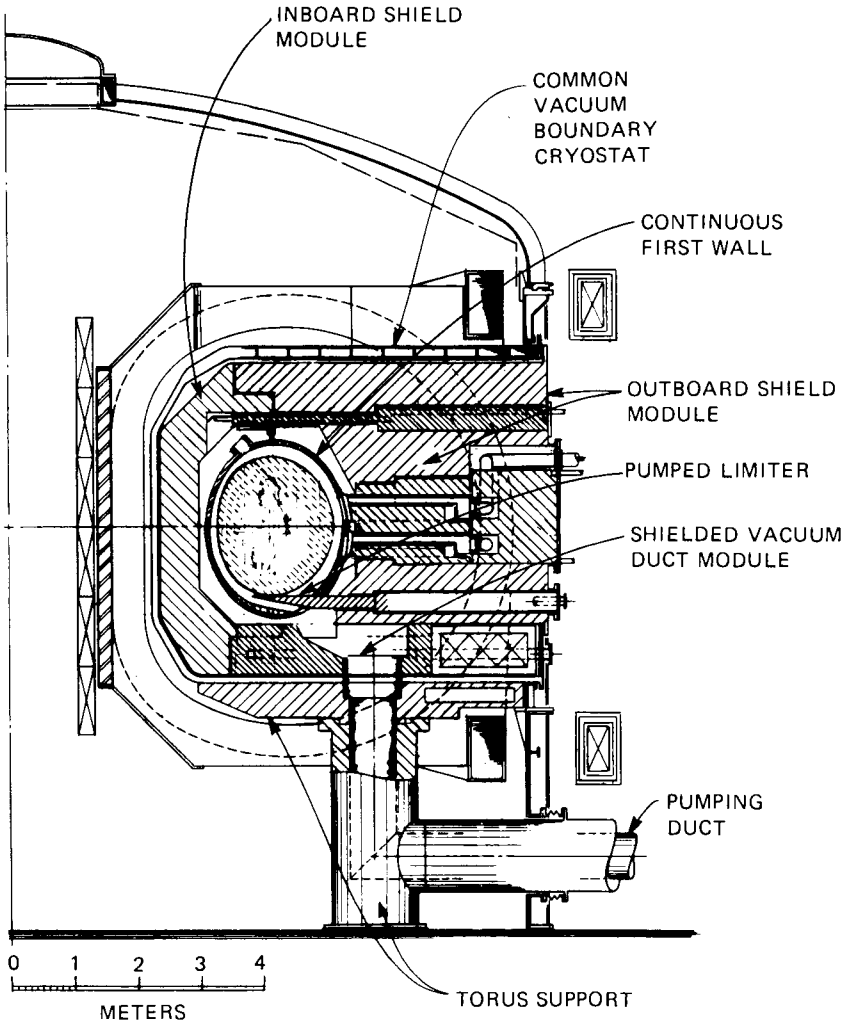

Fig. 6-20. General configuration of torus structures.

panels of the outboard shield module, pumped limiter, and vacuum duct module. Figure 6-21 shows the vacuum boundaries for the plasma and vessel vacuums and also shows the cryostat as a common boundary. Figure 6-22 shows an exploded view of the cryostat. Cryostat ring and window modules are welded together.

6.4.3.2 Shield

The shielding torus is composed of three major modules — inboard, outboard, and vacuum duct modules. The removal of the outboard modules permits the removal of the first wall sectors. The inboard shield module is 62 cm thick, and the outboard shield is 120 cm thick at the plasma centerline. The primary choice of material for the shielding is stainless steel (60% 316 SS, 10% H_2O, 30% B_4C). Tungsten (80% W, 10% H_2O, 10% 316 SS) has also been evaluated and is discussed in Sect. 5.4.

6.4.3.3 Limiter

The interface configuration of the pumped limiter with the continuous first wall is shown in Fig. 6-23. The limiter is divided into removable segments in each shield sector. The line of tangency between the plasma and the top surface of the limiter is 30 cm from the limiter tip. The limiter installation requires penetrations through the outboard shield and first wall structures. Limiter assembly techniques, material makeup, cooling methods, and expendable protective surfaces are similar to those specified for the FED Baseline device and are described in more detail in Ref. 8.

6.4.3.4 Torus support

The major torus structures are supported on a toroidal platform mounted on cylindrical pedestals. These structures are shown in Fig. 6-20. A pedestal is provided under each of the 12 sectors of the torus. Dead weight and seismic loads of the torus structures are transmitted to the floor of the building through these pedestals. Each

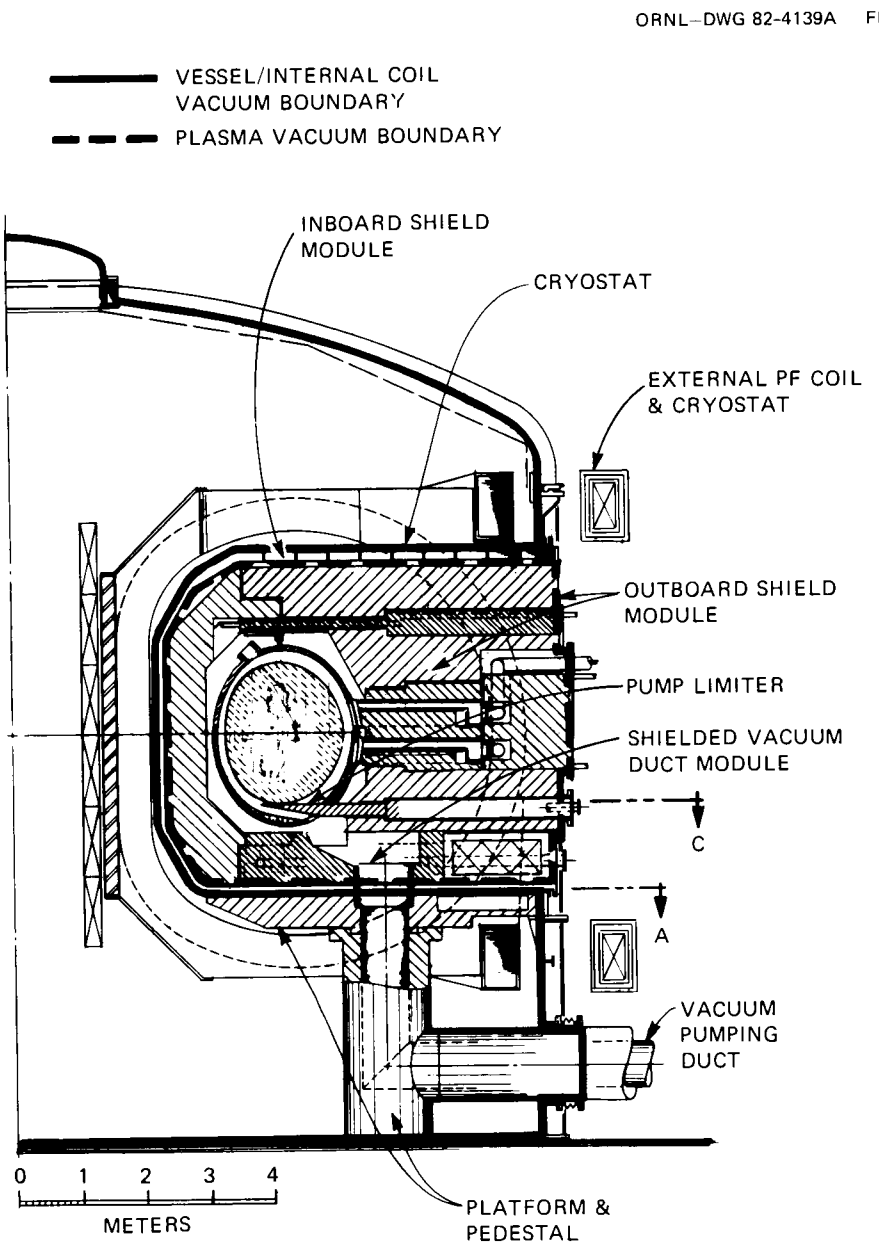

Fig. 6-21. Plasma and vessel vacuum boundary.

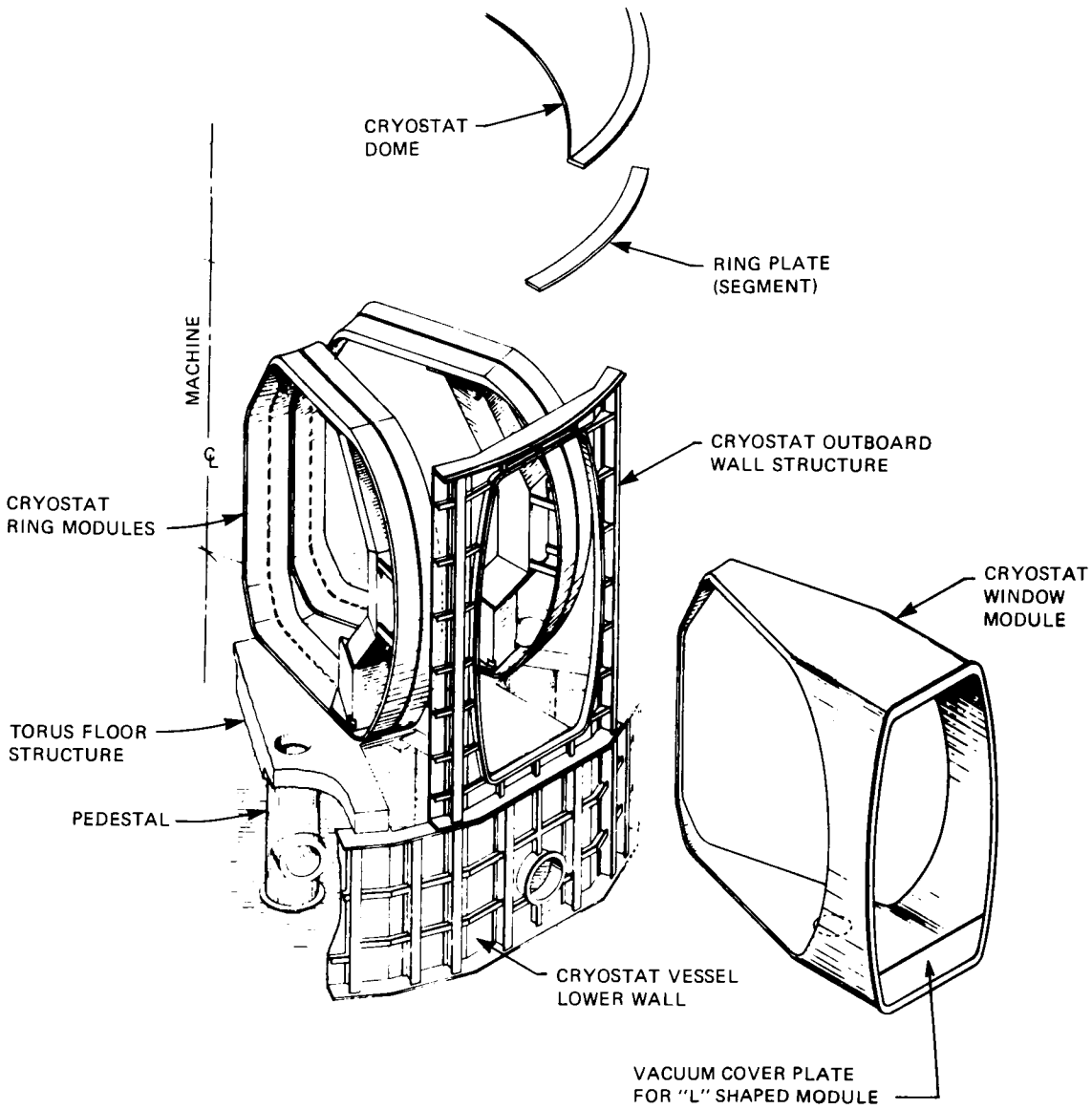

Fig. 6-22. Configuration of common vacuum boundary at the cryostat.

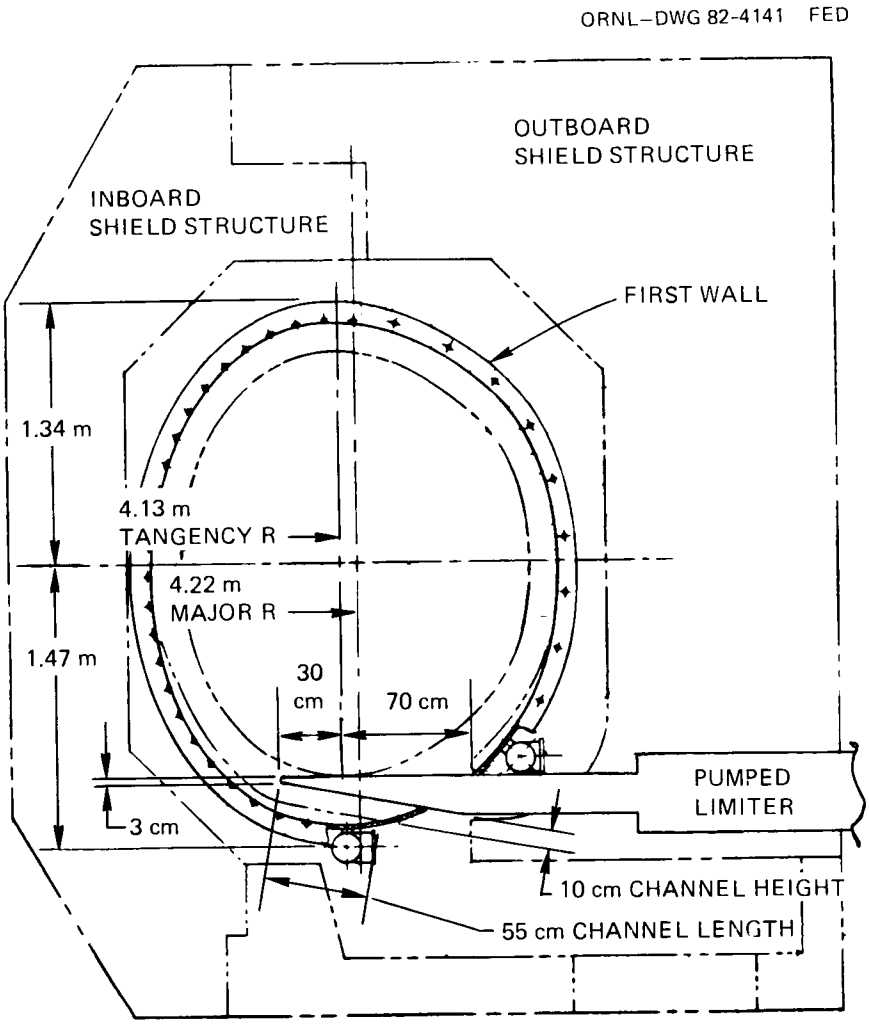

Fig. 6-23. Interface configuration of first wall and limiter.

pedestal also serves as the plasma vacuum pumping duct, which is connected to the shielded vacuum duct module by bellows. The pedestal walls also provide shielding for the vacuum duct.

The support platform and pedestals are sized according to AISI steel construction code requirements. Since all support structure is assumed to be nonmagnetic, type 304 stainless steel has been designated as the primary choice of materials.

6.4.3.5 First wall segmentation

The first wall is a thin-walled, toroidal shell that is moderately elliptical in cross section, as shown in Fig. 6-24. The shell is divided into twelve 30° sectors joined together mechanically to form a continuous first wall in which the plasma is confined. It is made of a copper alloy, Cu AMAX-MZC, with double-wall construction and passages for active water cooling. The total shell thickness is 1.5 cm. The inner surface of the wall closely conforms to the shape of the plasma and is separated by the scrapeoff layer. The continuous wall provides a low resistance, toroidal current path. Armor tiles are installed on the lower inside circumference of the first wall near the pump limiter to account for locally enhanced charge-exchange erosion.

It is recognized that surfaces close to the plasma will be subjected to life-limiting conditions. The first wall shell is segmented to permit replacement. The 12 sectors of the shell are removable through the cryostat window modules between the TF coils by direct radial extraction. Machined ring flanges are attached to each end of the shell to join the sectors together. Each sector is supported by a single vertical linkage attached to the shell structural rib that runs in the toroidal direction above the shell center of mass. The linkage is installed in a support channel in the top of the inboard shield module. A maintenance access door is provided in the outboard wall of each shell sector.

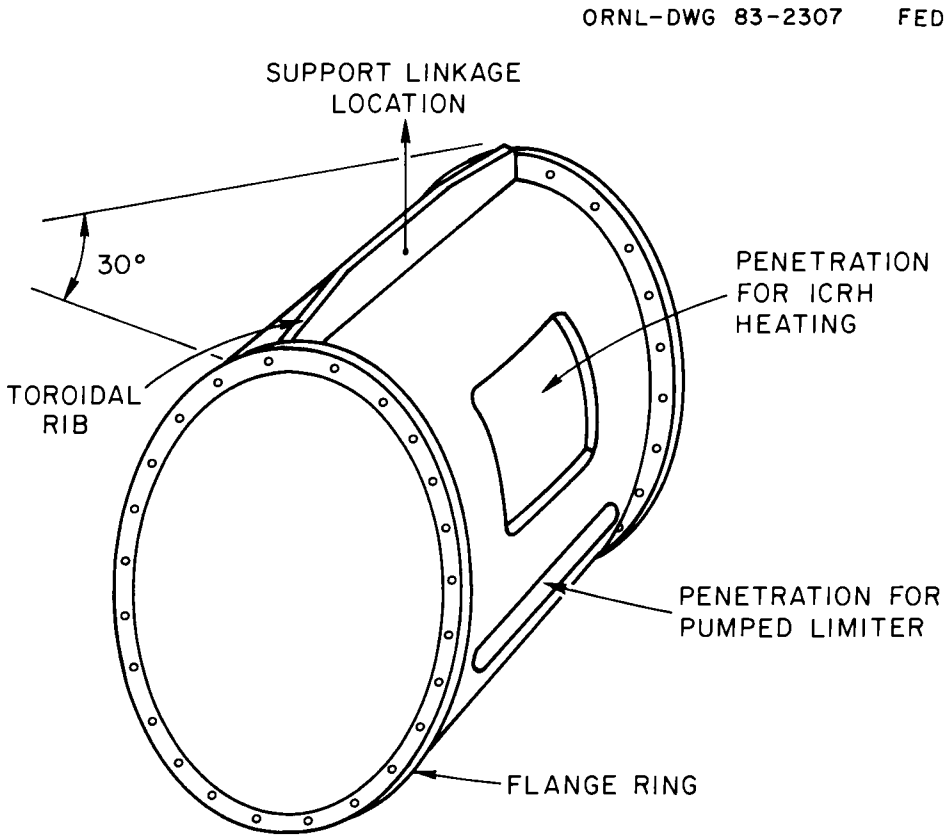

Fig. 6-24. Typical first wall shell sector.

6.4.3.6 Joint attachment concepts

Shell sectors are joined together mechanically. Two methods of joining the sectors were evaluated — bolting and clamping with a continuous articulated band. Bolting was selected as the primary method. The attachment design must provide for clamping the sector rings together with a minimum face pressure of 0.7 MPa (100 psi) at the ring joints. This contact pressure ensures a current path across the joint with a resistance low enough ($\sim$1 $\mu\Omega$ per joint) to prevent arc welding when high eddy current is induced.

A concept for the bolted ring joint is shown in Fig. 6-25. The rings are bolted together from the inside of the shell. Pockets for the bolts are machined in the ring flange, allowing the bolt, washer, and nut to be assembled before installation. The cutout for the nut is sized to trap the nut so that only a torquing motion on the bolt seat is required. Based on a bolt spacing of 15 cm (5.9 in.), fifty-two 12-mm bolts would be required.

The option of bolting only the inboard half of the ring joint from inside the shell and bolting the outboard half of the ring joint from outside the shell is also viable. This method has the advantages of better access to the outside bolts and the use of larger bolts with greater spacing (fewer bolts required). The disadvantage is that a different set of installation tools would be required if a different-size bolt were used. A thin recessed surface on the inside periphery of each ring face would allow the bolts to be cut during disassembly if required.

The option of a clamping band is also considered. The band is made of spool-shaped rollers connected by links. The tension in the links induces an inward radial force on the spools, which clamps the rings together by a wedging action. A single bolt connects the free ends of the strap and is used to provide the tension in the band links. The joint configuration is shown in Fig. 6-26.

The bolting method has the following distinct advantages over the clamping method:

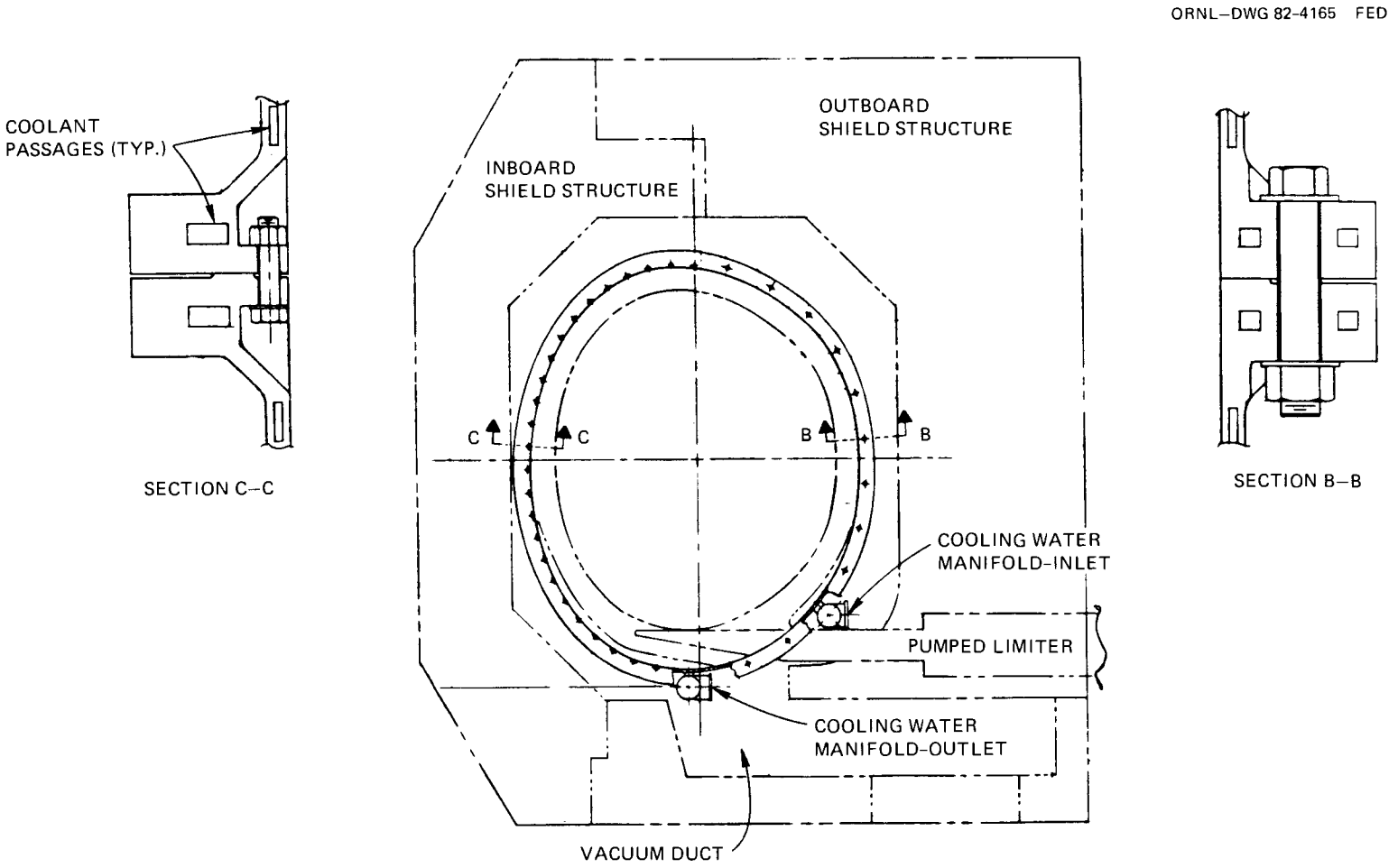

Fig. 6-25. View inside sector at bolted ring joint.

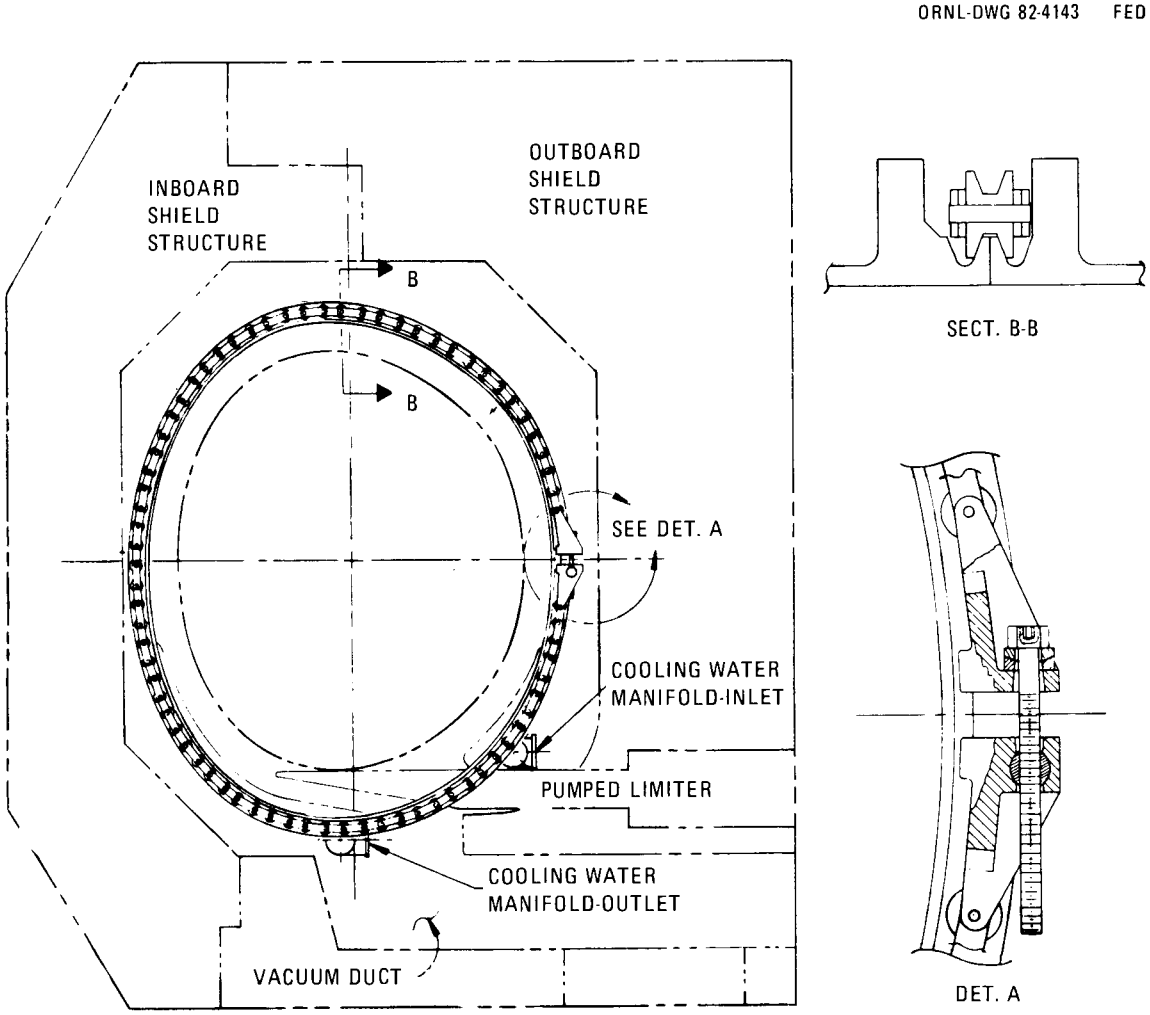

Fig. 6-26. View inside sector at clamped ring joint.

1. A predictable, uniform contact pressure can be established and maintained across the joint.
2. Bolting does not load the first wall shell and the rings (except for compression at the face of the rings).
3. Bolting allows a lower profile ring at the joint.
4. Bolting is an existing technique; the clamp assembly would be unique.
5. The cost of bolts and spares is less than the clamp assembly cost.
6. The operating temperature of the bolts (405°C for tantalum) is much lower than the clamp roller temperature (1400°C for tantalum).

Disadvantages to the bolting method are as follows:

1. Bolting requires an access door or cutout in the outboard first wall shell to provide access to the bolts.
2. Although the installation procedure for each bolt is a simple process, the relatively large number of bolts (52) will make the overall installation process lengthy and tedious using remote handling equipment.

6.4.4 Structural Considerations

Given the selection of the material, coolant, and mechanical configuration of the first wall, a quantitative assessment of its mechanical structure becomes possible. The structural considerations include an analysis of shell size, sector-to-sector flange mechanical loads and support, penetrations, sector support linkage, and installation.

The first wall sector structure was analyzed to define required thickness for the top support beam and poloidal ring flanges. Adequacy of the baseline shell thickness to take toroidal loads was also evaluated, and shell deflections were calculated.

6.4.4.1 Shell sizing

Shell sizing showed that the baseline skin thickness (0.5 cm) should be adequate to carry toroidal loads under dead weight and seismic loads. The analysis was based on stability requirements of the outboard

wall. The dead weight and vertical 1-g seismic load result in compressive toroidal internal loads in the outboard shell. This internal load was approximated using an equation for a toroidal shell subjected to equal and opposite vertical loads on the top and bottom,

$$F = \left(\frac{0.925p\sqrt[3]{1 - \nu^2}}{4\pi b} \right)^3 ab/t^2 ,$$

where

f = maximum compressive toroidal membrane running load,
p = load (twice shell dead weight to account for seismic load),
t = shell membrane thickness,
a = torus minor radius (1.25 m),
b = torus major radius (4.2 m),
ν = Poisson's ratio.

The allowable load was calculated based on stability of a torus subjected to a uniform external pressure. Nondimensional buckling curves[12] are shown in Fig. 6-27. These curves provide values of critical buckling pressure (P_{CR}) as a function of major radius, minor radius, solid wall thickness (t ≈ total wall depth), and material modulus of elasticity. The critical pressure was converted to an equivalent internal circumferential running load $F_{CR} = P_{CR}R$, where R was taken as the maximum outer shell radius (≈5.3 m).

The applied and allowable internal loads for the copper shell are compared in Fig. 6-28. Results indicate that the baseline wall dimension of 0.5-cm skin thickness is adequate to resist buckling, since the allowable load is greater than the applied load.

6.4.4.2 Sector-to-sector flange

Bolted flange. The bolted flange provides a positive approach to achieving sector-to-sector electrical contact. Control of bolt loads is dependent on the bolt torque. A wide range (factor of ≈2) can be expected in the bolt load for a given torque (function of bolt material,

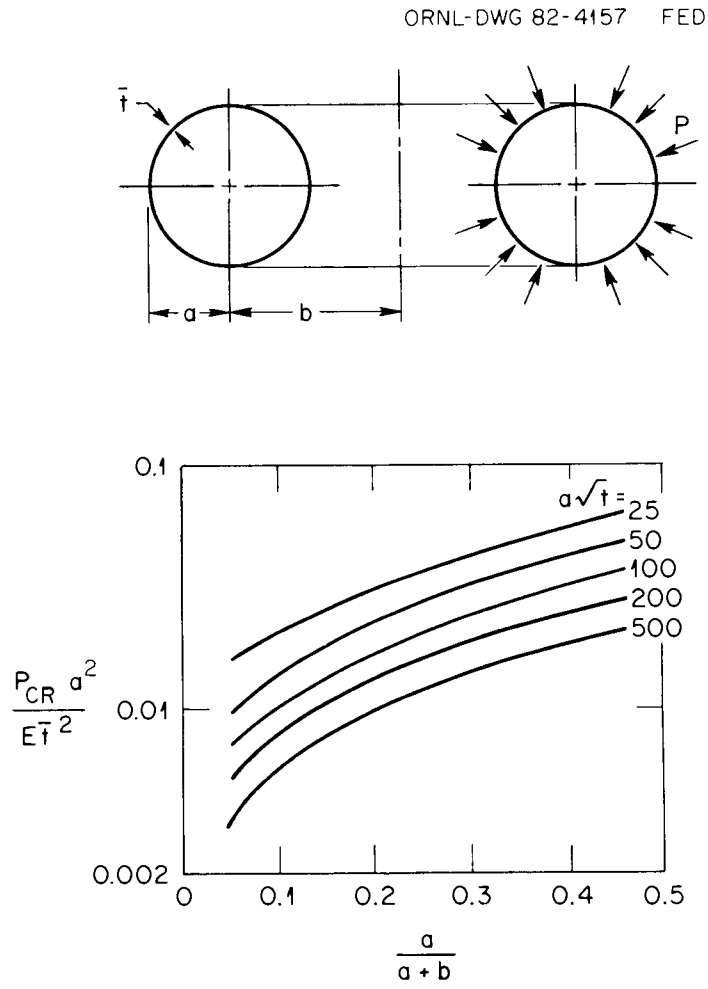

Fig. 6-27. Nondimensional buckling curves for toroidal shells under uniform external pressure.

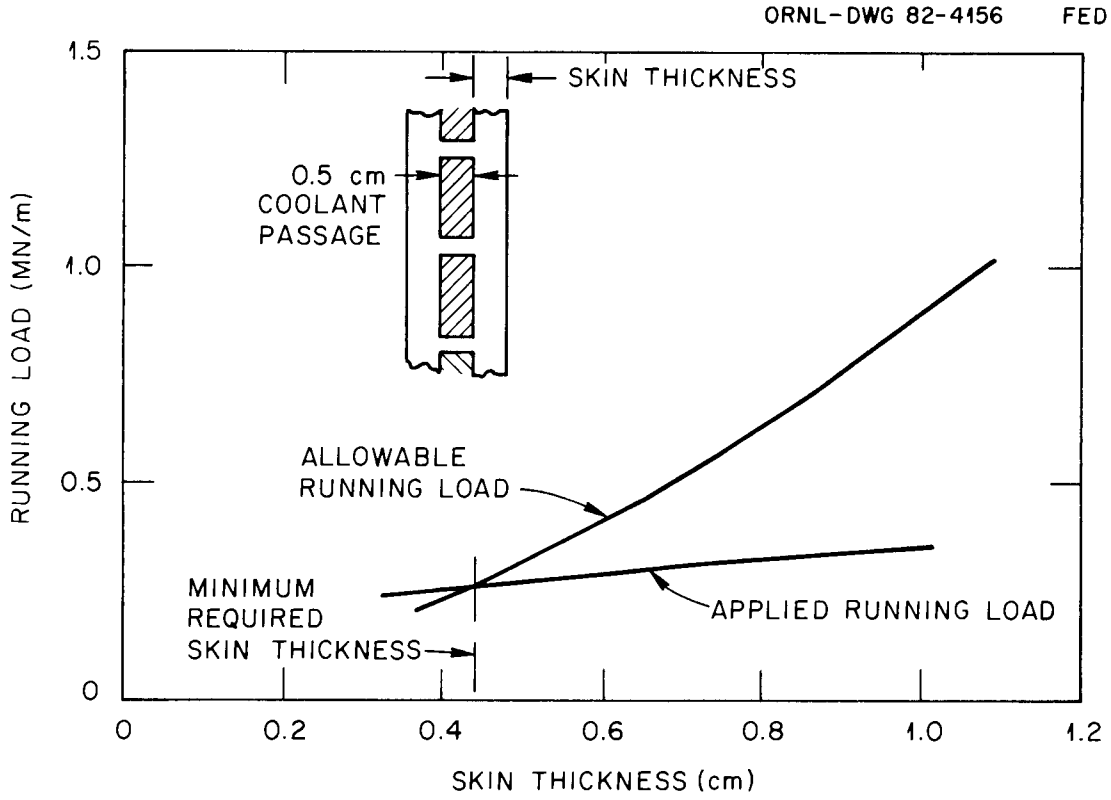

Fig. 6-28. Vessel applied and allowable running loads.

etc.). A bolt torque of 17 kg (150 in.·lb) for the 12.7-mm (0.5-in.) bolts spaced 15 cm (6 in.) apart represents a range in bolt stress from 55 MPa to 96 MPa (8 ksi to 14 ksi), based on steel bolt data. The minimum of these represents a sector-to-sector clamping load of 14.3-kg (130-psi) clamping pressure. Thus, the required minimum clamping pressure of 0.7 MPa (100 psi) is obtained with very modest bolt stresses and torques.

Expansion of the bolts due to temperature rise during operation can result in either tightening or loosening of the bolts. Bolt temperatures for several bolt materials are shown in Table 6-15. Stainless steel and titanium bolts exceed acceptable material temperatures. Both tantalum and tungsten bolts have acceptable operating temperatures. Tantalum (Ta-10 W) is preferred because of its higher elongation. Using the average bolt temperatures of 580°C and 370°C at the outboard and inboard sides of the shell, respectively, and a copper flange temperature of 200°C, the differential expansions of the bolt and the flange are reasonably well matched. For the higher bolt temperature, a relaxation of the bolt load of approximately 30% occurs. For the lower bolt temperature, an increase in bolt stress to approximately the yield stress occurs. Neither of these effects should cause any problem with the operating characteristics of the shell.

Clamped flange. The flange rings at the ends of each sector take bending loads caused by the shell dead weight and seismic loads. In addition to these loads, bending moments caused by clamping the flanges together were used in sizing the flanges. This approach results in some conservatism in the ring flange dimensions for the baseline bolted flange design. However, the approach would allow later changes to the clamped flange design without changing the overall flange dimensions.

The maximum total bending moment of 117,700 lb requires copper edge rings with a depth of 10.0 cm and a width of 5.0 cm. Most of the bending moment (67%) is due to dead weight and seismic loads.

Table 6-15. FED-A bolt temperatures

Bolt material	Location	Maximum temperature (°C)	Average temperature (°C)
Stainless steel	Outboard	780	600
	Inboard	570	500
Tungsten	Outboard	400	310
	Inboard	305	290
Titanium	Outboard	650	510
	Inboard	640	550
Tantalum (Ta-10 W)	Outboard	780	580
	Inboard	405	370

6.4.4.3 Mechanical loads and support

Dead weight and seismic loads. A free body diagram of the torus under dead weight and seismic loads is shown in Fig. 6-29. The dead weight for determining the ring flange loads was based on two copper skins with a 1.8-cm total thickness. This is the design for a 1-s skin time and represents a conservative weight for sizing the rings. The 1.8-cm skin thickness results in a sector weight of approximately 28,500 N (6400 lb) or a total torus weight of 342,000 N (76,800 lb). Seismic loads of 1 g in the vertical and horizontal directions were included simultaneously. The vertical load is taken equally by the supports located at the top center of each of the 12 sectors. The horizontal load is reacted by vertical loads and by horizontal (shear) loads at the supports. The supports are designed to slide radially to accommodate thermal expansion of the entire torus. Therefore, the horizontal shear is taken as toroidal loads at the supports.

The vertical shell loads are assumed to be sheared into the rings at each end of each sector. These rings are supported by a toroidal beam located at the top of each sector. The resulting bending moment distributions in the rings are shown in Fig. 6-30. It can be noted that the region of maximum bending moment is within a $\pm 10^{\circ}$ angle of the support point.

Ring clamping loads. The objective of the clamping design described in Sect. 6.4.4.2 is to provide contact pressure between adjacent sectors (to give the desired electrical current path) and at the same time provide for easy maintenance. The wedging approach for obtaining this contact, provided by the strap design, results in a radial component of load. These radial loads result in bending moments and axial loads in the clamping strap (or linkage).

Two basic approaches were considered for clamping the vessel sectors. These were a sliding strap (Marmon clamp) and a linkage roller design. In each case, the clamping is achieved by tightening an adjustment bolt at the outboard midplane of the shell. Because of friction, the load in the sliding strap varies as a function of the poloidal

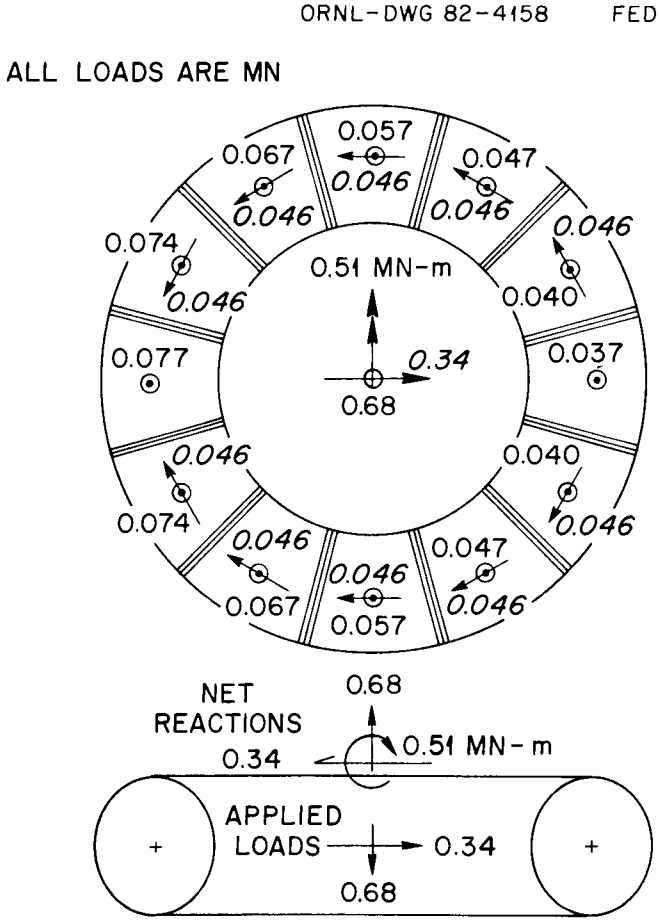

Fig. 6-29. Free body of torus under dead weight and seismic loads.

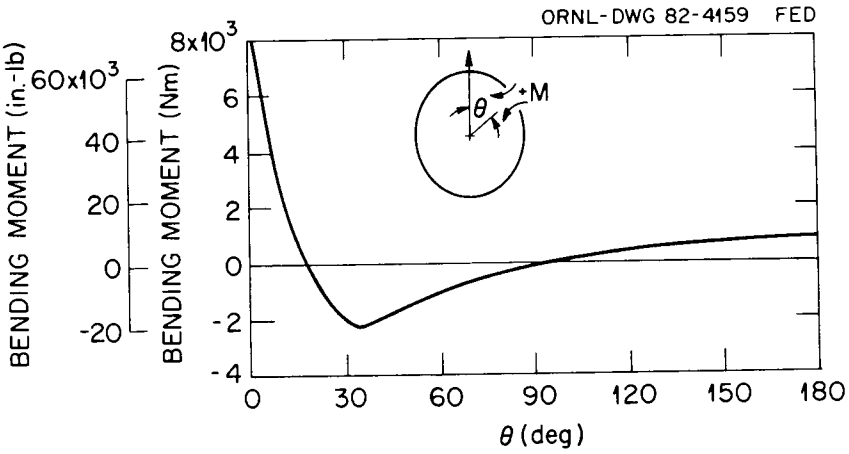

Fig. 6-30. Ring bending movement distribution due to dead weight seismic loads.

distance from the adjustment bolt. The radial load between the strap and ring and therefore the sector-to-sector clamping pressure are directly proportional to the strap load.

Resulting distributions of the sector-to-sector clamping loads are shown in Fig. 6-31. In the case of no friction, the strap load is constant. In the case of a 0.5 coefficient of friction, the load 180° away from the adjustment bolt is zero. For a coefficient of friction of 0.19, the load at $\theta = 180°$ drops off to 50% of that at the adjustment bolt. In each case, a cosine friction load distribution and a circular ring shape were assumed. Results indicate that a higher strap load will have to be provided to achieve the desired average clamping pressure. Additionally, for typical coefficients of friction (e.g., 0.39 for steel on steel in air and 1.05 for aluminum on aluminum) it may be difficult to achieve any clamping pressure along the inboard portion of the shell.

The roller linkage design for achieving sector-to-sector clamping is intended to provide as uniform a load as possible by eliminating friction between the strap and the flange. The shell elliptical shape, however, will result in a poloidal load variation. Bending and axial loads in the elliptical rings were calculated for the two radial load distributions shown in Fig. 6-32. The ring bending moments that result from these load distributions are intended to provide upper and lower bounds to the bending moments expected and to provide a basis for sizing the rings.

Bending moments in the sector rings were calculated for a sector-to-sector clamping load of 0.1 MPa (100 psi) over a 5-cm ring depth, as shown in Fig. 6-33(a). The dummy load method of structural analysis and numerical integration were used to solve for the internal ring bending moments, axial loads, and deflections. Bending moment distributions for the two assumed poloidal clamping load distributions are shown in Fig. 6-33(b). Results show that the load distribution has a significant effect on the ring bending moments. For purposes of sizing the ring flanges, the peak bending moment of 40,000 in.·lb (for the uniform clamping load) is superimposed on the 77,700-in.·lb moment resulting from dead weight and seismic loads. Both these moments occur near the

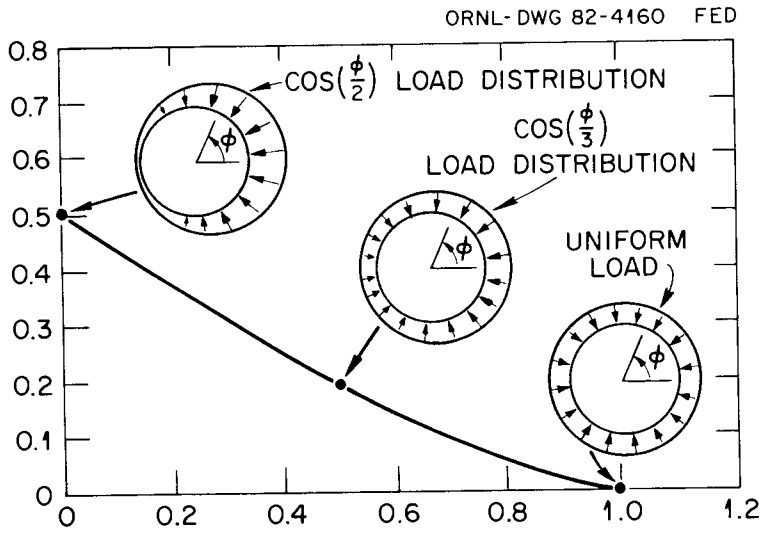

Fig. 6-31. Effect of coefficient of friction on sliding strap clamping load distribution.

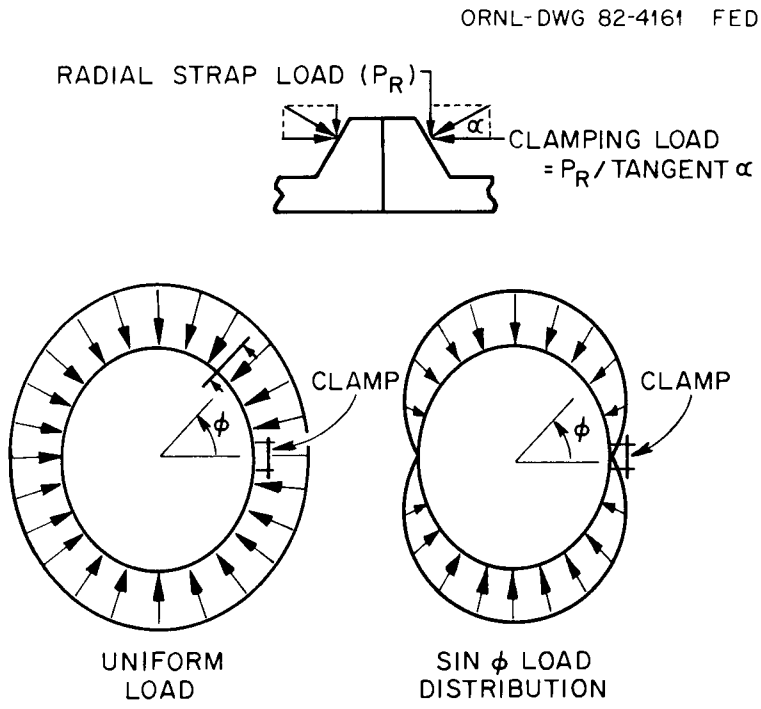

Fig. 6-32. Assigned load distribution for roller linkage clamping on elliptical rings.

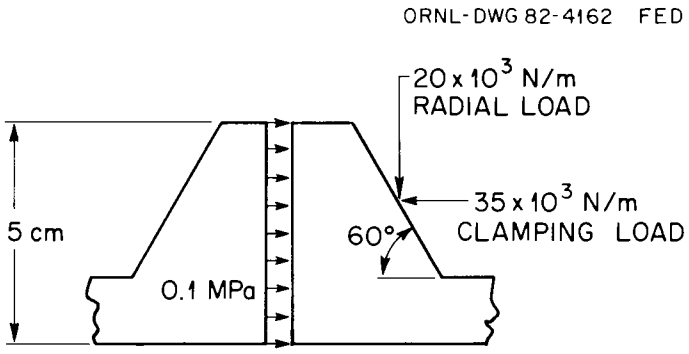

Fig. 6-33(a). Ring clamping geometry assumed for ring bending calculations.

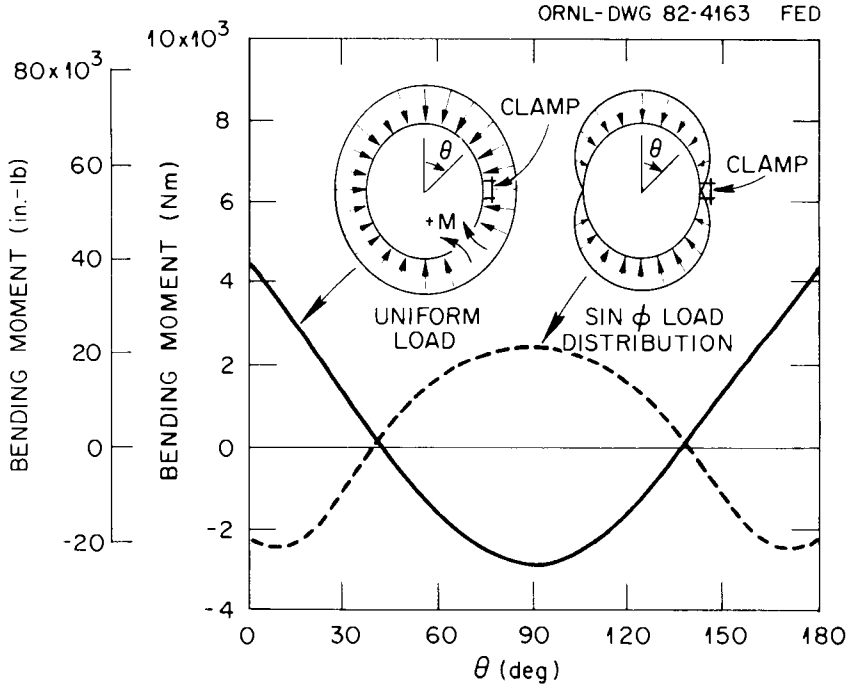

Fig. 6-33(b). Elliptical shell ring bending movements due to clamping loads.

top of the ring and result in tension on the outside of the ring. Thus, the clamping load is approximately 35% of the total load. The total load should be conservative, since a nonuniform clamping load similar to the cosine distribution is more likely for the elliptical shell.

The ring bending moments shown in the figures are applied to each pair of rings at the sector-to-sector joint. Copper rings with a depth of 10.0 cm and a width of 5.0 cm are adequate to take the maximum bending moment. The ring can be tapered to smaller dimensions away from the support point.

Clamping tension load and temperature. The maximum strap tension loads, due to clamping the sectors together, are 6300 lb and 3300 lb for the uniform distribution and cosine distribution shown in Fig. 6-33(a), respectively.

Because of nuclear heating, the clamping strap operates at a high temperature (1200°C) and must be fabricated using a refractory metal such as tantalum or tungsten. Although the coefficients of thermal expansion of these materials are relatively low, the differential expansion between the clamping strap and the copper rings is approximately 4.0 cm. Thus, an active means of controlling the strap tension will be required to maintain the electrical contact from sector to sector.

Top support beam sizing. The top support beam was analyzed as a simply supported beam with a midspan load of 770,000 N (17,300 lb). A rectangular cross-section copper beam with a depth of 20 cm and a width of 7.5 cm is adequate to carry the maximum bending moment at the center of this beam. The beam can be tapered to a depth of 10 cm at the ring flanges. The maximum bending moment in the beam can be reduced significantly by adding intermediate poloidal rings to the shell structure.

Shell deflections and thermal expansion. Deflections of the copper rings, under dead weight, seismic load (as a static load), and clamping loads, are shown in Table 6-16. The radial thermal growth of the outboard shell surface during operation is 1.0, 1.7, and 1.6 cm for the copper, stainless steel, and aluminum candidate shell materials, respectively. These expansions will have to be accommodated by the shell support system and by components attached at ports. The deflections

Table 6-16. Baseline shell deflections

Load	Deflection (cm)
Dead weight	0.38
Seismic	0.65
Clamping (uniform)	0.05
Clamping (cosine)	-0.05

cited are based on approximate average shell temperatures for the design thickness for each of the materials (e.g., 0.5-cm skins for copper, maximum thicknesses for stainless steel). These average temperatures are 120°C, 210°C, and 150°C for copper, stainless steel, and aluminum, respectively. Larger deflections will occur during bakeout conditions.

6.4.4.4 Penetrations

First wall penetrations are required for machine functions such as fueling, plasma heating, testing, diagnostics, particle removal, and pumped limiter. Local cutouts and/or windows will be provided to meet these requirements. Since the first wall is not a vacuum boundary, it is not necessary to make a seal between the penetrations and the first wall.

Anticipated penetrations are as follows:

1. Fueling systems. One sector will be devoted to fueling components similar to the FED Baseline machine (Ref. 8). Fueling will require two 6-cm holes in the first wall at the horizontal centerline.
2. Pumped limiter/vacuum duct. These components establish the plasma edge and remove helium ash and hydrogen particles from the plasma. The single cutout in each sector of the first wall for these components measures approximately 60 cm poloidally by 2.6 m toroidally running from one end of the first wall sector to the other.
3. Plasma heating. Two electron cyclotron resonance heating (ECRH) penetrations approximately 6 cm in diameter are required in every sector. A cutout measuring approximately 1.2 m poloidally by 0.6 m toroidally is required for the lower hybrid resonance heating (LHRH) launcher port in two sectors. Additionally, two first wall sectors will have two cutouts for ion cyclotron resonance heating (ICRH) launchers. Each cutout will measure 0.4 m poloidally by 2.0 m toroidally. Figure 6-24 shows some of the cutouts required.
4. Testing. Test modules requiring a direct view of the plasma will also require cutouts in the first wall shell. Although testing requirements are undefined, it is anticipated that the maximum test area available for each sector is about 1.5 m^2.

5. Diagnostics. Instrumentation requiring direct access to the plasma will require a cutout in the first wall sectors. The diagnostic requirements are assumed to be similar to the FED Baseline.[8]

Future studies are required to evaluate the overall impact of the various cutouts in the continuous first wall from performance, structural, and electrical standpoints.

Access doors, or cutouts for maintenance access, are required in all sectors of the first wall shell that do not have large cutouts for major components such as ICRH, LHRH, or test modules. Future studies will determine this requirement.

Each sector of the continuous first wall is actively cooled by water. Coolant flows in the poloidal direction through built-in coolant passages in the shell, as shown in Fig. 6-34. Inlet and outlet water manifolds are attached to the shell above and below the limiter cutout, respectively. Two sets of manifolds are required in order to minimize their size. Coolant passages approaching cutouts merge with a single, larger coolant passage running around the periphery of the cutout. Coolant passages have been sized to prevent the water coolant from boiling during operation.

6.4.4.5 Sector support linkage

Each first wall sector is supported vertically by a single support linkage assembly above the center of mass along the sector midpoint radial centerline. The pivoting, double-pinned joint is shown in Fig. 6-35. The linkage assembly consists of an internally threaded T-bar, a threaded clevis, and another clevis connected through pins. The T-bar has spherical surfaces that allow the bar to pivot slightly, and the internal threads provide capability for vertical alignment of the sectors by rotation of the T-bar. The clevises are pinned together and the bottom clevis is pinned to the structural rib of the first wall shell, running toroidally above the center of mass. Outward thermal growth of the continuous first wall is unrestrained since the linkage assembly pivots about the upper pin, rocking on the spherical surface of the T-bar.

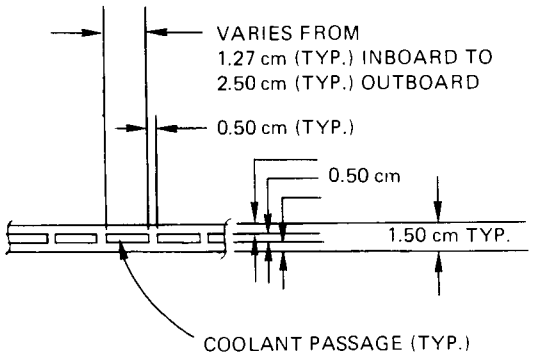

SECTION F–F
TYP. SHELL CROSS SECTION

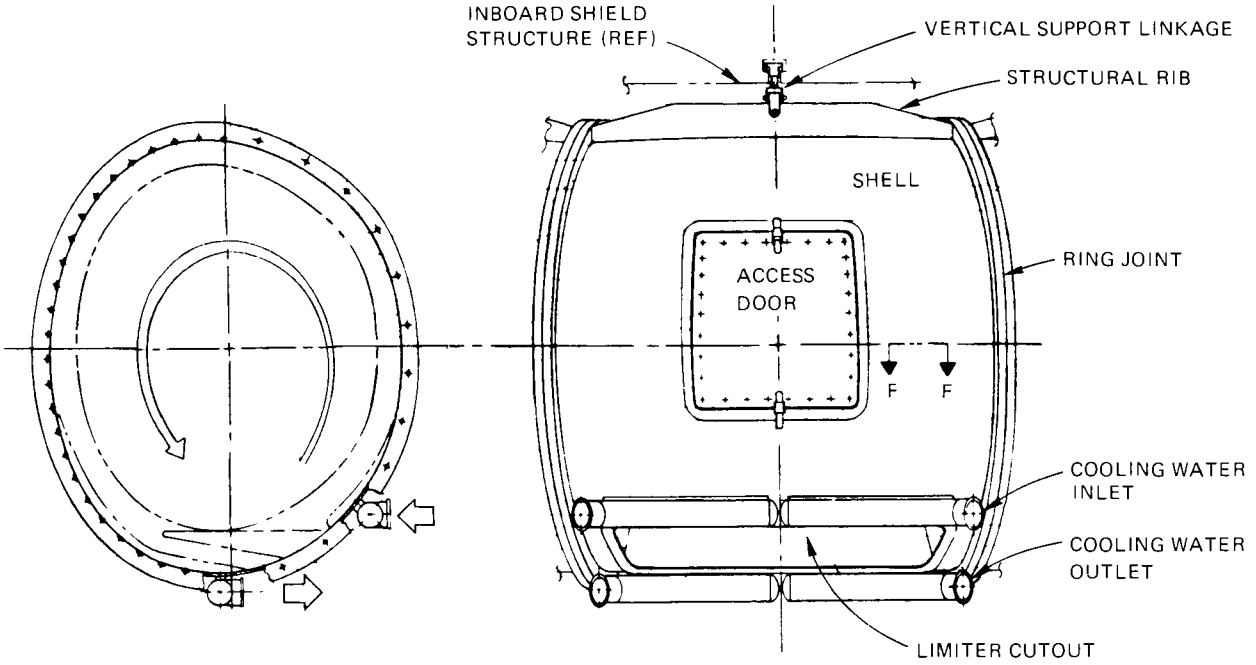

Fig. 6-34. Coolant flow path through first wall sector.

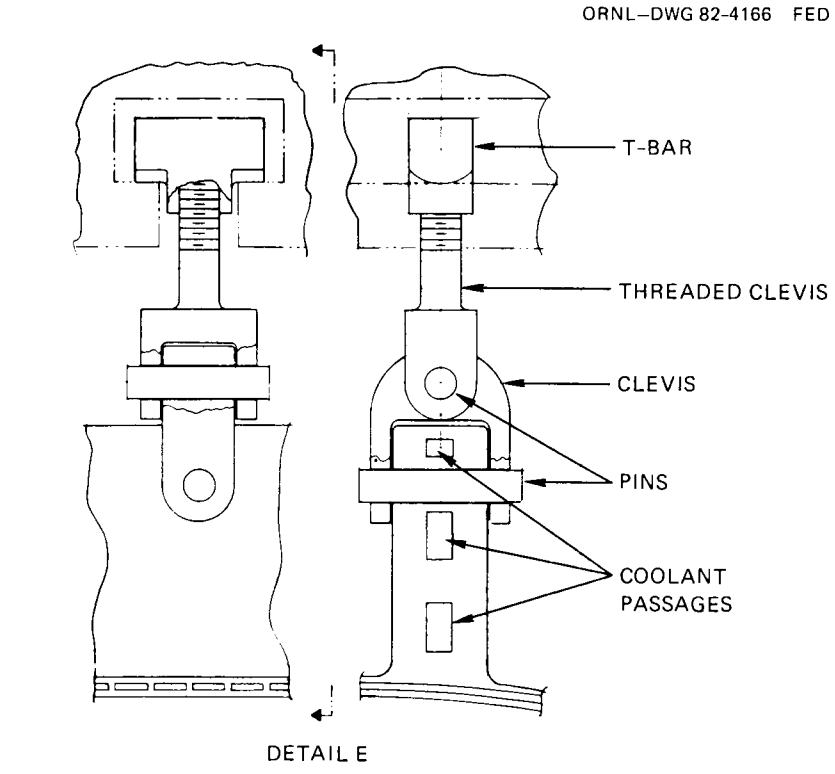

Fig. 6-35. Sector support linkage.

Restraining the first wall shell under seismic loading conditions will be addressed in future studies.

6.4.4.6 Installation approaches

The first wall is one of the major components of the torus, as shown in Fig. 6-20. Once construction has proceeded through the installation of the common vacuum cryostat, the following sequence of installation of major torus structures would occur:

1. inboard shield module,
2. shielded vacuum duct module,
3. continuous first wall,
4. 3-piece TF coil shield posts,
5. outboard shield module, and
6. pumped limiter.

The sequence of events for installing the first wall sectors with the bolted joints is as follows:

1. An access door or cutout in the outboard first wall shell is required to install the bolts on the inboard periphery of the joint from the inside of the shell. Remove this access door before bolt installation.
2. Insert each first wall sector, with support linkage assembly attached, into the torus cavity by inserting the T-bar of the assembly into the support channel in the inboard shield module (Fig. 6-35). The sector is then permitted to hang free from the clevis.
3. Align each sector-to-sector joint, mating the end rings so that bolt holes match.
4. If the design option of using large bolts on the outboard periphery of the shell was adopted, install the large bolts at this time.
5. Install all (or remaining small) bolts in the cutouts along the inside periphery of the ring joint from the inside of the shell.
6. Reinstall the access door, if provided in the design.

6.5 CONCLUSIONS AND RECOMMENDATIONS

Under the assumption of the necessity and the utility of a closely fitted, continuous, conducting first wall in FED-A, we have taken a preliminary look at its design criteria and concepts. The results suggest that a water-cooled copper (e.g., AMAX-MZC alloy) first wall shell provides the best combination of electrical conductivity, neutron transparency, and reactor-relevant heat removal of the three materials examined (others were 316 SS and Al 5083). The copper shell can simultaneously satisfy time constants around 0.5 s, tritium breeding ratios of about 1.2, and coolant temperatures as high as 320°C. Aluminum temperatures are limited to 200°C, and the electrical resistance of stainless steel is limited to values above 120 $\mu\Omega$, resulting in a time constant of 0.05 s.

The simple bolted technique for joining the shell sectors offers a high potential for good electrical continuity. Development of a special remotely operated tool for installing and tightening the bolts is required. No structural difficulties are indicated for this first wall concept (with a separate vacuum boundary) by our preliminary considerations.

Penetrations in the shell for such auxiliary functions as ICRH heating and the pumped limiter will cause induced currents in the shell to travel poloidally. This is expected to cause forces that have yet to be examined.

Design analysis of the continuous first wall concept should be continued with emphasis on the following tasks:

1. support linkage design with special effort on thermodynamic performance,
2. tool definition for remotely installing the bolts,
3. providing adequate response to seismic accelerations,
4. coolant flow geometries that minimize the effects of temperature gradients,
5. evaluation of induced eddy current forces, and
6. maintenance equipment requirements for holding and aligning sectors while structural and coolant hookups are made.

REFERENCES

1. F. Schneider, "Operation of the ASDEX Feedback System," *Proceedings of the 11th Symposium on Fusion Technology, Oxford, 1980*, p. 1027.
2. H. J. Avci et al., "The Use and Performance of Graphite and Metal ISSECS in TOKAMAK Fusion Reactors," *Nucl. Eng. Des.* 45, 285-310 (1978).
3. W. Engle, Jr., *A User's Manual for ANISN, A One Dimensional Discrete Ordinates Code with Anisotropic Scattering*, ORGDP-K-1963, Union Carbide Corp. Nuclear Div., Oak Ridge Gaseous Diffusion Plant, 1967.
4. R. W. Roussin et al., *The CTR Processed Multigroup Cross Section Library for Neutronics Studies*, ORNL/RSIC-37, Union Carbide Corp. Nuclear Div., Oak Ridge Natl. Lab.
5. Y. Gohar and M. A. Abdou, *MACKLIB-IV, A Library of Nuclear Response Functions Generated with MACK-IV Computer Program from ENDF/B-IV*, ANL/FPP/TM-106, Argonne Natl. Lab., Argonne, Ill.
6. M. I. Baskes, K. L. Wilson, and W. Bauer, FED-INTOR/TRIT/81-01 and FED-INTOR/TRIT/82-4.
7. M. I. Baskes, Sandia National Laboratories, Livermore, California, personal communication to F. W. Wiffen, Oak Ridge National Laboratory, September 30, 1982.
8. P. H. Sager et al., *Engineering Studies for FED Baseline*, ORNL/FEDC-82/2, Union Carbide Corp. Nuclear Div., Oak Ridge Natl. Lab., 1983.
9. INTOR.
10. *STARFIRE — A Commercial Tokamak Fusion Power Plant Study*, ANL/FPP-80-1, Argonne Natl. Lab., Argonne, Ill., 1980.
11. J. Murray, personal communications.
12. L. H. Sobel and W. Flugge, "Stability of Toroidal Shells Under Uniform External Pressure," *AIAA J.* 5, 425 (1967).

7. CURRENT DRIVE AND HEATING DESIGN CONCEPTS

This chapter discusses the engineering concepts and evaluations of the current drive and heating equipment for the FED-A, carried out during FY 1982. Early in the effort, a number of approaches to current drive were configured. It became apparent that incorporating all options in the FED-A would require a large cost increase. A comparative assessment was needed to elucidate appropriate combinations of current drive and heating for FED-A operation. To carry this out, we proceed first with a discussion of the possible roles of current drive and heating in operating FED-A (Sect. 7.1), followed by an evaluation of the merit of various combinations of current drive and heating schemes (Sect. 7.2). Then the preconceptual design descriptions of various current drive components and how they interface in the FED-A device are discussed (Sect. 7.3).

7.1 CURRENT DRIVE AND HEATING PHILOSOPHIES

7.1.1 Current Drive

Three major current drive philosophies are discussed here: (1) full inductive capability (present transformer), (2) quasi-steady-state current operation (weak transformer), and (3) steady-state burn (no transformer). The current drive options and approaches appropriate for each of these philosophies are summarized below.

1. Full inductive capability

With this philosophy, the full inductive current drive capability is retained in the transformer of FED-A. There is a 67-V•s capability built into the poloidal system on FED. During start-up, 63 V•s is used. This is supplied by 24 V•s from the EF coils and 39 V•s from the OH transformer. During the 100-s burn, the OH transformer expends its final 4 V•s.

2. Quasi-steady-state current drive

The quasi-steady-state current drive operation involves only a weak transformer. A long pulse (>1000-s) burn operation is assumed where the transformer current drive is supplemented by one or a combination of the heating options (LHRH, FWIC, or REB). Alternatively, the transformer can be recharged by an rf drive system, as suggested in Sect. 4.2. We envision three approaches for this philosophy using the LHRH option. Depending on the resolution of the high density limitation associated with LHRH current drive, one or more of these would be appropriate. If acceptable drive efficiency cannot be achieved at high density (10^{14} cm^{-3}), then LHRH can be used to drive current during the initial low density current start-up before the densification phases. The full capacity of a weak transformer can then be used to provide inductive current maintenance at high density for $\sim$1000 s of burn.

A second approach uses the same start-up and burn drive, but the density is then allowed to drop to a level where the LHRH can drive current at high efficiency. At this density, the LHRH not only maintains the plasma current but also drives the current in the OH coil primary, thus fully recharging the transformer for the next burn pulse.

In the third approach, LHRH would operate at both low and high densities (densification and maintenance phases) but not during start-up. Here the weak transformer is used for start-up, and LHRH drives through densification into burn.

As a secondary option, the FWIC is suggested for current maintenance at high density (Sect. 4.3). Hence, the third approach where the weak transformer effects start and FWIC maintains the current during burn may be considered.

The experimental evidence for relativistic electron beams is limited, but it suggests that current start-up and maintenance may be possible (Sect. 4.5). There are engineering concerns about possible breakdown in the vacuum coaxial transmission line supplying the REB diodes during start-up. We include an REB–weak transformer case in which current is provided from the transformer during start-up and then maintained by REB.

3. Steady-state burn

This is the "no transformer" case. The primary option (LHRH) and a secondary option (REB) are candidates for current start-up without a transformer. All options are considered appropriate for current maintenance except that LHRH may have a density limitation. Therefore, there are six possible combinations: LHRH start with LHRH, FWIC, or REB maintenance and REB start with REB, LHRH, or FWIC maintenance. Some theories on the LHRH density limitation state that an abundance of high energy electrons is needed for high efficiency current drive. If this is true, a combination of REB or FWIC supplying energetic electron heating in conjunction with LHRH might be attractive from a physics point of view; however, it is cumbersome from an engineering standpoint. These cases are summarized in Table 7-1 along with those noted above.

7.1.2 Heating Philosophy

For purposes of discussion, we divide the heating into three stages or phases: (1) assisting current start-up (ionization of the fill gas and heating the electrons), (2) heating to burn or ignition (bulk heating), and (3) heating drive (maintaining plasma during burn $Q < \infty$). The heating techniques considered here are ECRH, LHRH, and ICRH.

1. Baseline ECRH-ICRH

The FED Baseline design assumes ECRH early in start-up and then supplements it with low power ($\sim$5-MW) ICRH proton minority heating. At about 5 keV the power is stepped up to 50 MW for bulk heating. This high power is required to accomplish the bulk heating in 6 s. FED-A uses up to 25 MW of rf power and takes a longer time for start-up and bulk heating. During burn, the baseline requires 36 MW with $Q = 5$ to obtain 180 MW of fusion power. FED-A is an ignited machine.

Table 7-1. Current drive philosophy summary

1. Full inductive (present transformer) — All current is driven from the PF coil set (∿100-s burn)
2. Quasi-steady-state current operation (weak transformer)
   - 2.1 Primary option (LHRH)
     - 2.1.1 LHRH (density limited) — LHRH assists current drive of the transformer during start-up (greatly reduces start-up volt-seconds). After limiting density is reached during densification, the weak transformer drives current all through the long pulse (>1000-s) burn.
     - 2.1.2 LHRH (modulated density) — same as 2.1.1, but at the end of burn the density is lowered to a level where LHRH is effective and current is maintained in the plasma and induced into the OH primary to "recock" the transformer for the next burn pulse.
     - 2.1.3 LHRH (not limited at high density but cannot start up current) — weak transformer is used for start-up; LHRH takes over to maintain current throughout the long pulse (>1000-s) burn.
   - 2.2 Secondary option (FWIC) — weak transformer is used for start-up. FWIC maintains the current drive.
   - 2.3 Secondary option (REB) — if current start-up is limited (either engineering or physics considerations) to current maintenance, then same as 2.2 but with REB.
3. Steady-state burn (no transformer)
   - 3.1 LHRH start-up current drive with
     - 3.1.1 LHRH current maintenance,
     - 3.1.2 FWIC current maintenance, or
     - 3.1.3 REB current maintenance
   - 3.2 REB start-up current drive with
     - 3.2.1 LHRH current maintenance,
     - 3.2.2 FWIC current maintenance, or
     - 3.2.3 REB current maintenance

2. ECRH-FWIC Multiplex

A variation of this would use the FWIC current drive equipment in a time-multiplexed fashion. During heating, for example, there could be a 2-s cycle. During the first half of the cycle the FWIC frequency could be transmitted; during the second half a harmonic frequency of one of the majority species could be transmitted for heating. The plasma thermal and electrical time constant would be such that both plasma temperature and current would be maintained with only minor variations due to the pulsed nature of the drive. After ignition, only the FWIC current drive frequency would be transmitted. Note that during the multiplex mode the average power is only one-half the peak power.

3. ECRH-ECRH

Other sequences using ECRH for both the start-up and bulk functions are possible. The start-up arrangement would be similar to the baseline. An ECRH wave is launched from the high field side with an extraordinary (X) mode. Additional ECRH power from the low field side using the ordinary (O) mode would provide bulk heating.

4. ECRH-LHRH

Finally, the combination of ECRH and LHRH for start-up and bulk heating, respectively, is another possibility. Experimental data for slow wave (SW) LHRH have been sparse. Some data from heating experiments on JFT-2[1] indicate heating efficiencies of 2-3 $eV/kW \cdot 10^{13}$ cm^{-3}. There are, however, concerns about heating reactor-relevant, hot, dense plasmas and uncertainties in wave penetration and loss mechanisms. Fast wave (FW) heating is being given some consideration at PPPL. In this study, LHRH is considered as a class or technique, and no distinction is made between SW and FW heating. These heating philosophies are summarized in Table 7-2.

Table 7-2. Heating philosophy summary

1. Baseline ECRH-ICRH

   ECRH plasma initiation and start-up supplemented by 5 MW of proton minority heating. Bulk heating is ICRH at the second harmonic of deuterium. Burn drive for $Q < \infty$ is also at the second harmonic of deuterium.

2. ECRH-FWIC Multiplex

   Plasma initiation and start-up same as baseline. Harmonic frequency of proton minority during densification phase is alternated (time-multiplexed) with the FWIC current drive frequency. After ignition frequency remains set at current drive.

3. ECRH-ECRH

   Plasma initiation and start-up same as baseline. ECRH bulk heating is done with high power launched from the low field side in the ordinary mode.

4. ECRH-LHRH

   Plasma initiation and start-up same as baseline, but LHRH replaces ICRH. Densification/bulk heating done with LHRH.

7.2 SELECTION OF CURRENT DRIVE AND HEATING SCENARIOS

Among the possible combinations of current drive and heating philosophies, Table 7-3 summarizes 40 feasible cases. Many among these are considered undesirable from an engineering standpoint because of cost. There are 28 relatively desirable cases (circled in Table 7-3) that use at least two but not more than four techniques.

A set of criteria for evaluating the merit of these cases is given in Table 7-4. We define merit based on these criteria as follows:

$$\text{merit} = \frac{\text{burn time factor} \times \text{credibility}}{\text{access } (m^2) \times 10^8 \ (\$/m^2) + (\text{component capital cost})} .$$

Examples of assigned technical credibility, cost and power density, and the FED-A reference parameters are given in Tables 7-5, 7-6, and 7-7, respectively. The scientific basis given in Table 7-5 is roughly consistent with the discussion of Chap. 4. The burn time factor is assumed to be 0.1 for a 100-s inductively driven burn, 1.0 for quasi-steady-state operation, and 10 for steady-state burn.

The current drive and heating scenarios with the highest merits as defined above are given in Table 7-8. Although the assumptions of performance, credibilities, cost, and impact are somewhat arbitrary, the following observations are of interest.

1. Nine out of ten use LHRH due to its modest impact, high physics credibility, and engineering credibility.
2. The top three scenarios use modulated density with LHRH current drive due to quasi-steady-state operation and high physics and engineering credibility.
3. Eight out of ten use a weak transformer due to low impact, 1000-s burn time, and high credibility.
4. The order of merit for heating is ICRH, ECRH, and LHRH, due to lowest cost and highest credibility for ICRH, lowest usage of vacuum vessel area and good credibility for ECRH, and modest cost and vacuum vessel area usage for LHRH.

Table 7-3. Scenario summaries

Case	Scenario Designation	Start up Techniques						Drive to operating point Techniques						Maintenance Techniques						X = Full Time F = Full Transf. W = Weak Transf. N = No Transf. M = Multi-plexed P = Part Time * = If Q<∞ - = Negligible
		OH	EC	IC	LH	FW	REB	OH	EC	IC	LH	FW	REB	OH	EC	IC	LH	FW	REB	
	Heat Option	-	X	P						X						X*				
	Current Option																			
1.	1.0	F						F						F						
2.	2.1.1	W			X			W			P			W						
3.	2.1.2	W			X			W			P			W			P			
4.	2.1.3	W						W			X			W			X			
5.	2.2	W						W				P						X		
6.	2.3	W						W					P						X	
7.	3.1.1	N			X						X						X			
8.	3.1.2	N			X						P	P					X			
9.	3.1.3	N			X						P		P						X	
10.	3.2.1	N					X				P		P				X			
11.	3.2.2	N					X					P	P					X		
12.	3.2.3	N					X						X						X	
	Heat Option	-	X			MP		-				M		-				M*		
13.	1.0	F						F						F						
14.	2.2	W				MP		W				M		W				M		
15.	3.1.2	N			X			N			P	M		N				M		
16.	3.2.2	N					X	N				M	P	N				M		

Table 7-3 (continued)

Case	Scenario Designation	Start up Techniques						Drive to operating point Techniques						Maintenance Techniques						X = Full Time F = Full Transf. W = Weak Transf. N = No Transf. M = Multi-plexed P = Part Time * = If Q<∞ - = Negligible
		OH	EC	IC	LH	FW	REB	OH	EC	IC	LH	FW	REB	OH	EC	IC	LH	FW	REB	
	Heat Option	-	X					-	X					-	X					
(17)	1.0	F						F						F						
(18)	2.1.1	W			X			W			P			W						
(19)	2.1.2	W			X			W			P			W			P			
(20)	2.1.3	W						W			X			W			X			
(21)	2.2	W						W				P						X		
(22)	2.3	W						W					P	W					X	
(23)	3.1.1	N			X			N			X			N			X			
24.	3.1.2	N			X			N			P	P		N				X		
25.	3.1.3	N			X			N			P		P	N					X	
	Heat Option	-	X					-	X						X*					
	Current Option																			
26.	3.2.1	N					X				P		P				X			
27.	3.2.2	N					X					P	P					X		
(28)	3.2.3	N					X						X						X	
	Heat Option	-	X					-	P		P						X			
	Current Option																			
(29)	1.0	F						F						F						
(30)	2.1.1	W			X			W			P			W						
(31)	2.1.2	W			X			W			P			W			P			

Table 7-3 (continued)

Scenario Designation		Start up Techniques						Drive to operating point Techniques						Maintenance Techniques						X = Full Time F = Full Transf. W = Weak Transf. N = No Transf. M = Multiplexed P = Part Time * = If Q<∞ - = Negligible
Case		OH	EC	IC	LH	FW	REB	OH	EC	IC	LH	FW	REB	OH	EC	IC	LH	FW	REB	
	Heat Option	-	X					-	P		P						X			
	Current Option																			
(32)	2.1.3	W						W			X						X			
(33)	2.2	W						W				P						P		
34.	2.3	W			X			W					P						X	
(35)	3.1.1	N			X						X						X			
(36)	3.1.2	N			X						P	P						X		
37.	3.1.3	N			X						P		P						X	
	Heat Option	-	X					-	P		P			-			X			
	Current Option																			
(38)	3.2.1	N					X				P		P				X			
(39)	3.2.2	N					X					P	P					X		
(40)	3.2.3	N					X						X						X	

Table 7-4. Evaluation criteria

1. Potential performance (e.g., burn time)
2. Technical credibility (including scientific and technological basis)
3. Impact on device interface (e.g., access requirement)
4. Impact on device cost

Table 7-5. Technical credibilities assigned to various current drive and heating techniques

	Scientific basis	Technological basis	Technical credibility
REB	0.1	0.1	0.01
LHRH current maintenance	0.2	1.0	0.2
LHRH current start-up	0.8	1.0	0.8
LHRH bulk heating	0.5	0.8	0.4
ICRH bulk heating	1.0	1.0	1.0
ECRH start-up heating	1.0	1.0	1.0
ECRH bulk heating	0.8	0.8	0.64
Transformer	1.0	1.0	1.0
FWIC current maintenance	0.1	0.8	0.08
FWIC bulk heating	1.0	1.0	1.0

Table 7-6. Cost, power density, and efficiency assumptions used for current drive and heating

1.	Capital cost	ECRH	6 $/W	
		LHRH	3 $/W	
		ICRH	1.5 $/W	
		REB	0.9 $/W	
2.	Power density	ECRH	10 kW/cm^2	
		LHRH	5 kW/cm^2	
		ICRH	2 kW/cm^2	
		REB	0.25 kW/cm^2	
3.	Efficiency			
	Heating	ICRH	3-6 eV/kW·10^{13}	Assumed 3 eV/kW·10^{13} for the study
		LHRH	2-3 eV/kW·10^{13}	
		ECRH	3 eV/kW·10^{13}	
	Current drive	FWIC	0.2 A/W	Assumed 0.1 A/W for the study
		LHRH	0.1-2 A/W	
		REB	2.25 A/W	
		ECRH	0.1 A/W	

Table 7-7. FED-A plasma parameters

Temperature	10 keV
Density	$1.6 \cdot 10^{14}$ cm^{-3}
Q	∞
P_{fusion}	255 MW
Plasma current	4 MA
Start-up (ECRH)	
Power	3.5 MW
Frequency	120 GHz
Bulk heating power (LHRH)	25 MW
Start-up current drive	
Power	20 MW
Frequency	1-3 GHz
Maintenance current drive	
Power	25 MW
Frequency	1-5 GHz

Table 7-8. Current drive and heating approaches with highest merit

Rank	Merit	Current drive technique	Heating technique	Transformer
1	2.0	Modulated n_e LHRH	ICRH	Weak
2	1.1	Modulated n_e LHRH	ECRH	Weak
3	0.85	Modulated n_e LHRH	LHRH	Weak
4	0.55	High n_e LHRH	ICRH	Weak
5	0.46	High n_e LHRH	ECRH	Weak
6	0.41	FWIC	FWIC	Weak
7	0.33	All n_e LHRH	ICRH	No
8	0.25	Low n_e LHRH	ICRH	Weak
9	0.24	All n_e LHRH	ECRH	No
10	0.24	FWIC, high n_e LHRH	ICRH, LHRH	Weak

Reassessment of the merits of various current drive and heating scenarios should continue as additional technical understanding is obtained in the R&D programs.

7.3 EQUIPMENT CONFIGURATION

The systems evaluated as part of the scenario assessments discussed in Sect. 7.2 are described. Each configuration is an example of the equipment required to perform either the current drive or the heating function. Emphasis has been placed on current drive, since heating systems were covered in some detail last year for FED. Based on this year's effort, the primary current drive approach, LHRH, was a good choice and will receive the most attention. The secondary options are FWIC and REB. The electron cyclotron heating (ECH) and current drive system should be similar in nature to the ECH system described in the 1981 FED Baseline concept[2] and is not discussed here. Following discussion of the current drive options, there is a review of the heating options.

7.3.1 Lower Hybrid Current Drive Design Concepts

This description outlines the FED-A preconceptual design. After a brief summary of the requirements, the discussion proceeds with a description of the device-launcher interface design, considerations of the launcher design (sizing and arrangement), rf generator design, and array modeling. The discussion concludes with a brief review of engineering concerns associated with LHRH implementations on large devices such as FED-A and INTOR.

Requirements

The requirements for the current drive start-up and maintenance functions are given in Table 7-9. The frequency ranges for the two functions are different enough to require two separate systems. Both system polarizations are set parallel to the toroidal field and launch

Table 7-9. Reference working parameters for FED-A current drive

Description	Start-up	Maintenance
Lower hybrid current		
Rise time	20 s	Steady state
Power	10-20 MW	25 MW
Position	Top or bottom	
Frequency	1-3 GHz	1-5 GHz
Mode	Ordinary	
Others (REB, FWIC, ECH)	TBD[a]	TBD

[a] To be determined.

the slow wave. A top or bottom launch is preferred. A bottom launch position is probably precluded by the presence of the limiter. In addition to these requirements, there are the guidelines and assumptions in Table 7-10.

Interface design description

Figure 7-1 shows three views of the device-launcher interface. Starting at the plasma, there is a bend of $\sim 45°$ to allow ingress through the plasma shell. This provides a "near-top" launch and leaves the shell support structure intact. Following this first bend, there is a straight section that penetrates ~ 1 m of nuclear shield. At this point there is a right-angle bend downward. Behind the 1-m shield, the straight section contains a vacuum break (rf window). Here, the neutron flux is reduced by $\gtrsim 2$ orders of magnitude to $\sim 4 \times 10^{12}$ n/cm^2•s. A beryllium oxide (BeO) window should not reach the radiation damage threshold for a few full power years. This neutron flux attenuation is lowered by the water-and-steel composition of a high percentage of the launcher volume and its support structure. Two subsequent 90° bends in the waveguide structure effect an exit through the vacuum boundary just above the limiter. This series of bends through the shield is sufficient to reduce the neutron flux to $\lesssim 10^5$ n/cm^2•s and removes the need for further shielding of the waveguide.

The 192 waveguides are grouped in subarrays of 8 elements each (see Fig. 7-2). The connectors at the vacuum boundary and the windows are planned to be an 8-channel assembly. Maintenance of the launcher is on a subarray basis. To gain access to some of the inner subarrays, disassembly of the outer subarrays will be required. These 8-channel assemblies will be formed to the required contour with flanged connections only at the rf window and at the vacuum boundary outside the shield. For the FED-A, the "patch" between these connectors and the floor-mounted panel is done with flexible waveguide. This floor penetration is behind the outboard leg of the TF coil between the limiter access areas. This patch connection was arranged to allow accessibility to

Table 7-10. LHRH guidelines and assumptions

Description	Value
Maximum power density	5-10 kW/cm^2
Element size	1.1×12 cm^2
Plasma edge density slope	$\sim 10^{11}$-10^{12} cm^{-4}
Neutron flux at the plasma shell	$4 \cdot 10^{14}$ $n/cm \cdot s$

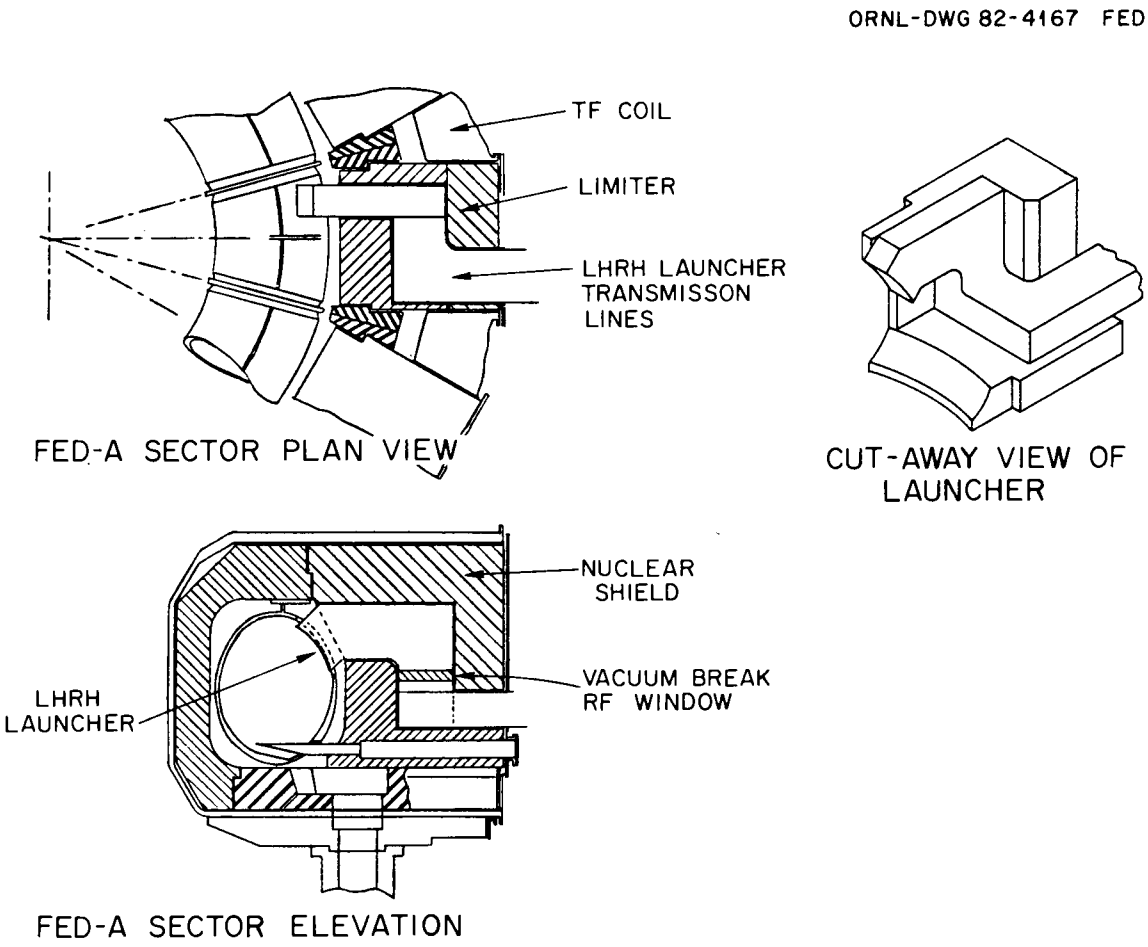

Fig. 7-1. A top launch interface for current drive on FED-A.

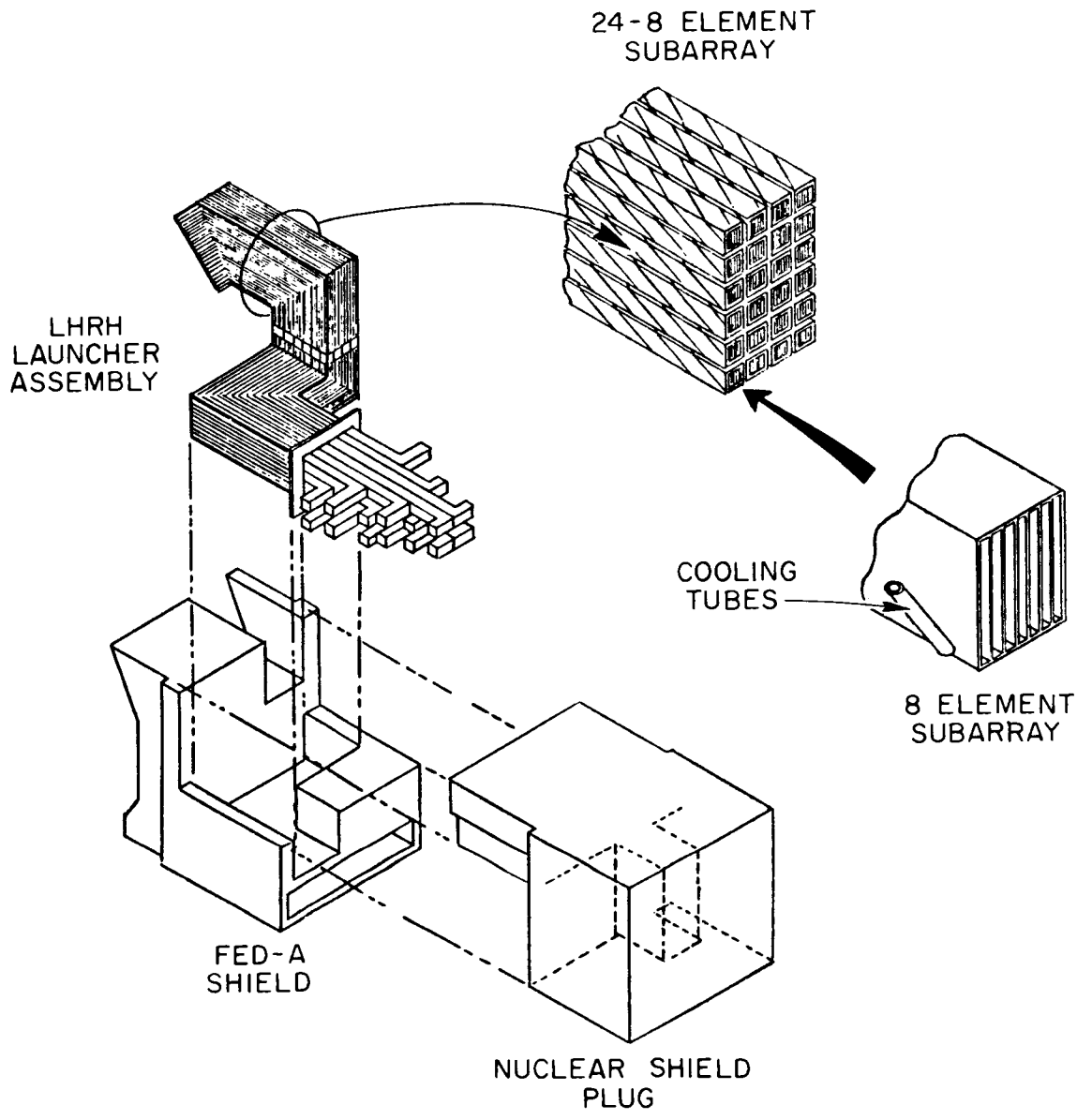

Fig. 7-2. Details of the LHRH current drive launcher assembly.

each 8-channel connector without disturbing others. Below the floor, outside the reactor room/hall, the 192 waveguides can be combined into 32 waveguides with 6-way dividers, each driven by a separate klystron.

Launcher design considerations

Experimental results on PLT and Alcator indicate that power densities of 5-10 kW/cm^2 are reasonable for LHRH at these frequencies. A conservative approach assuming only 5 kW/cm^2 was used for the FED-A design concept. Design problems in routing a large number of waveguides through a thick (>1-m) shield, as required for FED-A, make minimizing the size and number of connections a critical consideration. Although window failures from radiation damage are not expected to be a problem, the launcher should be designed to allow replacement of the window in the hot cell. This suggests a single flanged connection for a block of waveguides. This approach is proposed.

Launcher sizing and configuration

Table 7-11 gives the characteristics of the LHRH system. The port sizing for the current maintenance function was done as follows. Dividing the 25 MW required by the maximum power density, 5-10 kW/cm^2, gives an element area of 2500 to 5000 cm^2. Assuming each element has an area of approximately 13 cm^2, it takes 192 to 384 elements. Figure 7-3 shows one candidate layout for 192 elements using subarrays. Two such ports are employed. There are four 8-waveguide subarrays (grills) arranged in a line (line array). The spacing between these subarrays is 2.8 cm (equivalent to two elements). In the orthogonal (poloidal) direction there are six of these line arrays, again spaced 2.8 cm apart. This spacing allows space for structure and a 1-cm-OD cooling line around each subarray bundle of eight waveguides. The aspect ratio (toroidal width to poloidal height) could be increased, since there is ample additional space between TF coils (see Fig. 7-1); however, this would sharpen the spectrum ($\Delta n_{\parallel}$) and might reduce the current drive efficiency. With such a large number of waveguides, there is concern

Table 7-11. LHRH current drive characteristics

1.	Function	Start-up	Maintenance
2.	Power	20 MW	25 MW
3.	Pulse length	10-20 s	>1000 s
4.	Frequency	1-2 GHz	2-2.5 GHz
5.	Launcher mode	0	0
6.	Launcher position[a]	Top or bottom	Top or bottom
7.	Launcher type	Grill	Grill
8.	Launcher size, W × H	0.021 m × 0.22 m	0.011 m × 0.12 m
9.	Number of launchers/port	12	24
10.	Number of ports	1	2
11.	Phasing (waveguide to waveguide)	∿90°	∿90-120°
12.	Launcher power density	∿5 kW/cm^2	∿5 kW/cm^2
13.	Transmission line	3.5 × 22 cm^2 waveguide	1.1 × 12 cm^2 waveguide
14.	rf generator	40 0.5-MW klystrons	24 0.5-MW klystrons/port

[a]Position with respect to the plasma edge is also needed.

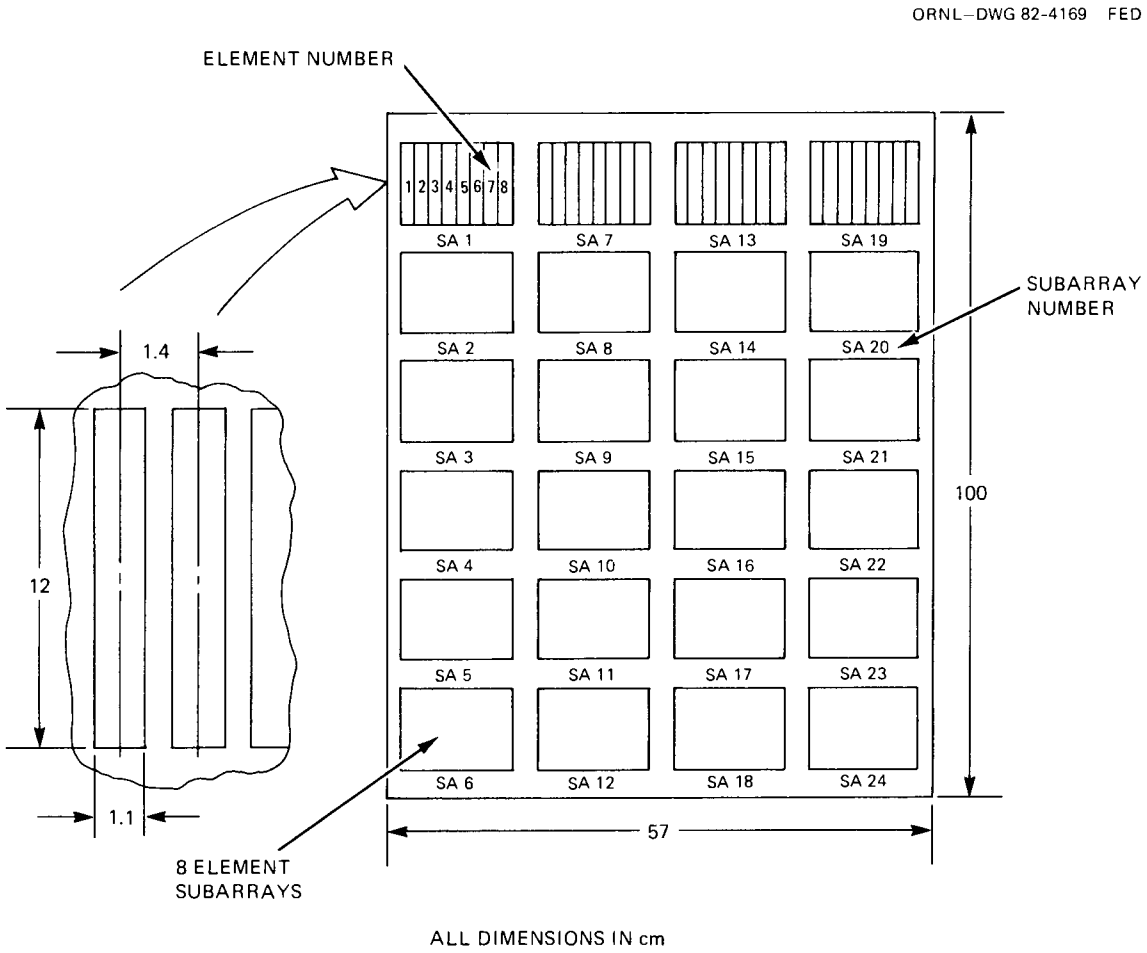

Fig. 7-3. An array of subarrays form the LHRH launcher port.

about the most effective way to connect them to the rf generator. Repair of the launcher assembly elements will involve significant disassembly. Array operation should therefore sustain failure of one or more elements. This is the desirable quality of graceful degradation and is dependent on the rf power amplifier connections.

Power amplifier arrangement

The arrangement of subarrays lends itself well to a modular connection of a number of modest power level amplifiers. For FED-A, the availability of these amplifiers in the near future was a consideration. This arrangement was compatible with a klystron size (500 kW) that could supply six elements from a single tube. It takes 32 of these tubes to drive the 192 elements. There is one tube allocated to each column of four sectors, as shown in Fig. 7-4. Figure 7-5 shows details of such an arrangement. Note that a klystron drives one element in each of six subarrays. With this arrangement, the impact on the grill's spectrum from a klystron failure is small. The phase advance between neighboring elements of the grill is commanded in columns by a single lower power phase shifter at the input of each of the klystrons. These 32 klystrons, at 500 kW each, supply $\sim$16 MW, less losses. Two such arrays or ports will provide $\gtrsim$25 MW to the plasma. (Note that in the arrangement of Fig. 7-4, there is a space between subarrays. This is assumed to be the equivalent of two elements. This space is used for structure, cooling headers, etc. With this spacing between subarrays, the klystron phase-shifts by the equivalent of two elements between subarrays, so the phase of klystron 1A leads, by $10\Delta\phi$, the phase of klystron 1B.)

Driver and modulator arrangements

From the standpoint of failure effects, the driver configuration that provides excitation to the 32 klystrons must be given special attention. One driver could supply eight klystrons (equivalent to a full sector). Losing a driver would result in one-quarter of the elements being down. This can be avoided by using the same set of four

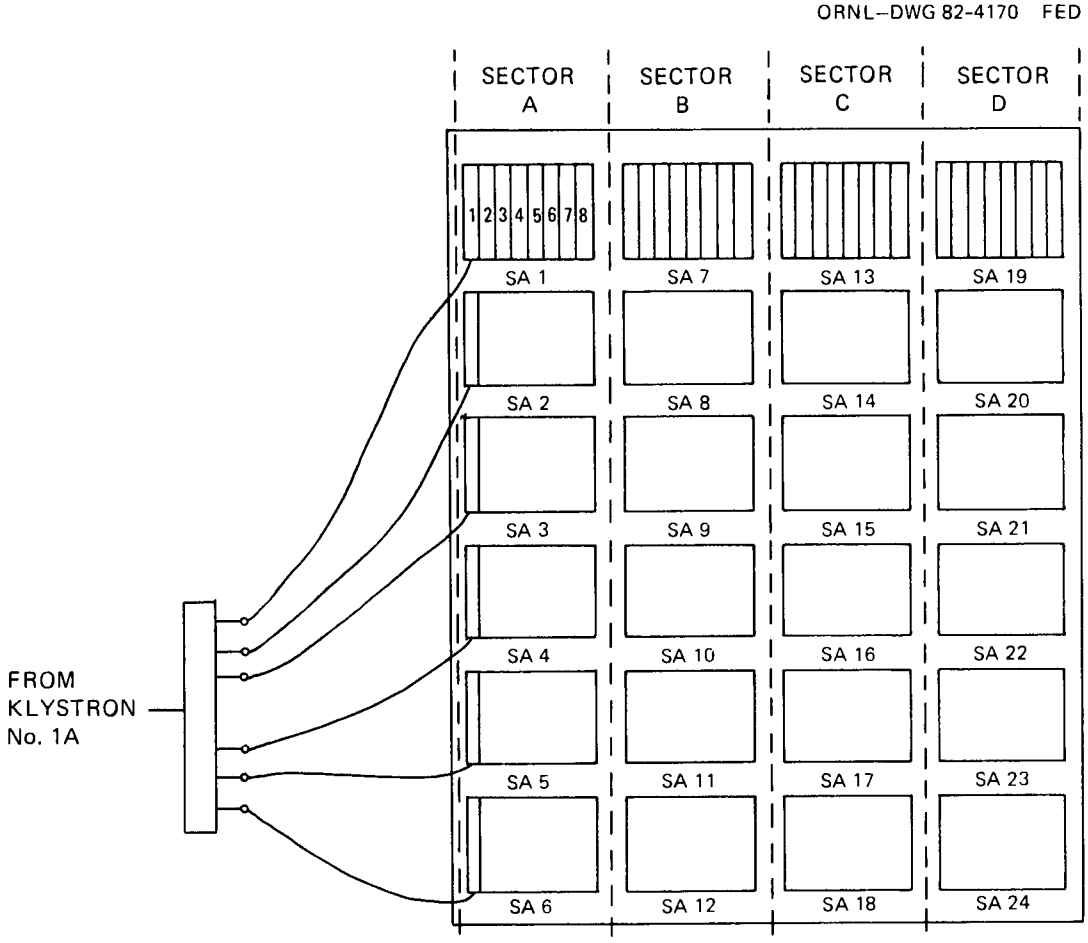

Fig. 7-4. Klystrons assigned to sectors.

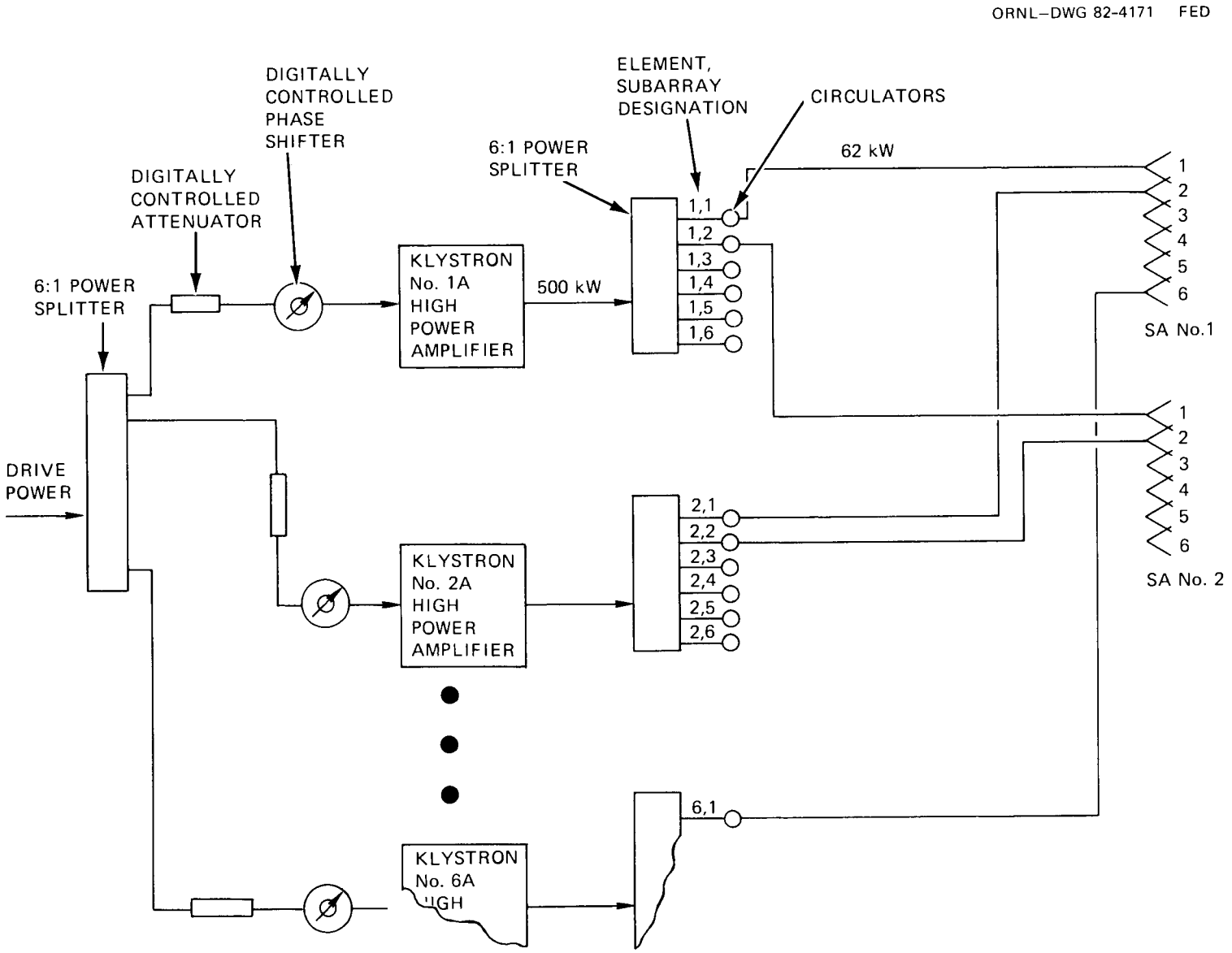

Fig. 7-5. Klystron connections are chosen to enable use of simple, low power phase shifters.

drivers connected as shown in Fig. 7-6. Each sector excitation output is derived from two driver amplifiers. A loss of one driver amplifier results in only a reduction (6 dB) in the drive level, not a complete loss of drive to a sector. Since the high power klystron amplifiers are operated in saturation,* a reduction in drive level can be tolerated.

There are separate modulators for each klystron, as shown in Fig. 7-7. One power supply feeds four klystrons. The loss of a modulator takes out one element in every subarray of a single sector (six elements). A power supply failure takes out one element of each subarray in all sectors (24 elements).

Array modeling

In this preconceptual design effort, the choice of element (waveguide) width, element spacing, and array extent (in both the poloidal and toroidal directions) was considered. The approach taken was to arrange the 192 elements as described above, based on experience and judgment, and then to examine this configuration with computer models. For example, some modeling of current drive efficiency versus spectral width of the main response has been done.[3] Indications are that a $\Delta n_{\parallel} \gtrsim 0.1$ is reasonable, if not optimum. More work is needed to determine an upper bound. The baseline arrangement has a spectral width of 0.2. No conclusions have been made about the correlation of spectral width and heating, nor has the impact of spectral width in the orthogonal direction been investigated. For the baseline arrangement, since the array extent is 50% larger in the poloidal direction, the spectral width will be correspondingly less. The choice of element spacing has not been evaluated quantitatively for its impact on current drive efficiency. There are engineering advantages to wider element spacing; fewer, but larger, waveguides would simplify the launcher assembly. However, a large element spacing has an ambiguous response closer to the desired

*Amplifier drive is set beyond the linear range of the output tube.

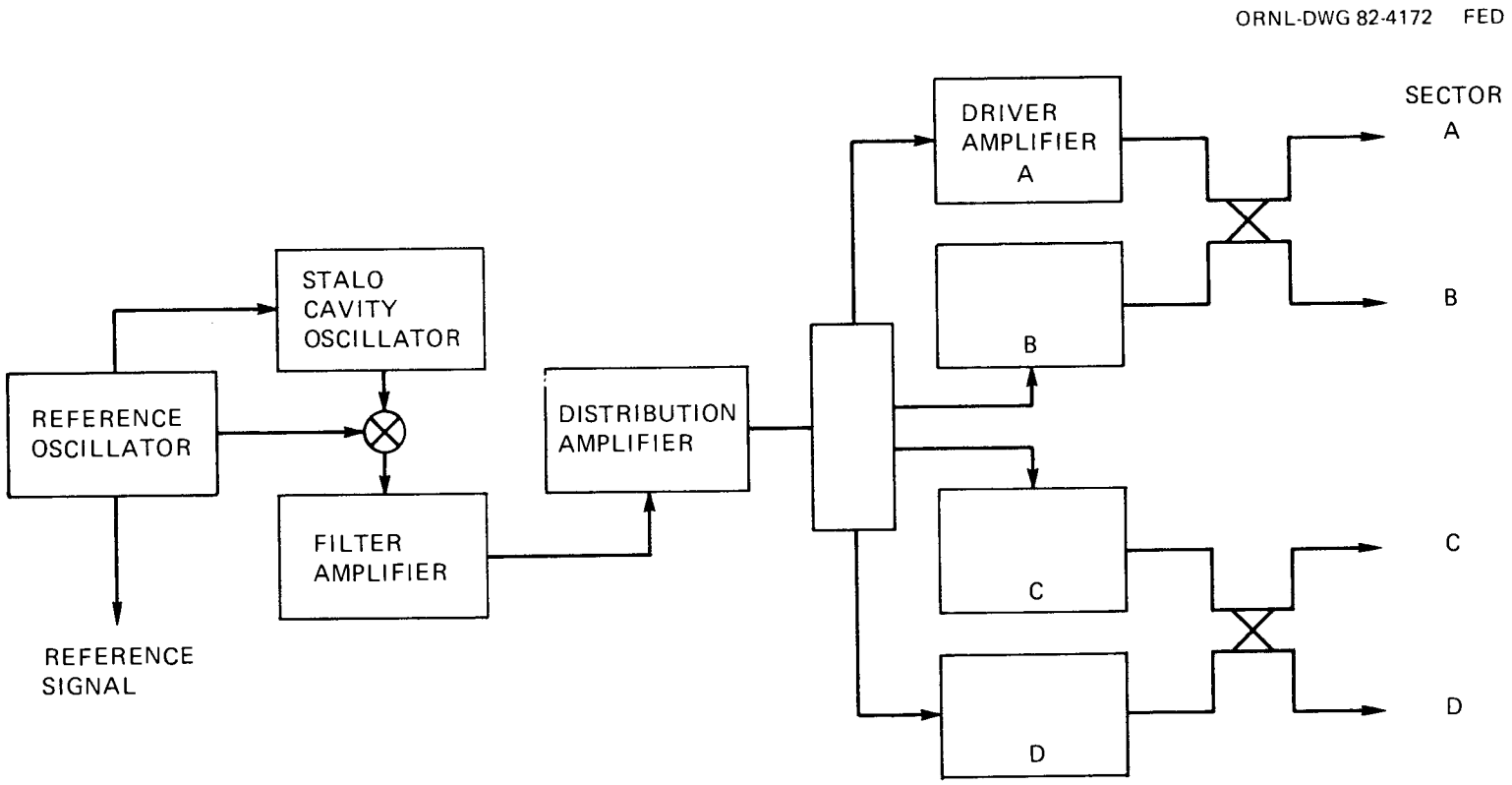

Fig. 7-6. LHRH exciter configuration for inherent redundancy.

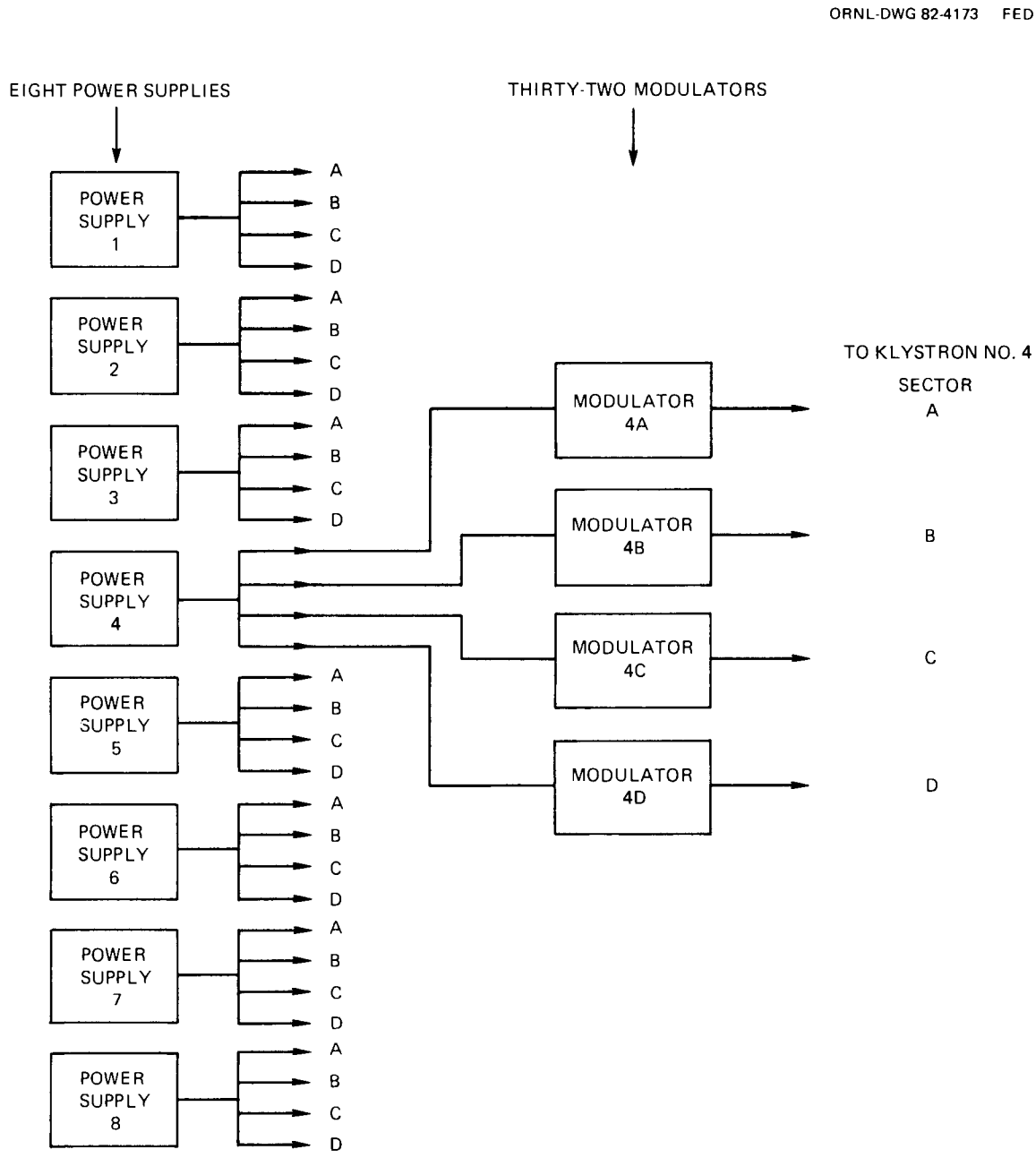

Fig. 7-7. Power supply. Modulator arrangement features individual control.

response in $n_{\parallel}$ space. Since these ambiguous responses can drive current in the wrong direction, it is important that they be positioned where they have minimal impact. These considerations and others, including failure effects, were evaluated using Brambilla grill[4,5] theory and a parametric study.

Figure 7-8 shows a line array of subarrays (one row from the LHRH launcher port) with their excitations in phase and amplitude. The phase function is shown as a linear ramp. In the implementation, the phase is set with a modulo 2π; that is, $\phi = \Phi - 2\pi n$, so that a phase of $9\pi/2$ is equivalent to $9\pi/2 - 2\pi n = \pi/2$ for $n = 2$. Note that the spaces between the subarrays are modeled as elements with zero amplitude and the phase function continued. By superposition, the array of subarrays will have a spectrum from a 38-element array with all elements with an amplitude of 1 plus that of an array of six elements (representing the missing elements) with an amplitude of -1. (This missing element array is shown in Fig. 7-9.) The spectrum for the array of subarrays at cutoff point ($\omega_{pe} = \omega$) is shown in Fig. 7-10. The main (desired) response is at $n_{\parallel} = 2.2$ for the proposed element spacing and a differential phase of $\pi/2$. The missing element array's spectrum is shown in Fig. 7-11. Here $n_{\parallel} = 0.44$ results from an average elemental phase differential of $\pi/10$. Note that this peak also appears in the spectrum for the array of subarrays as a secondary peak, still at $n_{\parallel} = 0.44$, but its amplitude is only $\sim$0.035 compared to unity for the desired response. This relative amplitude is due to the difference in (1) the number of elements in this array (6 vs 32) and (2) the element response at $n_{\parallel} = 0.44$ vs $n_{\parallel} = 2$.

This modeling of subarrays gives insight into failure effects analyses. In a like manner, the impact on the spectrum due to a failure of a klystron would be secondary responses and a loss in the peak of the main response by a factor equal to the number of active elements divided by 32.

The response of the grill with failed components is dependent on the makeup of the grill's spectrum. The spectrum is the product of three spectra: those of the element, the subarray, and the line array. A pictorial representation of these responses is shown in Fig. 7-12.

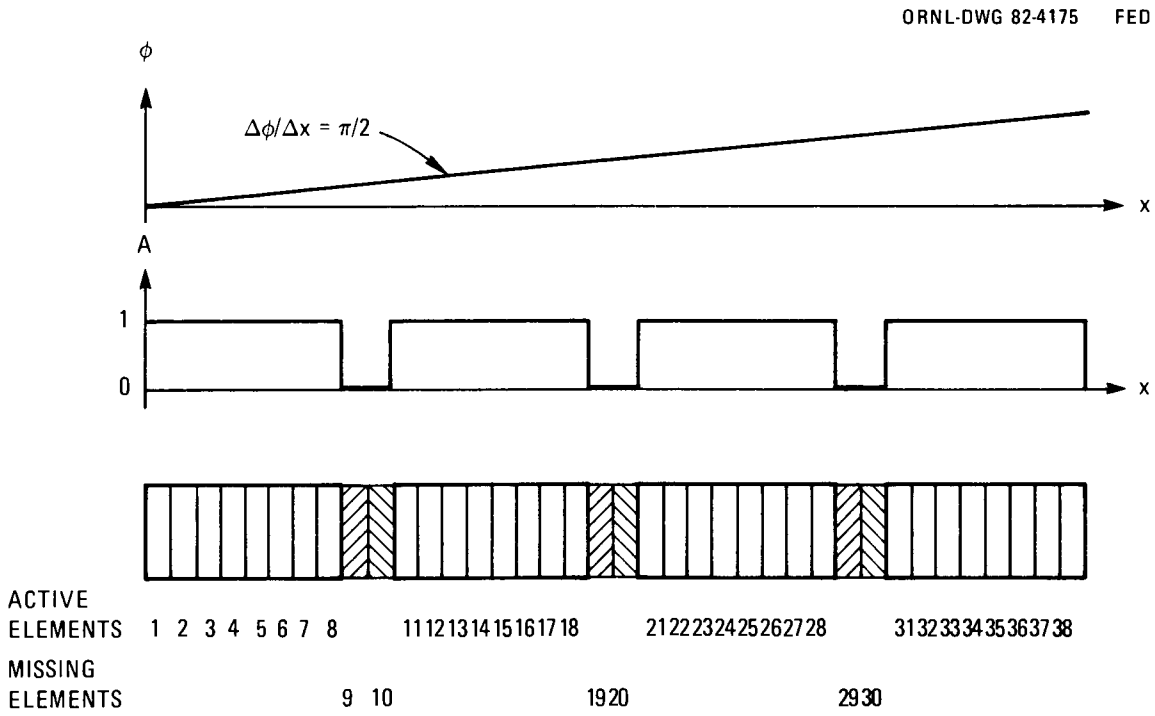

Fig. 7-8. One row of the launcher port is modeled.

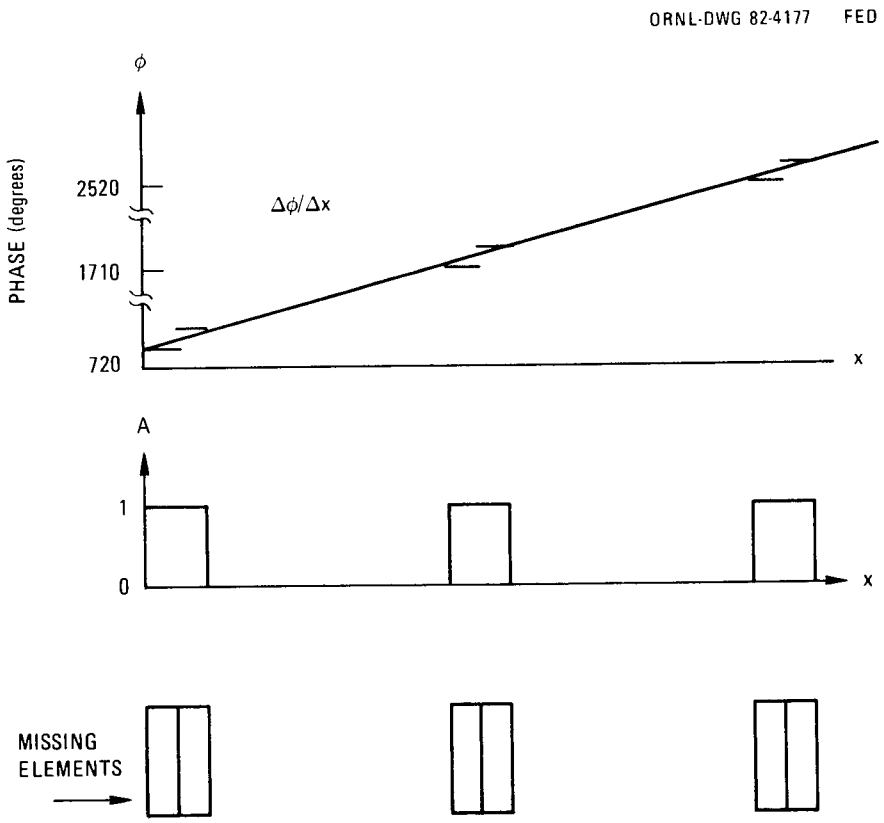

Fig. 7-9. Spaces corresponding to missing elements form the array modeled here.

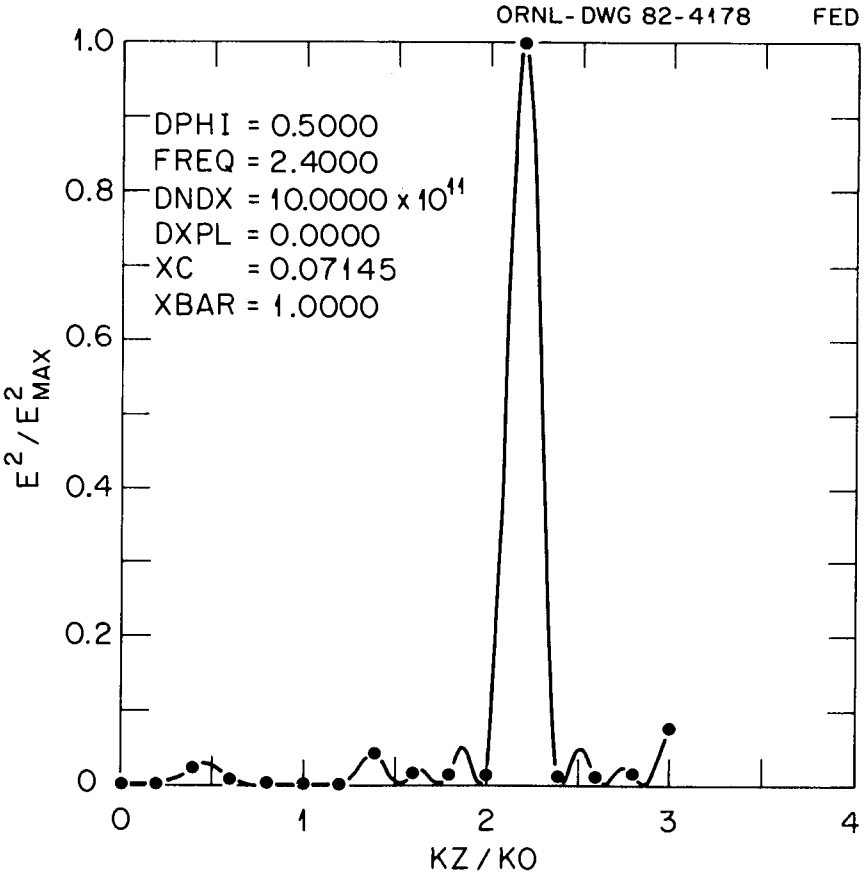

Fig. 7-10. A sharp spectrum is formed by the LHRH current drive launcher.

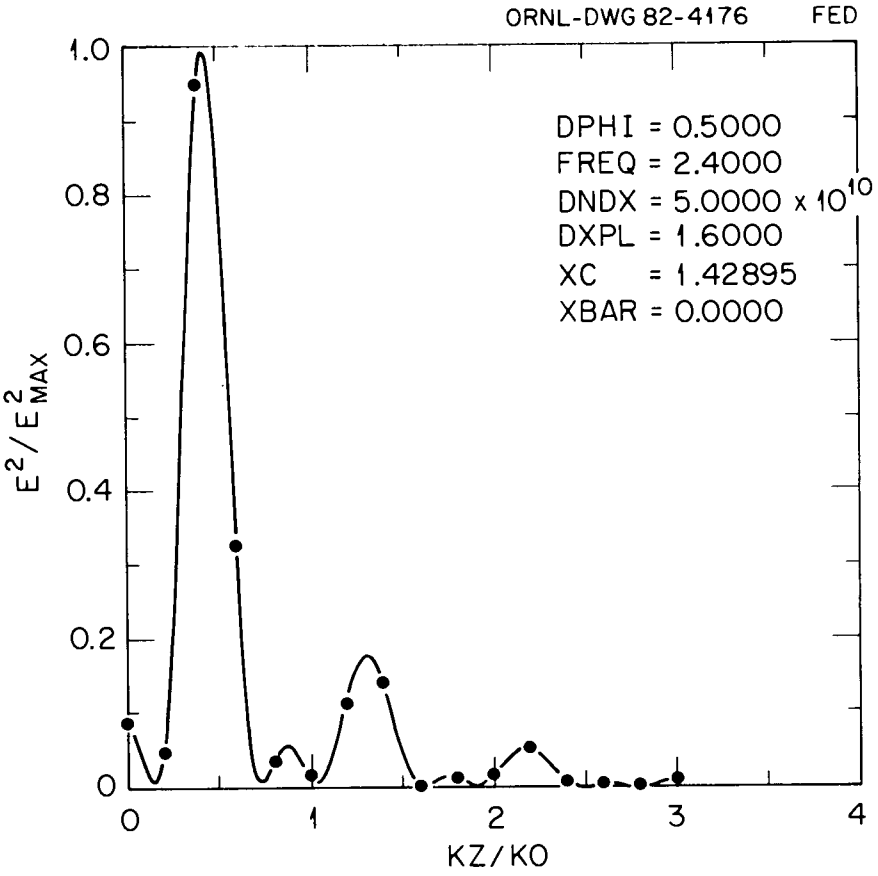

Fig. 7-11. The missing element array's spectrum is centered at 0.44.

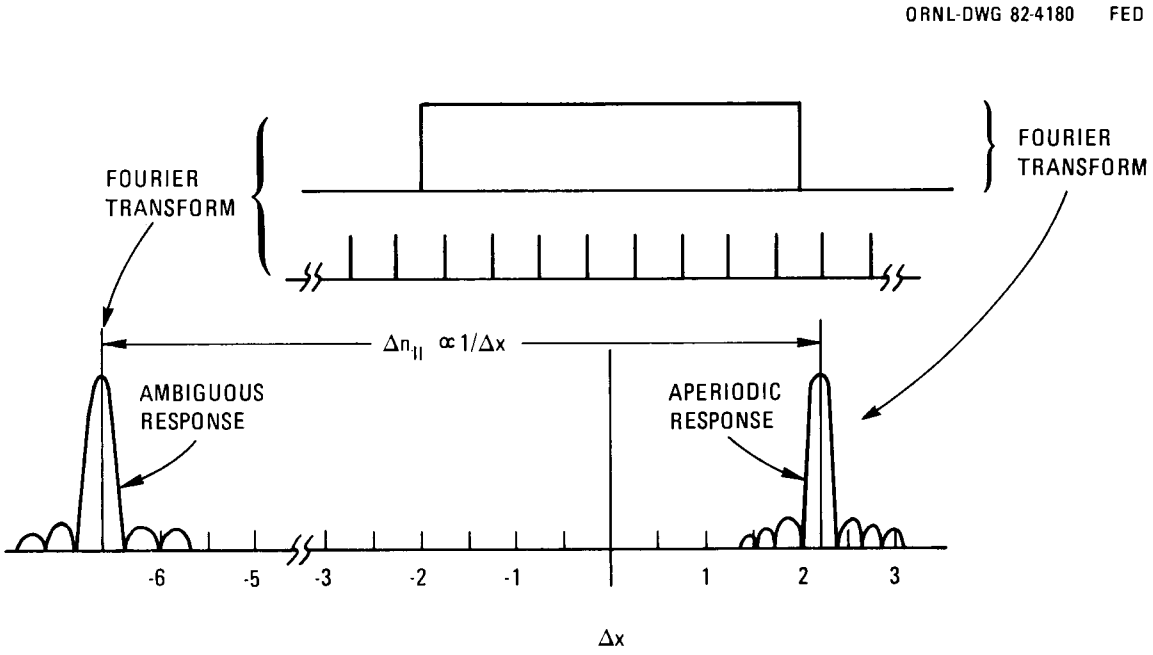

Fig. 7-12. Ambiguities result from a sampled aperture.

The spectral width of each is inversely proportional to the aperture width. Note that the element is modeled here as a delta function (infinitely thin aperture), the Fourier transform of which is isotropic response. (In practice, the element has a width $\sim$ 1.1 cm.) The fallaway from the isotropic pattern modeled for $n_{\|} > 1$ is due to the presence of the evanescent region. The element response does not steer. It is fixed and centered at $n_{\|} = 0$. The subarray pattern does steer, and since it has an aperture corresponding to only eight elements, it has a main response width $\sim$4 times that of the line array and lower amplitude. Finally, the line array response is the summation of 4 subarrays with the aperture extent of 38 elements and has a correspondingly sharp response in $n_{\|}$ space. As the array is steered away from $n_{\|} = 1$, the response is expected to decrease following the element's response. Any spurious responses due to failed elements are also modified by the multiplication of the element response. A spurious response such as the secondary peak of the missing element pattern noted above is enhanced if it falls higher up ($n_{\|} = 0.44$) on the element pattern than the desired response ($n_{\|} = 2.2$).

In the design of a grill (array) there is a choice of element spacing to be made. Two elements spaced far apart, equal to the 38-element spacing, could have a main response as sharp as that of the full 38-element array. This would not be a satisfactory configuration, however, because of the large number of ambiguous responses (see Fig. 7-13). The spacing between ambiguities is inversely proportional to the element spacing. This point is conveyed in Fig. 7-12. Note that the ambiguous response could drive current in the wrong direction (compared to that of the desired response). For the baseline array, the element spacing was chosen to be 1.4 cm or 0.112 wavelengths at f = 2.4 GHz. This places the ambiguity far away at $n_{\|} = -6.6$. At this position the element response and/or evanescence attenuates the ambiguity. Landau damping takes place on any residue and no significant counter-current is generated. Figure 7-14 shows a comparison of the ambiguous response for two spacings.

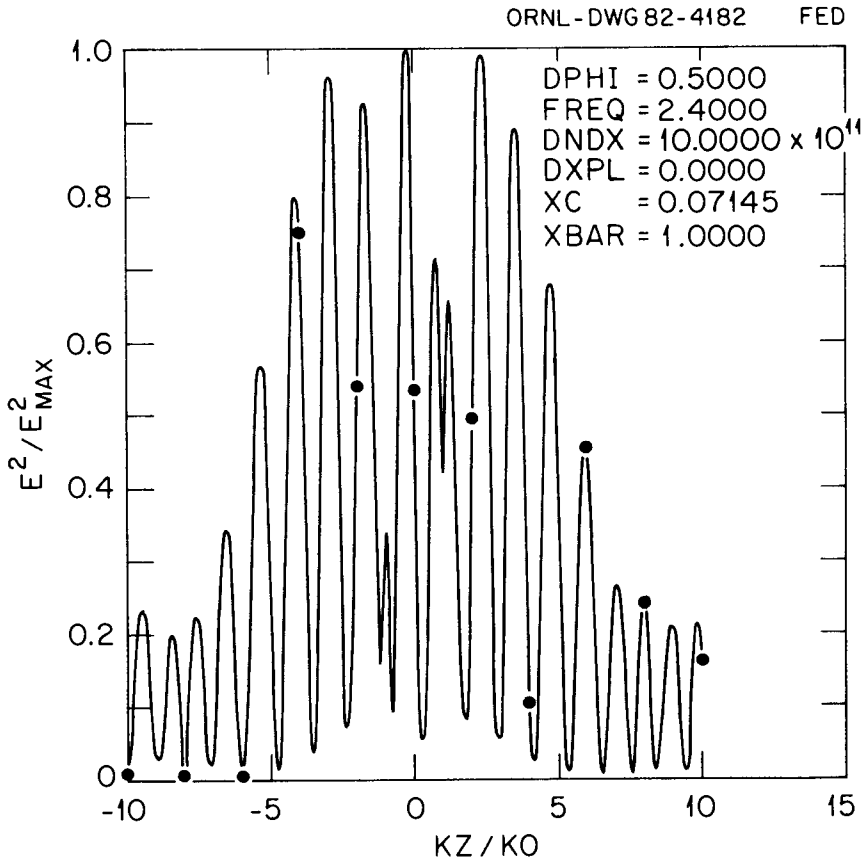

Fig. 7-13. A 2-element array has the same $\Delta n_{\|}$ but many ambiguities.

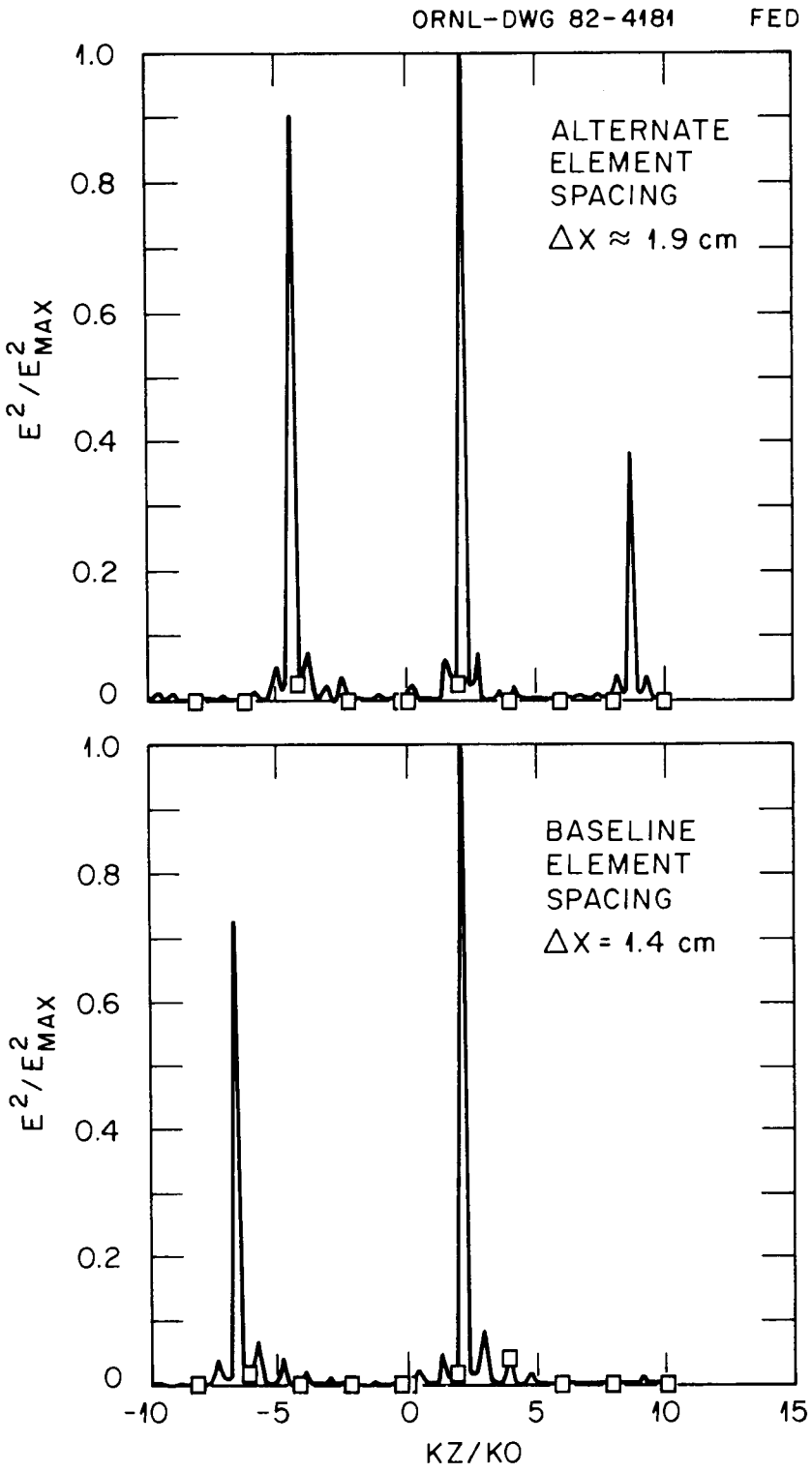

Fig. 7-14. Increasing the waveguide spacing moves the ambiguous response in closer.

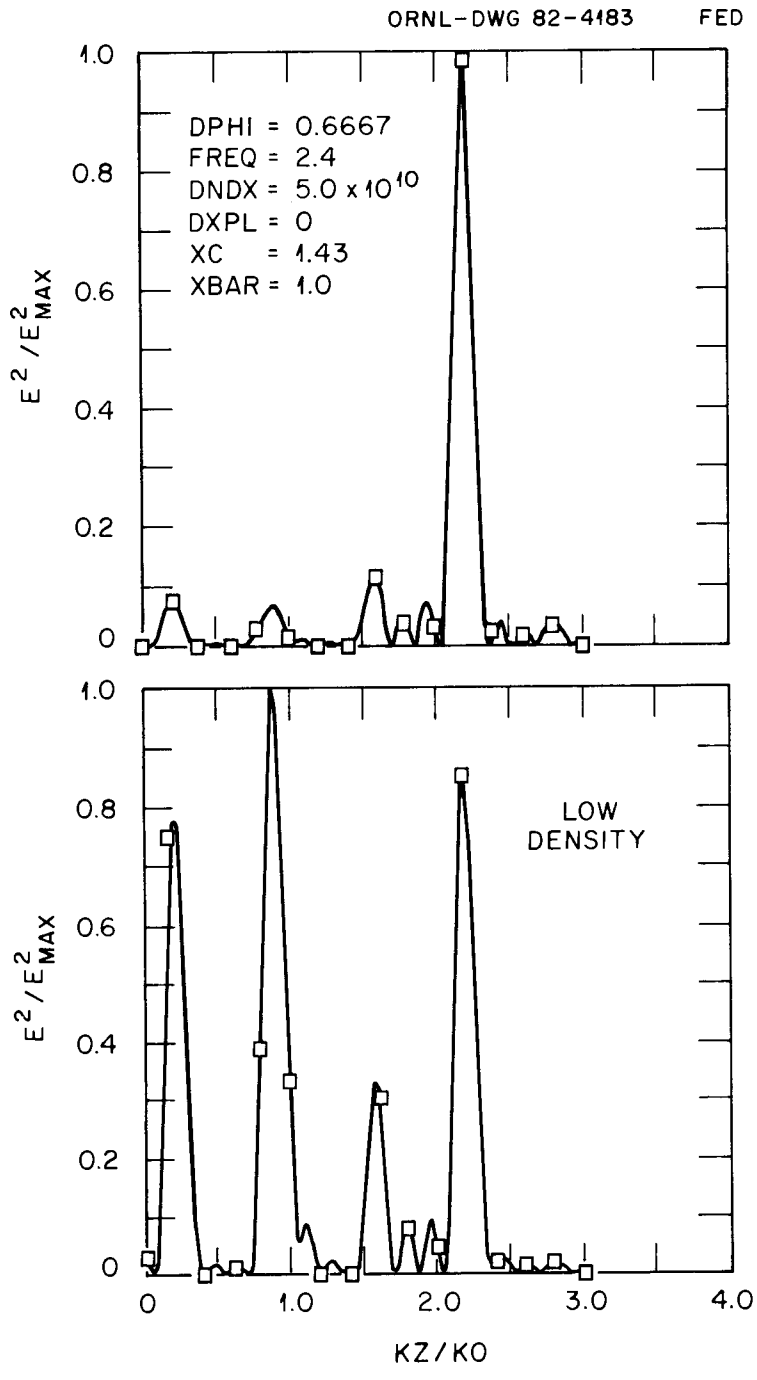

Fig. 7-15. Low edge density degrades the launcher spectrum.

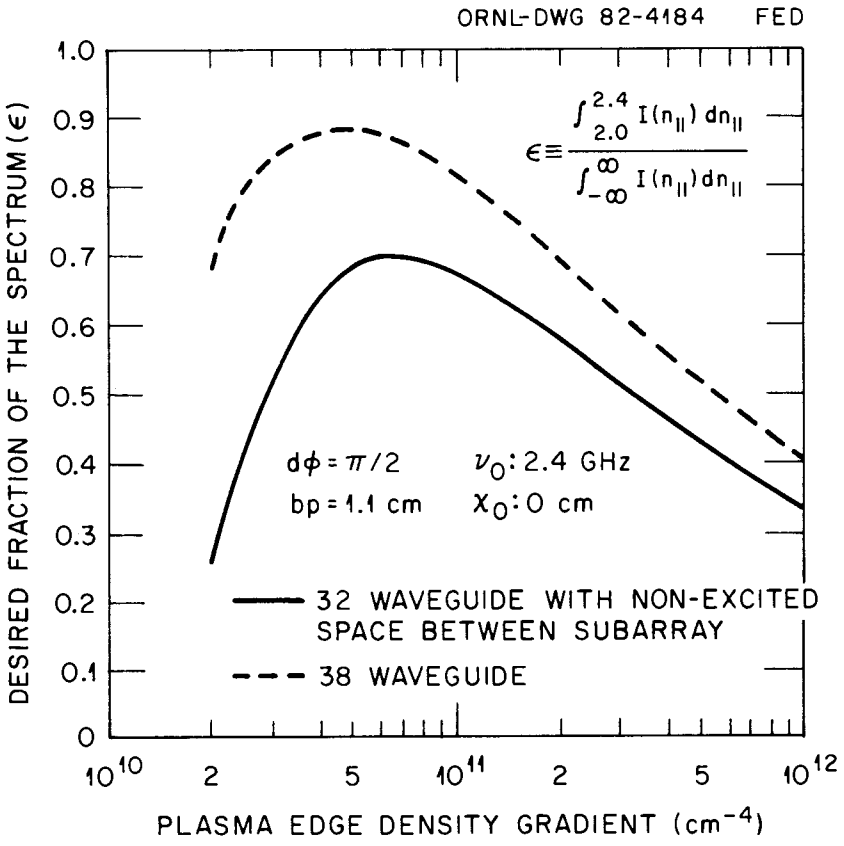

Fig. 7-16. Optimum coupling occurs at a plasma edge density of $\sim 10^{11}$.

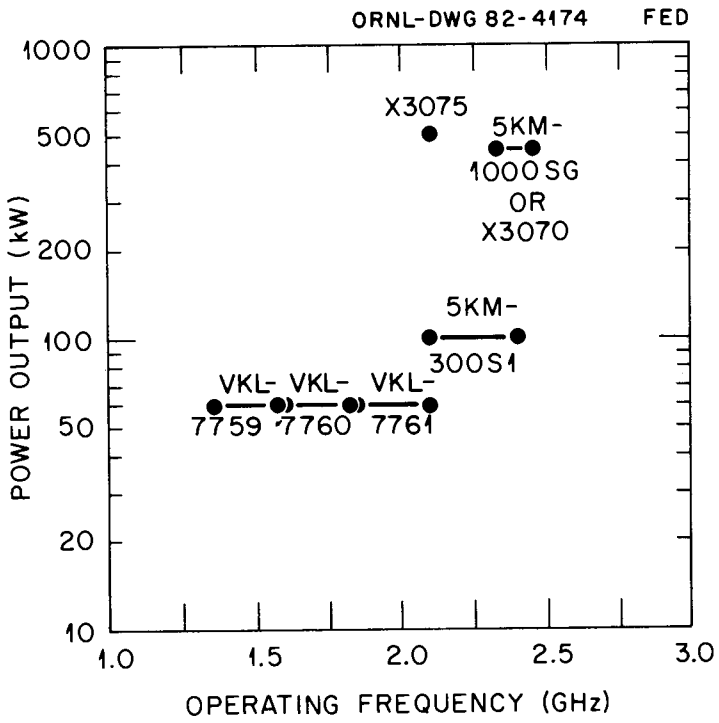

Fig. 7-17. Frequencies available in high power tubes. High power klystron availability is a concern.

Table 7-12. FWIC current drive system characteristics

	Value
Function	Current maintenance
Power	35 MW
Pulse length	>1000 s to steady state
Frequency	∿200 MHz
Launcher mode	X
Launcher type	Interleaved ridge-loaded waveguide phased at 90°
Launcher size, W × H	∿1.0 m × 1.5 m
Number of launchers	2-4
Launcher power density	TBD[a]
Transmission line	9-in. coax
rf generator	TBD (tube development)
Launcher position	Midplane

[a]To be determined.

An important point in the design of the current drive system has to do with the array position with respect to the plasma. For FED-A, the density 8 cm away from the plasma edge is $\sim 10^{12}$. At this point, the particle and heat fluxes are low enough to expect survival of the launcher. The coupling is good. At very low densities, near the shell wall, the coupling to the slow wave diminishes, and spurious responses due to spacing between the subarrays or failed elements grow in relative amplitude (see Fig. 7-15). Hence the launcher should be positioned in the plasma edge region, where the density is at least 10^{11} or 10^{12}. Figure 7-16 shows the impact of edge density on coupling to the desired spectrum.

Engineering concerns

From an engineering standpoint, the LHRH regime has few concerns because most components are available. One possible exception is the klystron. There are a limited number of frequencies available in high power tubes (see Fig. 7-17). Beyond this small set, tubes must be developed. In most cases this amounts to the scaling in frequency of an existing design. Vacuum breaks or rf windows have been developed for nonreactor applications like PLT, which uses an alumina window. For FED-A, a similar approach using a beryllium oxide window positioned beyond a shielded bend in the waveguide is proposed. The material and brazing technology are available, and only the specific configuration is needed for the design.

7.3.2 Fast Wave Ion Cyclotron Current Drive Design Concepts

Fast wave ion cyclotron (FWIC) current drive couples to electrons, and therefore its title is something of a misnomer. The frequency ($\sim$200 MHz) used is well above the ion cyclotron resonance frequency. Table 7-12 summarizes the requirements for FWIC. The required power level is higher (35 MW vs 25 MW). A small grill with a steering capability is required. The polarization is perpendicular to the toroidal field. Current maintenance is thought to be the only practical task for

FWIC at this time. The wave can be launched from the outboard wall at the midplane. The requirements, with the exception of frequency, are enough like those of ICRH to suggest multiplexing the two functions through a single set of launchers.

Figure 7-18 shows the configuration developed for FWIC current drive. Each 3-MW module requires four RCA 6950 power tetrodes. Low power phase shifters (digitally controlled) are used to set the differential phase for steering the spectrum to the desired $n_{\|}$. Two modules are combined to drive a single element at approximately 5 MW. These elements are interleaved ridge-loaded waveguides (suggested by F. Perkins, PPPL).[6] The launchers can be arranged in one or two pairs per window. Because one of the two elements is inverted (with respect to the other) the phase must also be inverted (180°). This phase shift is in addition to any differential phase that is required for steering. The spectrum in $n_{\|}$ of the launcher will be rather wide since the aperture is a fraction of a wavelength. With 10 MW per 2-element launcher, it takes about four sets of launchers to inject the specified 35 MW. Four sets of modules require 64 high power tubes (RCA 6950).

A brief survey of high power tubes was taken, and the results are plotted in Fig. 7-19. The only tube that could meet the requirements was the RCA 6950. There are two engineering concerns with this situation. First, this tube is about 20 years old and could be improved in efficiency and bandwidth. Second, the power level is less than optimum for the specified power of 35 MW. With this tube, many levels of combining tend to reduce efficiency and increase cost. From a programmatic standpoint there is concern about lead time and/or development cost. It would take about 4 years to produce enough tubes to operate at 35 MW with present production and testing facilities. The other approach is to develop a high power tube at about 5 MW. The configuration would then have only eight sockets (one per launcher), and the efficiency and cost situation would be improved. From an overall standpoint, the program time may be about the same, since developing a new tube could take 2 years and production of eight or ten tubes another 2 years. With consideration of future experiments at higher TF levels

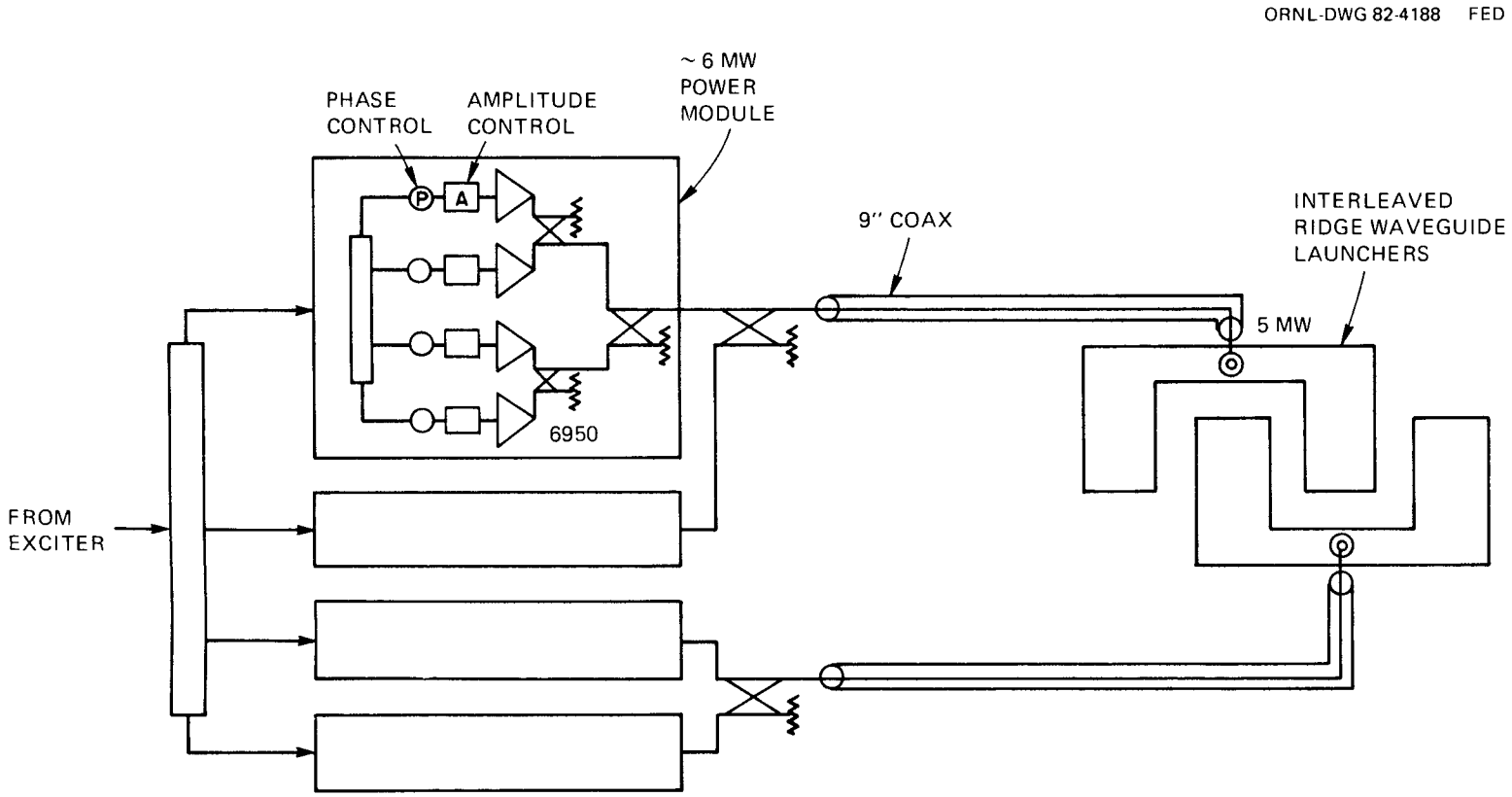

Fig. 7-18. Phased high power ICRF modules provide drive for interleaved launchers.

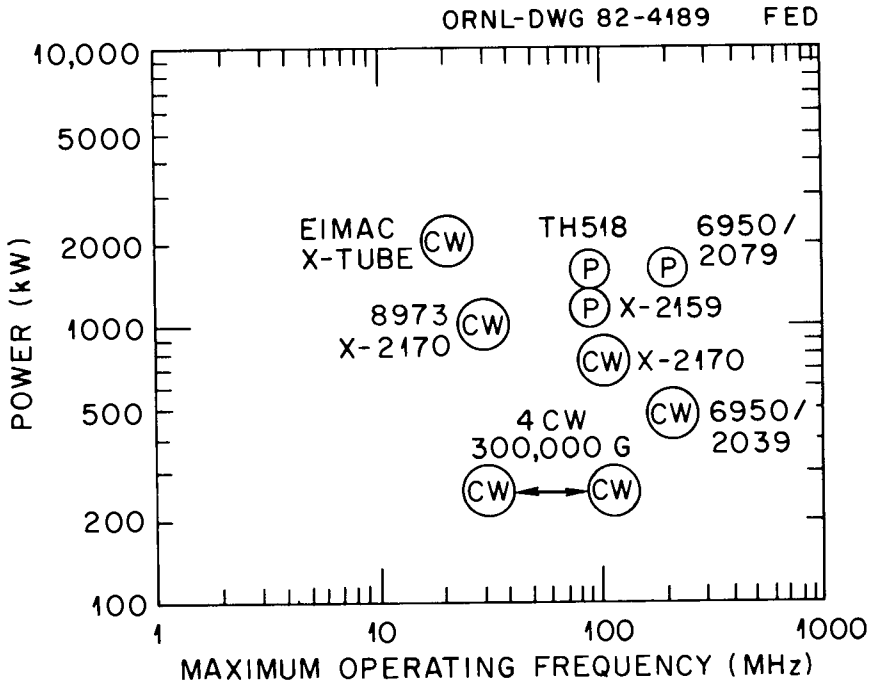

Fig. 7-19. At 200 MHz, the 6950 is the best high power tube.

and second and higher harmonic heating, investment in a new tube seems appropriate.

The other major component of concern from an engineering standpoint is the launcher. There are three main points. First is the power handling capability in the environment imposed by the FED-A and its plasma. The presence of gas and/or plasma in the waveguide will severely degrade the insertion phase and power handling characteristics. Because this launcher is only used after the plasma is established (i.e., during the current maintenance phase), it is expected that the density in the waveguide will be low enough to preclude breakdown and insertion phase variations. This has not been demonstrated as yet. For a near-vacuum ($P < 10^{-5}$ torr) case the launcher should have no problem handling 5 MW per waveguide — 10 MW total. The second point is the concern about the viability of the launcher in the harsh neutron environment. It is expected that the neutron flux at the wall will be about 10^{14} n/cm^2•s. The launcher will be constructed of stainless steel, with the only other material being a ceramic for the vacuum break (window) at the back of the launcher. This ceramic will have a radiation-damage-imposed lifetime of about 0.3 full power years. For reasonable FED-A operational duty factors (15-30%), a changeout might be expected every 1 or 2 years during the period of full performance. The third and final point is the bandwidth of the launcher. For the current drive function alone, only one frequency ($\sim$200 MHz) is required and very little bandwidth. If it is desired to multiplex the ICH frequency ($\sim$70 MHz) with this 200-MHz signal through a single launcher, then bandwidth is a consideration. Figure 7-20 shows the configuration for a multiplexed system with two frequencies. Most launcher designs are optimized in a narrow band ($\sim$10% of center frequency), but in principle there is no reason why a design that operates at 70 MHz could not be made to work at 200 MHz. In summary, the FWIC launcher requires development, including testing in a simulated environment. This need has been identified on numerous occasions in past for other ICRF launchers.

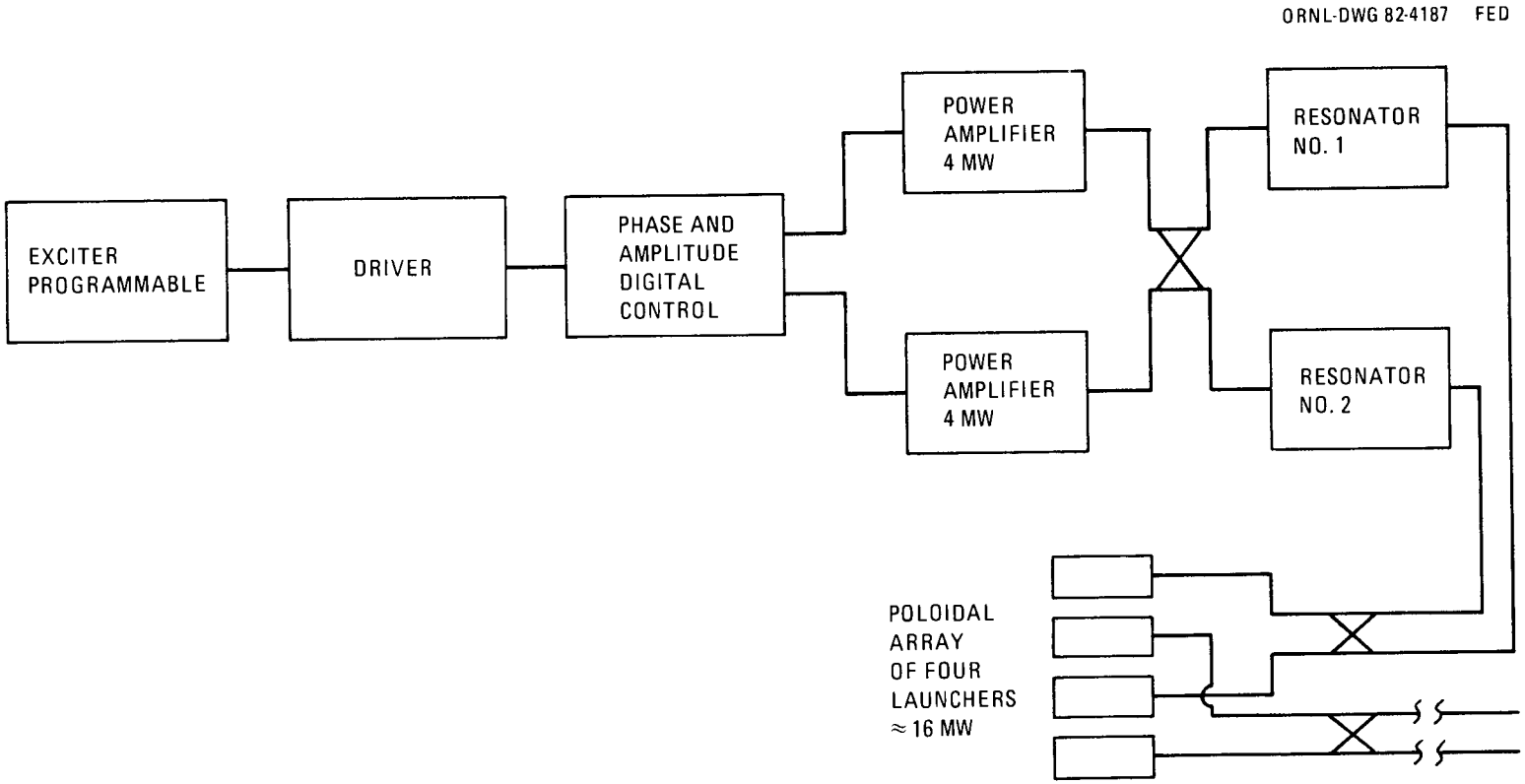

Fig. 7-20. Hybrid combining and phase shifters allow frequency multiplexing.

7.3.3 Relativistic Electron Beam Current Drive Design Concept

Relativistic electron beam (REB) application to the heating and current drive functions of tokamaks is relatively new.[7] Some limited experiments have been done on Macrotor at UCLA.[8] Current drive efficiencies were reported in the DEMO study.[9] Equipment development has been carried out. The results of these efforts are encouraging, but this technique has never been demonstrated on a reasonably large machine, like PLT or Doublet III.

The FED-A REB proposed characteristics (as suggested by D. Ehst[10]) are listed in Table 7-13. A sketch of the candidate interfaces is shown in Fig. 7-21. The 1000-cm^2 diode cathode is positioned in the plasma scrapeoff region (3-8 cm from the plasma edge). A tapered vacuum coaxial line supplies the diode. Because of the neutron containment needs, the line goes through two bends in the toroidal plane. This reduces the neutron flux at the vacuum break by one or two orders of magnitude from the first wall value of 10^{14} $n/cm^2 \cdot s$. As noted in the table, the center conductor of this vacuum section is cantilevered off the vacuum window. The vacuum window has a double insulator, which provides better structural support and gives a measure of redundancy against failures of the window, which could allow insulating oil from the transmission line into the vacuum vessel. There are two diodes, each carrying a 13-kA pulse at 1.5 MeV for a pulse length of 100 μs. The rationale for the selection of pulse length is detailed in Ref. 9. In brief, the power injected is required to be enough to overcome the plasma I^2R losses. This dictates a minimum power level from which the injected charge is calculated. The diode current times the pulse duration gives the injected charge. Short pulses of, say, 1 μs require very high currents (in this case 1.3 MA). This would require large transmission line conductors and large diodes. Very long pulses affect pulse generator design. A compromise was selected at 100 μs and 13 kA (per diode). The 80- by 13-cm diode size was another carefully chosen parameter. It is desirable to minimize the size of the diode. The current density of the diode is limited by the plasma edge conditions to a maximum of $\sim$130 kA/m^2; hence, the area was $\sim$0.1 m^2.

Table 7-13. REB characteristics

FED-A interface	
Injection points	Midplane or limiter duct
Injection position	3-8 cm from plasma edge
Number of diodes	2
Diode configuration mounting	Diode on conductor cantilevered from vacuum window
Size	$\sim 80 \times 13$ cm^2
Electrical	
Current	13 kA/diode
Voltage	1.5 MeV
Pulse length (s)	
Subpulse	100×10^{-6}
Burst	TBD
Pulse repetition period	1
Transmission line	Tapered vacuum section $\sim$50 cm in diameter Oil-filled section $\sim$85 cm in diameter

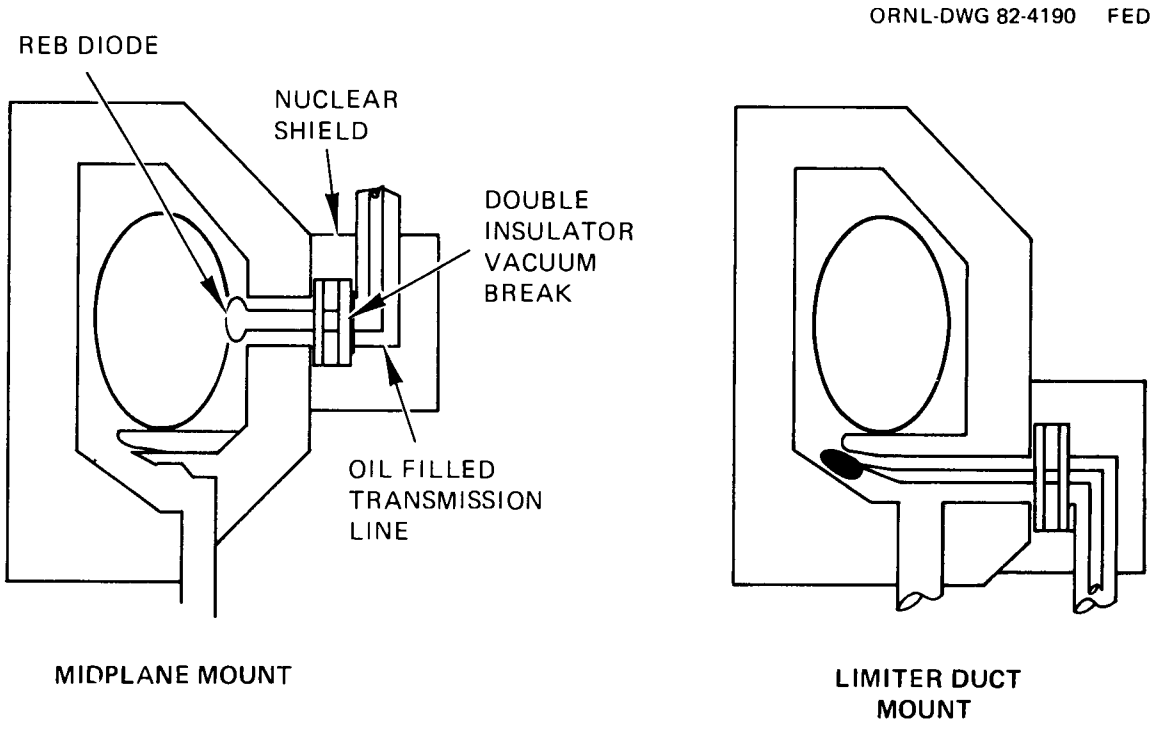

Fig. 7-21. Two candidate REB/FED-A interface designs.

In selecting the beam energy, the higher kinetic energies resulted in better current drive efficiency but a larger voltage insulation problem. If the voltage is too low, the beam will not cross flux lines and will hit the diode on return path. Again, a compromise at 1.5 MeV was reached.

Figure 7-22 shows the overall equipment configuration. Six sets of motor-driven compulsators, each supplying a 20:1 step-up transformer, are arranged in a series connection. Each transformer has ∿250 kV at the secondary, thereby producing a 1.5-MV pulse for transmission through the oil-filled transmission line. The choice of a compulsator approach over the pulse-forming network was made based on a number of engineering considerations. This approach eliminates the need for high voltage (100- to 500-kV) switching, is simple, and has a longer life. At the FED-A interface, the oil-filled line (50 cm in diameter) enters a rather massive nuclear shield in which the line makes two right-angle bends before entering the double insulator window. The right-angle bends circumvent neutron streaming through the large (50-cm-diam) bulk shield penetration. The insulators of the vacuum break are 2 m in diameter.

A number of engineering concerns were identified but not properly addressed due to limited resources. The first of these has to do with the viability of the diode positioned in the plasma scrapeoff region. At 8 cm from the plasma edge, a diode constructed like the limiter (∿5-cm graphite brazed to copper) could last 8-10 years at the midplane location. Figure 7-23 shows the basis for this in terms of heat flux and erosion for the two suggested locations. At 3 cm, the life expectancy would be well below 1 year due to the combined effects of heat flux and erosion. The limiter location is a considerably harsher environment and is not favored.

Another area of concern is breakdown due to gas in the "vacuum" transmission line. The voltage is much higher (megavolts vs tens of kilovolts) than that encountered with rf launchers. Because the actual conditions in the scrapeoff region are not known or are difficult to model, this concern needs to be addressed through experimentation.

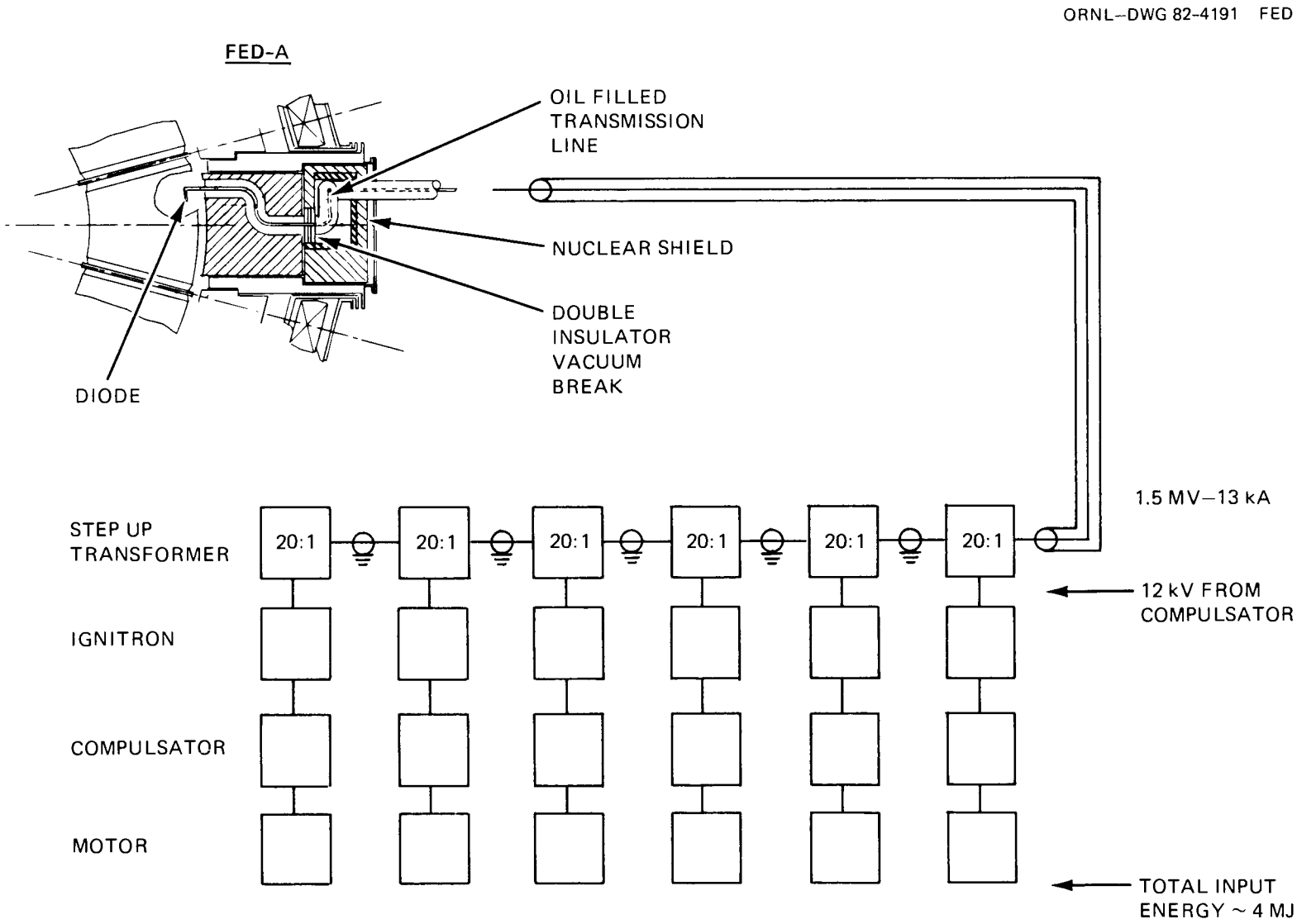

Fig. 7-22. A 1.5-MeV pulse is generated by a series combination of compulsators.

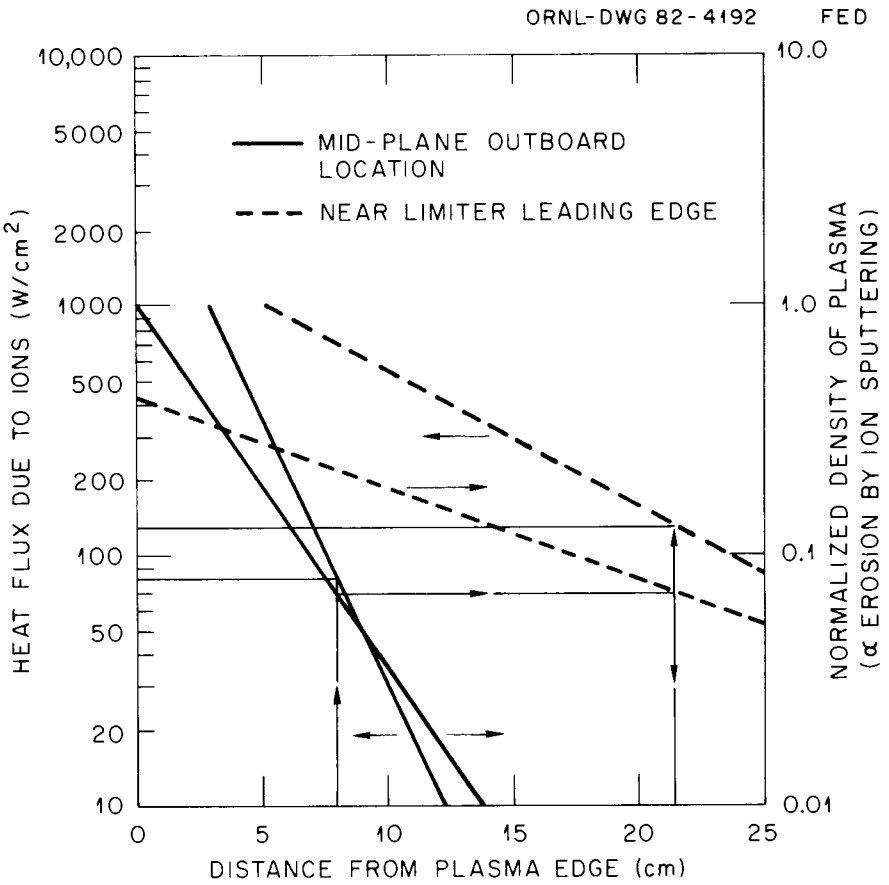

Fig. 7-23. A midplane position for the REB diode has a less severe environment.

Component development of compulsators, diodes, and vacuum breaks is needed. This is a relatively new technology, and there is much to be done to raise it to a level of confidence comparable to rf or neutral beam injection. On the positive side, it appears to be simple, it requires little equipment in the reactor hall (and that is easily maintained), the majority of the complex equipment is outside in a hands-on area, and the direct capital cost could be much lower.

7.3.4 Heating Design Concepts

Baseline option

The FED developed in FY 1981[2] uses ECRH for start-up and ICRH for bulk heating. These systems provided 1-2 MW of ECRH at 80-100 GHz and 50 MW of bulk heating at 54 MHz. Figures 7-24 and 7-25 summarize these two systems' configurations. FED-A needs 3.5 MW at 120 GHz of start-up assist and 25 MW of bulk heating power. A higher field is planned, resulting in a higher ECRH frequency. The bulk heating power is reduced because the bulk heating time is extended; recently, the rf heating efficiency experiments have consistently indicated better heating than with neutral beams. To meet the FED-A bulk heating needs, two of the launcher-rf generator sets shown in Fig. 7-24 would suffice. During the FY 1982 effort on the INTOR project, investigations into launcher coupling indicated that the FED Baseline launcher may require more poloidal extent. For FED-A the baseline launcher (ridge-loaded waveguide) would consist of two to four such launchers stacked in the poloidal direction (see Fig. 7-26). With four launchers, either two sets of two per TF window segment or all four in a single window would be acceptable from a bulk heating standpoint. Further, with four launchers, the final combiner in the rf generator (see Fig. 7-24), where the two 8-MW signals are combined, could be eliminated and 8 MW supplied per launcher. This would give nearly 25% redundancy, since three out of four launchers could supply $\sim$24 MW. From the standpoint of mechanical stability of the plasma shell, two sets of two are favored.

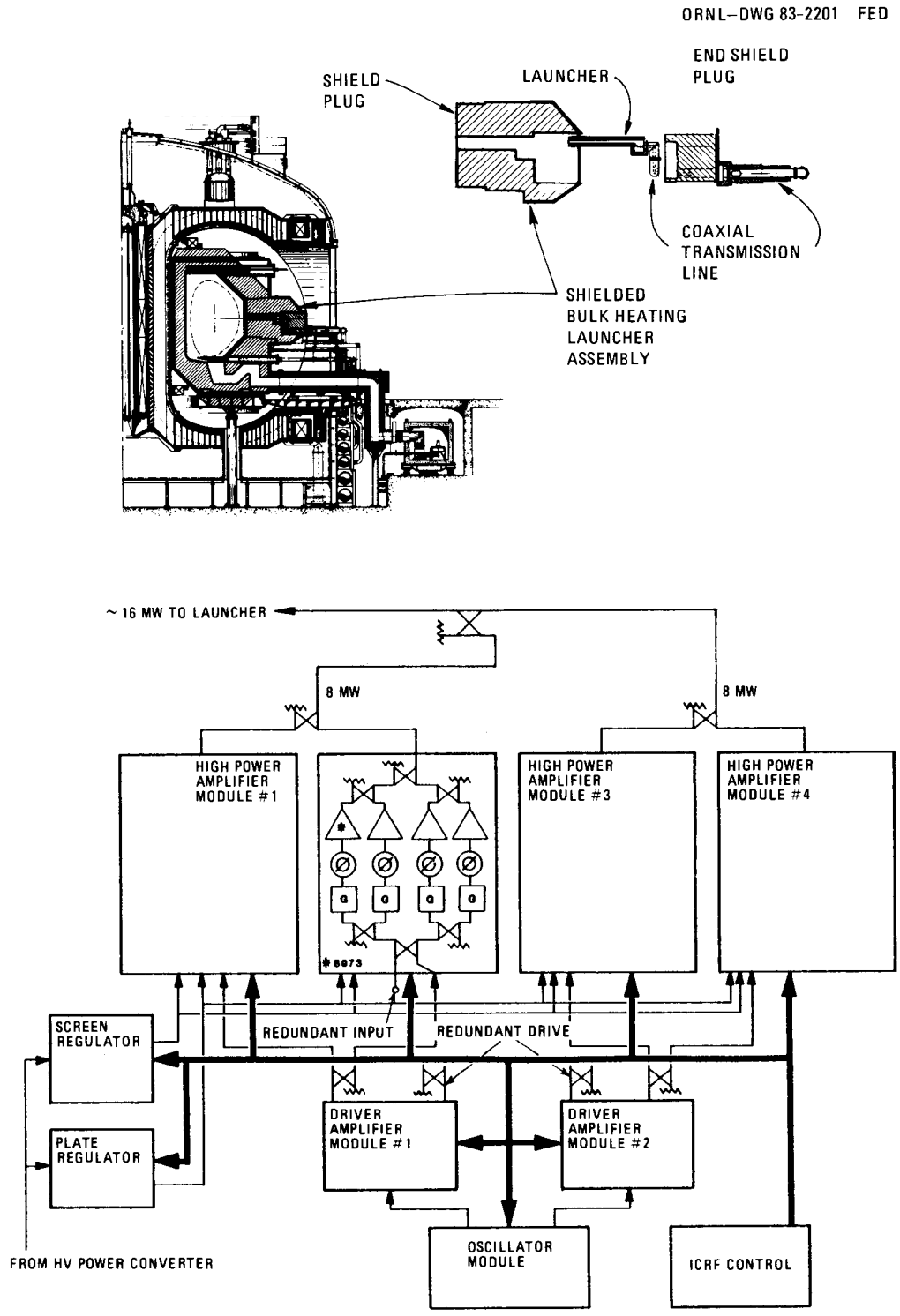

Fig. 7-24. The bulk heating system (figures taken from the FED Baseline description).

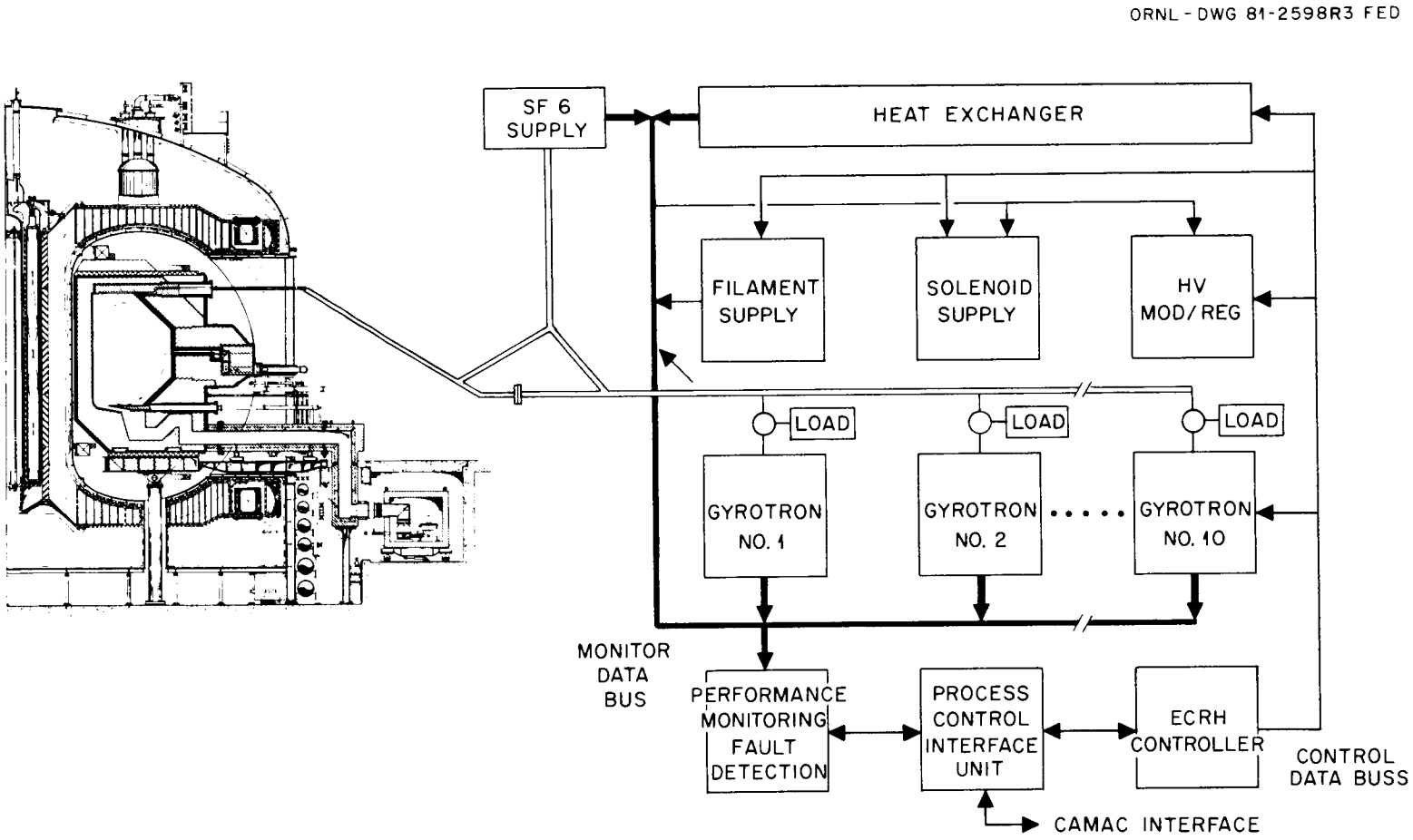

Fig. 7-25. Separate strings of gyrotrons and launchers provide ECRH power for start-up.

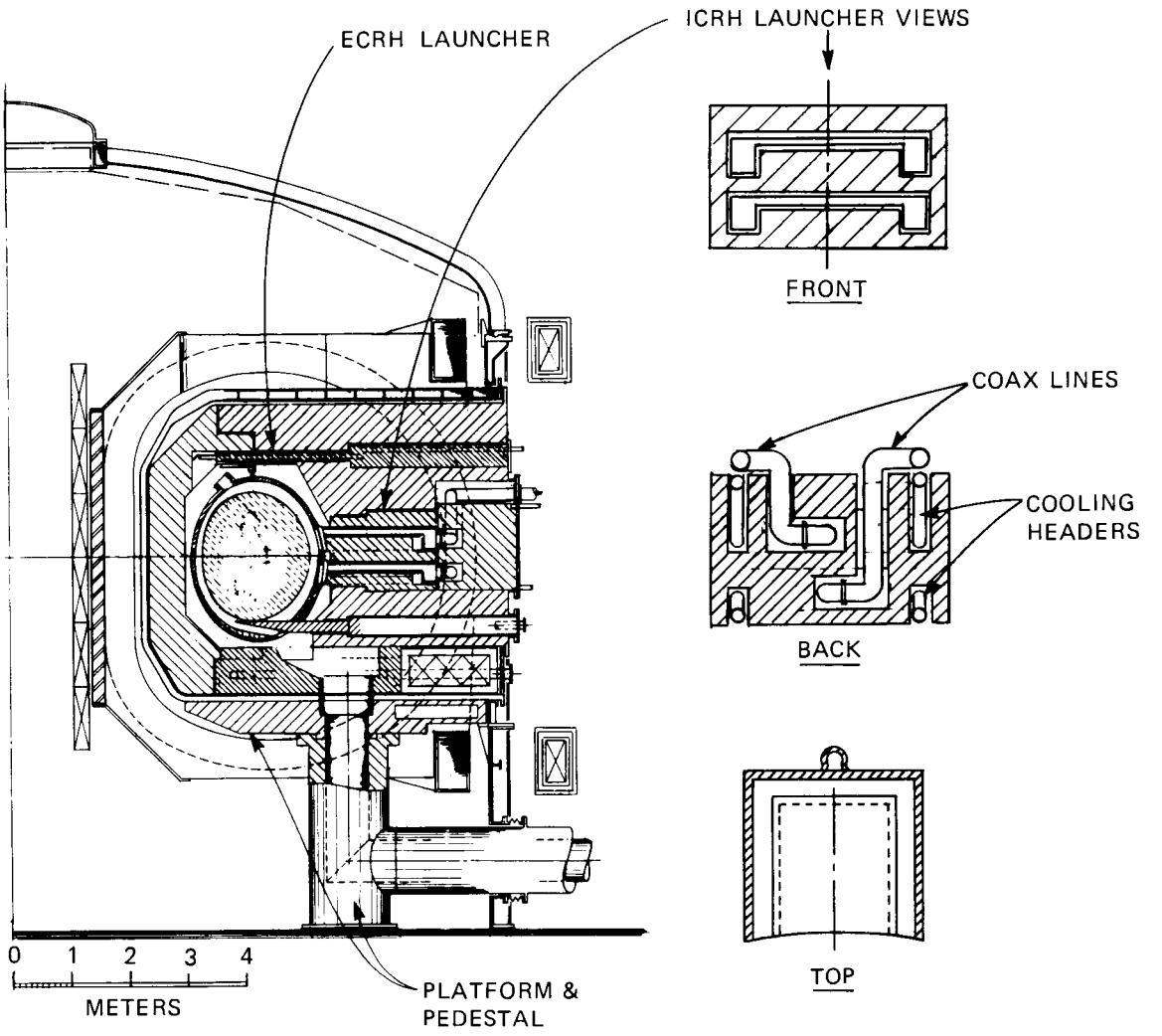

Fig. 7-26. A stack of two ICRH launchers is arranged for interface with the FED-A.

Figure 7-27 shows another ICRH launcher concept considered for INTOR. It features a planar array of 16 loop antennas, each driven by a separate amplifier with phase control. There is a vacuum boundary in front of each loop, which improves the power handling capability. Maintenance can be performed on a single element of the array if required. Performance modeling of this approach has not been completed. One disadvantage of this array design is that it is very narrow band.

The ECRH system would be essentially the same, except there would be two launchers per TF coil window section — 24 total. Presently, 28-GHz cw and 60-GHz pulsed gyrotrons are available. The 60-GHz cw tube should be available in mid-1983. These tubes have a nominal power output rating of 200 kW; however, one 28-GHz tube has operated for hours at over 300 kW. A pulsed tube has been tested at well over 100 GHz but for short (microseconds) pulses. For FED-A, gyrotrons of 24-250 kW are proposed to generate 6 MW at 120 GHz, providing 3.6 MW to the plasma chamber for start-up. ECRH is also considered for bulk heating. This approach has been unattractive in the past because of the low tube power. However, starting in FY 1983, there are four candidate tube developments for a 1-MW gyrotron. With only 25 MW required for bulk heating, ECRH may become quite attractive in the next few years.

Other options

It would be desirable to have one set of equipment perform all three functions of (1) start-up assist (both heating and current), (2) bulk heating, and (3) current maintenance. With this thought in mind, the FED-A parameter list calls for LHRH to perform bulk heating. To date, attempts at ion heating with LHRH have been mostly unsuccessful. An experiment on JFT-2 probably represents the best results.[1] Indications were that 2-3 eV/kW $\times$ 10^{13} cm^{-3} heating efficiency was being observed. In most other experiments results were not consistent or repeatable. Recently, consideration has been given to the recognized fact that LHRH heats electrons rather well. If this heat can then be transferred to the ions, perhaps LHRH could be used for both heating and current drive. Based on PLT current drive experiments, 60% of the heating can be

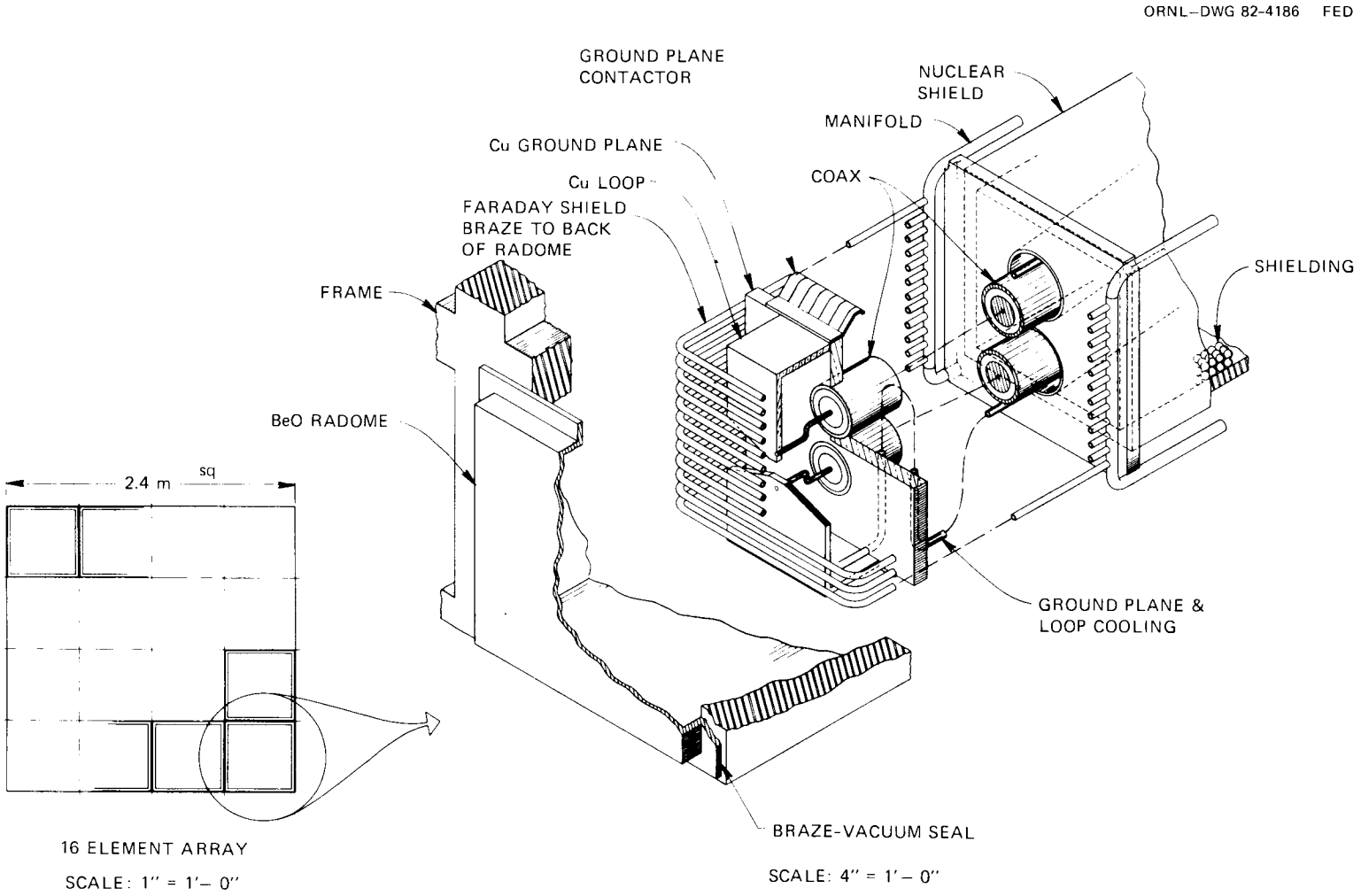

Fig. 7-27. An array of loops concept developed for INTOR may have application on FED-A.

supplied by the current drive system. It is not clear what the characteristics of a LHRH bulk heating would be in terms of frequency, $n_{\|}$, launching point, etc. (This is why they have not been specified.) If the characteristics are significantly different, a second set of equipment is required. Compared to the FED Baseline, this would be an expensive approach. The general configuration for bulk heating would be very similar to that of the current drive experiment.

Fast wave ion cyclotron heating heats electrons also. Hence any approach that is workable for LHRH may be applicable to FWIC. With regard to the use of REB for bulk heating, there was some evidence that heating is possible. However, data are sparse. Again, the configuration requirements have not been specifically stated for REB bulk heating, but there is no reason to believe the equipment would be significantly different than that for current drive.

7.4 SUMMARY AND CONCLUSIONS

During this year's effort, the topics addressed were (1) current drive and heating philosophies, (2) evaluation and selection of current drive and heating options, and (3) equipment configurations. In the course of study we have defined both current drive and heating philosophies. When these were considered separately or in combination to perform the full set of functions required for the tokamak devices operation, some 48 possible options were created. Based on current information, scientific and technological credibility values were assigned to each current drive and heating approach. Approaches such as LHRH current drive or ICRH bulk heating have high credibility because of their supporting experimental data. These credibility factors were used to weight the outcome of evaluations of performance to impact ratios.

We conclude that, in general, LHRH and low density current drive in conjunction with a weak transformer have the highest merit at this time. The baseline heating approach was preferred for start-up assist and bulk heating. The method used in the selection of options is a standard systems engineering technique, which is designed to be as objective as

possible. The outcome becomes subjective through the assignment of credibility factors. With breakthroughs in the technology advancement or physics understanding, there will be a need to revisit the selection process.

Most of the equipment configuration effort concentrated on the LHRH current drive design. Its component designs were based on present-day technology. Some emphasis was placed on availability because there is greater need for high availability in a device approaching steady-state operation. Inherent redundancy using modules was incorporated in these designs so that partial failure had minimal impact on system performance, thus increasing the mean time between failures. This modular construction was proposed where possible to reduce the mean time to repair. One of the critical areas is the launcher. A workable interface for the top launch was developed using a 24-subarray (each subarray a module) approach. The GRILL code was useful in the investigation of the failure effects.

A start was made on design trade-off techniques for grills, examining such parameters as number and size of waveguides, waveguide spacing, launcher position, grill size and shape, etc. Effects such as the impact of the grill's spectral width on current drive efficiency or the amount of countercurrent driven by the ambiguous responses of the grill are not well understood at this time. We need this understanding if we are to make intelligent design choices for large devices where tens of megawatts and hundreds of waveguides are required.

The secondary options using REB and FWIC have potential because of their relatively low device impact. Their high marks in performance to impact ratio were heavily weighted by low credibility. The problem is a lack of experimental evidence. As discussed in Sect. 4.3, the main concern is with alpha damping. If these experiments indicate that FWIC is credible, it would radically change the selection outcome. A multiplexed FWIC system was found to be very attractive. Using the same apparatus with multiplexed frequency operation is very cost-effective. The REB approach current lacks a significant demonstration on a device

of reasonable size. There are concerns about the technology of REB, particularly with regard to the interface with the device, such as diode matching and viability, transmission line breakdown, and shielding. This is a relatively simple approach and should have low cost and easier remote maintenance.

The main point to be made about the heating options is that while the baseline approach (developed last year for FED) looks credible, it would be desirable to have one system perform all the functions. If the LHRH system could heat or the ICRH system drive the current, that would greatly reduce cost and interface impact.

REFERENCES

1. T. Imat et al., "LHRF Heating Experiment in JFT-2," in *Proceedings of the 4th Topical Conference on Radiofrequency Plasma Heating*, University of Texas, Austin, 1981.
2. *Fusion Engineering Device Design Description*, ORNL/TM-7948, Union Carbide Corp. Nuclear Div., Oak Ridge Natl. Lab., 1981.
3. H. Iida, "Parametric Study of LH Current Drive for a FED-A Design," unpublished memorandum, 1982.
4. M. Brambilla, *Nucl. Fusion* 16, 47 (1976).
5. C. D. Boley, Argonne Natl. Lab., "GRILL: A Code to Calculate the Spectrum of Lower Hybrid Waves Launched by a Brambilla Waveguide Array."
6. F. Perkins, paper presented at the Workshop on Advanced Plasma Performance in FED, Fusion Engineering Design Center, Oak Ridge, Tenn., Dec. 14-15, 1981.
7. V. Bailey, Physics International, personal communication with Y-K. M. Peng, Oak Ridge National Laboratory, Oak Ridge, Tenn., Dec. 17, 1981.
8. V. Bailey et al., "Injection of REB into a Tokamak for Current Drive: Experimental Results," presented at the 4th Topical Conference on HP Electron and Ion Research and Technology, Palaiseau, France, June 29, 1981.
9. *A Demonstration Tokamak Power Plant Study. Interim Report*, ANL/FPP/TM-154, Argonne Natl. Lab., Argonne, Ill.
10. D. A. Ehst, Argonne Natl. Lab., "FED Innovative Concepts: REB Current Drive," presentation, Atlanta, Ga., Mar. 10, 1982.

8. MAGNETICS AND CONFIGURATION

The FED-A concept studies have centered around low q, high beta, noninductive current drive, and the impact of these factors on the major device parameters and component designs. The device magnetics and configuration represent a specific basis on which design assessments and systems trade studies (Chap. 5) are quantified and hence are necessary parts of the FED-A studies.

In this chapter, the plasma poloidal field (PF) configurations, PF coil locations, and coil current waveforms appropriate for quasi-steady-state current drive operations are reviewed in Sect. 8.1. Section 8.2 discusses the magnet concepts of FED-A, accounting for the impact of quasi-steady-state operation with 1000-s burn and a reduced number of plasma current and burn pulses. In support of the FED-A systems trade studies (Sect. 5.2.4) on variation of the maximum magnetic field from 8 T to 12 T, a relatively detailed discussion of the major toroidal field (TF) coil design parameters for this range of field is also included. Section 8.3 summarizes the FED-A configuration, highlighting areas where it differs from the FED Baseline approach.

8.1 POLOIDAL FIELD CONFIGURATION CONCEPTS

D. J. Strickler, K. E. Rothe, and Y-K. M. Peng (FEDC/ORNL)

The assumption of a low q (q_ψ = 1.8, where q_ψ is the flux-surface-averaged safety factor at the plasma edge), nearly circular (elongation $\kappa \sim 1.1$-1.2) plasma in FED-A leads to the possibility of a simplified poloidal field (PF) coil system. In particular, shaping coils are greatly reduced in size compared with designs assuming elongated and D-shaped plasma cross sections, directly influencing the complexity of the configuration and contributing to the overall objectives of FED-A, that is, simplified engineering and lower cost. Further simplification in the PF system is achieved by coupling the fields of the ohmic heating (OH) and equilibrium field (EF) coil sets, thus reducing the number of coils and lowering the total ampere-turns. This concept allows the

magnetic energy stored in the coil system to be used for both current buildup and plasma equilibrium.

Aside from structural and maintenance implications, large shaping coils with current in the same direction as the plasma current I_p tend to reduce the overall volt-second capability of the PF system. The assumption of a nearly circular plasma leads to the possibility of eliminating the D-shaping coil, as is evident in Table 8-1, where the shaping coil current changes sign between $\kappa = 1.0$ and $\kappa = 1.2$. The FED systems code studies (see Sect. 5.2) based on these PF system data show that, if no significant beta improvement is evident with elongation, cost considerations strongly favor near-circular plasmas. An additional feature of circular plasmas is a favorable field index,

$$n = \frac{-R}{B_v} \frac{\partial B_v}{\partial R} ,$$

important for vertical stability ($n > 0$), also shown in Table 8-1.

Based on MHD equilibrium requirements, a PF system consisting of a central OH solenoid, two outer EF coils, and two small shaping coils (carrying a maximum of 1 MA to minimize the effect of fields of the OH solenoid during the early stages of start-up) is adequate for an expanding radius start-up scenario. All PF coils are external to the TF coils and are assumed to be superconducting.

The prospect of current drive in FED-A leads to several possible scenarios for steady-state operation. Included among these is a cyclic density mode in which lower hybrid current drive (LHCD) allows the OH solenoid to be periodically recharged. This option presents specific equilibrium requirements for plasma position and shape control.

8.1.1 Coil Locations

The FED-A PF system consists of three superconducting coil sets positioned external to the TF coils, as shown in Fig. 8-1. A design requirement that the inductive capability for a 100-s pulse be retained

Table 8-1. Plasma and coil currents for a high beta ($\langle\beta\rangle$ = 7%) FED-A plasma as the elongation is varied. Coil locations are (see Fig. 8-1) R_{EF_1} = 3.0 m, Z_{EF_1} = ±4.8 m, and R_{EF_2} = 9.5 m; Z_{EF_2} = ±4.0 m

κ	1.0	1.2	1.4	1.6
δ	0.0	0.1	0.2	0.3
n	0.24	-0.33	-0.71	-0.95
I_p	3.5	4.2	5.0	6.2
I_{EF_1}	-3.6	0.6	4.0	6.9
I_{EF_2}	-3.2	-4.4	-5.2	-6.1

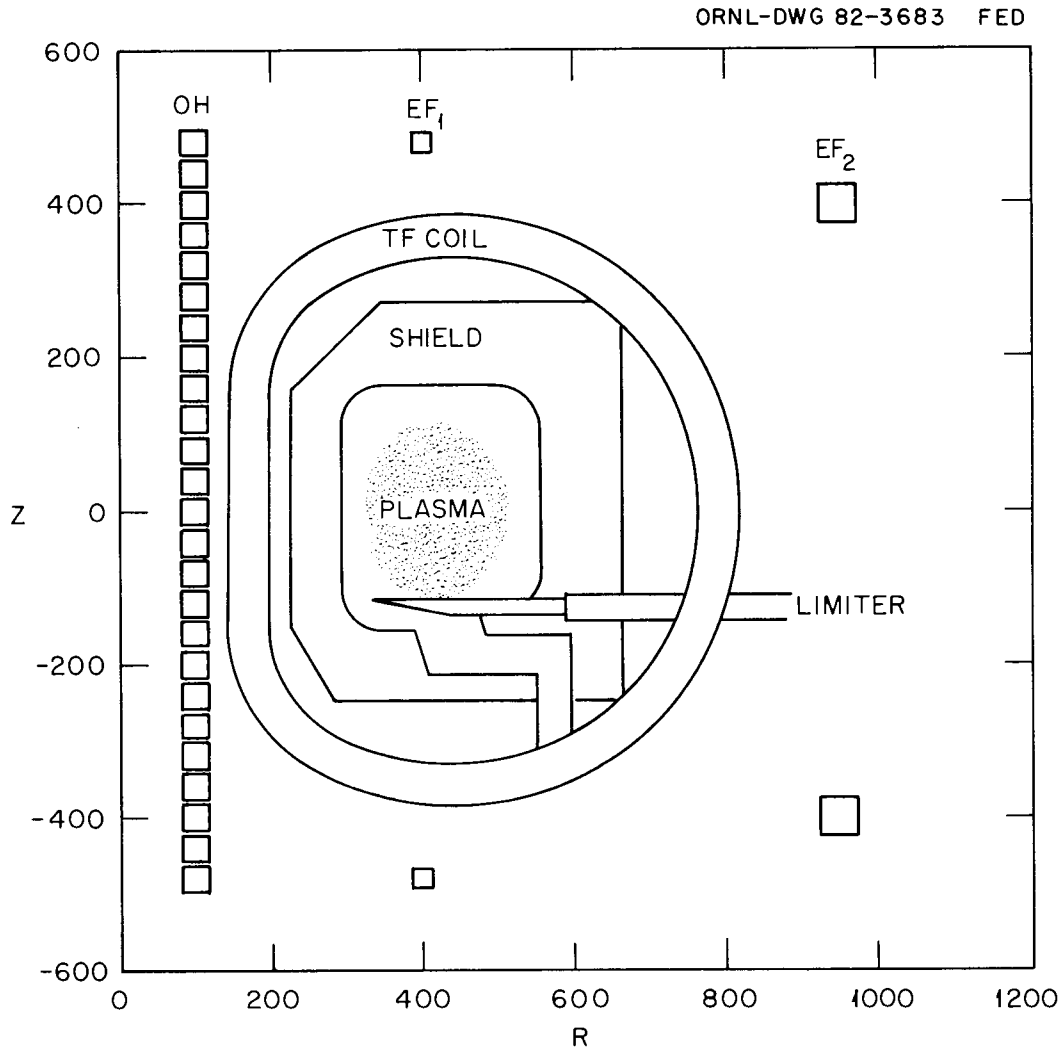

Fig. 8-1. The FED-A PF system consists of three superconducting coil sets: the central ohmic heating solenoid (OH), small shaping coils (EF_1), and outboard equilibrium field coils (EF_2).

implies the need for a large central solenoid (OH) carrying a maximum current of 50 MA to provide a capability of >30 V·s. Small shaping coils (EF_1) cancel the field of the OH solenoid during the early stages of start-up and assist in the mild elongation of the plasma. The vertical location of these coils is limited only by the TF coil size, and the plasma shape is not extremely sensitive to their radial position, taken to be R_s = 4 m in the present calculations. The outboard coils (EF_2) were positioned to satisfy configuration constraints, and their vertical location was varied to give the plasma a small elongation during high beta operation. To obtain coil currents, the tokamak equilibrium equation was solved while iteratively adjusting the currents in some subset of the given coil locations so that the plasma boundary (i.e., the flux surface intersecting a prescribed limiter point on the midplane) intersects a given set of points describing the desired plasma shape. If there are more boundary points than there are variable coil current groups, this is solved as an approximation (least squares with a regularization term) problem.[1] Coil locations, together with maximum ampere-turns, are given in Table 8-2.

8.1.2 Start-Up Requirements

In simulating the PF coil current requirements for start-up in FED-A, we have assumed that the plasma characteristics follow an analysis similar to that described in Ref. 2, based on an rf-assisted, expanding radius start-up consisting of ECRH preheating, current initiation, and significant LHRH power (12.5 MW) as the minor radius and plasma current are increased. A slow start-up time of 20 s reflects the need for fields to penetrate a highly conducting vessel. Plasma parameters at high beta for this sequence are R_o = 4.3 m, a = 1.2 m, B_t = 3.4 T, and I_p = 4.3 MA.

During the early stages of start-up ($0 \leq t \leq 0.3$ s), if no shaping coil is present, the small radius plasma in contact with an outboard limiter [Fig. 8-2(a)] tends to have an elongation $\kappa < 1.0$ and, in the extreme case, a field index $n > 10$. For a negligible plasma beta, the field curvature here is dominated by the effect of the OH fields and

Table 8-2. Coil locations and maximum ampere-turns.
Coils are symmetric about Z = 0

	R_{min} (m)	R_{max} (m)	Z_{min} (m)	Z_{max} (m)	I_{max} (m)
OH	0.80	1.20	-5.00	5.00	50.00
EF_1	3.87	4.13	4.67	4.93	1.00
EF_2	9.20	9.80	3.70	4.30	5.00

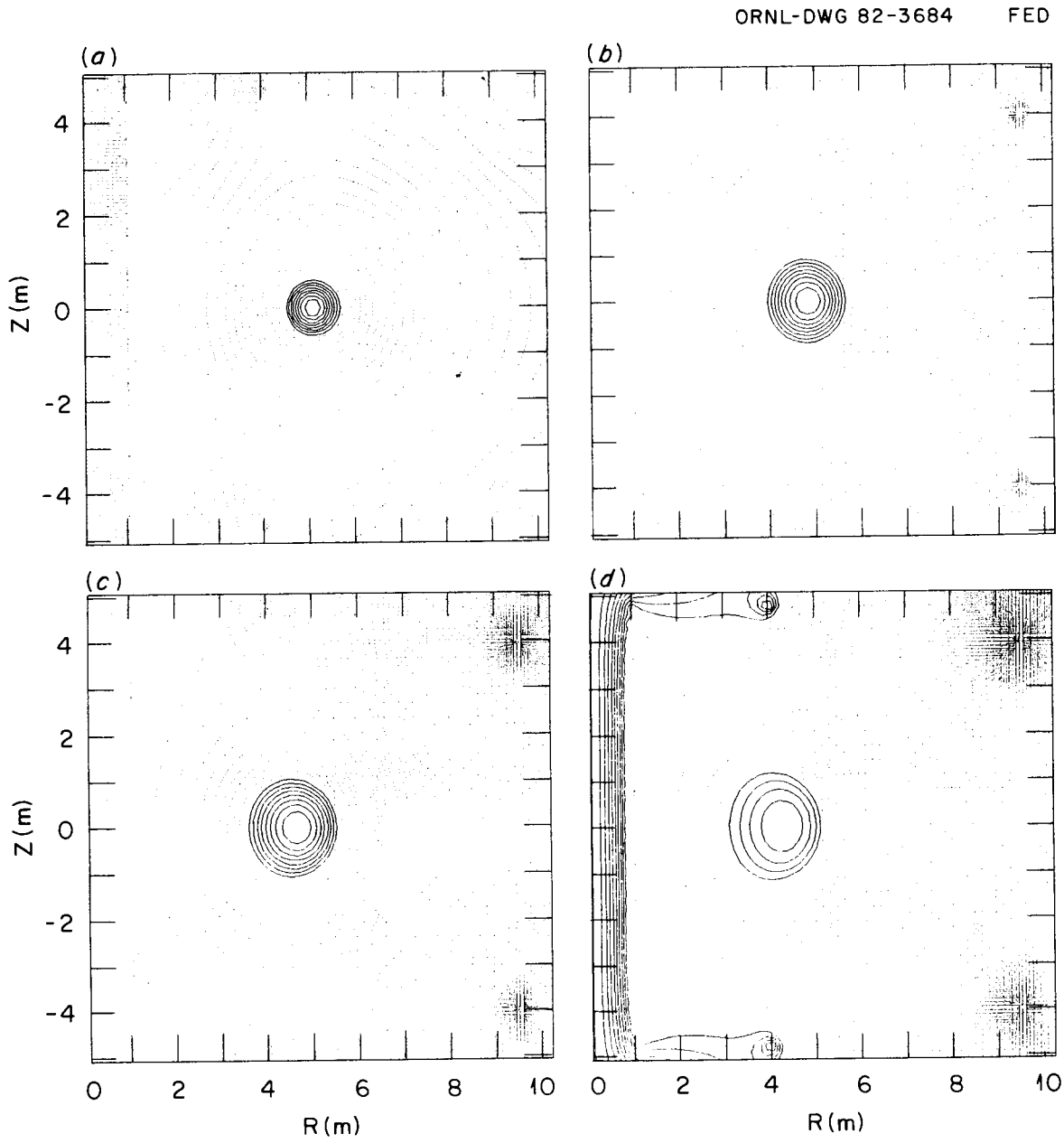

Fig. 8-2. FED-A poloidal flux surfaces during the 20-s, rf-assisted, expanding radius start-up.

is strongly concave inward [Fig. 8-3(a)]. Such a plasma would be subject to radial instability. This situation is shown to improve if small shaping coils (I_s = 1 MA) are placed at R = 4.0 m, Z = ±4.8 m, as is shown in Fig. 8-3(b). With outer EF coils located at R = 9.5 m, Z = ±4.0 m, the coil current requirements for this sequence of equilibria are presented in Table 8-3. The field index through the start-up phase for this system is shown in Fig. 8-4.

8.1.3 Quasi-Steady-State Current Drive Requirements

Assuming current drive is successful at relatively low density ($n_e \sim 10^{13}$ cm^{-3}), a possible cyclic density mode of quasi-steady-state operation is presented in Fig. 8-5. Following a 20-s start-up, LHCD is periodically in effect for ∿100-s intervals, during which the OH solenoid is recharged to its original (maximum) current. The OH solenoid then discharges during ∿1000-s intervals, in which heating and densification raise the plasma beta to $\langle\beta\rangle$ = 4-5%.

The EF coil currents must then respond to these oscillating changes in the field of the OH transformer and the plasma pressure to maintain MHD equilibrium. With a steady-state current of 1 MA in the shaping coil EF_1, the required outer coil currents (EF_2) are shown in Fig. 8-6. Figure 8-7 shows the poloidal flux surfaces that result in this mode of operation.

8.2 MAGNET DESIGN

The FED-A magnet systems design is similar to the FED Baseline with some important differences. The FED-A is essentially a steady-state device that is subjected to relatively few pulses (∿30,000). This allows components with higher design stresses, which lead to lower weights and costs. The OH solenoid is designed to operate at a peak field of 8 T, compared with 7 T in the baseline. This change results in a lower radius OH solenoid, which leads to a lower cost for the solenoid, as well as for the whole machine. A new TF winding approach is adopted that makes the winding cross section in the nose and outboard regions identical; that is, the wedge-shaped winding cross section is oriented in the same direction in both locations. This type of winding can only

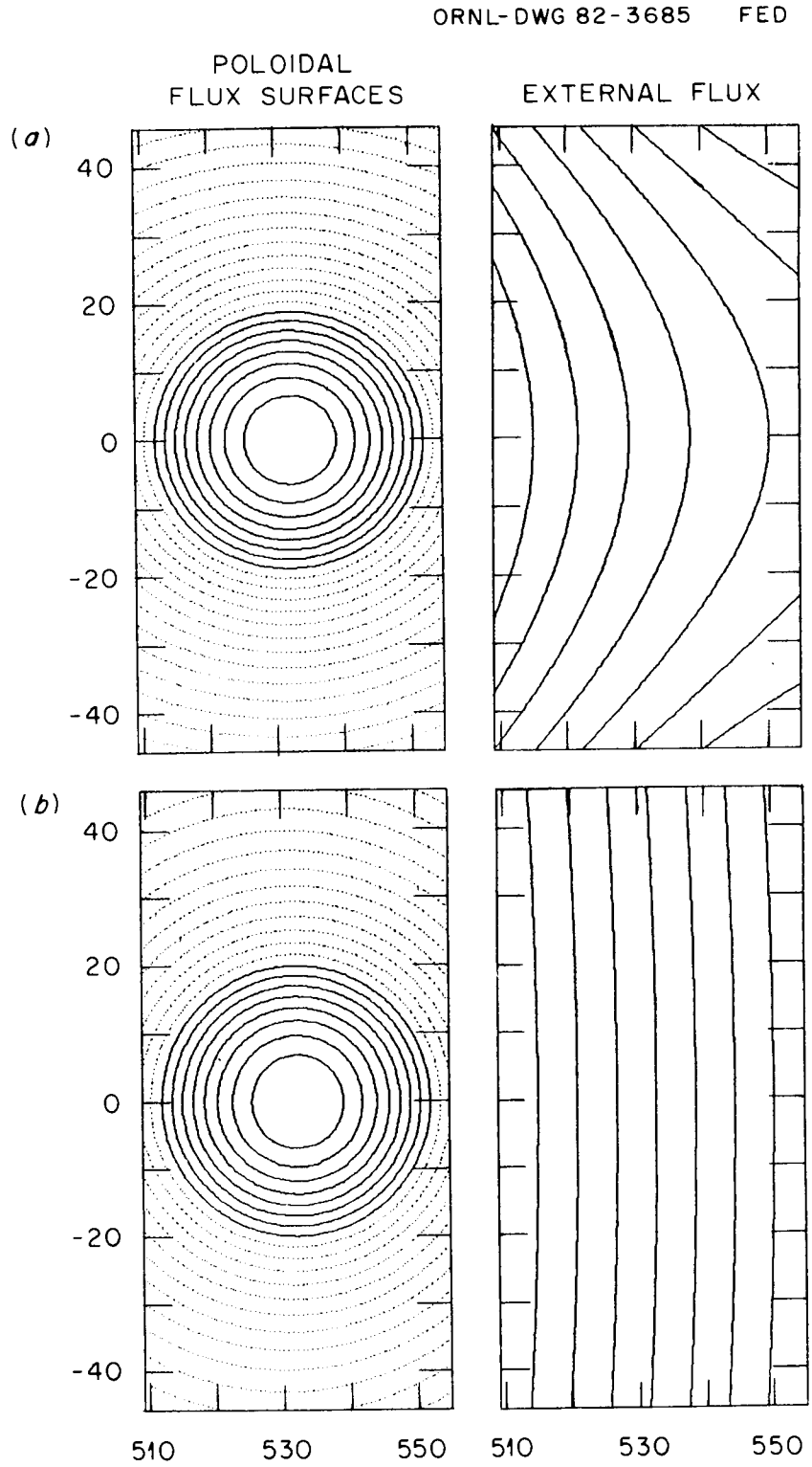

Fig. 8-3. During early stages of the expanding radius start-up, the equilibrium vertical field tends to be strongly concave inward (a) when shaping coils are not used. The field index improves (b) when a small shaping coil is present.

Table 8-3. PF coil currents for 20-s expanding radius start-up

	time (s)				
	0.3	2.0	6.0	10.0	20.0
R_o (m)	5.32	5.03	4.75	4.57	4.32
a (m)	0.20	0.49	0.77	0.95	1.20
κ	1.00	1.02	1.06	1.10	1.20
I_p (MA)	0.06	0.43	1.27	2.15	4.30
I_{OH} (MA)	58.50	49.25	27.50	6.00	-48.00
I_{EF_1} (MA)	1.01	0.96	0.85	0.75	0.82
I_{EF_2} (MA)	0.22	-0.10	-0.83	-1.58	-3.94

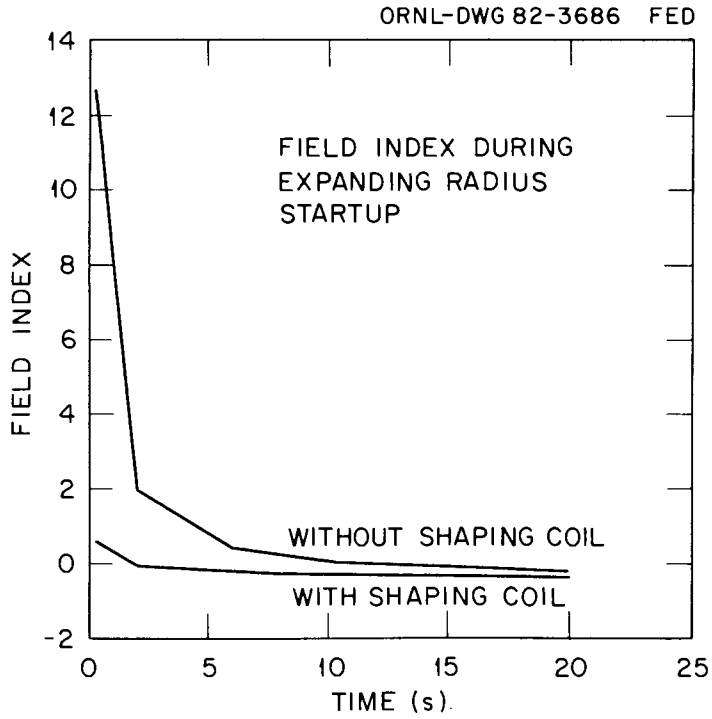

Fig. 8-4. The field index $n = -\frac{R}{B_v}\frac{\partial B_v}{\partial R}$ during the expanding radius start-up with and without a shaping coil.

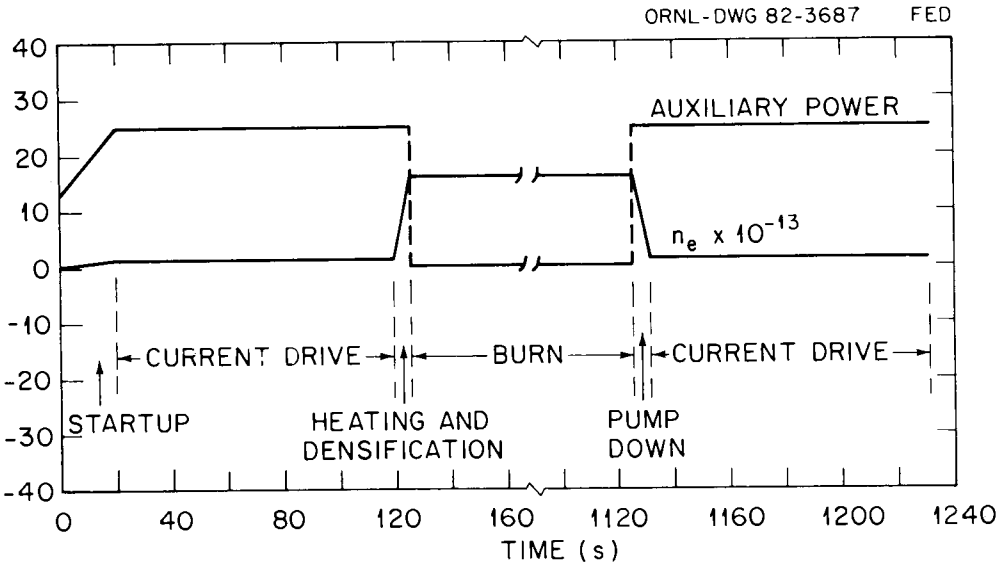

Fig. 8-5. A possible cyclic density mode of quasi-steady-state operation where lower hybrid current drive is periodically in effect at low density for 100-s intervals, during which the OH solenoid is recharged.

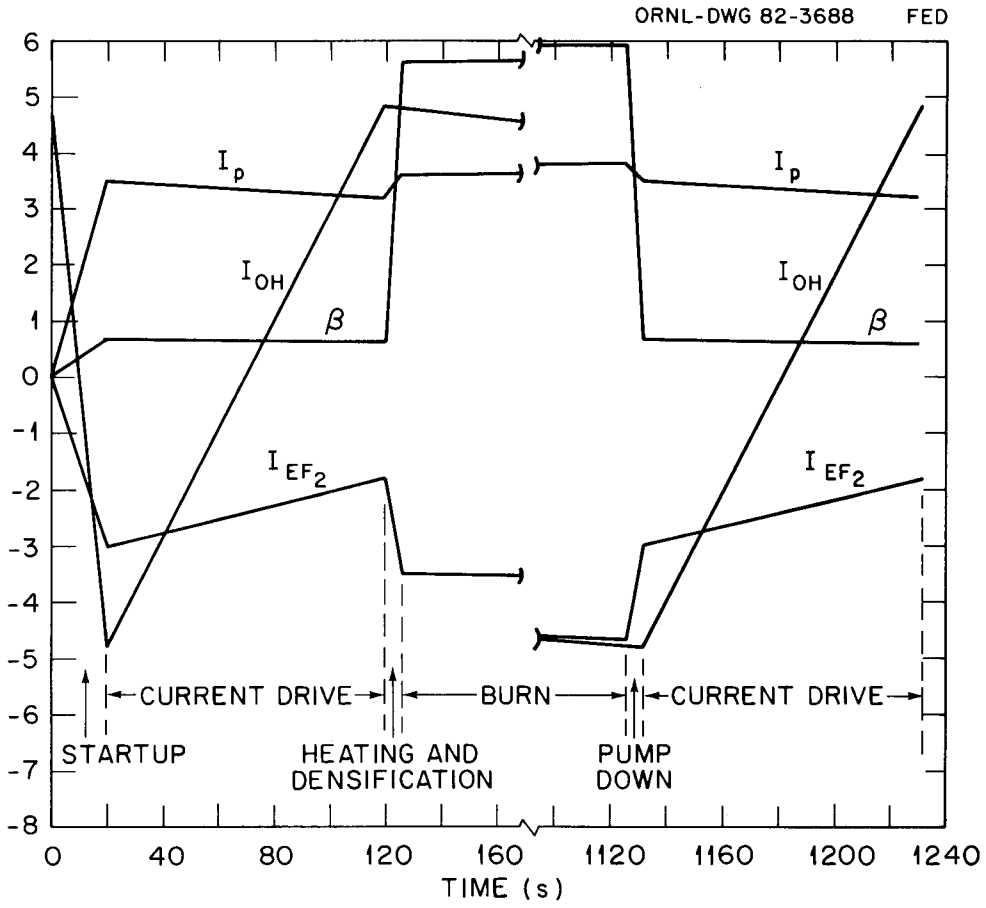

Fig. 8-6. Poloidal field coil current waveforms satisfying plasma MHD equilibrium requirements during quasi-steady-state operation with current drive.

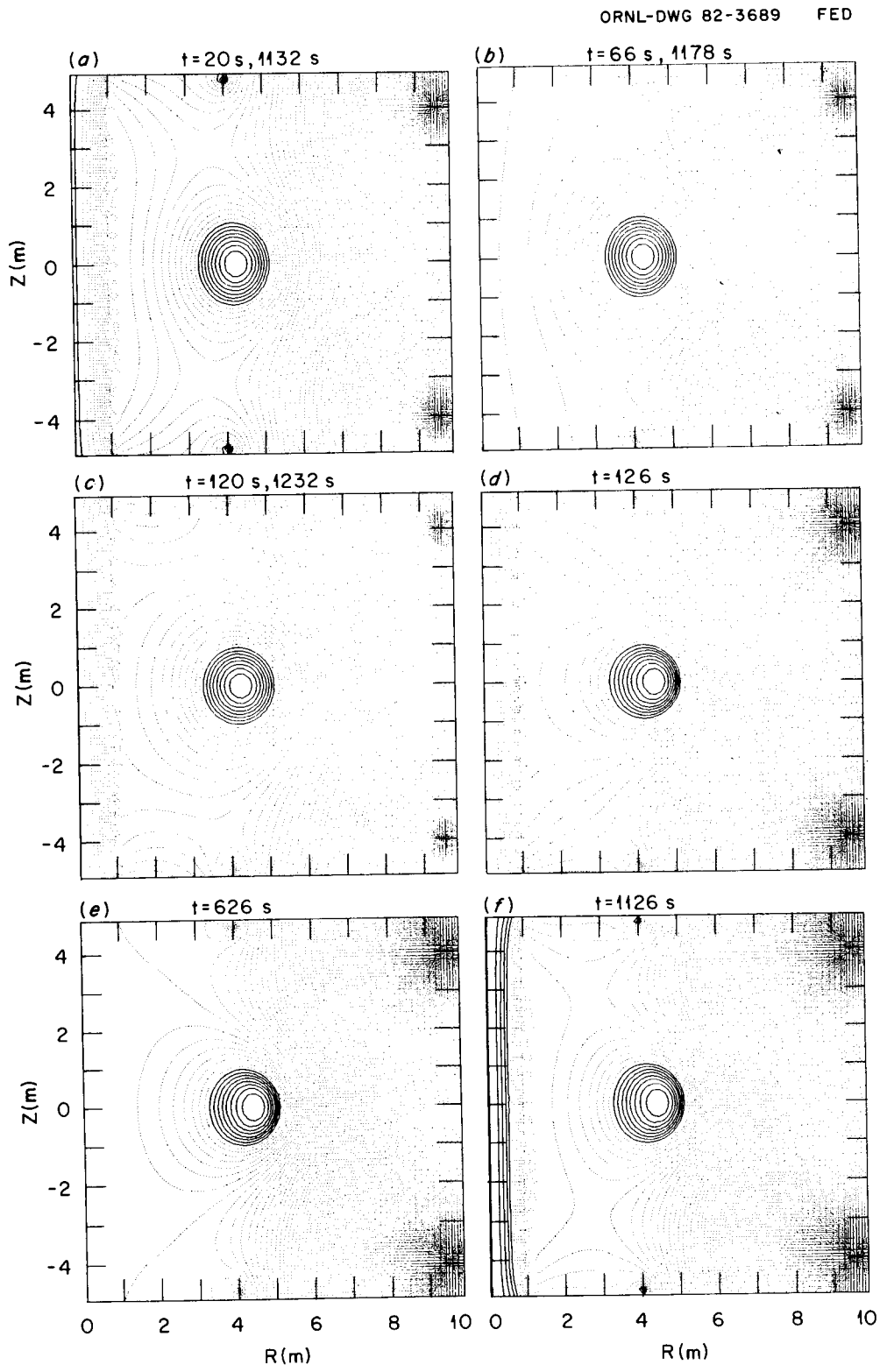

Fig. 8-7. Equilibrium poloidal flux surfaces during various stages of the cyclic density, quasi-steady-state operation shown in Figs. 8-5 and 8-6.

be achieved if the conductor is wound in pancake fashion instead of layer fashion. This winding approach, however, leads to placement of the outboard leg at a smaller radius, which results in significant savings in the overall machine cost.

All the above concepts are of general nature and can be applied to any machine. They are incorporated in the FED-A machine for the first time, however.

8.2.1 Design Requirements

The magnet system provides both plasma confinement and control functions. The FED-A magnet system is required to provide a toroidal field of 5 T at the plasma axis, which results in 10 T at the TF coil winding. The machine has three PF coils — an OH solenoid and two EF ring coils. Peak field at the solenoid winding is 8 T. All coils of the machine are superconducting. Assuming quasi-steady-state operation, the total number of full field pulses is 30,000. Each full field pulse has 10 burn pulses. Length of the burn pulse is determined by the full volt-second capability of the OH solenoid. The burn pulse is terminated when the OH solenoid volt-seconds are completely exhausted. It is then necessary to recharge the solenoid. During this recharging period, the plasma current is maintained at its initial value by the current drive equipment. The burn pulse is initiated again as soon as the OH solenoid is fully recharged. The plasma vessel has a high conductivity shell, which eliminates or mitigates the possibility of plasma disruptions.

8.2.2 General System Description

The FED-A magnet system is shown schematically in Fig. 8-8. Major parameters and features are summarized in Table 8-4. The machine has 12 TF coils, with a peak field of 10 T achieved by use of NbTi cable conductors cooled with a forced flow of 3 K supercritical helium. Alternatively, NbTi winding cooled with 1.8 K superfluid helium pool or Nb_3Sn winding cooled with 4.5 K helium can be employed. The intercoil support structure takes the form of ring beams placed on the top and

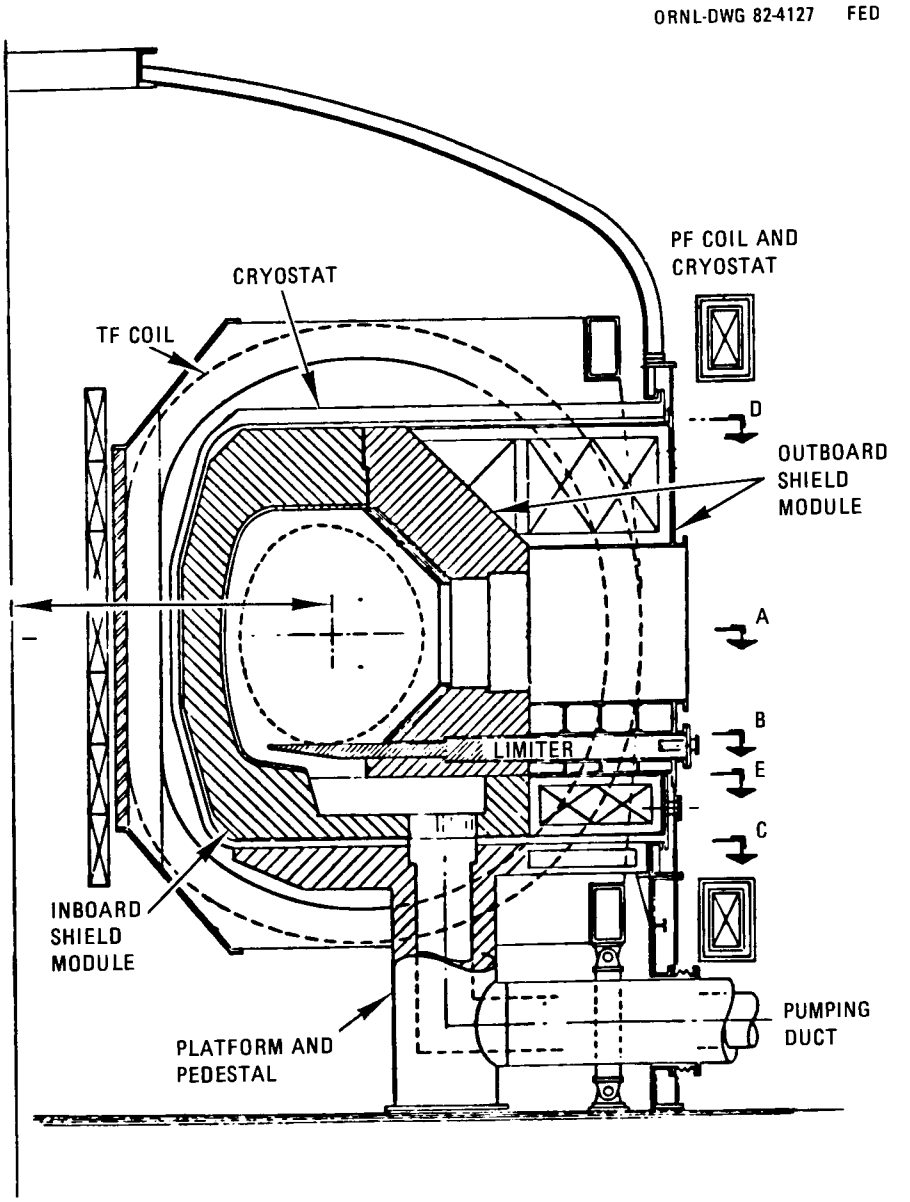

Fig. 8-8. FED-A magnet system configuration.

Table 8-4. FED magnet system parameters

Parameter	Value
Major axis	4.6 m
Field on axis	5.0 T
Number of full field pulses	30,000
Number of burn pulses in each full field pulse	10
Lifetime	10 years
TF coils	
Number	12
Conductor	NbTi
Design field at winding	10 T
Winding bore	5.2 m × 6.3 m
Maximum permissible radiation dose	10^9 rad
Ampere-turns per coil	8.76 MAT
Overall current density	1500 A/cm^2
Operating current	20 kA
Stored energy/coil	0.93 GJ
Coil mean perimeter	20.6 m
Bucking post	
Outside radius	1.63 m
Inside radius	1.35 m
OH coil	
Volt-seconds	44 Wb
Conductor	NbTi
Maximum field at coil	8 T
Charging time	26 s
Discharge time (+7 to -7 T)	26 s
Length of central solenoid	6.5 m
Winding current density	1400 A/cm^2
Stored energy in the solenoid	∿700 MJ

Table 8-4 (continued)

Parameter	Value
EF coils	
Volt-seconds	26 Wb
Conductor	NbTi
Field at EF coils	<7 T
Charging time	26 s
Discharging time	26 s
Winding current density	1400 A/cm^2

bottom of the outboard legs of the TF coils. All TF coils are enclosed in a single vacuum vessel. One of the vessel walls is common with the plasma vacuum vessel.

The OH solenoid has a capability of 55 MAT and provides 44 V•s with full bipolar swing of its current. The OH solenoid is designed for an 8-T peak field capability that can be achieved with NbTi windings employing pool-boiling or forced-flow liquid helium cooling concepts. The 8-T OH solenoid designs employing both cooling concepts are provided in the 1982 FED Baseline report.

The two EF ring coils are located outside the bore of the TF coils. Each coil has 3.5-MAT capability and provides 13 V•s. Thus, the total volt-second capability of the PF system is 70 V•s.

The EF coils can also be designed by using NbTi windings cooled with 4.5 K pool-boiling helium or forced-flow helium. Design of such coils is discussed in the 1982 FED Baseline report.

The structural design of the FED-A magnet system is based on an allowable stress of 40 ksi, compared with 31 ksi for the FED Baseline (at 10 T). The allowable stress for FED-A is higher because its number of pulses is considerably lower than the baseline number. The allowable stresses are determined on the basis of structural design criteria, which are similar to those used in other large superconducting magnet programs such as the Large Coil Program (LCP) and the Mirror Fusion Test Facility (MFTF).

8.2.3 Toroidal Field Coil Design

The TF system consists of 12 coils. The maximum field at a TF coil is 10 T; that provides 5 T on the plasma axis. The coils have bore dimensions of 5.2 m × 6.3 m. Each coil has 8.8 MA for producing the desired field. The maximum permissible nuclear radiation dose at the coils is 10^9 rad. The coils are sized on the basis of NbTi forced-flow conductors cooled with 3 K supercritical helium. The magnets are designed to accommodate a 20% increase in the resistivity of copper in the conductor over the 10-year lifetime of the machine. A lower increase in resistivity will result in small reductions in conductor cost, but it

would then be necessary to periodically warm up the magnets to anneal out the increased copper resistivity effect. Because the FED-A has 30,000 full field pulses, compared with 76,000 (10-T) pulses for the FED Baseline, the design stress is 30% higher for the FED-A coils.

8.2.3.1 Coil winding design concept

The peak field requirement for the TF coils is 10 T. The configuration of the coils is shown in Fig. 8-8. The TF coils can use all three concepts considered for the 1981 FED Baseline design: Nb_3Sn/NbTi pool-boiling or forced-cooled conductor at 4.2 K, NbTi pool-boiling conductor at 1.8 K (superfluid helium), and NbTi forced-cooled conductor at 3 K (supercritical helium). The winding cavity size is adequate to accommodate any of the options. The forced-cooled option using the NbTi internally cooled cabled superconductor (ICCS) is selected for illustrative design of the TF coils.

The TF coil winding design details are similar to those of the FED Baseline. The conceptual design parameters of the TF coils are given in Table 8-5. A schematic of the winding configuration in the inboard region is shown in Fig. 8-9. The coils employ pancake-type winding using an ICCS and consist of 22 full pancakes of 14 turns and 4 partial pancakes. The ICCS conductor is identical to the one used for the FED Baseline (NbTi strands in a steel conduit). The conductor is cooled by supercritical forced-flow helium with a maximum outlet temperature of 3.1 K. The conductor is co-wound with a C-shaped stainless steel channel to support the magnetic loads. The conductor-in-channel is insulated with wraps of Kapton and fiberglass tape. The assembled winding is vacuum impregnated with an epoxy potting compound, which provides additional electrical insulation.

The designs for helium manifolding connections, splices, and current leads are similar to the FED Baseline. The nuclear heating rate at the TF coil in the inboard region is less than 2 mW/cm^3 with a 62-cm shield thickness. This heat load is smaller than that in the FED Baseline design ($\sim$3 mW/cm^3). The ac losses in the winding are also expected

Table 8-5. Conceptual design parameters for TF coil

Parameter	Value
Number of TF coils	12
Field on plasma axis	5.0 T
TF ripple (peak to average), edge	1.0%
Plasma major radius	4.2 m
Peak field at the windings	10.0 T
Ampere-turns/coil	8.76 MAT
Operating current	27.4 kA
Conductor winding current density	2200 A/cm^2
Number of turns	330
Number of full pancakes	22
Number of partial pancakes	4
Maximum operating temperature	3.1 K
Maximum operating pressure	5.0 atm
Maximum discharge voltage	6 kV
Maximum radiation dose	10^9 rad
Maximum number of pulses	30,000
Stored energy/coil	$\sim$925 MJ

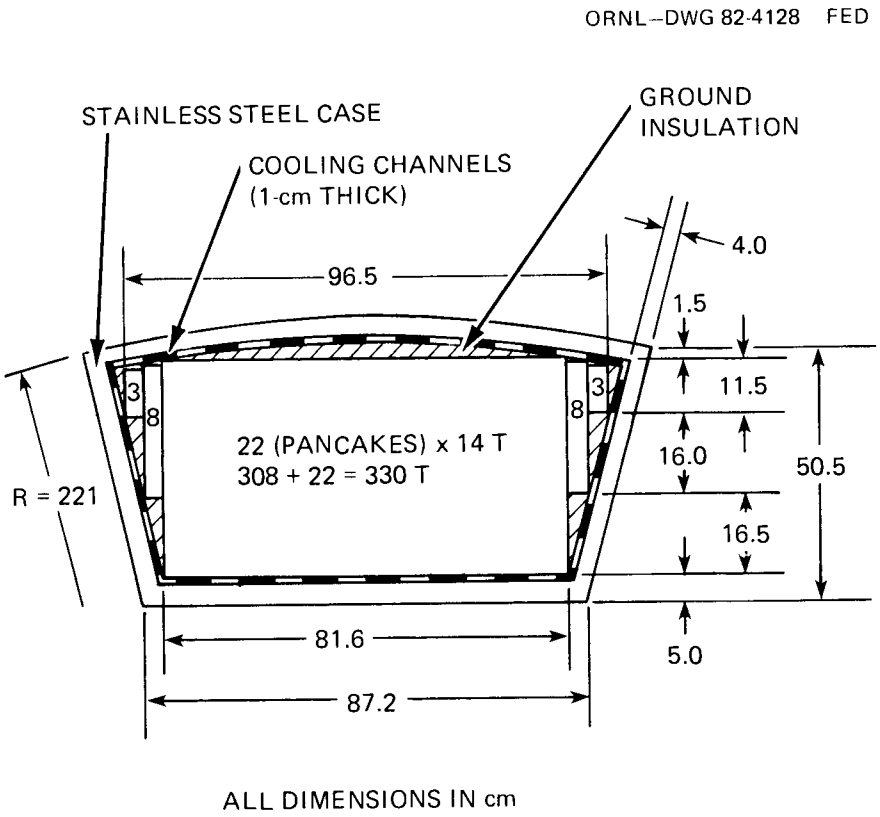

Fig. 8-9. TF winding configuration in the inboard region.

to be less than the FED Baseline. Both of these conditions ensure cryostable operation of the TF windings.

8.2.3.2 Winding layout concept

The FED-A configuration drawing shows a TF coil winding pack in which the side pancakes (partial pancakes) are against the bobbin ring in the inboard region but against the opposite wall of the case in the outboard window region. This winding configuration, which is used in the interest of improved access between TF coils, is not realizable using the conventional winding technique planned for the FED Baseline.

An alternate winding concept has been developed to achieve the desired winding configuration. The procedure involves winding the side pancakes on a different axis than that used for the central pancakes. The result is that in the outboard region, the side pancakes are moved radially outboard of the position they would occupy if the coil were wound conventionally.

For a given TF coil size, the proposed winding method affords a larger access opening between TF coils. Similarly, for a specified opening, the new winding technique permits use of smaller TF coils (i.e., outboard leg moved radially inward), which favorably impacts the overall device size.

Figure 8-10 shows the cross section in the inboard and outboard regions of a conventionally wound TF coil. The winding cross section is composed of a central rectangular region plus two smaller rectangular portions, one on either side of the central region. In the inboard region, this shape is well suited to the available space. In the outboard region, the arrangement is wasteful of space because the side rectangles are against the bobbin ring, limiting the access between adjacent TF coils.

If the winding cross section in the outboard region were such that the side rectangles were moved radially outward to be against the opposite wall of the case, the case cross section could be more closely contoured to the winding, as schematically indicated in Fig. 8-11. The result would be an increase in access between adjacent TF coils or,

ORNL-DWG 83-2289 FED

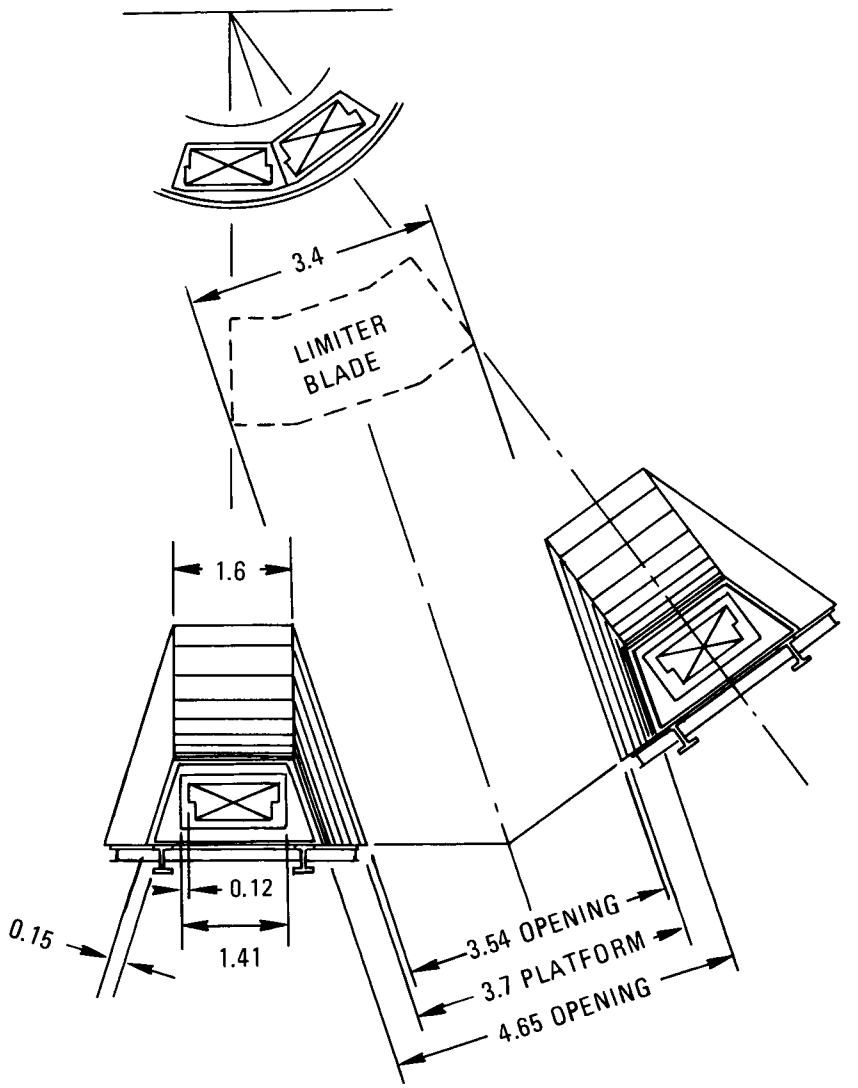

Fig. 8-10. TF coil cross section, showing access between TF coils.

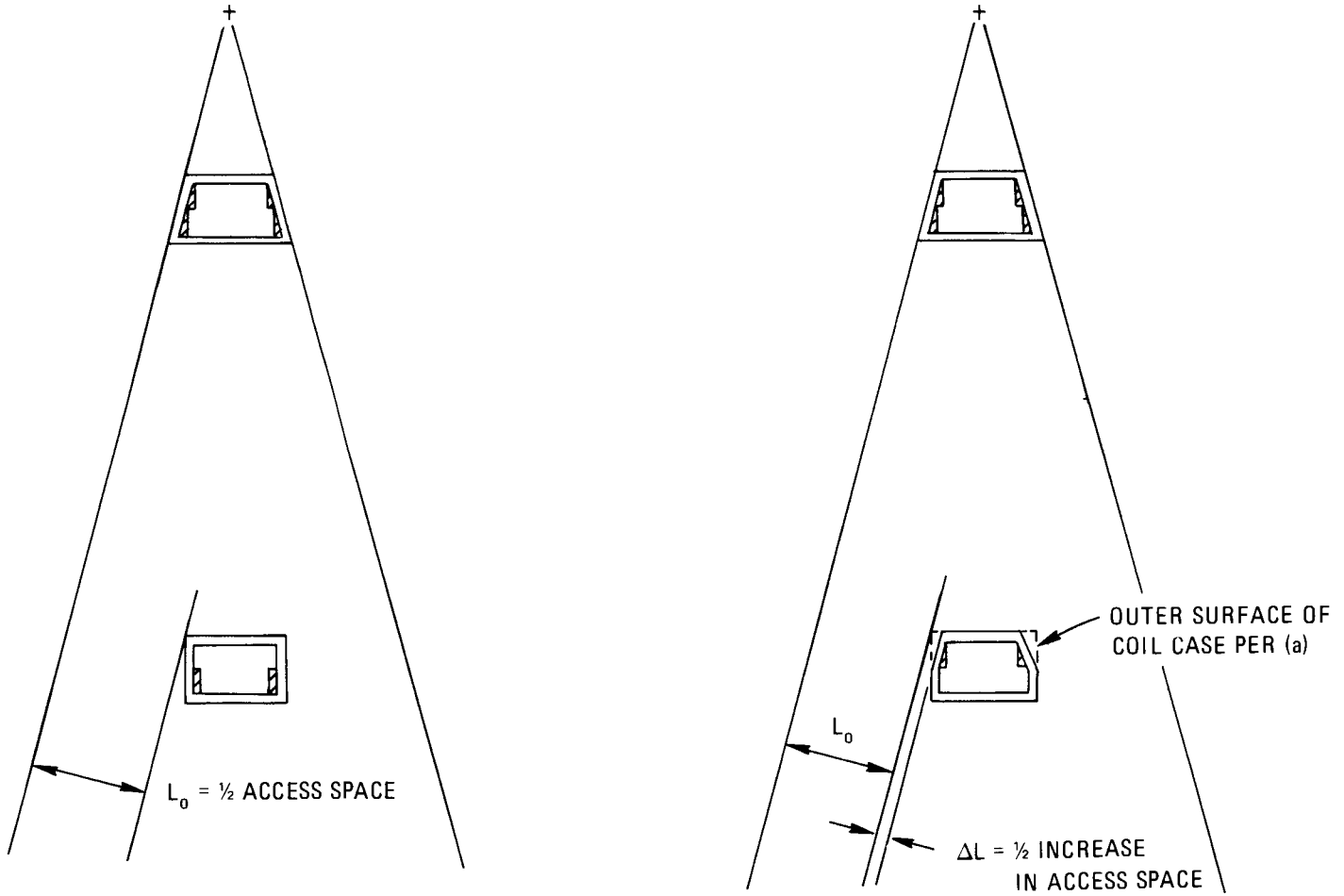

(a) CONVENTIONAL WINDING

(b) ALTERNATE WINDING CONCEPT

Fig. 8-11. Increase in access space due to new winding technique.

conversely, an opportunity to move the outboard leg of the coil radially inward while maintaining the original access between coils.

The practicality of this space-saving innovation depends upon finding a winding technique that will realize the desired winding layout in the outboard region. The technique to be described is suitable for a pancake-wound winding, although not for a layer-wound winding.

A pancake-wound winding using the configuration shown in Fig. 8-10 uses several partial pancakes on each side of the winding. The space inside the case that is not occupied by turns of conductor is occupied by a G-10 filler. In the inboard region, the cross section of the filler on each side of the winding is composed of two triangles. Over the remainder of the coil, the overall coil case cross section is rectangular, with a rectangular cross-section filler on each side of the winding.

In the outboard window region of the coil, it is proposed to use the coil case cross section shown in Fig. 8-11(b). Use of this cross section is responsible for the improved access between TF coils. Fabrication of this cross section would be somewhat more complex and costly than a simple rectangular cross section but is considered within present-day capabilities. In this region of the coil, the G-10 filler cross section on each side of the coil would change from rectangular to triangular.

Between the inboard region and the outboard window region, the present rectangular coil case cross section is maintained. However, over this portion of the coil, the single rectangular cross-section filler on each side of the winding is replaced by two variable cross-section (i.e., tapered) fillers, as schematically indicated in Fig. 8-12. The portion of the TF coil over which the variable cross-section fillers are used begins at the tangency point between the arcs of radius R_1 and R_3. The exact extent of the transition region, as well as the radius of curvature of the transition region [see Fig. 8-12(b)], is determined by the need to maintain a smooth tangency at the two ends of the transition region. The radius of curvature R_2' shown in Fig. 8-12(b) can be easily calculated and, in general, is slightly less than the

ORNL-DWG 83-2291 FED

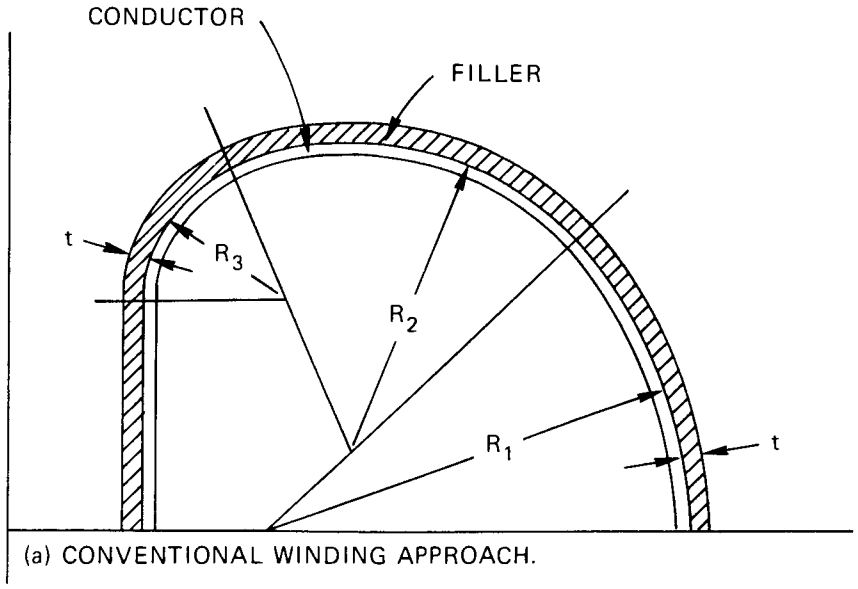

(a) CONVENTIONAL WINDING APPROACH.

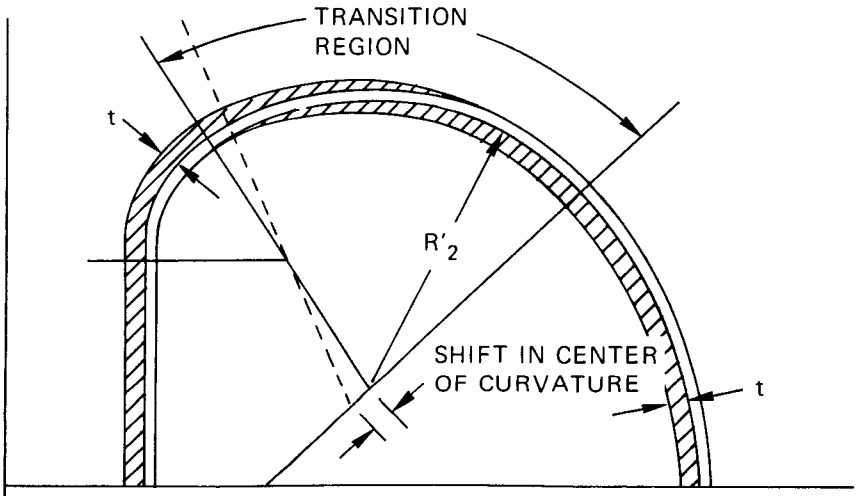

(b) PROPOSED WINDING APPROACH.

Fig. 8-12. Comparison of winding approaches for side pancakes.

radius of curvature R_2 shown in Fig. 8-12(a) for the conventional winding scheme. Figure 8-13 shows an isometric view of the proposed winding configuration.

Calculations using representative TF coil cross-section dimensions indicate that for a given TF coil size, use of the proposed winding concept increases the access space between TF coils by an amount $2\Delta L \approx 18$ cm, where ΔL is shown in Fig. 8-11(b). On the other hand, if it is desired to maintain a given access space, use of the new winding concept permits moving the outer leg of the TF coil radially inward by about 34 cm.

8.2.3.3 Impact of number of pulses on structural design

The structural design criteria used in the analysis of all magnet system components for which FEDC has design responsibility include a limit on peak tensile stress. This limit is based on the assumed existence of a structural flaw that can grow under the action of a cyclic stress, with the potential for eventual fracture. The size of the assumed flaw is taken as the largest defect that can escape detection during ultrasonic testing.

In typical pulsed tokamak applications, this criterion leads to a design-allowable stress for cyclically loaded components that is only a small fraction of the material yield strength. While the allowable stress is a function of the number of pulses for which the device is to be designed, the number of cycles is nearly always high enough so that this criterion is more restrictive than companion criteria, which limit primary membrane and bending stresses to fractions of yield and ultimate strength.

Figure 8-14 shows the allowable stress as a function of the required number of pulses for a range of initial flaw sizes. In drawing these curves, it is assumed that all pulses are of the same amplitude; if this is not the case, an equivalent number of pulses of a single amplitude can be defined. For example, the FED Baseline device is designed to withstand a combination of 8- and 10-T pulses. Since the stress level in a given structure varies as the square of the field, the amount of

ORNL–DWG 83-2292 FED

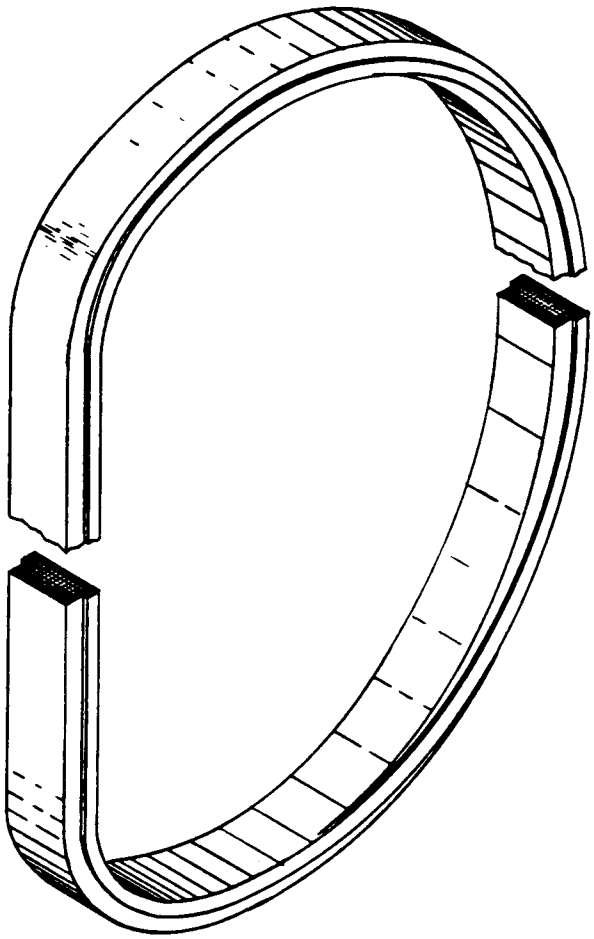

Fig. 8-13. Isometric view of proposed winding configuration.

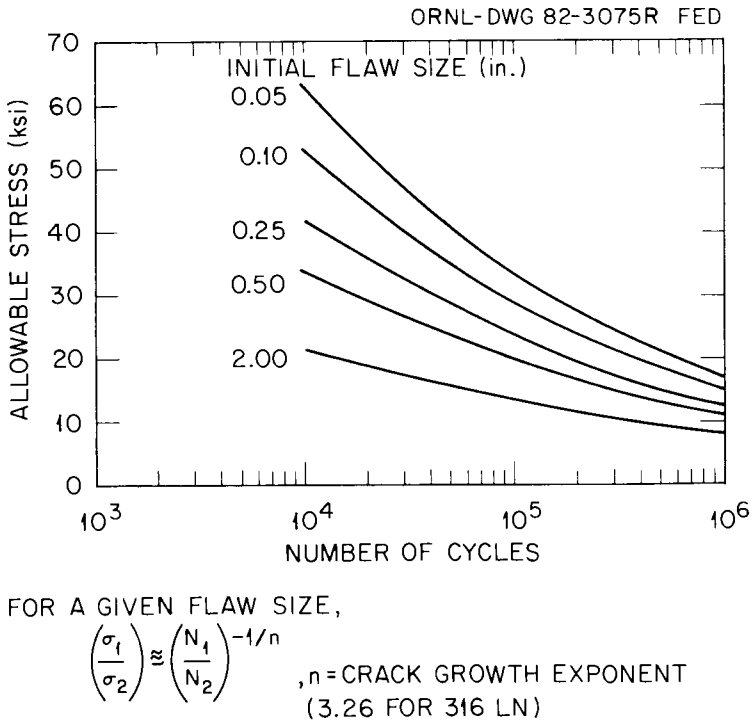

FOR A GIVEN FLAW SIZE,

$$\left(\frac{\sigma_1}{\sigma_2}\right) \cong \left(\frac{N_1}{N_2}\right)^{-1/n}$$

, n = CRACK GROWTH EXPONENT (3.26 FOR 316 LN)

Fig. 8-14. Allowable stress vs number of cycles for selected initial flaw sizes (316 LN material).

crack growth resulting from one 8-T pulse can be related to the amount of crack growth due to one 10-T pulse. From a fatigue damage standpoint, the "equivalent" number of 10-T pulses (with no 8-T pulses superposed) is the number of 10-T pulses needed to cause an initial flaw to grow to the same size as the specified combination of 8- and 10-T pulses.

The FED-A device is required to withstand 30,000 cycles, all between 0 and 10 T. If the initial flaw size is taken as 0.1 in., the allowable stress (from Fig. 8-14) is 40 ksi. In contrast, the FED Baseline device must withstand 250,000 cycles between 0 and 8 T plus 25,000 cycles between 0 and 10 T. The combination of 8- and 10-T pulses is equivalent to 75,600 pulses, all at 10 T. If the initial flaw size is again taken as 0.1 in., the allowable stress (Fig. 8-14) for the FED Baseline is 31 ksi (when the device operates at the 10-T level). Although the FED-A cycle requirement at first appears an order of magnitude less severe than that of the FED Baseline, most of the FED Baseline pulses are at a lower field level, at which the rate of flaw growth is greatly reduced. When compared on a consistent basis, the FED-A cycle requirement is about 40% as severe as that of FED Baseline (30,000 vs 75,600).

The section thickness of structural components that carry mostly membrane loads varies inversely as the allowable stress, whereas the section thickness of components that carry mostly bending loads varies inversely as the square root of the allowable stress. Figure 8-14 shows that for a given flaw size, the allowable stress varies approximately as the number of cycles to the power -0.3. Consequently, large changes in cycles are needed to significantly change the section thickness; in the case of a component that carries mostly bending loads, an order of magnitude reduction in cycles reduces the section thickness by about 30%.

8.2.3.4 Comparison of 8-T, 10-T, and 12-T TF coils

Alternate winding concepts were considered for the TF coils with peak field capabilities of 8 T, 10 T, and 12 T. These concepts are based on ongoing superconducting coil development programs such as LCP, the 12-T programs, ORNL's advanced conductor program, and other related programs. Overall winding configurations are developed for the three peak fields on the basis of credible winding current densities and structural needs.

The TF coil windings employ NbTi conductors for fields up to 10 T and Nb_3Sn conductors for fields between 10 and 12 T. The 8-T TF coil design concept is based on LCP technology for a pool-boiling or forced-flow mode of cooling (operating temperature of 4 K). The 10-T TF coils can be either superfluid helium bath-cooled ($\sim$1.8 K) based on the GA 12-T program or forced-cooled (at $\sim$3 K) based on ORNL's forced-flow conductor development program. The 12-T coils can have a hybrid Nb_3Sn and NbTi winding in a single cavity with pool-boiling or forced-flow cooling concepts. Alternatively, a 10-T portion can be made from NbTi forced-flow conductor cooled with 3 K supercritical helium and a 10- to 12-T portion made from Nb_3Sn conductor employing pool-boiling or forced-flow cooling. Various TF coil requirements and winding options are discussed below.

TF coil requirements. The TF coil requirements for FED-A are listed in Table 8-6. A variety of TF coil designs can meet these requirements. The plasma major radius may vary from 4.3 m to 4.8 m, as determined by system configuration and cost studies.[1] The peak magnetic fields on the coils range from 8 to 12 T with a ripple (peak-to-average) requirement of 1%. The TF coils must retain their cryostability during normal pulse operation and plasma disruption.

Toroidal field coils are subjected to in-plane and out-of-plane magnetic loads. The coil support structure must provide support for these magnetic loads and seismic and gravity loads and must be able to withstand 30,000 full field pulses.

Table 8-6. TF coil requirements

- Plasma major radius — 4.3 to 4.8 m
- Peak magnetic field — 8, 10, and 12 T
- TF ripple (peak to average), edge — 1%
- TF coil must operate in cryostable mode during
  - — normal pulse operation
  - — plasma disruption
- Magnet structure must withstand
  - — 30,000 full field pulses
  - — magnetic, seismic, and gravity loads
- Winding insulation must have acceptable structural and electrical properties after accumulating $\sim 10^9$-rad neutron fluence over the lifetime of the machine

TF coil winding concepts. The preliminary locations and currents for the PF coils as used for evaluation of the various TF coil concepts are shown in Fig. 8-8 and are used for sizing TF coil support structures. The winding options for 8, 10, and 12 T are listed in Table 8-7. The 8-T winding employs the NbTi conductor with pool-boiling or forced-flow cooling (at 4.2 K). The 10-T windings are made of cable-type NbTi conductor, but it is necessary to operate the winding at reduced temperature ($\sim$3 K for forced flow and 1.8 K with superfluid helium). For the 10- to 12-T winding portion, it is necessary to use Nb_3Sn with forced-flow or pool-boiling cooling. The achievable winding current densities at 8, 10, and 12 T are approximately 2500, 2200, and 2100 A/cm^2, respectively.

The conceptual design parameters for the three options are given in Table 8-8. The schematic cross section of the TF coils in the inboard region is shown in Figs. 8-15 through 8-17 for these options. Appropriate conductors used in each case are also shown in these figures. The coil windings are pancakes or layers, depending on the choice of the conductor. The overall cross section of the coils increases as a function of peak field. The coil case thickness is smaller than the FED Baseline. This is due to the lower number of pulses (30,000) for FED-A, which permits the use of higher design stresses for sizing the structures.

The state of the art of the various conductor candidates is summarized in Table 8-9. The technology base for the NbTi pool-boiling conductors up to 8-T operation is adequate. The LCP operation will provide the database for 8-T coils using the NbTi forced-cooled option, which could be extended to 10 T at reduced temperatures. However, fabrication experience with large Nb_3Sn windings is not adequate. The MIT 12-T program and Westinghouse LCP coil will provide some basis in this area. Similarly, the basis for the winding concepts using superfluid helium is being developed under the GA 12-T program.

Table 8-7. TF coil winding options

	8-T winding	10-T winding	12-T winding
Conductor	NbTi	NbTi	NbTi + Nb_3Sn
Cooling mode	PB,[a] FF[b]	PB, FF	PB, FF
Operating temperature	4.2 K	1.8 K, 3 K	4.2 K
Possible options	NbTi/PB/4.2 K NBTi/FF/4.2 K	NbTi/PB/1.8 K NbTi/FF/3 K	Nb_3Sn/PB/4.2 K Nb_3Sn/FF/4.2 K
Database	LCP	PB: GA 12-T program FF: ORNL conductor development	PB: GE or GD 12-T concepts FF: MIT/$\overline{W}$ 12-T program
Achievable winding current density (A/cm^2)	2500	2200	2100

[a] PB — pool-boiling.

[b] FF — forced-flow.

Table 8-8. TF coil concepts for FED-A

Parameter	8-T	10-T	12-T
Major radius (m)	4.32	4.65	4.89
Field on axis (T)	3.6	4.6	5.6
Peak field at the winding (T)	8	10	12
Ampere-turns/coil (MAT)	7.62	10.7	13.6
Operating current (kA)	20	25.5	25.5
Winding current density (A/cm^2)	2500	2200	2100
Overall current density (A/cm^2)	1510	1430	1350
Cooling mode	PB[a]/FF[b]	PB/FF	PB/FF
Operating temperature (K)	4.2	1.8/3	4.2
Clear bore (m^2)	6 × 7.5	6 × 7.5	6 × 7.5
Winding concept and material	Pancake-wound, NbTi	Pancake-wound, NbTi	Pancake-wound, NbTi/Nb_3Sn

[a] PB — pool boiling.

[b] FF — forced flow.

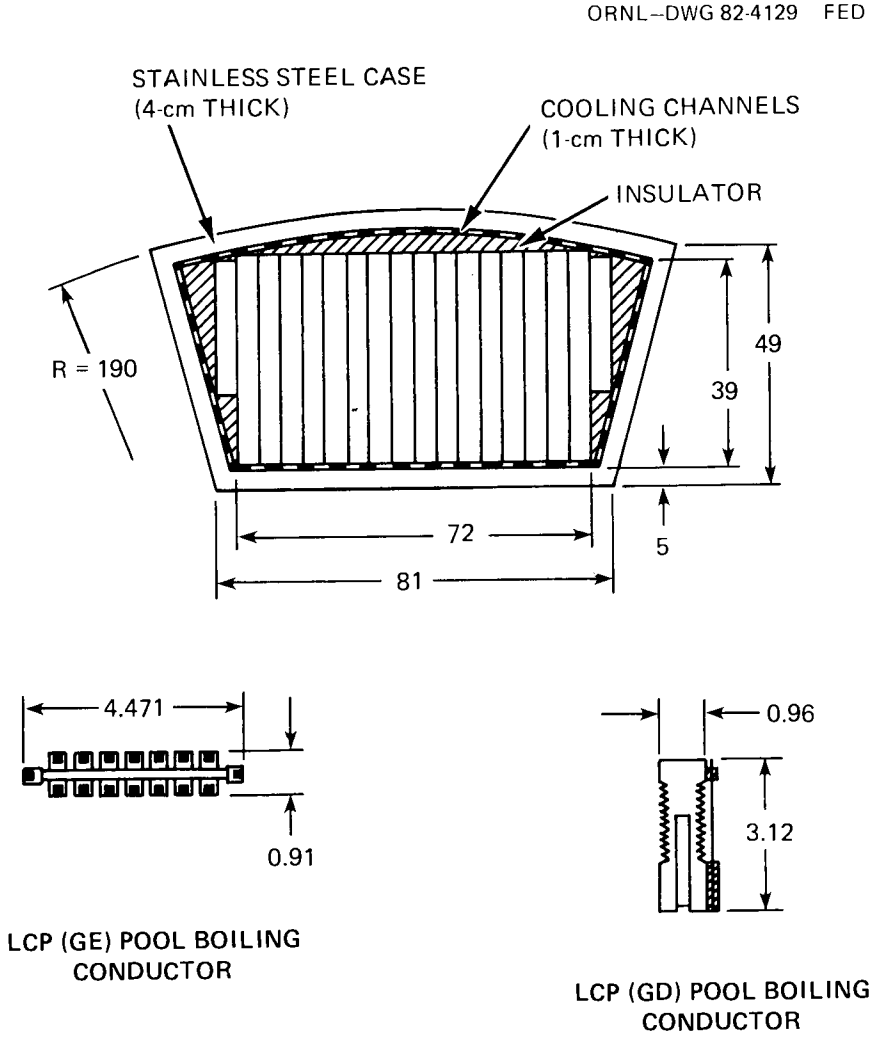

Fig. 8-15. 8-T TF coil design concept.

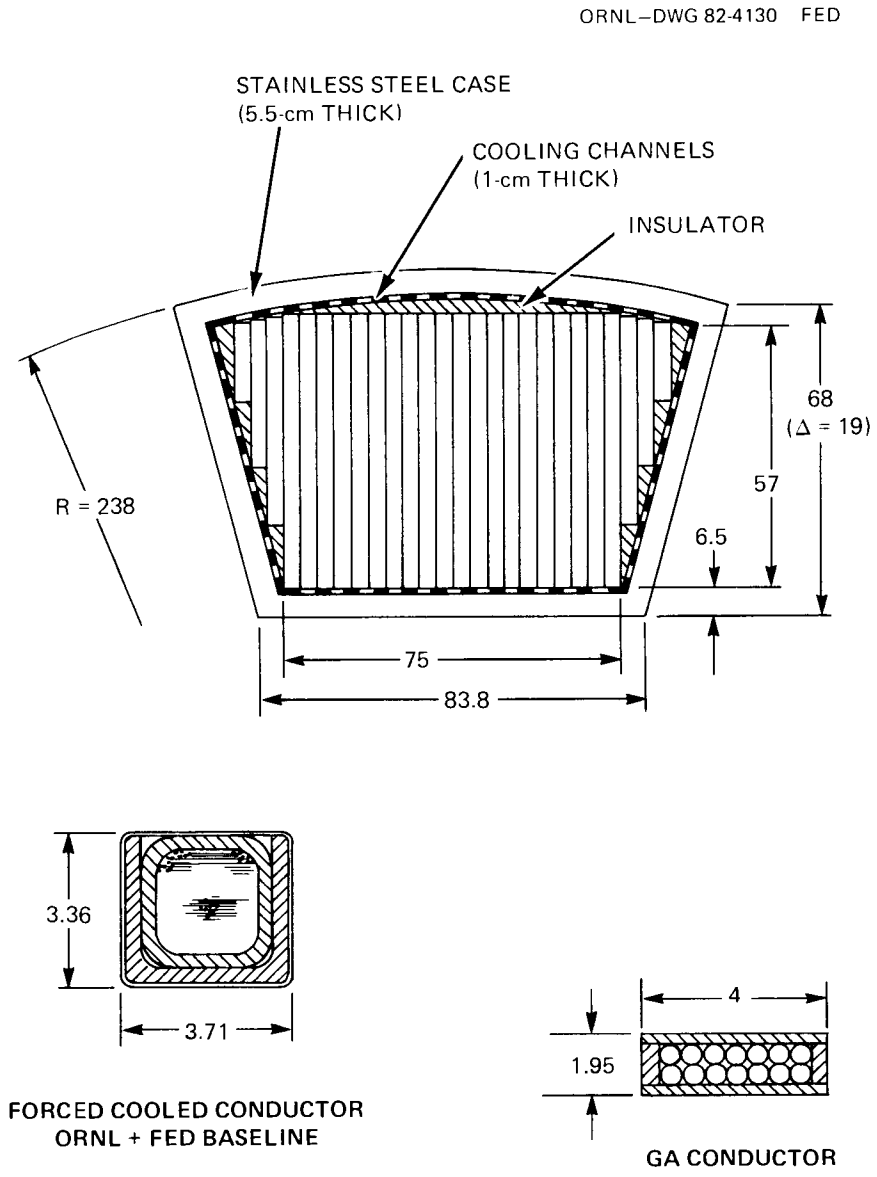

Fig. 8-16. 10-T TF coil design concept.

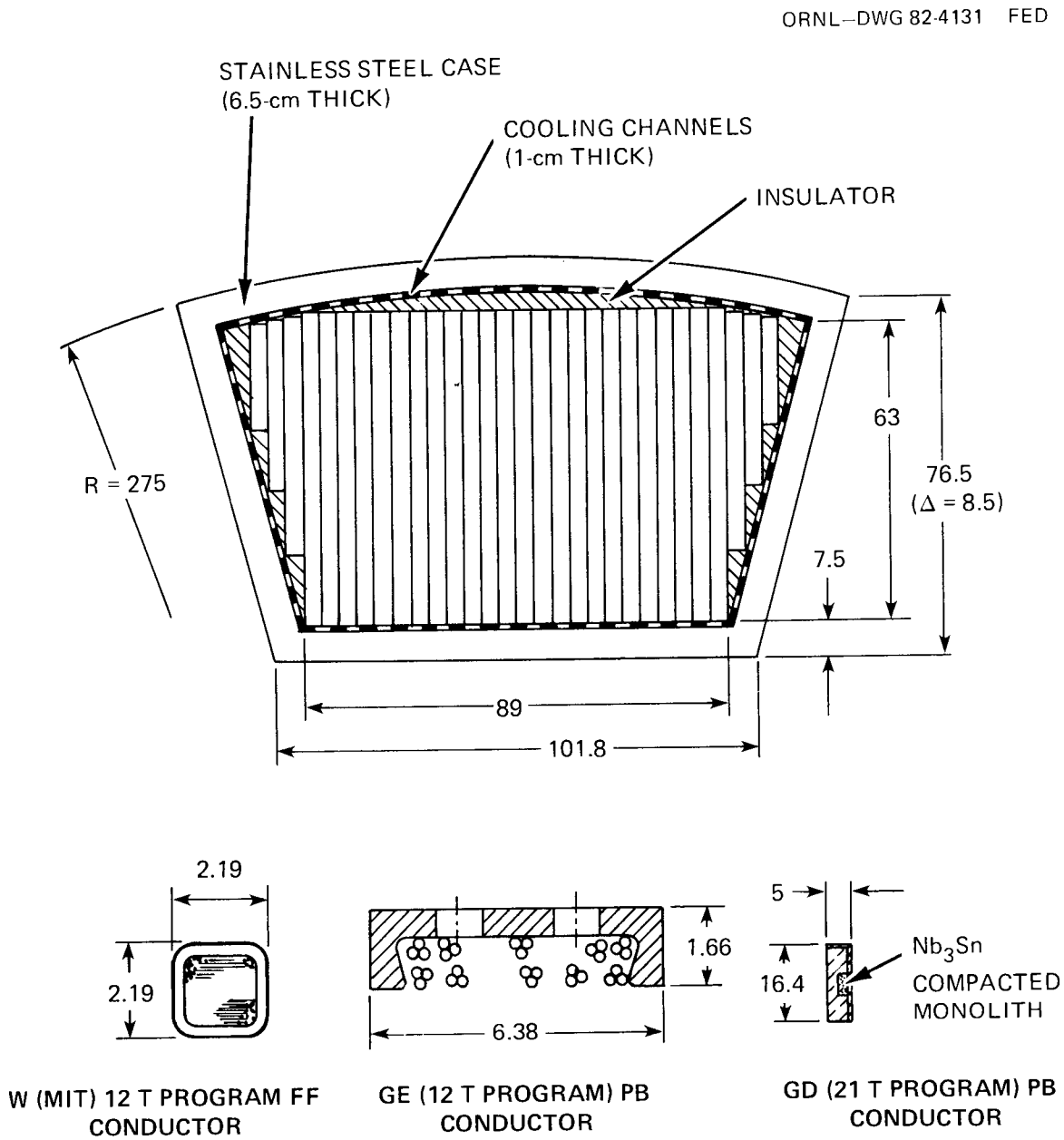

Fig. 8-17. 12-T TF coil design concept.

Table 8-9. Comparison of conductor state-of-the-art performance depends on conductor capabilities

Options	Advantages	Disadvantages
NbTi pool boiled at 4.2 K	Extensive LCP design experience	Peak field limited to 8 T
NbTi forced cooled at 4.2 K	LCP will provide database	Peak field limited to 8 T, but higher fields are possible at lower temperature ($\sim$3 K)
NbTi pool boiled at 1.8 K	Fabrication experience with NbTi cable-type conductor	Limited experience with superfluid helium system
Nb_3Sn pool boiled at 4.2 K	Large body of design/operational experience	Fabrication technology not matured
Nb_3Sn forced cooled at 4.2 K	Improved heat transfer Higher current density More reliable insulation Helium vessel not needed	Limited experience with forced-flow cooling Fabrication technology not matured

8.2.4 Poloidal Field Coil Design

The PF system consists of three coils, an OH solenoid and two EF ring coils. The OH coil is primarily used for inductive heating of the plasma. The EF coils shape the plasma cross section and provide the vertical field necessary to maintain the plasma in equilibrium.

The PF coil locations and coil current ratings are given in Fig. 8-8. The PF coil configuration is designed to satisfy plasma stability requirements and to provide the required volt-seconds (see Table 8-4) for the start-up and burn phases. Maximum field at the OH solenoid winding is limited to 8 T — the field is much lower at the EF ring coils. The coils are designed to be cryostable with normal heat loads such as winding losses, coil case losses, lead and joint losses, and heat load generated by transient conductor motion. Their structural design is adequate to support magnetic loads, gravity loads, a 1-g seismic load (laterally and vertically), and operating pressure differential.

The machine is designed for a total of 30,000 full field pulses. Each full field pulse has 10 burn pulses. The OH solenoid goes through full bipolar swing during each burn pulse; therefore, the total number of pulses for the solenoid is 600,000 (= $2 \times 10 \times 30{,}000$). The FED Baseline solenoid has the same number of pulses. Therefore, the designs of the solenoids for FED-A and FED Baseline are almost identical. On the other hand, the EF ring coils are subjected to 30,000 pulses, which is much less than that for the FED Baseline. As discussed in Sect. 8.2.2, higher design stresses can be used for sizing structures for these magnets.

8.2.4.1 Ohmic heating solenoid design

The solenoid employs NbTi superconducting winding. The winding can be cooled with pool-boiling helium or forced-flow helium. The pool-boiling, helium-cooled design is based on the conductor developed by LANL for their 20-MJ pulsed coil. The conductor design can be considerably simplified because the FED-A start-up time ($\sim$26 s) is considerably

longer than that for the LANL 20-MJ coil (1-2 s) and the FED Baseline (6-12 s). The basic conductor is rated for 50 kA and is built up from multiple strands of NbTi. Detailed descriptions of the conductor, the winding configuration, and the performance analysis are provided in the 1982 FED Baseline report. The FED-A solenoid will be of similar design.

The forced-flow, helium-cooled design is attractive because the solenoid has a potential of being more compact. The coil employs conductor similar to that used in the TF coils of the 1981 FED Baseline but with some modifications to account for the pulsing nature of the OH solenoid. The conceptual design of the OH solenoid was developed for the FED Baseline and is described in the 1982 FED Baseline report. The solenoid is designed to withstand the electromagnetic loads and to provide cryostable operation. The FED-A solenoid design will be similar.

8.2.4.2 Ring coil design

FED-A has two ring coils. They can be designed using the pool-boiling or forced-flow helium cooling systems. The conductor is NbTi optimized for the EF coil operating field. The ring coil designs were developed for the FED Baseline using the two cooling concepts. These designs are described in the 1982 FED Baseline report. The FED-A coils will be similar in design but will be modified to reflect lower conductor and structure costs caused by the lower number of pulses in FED-A.

8.3 OVERALL MECHANICAL CONFIGURATION

The FED 400 configuration concept has been applied to FED-A using the FED-A design specifications. The results are reflected in the elevation and plan view drawings shown in Figs. 8-18 and 8-19. The main design features include:

1. 12 TF coils and 12 torus sectors,
2. a combined vacuum boundary between the superconducting magnet system and the torus plasma chamber,

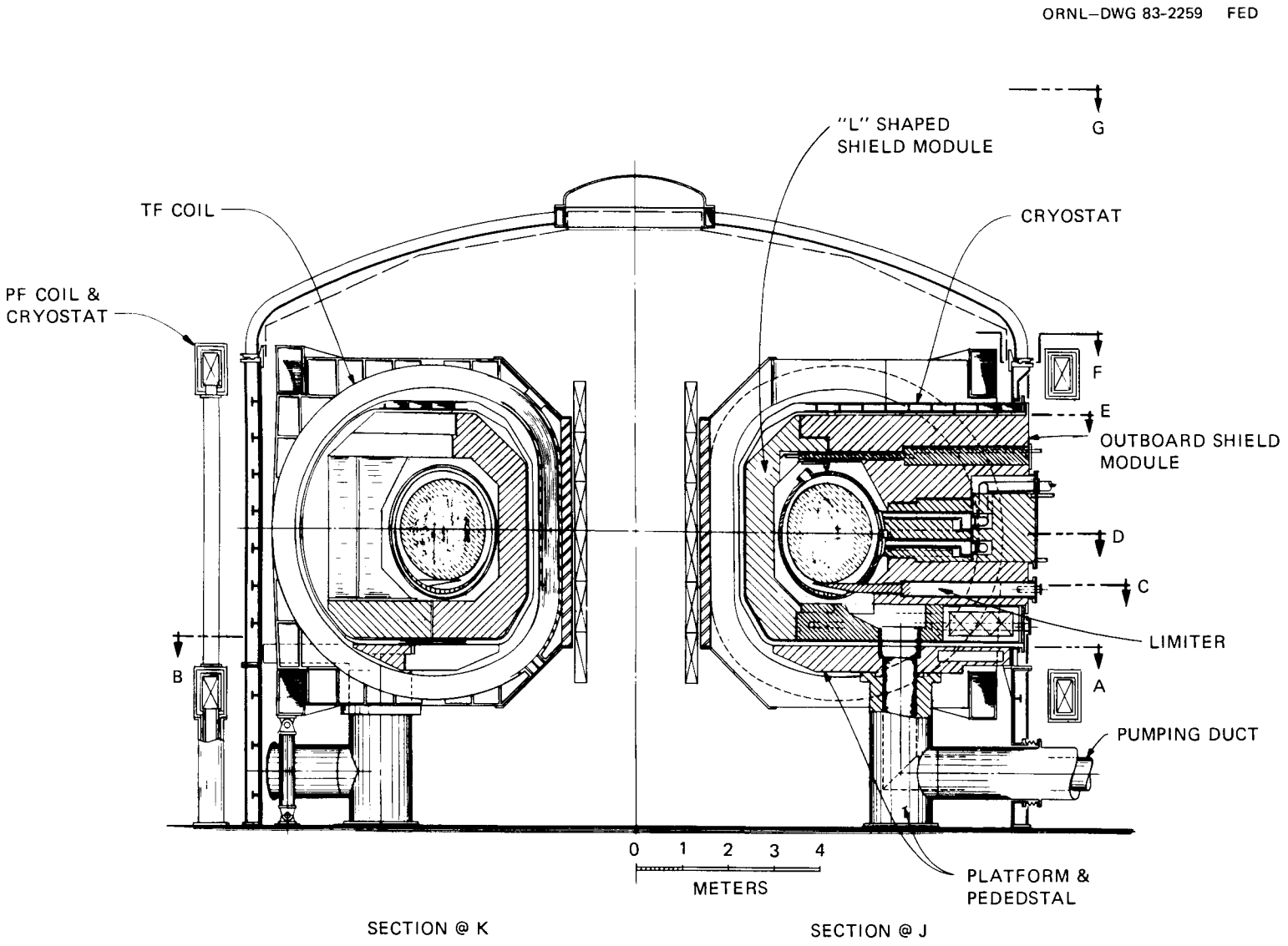

Fig. 8-18. FED-A elevation view.

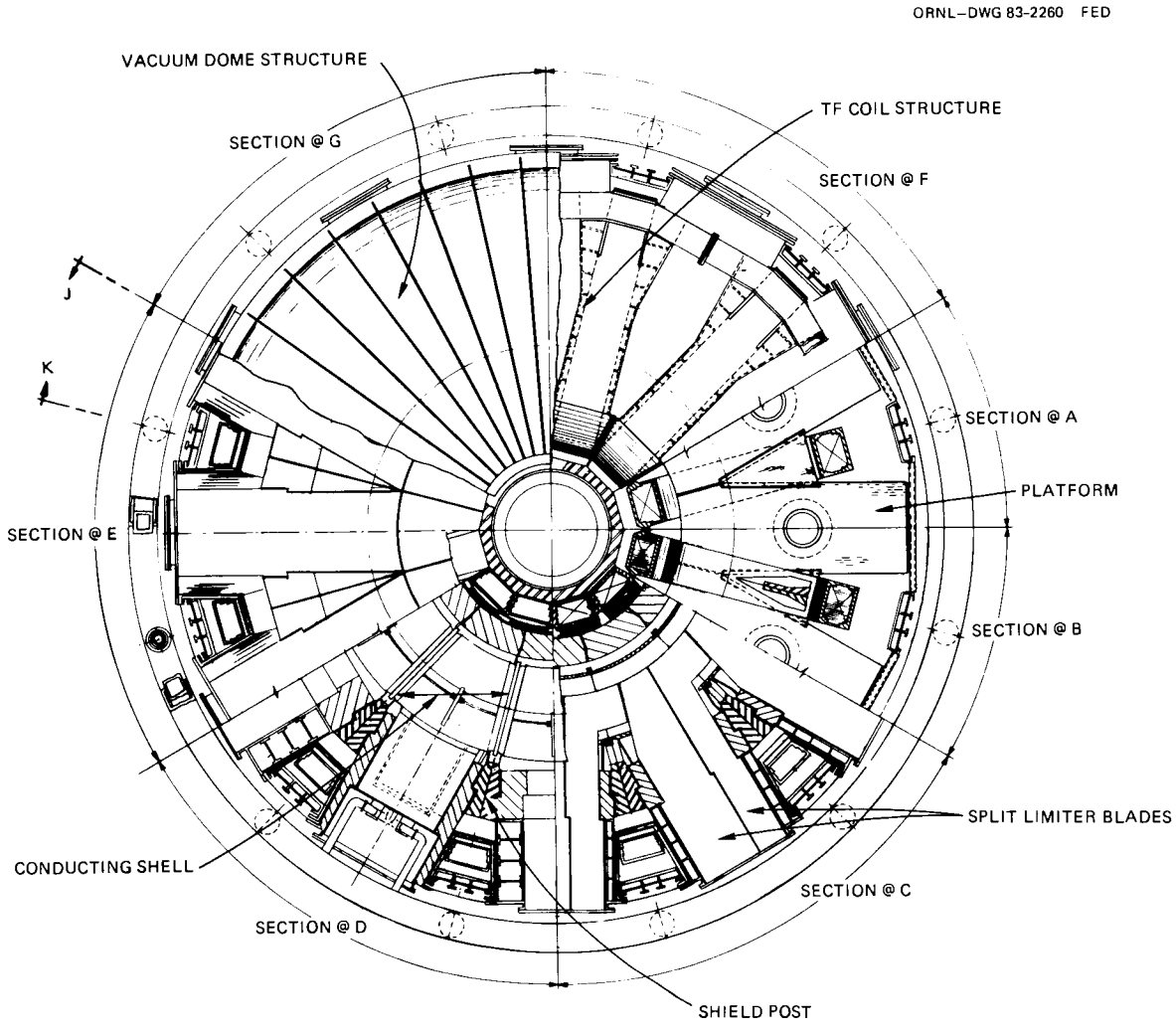

Fig. 8-19. FED-A plan view.

3. a lower outboard EF coil located in a separate vacuum boundary,
4. a torus shell located inside the shield module, and
5. vacuum pump ducts providing the gravity support for the torus.

The arrangement of components around the device is illustrated in Fig. 8-20. The allocation of testing and diagnostics areas has not been defined at this time.

8.3.1 Torus

The torus configuration had to be modified from the original FED 400 concept to provide access to install the torus shell. In lieu of removing a full torus sector, the torus sector was split into two major submodules: a semipermanent L-shaped module and a removable shield module (see Fig. 8-21). The L-shaped modules are first installed using a transport device, as shown in Fig. 8-22. Note that a smaller shield plug is removed from the bottom of the L-shaped module to allow the transport device to engage the module. After the L-shaped module is in place and checked out, a vacuum cover plate is welded to the combined vacuum boundary structure in the region in front of the shield module (see Fig. 8-23). The installation of the torus shell structure follows. The configuration details of the combined vacuum boundary are also shown in Fig. 8-23, including the cryostat modules that lie under each TF coil, a semipermanent window module that wedges between the ring modules and is joined to a permanent outboard wall structure, a permanent lower wall structure surrounding the bottom of the device, and a torispherical dome forming the vacuum boundary at the top of the device. All module interface joints are made with a continuous in-plane structure tie and vacuum seal weld, which forms an annulus for leak detection. The outboard wall structure can be electrically broken if required.

8.3.2 Poloidal Field System

The important reactor design consideration with regard to the PF configuration is the placement of the three EF coils, the lower high beta divertor coil and the two outboard EF coils.

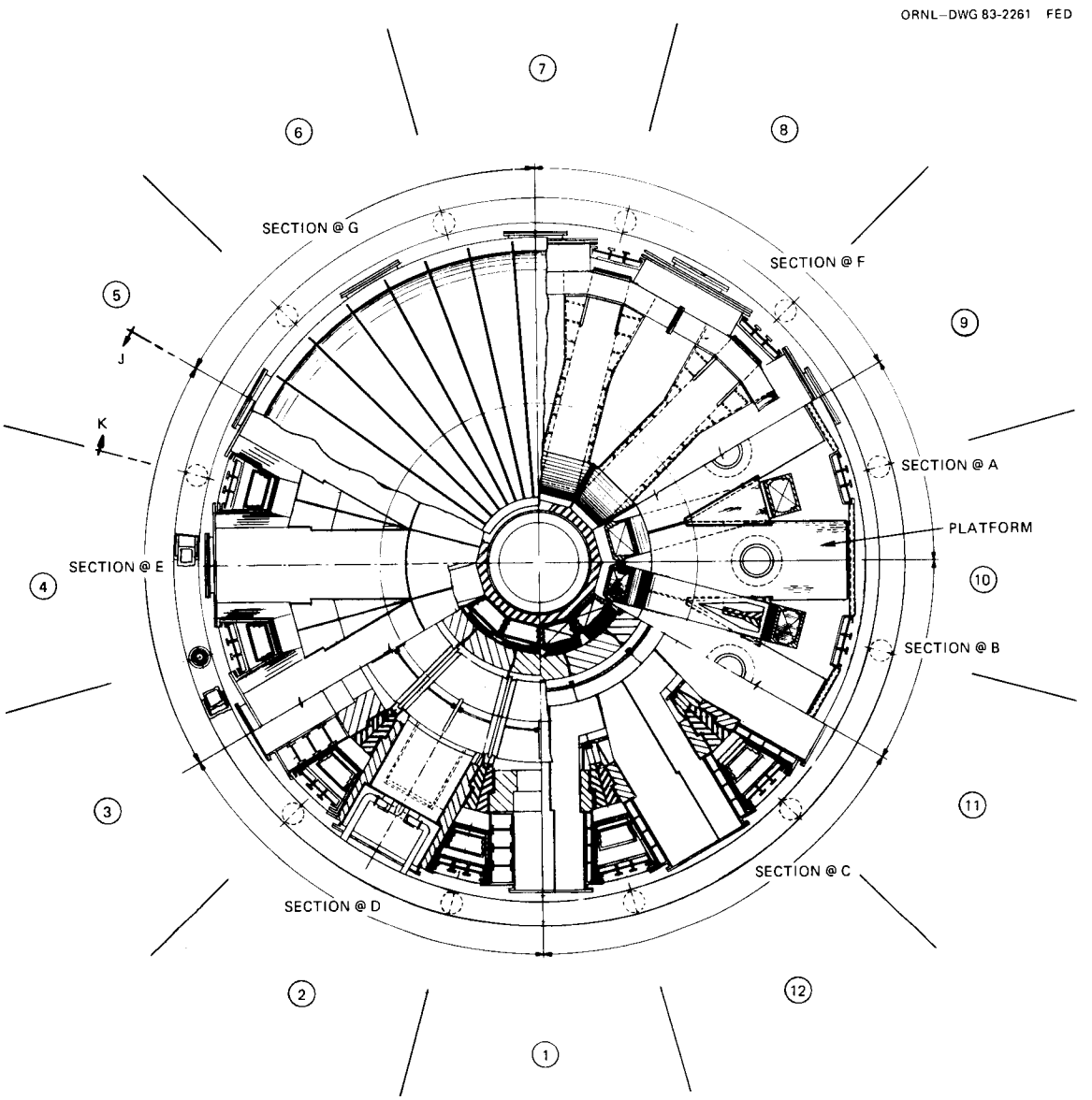

COMPONENT	SECTOR POSITION
PELLET INJECTOR	1
ICRH	2 PER SECTORS 2 - 4
LHRH	6
ECRH	2 PER SECTORS 1 THRU 12

Fig. 8-20. Component arrangement around FED-A device.

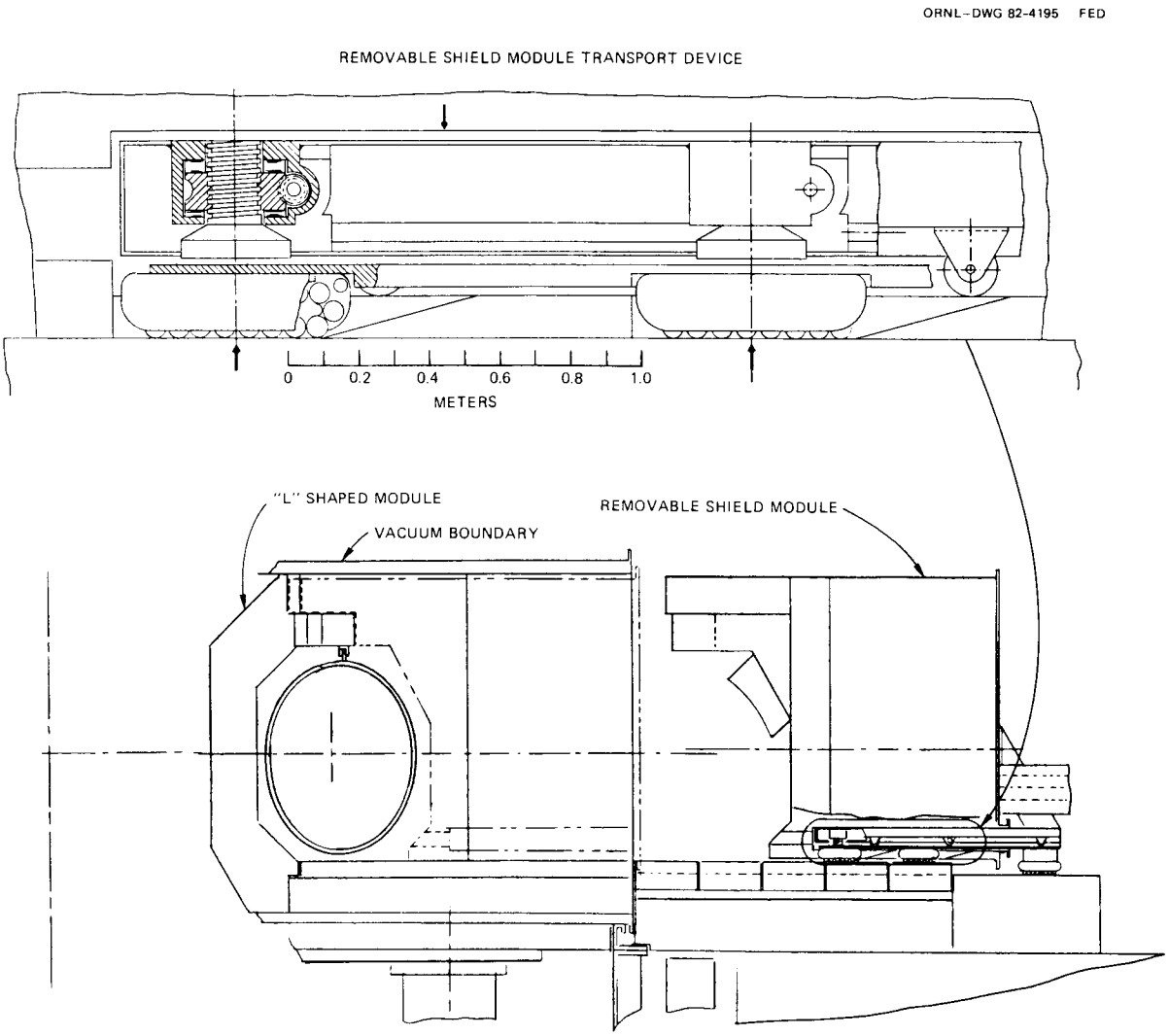

Fig. 8-21. Torus module segmentation approach.

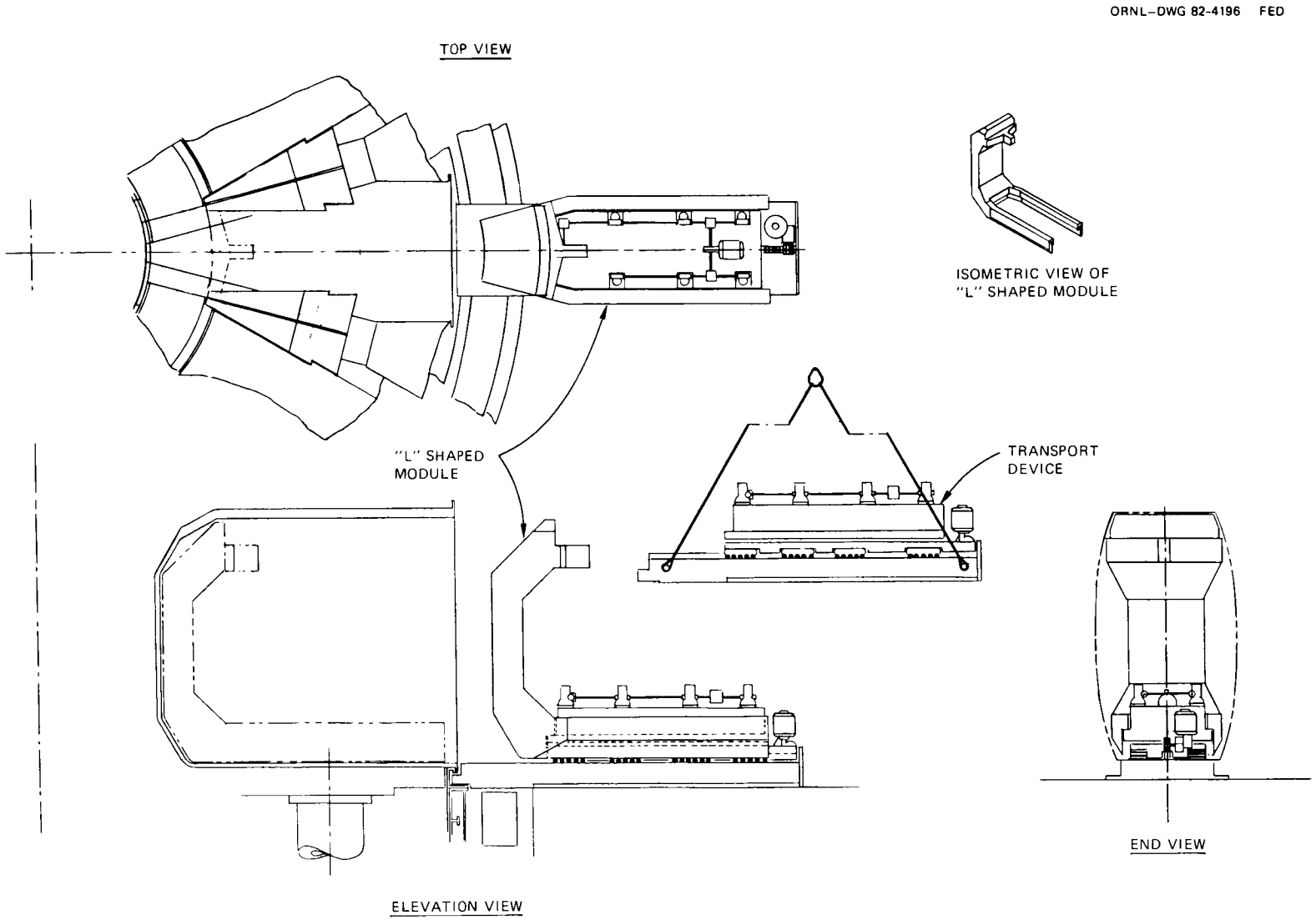

Fig. 8-22. Installation devices for L-shaped module.

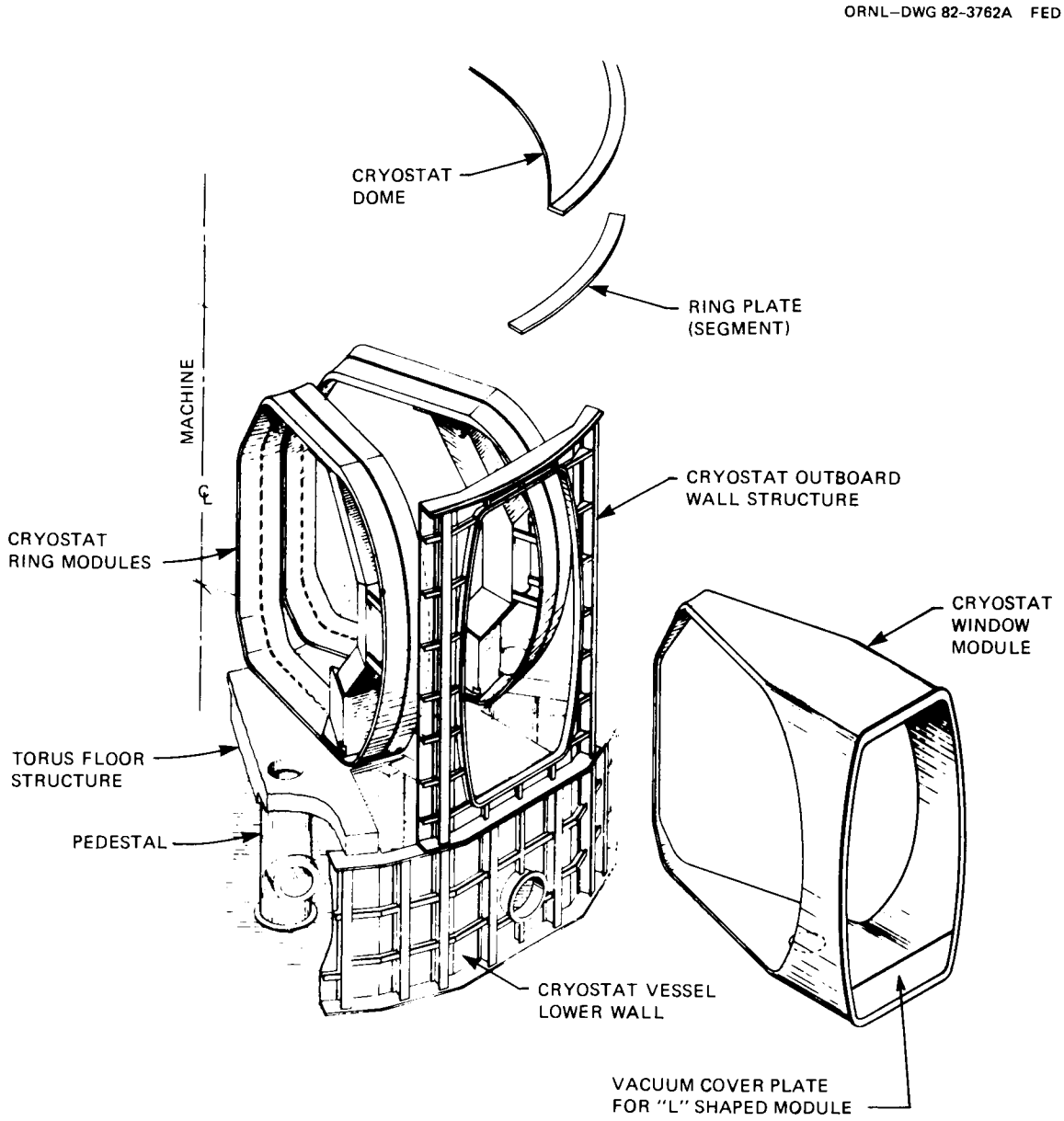

Fig. 8-23. Combined vacuum boundary structural arrangement.

The maintenance scenario has been simplified by locating the outboard EF coils in a separate vacuum boundary independent of the remaining superconducting magnet system. Only those components and lines protruding past the inner radius of the outboard EF coils must be removed for maintenance; the outboard EF coils only are warmed up, the EF coil vertical supports are detached, and the coils are removed. The TF coil maintenance approach involves removing the TF coil vertically, retaining a fixed outboard wall vacuum structure; therefore, maintenance is independent of the outboard EF coils. Cryogenically, the outboard EF coils can be isolated from the warm structure in the same manner as the TF coil system. By incorporating a glass isolation section and a nitrogen barrier, the thermal heat load should be minimized. All things considered, incorporating the outboard EF coils in a separate vacuum boundary considerably improves the maintenance and availability of the tokamak design, while no incurring real cost penalties.

Since the FED-A plasma is only slightly elongated, a set of relatively low current, D-shaped coils was located in the inboard region of the device, inside the torus vacuum/torus support columns (see Fig. 8-18). The coils at the bottom of the device can be removed through an access tunnel provided under the device.

8.3.3 Toroidal Field System

A TF coil structural design concept has been incorporated in the FED-A configuration that has modified the structure between TF coils along the top and bottom (see Fig. 8-24). The local structure that was used to stiffen the case was increased and flared outward locally to pick up the outer ring beam structure. Bolted TF coil interfaces are located between TF coils along the inboard region of the TF coil corners and at the midsection of the upper ring beam. The upper ring beam was turned inward to provide bolt access around the joint to prevent interference with the upper outboard EF coil. A preliminary decision has been made to retain a continuous lower ring beam to provide a datum for the initial erection of the TF coils. The lower outboard corner of the TF coil would be bolted to this beam.

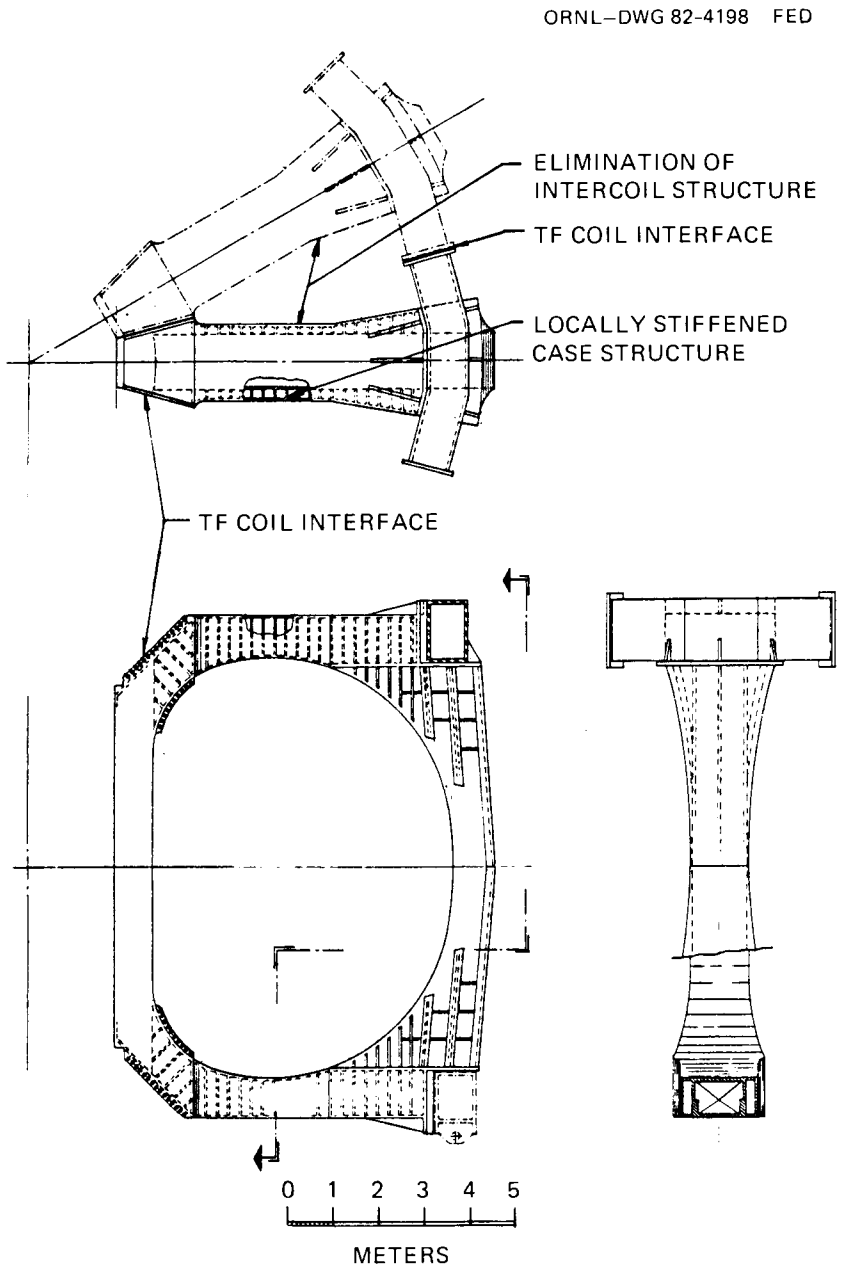

Fig. 8-24. TF coil structural design concept.

A preliminary structural analysis of this concept was performed on the FED Baseline reactor design using a pumped limiter loading condition. The results show that the proposed concept appears feasible. The motivation behind this TF coil structural arrangement is threefold:

1. The structural interface between TF coils is concentrated in four places, which will improve the maintenance of the TF system.
2. The intercoil structure is eliminated, reducing the number of parts (therefore cost) and the eddy current heating associated with it.
3. Direct torus access is made available for the vacuum ducts, magnetic electrical leads, helium coolant lines (for forced-flow TF coils), and diagnostics.

8.3.4 Impurity Control

In order to allow sufficient sidewall area for the torus shell in the region of the limiter, a split limiter module was incorporated in the FED-A design (see Fig. 8-25). The two-piece limiter module is extracted in the following sequence:

1. The unrestricted limiter module is extracted in a straight-line motion once the divertor vacuum door is removed.
2. A manipulator device is inserted and attached to the remaining limiter module.
3. The manipulator device pulls the limiter module to clear it from any sidewall osbstructions. At this point the remaining limiter module can be extracted in a straight-line motion.

Clear access space has been provided around the machine in the region of the limiter to allow the limiter blades to be removed without interfering with any peripheral equipment or service lines.

8.3.5 Heating System

Three rf heating systems have been defined for the FED-A device. They include: (1) electron cyclotron resonance heating (ECRH) to assist the plasma current start-up, (2) ion cyclotron resonance heating (ICRH)

ORNL-DWG 82-4197 FED

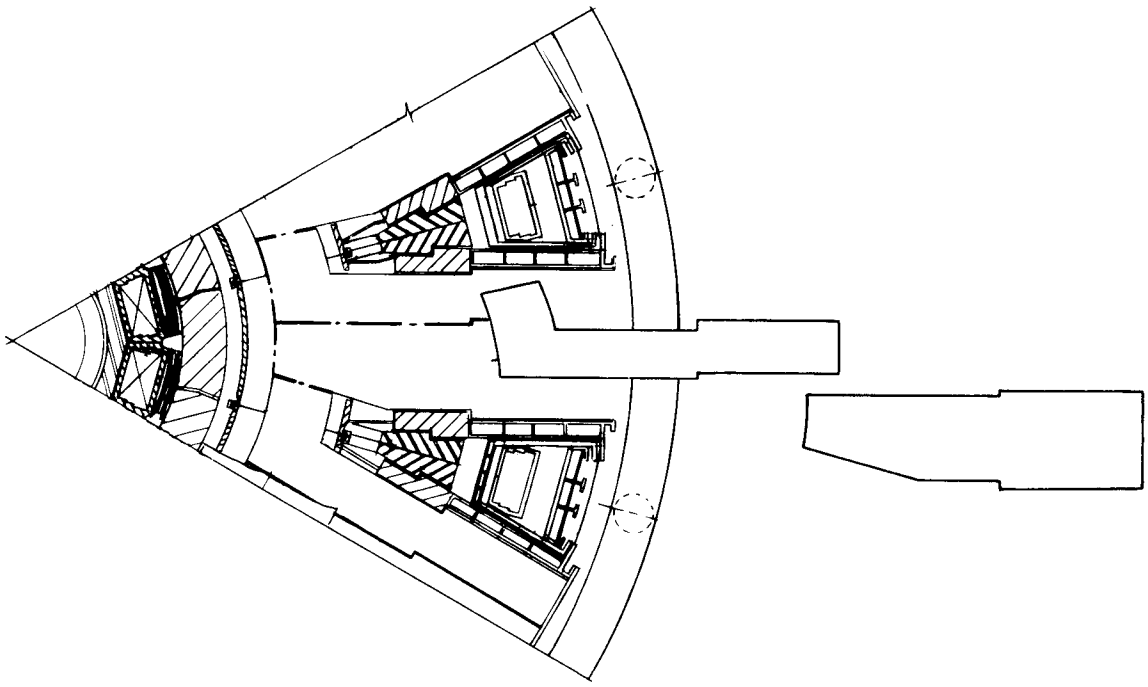

Fig. 8-25. FED-A split limiter arrangement.

for bulk heating to burn or ignition, and (3) lower hybrid resonance heating (LHRH) to maintain the plasma current during burn. Figure 8-26 illustrates the ICRH and ECRH system interface with the torus, and Fig. 8-27 shows the torus interface with the LHRH system. The distribution of the rf heating components around the device can be found in Fig. 8-20.

Each component interfaces with the torus module in a manner that allows effective maintenance of all systems. The waveguides, coolant, and electrical leads to the rf components are contoured to follow a path around the limiter access space and are concentrated in an area behind the outboard leg of the TF coils. A detailed description of the rf component designs can be found in Sect. 7.3.

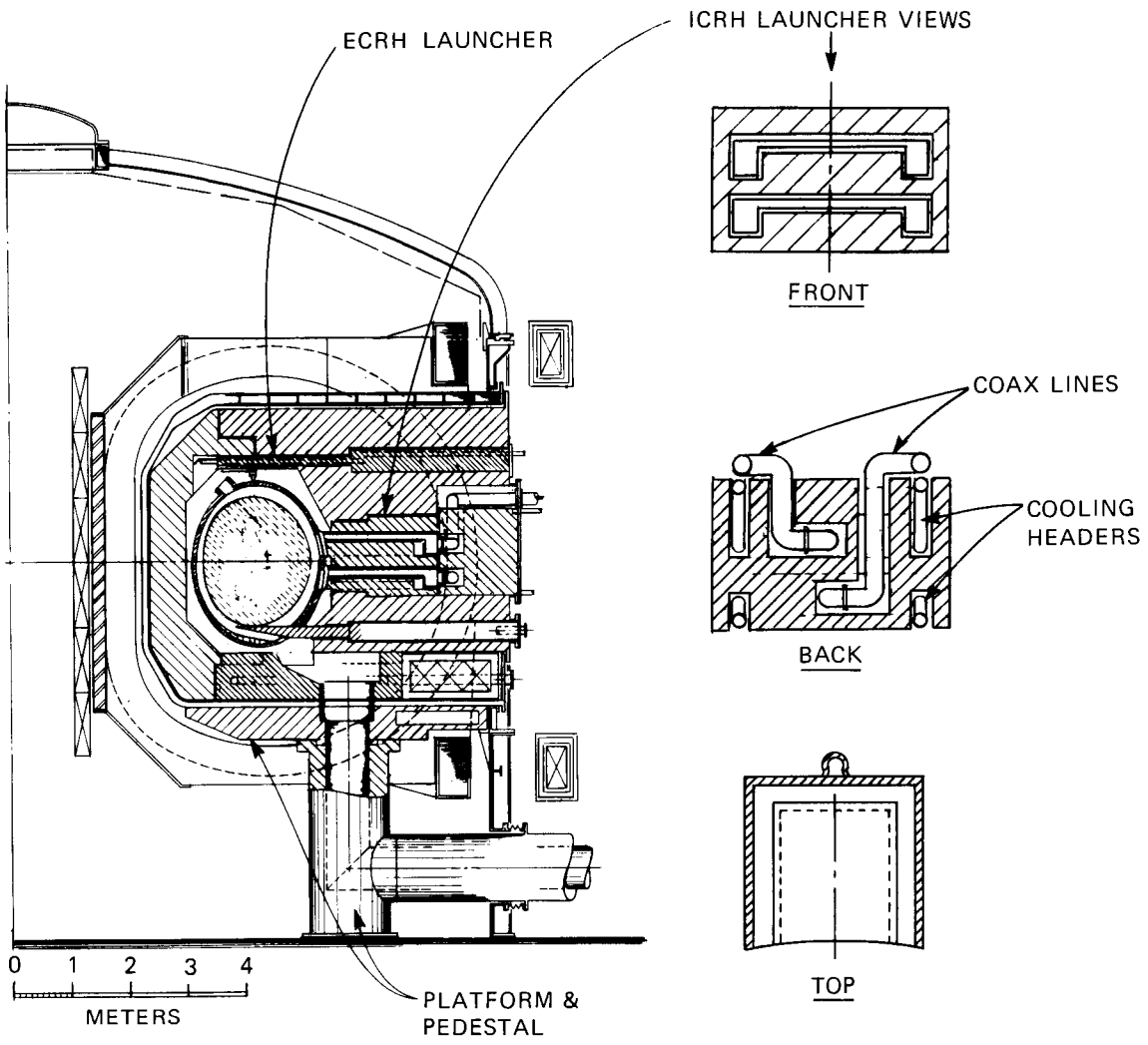

Fig. 8-26. ICRH and ECRH interface with torus.

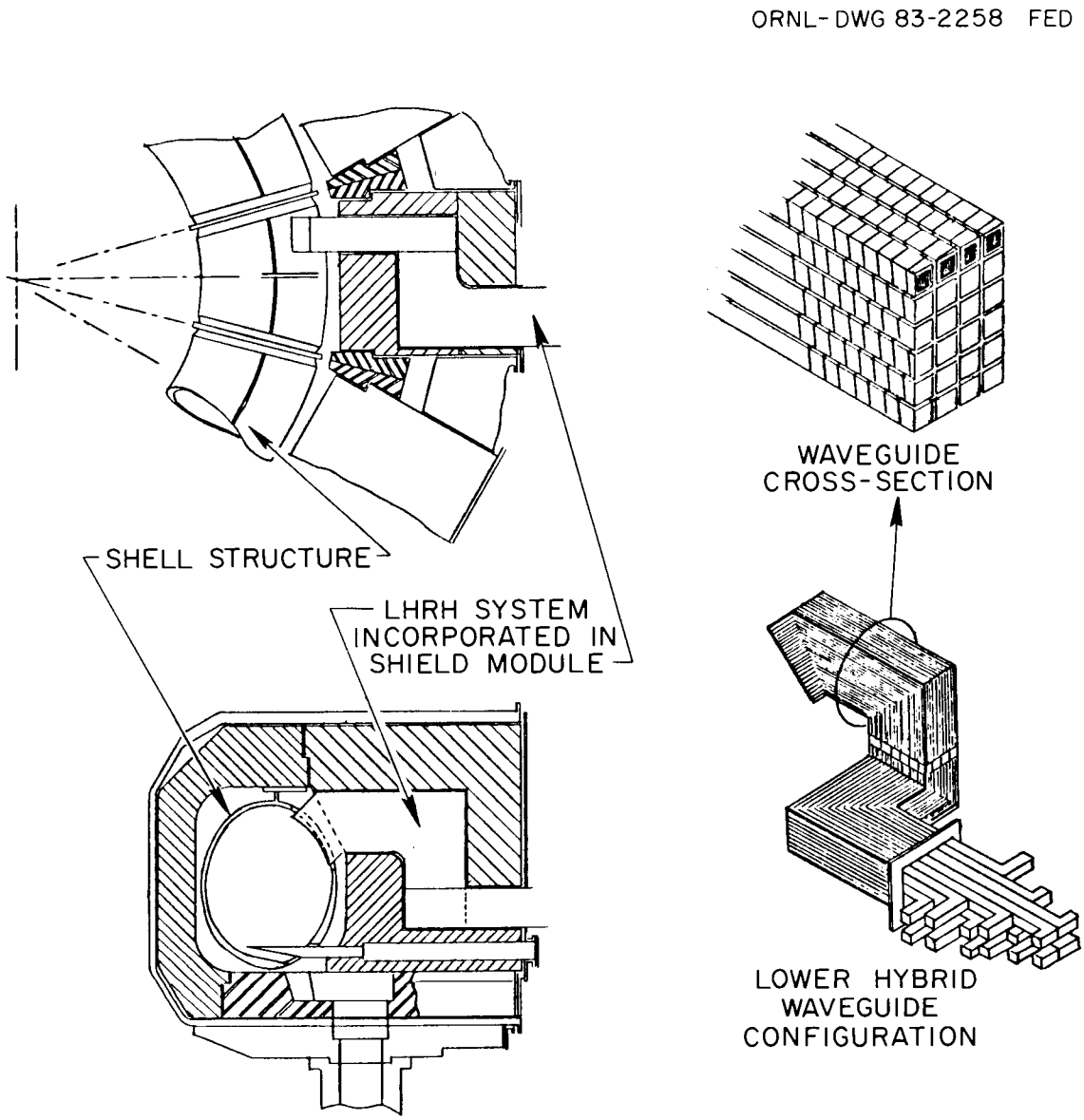

Fig. 8-27. LHRH interface with torus.

REFERENCES

1. D. J. Strickler and Y-K. M. Peng, "The Poloidal Field System of the Fusion Engineering Device," in *Proceedings of the 9th Symposium on Engineering Problems of Fusion Research*, vol. I, IEEE, New York, 1981, p. 515.
2. S. K. Borowski, Y-K. M. Peng, and T. Kammash, *RF-Assisted Current Startup in the Fusion Engineering Device (FED)*, ORNL/TM-8319, Union Carbide Corp. Nuclear Div., Oak Ridge Natl. Lab., August 1982.

9. COST AND SCHEDULE

One of the major elements of the FED-A studies is to assess the cost-effectiveness of incorporating the advanced physics assumptions of low q, high beta, and partial noninductive current drive. While Chap. 5 has dealt with the comparison among various candidate FED-A designs, this chapter provides a more detailed cost estimate of the chosen design to allow comparisons with the FED Baseline. In constant 1981 dollars, the FED-A is estimated to be about 30% less in direct total cost than the baseline, based on nearly identical costing algorithms.

9.1 COST

The capital cost for FED-A was estimated using costing algorithms and unit cost values obtained from current fusion projects (TFTR, TSTA, LCP, and JET) and from data supplied by architectural engineering firms for large construction projects. The capital cost for FED-A is consistent with the quantities of materials, building sizes, electrical power requirements, and stored energy requirements associated with the tokamak parameters shown in Table 5-15.

The following assumptions were made in developing the cost projection for FED-A:

- All costs are based on constant 1981 dollars.
- Direct capital costs include all costs associated with component procurement and fabrication, including shipping to the construction site.
- Indirect capital costs include engineering design and project management as well as all equipment installation and assembly at the construction site.
- A 30% contingency is included in the total cost.
- The estimate is only for the FED construction project and does not include any operating or maintenance costs, spare parts, fuel, associated research and development, transmission lines, or decommissioning.

- Direct capital costs were estimated by applying unit cost values and algorithms that have been developed as part of the FEDC systems code.
- The indirect costs for engineering (45%), installation, and assembly (15%) are based on fixed percentages of the direct costs and represent a best judgment based on recent large DOE projects.

The capital cost for FED-A is presented by system in Table 9-1 together with some key cost values for the 1981 FED Baseline. The direct capital cost is $729 million, and the indirect capital cost is $437 million, giving a total (direct plus indirect) cost of $1.167 billion. Adding a 30% contingency brings the total cost to $1.517 billion. A 30% reduction in cost from the baseline is seen as a result of major cost reductions in magnet systems, torus, cooling systems, electrical systems, and vacuum pumping systems.

9.2 FED-A CONSTRUCTION SCHEDULE PROJECTION

The preliminary FED-A construction schedule projection described in this section is based on the schedule projection developed for the FED Baseline (documented in Ref. 1). The following subsections describe the methodology and ground rules employed in developing the baseline schedule, the construction schedule phases that make up the overall schedule, and the FED-A schedule preparation and characteristics.

9.2.1 Schedule Methodology and Ground Rules

The FED Baseline schedule was developed by first estimating the design, procurement, fabrication, and installation time spans for each major machine component and then developing an overall construction schedule that was compatible with the subsystem schedules, the required machine assembly sequence, and the construction schedule for the facilities necessary to house the machine.

The schedule developed for the FED Baseline was predicated on the following ground rules for the start of the project:

- The beginning of preliminary design (i.e., the start of Title I) serves as the starting point for the schedule.

Table 9-1. Comparison of cost estimates for FED-A and FED Baseline (in millions of 1981 dollars)

			FED-A	FED Baseline
1.	Magnet system		151.5	312.2
	TF coil	97.2		
	PF coil	35.1		
	Intercoil structure	4.0		
	Bucking cylinder	3.7		
	Cryostat	11.5		
2.	Torus		120.4	161.9
	Shell	17.7		
	Armor	0.7		
	Shield	86.8		
	Pumped limiter module	8.1		
	Torus support	7.1		
3.	Cooling systems		18.8	38.5
	Refrigeration	7.5		
	Heat transport loops	5.8		
	Cooling tower	5.5		
4.	Tritium and fuel handling		48.2	54.0
	Primary fuel cycle	6.4		
	Secondary systems	16.0		
	Tritium system data acquisition	9.1		
	Tritium cleanup (room)	12.7		
	Fuel injector	4.0		
5.	Plasma heating		97.3	89.0
	Bulk heating			
	LHRH	83.3		
	Shielding	2.1		
	Preheating (ECRH)	11.9		
6.	Electrical systems		29.0	99.1
	PF electrical	15.1		
	TF electrical	4.7		
	ac power	9.2		
7.	Vacuum pumping system		8.3	24.0
	Vacuum duct	4.1		
	Vacuum pumps	4.2		
8.	Instrumentation and control		67.0	67.0
	Diagnostics	42.0		
	Information and control systems	25.0		

Table 9-1 (continued)

		FED-A	FED Baseline
9. Maintenance equipment		60.4	60.4
Reactor cell	33.3		
Hot cell	27.1		
10. Facilities		128.2	138.6
Reactor cell	31.6		
Hot cell	35.0		
Cooling system structures	1.1		
Cryogenic refrigeration building	1.0		
Radiation waste building	4.3		
Administration building	4.3		
Mockup and shop building	13.5		
Power supply and energy storage building	2.9		
Diesel generator building	0.4		
Tritium processing building	8.1		
Ventilation building and stack	13.7		
Site improvements	12.3		
Total direct cost		729.1	1044.7
11. Indirect costs			
Engineering and management (45%)		328.1	
Installation (15%)		109.4	
Total (direct + indirect)		1166.6	
Contingency (30%)		350.0	
Total cost		1516.6	

- A satisfactory conceptual design has been completed and approved.
- Major contractors (e.g., project management, construction, management, organizations responsible for major component design, architect/engineering firms, etc.) have been selected and are ready to begin work.
- The construction site has been selected, and the environmental impact statement has been completed and approved.

These ground rules are generic in nature and are considered to be applicable to FED-A, as well as to the FED Baseline or other tokamak devices.

9.2.2 FED-A Construction Schedule Phases

The overall construction schedule, as developed for the FED Baseline, is divided into five phases. In Phase I, a preliminary design is carried out and appropriate preliminary design reviews are conducted. The site is prepared, the safety review is completed, and construction approval is received. Component design and procurement activities for long-lead-time items are also initiated during this phase. The Phase I effort was estimated to require 24 months for the FED Baseline. This time span is also considered to be a reasonable but slightly conservative projection for FED-A, since the overall configuration, site size, and safety considerations are similar to the FED Baseline. Future detailed definition of the FED-A Phase I schedule may result in a reduction in time span, due to simplifications in the PF coil system and the TF coil case and support structure design.

Phase II starts with commencement of actual construction activities on the tokamak building. During this phase, the tokamak reactor building construction is taken to the point where device component installation can begin. In the FED Baseline schedule, Phase II was estimated to take 21 months. As in the case of Phase I, this duration is considered to be a reasonable but somewhat conservative projection for FED-A, pending a more detailed definition of reactor building size and form factor requirements. Reactor building construction time may drop because

FED-A is smaller than the baseline (diameter/height of 17 m/14 m for FED-A vs 23 m/18.5 m for the baseline device).

Phases III and IV cover the installation of major subsystems. In the baseline, Phase III encompassed installation of magnetic system components, including the bucking cylinder; TF, EF, and OH coils; TF coil support structure; and the cryostat. This phase culminated in a checkout of the magnetic system and required 22 months. Phase IV covered installation of all other major components and associated piping, electrical and mechanical equipment, cabling, and instrumentation. This phase required 16 months; its completion constrained the start of preoperational testing.

Direct comparison of FED-A and FED Baseline designs with respect to Phases III and IV of the construction schedule was found to be impractical, since the two devices are different in design approach and use different assembly sequences and schedule logic. The FED-A schedule does not have a clear demarcation between Phases III and IV. Consequently, for FED-A, these phases have been combined into a single phase, component installation.

The final phase of the construction schedule is the preoperational testing of the completed device. All construction and installation necessary for initial device operation must be complete prior to this phase. Nine months were allowed for this phase (which now would become Phase IV for FED-A) in the FED Baseline. Pending future detailed schedule studies, this duration is considered appropriate for FED-A. Section 9.2.3 describes the steps used in developing the FED-A construction schedule and the order of component installation.

9.2.3 FED-A Schedule: Preparation and Characteristics

The five basic steps employed in developing the FED-A schedule were as follows:

- Use Phases I and II directly from the FED Baseline schedule. These phases cover the period from the start of preliminary design to the start of machine component assembly in the reactor building.

- Establish the order of assembly into the machine of each major component.
- Determine when each major component will be available for assembly into the machine.
- Lay out a schedule for equipment installation that uses the specified assembly sequence and accommodates the availability of the major machine components for installation.
- Add to the schedule event "equipment installation complete" a 9-month period to accommodate preoperational checkout of the machine.

As noted above, the first two phases (comprising a total of 45 months) and the final phase (9 months of preoperational testing) have been taken from the FED Baseline and applied directly to the FED-A schedule. The area of major difference from the baseline is that of component installation, where differences in design necessitate a different assembly sequence for FED-A.

The revised assembly sequence was established by a review of the FED-A drawings and consultation with the engineers. Installation time spans for similar components were taken from the baseline schedule. Where possible, parallel installation or overlaps in installation were employed to reduce schedule time. The resulting installation sequence of major components is listed below and shown in Fig. 9-1, which depicts the overall FED-A schedule. Figure 9-2 shows the major components and their location in the machine. The installation sequence is:

1. platform and pedestal,
2. bucking cylinder,
3. TF coils and intercoil support structure,
4. cryostat outboard walls,
5. OH solenoid [in parallel with (4)],
6. cryostat ring segments and window modules,
7. inboard and lower shield elements,
8. continuous first wall,
9. outboard shield elements,
10. upper and lower PF coils,

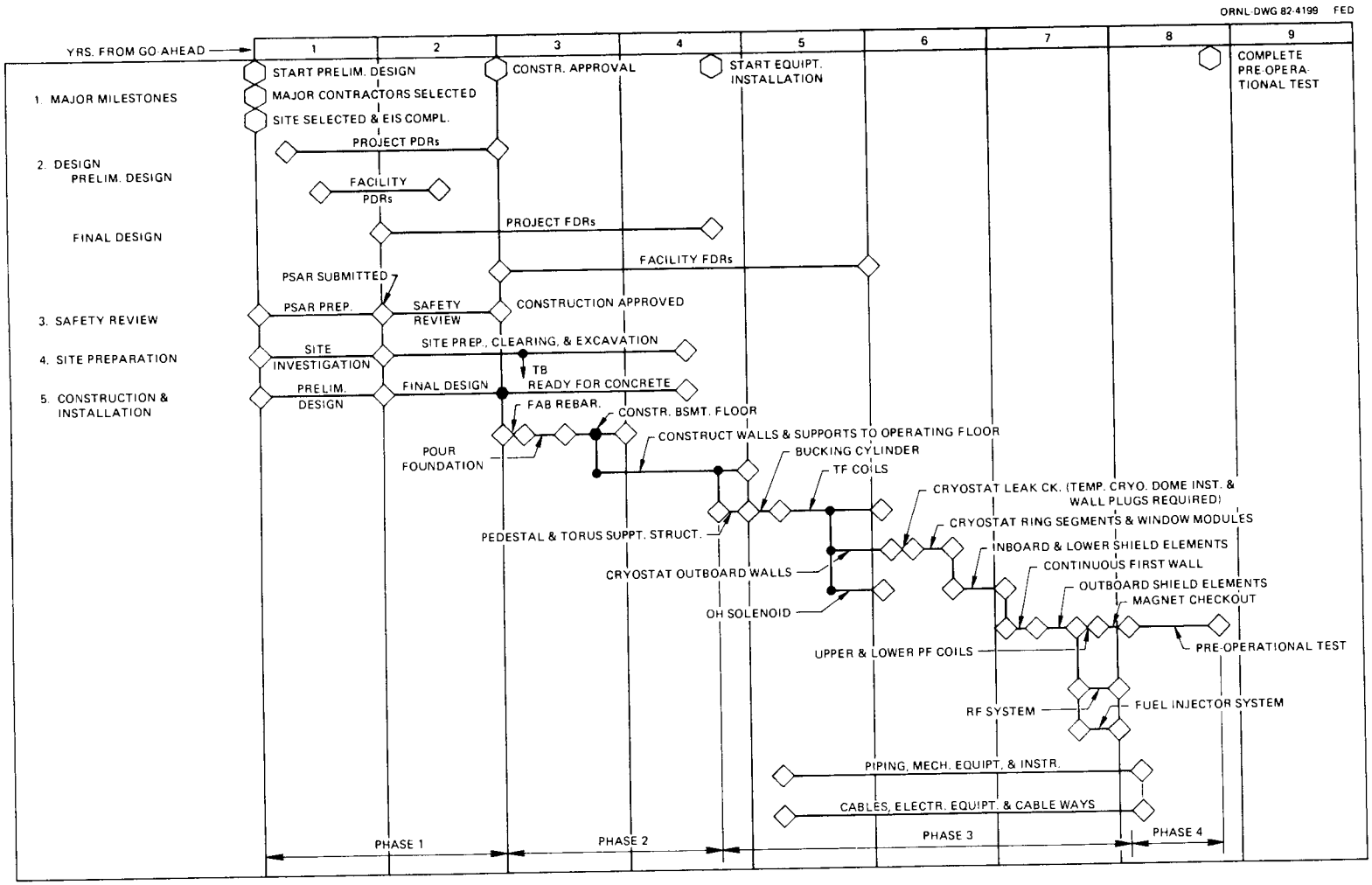

Fig. 9-1. FED-A construction schedule.

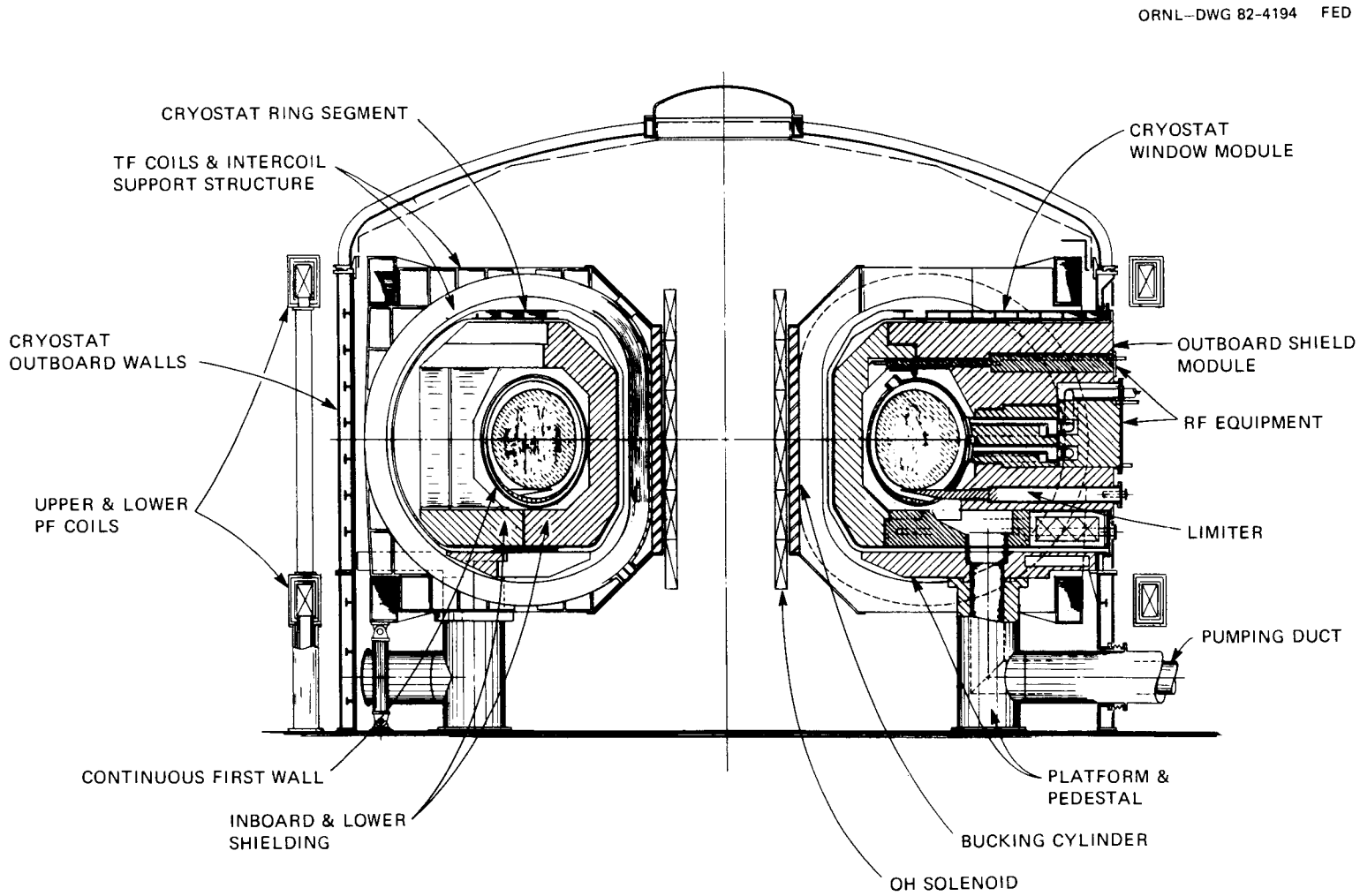

Fig. 9-2. FED-A major components.

11. rf equipment [in parallel with (6)],
12. fuel injection equipment [in parallel with (6) and (11)],
13. piping, mechanical equipment, and instrumentation, and
14. cables, electrical equipment, and cable ways.

As in the case of the baseline, four additional months (after installation of the superconducting PF coils) are allowed for completion of items 12 and 13 above. These activities are initiated at the time of first component installation and are continued in parallel throughout the installation period. Also required, but not shown in the schedule, is the installation of peripheral equipment (pumps, valves, etc.). Based on experience with the FED Baseline, it is not anticipated that these items will be schedule drivers.

9.2.4 Availability of Each Major Component

The availability of each major component for its required installation time was determined in a two-step process. Step 1 entailed determination of the time required to design, negotiate procurement, and complete fabrication of each major component. This was done by comparing the FED-A components to similar FED Baseline components and determining, with the aid of cognizant FEDC engineers, whether the design and manufacturing time span for a given component should be longer, shorter, or the same as that of its FED Baseline counterpart. The output of this step is the identification of the time at which each major component is available for installation in the machine. Step 2 calls for comparison of the date at which each component is available vs the date at which availability is required. Results indicate that three items, the inboard and lower shield elements, the bucking cylinder, and the TF coils, exhibit zero slack with respect to required installation dates. The OH coil shows one month of slack, and the remaining items appear to satisfy required installation dates. It is anticipated that corrective actions can be applied to improve zero slack conditions when the schedule is subjected to detailed definition.

The total time span from go-ahead to completion of preoperational testing for FED-A is projected to be 94 months. It should be noted that the schedule as shown allows no time for contingencies, redirections, or major design changes. On the other hand, it is believed that the installation time spans used for FED-A may be conservative in some areas, due to such factors as simpler PF coil installation requirements, smaller TF coils with simpler intercoil structure, and deletion of the spool structure used in the baseline configuration. On balance, it is believed that the schedule depicted in Fig. 9-1 represents a reasonable initial projection for the FED-A machine.

REFERENCE

1. C. A. Flanagan, D. Steiner, and G. E. Smith, eds., *Fusion Engineering Device Design Description*, vol. 1, ORNL/TM-7948, Union Carbide Corp. Nuclear Div., Oak Ridge Natl. Lab., December 1981.

ORNL/FEDC-83/1
Dist. Category UC-20 c,d

INTERNAL DISTRIBUTION

1. S. E. Attenberger
2. F. W. Baity
3. R. J. Barrett
4. T. G. Brown
5. B. A. Carreras
6. R. E. Clausing
7. B. A. Cramer
8. O. C. Eldridge
9. J. C. Glowienka
10. G. E. Gorker
11. J. T. Hogan
12. J. A. Holmes
13. R. J. Hooper
14. W. A. Houlberg
15. B. L. Hunter
16. H. Iida
17. P. W. King
18. V. D. Lee
19. C. M. Loring
20. D. H. Metzler
21. J. R. Mihalczo
22. J. G. Murray
23. W. D. Nelson
24. R. L. Reid
25. W. T. Reierson
26. J. A. Rome
27. K. E. Rothe
28. P. H. Sager
29. J. Sheffield
30. M. J. Saltmarsh
31. T. E. Shannon
32. P. T. Spampinato
33. V. C. Srivastava
34. N. A. Uckan
35. T. Uckan
36. K. F. Wu
37. S. K. Borowski
38. J. R. Haines
39. D. L. Hillis
40. L. M. Hively
41. S. S. Kalsi
42. J. F. Lyon
43. J. A. O'Toole
44. D. J. Strickler
45. F. W. Wiffen
46. J. Wilgen
47-51. Y-K. M. Peng
52-53. Laboratory Records Department
54. Laboratory Records, ORNL-RC
55. Document Reference Section
56. Central Research Library
57. Fusion Energy Division Library
58. Fusion Energy Division Reports Office
59. ORNL Patent Office

EXTERNAL DISTRIBUTION

60. M. A. Abdou, Associate Director, FPP/207, Argonne National Laboratory, 9700 South Cass Avenue, Argonne, IL 60439
61. N. A. Amherd, Fusion Power Program, Advanced Systems Department, Electric Power Research Institute, P.O. Box 10412, Palo Alto, CA 94304
62. J. L. Anderson, CMB-3, Mail Stop 348, Los Alamos National Laboratory, P.O. Box 1663, Los Alamos, NM 87545
63. M. Anderson, Tennessee Valley Authority, 1300 Commerce Bank Building, Chattanooga, TN 37401
64. O. A. Anderson, Lawrence Berkeley Laboratory, University of California, Berkeley, CA 94720
65. D. J. Anthony, Advanced Power Program, Advanced Energy Programs Department, Building 2, Room 551, General Electric Company, Schenectady, NY 12345

66. C. C. Baker, FPP/208, Argonne National Laboratory, 9700 South Cass Avenue, Argonne, IL 60439
67. T. H. Batzer, L-536, Lawrence Livermore National Laboratory, P.O. Box 808, Livermore, CA 94550
68. J. E. Baublitz, Office of Fusion Energy, Department of Energy, Washington, DC 20545
69. W. Bauer, Physical Research Division, Sandia National Laboratories-Livermore, Livermore, CA 94550
70. J. F. Baur, GA Technologies, Inc., P.O. Box 81608, San Diego, CA 92138
71. D. S. Beard, Office of Fusion Energy, Office of Energy Research, Mail Stop G-256, U.S. Department of Energy, Washington, DC 20545
72. R. J. Beeley, ETEC, Rockwell International, P.O. Box 1449, Canoga Park, CA 91304
73. D. C. Berkey, Vice President & General Manager, Energy System and Technology Division, General Electric Company, P.O. Box 7600, Stamford, CT 06904
74. K. L. Black, Department E452, McDonnell Douglas Astronautics Company, P.O. Box 516, St. Louis, MO 63166
75. R. Botwin, C47-05, Grumman Aerospace Corporation, P.O. Box 31, Bethpage, NY 11714
76. W. B. Briggs, McDonnell Douglas Astronautics Company, P.O. Box 516, St. Louis, MO 63166
77. G. Bronner, Princeton Plasma Physics Laboratory, P.O. Box 451, Princeton, NJ 08544
78. J. N. Brooks, FPP/207, Argonne National Laboratory, 9700 South Cass Avenue, Argonne, IL 60439
79. S. C. Burnett, GA Technologies, Inc., P.O. Box 81608, San Diego, CA 92138
80. J. D. Callen, Department of Nuclear Engineering, University of Wisconsin, Madison, WI 53706
81. V. S. Chan, GA Technologies, Inc., P.O. Box 81608, San Diego, CA 92138
82. R. G. Clemmer, Fusion Power Program, Argonne National Laboratory, 9700 South Cass Avenue, Argonne, IL 60439
83. D. R. Cohn, MIT Plasma Fusion Center, 167 Albany Street, Cambridge, MA 02139
84. W. S. Cooper, Lawrence Berkeley Laboratory, University of California, Berkeley, CA 94720
85. J. W. Coursen, C36-05, Grumman Aerospace Corporation, P.O. Box 31, Bethpage, NY 11714
86. R. W. Conn, School of Chemical, Nuclear, and Thermal Engineering, Boelter Hall, University of California, Los Angeles, CA 90024
87. J. G. Crocker, EG&G Idaho, P.O. Box 1625, Idaho Falls, ID 83401
88. A. E. Dabiri, Energy Systems and Conservation Division, Science Applications, Inc., P.O. Box 2351, La Jolla, CA 92038
89. C. C. Damm, L-441, Lawrence Livermore National Laboratory, P.O. Box 808, Livermore, CA 94550
90. R. C. Davidson, Massachusetts Institute of Technology, 77 Massachusetts Avenue, Cambridge, MA 02139
91. N. A. Davies, Office of Fusion Energy, Office of Energy Research, Mail Station G-256, U.S. Department of Energy, Washington, DC 20545

92. J. W. Davis, E457, Building 81/1/B7, McDonnell Douglas Astronautics Company, P.O. Box 516, St. Louis, MO 63166
93. M. J. Davis, Sandia National Laboratories, P.O. Box 5800, Albuquerque, Albuquerque, NM 87185
94. S. O. Dean, Director, Fusion Energy Development, Science Applications, Inc., 2 Professional Drive, Suite 249, Gaithersburg, MD 20760
95. J. F. Decker, Office of Fusion Energy, Department of Energy, Mail Stop G-256, Washington, DC 20545
96. D. DeFreece, E451, Building 81/1/B7, McDonnell Douglas Astronautics Company, P.O. Box 516, St. Louis, MO 63166
97. A. Deitz, Princeton Plasma Physics Laboratory, P.O. Box 451, Princeton, NJ 08544
98. D. A. Dingee, Program Manager, Fusion Technology, Pacific Northwest Laboratories, Battelle Boulevard, Richland, WA 99352
99. J. N. Doggett, L-441, Lawrence Livermore National Laboratory, P.O. Box 808, Livermore, CA 94550
100. H. Dreicer, Division Leader, CRT, Los Alamos National Laboratory, P.O. Box 1663, Los Alamos, NM 87545
101. D. Ehst, Argonne National Laboratory, 9700 South Cass Avenue, Argonne, IL 60439
102. G. A. Eliseev, I. V. Kurchatov Institute of Atomic Energy, P.O. Box 3402, 123182 Moscow, U.S.S.R.
103. W. R. Ellis, Office of Fusion Energy, Department of Energy, Mail Stop G-256, Washington, DC 20545
104. B. A. Engholm, GA Technologies, Inc., P.O. Box 81608, San Diego, CA 92138
105. H. P. Eubank, Princeton Plasma Physics Laboratory, P.O. Box 451, Princeton, NJ 08544
106. F. Farfaletti-Casali, Engineering Division, Joint Research Center, Ispra Establishment, 21020 Ispra (Varese), Italy
107. J. J. Ferrante, Manager, Building 36-241, Large Superconducting Program, General Electric Company, 1 River Road, Schenectady, NY 12345
108. J. File, Princeton Plasma Physics Laboratory, P.O. Box 451, Princeton, NJ 08544
109. P. A. Finn, Fusion Power Program, Argonne National Laboratory, 9700 South Cass Avenue, Argonne, IL 60439
110. H. K. Forsen, Bechtel Group, Inc., Research & Engineering, P.O. Box 3965, San Francisco, CA 94119
111. J. S. Foster, Jr., Building R4-2004, TRW Defense and Space Systems, 1 Space Park, Redondo Beach, CA 90278
112. T. K. Fowler, Associate Director for MFE, L-436, Lawrence Livermore National Laboratory, P.O. Box 808, Livermore, CA 94550
113. J. W. French, EBASCO Services, Inc., Forrestal Campus, CN-59, Princeton University, Princeton, NJ 08544
114. H. P. Furth, Director, Princeton Plasma Physics Laboratory, P.O. Box 451, Princeton, NJ 08544
115. J. G. Gavin, Jr., President, A01-11, Grumman Aerospace Corporation, P.O. Box 31, Bethpage, NY 11714
116. G. Gibson, Westinghouse Electric Corporation, Fusion Power Systems Department, P.O. Box 10864, Pittsburgh, PA 15236

117. J. R. Gilleland, Manager, Fusion Project, GA Technologies, Inc., P.O. Box 81608, San Diego, CA 92138
118. V. A. Glukhikh, Scientific-Research Institute of Electro-Physical Apparatus, 188631 Leningrad, U.S.S.R.
119. M. Y. Gohar, Argonne National Laboratory, 9700 South Cass Avenue, Argonne, IL 60439
120. W. D. Goins, Tennessee Valley Authority, 1300 Commerce Union Bank Building, Chattanooga, TN 37401
121. D. A. Goldberg, Lawrence Berkeley Laboratory, University of California, Berkeley, CA 94720
122. R. Goldston, Princeton Plasma Physics Laboratory, P.O. Box 451, Princeton, NJ 08544
123. M. B. Gottlieb, Princeton Plasma Physics Laboratory, P.O. Box 451, Princeton, NJ 08544
124. R. W. Gould, Department of Applied Physics, California Institute of Technology, Pasadena, CA 91109
125. M. W. Griffin, Department E236, McDonnell Douglas Astronautics Company, P.O. Box 516, St. Louis, MO 63166
126. C. R. Head, Office of Fusion Energy, Department of Energy, Mail Stop G-256, Washington, DC 20545
127. C. D. Henning, Lawrence Livermore National Laboratory, P.O. Box 808, Livermore, CA 94550
128. G. K. Hess, Office of Fusion Energy, Department of Energy, Mail Stop ER-701, Washington, DC 20545
129. T. Hiraoka, JT-60 Project Office I, Japan Atomic Energy Research Institute, Tokai Research Establishment, Tokai, Ibaraki, Japan
130. R. L. Hirsch, Manager, Synthetic Fuels Research, Exxon Research and Engineering Company, P.O. Box 4255, Baytown, TX 77520
131. J. J. Holmes, Westinghouse-Hanford Engineering Development Laboratory, P.O. Box 1970, Richland, WA 99352
132. W. G. Homeyer, GA Technologies, Inc., P.O. Box 81608, San Diego, CA 92138
133. J. C. Hosea, Princeton Plasma Physics Laboratory, P.O. Box 451, Princeton, NJ 08544
134. D. Hwang, Princeton Plasma Physics Laboratory, P.O. Box 451, Princeton, NJ 08544
135. G. J. Inukai, Department E231, McDonnell Douglas Astronautics Company, P.O. Box 516, St. Louis, MO 63166
136. D. L. Jassby, Princeton Plasma Physics Laboratory, P.O. Box 451, Princeton, NJ 08544
137. J. B. Joyce, Princeton Plasma Physics Laboratory, P.O. Box 451, Princeton, NJ 08544
138. R. A. Krakowski, CTR-12, Mail Stop 641, Los Alamos National Laboratory, P.O. Box 1663, Los Alamos, NM 87545
139. G. L. Kulcinski, University of Wisconsin, Department of Nuclear Engineering, Engineering Research Building, Room 439, 1500 Johnson Drive, Madison, WI 53706
140. D. L. Kummer, McDonnell Douglas Astronautics Company, P.O. Box 516, St. Louis, MO 63166
141. T. S. Latham, Mail Stop 44, United Technologies Research Center, Silver Lane, East Hartford, CT 06108
142. L. R. Ledman, Office of Fusion Energy, Department of Energy, Mail Stop G-256, Washington, DC 20545

143. L. M. Lidsky, MIT Plasma Fusion Center, 167 Albany Street, Cambridge, MA 02139
144. E. F. Lowell, General Manager, Energy Systems Programs Department, Building 2-455, General Electric Company, 1 River Road, Schenectady, NY 12345
145. C. S. Liu, GA Technologies, Inc., P.O. Box 81608, San Diego, CA 92138
146. D. J. McFarlin, Mail Stop 44, United Technologies Research Center, Silver Lane, East Hartford, CT 06108
147. R. McGrath, Fusion Power Program, Argonne National Laboratory, 9700 South Cass Avenue, Argonne, IL 60439
148. V. A. Maroni, CEN/205, Argonne National Laboratory, 9700 South Cass Avenue, Argonne, IL 60439
149. W. Marton, Office of Fusion Energy, Office of Energy Research, Mail Station G-256, U.S. Department of Energy, Washington, DC 20545
150. L. G. Masson, EG&G Idaho, Idaho National Engineering Laboratory, P.O. Box 1625, Idaho Falls, ID 83401
151. D. G. McAlees, Exxon Nuclear Company, Inc., 777 106th Avenue, NE, Bellevue, WA 98009
152. D. M. Meade, Princeton Plasma Physics Laboratory, P.O. Box 451, Princeton, NJ 08544
153. A. T. Mense, Building 107, Post B2, McDonnell Douglas Astronautics Company, P.O. Box 516, St. Louis, MO 63166
154. L. Michaels, Princeton Plasma Physics Laboratory, P.O. Box 451, Princeton, NJ 08544
155. D. Mikkelsen, Princeton Plasma Physics Laboratory, P.O. Box 451, Princeton, NJ 08544
156. R. L. Miller, GA Technologies, Inc., P.O. Box 81608, San Diego, CA 92138
157. R. G. Mills, Princeton Plasma Physics Laboratory, P.O. Box 451, Princeton, NJ 08544
158. J. T. D. Mitchell, Culham Laboratory, Abingdon, Oxon OX14 3DB, United Kingdom
159. R. W. Moir, Lawrence Livermore National Laboratory, P.O. Box 808, Livermore, CA 94550
160. D. B. Montgomery, MIT Plasma Fusion Center, 167 Albany Street, Cambridge, MA 02139
161. K. Moses, R-1/1078, TRW Defense and Space Systems, 1 Space Park, Redondo Beach, CA 90278
162. R. E. Muller, Aerojet Manufacturing Company, P.O. Box 4210, Fullerton, CA 92934
163. A. E. Munier, Grumman Aerospace Company, P.O. Box 31, Bethpage, NY 11714
164. M. R. Murphy, Office of Fusion Energy, Department of Energy, Washington, DC 20545
165. R. E. Nygren, FPP/207, Argonne National Laboratory, 9700 South Cass Avenue, Argonne, IL 60439
166. T. Ohkawa, GA Technologies, Inc., P.O. Box 81608, San Diego, CA 92138
167. M. Okabayashi, Princeton Plasma Physics Laboratory, P.O. Box 451, Princeton, NJ 08544
168. D. Overskei, GA Technologies, Inc., P.O. Box 81608, San Diego, CA 92138

169. R. R. Parker, Francis Bitter National Magnet Laboratory, 170 Albany Street, Cambridge, MA 02139
170. B. Pease, Culham Laboratory, Abingdon, Oxon OX14 3DB, United Kingdom
171. M. Pelovitz, Princeton Plasma Physics Laboratory, P.O. Box 451, Princeton, NJ 08544
172. F. W. Perkins, Princeton Plasma Physics Laboratory, P.O. Box 451, Princeton, NJ 08544
173. M. Petravic, Princeton Plasma Physics Laboratory, P.O. Box 451, Princeton, NJ 08544
174. M. Porkolab, Massachusetts Institute of Technology, 77 Massachusetts Avenue, Cambridge, MA 02139
175. D. E. Post, Princeton Plasma Physics Laboratory, P.O. Box 451, Princeton, NJ 08544
176. L. K. Price, Department of Energy, Oak Ridge Operations, P.O. Box E, Oak Ridge, TN 37830
177. R. E. Price, Office of Fusion Energy, Office of Energy Research, Mail Station G-256, Washington, DC 20545
178. D. H. Priester, Office of Fusion Energy, Department of Energy, Washington, DC 20545
179. F. A. Puhn, GA Technologies, Inc., P.O. Box 81608, San Diego, CA 92138
180. J. Purcell, GA Technologies, Inc., P.O. Box 81608, San Diego, CA 92138
181. R. V. Pyle, University of California, Lawrence Berkeley Laboratory, Berkeley, CA 94720
182. J. M. Rawls, GA Technologies, Inc., P.O. Box 81608, San Diego, CA 92138
183. P. J. Reardon, Princeton Plasma Physics Laboratory, P.O. Box 451, Princeton, NJ 08544
184. M. Roberts, Office of Fusion Energy, Department of Energy, Mail Stop G-256, Washington, DC 20545
185. J. D. Rogers, Los Alamos National Laboratory, P.O. Box 1663, Los Alamos, NM 87545
186. F. L. Robinson, Tennessee Valley Authority, 1300 Commerce Bank Building, Chattanooga, TN 37401
187. M. L. Rogers, Monsanto Research Corporation, Mound Laboratory Facility, P.O. Box 32, Miamisburg, OH 45342
188. M. N. Rosenbluth, RLM 11.218, Institute for Fusion Studies, University of Texas, Austin, TX 78712
189. L. Ruby, Lawrence Berkeley Laboratory, University of California, Berkeley, CA 94720
190. P. H. Rutherford, Princeton Plasma Physics Laboratory, P.O. Box 451, Princeton, NJ 08544
191. D. D. Ryutov, Institute of Nuclear Physics, Siberian Branch of the Academy of Sciences of the U.S.S.R., Sovetskaya St. 5, 630090 Novosibirsk, U.S.S.R.
192. M. M. Sabado, EBASCO Services, Inc., A Site, Building 1-A, Forrestal Campus, Princeton, NJ 08544
193. J. A. Schmidt, Princeton Plasma Physics Laboratory, P.O. Box 451, Princeton, NJ 08544
194. J. Schultz, MIT Plasma Fusion Center, 167 Albany Street, Cambridge, MA 02139

195. F. R. Scott, Electric Power Research Institute, P.O. Box 10412, Palo Alto, CA 94304
196. G. Sheffield, Princeton Plasma Physics Laboratory, P.O. Box 451, Princeton, NJ 08544
197. C. E. Singer, Princeton Plasma Physics Laboratory, P.O. Box 451, Princeton, NJ 08544
198. T. J. M. Sluyters, Accelerator Department, Brookhaven National Laboratory, Upton, NY 11973
199. D. Smith, Materials Science Division, Argonne National Laboratory, 9700 South Cass Avenue, Argonne, IL 60439
200. G. E. Smith, Grumman Aerospace Corporation, P.O. Box 31, Bethpage, NY 11714
201. R. I. Smith, Board Chairman, Public Service Electric and Gas Company, 80 Park Place, Newark, NJ 07101
202. L. Soroka, Lawrence Berkeley Laboratory, University of California, Berkeley, CA 94720
203. L. Southworth, GA Technologies, Inc., P.O. Box 81608, San Diego, CA 92138
204. I. Spighel, Lebedev Physical Institute, Leninsky Prospect 53, 117924 Moscow, U.S.S.R.
205. W. M. Stacey, Jr., Georgia Institute of Technology, School of Nuclear Engineering, Atlanta, GA 30332
206. E. Stern, Grumman Aerospace Corporation, CN-59, Forrestal Campus, Princeton, NJ 08540
207. L. D. Stewart, Princeton Plasma Physics Laboratory, P.O. Box 451, Princeton, NJ 08544
208. W. Stodiek, Princeton Plasma Physics Laboratory, P.O. Box 451, Princeton, NJ 08544
209. P. M. Stone, Office of Fusion Energy, Office of Energy Research, Mail Station G-256, Washington, DC 20545
210. I. N. Sviatoslavsky, Room 33, Engineering Research Building, 1500 Johnson Drive, University of Wisconsin, Madison, WI 53706
211. T. Tamano, GA Technologies, Inc., P.O. Box 81608, San Diego, CA 92138
212. R. E. Tatro, Manager, Energy Systems, M.Z. 16-1070, General Dynamics-Convair Division, P.O. Box 80847, San Diego, CA 92138
213. F. Tenney, Princeton Plasma Physics Laboratory, P.O. Box 451, Princeton, NJ 08544
214. F. Thomas, B-20-5, Grumman Aerospace Corporation, Bethpage, NY 11714
215. K. I. Thomassen, Lawrence Livermore National Laboratory, P.O. Box 808, Livermore, CA 94550
216. R. J. Thome, Francis Bitter National Magnet Laboratory, 170 Albany Street, Cambridge, MA 02139
217. S. L. Thomson, Bechtel Group, Inc., P.O. Box 3965, San Francisco, CA 94119
218. V. T. Tolok, Kharkov Physical-Technical Institute, Academical St. 1, 310108 Kharkov, U.S.S.R.
219. C. Trachsel, McDonnell Douglas Astronautics Company, P.O. Box 516, St. Louis, MO 63166
220. J. R. Treglio, General Dynamics-Convair Division, P.O. Box 80847, San Diego, CA 92138

221. A. W. Trivelpiece, Office of Energy Research, Department of Energy, Washington, DC 20545
222. L. R. Turner, Fusion Power Program, Argonne National Laboratory, 9700 South Cass Avenue, Argonne, IL 60439
223. M. A. Ulrickson, Princeton Plasma Physics Laboratory, P.O. Box 451, Princeton, NJ 08544
224. E. H. Valeo, Princeton Plasma Physics Laboratory, P.O. Box 451, Princeton, NJ 08544
225. T. C. Varljen, Westinghouse Electric Corporation, P.O. Box 10864, Pittsburgh, PA 15236
226. R. Varma, Physical Research Laboratory, Navangpura, Ahmedabad, India
227. H. F. Vogel, Los Alamos National Laboratory, P.O. Box 1663, Los Alamos, NM 87545
228. A. Wait, Building 36-421, General Electric Company, 1 River Road, Schenectady, NY 12345
229. K. E. Wakefield, Princeton Plasma Physics Laboratory, P.O. Box 451, Princeton, NJ 08544
230. D. Weldon, Los Alamos National Laboratory, P.O. Box 1663, Los Alamos, NM 87545
231. J. C. Wesley, GA Technologies, Inc., P.O. Box 81608, San Diego, CA 92138
232. S. Whitley, Tennessee Valley Authority, 1300 Commerce Bank Building, Chattanooga, TN 37401
233. W. R. Wilkes, Monsanto Research Corporation, Mound Laboratory Facility, P.O. Box 32, Miamisburg, OH 45342
234. J. E. Wilkins, EG&G Idaho, Idaho National Engineering Laboratory, P.O. Box 1625, Idaho Falls, ID 83401
235. H. Willenberg, Mathematical Sciences Northwest, Inc., P.O. Box 1887, Bellevue, WA 98009
236. J. E. C. Williams, Francis Bitter National Magnet Laboratory, 170 Albany Street, Cambridge, MA 02139
237. P. Willis, Building 23, Room 298, General Electric Company, 1 River Road, Schenectady, NY 12345
238. T. F. Yang, MIT Plasma Fusion Center, 167 Albany Street, Cambridge, MA 02139
239. H. H. Yoshikawa, W/A-62, Hanford Engineering Development Laboratory, P.O. Box 1970, Richland, WA 99352
240. K. M. Young, Princeton Plasma Physics Laboratory, P.O. Box 451, Princeton, NJ 08544
241. N. E. Young, EBASCO Services, Inc., Princeton Plasma Physics Laboratory, P.O. Box 451, Princeton, NJ 08544
242. K. M. Zwilsky, National Materials Advisory Board, National Academy of Sciences, 2101 Constitution Avenue NW, Washington, DC 20418
243. Bibliothek, Max-Planck Institut fur Plasmaphysik, D-8046 Garching bei Munchen, Federal Republic of Germany
244. Bibliothek, Institut fur Plasmaphysik, KFA, Postfach 1913, D-5170 Julich, Federal Republic of Germany
245. Bibliotheque, Centre de Recherches en Physique des Plasmas, 21 Avenue des Bains, 1007 Lausanne, Switzerland
246. Bibliotheque, Service du Confinement des Plasmas, CEA, B.P. No. 6, 92 Fontenay-aux-Roses (Seine), France

247. Documentation S.I.G.N., Department de la Physique du Plasma et de la Fusion Controlee, Association EURATOM-CEA, Centre d'Etudes Nucleaires, B.P. 85, Centre du Tri, 38041 Grenoble, Cedex, France
248. Library, Centre de Recherches en Physique des Plasmas, 21 Avenue des Bains, 1007 Lausanne, Switzerland
249. Library, Culham Laboratory, UKAEA, Abingdon, Oxon, OX14 3DB, England
250. Library, FOM Instituut voor Plasma-Fysica, Rijnhuizen, Jutphaas, Netherlands
251. Library, Institute of Physics, Academia Sinica, Beijing, Peoples Republic of China
252. Library, Institute for Plasma Physics, Nagoya University, Nagoya 464, Japan
253. Library, International Centre for Theoretical Physics, Trieste, Italy
254. Library, JET Joint Undertaking, Abingdon, Oxfordshire, OX14, DB, England
255. Library, Laboratoria Gas Ionizzati, Frascati, Italy
256. Plasma Research Laboratory, Australian National University, P.O. Box 4, Canberra, ACT 2000, Australia
257. Thermonuclear Library, Japan Atomic Energy Research Institute, Tokai, Naka, Ibaraki, Japan
258. Library, Plasma Physics Laboratory, Kyoto University, Gokasho Uji, Kyoto, Japan
259. Office of the Assistant Manager for Energy Research and Development, Department of Energy, Oak Ridge Operations, Oak Ridge, TN 37830

260-463. Given distribution as shown in TID-4500, Magnetic Fusion Energy, (Distribution Category UC-20 c,d: Reactor Materials and Fusion Systems)

☆U.S. GOVERNMENT PRINTING OFFICE 1983 646 055 75